UCLouvain

in cotutelle with Alma Mater Studiorum - Università di Bologna

From Dark Matter to Dark Sectors: Exploring Signatures at Multiple Scales

Doctoral dissertation presented by

Daniele Massaro

in fulfilment of the requirements for the degree of Doctor in Sciences.

Thesis Jury

Prof. Philippe Ruelle	President	Université Catholique de Louvain
Prof. Fabio Maltoni	Supervisor	Université Catholique de Louvain
Prof. Silvia Pascoli	Supervisor	Università di Bologna
Prof. Marco Drewes		Université Catholique de Louvain
Prof. Ilaria Brivio		Università di Bologna
Prof. Filippo Sala		Università di Bologna
Prof. Michel Tytgat		Université Libre de Bruxelles

May, 2024

Alla mia famiglia.

"You - you alone - will have the stars as no one else has them"
"What are you trying to say?"
"In one of the stars I shall be living. In one of them I shall be laughing. And so it will be as if all the stars were laughing, when you look at the sky at night. . . You - only you - will have stars that can laugh!"
And he laughed again.
"And when your sorrow is comforted (time soothes all sorrows) you will be content that you have known me. You will always be my friend. You will want to laugh with me. And you will sometimes open your window, so, for that pleasure. . . And your friends will be properly astonished to see you laughing as you look up at the sky! Then you will say to them, 'Yes, the stars always make me laugh!' And they will think you are crazy. It will be a very shabby trick that I shall have played on you. . . "
And he laughed again.
"It will be as if, in place of the stars, I had given you a great number of little bells that knew how to laugh. . . "

The Little Prince
Antoine de Saint-Exupéry

Acknowledgments

"Did you do it?"
"Yes."
"What did it cost?"
"Everything."

—Thanos and Gamora

Avengers: Infinity War
Anthony Russo, Joe Russo

Many people say PhD is tough, energy-draining and frustrating. Others describe it as wholesome, satisfying and rewarding. For me, it was all these things together, and I am really glad I did it. The PhD taught me how to endure through failures, not by avoiding them, but by building on top of them, and be successful at the end. Nothing works on the first attempt, and everything seems obscure. This is part of the game, nearly everyone experiences the same. You are not alone, indeed. PhD allows you to meet a lot of people you can share your journey with. I had the opportunity of meeting amazing people, both within and outside academia, with whom I shared some of the greatest experiences in my life, and who supported, cheered, motivated and celebrated with me in these four years. My journey would not have been the same without them.

First, I am deeply grateful to my supervisors, Prof. Fabio Maltoni and Prof. Silvia Pascoli, for their constant support, help and motivation throughout these four years. I will always be thankful for having taught me how to develop the "physics intuition", namely the ability to fully understand a problem, by asking a lot of questions on every little detail and to be curious even on the small things that are usually taken for free, be it the behavior of a certain curve in a plot, or an inconsistency in a simulation. I will never forget your ability in immediately spotting the most important issues of a certain topic, providing helpful and perfectly on point solutions to any problem I had during my research. Thank you also for having set up a cotutelle with the Université Catholique de Louvain, which allowed me to spend a lot of time at the *Centre for Cosmology, Particle Physics and Phenomenology* (CP3) in Louvain-la-Neuve, and I want to express my gratitude to all the CP3 staff for having hosted me in these years.

A special thank to Dr. Chiara Arina for her constant availability and patience in helping me with whatever I had a problem with, and for the precious comments on my thesis. It was very nice to share many projects with you in these years.

I want to thank Dr. Matheus Hostert for the steady support and kindness. Thank you for the patience and the time you dedicated in listening and solving my doubts. Your ability of explaining everything in simple terms is truly a feat.

A special thank goes to Dr. Mattia Di Mauro, who really represented a light in the dark in one of the toughest periods of my PhD. Working together, collaborating both on MadDM and on the paper, boosted my motivation, and I really needed it.

Then, I would like to thank Jaime Hoefken, the best office mate one could ask for, always ready to help and to share a laugh. It has been great to listen to your stories and to share many Italian meals together. And Dr. Asli Abdullahi, for her invaluable help, for the many discussions and the nice chats at the end of the meetings. I am also grateful to Dr. Mark Ross-Lonergan, for the many times you helped me understand the experimental side of physics.

A huge thank to Dr. Jan Heisig for your support, especially during the initial steps of my PhD, my first talks and my first paper. I am also thankful to Dr. Olivier Mattelaer, for the many discussions and for the help with MadGraph and MadDM debugging, your input has been invaluable.

A special thank to Prof. Georgia Karagiorgi, for having invited me to spend few months at the Columbia University in the City of New York, one of the most exciting experiences of my life. Your support and your enthusiasm have been a great source of inspiration, and I am very glad to have had the chance to work with you. During that experience, I also had the opportunity to meet Ibrahim and Daphne, who are two of the most amazing people I have ever met. I am very grateful for the time we spent together, for taking me on walks around New York, and for the many meals we shared. Thank you also for your patience in listening to me talking about Italian food, for the many laughs and the Formula 1 races we watched together. I am looking forward to meeting you again.

Un grazie enorme a Federico De Lillo, per la sua costante compagnia in questi quattro anni, per le lunghe chiacchierate di conforto, per le passeggiate intorno a Louvain-la-Neuve e le mangiate a O'Tacos.

Voglio ringraziare anche tutti gli amici con cui ho condiviso moltissime serate, birre e gare di Formula 1 a Louvain-la-Neuve, in particolare Tommaso, Jonathan e Simone. E naturalmente al gruppo di Bologna, in particolare Luca, Gian Marco e Riccardo, per i pranzi condivisi e le infinite chiacchierate su One Piece.

Vorrei inoltre ringraziare il gruppo d'improvvisazione teatrale di Scandiano, per avermi fatto scoprire un nuovo mondo di emozioni e spontaneità. Un grazie speciale a Daniele, Eleonora, Roberto, Aurora, Elisa e Luca, per avermi accompagnato in questo nuovo capitolo della mia vita e per l'influenza positiva che avete riversato su di me negli ultimi mesi.

Non posso che ringraziare il mio gruppo di amici di sempre: Jack, Ruo, Piffe, Jambo, Porro e Fabio, per avermi sempre supportato e incoraggiato, e per avermi fatto sentire a casa, anche quando ero dall'altra parte del mondo. Nonostante abbia passato la maggior parte del mio dottorato in viaggio, siete sempre stati presenti, e condividere momenti con voi mi ha aiutato a vivere questa esperienza in modo più sereno. Mi rendo davvero conto di quanto sia fortunato ad avere amici come voi. In particolare, un grazie speciale a Jack e Ruo, il vostro supporto negli ultimi mesi è stato fondamentale.

Vorrei ringraziare anche Federica. Il tuo supporto e la tua comprensione, durante il tempo passato insieme in questi anni, è stato essenziale per arrivare fino a qui. Hai saputo ascoltarmi e incoraggiarmi, motivandomi a dare il meglio.

Infine, un enorme grazie alla mia famiglia. Sono certo che starmi intorno abbia richiesto una dose di pazienza non indifferente. Un grazie a mio padre e mia madre, per le vostre parole di conforto e il vostro supporto incondizionato, che mi ha aiutato a superare i momenti più difficili. Un grazie ai miei fratelli, per le giornate passate insieme a giocare a Formula 1, Terraforming Mars, e per la profonda fiducia che mi avete sempre dimostrato. Queste poche righe non sono sufficienti a esprimere la mia gratitudine.

I also acknowledge support from the following grants:

- Innoviris ATTRACT 2018 104 BECAP 2 agreement;
- European Union's Horizon 2020 research and innovation programme under the Marie Skłodowska-Curie grant agreement No 777822 - GHAIA;
- European Union's Horizon Europe research and innovation programme under the Marie Skłodowska-Curie Staff Exchange grant agreement No 101086085 - ASYMMETRY.

Abstract

The quest to understand the nature of dark matter is one of the most compelling challenges in modern physics. This dissertation investigates various dark matter models, aiming to establish connections between theory and observations. Beginning with indirect detection searches, we focus on dark matter annihilation into monochromatic photon lines. We examine the potential of this signature by constraining a top-philic dark matter model and the inert doublet model, using Fermi-LAT and HESS experimental data. We explore the singlet scalar Higgs portal model on the resonance region, combining data from the galactic center, dwarf galaxies and antiprotons. The model accommodates these measurements along with the relic density, while being unchallenged by current direct detection and collider constraints. We also investigate the phenomenology of superheavy decaying dark matter, constraining its lifetime on the basis of gamma-rays and future neutrino observations. Furthermore, we introduce light dark sectors, focusing on Standard Model extensions featuring a vector portal, involving a new dark gauge symmetry with a kinetically mixed dark photon. In particular, we focus on light dark photons, proposing models containing multiple dark fermions, generalizing the idea of the inelastic dark matter. We probe these rich dark sector models by searching for semi-visible dark photon decays, where electron-positron pairs are produced alongside missing energy. This decay pattern allows recasting and relaxing the main constraints, opening new regions of the parameter space, that can account for the anomalous magnetic moment of the muon, and be tested in the future. Finally, we present a search for electron-positron pairs produced within dark sector models in the MicroBooNE experiment, where heavier dark fermions are produced by beam neutrinos upscattering, further decaying to electron-positron pairs. This search has the potential to probe the parameter space that could provide an explanation for the MiniBooNE low-energy excess.

Résumé

La recherche de la nature de la matière noire est l'un des défis les plus importants de la physique moderne. Cette thèse étudie différents modèles de matière noire, dans le but d'établir des liens entre la théorie et les observations. En commençant par des recherches de détection indirecte, nous nous concentrons sur l'annihilation de la matière noire en photons monochromatiques. Nous examinons le potentiel de cette signature en contraignant un modèle de matière noire top-phile et le modèle du doublet inerte, en utilisant les données expérimentales de Fermi-LAT et HESS. Nous explorons le modèle du singlet scalaire avec portail de Higgs dans la région de résonance, en combinant les données du centre galactique, des galaxies naines et des antiprotons. Le modèle tient compte de ces mesures ainsi que de la densité relique, tout en n'étant pas remis en cause par les contraintes actuelles de la détection directe et des collisionneurs. Nous étudions également la phénoménologie de la matière noire super-lourde qui se désintégre, en contraignant sa durée de vie sur la base des rayons gammas et des futures observations de neutrinos. En outre, nous introduisons les secteurs sombres légers, en nous concentrant sur les extensions du modèle standard comportant un portail vectoriel, impliquant une nouvelle symétrie de jauge sombre avec un photon sombre cinétiquement mélangé. En particulier, nous nous concentrons sur les photons sombres légers, en proposant des modèles contenant de multiples fermions sombres, généralisant l'idée de la matière noire inélastique. Nous sondons ces riches modèles du secteur sombre en recherchant des désintégrations de photons sombres semi-visibles, où des paires électron-positron sont produites en même temps que l'énergie manquante. Ce modèle de désintégration permet de remanier et d'assouplir les principales contraintes, en ouvrant de nouvelles régions de l'espace des paramètres, qui peuvent expliquer l'anomalie du moment magnétique du muon, et être testées à l'avenir. Enfin, nous présentons une recherche de paires électron-positron produites dans des modèles de secteur sombre dans l'expérience MicroBooNE, où des fermions sombres plus lourds sont produits par la diffusion ascendante de neutrinos de faisceau, et se désintègrent ensuite en paires électron-positron. Cette recherche a le potentiel de sonder l'espace des paramètres qui pourrait fournir une explication pour l'excès à basse énergie de MiniBooNE.

Sommario

La ricerca della materia oscura è una delle sfide più avvincenti della fisica moderna. Questa tesi indaga diversi modelli di materia oscura, con l'obiettivo di stabilire connessioni tra teoria e osservazioni. Iniziando con le ricerche di rivelazione indiretta, ci concentriamo sull'annichilazione della materia oscura in fotoni monocromatici. Esaminiamo il potenziale di questo segnale vincolando un modello di materia oscura top-philic e il modello inert doublet, utilizzando i dati sperimentali di Fermi-LAT e HESS. Esploriamo il modello singlet scalar Higgs portal nella regione di risonanza, combinando i dati del centro galattico, delle galassie nane e degli antiprotoni. Il modello si adatta a queste misure e all'abbondanza attuale di materia oscura, e non è vincolato dagli attuali limiti della rivelazione diretta e acceleratori. Analizziamo anche la fenomenologia del decadimento della materia oscura superpesante, vincolando la sua vita media sulla base delle misure sui fotoni e delle future osservazioni di neutrini. Inoltre, introduciamo i settori oscuri leggeri, concentrandoci sulle estensioni del Modello Standard caratterizzate da un portale di tipo vettoriale, che comporta una nuova simmetria di gauge oscura con un fotone oscuro cineticamente misto. In particolare, ci concentriamo sui fotoni oscuri leggeri, proponendo modelli contenenti molteplici fermioni oscuri, generalizzando l'idea della materia oscura anelastica. Sondiamo questi ricchi modelli di settore oscuro cercando decadimenti semi-visibili di fotoni oscuri, in cui vengono prodotte coppie elettrone-positrone insieme a energia mancante. Questo modello di decadimento permette di riformulare e rilassare i principali vincoli, aprendo nuove regioni dello spazio dei parametri, che possono spiegare il momento magnetico anomalo del muone ed essere testate in futuro. Infine, presentiamo una ricerca di coppie elettrone-positrone prodotte all'interno di modelli di settore oscuro nell'esperimento MicroBooNE, dove fermioni oscuri più pesanti sono prodotti dall'upscattering di neutrini del fascio, decadendo infine in coppie elettrone-positrone. Questa ricerca ha il potenziale per sondare lo spazio dei parametri che potrebbe fornire una spiegazione per l'eccesso di eventi a bassa energia di MiniBooNE.

Associated publications

[1] Arina, C., Heisig, J., Maltoni, F., **DM**, Mattelaer, O., "Indirect dark-matter detection with MadDM v3.2 – Lines and Loops". *Eur. Phys. J. C* 83.3 (2023), p. 241. DOI: 10.1140/epjc/s10052-023-11377-2;

[2] Di Mauro, M., Arina, C., Fornengo, N., Heisig, J., **DM,** "Dark matter in the Higgs resonance region". *Phys. Rev. D* 108.9 (2023), p. 095008. DOI: 10.1103/PhysRevD.108.095008;

[3] Allahverdi, R., Arina, C., Chianese, M., Cicoli, M., Maltoni, F., **DM**, Osiński, J. K., "Phenomenology of superheavy decaying dark matter from string theory". *JHEP* 02 (2024), p. 192. DOI: 10.1007/JHEP02(2024)192;

[4] Abdullahi, A. M., Hostert, M., **DM**, Pascoli, S., "Semi-Visible Dark Photon Phenomenology at the GeV Scale". *Phys. Rev. D* 108.1 (2023), p. 015032. DOI: 10.1103/PhysRevD.108.015032.

During my PhD, I have published other works of research not presented in this manuscript:

[5] Abdullahi, A. M., Hoefken Zink, J., Hostert, M., **DM**, Pascoli, S., "DarkNews: A Python-based event generator for heavy neutral lepton production in neutrino-nucleus scattering". *Comput. Phys. Commun.* 297 (2024), p. 109075. DOI: 10.1016/j.cpc.2023.109075;

[6] Mongillo, M., Abdullahi, A., Oberhauser, B. B., Crivelli, P., Hostert, M., **DM**, Bueno, L. M., Pascoli, S., "Constraining light thermal inelastic dark matter with NA64". *Eur. Phys. J. C* 83.5 (2023), p. 391. DOI: 10.1140/epjc/s10052-023-11536-5;

[7] Abdullahi, A. M., Hoefken Zink, J., Hostert, M., **DM**, Pascoli, S., "A panorama of new-physics explanations to the MiniBooNE excess" (Aug. 2023). arXiv: 2308.02543 [hep-ph].

Contents

1 Introduction 1

I State of the art 5

2 The Standard Model: a starting point 7
- 2.1 Particle content and interactions . . . 8
- 2.2 The Standard Model Lagrangian . . . 9
- 2.3 Fermion mass terms and mixing . . . 14
- 2.4 Uncharted landscapes: when the Standard Model is not enough 16
- 2.5 A deeper look into the neutrino sector . . . 17
  - 2.5.1 Neutrino masses . . . 18
  - 2.5.2 Type-I seesaw mechanism . . . 21
  - 2.5.3 Anomalies in neutrino experiments . . . 23
- 2.6 Extending the Standard Model: a brief summary of supersymmetry 26
  - 2.6.1 Super-Poincaré group . . . 26
  - 2.6.2 Superfields . . . 27
  - 2.6.3 Minimal Supersymmetric Standard Model . . . 28

3 Dark matter: evidence and detection 31
- 3.1 Chronicles of the unseen: how dark matter came to be . . . 32
  - 3.1.1 The challenge of missing mass . . . 33
  - 3.1.2 Galaxies rotation curves . . . 33
  - 3.1.3 Gravitational lensing . . . 35
  - 3.1.4 Cosmic microwave background . . . 37
  - 3.1.5 An alternative: modified gravity paradigm . . . 40
- 3.2 Dark matter candidates . . . 40
  - 3.2.1 Relic neutrinos . . . 42
  - 3.2.2 Sterile neutrinos . . . 43
  - 3.2.3 Axions . . . 44
  - 3.2.4 Supersymmetric particles . . . 44
  - 3.2.5 Primordial black holes . . . 45
- 3.3 Deciphering Universe dynamics: the Boltzmann equation . . . 45
- 3.4 The miracle of WIMPs . . . 53
- 3.5 Coannihilation . . . 55
- 3.6 Hunting for dark matter . . . 57
- 3.7 Indirect detection . . . 58
  - 3.7.1 Dark matter distribution . . . 60

3.7.2 Neutral particles . . . 61
3.7.3 Particle spectra . . . 64
3.7.4 Cosmic rays . . . 65
3.7.5 Indirect searches summary . . . 65
3.7.6 Recorded excesses . . . 70
3.8 Direct detection . . . 72
3.8.1 Astrophysics: the dark matter velocity distribution . . . 72
3.8.2 Recoil energy and rate . . . 73
3.8.3 Cross sections . . . 74
3.8.4 Experimental searches . . . 75
3.9 Collider searches . . . 77

4 Light dark sectors: the role of dark photon 79
4.1 The portal connections between dark sectors and the Standard Model . . . 80
4.1.1 The neutrino portal . . . 80
4.1.2 The scalar portal . . . 81
4.1.3 The vector portal . . . 81
4.2 The dark photon . . . 82
4.3 Model independent bounds . . . 88
4.3.1 Visible resonance searches . . . 88
4.3.2 Deep-inelastic scattering . . . 88
4.3.3 Electroweak precision observables . . . 90
4.3.4 Meson decays . . . 90
4.3.5 Anomalous magnetic moments of electron and muon . . . 90
4.3.6 Belle-II . . . 95
4.4 An example of a dark sector model: the three-portal model . . . 96
4.4.1 The scalar portal . . . 97
4.4.2 The vector portal . . . 99
4.4.3 The neutrino portal and the neutrino mass basis . . . 101
4.5 A look at the MiniBooNE LEE from a dark sector point of view . 104

II Phenomenology of dark matter models 107

5 Loop-induced dark matter annihilation and γ-lines phenomenology 109
5.1 Gamma-ray line phenomenology and constraints . . . 111
5.2 Loop-induced processes in MadDM . . . 115
5.2.1 The MadLoop interface . . . 115
5.2.2 Generate loop-induced annihilation processes in MadDM 118
5.3 Physics applications . . . 119
5.3.1 Simplified top-philic dark matter model . . . 119
5.3.2 Inert doublet model . . . 123
5.4 Summary . . . 128

6 Dark matter on the Higgs resonance **131**
6.1 Singlet scalar Higgs portal model 133
6.1.1 Overview 133
6.1.2 Annihilation cross section 134
6.1.3 Source energy spectra 138
6.2 Relic density 138
6.3 Collider searches 142
6.4 Direct detection 143
6.5 Indirect detection 145
6.5.1 The γ-rays from the galactic center and dwarf galaxies . 146
6.5.2 Antiproton flux 148
6.6 Combined results from direct, indirect, collider searches and cosmology 149
6.6.1 The S particle as dominant dark matter component . . . 149
6.6.2 The S particle as subdominant dark matter component . 151
6.6.3 Results without the GCE and upper limits from cosmic antiprotons 154
6.7 Summary 155

7 Phenomenology of superheavy decaying dark matter from string theory **157**
7.1 Superheavy dark matter from string theory 159
7.1.1 Generic features of 4-dimensional string models 159
7.1.2 The string theory model 160
7.1.3 Decaying dark matter and three-body decay spectra . . . 161
7.2 Astrophysical signatures of superheavy decaying dark matter . 162
7.2.1 Theoretical astrophysical fluxes 163
7.2.2 Future neutrino telescopes 164
7.2.3 Current γ-ray experiments 166
7.3 Methodology and energy spectra 166
7.4 Neutrino and γ-ray bounds for three-body decays 170
7.5 Summary 175

III Dark photons and dark sectors **177**

8 Semi-visible dark photons below the GeV scale **179**
8.1 Semi-visible dark photons 181
8.1.1 Two HNFs 185
8.1.2 Three HNFs 188
8.1.3 Four HNFs 192
8.1.4 Mixing with light neutrinos 194
8.2 Reinterpreting constraints on invisible Z' 196
8.2.1 BaBar monophoton search 197

8.2.2 NA64 dark photon searches . . . 199
8.2.3 Other limits from beam dumps . . . 204
8.3 Results . . . 205
8.3.1 Inelastic Dark Matter (BP1a, b) . . . 206
8.3.2 Mixed-inelastic Dark Matter (BP2a, b) . . . 213
8.3.3 Inelastic Dirac Dark Matter (BP3a–d) . . . 217
8.3.4 Three HNFs (BP4a–c, BP5) . . . 223
8.4 Prospects and constraints on HNL and dark matter interpretations 226
8.4.1 HNFs as dark matter candidates . . . 226
8.4.2 HNFs as HNLs . . . 229
8.4.3 Prospects for detection . . . 230
8.5 Summary . . . 234

9 Search for dark sector-produced e^+e^- pairs in MicroBooNE 237
9.1 Analysis overview . . . 240
9.1.1 The model . . . 240
9.1.2 The DarkNews event generator . . . 245
9.1.3 Goals and methods . . . 246
9.2 Generating model predictions . . . 247
9.2.1 The master benchmark . . . 247
9.2.2 Building the reweighting map . . . 248
9.2.3 Decay filter . . . 250
9.2.4 Other reweighted quantities . . . 252
9.2.5 Reweighting summary . . . 254
9.2.6 Modeling the dirt upscattering signal . . . 255
9.3 Analysis selection . . . 256
9.3.1 Development . . . 256
9.3.2 Final selection . . . 257
9.3.3 Predictions . . . 260
9.3.4 Efficiencies . . . 260
9.4 Systematic uncertainties . . . 261
9.5 Sensitivities . . . 262
9.6 Summary . . . 267

10 Conclusions 269

A Notation 275
A.1 Field theory . . . 275
A.1.1 Metric tensor . . . 275
A.1.2 Pauli matrices . . . 275
A.1.3 Dirac matrices . . . 276
A.1.4 Spinors . . . 276
A.1.5 Charge conjugation . . . 277
A.1.6 Standard Model fields and indices . . . 278

A.2 Abbreviations 279
A.3 Units 279

B A brief review of cosmology **281**
B.1 The Friedmann equations 281
B.2 Composition of the Universe 282
B.3 Equilibrium thermodynamics 284
B.4 Entropy 287
B.5 Structure formation 288

C MadDM v3.2 **291**
C.1 Astrophysics of γ-ray lines 291
C.1.1 The $\mathcal{J}$-factor computation 291
C.1.2 $\mathcal{J}$-factor density profiles in MadDM 302
C.1.3 Details on experimental data 304
C.2 Merging algorithm for multiple lines features 306

Bibliography **309**

List of Figures

2.1 The MiniBooNE LLE energy distribution. 24

3.1 Hydrogen surface density profile and rotation curves of the galaxies studied by Rogstad and Shostak. 35
3.2 Composite image of the Bullet Cluster. 36
3.3 Temperature power spectrum recorded by the Planck experiment in 2018. 38
3.4 Numerical solutions for the Boltzmann equation, for different cases of masses and cross sections. 52
3.5 Graphical representation of the detection methods of dark matter, involving interactions with the Standard Model. 58
3.6 Summary of SI dark matter-nucleon scattering cross section parameter space, with experiments, future sensitivities and the neutrino fog. 77

4.1 Model independent bounds on kinetic mixing ε and limits assuming invisible dark photon decays. 89
4.2 The tree-level photon-lepton coupling mediated by the intrinsic magnetic moment. 91
4.3 One-loop correction diagram to the lepton magnetic moment. . 91
4.4 Dark photon one-loop correction to the lepton's anomalous magnetic moment. 92

5.1 LO $2 \to 2$ annihilation and coannihilation diagrams for the simplified top-philic model. 121
5.2 The $2 \to 3$ process $\chi\chi \to W^+ b\bar{t}$; the process $\chi\chi \to W^- \bar{b}t$ has the same topology. 122
5.3 Higgs-mediated loop-induced annihilation for the top-philic model. 122
5.4 Loop-induced annihilation diagrams in γX for the top-philic model. Loop-induced annihilation diagrams in gg have the same topology. 123
5.5 Parameter space for the top-philic model in λ_χ vs m_χ. 124
5.6 Subset of the loop-induced annihilation diagrams in γX for the IDM model. 127
5.7 Cross section for the loop-induced dark matter annihilation into $\gamma\gamma$ and γZ for the IDM as a function of m_{h_0}. 128

6.1 Tree-level annihilation Feynman diagrams of the singlet scalar Higgs portal model. 134
6.2 Loop-induced Feynman diagrams for annihilation into a pair of gluons. 134
6.3 Annihilation cross section and branching ratio of the different channels as function of λ_{HS} and m_S, respectively. 136
6.4 The relic density of the SHP model in a λ_{HS} vs m_S plot and comparison between the two scenarios assuming or not kinetic equilibrium during freeze-out. 141
6.5 The 95 % CL upper limits for invisible Higgs width constraints in λ_{HS} vs m_φ parameter space. 143
6.6 The 90 % CL upper limits for direct detection experiments in λ_{HS} vs m_S parameter space. 144
6.7 Best-fit of the GCE SED for the SHP model and χ^2 contour. . . . 147
6.8 Combined fit to cosmic particle flux data (GCE, dSph, antiprotons) with relic density, direct detection and collider constraints. 150
6.9 Same as in fig. 6.8 but for various values of the fraction ξ of dark matter. 152
6.10 Best-fit regions of the combined cosmic particle flux data compatible with thermal freeze-out in the λ_{HS} vs ξ plane. 153
6.11 Same as in figs. 6.8 top left and 6.8 top right but rescaling all predicted astrophysical signals by the fraction ξ of dark matter predicted by the relic density computation for each point. 153
6.12 Same as in fig. 6.8 top right but with the upper limits derived from CR antiprotons flux. 154

7.1 Feynman diagrams for neutralino decay in RPV MSSM. 162
7.2 Comparison between the shower spectra in γ and ν for three and two-body decay patterns. 170
7.3 Current γ-ray lower bounds on dark matter lifetime as a function of the dark matter mass in the case of a dark matter candidate with a three-body decay pattern, for different experiments and RPV channels. 171
7.4 Projections for neutrino limits on the dark matter lifetime as a function of the dark matter mass in the case of a dark matter candidate with a three-body decay pattern, for different future experiments and RPV channels. 172
7.5 Comparison between the combined γ-ray constraints and the neutrino projections on the dark matter lifetime in the case of a dark matter candidate with a three-body decay pattern, for different RPV channels. 173

7.6 Upper bounds on the RPV couplings from current γ-ray and future neutrino data, as a function of the dark matter mass in the case of a neutralino candidate. 174
7.7 Upper bounds on the string coupling as a function of the ratio between mediator and dark matter masses, with fixed dark matter mass in the case of a neutralino candidate. 175

8.1 Feynman diagrams for the iDM model. 188
8.2 Feynman diagrams for the mixed-iDM model. 191
8.3 Feynman diagrams for the three Majorana fermions model. . . . 192
8.4 Feynman diagrams for the i2DM model. 194
8.5 The signatures of semi-visible dark photons at e^+e^- colliders. . 197
8.6 The signatures of semi-visible dark photons at the NA64 experiment. 200
8.7 Parameter space ε vs $m_{Z'}$ for the iDM model (BP1a, BP1b). . . . 209
8.8 Parameter space ε vs $m_{Z'}$ for the iDM model (BP1a, BP1b), with multiple BaBar recasts, with varying energy threshold. 210
8.9 Parameter space α_D vs $m_{Z'}$ for the iDM model. 211
8.10 Parameter space Δ_{21} vs $m_{Z'}$ for the iDM model. 212
8.11 Parameter space ε vs $m_{Z'}$ for the mixed-iDM model (BP2a, BP2b). 214
8.12 Parameter space Δ_{21} vs α for the mixed-iDM model. 215
8.13 Relic density for the mixed-iDM model in ε vs $m_{Z'}$ parameter space. 216
8.14 Parameter space ε vs $m_{Z'}$ for the i2DM model (BP3a, BP3b). . . 219
8.15 Same as fig. 8.14, but for BP3c and BP3d. 220
8.16 Parameter space Δ_{21} vs β for the i2DM model. 221
8.17 Relic density and CMB limits for the i2DM model in ε vs $m_{Z'}$ parameter space. 222
8.18 Parameter space ε vs $m_{Z'}$ for the 3 HNFs models (BP4a, BP4b). . 224
8.19 Same as fig. 8.18, but for BP4c and BP5. 225

9.1 The upscattering diagram for the $(3+2)$ model. 242
9.2 Truth-level distributions for the benchmark points. 248
9.3 The decay filter procedure. 251
9.4 The dirt model used in the analysis. 255
9.5 The BDT scores distributions for the final selection. 258
9.6 The analysis validation, MC-data comparison. 259
9.7 Final predicted spectra for Run1–3 data 260
9.8 Sensitivities for the MicroBooNE experiment. 265
9.9 Sensitivities for the MicroBooNE experiment (cont.). 266

C.1 The 2-dimensional projections for the $\mathcal{J}$-factor integration regions, including a mask, that can be computed with MadDM. 293
C.2 Graphical example of the merging algorithm. 307

List of Tables

2.1 Fields content of the Standard Model. 9
2.2 Standard Model particles electroweak charges: electric charge, isospin and hypercharge. 11
2.3 Chiral superfields of the MSSM. 28
2.4 Vector superfields of the MSSM. 29

3.1 Values of x_f for different masses and cross sections for a weak-scale coupled particle. 53

4.1 The vector and axial-vector couplings of the Standard Model fermions with the Z and Z' bosons. 87
4.2 The field content of the three-portal model. 97
4.3 The vector and axial-vector couplings of the dark-charged fermions with the Z and Z' bosons. 101

7.1 Three-body neutralino final states induced by the RPV vertices. 167

8.1 Summary of the benchmark models considered, with the HNF spectra and dark photon interaction vertices. 184
8.2 Benchmark models parameters. 205

9.1 The four benchmark scenarios considered in the analysis. 244
9.2 The parameters of the four benchmark points. 245
9.3 The binning scheme used for the reweighting map. 249
9.4 The final selection cuts. 257

C.1 The integration regions on the basis of the input parameters. . . 301

Chapter 1

Introduction

> Fra cent'anni diranno che sono uno che ha scoperto l'acqua calda.
>
> ENZO FERRARI

In the early 17th century, in the quiet solitude of his study, a young Galileo Galilei pointed his rudimentary, homemade, telescope to the sky for the first time. His observations unveiled a new world made of planets, moons and stars, in a relentless celestial dance, shattering the prevailing geocentric model of the Universe. His studies and discoveries, together with those of other scientists of the time, marked the beginning of the scientific revolution and formalized the scientific method, which is still the basis of modern science. Centuries later, it was the turn of the quantum revolution to change our understanding of the world. Physics underwent a profound paradigm shift, where reality itself was redefined, from the classical, deterministic view, to a probabilistic one, made of wave functions and quantum states. In this new framework, the brilliant minds of the 20th century formalized the laws of nature in a set of particles and interactions, laying down the foundations of particle physics. The Standard Model of particle physics is the result of this process, and it is the most successful theory in the history of science.

Fast-forward to the present, where it is our turn to push the boundaries of our knowledge of the Universe. The technological progress of the last decades has allowed us to probe the Universe at a level of detail never reached before, unveiling new phenomena, out of the reach of the Standard Model. Observations have shown that the luminous matter we see in the Universe is only a small fraction of the total matter content. Galaxies seem to be heavier than what it is observed, and studies on large scale structure formations, gravitational lensing and the cosmic microwave background radiation, all point to the existence of a new form of non-luminous matter, called dark matter. The dark matter problem is certainly one of the major issues in modern physics, and it is driving the theoretical and experimental research in the whole world since few decades. Many speculations have been made on the nature of dark matter, and the most explored so far is that it is made of one or more new particles, still unknown to us. To accommodate these particles, theoretical research is focused on providing consistent extensions of the Standard Model. Some of them will be discussed in this thesis.

Another compelling evidence of the need of new physics beyond the Standard Model is the problem of neutrino masses. Neutrinos are the most elusive particles of the Standard Model, and their properties are still largely unknown, they are neutral, and they interact only via the weak force. Multiple experiments have shown that neutrinos must have a non-zero mass, in contrast with the prediction of the Standard Model. The neutrino sector is certainly the more mysterious part of the Standard Model, and it is the subject of intense experimental research. In this context, many searches showed some intriguing anomalies, that could be explained by extensions of the neutrino sector with new particles and interactions. Such extensions may also be able to accommodate neutrino masses.

We can recognize a trend: the theoretical approach to the problems of dark matter and neutrino masses is to extend the Standard Model with new particles and interactions. Perhaps, all these problems can be connected, and the hypothetical new particles may be part of a bigger picture: a new rich hidden sector. Rich hidden sectors are extensions of the Standard Model where multiple new particles and interactions are added. In general, they are secluded from the Standard Model itself, if not for the presence of specific mediators. When the scale of these hidden sectors is below the electroweak scale, we will refer to them as (light) dark sectors, following the common nomenclature. It is not difficult to think to connect the neutrino sector to a new dark sector, given the elusiveness of neutrinos. Indeed, dark sectors can be thought as parallel worlds, linked to the Standard Model via the so-called portal interactions, where possibly new particles acting as mediators can couple to both worlds. These extensions can offer a theoretical framework to develop new physics beyond the Standard Model, while providing an optimal experimental target for their search in the form of the portal interactions. Portal interactions can have different forms, depending on the type of particles they mediate. In this thesis, we will focus on the vector portal, where a new dark force is added to the Standard Model, with the mediator being a new vector boson, called dark photon.

The thesis is organized into three parts.

In part I, we will review the state of the art of the theoretical and experimental research on dark matter and dark photons. In particular, chapter 2 will introduce the Standard Model of particle physics, describing its particle content and interactions, while briefly summarizing its main issues. Additionally, the neutrino masses problem will be discussed, along with the main methods to extend the Standard Model to accommodate them, and one of the most promising experimental anomalies recorded in the neutrino physics will be examined. Chapter 3 will be entirely devoted to the dark matter problem. We will review the experimental and observational evidences in favor of dark matter, and we will discuss the main particle and non-particle candidates that the scientific community has proposed to explain it. Emphasis will be given to the thermal evolution of dark matter in the Universe, and the main detection methods employed today will be described. Finally, chapter 4 will introduce light dark sectors and the dark photon. First, we will discuss the portal couplings, introducing the dark photon as the mediator of the vector portal. Then, we will present the main experimental constraints on its properties, and finally an example of a dark sector model containing the three portal couplings will be described.

In part II, we will discuss the phenomenology of various simple dark matter models, made of a single dark matter candidate and one (or more) mediators between the Standard Model and the dark matter itself. Chapter 5 will be devoted to a phenomenological study of the γ-line signature of dark matter annihilation. This signal can be produced by the annihilation of dark matter into two photons, or a photon and another neutral particle, and it is characterized by a monochromatic photon spectrum. It is a smoking-gun signature, because of the low background contamination that otherwise would affect the dark matter searches. Experiments like Fermi-LAT and HESS have set constraints on this signal, and we will discuss their bounds within two dark matter models. In chapter 6, we will focus on the singlet scalar Higgs portal model, one of the simplest extensions of the Standard Model that can accommodate dark matter, by adding a single scalar and a Higgs portal on top of the Standard Model. We will perform an in-depth study of this model, considering the parameter space on the Higgs resonance region, where the dark matter mass is half of the Higgs boson mass. Constraints from indirect, direct and collider searches will be discussed, and a detailed analysis of the relic density will be performed. Finally, in chapter 7, we will consider a string theory model able to generate a superheavy dark matter candidate, with a mass scale of the order 10^{10} GeV, that can decay into three fermions. We will perform a phenomenological study of this model, studying the particles spectra coming from the showering of the dark matter decay products and constraining the dark matter lifetime on the basis of γ-rays observations and future neutrino telescopes sensitivities.

In part III, we will focus on dark sector models based on the dark photon portal. In chapter 8, many dark photon-based dark sector models will be considered, where the dark photon is assumed to be lighter than the GeV scale. Specifically, the dark photon will be able to decay semi-visibly, producing both invisible states, in the form of other stable dark sector particles, and e^+e^- pairs, which can then be targeted by experimental searches. This approach would make possible to relax the constraints on invisible dark photon decays, and we will perform a phenomenological study on different models, considering all the possible bounds on their parameter space. In chapter 9, a search for e^+e^- pairs produced by a dark sector model will be presented. We will study the sensitivity of the MicroBooNE experiment to this model, discussing the main technical aspects of the analysis and the main ways to perform an efficient simulation on the full parameter space.

Finally, in chapter 10, we will summarize the results of this thesis, and we will discuss the future perspectives of the research on dark matter and dark sectors.

Part I

State of the art

Chapter 2

The Standard Model: a starting point

The Guide is definitive.
Reality is frequently inaccurate.

The Hitchhiker's Guide to the Galaxy
DOUGLAS ADAMS

The Standard Model of particle physics is the most complete *rulebook* in our hands to describe the fundamental constituents of matter and their interactions. It was developed throughout the second half of the last century, and it takes its fundamental roots from the first experimental evidences of the existence of subatomic particles. The Standard Model is a gauge theory based on the local symmetry group $\mathrm{SU}(3)_\mathrm{C} \times \mathrm{SU}(2)_\mathrm{L} \times \mathrm{U}(1)_\mathrm{Y}$, related respectively to colors, left-handed chirality and weak hypercharge. It is a Quantum Field Theory that describes three of the four fundamental interactions: the electromagnetic, the weak and the strong interactions. Its success is remarkable, because the Standard Model has been able to not only describe a plethora of experimental results and phenomena that have been observed in the last decades, but also to predict new particles and interactions, which have been later discovered. One of the most successful examples is the prediction of the Higgs boson and the Higgs mass mechanism, necessary to justify the mass of the elementary particles and of the weak gauge bosons. The Higgs boson was discovered in 2012 at the Large Hadron Collider (LHC) at CERN [8, 9]. In this chapter we give a brief overview of the Standard Model, focusing mainly on the electroweak sector, which is the most relevant for the phenomenology of this thesis. We will describe its particle content interactions in § 2.1. The Standard Model Lagrangian will be introduced in § 2.2 along with the electroweak symmetry breaking. A deeper look at the mass terms and the fermion mixing will be given in § 2.3. In § 2.5 we will discuss some features of the neutrino sector, proposing some theoretical avenues to explain the neutrino masses. Finally, in § 2.6 we will review the theory of Supersymmetry, which is one of most possible extensions of the Standard Model.

2.1 Particle content and interactions

The Standard Model is a non-Abelian gauge theory, based on the symmetry group $SU(3)_C \times SU(2)_L \times U(1)_Y$. The group $SU(3)_C$ is the symmetry group of the strong interaction, also known as Quantum Chromodynamics (QCD), while $SU(2)_L \times U(1)_Y$ is the symmetry group of the electroweak interaction, characterized by left-handed chirality. When we talk about symmetry, we are referring to the invariance of the physics under a certain transformation. In particle physics, we can define *global* and *local* symmetries. A global symmetry is a transformation that acts on the fields of the theory, but it does not depend on the spacetime coordinates, e.g. a rotation of the fields. On the contrary, local symmetry transformations depend on the spacetime coordinates. Standard Model symmetries, or gauge symmetries, are local. The invariance under gauge transformations makes the Standard Model a theory that contains both particles and interactions.

The elementary particles of the Standard Model are divided into two categories: fermions and bosons. Fermions are the building blocks of matter: all the elementary particles constituting the matter are fermions with spin 1/2. There exists two classes of fermions on the basis of their interactions: quarks are strongly interacting particles, and they possess the charge of the strong interacting force (the color), while leptons are not. The interactions between particles are determined by the gauge groups, which introduces a certain number of *force carriers* of bosonic nature and having spin 1. In particular, $SU(3)_C$ introduces eight gauge bosons, the gluons g, while the block $SU(2)_L \times U(1)_Y$ introduces four gauge bosons, $W^{\pm}$, Z and the photon γ. To satisfy gauge invariance, it is not possible to write explicit mass terms for either the gauge bosons or the fermions. In the case of gluons and the photon, this is not a problem, because they are massless particles. However, $W^{\pm}$, Z and the fermions are massive particles, so we need to introduce a mechanism to consistently provide a mass term for them. The introduction of the Higgs mechanism and of the electroweak symmetry breaking is the solution to this problem.

Before delving into the Standard Model Lagrangian, we need to introduce the mathematical description of bosons and fermions, on the basis of the formalism of Quantum Field Theory. Each particle is described by a field, which is a function of the spacetime coordinates. Fields transform under the action of a certain representation of the gauge group in different ways, depending on the spin of the particle and on its charge under that interaction (if it does not have a charge, then it is a singlet). Because of the chiral nature of the weak interaction, only left-handed particles are charged under $SU(2)_L$. This can be parametrized by the introduction of left-handed $SU(2)_L$ doublets, and right-handed $SU(2)_L$ singlets. Quarks and leptons will be organized in such doublets and singlets. Given right-handed neutrinos are singlets under all

Table 2.1: Fields content of the Standard Model. The first column shows the field, the second column shows the representation under the gauge group $SU(3)_C \times SU(2)_L \times U(1)_Y$, in the case of $U(1)_Y$ we indicate the value of the hypercharge. The index i marks the generation, u_i and d_i are up-type and down-type quarks respectively, ℓ_i is a charged lepton.

Field	$SU(3)_C \times SU(2)_L \times U(1)_Y$
Fermions	
$Q_i = \begin{pmatrix} u_{iL}^T & d_{iL}^T \end{pmatrix}^T$	$(\mathbf{3}, \mathbf{2}, 1/3)$
u_{iR}	$(\mathbf{3}, \mathbf{1}, 4/3)$
d_{iR}	$(\mathbf{3}, \mathbf{1}, -2/3)$
$L_i = \begin{pmatrix} \nu_{iL}^T & \ell_{iL}^T \end{pmatrix}^T$	$(\mathbf{1}, \mathbf{2}, -1)$
ℓ_{iR}	$(\mathbf{1}, \mathbf{1}, -2)$
Gauge bosons	
B_μ	$(\mathbf{1}, \mathbf{1}, 0)$
W_μ^a	$(\mathbf{1}, \mathbf{3}, 0)$
G_μ^b	$(\mathbf{8}, \mathbf{1}, 0)$
Higgs	
H	$(\mathbf{1}, \mathbf{2}, 1)$

gauge groups, they do not exist in the Standard Model. Moreover, both quarks and leptons are organized in three generations. In tab. 2.1 we summarize the fields content of the Standard Model along with their charges. The matter fields always transform under the fundamental representation of the gauge group, while the gauge fields transform under the adjoint representation.

2.2 The Standard Model Lagrangian

The full Standard Model Lagrangian can be written as:

$$\begin{aligned} \mathcal{L}_{SM} = \sum_f \overline{\psi_f} i \not{\mathcal{D}} \psi_f - \frac{1}{4} B_{\mu\nu} B^{\mu\nu} - \frac{1}{4} W^a_{\mu\nu} W^{a\mu\nu} - \frac{1}{4} G^b_{\mu\nu} G^{b\mu\nu} \\ - \left((\overline{\mathbf{Q}} \widetilde{H}) Y_u \mathbf{u}_R + (\overline{\mathbf{Q}} H) Y_d \mathbf{d}_R + (\overline{\mathbf{L}} H) Y_\ell \boldsymbol{\ell}_R + \text{h.c.} \right) \\ + (\mathcal{D}_\mu H)^\dagger \mathcal{D}^\mu H - V(H) \,. \end{aligned} \tag{2.1}$$

We define the following terms (notice that any generation index has been dropped in favor of the cleaner vector notation):

- ψ_f is the fermion field, where f is a generic doublet or weak singlet fermion field, as the ones described in tab. 2.1;

- $\mathcal{D}_\mu$ is the covariant derivative, defined as

$$\mathcal{D}_\mu = \partial_\mu - i\frac{g'}{2}YB_\mu - i\frac{g}{2}\sigma^a W^a_\mu - i\frac{g_s}{2}\lambda^b G^b_\mu\,, \tag{2.2}$$

  where g_s, g and g' are the coupling constants for the strong, weak and electromagnetic interactions, respectively, while σ^a, $a \in \{1, 2, 3\}$ are the Pauli matrices and λ^b, $b \in \{1, \ldots, 8\}$ are the Gell-Mann matrices;

- $B^{\mu\nu}$, $W^{a\mu\nu}$ and $G^{b\mu\nu}$ are the field strength tensors for the gauge fields B_μ, W^a_μ and G^b_μ respectively;

- Y_u, Y_d and Y_ℓ are the Yukawa coupling matrices for the up-type quarks, down-type quarks and charged leptons respectively, and they are part of the mass terms;

- H is the $SU(2)_L$ Higgs doublet:

$$H = \begin{pmatrix} H^+ \\ H_0 \end{pmatrix}\,, \tag{2.3}$$

  and $\widetilde{H} = i\sigma^2 H^*$ is its conjugate;

- $V(H)$ is the Higgs potential:

$$V(H) = -\mu^2 H^\dagger H + \frac{\lambda}{2}(H^\dagger H)^2\,, \tag{2.4}$$

  where $\mu^2 > 0$.

The Lagrangian of the Standard Model as it is written in eq. (2.1) already contains the ingredients to describe the electroweak symmetry breaking. This theory was developed in 1964 by Robert Brout, François Englert, Gerald Guralnik, Carl Hagen, Tom Kibble and Peter Higgs [10–13], and it is known as the Brout-Englert-Higgs mechanism. The electroweak unification is based on the spontaneous symmetry breaking, which allows writing

$$SU(1)_L \times U(1)_Y \to U(1)_{em}\,, \tag{2.5}$$

where the new gauge group is the electromagnetic group $U(1)_{em}$. In this context, it is possible to write a relation between the charges of the gauge groups participating in the electroweak unification, that is

$$Q_e = I_3 + \frac{Y}{2}\,, \tag{2.6}$$

known as the Gell-Mann–Nishijima formula, which relates the isospin charge I_3 of the $SU(2)_L$ group and the hypercharge Y of the $U(1)_Y$ group to the electric

Table 2.2: Standard Model particles electroweak charges: electric charge, isospin and hypercharge.

Field	Q_e	I_3	Y
$\begin{pmatrix} u_{iL} \\ d_{iL} \end{pmatrix}$	$2/3$ $-1/3$	$1/2$ $-1/2$	$1/3$
u_{iR}	$2/3$	0	$4/3$
d_{iR}	$-1/3$	0	$-2/3$
$\begin{pmatrix} \nu_{iL} \\ \ell_{iL} \end{pmatrix}$	0 -1	$1/2$ $-1/2$	-1
ℓ_{iR}	-1	0	-2
$\begin{pmatrix} H^+ \\ H_0 \end{pmatrix}$	1 0	$1/2$ $-1/2$	1

charge Q_e. In tab. 2.2 we summarize the charges of the particles of the Standard Model under the electroweak gauge group.

We now delve into the electroweak symmetry breaking mechanism. The Higgs potential in eq. (2.4) is a function of the Higgs field H, and it is easy to see that it can be minimized for a non-zero value of the field,

$$H^\dagger H = \frac{2\mu^2}{\lambda} \doteq \frac{v_H^2}{2}\,, \tag{2.7}$$

where we define the vacuum expectation value (VEV) of the Higgs field $v_H \approx 246\,\text{GeV}$. We notice the minimum is not constituted by a single point, rather the various minima are distributed in a circle, and this corresponds to the theory having an infinite amount of vacua. When choosing a certain vacuum, we induce a spontaneous symmetry breaking, with the new vacuum being

$$\langle 0|H|0\rangle = \frac{1}{\sqrt{2}}\begin{pmatrix} 0 \\ v_H \end{pmatrix}. \tag{2.8}$$

The Higgs field can be expanded around the chosen VEV, obtaining

$$H = \frac{1}{\sqrt{2}}\begin{pmatrix} G_1^+ + iG_2^+ \\ v_H + h + iG_3^0 \end{pmatrix}, \tag{2.9}$$

where G_1^+, G_2^+ and G_3^0 are the so-called Goldstone bosons, while h is the Higgs boson. The Goldstone bosons are massless bosons that always appear in the spontaneous symmetry breaking of a gauge theory and constitute degrees of freedom that are not physical. It is possible to perform a gauge transformation to *remove* the Goldstone bosons from the theory. This transformation *fixes* the gauge of the theory, and it is called unitary gauge, so that eq. (2.9) becomes

$$H = \frac{1}{\sqrt{2}} \begin{pmatrix} 0 \\ \nu_H + h \end{pmatrix} . \tag{2.10}$$

We can expand the covariant derivative of the Higgs field: After electroweak symmetry breaking we obtain

$$\begin{aligned}
(\mathcal{D}_\mu H)^\dagger \mathcal{D}^\mu H = \frac{1}{2}\partial_\mu h\, \partial^\mu h + \frac{1}{8}\begin{pmatrix} 0 & \nu_H + h \end{pmatrix} \begin{pmatrix} gW^3_\mu + g'B_\mu & g\left(W^1_\mu - iW^2_\mu\right) \\ g\left(W^1_\mu + iW^2_\mu\right) & -gW^3_\mu + g'B_\mu \end{pmatrix} \\
\times \begin{pmatrix} gW^{3\mu} + g'B^\mu & g\left(W^{1\mu} - iW^{2\mu}\right) \\ g\left(W^{1\mu} + iW^{2\mu}\right) & -gW^{3\mu} + g'B^\mu \end{pmatrix} \begin{pmatrix} 0 \\ \nu_H + h \end{pmatrix} \\
= \frac{1}{2}\partial_\mu h\, \partial^\mu h + \frac{g^2}{8}\left(W^1_\mu - iW^2_\mu\right)\left(W^{1\mu} + iW^{2\mu}\right)\left(\nu_H^2 + 2\nu_H h + h^2\right) \\
+ \frac{g^2}{8} W^3_\mu W^{3\mu}\left(\nu_H^2 + 2\nu_H h + h^2\right) + \frac{g'^2}{8} B_\mu B^\mu \left(\nu_H^2 + 2\nu_H h + h^2\right) \\
+ \frac{gg'}{4} W^3_\mu B^\mu \left(\nu_H^2 + 2\nu_H h + h^2\right) .
\end{aligned} \tag{2.11}$$

We can now collect the mass terms and write the mass matrix as

$$\mathcal{L} \supset \frac{1}{2}\begin{pmatrix} B_\mu & W^3_\mu \end{pmatrix} \frac{\nu_H^2}{4} \begin{pmatrix} g'^2 & -gg' \\ -gg' & g^2 \end{pmatrix} \begin{pmatrix} B^\mu \\ W^{3\mu} \end{pmatrix} . \tag{2.12}$$

It is possible to diagonalize the mass matrix using one single rotation,

$$\mathcal{R}(\vartheta_w)^T \begin{pmatrix} g'^2 & -gg' \\ -gg' & g^2 \end{pmatrix} \mathcal{R}(\vartheta_w) = \begin{pmatrix} 0 & 0 \\ 0 & g^2 + g'^2 \end{pmatrix} , \tag{2.13}$$

where:

$$\mathcal{R}(\vartheta_w) = \begin{pmatrix} \cos(\vartheta_w) & -\sin(\vartheta_w) \\ \sin(\vartheta_w) & \cos(\vartheta_w) \end{pmatrix} , \tag{2.14}$$

with ϑ_w defined as the Weinberg angle, and

$$\sin(\vartheta_w) = \frac{g'}{\sqrt{g^2 + g'^2}} , \tag{2.15a}$$

$$\cos(\vartheta_w) = \frac{g}{\sqrt{g^2 + g'^2}} , \tag{2.15b}$$

$$\tan(\vartheta_w) = \frac{g'}{g} . \tag{2.15c}$$

Finally, we can write the mass terms of eq. (2.11) in a compact form, that is

$$\mathcal{L} \supset \frac{1}{2} m_Z^2 Z_\mu Z^\mu + m_W^2 W_\mu^+ W^{-\,\mu}\,, \tag{2.16}$$

where we have the following definitions:

$$Z_\mu = \frac{1}{\sqrt{g^2 + g'^{\,2}}} \left(g W_\mu^3 - g' B_\mu \right), \tag{2.17a}$$

$$A_\mu = \frac{1}{\sqrt{g^2 + g'^{\,2}}} \left(g B_\mu + g' W_\mu^3 \right), \tag{2.17b}$$

$$W_\mu^\pm = \frac{1}{\sqrt{2}} \left(W_\mu^1 \mp i W_\mu^2 \right). \tag{2.17c}$$

The gauge boson masses result

$$m_Z = \frac{v_H}{2} \sqrt{g^2 + g'^{\,2}}\,, \tag{2.18a}$$

$$m_A = 0\,, \tag{2.18b}$$

$$m_W = m_Z \cos(\vartheta_w)\,. \tag{2.18c}$$

It is possible to obtain the interactions between the gauge bosons and the fermions by expanding the covariant derivative in the kinetic terms of the fermion fields, obtaining charged current and neutral current interactions, resulting, respectively,

$$\mathcal{L}_{cc} = \frac{g}{\sqrt{2}} \left(J_\mu^+ W^{+\,\mu} + J_\mu^- W^{-\,\mu} \right), \tag{2.19}$$

$$\mathcal{L}_{nc} = e\, A_\mu J_{em}^\mu + \frac{g}{2\, c_w} Z_\mu J_{nc}^\mu\,, \tag{2.20}$$

where the electric charge e is defined as

$$e = g \sin(\vartheta_w)\,. \tag{2.21}$$

We can explicitly define the following charged, electromagnetic and neutral currents, respectively as

$$J_\mu^+ = \sum_i \overline{\nu'_{iL}} \gamma_\mu \ell'_{iL} + \overline{u'_{iL}} \gamma_\mu d'_{iL}\,, \tag{2.22}$$

$$J_\mu^- = J_\mu^{+\,\dagger}\,, \tag{2.23}$$

$$J_\mu^{em} = \sum_f \overline{\psi'_f} \gamma_\mu Q_e^f \psi'_f\,, \tag{2.24}$$

$$J_\mu^{nc} = \sum_f \overline{\psi'_f} \gamma_\mu \left(I_3^f\, P_L - Q_e^f\, s_w^2 \right) \psi'_f\,. \tag{2.25}$$

2.3 Fermion mass terms and mixing

Including the fermion masses in the Lagrangian is not straightforward as simply writing the spin-1/2 mass term, that is, for a generic Dirac fermion ψ,

$$\mathcal{L} \supset m_\psi \overline{\psi_L} \psi_R + \text{h.c.}\,, \tag{2.26}$$

because this term violates gauge invariance. The solution comes from using the Higgs mechanism allowing us to write gauge-invariant mass terms, which will yield the fermion masses after the electroweak symmetry breaking. The fermion mass terms have been already introduced in eq. (2.1), by means of the Yukawa coupling matrices Y_u, Y_d and Y_ℓ, as

$$\mathcal{L}_{\text{SM}} \supset -(\overline{\mathbf{Q}}\widetilde{H}) Y_u \mathbf{u}_R - (\overline{\mathbf{Q}} H) Y_d \mathbf{d}_R - (\overline{\mathbf{L}} H) Y_\ell \boldsymbol{\ell}_R + \text{h.c.}\,. \tag{2.27}$$

We can expand eq. (2.27) with the results of the electroweak symmetry breaking, obtaining

$$\mathcal{L}_{\text{SM}} \supset -\frac{v_H + h}{\sqrt{2}} \left(\overline{\mathbf{u}'_L}\, Y_u \mathbf{u}'_R + \overline{\mathbf{d}'_L}\, Y_d\, \mathbf{d}'_R + \overline{\boldsymbol{\ell}'_L}\, Y_\ell \boldsymbol{\ell}'_R \right) + \text{h.c.}\,, \tag{2.28}$$

where the matrices Y_u, Y_d, Y_ℓ are in general non-diagonal. This implies that the states in eq. (2.28) do not have definite masses, and they are called flavor eigenstates. Subsequently, to obtain the physical states of each particle, we need to diagonalize the Yukawa matrices. In the following we will indicate the flavor states with a prime, and the mass states without it. We define the following unitary transformations between flavor and mass states

$$\mathbf{u}_L = V_L^{u\dagger} \mathbf{u}'_L\,, \tag{2.29a}$$
$$\mathbf{u}_R = V_R^{u\dagger} \mathbf{u}'_R\,, \tag{2.29b}$$
$$\mathbf{d}_L = V_L^{d\dagger} \mathbf{d}'_L\,, \tag{2.29c}$$
$$\mathbf{d}_R = V_R^{d\dagger} \mathbf{d}'_R\,, \tag{2.29d}$$
$$\boldsymbol{\ell}_L = V_L^{\ell\dagger} \boldsymbol{\ell}'_L\,, \tag{2.29e}$$
$$\boldsymbol{\ell}_R = V_R^{\ell\dagger} \boldsymbol{\ell}'_R\,, \tag{2.29f}$$

so that we can cast each term of eq. (2.28) as

$$\overline{\mathbf{u}'_L}\, Y_u \mathbf{u}'_R = \overline{\mathbf{u}_L} (V_L^{u\dagger} Y_u V_R^u) \mathbf{u}_R = \overline{\mathbf{u}_L}\, \hat{Y}_u \mathbf{u}_R\,, \tag{2.30a}$$
$$\overline{\mathbf{d}'_L}\, Y_d \mathbf{d}'_R = \overline{\mathbf{d}_L} (V_L^{d\dagger} Y_d V_R^d) \mathbf{d}_R = \overline{\mathbf{d}_L}\, \hat{Y}_d \mathbf{d}_R\,, \tag{2.30b}$$
$$\overline{\boldsymbol{\ell}'_L}\, Y_\ell \boldsymbol{\ell}'_R = \overline{\boldsymbol{\ell}_L} (V_L^{\ell\dagger} Y_\ell V_R^\ell) \boldsymbol{\ell}_R = \overline{\boldsymbol{\ell}_L}\, \hat{Y}_\ell \boldsymbol{\ell}_R\,, \tag{2.30c}$$

obtaining

$$\begin{aligned}\mathcal{L}_{\rm SM} &\supset -\frac{v_H + h}{\sqrt{2}}\left(\overline{\mathbf{u}_L}\,\hat{Y}_u \mathbf{u}_R + \overline{\mathbf{d}_L}\,\hat{Y}_d\,\mathbf{d}_L + \overline{\boldsymbol{\ell}_L}\,\hat{Y}_\ell \boldsymbol{\ell}_L\right) + \text{h.c.} \\ &= -\frac{v+h}{\sqrt{2}}\sum_i \overline{u_{iL}}\,\hat{y}^i_u u_{iR} + \overline{d_{iL}}\,\hat{y}^i_d d_{iL} + \overline{\ell_{iL}}\,\hat{y}^i_\ell \ell_{iL} + \text{h.c.}\,,\end{aligned} \tag{2.31}$$

where we have defined the diagonal Yukawa matrices $\hat{Y}_u$, $\hat{Y}_d$ and $\hat{Y}_\ell$. Eq. (2.31) shows that the fermion mass terms are proportional to the Higgs field VEV, and that the mass term itself is accompanied by a coupling between the fermion and the Higgs boson:

$$\begin{aligned}\mathcal{L}_{\rm SM} \supset -\sum_i m^i_u\,\overline{u_{iL}}u_{iR} + m^i_d\,\overline{d_{iL}}d_{iL} + m^i_\ell\,\overline{\ell_{iL}}\ell_{iL} + \text{h.c.} \\ -\sum_i \frac{m^i_u}{v_H} h\,\overline{u_{iL}}u_{iR} + \frac{m^i_d}{v_H} h\,\overline{d_{iL}}d_{iL} + \frac{m^i_\ell}{v_H} h\,\overline{\ell_{iL}}\ell_{iL} + \text{h.c.}\end{aligned} \tag{2.32}$$

where the masses are defined as

$$m^i_u = \frac{v_H}{\sqrt{2}}\hat{y}^i_u\,, \tag{2.33a}$$

$$m^i_d = \frac{v_H}{\sqrt{2}}\hat{y}^i_d\,, \tag{2.33b}$$

$$m^i_\ell = \frac{v_H}{\sqrt{2}}\hat{y}^i_\ell\,. \tag{2.33c}$$

We can now recast the charged and neutral currents under the mass eigenstates, by using the transformations defined in eq. (2.29). For the charged current in eq. (2.22) we obtain:

$$\begin{aligned}J^+_\mu &= \overline{\boldsymbol{\nu}'_L}\,\gamma_\mu V^\ell_L \boldsymbol{\ell}_{iL} + \overline{\mathbf{u}_L}(V^{u\dagger}_L V^d_L)\gamma_\mu \mathbf{d}_L\,, \\ &= \overline{\boldsymbol{\nu}_L}\,\gamma_\mu \boldsymbol{\ell}_L + \overline{\mathbf{u}_L}\,V_{\rm CKM}\,\gamma_\mu \mathbf{d}_L\,.\end{aligned} \tag{2.34}$$

We can draw two important conclusions from this result:

- the leptonic charged current does not change under the transformation: this happens because we can always redefine the neutrino fields to absorb the transformation. This is a consequence of the massless nature of neutrinos in the Standard Model, so that any linear combination of them is still a massless field:

$$\boldsymbol{\nu}_L = V^{\ell\dagger}_L \boldsymbol{\nu}'_L\,, \tag{2.35}$$

  and $\nu_{\alpha L}$, $\alpha \in \{e, \mu, \tau\}$ are called flavor neutrino fields;

- the quark charged current is not diagonal, and it is proportional to the Cabibbo-Kobayashi-Maskawa (CKM) matrix V_{CKM} [14, 15], defined as:

$$V_{CKM} = V_L^{u\dagger} V_L^d \,. \tag{2.36}$$

  The CKM matrix parametrizes the mixing between the quarks, allowing the transitions between different generations.

For the neutral current in eq. (2.25), we obtain:

$$\begin{aligned} J_\mu^{nc} &= \sum_f \overline{\psi'_{fL}}\, \gamma_\mu g_L^f\, \psi'_{fL} + \overline{\psi'_{fR}}\, \gamma_\mu g_R^f\, \psi'_{fR} \\ &= \sum_f \overline{\psi_{fL}}\, \gamma_\mu g_L^f\, V_L^{f\dagger} V_L^f\, \psi_{fL} + \overline{\psi_{fR}}\, \gamma_\mu g_R^f\, V_R^{f\dagger} V_R^f\, \psi_{fR} \\ &= \sum_f \overline{\psi_{fL}}\, \gamma_\mu g_L^f\, \psi_{fL} + \overline{\psi_{fR}}\, \gamma_\mu g_R^f\, \psi_{fR} \,, \end{aligned} \tag{2.37}$$

where we have defined the couplings g_R^f and g_L^f. This result comes from the unitarity of the transformation matrices. We notice that the neutral current is the same for the mass and flavor eigenstates, and that the couplings are diagonal.

2.4 Uncharted landscapes: when the Standard Model is not enough

Despite the incredible achievements of the Standard Model in explaining the fundamental interactions of nature with a striking precision, some questions remain unanswered. A more complete theory, possibly extending the Standard Model, is needed to explain its shortcomings. In the following, we will briefly discuss some of these open questions:

- **neutrino masses**: the Standard Model assumes neutrinos are massless. However, experimental evidences show that neutrinos can oscillate, and this phenomenon implies that neutrinos have non-zero masses [16–18]. The absence of neutrino masses within the Standard Model framework indicates the need for an extension to accommodate new neutrino mass terms. These extensions can be made with the introduction of new particles and interactions;
- **dark matter**: astronomical observations show that the baryonic matter we can observe in the Universe is just a small fraction of the total matter, and a significant portion of it is non-baryonic, and it is known as dark matter. Dark matter has been observed through its gravitational effects, in particular concerning the rotation curves of galaxies [19] and the effects

on structure formation in the Universe [20], see chapter 3 for a discussion on the dark matter problem. However, the nature of dark matter is still unknown, and it is not described by the Standard Model;

- **strong CP problem** [21]: within the QCD theory, it is possible to extend the QCD Lagrangian with the addition of the following term [22], that respects all the Standard Model symmetries, but breaks the charge-parity symmetry (CP),

$$\mathcal{L}_{\rm QCD} \supset \vartheta \frac{g_s^2}{32\pi^2} G^b_{\mu\nu} \widetilde{G}^{b\mu\nu} \,, \tag{2.38}$$

  where the dual field strength tensor is defined as $\widetilde{G}^{b\mu\nu} = \frac{1}{2}\varepsilon^{\mu\nu\rho\sigma}G^b_{\rho\sigma}$. For values of the parameter $\vartheta \neq n\pi$, $n \in \mathbb{Z}$, this term introduces a CP violation that makes the neutron electric dipole moment higher than expected. So, in order to maintain that effect under control, one needs at least $|\vartheta| < 10^{-9}$ [23]. However, there is no reason to expect ϑ to be so small, and it is not clear why CP-violating effects are so suppressed. The introduction of the axion [24] is a possible solution to this problem, see § 3.2;

- **hierarchy problem**: the large hierarchy between the electroweak scale, characterized by the mass of the Higgs boson, and the Planck scale raises questions about the naturalness of the SM. The Higgs boson mass receives quantum corrections that are sensitive to high energy scale, so it is unnatural for it to have a mass compatible with the electroweak scale;

- **gravity**: the Standard Model is able to successfully describe three of the four fundamental interactions, and it does not include gravity. The formulation of a quantum theory of gravity is still an open problem, and it is not clear how to include it along with the other interactions in the Standard Model.

2.5 A deeper look into the neutrino sector

As we have seen in § 2.4, neutrino masses are not included in the Standard Model, while, on the other hand, neutrino flavor oscillations have been observed, confirming that neutrinos must have a mass, despite very small. From a theoretical point of view, the idea of neutrino oscillations was first proposed by B. Pontecorvo in 1957 [25] and 1958 [26]. Later on, in 1962, Z. Maki, M. Nakagawa, S. Sakata discussed the idea of neutrino flavor mixing, introducing a “virtual transmutation” of $\nu_\mu \to \nu_e$ [27]. In the same period, the first experiments looking for solar neutrinos were designed. The first results were published by the Homestake experiment in 1968 [28], and show a deficit in the observed number of electron neutrino events with respect to the theoretical predictions provided by the Standard Model, a fact that became known as the *solar neutrino problem*. Later on, also measurements on the atmospheric neutrino flux, from the Irvine-Michigan-Brookhaven (IMB) experiment [29] and the Kamiokande experiment [30], detected a deficit in the expected number of neutrino events, related to muon flavor neutrinos. In 1998, the Super-Kamiokande experiment [18] provided the first experimental evidence of neutrino oscillations, confirming the same behavior observed in the case of atmospheric neutrinos. It was followed by the Sudbury Neutrino Observatory (SNO) experiment [16, 17], that detected neutrino oscillations also in the case of solar neutrinos, by measuring both the electron neutrino flux and the cumulative flux of all neutrino flavors. It was then clear that the deficits in neutrino events recorded both for solar and atmospheric neutrinos were due to flavor oscillations, happening while neutrinos were traveling from their production point (the Sun or the atmosphere) to the detector.

However, the existence of the neutrino oscillations poses an important problem on the Standard Model. Oscillations require neutrinos to have a non-zero mass, so that it is necessary to extend the Standard Model to include neutrino masses.

2.5.1 Neutrino masses

Dirac mass

The first possibility to introduce neutrino masses is to add a Dirac mass term to the Standard Model Lagrangian, in the same way as lepton masses have been obtained. This implies the addition of the right-handed neutrino fields $\nu_{\alpha R}$, which is a singlet under all the symmetries of the Standard Model. We can write a new mass term identical to the ones defined in eq. (2.27):

$$\mathcal{L} \supset -\left(\overline{\mathbf{L}}\widetilde{\mathrm{H}}\right)\mathrm{Y}_\nu \boldsymbol{\nu}_R + \mathrm{h.c.}\,. \tag{2.39}$$

Additionally, the number of these neutrinos is not fixed by the theory, and one could work with a different number of them, even lower than three. This specific scenario, with the choice of three right-handed neutrinos, is known as the minimally extended Standard Model. After the electroweak symmetry breaking, eq. (2.39) becomes:

$$\mathcal{L} \supset -\frac{v_H + h}{\sqrt{2}}\,\overline{\boldsymbol{\nu}'_L}\,\mathrm{Y}_\nu \boldsymbol{\nu}'_R + \mathrm{h.c.}\,, \tag{2.40}$$

where we recovered the notation with prime fields to indicate the flavor eigenstates. Subsequently, we can perform a unitary transformation to obtain the mass eigenstates, in the same way as it was performed in eq. (2.29):

$$\mathbf{n}_L = V_L^{\nu\dagger} \boldsymbol{\nu}'_L = \begin{pmatrix} \nu_{1L} \\ \nu_{2L} \\ \nu_{3L} \end{pmatrix} , \tag{2.41a}$$

$$\mathbf{n}_R = V_R^{\nu\dagger} \boldsymbol{\nu}'_R = \begin{pmatrix} \nu_{1R} \\ \nu_{2R} \\ \nu_{3R} \end{pmatrix} , \tag{2.41b}$$

so that

$$\overline{\boldsymbol{\nu}'_L}\, Y_\nu \boldsymbol{\nu}'_R = \overline{\mathbf{n}_L} \big(V_L^{\nu\dagger} Y_\nu V_R^\nu\big) \mathbf{n}_R = \overline{\mathbf{n}_L}\, \hat{Y}_\nu \mathbf{n}_R \,, \tag{2.42}$$

obtaining

$$\mathcal{L} \supset -\frac{v_H + h}{\sqrt{2}} \overline{\boldsymbol{\nu}_L}\, \hat{Y}_\nu \boldsymbol{\nu}_R + \text{h.c.} = -\frac{v_H + h}{\sqrt{2}} \sum_i \overline{n_{iL}}\, \hat{y}^i_\nu n_{iR} + \text{h.c.} \,. \tag{2.43}$$

Finally, we can conclude that massive Dirac neutrino can couple to the Higgs boson in the same way as leptons and quarks, with a coupling proportional to the neutrino mass:

$$\mathcal{L} \supset -\sum_i m^i_\nu\, \overline{\nu_{iL}} \nu_{iR} - \sum_i \frac{m^i_\nu}{v_H} h\, \overline{\nu_{iL}} \nu_{iR} + \text{h.c.} \,, \tag{2.44}$$

with the neutrino Dirac mass defined as:

$$m^i_\nu = \frac{v_H}{\sqrt{2}} \hat{y}^i_\nu \,. \tag{2.45}$$

Despite this solution is very elegant and compatible with the same mass mechanism giving mass to the other fermions, it requires the Yukawa couplings $\hat{y}^i_\nu$ to be tiny, given we expect neutrinos to have a very small mass.

We can now recover the expression of the charged current, in light of the new neutrino mass term:

$$J^+_\mu = \overline{\mathbf{n}_L}\, \gamma_\mu \big(V_L^{\nu\dagger} V_L^\ell\big) \boldsymbol{\ell}_L = \overline{\mathbf{n}_L}\, \gamma_\mu U^\dagger \boldsymbol{\ell}_L \,, \tag{2.46}$$

and we define the Pontecorvo-Maki-Nakagawa-Sakata mixing matrix U:

$$U = V_L^{\ell\dagger} V_L^\nu \,. \tag{2.47}$$

Furthermore, we can define the flavor neutrino fields $\boldsymbol{\nu}_L$:

$$\boldsymbol{\nu}_L = U \mathbf{n}_L \,. \tag{2.48}$$

The flavor neutrino field is the neutrino field produced along with the same flavor lepton in charged current interactions.

Majorana mass

A Dirac fermion can always be written as the sum of the two chiral components,

$$\psi = \psi_L + \psi_R \,. \tag{2.49}$$

However, there is no reason to assume these two components to be independent one from the other. In particular, through the charge-conjugation transformation, it is possible to produce a right-handed field from a left-handed one, and vice versa. In this context, one could write:

$$\psi_R = \psi_L^c \,, \tag{2.50}$$

which implies a Dirac fermion can be written using only the left-handed component

$$\psi = \psi_L + \psi_L^c \,. \tag{2.51}$$

This has the rather curious consequence of making the Dirac fermion equal to its charge-conjugate, a fact known as the Majorana condition:

$$\psi = \psi^c \,. \tag{2.52}$$

In this case, we say ψ is a Majorana fermion. The Majorana condition implies that the fermion is its own antiparticle.

Assuming neutrinos to be Majorana fermions, it is possible to write a mass term using only the left-handed component:

$$\mathcal{L} \supset -\frac{1}{2}\overline{\boldsymbol{\nu}_L^c}\, M_\nu \boldsymbol{\nu}_L + \text{h.c.} = \frac{1}{2}\boldsymbol{\nu}_L^T\, \mathcal{C}^\dagger M_\nu \boldsymbol{\nu}_L + \text{h.c.}\,. \tag{2.53}$$

The left-handed neutrino has $I_3 = \frac{1}{2}$ and $Y = -1$, so that means the mass term just written has $I_3 = 1$ and $Y = -2$, and it is not gauge-invariant under the Standard Model symmetries. To justify the Majorana mass term, we need to introduce a new gauge-invariant term that would be able to generate it after the electroweak symmetry breaking. Such term can be obtained in the Standard Model effective field theory as a dimension-5 operator, known as the Weinberg operator [31]:

$$\mathcal{L}_5 \supset \frac{c_5^{\alpha\beta}}{\Lambda}\left(\overline{L_\alpha^c}\widetilde{H}\right)\left(\widetilde{H}^\dagger L_\beta\right) + \text{h.c.}\,, \tag{2.54}$$

where α and β are the flavor indices, $c_5^{\alpha\beta}$ is the Wilson coefficient. This new operator is non-renormalizable, and it is suppressed by the energy scale of the new physics Λ. Neutrino masses are generated after electroweak symmetry breaking:

$$\mathcal{L}_5 \to \frac{c_5^{\alpha\beta} v_H^2}{2\Lambda} \overline{\nu_{\alpha L}^c} \nu_{\beta L} + \text{h.c.} \doteq m_\nu^{\alpha\beta} \overline{\nu_{\alpha L}^c} \nu_{\beta L} + \text{h.c.}\,, \tag{2.55}$$

where we defined the generated Majorana masses:

$$m_\nu^{\alpha\beta} = \frac{c_5^{\alpha\beta} v_H^2}{2\Lambda}\,. \tag{2.56}$$

2.5.2 Type-I seesaw mechanism

We will now discuss one of the simplest extensions of the Standard Model that can generate neutrino masses explaining naturally their smallness. In the simplest scenario, we assume only one single neutrino field ν_L. We proceed by adding a right-handed sterile neutrino field ν_R, which is a singlet under the Standard Model symmetries. In this situation, the Lagrangian can contain a Dirac mass term coupling ν_L with ν_R, as in eq. (2.39), and a Majorana mass term for ν_R, as in eq. (2.53) (a Majorana mass term for ν_L is not gauge-invariant, so we neglect it in this scenario):

$$\mathcal{L} \supset -(\overline{L}\widetilde{H}) Y_\nu \nu_R + \frac{1}{2} \nu_R^T \mathcal{C}^\dagger M \nu_R + \text{h.c.}\,. \tag{2.57}$$

It can be cast in a more compact form after electroweak symmetry breaking:

$$\mathcal{L} \supset \frac{1}{2} \begin{pmatrix} \nu_L^T & \nu_R^{c\,T} \end{pmatrix} \mathcal{C}^\dagger \begin{pmatrix} 0 & m_D \\ m_D & M \end{pmatrix} \begin{pmatrix} \nu_L \\ \nu_R^c \end{pmatrix} + \text{h.c.} = \frac{1}{2} \mathbf{N}_L^T \mathcal{C}^\dagger \mathbf{M}\, \mathbf{N}_L + \text{h.c.}\,, \tag{2.58}$$

which resembles the Majorana mass term. We define the Dirac mass $m_D \doteq Y_\nu v_H/\sqrt{2}$ and the multiplet:

$$\mathbf{N}_L = \begin{pmatrix} \nu_L \\ \nu_R^c \end{pmatrix}. \tag{2.59}$$

It is possible to diagonalize the mass matrix $\mathbf{M}$ by performing a unitary transformation, U, so that

$$n_L = U^\dagger \mathbf{N}_L\,, \tag{2.60}$$

$$U^T \mathbf{M} U = \hat{\mathbf{M}}\,, \tag{2.61}$$

where the massive neutrino fields are defined as the components of the multiplet $\mathbf{n}_L$, while $\hat{\mathbf{M}}$ is the diagonal mass matrix:

$$\hat{\mathbf{M}} = \begin{pmatrix} m_1 & 0 \\ 0 & m_2 \end{pmatrix} . \tag{2.62}$$

It is possible to assume the so-called seesaw limit:

$$m_D \ll M\,, \tag{2.63}$$

in this case the eigenvalues of the mass matrix can be written approximately as

$$m_1 \approx \frac{m_D^2}{M}\,, \tag{2.64a}$$

$$m_2 \approx M\,. \tag{2.64b}$$

The mixing matrix U is a single 2×2 rotation matrix, characterized by the mixing angle:

$$\tan(2\vartheta) \approx 2\frac{m_D}{M} \ll 1\,, \tag{2.65}$$

the remaining phases of U are chosen in order to give physical (positive) values to the neutrino masses*.

In order to estimate the neutrino masses in this scenario, we can use the upper limit on the sum of neutrino masses, coming from cosmological observations, $\sum_i m_i < 0.12\,\text{eV}$ [20], so that we can impose $m_1 = 0.12\,\text{eV}$. We can compute:

$$Y_\nu^2 \approx \frac{2m_1}{v_H^2} M \approx 4 \times 10^{-15}\left(\frac{M}{\text{GeV}}\right), \tag{2.66}$$

$$\vartheta^2 \approx \frac{m_1}{M} \approx 10^{-10}\left(\frac{M}{\text{GeV}}\right)^{-1} . \tag{2.67}$$

Both the Yukawa coupling and the mixing angle depend on the mass of the sterile neutrino M. The requirement of a *natural* value for the Yukawa coupling, $Y_\nu \approx \mathcal{O}(1)$, implies $M \approx \mathcal{O}(10^{15}\,\text{GeV})$.

This simplified scenario, known as the type-I seesaw mechanism, provides a natural explanation for the smallness of the neutrino masses, with a reasonable value for the Yukawa coupling, while assuming the existence of a new heavy sterile neutrino, at a mass scale close to the Planck scale, $10^{18}\,\text{GeV}$. This is a reasonable assumption, given we expect new physics to appear at these energy scales. Seesaw models are very popular in the literature for their ability to generate new physics from the neutrino sector, and they are the subject of many

*When diagonalizing $\mathbf{M}$ in this approximation, we would obtain m_1 with an opposite value with respect to the one indicated in eq. (2.64a). In order to recover a positive physical value, it is necessary to set the complex phases accordingly.

experimental searches. Many variants of seesaw models have been studied. In § 4.4, we will discuss an example of a more complicated model making use of the same concepts as seesaw models, but involving many different kinds of neutrinos.

2.5.3 Anomalies in neutrino experiments

Neutrino oscillations opened a new era for neutrino searches and experiments for the discovery of new physics. The possibility for neutrinos to have mass and to mix among different flavors has teased the theoretical community to propose a plethora of new models and mechanisms extending the Standard Model while being able to explain neutrino masses. On the experimental side, several experiments performed accurate measurements of neutrino properties and interactions, achieving a great success in understanding neutrino oscillations over large distances. However, the data collected so far show an incomplete picture of neutrino oscillations, with some tensions between different measurements. In particular, oscillations over short distances are not well understood, and some anomalies have been recorded by experiments. These anomalies are referred as short-baseline (SBL) anomalies, because of the technical features of the experiments that recorded them, characterized by baselines and energies of the order $L/E \approx \mathcal{O}(1\,\mathrm{km/GeV})$. The most significant anomaly is represented by the $\nu_\mu \to \nu_e$ conversion of neutrinos and antineutrinos, observed by both the Liquid Scintillator Neutrino Detector (LSND) [32–36], at $3.8\,\sigma$, and the MiniBooNE experiment [37–43], reaching $4.8\,\sigma$. The latter anomaly is commonly known as the MiniBooNE low-energy excess (LEE).

The MiniBooNE experiment and the LEE

The MiniBooNE experiment was a Čerenkov detector located at Fermilab, in the Booster Neutrino Beam (BNB). It was designed to search for $\nu_\mu \to \nu_e$ oscillations, with a baseline of $L = 541\,\mathrm{m}$, and it was equipped with a $12.2\,\mathrm{m}$ diameter spherical tank filled with $818\,\mathrm{t}$ of pure mineral oil. It had two different operational modes: in forward-horn-current (FHC, namely the neutrino mode), and reverse-horn-current (RHC, namely the anti-neutrino mode). The first results of the experiment were published between 2007 and 2009, in neutrino mode [37, 38], reporting an excess of 128.8 ± 43.4 electron-like events over the background, with a significance of $3\,\sigma$, for a total of 6.46×10^{20} Protons-on-target (POTs), in the energy range $E_\nu^{QE} = (200 \text{ to } 475)\,\mathrm{MeV}$, where E_ν^{CCQE} is the reconstructed neutrino energy of the charged-current quasi-elastic scattering (CCQE). This was later followed by an excess recorded in anti-neutrino mode with a significance of $2.8\,\sigma$, corresponding to 78.4 ± 28.5 excess events. The observation was performed on the energy range $E_\nu^{CCQE} = (200 \text{ to } 1250)\,\mathrm{MeV}$, with a total of 1.27×10^{21} POTs [39, 40]. In the later years, a careful study of

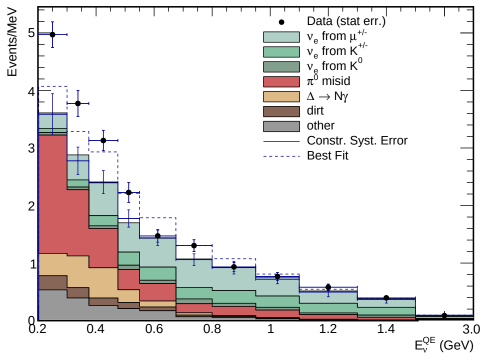

Figure 2.1: The MiniBooNE LLE energy distribution of the full dataset, compared to the expected background and the best-fit signal of a two-neutrino flavor oscillations model. Figure from [41, fig. 1].

the background was performed along with a collection of more data, allowing to increase the significance to $4.8\,\sigma$ [41, 42], with a final current measurement of electron-like events of 638.0 ± 52.1 (stat) $\pm$ 122.2 (sys), between the two operational modes. The anomaly is known as low-energy excess because most of the events are observed below $E_\nu^{QE} \approx 475\,\text{MeV}$. The excess is shown in fig. 2.1 [41]. The LEE is characterized by a mild preference for forward-going events, with a reconstructed angle of approximately 72 % of events with respect to the beam, satisfying $\cos(\vartheta_{\text{beam}}) \leqslant 0.9$. Moreover, most events occur within the first 8 ns of bunch timing, coinciding with neutrino scattering events in the detector.

Charged particles in the MiniBooNE chamber are measured thanks to the Čerenkov and scintillation light they produce. The Particle Identification (PID) capabilities of the detector are limited, and it is not possible to disentangle the signals coming from single electrons, single photons, collimated e^+e^- and $\gamma\gamma$ pairs, and they all appear as a typical electron-like event. The analysis of the various backgrounds sources is performed with *in-situ* measurements:

- intrinsic ν_e: related to the ν_e present in the neutrino beam, which are produced by the decay of charged kaons and muons; the kaon production rate was measured by SciBooNE [44];

- dirt: related to the neutrino interactions in the dirt surrounding the detector, which can produce single photons outside the detector; it is constrained by using topological and spatial cuts to isolate events close to the edge of the detector and pointing towards its center;

- $NC\pi^0$: related to the neutral current scattering producing the Δ baryon resonance, followed by its decay to neutrons and neutral pions $\Delta \to n\pi^0$;

the subsequent decay of π^0 into two photons can be misidentified if one of the photons escape the detector or the photons of the pairs are collinear;

- NC1γ: the Δ resonance can also decay to $\Delta \to n\gamma$, producing a single photon.

The NCπ^0 and NC1γ backgrounds are the most important, characterized by the largest uncertainties. They can easily mimic single electrons. They were constrained by direct measurement of the cross sections for neutral current single π^0 production on mineral oil, induced by neutrino and anti-neutrino interactions [45, 46]. These backgrounds have the potential of solving the LEE, indeed an enhancement of a 3.18 factor of the radiative Δ NC1γ background events is sufficient to give an excellent agreement with the data. This estimation justified searches for radiative Δ decays, which was performed by the MicroBooNE experiment [47].

The Short Baseline Neutrino program and the MicroBooNE experiment

The Short Baseline Neutrino (SBN) program at Fermilab is made of three Liquid Argon Time Projection Chambers (LArTPCs) located along the BNB, at different distances [48, 49]. The Short Baseline Near Detector (SBND) is the closest, located at approximately 100 m from the proton target; it is followed by MicroBooNE, placed at 470 m and finally by ICARUS at 600 m.

The MicroBooNE experiment recently completed its full data taking. Its main physics objective is to investigate the nature of the LEE. Thanks to the LArTPC technology, MicroBooNE is able to perform a detailed reconstruction of the neutrino interactions, with a good PID capability, and it is able to distinguish electrons and photons showers. The first results released by MicroBooNE aimed to test the radiative Δ hypothesis, looking at neutrino neutral current-induced Δ baryon production followed by its decay, producing a single photon [47]. The experiment rejected this hypothesis to be at the origin of the excess at the 94 % confidence level (CL). Notice that the search targeted events featuring a single photon-like electromagnetic shower with either no other activity in the detector, or one visible final-state proton. These events are commonly referred as 1γ0p and 1γ1p events, respectively. This means the single photon explanation is not fully precluded, as other non-resonant photon sources are not excluded, but it is unlikely to be coming from a Standard Model source. Furthermore, the MicroBooNE experiment also tested the hypothesis for the excess to be due to ν_e interactions. Neutrino interactions in the detector have the potential of producing visible electrons, developing in a single electromagnetic shower, possibly featuring hadronic activity along it. The MicroBooNE collaboration developed three analyses targeting different topologies [50]:

- deep-learning-based reconstruction [51]: for events with a single electron and a final-state proton, 1e1p;

- Pandora-based reconstruction [52]: for pionless events, $1e\mathrm{N}p0\pi$ ($\mathrm{N} \geqslant 1$) and $1e0p1\pi$;
- Wire-Cell-base reconstruction [53]: for inclusive ν_e scattering events, $1eX$, featuring all possible hadronic final states.

The comparison between MicroBooNE data and the MiniBooNE excess has been performed by using a signal template for the LEE, where the energy distribution was extracted by simple subtraction of the background prediction from the LEE signal. Indeed, this observable can then be related to a possible excess flux of ν_e in the BNB. The template was then used to compare consistently the ν_e data collected by the aforementioned analyses. All channels but the $1e0p1\pi$, found a deficit with respect to the prediction, with the $1e0p1\pi$ showing a mild excess in the lower energetic bin, which is also the less sensitive one. The results of these analyses show no excess of ν_e events, and the MicroBooNE collaboration concluded that the LEE is unlikely to be due to ν_e interactions.

2.6 Extending the Standard Model: a brief summary of supersymmetry

In this section we are briefly introducing the theory of Supersymmetry. In the beginning of 1970s, physicists considered adding a new symmetry able to relates bosons and fermions of the Standard Model [54–57], called Supersymmetry (SUSY). SUSY theories had a great success in the past decades, because they are able to solve some of the problems of the Standard Model, such as the hierarchy problem, while predicting the unification of the gauge couplings, which fostered many speculations regarding the existence of a unified theory at high energies.

2.6.1 Super-Poincaré group

In the framework of SUSY, the Poincaré symmetry of spacetime is extended by the introduction of a new set of symmetries involving fermionic partners for each bosonic particle. The mathematical structure governing these extended symmetries is encapsulated by the super-Poincaré group. The generators of the super-Poincaré group are the usual Poincaré generators, P_μ and $L_{\mu\nu}$, and the new fermionic generators Q_α and $\overline{Q}_{\dot\beta}$. Here, α and $\dot\beta$ are indices for two-component spinors representing different chiralities. The fermionic generators are characterized by the following anti-commutation relations:

$$\{Q_\alpha, \overline{Q}_{\dot\beta}\} = 2(\sigma^\mu)_{\alpha\dot\beta} P_\mu\,, \tag{2.68a}$$
$$\{Q_\alpha, Q_\beta\} = \{\overline{Q}_{\dot\alpha}, \overline{Q}_{\dot\beta}\} = 0\,, \tag{2.68b}$$

where σ^μ are the Pauli matrices. The commutation relations between the fermionic generators and the Poincaré generators are:

$$[Q_\alpha, P_\mu] = [\overline{Q}_{\dot\alpha}, P_\mu] = 0\,, \tag{2.69a}$$
$$[Q_\alpha, L_{\mu\nu}] = (\sigma_{\mu\nu})_\alpha{}^\beta Q_\beta\,, \tag{2.69b}$$
$$[\overline{Q}_{\dot\beta}, L_{\mu\nu}] = (\sigma_{\mu\nu})_{\dot\beta}{}^{\dot\gamma}\overline{Q}_{\dot\gamma}\,. \tag{2.69c}$$

The action of the operator Q_α on a state $|\psi\rangle$ produces a new state $|\psi'\rangle$ which is called superpartner of $|\psi\rangle$. The superpartner of a bosonic state $|B\rangle$ is a fermionic state $|F\rangle$ and vice versa:

$$Q_\alpha|B\rangle = |F\rangle\,, \tag{2.70}$$
$$Q_\alpha|F\rangle = |B\rangle\,. \tag{2.71}$$

The existence of superpartners is a straightforward solution to the hierarchy problem: the Higgs boson mass quantum corrections would be canceled by the contributions of the superpartners, so that the Higgs boson mass can remain at the electroweak scale.

2.6.2 Superfields

In SUSY, fields are extended and described as superfields, with a defined transformation under the super-Poincaré group. A superfield is a function defined on a superspace, the extended spacetime that includes both commuting and anticommuting operators. We introduce the Grassman coordinates ϑ^α, that are the fermionic coordinates on the superspace, while the bosonic coordinates are the regular spatial coordinates x^μ. The superspace is parametrized by $(x^\mu, \vartheta^\alpha, \vartheta^{\dot\alpha})$, and we can define a superfield $\Phi(x, \vartheta, \overline{\vartheta})$ as a function of the superspace coordinates. We can express superfields as power series expansions in ϑ and $\overline{\vartheta}$:

$$\begin{aligned}\Phi(x,\vartheta,\overline{\vartheta}) = {} & \varphi(x) + \vartheta\,\lambda(x) + \overline{\vartheta}\,\overline{\chi}(x) + \vartheta\,\vartheta\,A(x) + \overline{\vartheta}\,\overline{\vartheta}\,B(x) \\ & + \vartheta\sigma^\mu\,\overline{\vartheta}c_\mu(x) + \vartheta\,\vartheta\,\overline{\vartheta}\,\overline{\psi}(x) + \overline{\vartheta}\,\overline{\vartheta}\,\vartheta\rho(x) + \vartheta\,\vartheta\,\overline{\vartheta}\,\overline{\vartheta}\,D(x)\,.\end{aligned} \tag{2.72}$$

The irreducible representations of the super-Poincaré group are:

- chiral superfields, defined so that

$$\overline{D}_{\dot\alpha}\Phi = 0\,, \tag{2.73}$$

Table 2.3: Chiral superfields of the MSSM.

Superfield	Spin 0	Spin 1/2	$SU(3)_C \times SU(2)_L \times U(1)_Y$
Q_i	$(\tilde{u}_L, \tilde{d}_L)_i$	$(u_L, d_L)_i$	$(\mathbf{3}, \mathbf{2}, 1/6)$
$\overline{u}_i$	$\tilde{u}_{Ri}$	u_{Ri}	$(\mathbf{3}, \mathbf{2}, -2/3)$
$\overline{d}_i$	$\tilde{d}_{Ri}$	d_{Ri}	$(\mathbf{3}, \mathbf{2}, 1/3)$
L_i	$(\tilde{\nu}_L, \tilde{e}_L)_i$	$(\nu_L, e_L)_i$	$(\mathbf{1}, \mathbf{2}, -1/2)$
$\overline{e}_i$	$\tilde{e}_{Ri}$	e_{Ri}	$(\mathbf{1}, \mathbf{1}, 1)$
$\overline{\nu}_i$	$\tilde{e}_{Ri}$	e_{Ri}	$(\mathbf{1}, \mathbf{1}, 0)$
H_u	(H_u^0, H_u^+)	$(\tilde{H}_u^0, \tilde{H}_u^+)$	$(\mathbf{1}, \mathbf{2}, 1/2)$
H_d	(H_d^-, H_d^0)	$(\tilde{H}_d^-, \tilde{H}_d^0)$	$(\mathbf{1}, \mathbf{2}, -1/2)$

where D_α and $\overline{D}_{\dot{\alpha}}$ are the superspace derivatives, defined as

$$D_\alpha = \frac{\partial}{\partial \vartheta^\alpha} + i\sigma^\mu_{\alpha\dot{\alpha}}\overline{\vartheta}^{\dot{\alpha}}\partial_\mu\,, \tag{2.74a}$$

$$\overline{D}_{\dot{\alpha}} = -\frac{\partial}{\partial \overline{\vartheta}^{\dot{\alpha}}} - i\vartheta^\alpha\sigma^\mu_{\alpha\dot{\alpha}}\partial_\mu\,, \tag{2.74b}$$

- vector superfields, defined so that

$$V(x, \vartheta, \overline{\vartheta}) = V^\dagger(x, \vartheta, \overline{\vartheta})\,. \tag{2.75}$$

2.6.3 Minimal Supersymmetric Standard Model

The Minimal Supersymmetric Standard Model (MSSM) is the simplest supersymmetric extension of the Standard Model. In the MSSM, each particle of the Standard Model is associated to a superpartner, with the same quantum numbers, except for the spin. Superpartners of fermions are bosons, while superpartners of bosons are fermions. The superpartners of the Standard Model particles are called sparticles and a similar naming convention is used to refer to each superpartner singularly. Basically, each Standard Model fermion superpartner is a boson with the same name prepended by an "s" (so we will have *squarks* and *sleptons*), while each Standard Model boson superpartner is a fermion with the same name and the suffix "-ino" appended to it (so we have *photino*, *wino*, *bino*, . . .). The fields content of the MSSM is summarized in tabs. 2.3 and 2.4. The MSSM is equipped with two Higgs doublets, because when promoting the Standard Model Higgs field to a superfield, we are introducing new fermion fields in the theory, and we need to compensate that with a second Higgs doublet in order to cancel gauge anomalies. Sfermions are defined in terms of mass eigenstates, related to left and right-handed gauge states sfermions through 6×3 mixing matrices. Notice that there is only a left-handed sneutrino in the MSSM, so there is only a left-handed mixing matrix.

Table 2.4: Vector superfields of the MSSM.

Superfield	Spin 1/2	Spin 1	$SU(3)_C \times SU(2)_L \times U(1)_Y$
G	$\tilde{G}$	G	$(\mathbf{8}, \mathbf{1}, 0)$
W	$\tilde{W}^{\pm}, \tilde{W}^{0}$	$W^{\pm}, W^{0}$	$(\mathbf{1}, \mathbf{3}, 0)$
B	$\tilde{B}^{0}$	B^{0}	$(\mathbf{1}, \mathbf{1}, 0)$

In the Standard Model, there is no term that allows direct coupling between a particle and its superpartner. In addition, no supersymmetric particle has been observed so far. This allows us to formulate a conservation law, called R-parity, to be associated to each particle, and it is possible to introduce a new quantum number R defined as:

$$R = (-1)^{3(B-L)+2S}\,, \tag{2.76}$$

where B is the baryon number, L is the lepton number and S is the spin. The R-parity is defined as $R = +1$ for all Standard Model particles and $R = -1$ for all superpartners. The R-parity conservation implies that superpartners can only be produced in pairs and the lightest supersymmetric particle (LSP) is stable. Moreover, no supersymmetric particles can be produced from ordinary matter, consistently with observations so far.

The full Lagrangian of the MSSM is made of different terms, but its technicalities are beyond the scope of this thesis. However, it is noteworthy to mention a specific aspect of the MSSM potential, specifically the sector involving R-parity violation. Indeed, it is possible to extend the MSSM Lagrangian with terms that violates the R-parity conservation, called R-parity violating (RPV) terms. The RPV contribution to the MSSM superpotential is given by [58, 59]:

$$W_{\mathrm{RPV}} = \lambda LLE^c + \lambda' LQD^c + \lambda'' U^c D^c D^c\,, \tag{2.77}$$

where λ, λ' and λ'' are dimensionless coupling constants. The first and second terms violate lepton number conservation, while the third term violates baryon number conservation.

In more detail, eq. (2.77) reads:

$$W_{LLE} = \varepsilon^{\sigma\rho}\,\lambda_{ijk} L_{i\sigma} L_{j\rho} E^c_k\,, \tag{2.78a}$$
$$W_{LQD} = \varepsilon^{\sigma\rho}\,\lambda'_{ijk} L_{i\sigma} Q_{j\rho\alpha} D^c_{k\alpha}\,, \tag{2.78b}$$
$$W_{UDD} = 2\varepsilon^{\alpha\beta\gamma}\,\lambda''_{ijk} U^c_{i\alpha} D^c_{j\beta} D^c_{k\gamma}\,, \tag{2.78c}$$

where i, j, k are generation indices (with $k > j$), σ, ρ are $SU(2)_L$ indices, while α, β, γ are $SU(3)_C$ color triplet indices. These RPV terms have an interesting effect on the phenomenology of the MSSM [58, 59], because they allow a sfermion to decay into a pair of Standard Model particles. This has the interesting effect of making the LSP unstable. We will review the phenomenology of RPV MSSM in chapter 7.

Chapter 3

Dark matter: evidence and detection

If you only knew the power of the dark side.
—Darth Vader

Star Wars Episode V: The Empire Strikes Back
George Lucas

It is quite surprising how little we know about the Universe we live in. The Standard Model of particle physics, introduced in chapter 2, is a very successful theory that describes the fundamental constituents of matter and their interactions. It provides a complete description of the electromagnetic, weak, and strong interactions, and it has been tested with great precision in a wide range of experiments. However, astrophysical observations have shown that it is not enough to explain the entire energy content of the Universe. According to the latest measurements from the Planck experiment [20], the Standard Model only accounts for as little as 5 % of the total energy density of the Universe, what it is known as the *baryonic matter*. The rest of the energy content is made of *dark energy* (69 %) and *dark matter* (26 %). Dark matter is a kind of non-luminous matter that it can not be observed directly. It is remarkable that we know the exact quantity of dark matter the Universe hosts, but we are still unable to identify whether it is a particle or not, its interactions with the Standard Model and its cosmological origin. The answer to these questions has motivated extensive research in this field. In the past decades, massive efforts have been devoted to the study of dark matter, which have led to the development of many theoretical models and experimental searches. Still, the nature of dark matter remains one of the most intriguing mysteries of modern physics.

In this chapter, we are going to provide an in-depth review of the evidence for dark matter and the experimental searches that have been performed to detect it, updating [60, § 3]. In § 3.1, we will describe the historical path that has led to the modern concept of dark matter, following the reviews [61–63]. Then, in § 3.2, we will introduce the different dark matter candidates that have been proposed in the literature, while in § 3.3 we will introduce the mathematical formalism to study the Universe evolution, namely the Boltzmann equation, referring to [64, 65]. In §§ 3.4 and 3.5, we will focus on the so-called weakly interacting massive particles (WIMPs), which are the most popular candidates, describing their main properties and the theoretical motivations for their existence, considering the reviews [66, 67]. Finally, §§ 3.6–3.9 will be devoted to the experimental searches of dark matter, following [68–73].

3.1 Chronicles of the unseen: how dark matter came to be

Surprisingly, it is more than ninety years since the words *dark matter* have been used in their current meaning for the first time, by the astronomer Fritz Zwicky in 1933 [74]. In reality, the term has a long history in the astrophysical observations, and it was used to describe the presence of non-luminous matter in the Universe. Actually, one could even date back the first use of the *dark* adjective applied to astronomical bodies to the 19$^{\text{th}}$ century, when Lord Kelvin used it in a seminar [75]:

> "Many of our supposed thousand million stars, perhaps a great majority of them, may be dark bodies."

when discussing the Milky Way mass estimation on the basis of the velocity dispersion of the visible stars. Indeed, light has always been the prime method to survey the Universe. Astronomical objects can be observed by either the light they emit or the light they absorb, and in such case they can be observed as well as dark regions. The light collected from an object can be studied in order to infer its properties, such as its mass, temperature, chemical composition, and its distance from the observer. In particular, different objects emit or absorb light in different ways, and it is possible to quantify the emissivity by a quantity called light-to-mass ratio. Additionally, another way to infer the properties of an astrophysical object is to use the gravitational theory, which allows us to measure quantities like its mass by studying its gravitational interactions with close objects. The main point is that the two mass estimates, the one obtained from the light-to-mass ratio and the one obtained from the gravitational theory, can be different: the gravitational mass sometimes exceeds the luminous mass estimate. This discrepancy was the first reason that led to the term dark matter, so some kind of matter that can not be seen and that accounts for that discrepancy.

3.1.1 The challenge of missing mass

If we want to pinpoint the origin of the dark matter concept, we need to travel back around ninety years ago, in California (USA), where the astronomer Fritz Zwicky was working at the California Institute of Technology (Caltech). Zwicky was interested in the velocity distribution of the galaxies making up the Coma Cluster. He observed that the galaxies were moving too fast to be bounded together under the gravitational pull of the visible matter [74], concluding.

> "If this would be confirmed, we would get the surprising result that dark matter is present in much greater amount than luminous matter,"

that is actually referred as the first use of the words dark matter. Although, Zwicky was referring probably to cool stars and gases. Several studies followed the Zwicky's work, and the discrepancy between the gravitational mass and the luminous mass was confirmed in other clusters of galaxies, like the Virgo cluster by Sinclair Smith [76], or by observations of individual pairs or groups of galaxies [77, 78]. The problem of missing mass was taken seriously by the scientific community and was deeply discussed at the International Astronomical Union General Assembly in 1962 [79].

3.1.2 Galaxies rotation curves

The missing mass problem was just the beginning of the dark matter story. So far, dark matter was hypothesized to be found in the intergalactic space of the clusters of galaxies, but it was not yet clear whether it was present in the galaxies themselves. The first evidence of dark matter in galaxies came from the study of their rotation curves, that is the circular velocity profile of its stars and gas as a function of the distance from the center of the galaxy. Advancements in radio astronomy in the 1960s provided several methods to study the velocity distributions $v(r)$ until the edge of a galaxy. For example, the velocity of hydrogen clouds can be measured by the Doppler effect of the 21 cm line of neutral hydrogen, given its low level of absorption in the interstellar medium. Consider the most common galaxy shape, the spiral galaxy, which is composed of a central core (a disk and a bulge), containing the large part of galaxy mass and an outer region. Applying Newtonian gravitational law to such system we find:

$$v(r) = \sqrt{\frac{GM(r)}{r}} \,. \tag{3.1}$$

From luminous matter observations, the mass $M(r)$ enclosed in a sphere of radius r can be considered spherically symmetric and mostly entirely contained in the central core. That means $M(r)$ is constant in the outer region and the velocity profile of the stars and gas there is:

$$v(r) \propto r^{-1/2}\,, \tag{3.2}$$

expecting $v(r)$ to decrease with distance.

Needless to say, the observations did not match the prediction. The physicist Horace Babcock was the first one to provide an experimental result in this topic. In 1939, he presented the measurement of the rotation curve of galaxy M31 (i.e. Andromeda Galaxy) out to 20 kpc away from its center [80]. His findings show inexplicably high velocities at large radii, and he concluded that the mass distribution of M31 must have been different from the one predicted by the luminous matter distribution, which he computed approximating M31 to a sphere surrounded by a flattened ellipsoid. Later, in 1940, Jan Oort measured the rotation curve of the galaxy NGC 3115 [81], finding the same pattern as Babcock. He and his student, Hendik van de Hulst, measured the hydrogen velocity with the 21 cm line. They also measured the rotation curve of the galaxy M31 with the same method, obtaining results up to about 30 kpc away from the center, and confirming that the mass-to-light ratio was higher in the outer regions [82]. The measurement using the 21 cm line of hydrogen was performed again by Morton Roberts in 1966, confirming the previous results with more accuracy [83]. A step further in terms of quality was done by Kent Ford and Vera Rubin in 1970. Their strategy was based on the spectroscopic observation of M31 up to 31 kpc. They managed to determine the trend in the rotation velocity, characterized by a slow rise with increasing distance from the center of the galaxy, followed by an almost constant behavior for radial distances in the range (16 to 30) kpc [19], in complete contrast with the theoretical prediction of Newtonian gravitation applied only to luminous matter, in eq. (3.2). In the same year, we have the appearance of the first statement mentioning that additional mass was needed in the outer parts of the galaxies in order to account for galaxies rotational velocity observations. The physicist Ken Freeman compared the value of the radius at which the rotation curve velocity was observed to be maximum with the theoretical value obtained assuming an exponential distribution of matter, that is the distribution matching the observable luminous matter [84]. He stated

> "if [the data] are correct, then there must be in these galaxies additional matter which is undetected, either optically or at 21 cm. Its mass must be at least as large as the mass of the detected galaxy, and its distribution must be quite different from the exponential distribution which holds for the optical galaxy."

A few years later, David H. Rogstad and G. S. Shostak analyzed the rotation curves of the galaxies: M33, NGC 2403, IC 342, M101 and NGC 6946 [85], their results are shown in fig. 3.1. They observed the rotation curves do not decrease

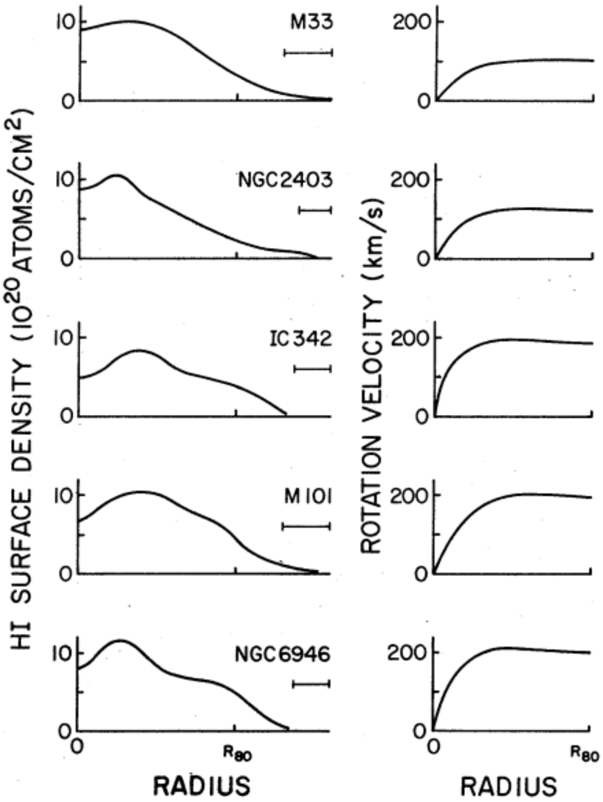

Figure 3.1: The hydrogen surface density profile (left) and the corresponding rotation curves (right) of the five galaxies studied by Rogstad and Shostak [85]. The bars under the galaxy names indicate the effective spatial resolution, while R_{80} is the radius containing the 80 % of the observed hydrogen. Figure from [85, fig. 1].

with distance, rather they remain flat. The same behavior was confirmed for other several galaxies in the following years.

3.1.3 Gravitational lensing

Another way to study the mass distribution of galaxies is to use the gravitational lensing effect [86]. The theory of General Relativity predicts that the presence of a mass distribution in the space-time can bend the light rays passing through it. This is due to the fact that the space-time is curved by the presence of mass, and the light rays follow the geodesics of the curved space-time. The deflection angle of the light rays emitted by a certain source is given by:

$$\alpha = \frac{4GM}{c^2 r}, \tag{3.3}$$

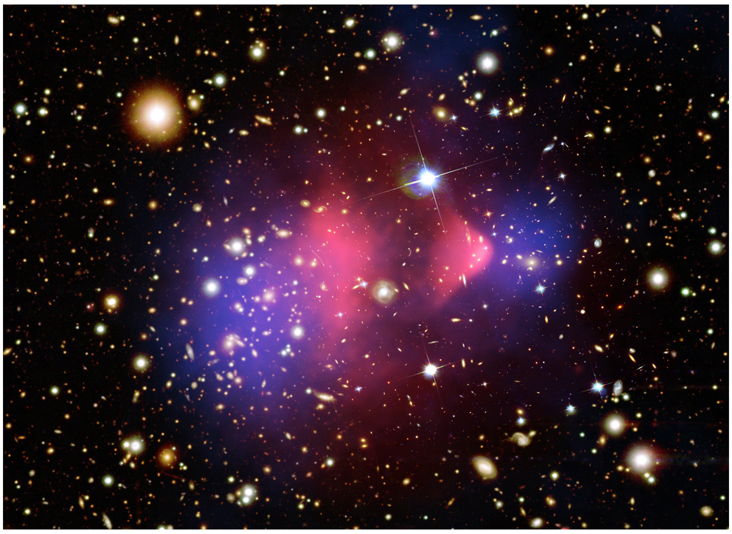

Figure 3.2: Composite image of the Bullet Cluster, the collision of a pair of galaxy clusters where one has passed through the other. Optical data from Magellan and Hubble Space Telescope shows galaxies (in orange and white), while Chandra X-ray reveals hot intracluster gas (pink). Gravitational lensing distortion reveals the mass of the cluster is dominated by dark matter (blue). Figure from [89].

where G is the gravitational constant, M is the mass of the lens and r is the distance between the source and the observer. Gravitational lensing is a powerful method to study the distribution of mass in galaxies and clusters of galaxies, and it has been used to confirm the presence of dark matter in galaxies [87, 88].

In this sense, one of the most famous examples is the cluster 1E0657-558, also known as the *Bullet Cluster*. It is the result of the collision between two smaller subclusters. When galaxy clusters collide, galaxies and dark matter are not expected to interact, and they pass through each other. However, intracluster gases, which constitute the bulk of the visible cluster mass, interact electromagnetically with each other and slow down. The fact the different components, gas, galaxies and dark matter, interact differently during the collision leads to the possibility to study them separately. This phenomenon translates in the gases to be stripped away from the two clusters, while dark matter and galaxies continue their motion. The result is that the intracluster gases are located in the middle of the two clusters, while the galaxies and the dark matter are located at the edges. This is exactly what has been observed in the Bullet Cluster, fig. 3.2, where the intracluster gases are shown in pink, while the galaxies and the dark matter are shown in orange and blue, respectively. The analysis of the Bullet Cluster has been performed in [90], where the X-ray emission of the intracluster gas has been observed with the Chandra telescope, computing the mass of the cluster. The gravitational lensing effect applied to the system showed that the mass distribution is not centered on the X-ray emission, but it is located at the edges of the cluster, where the galaxies are located. This is a clear evidence that the mass distribution is dominated by dark matter.

The example of the Bullet Cluster is also a clear proof able to rule out theories and scenarios that do not include dark matter, such as the Modified Newtonian Dynamics (MOND), see § 3.1.5. In that theory, the lensing would be expected to follow the baryonic matter distribution.

3.1.4 Cosmic microwave background

The Universe today is permeated by a microwave radiation field, called the Cosmic Microwave Background (CMB). The CMB is made of the photons that were released when the Universe was about 380 000 years old. At that time, the Universe was filled with a hot plasma of electrons and protons, and the photons were tightly coupled to it. The high temperatures of the plasma prevented the photons to travel freely through the Universe as they were constantly scattered by the electrons. As soon as the temperature dropped below the ionization energy of hydrogen, the electrons and protons combined to form neutral hydrogen atoms, and the photons were finally free to stream through the entire Universe. The decoupling of the photons from the hot plasma represents the so-called last scattering surface of the CMB. The CMB provides us with the information about the Universe at the time of the last scattering, and it is a powerful tool to study the cosmological parameters. In particular, the CMB is a black-body radiation with a temperature of 2.726 K and it is almost isotropic, with fluctuations of the order of $\Delta T/T \approx 10^{-5}$. Temperature fluctuations can be described with a multipole expansion in spherical harmonics on the celestial sphere:

$$\frac{\Delta T}{T}(\vartheta, \varphi) = \sum_{\ell=0}^{\infty} \sum_{m=-\ell}^{\ell} a_{\ell m} Y_{\ell m}(\vartheta, \varphi) \,. \tag{3.4}$$

From a statistical point of view, the multipole moments have zero mean, $\langle a_{\ell m} \rangle = 0$. Because of the Gaussian nature of the CMB fluctuations, the only relevant information is contained in the variance, known as the angular power spectrum C_ℓ:

$$C_\ell \doteq \langle |a_{\ell m}|^2 \rangle = \frac{1}{2l+1} \sum_{m=-\ell}^{\ell} |a_{\ell m}|^2 \,. \tag{3.5}$$

The power spectrum is used to estimate several cosmological parameters, because the current density perturbations are the result of the primordial density perturbations, imprinted in the CMB. Today the Planck experiment

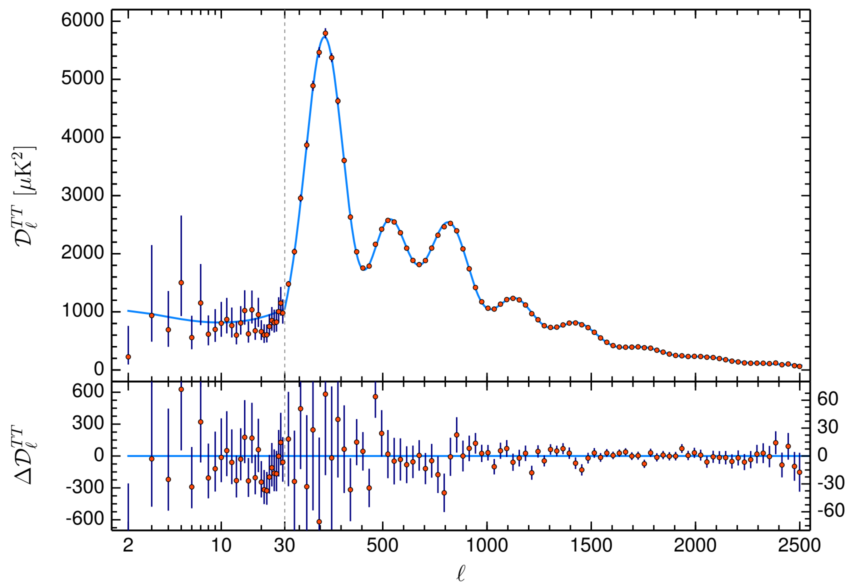

Figure 3.3: Temperature power spectrum recorded by the Planck experiment in 2018 [20]. On the x axis is the multipole ℓ, while on the y axis is the temperature variance. The cosmological model ΛCDM is assumed. Figure from [20, fig. 1].

[20] surveyed the CMB and performed precise measurements of its spectrum, which is shown in fig. 3.3. The Planck experiment assumes the cosmological model ΛCDM, which states that the Universe contains three major components: the cosmological constant Λ, related to dark energy, the cold dark matter and the ordinary matter, described by the Standard Model. The measurements of the different peaks of the spectrum allows us to compute the value of the density parameters of the Universe today:

- Radiation: $\Omega_{r0} \approx 5 \times 10^{-5}$;
- Matter: $\Omega_{m0} = 0.3153 \pm 0.0073$, that comprises baryonic matter ($\Omega_{b0} \approx 0.0493$) and dark matter ($\Omega_{DM0} \approx 0.264$);
- Dark Energy: $\Omega_{\Lambda 0} = 0.6847 \pm 0.0073$.

As we just mentioned, the CMB anisotropies can be linked to the primordial density perturbations, which are the seeds of the current density perturbations. Using the mathematical approach developed in app. B.5, we can trace how matter density perturbations have grown during the evolution of the Universe and compare the results with the observations, finally showing that the presence of dark matter was crucial to explain the current Universe structure. Adiabatic density perturbations can be described by temperature fluctuations of the same order, because of the relation $\rho \propto T^4$:

$$\delta_{dec} = \frac{\delta\rho}{\rho} \approx 3\frac{\Delta T}{T} \lessapprox 10^{-5} \,. \tag{3.6}$$

For baryonic matter, we can use eq. (B.51) and compute the value of the density perturbations today, δ_0:

$$\delta_0 = \frac{\delta_{dec}}{a_{dec}} a_0 \,. \tag{3.7}$$

For $a_0 = 1$, $\delta_{dec} \approx 10^{-5}$ and $a_{dec} \approx 1/1100$, we obtain

$$\delta_0 \approx 10^{-2} \,, \tag{3.8}$$

which does not agree with the observation, that is $\delta_0 \approx 10^2$: perturbations must grow faster. In the following, we will introduce the dark matter component in the game, and we will see how this modification can easily account for the observations. Baryonic perturbations start to grow only after equivalence, when the baryons decouple from radiation, see app. B.5 for reference. Dark matter, on the other hand, takes a different route. It decouples earlier than baryons, allowing its perturbations to grow right after the time of equivalence. In this way, dark matter perturbations are already present at the time of baryonic decoupling, and the *holes* left by the dark matter growth can act as seeds to speed up baryonic perturbations. This is the so-called baryon catch-up. Quantitatively, we can parametrize it from the Jeans equation in the general scenario of multi-component cosmological fluid, namely eq. (B.47), with $t > t_{dec}$,

$$\ddot{\delta}_{k,b} + 2H\dot{\delta}_{k,b} + 4\pi G\rho_0 \frac{k^2}{k_J^2}\delta_{k,b} - 4\pi G \sum_{i\in\{\text{ components }\}} \rho_{i,0}\delta_{k,i} = 0 \,, \tag{3.9}$$

where

$$\sum_{i\in\{\text{ components }\}} \rho_{i,0}\delta_{k,i} = \rho_{b,0}\delta_{k,b} + \rho_{DM,0}\delta_{k,DM} + \rho_{r,0}\delta_{k,r} \,, \tag{3.10}$$

We assume that the Universe is dominated by dark matter energy density, so $\rho_{DM,0} \gg \rho_{b,0}$, and, for growing perturbations, $k \ll k_J$, which allows us to neglect the term $v_s^2 k^2 a^{-2}$. We are left with

$$\ddot{\delta}_{k,b} + 2H\dot{\delta}_{k,b} - 4\pi G\rho_{DM,0}\delta_{k,DM} = 0 \,, \tag{3.11}$$

that has the following solution

$$\delta_{k,b}(t) = \delta_{k,DM}(t)\left(1 - \frac{a_{dec}}{a(t)}\right) . \tag{3.12}$$

We notice that the baryonic perturbations growth reaches the dark matter one, asymptotically as $a(t) \gg a_{dec}$. Taking into account this effect, we can find agreement with the observations.

3.1.5 An alternative: modified gravity paradigm

The dark matter paradigm is not the only way to explain the observations. Introducing a new kind of matter to account for the missing mass has given rise to speculations on the validity of Newton Law for such systems. The work of Mordehai Milgrom [91–93] has led to the development of the so-called MOND model, which modifies Newton Law for very low accelerations. The main feature of this model is its ability to describe stars and gas dynamics in galaxies without introducing a dark matter component. Its main result is the modification of the Newton Law:

$$F = m\frac{a^2}{a_0} \tag{3.13}$$

in the limit of very low accelerations, so that $a \ll a_0$, with $a_0 \approx 1.2 \times 10^{-10}\,\mathrm{m\,s^{-2}}$. The theory of MOND is quite successful in explaining the constant galactic rotation curves [94, 95] for hundreds of galaxies and manages to soften the mass discrepancy in galaxy clusters, though in that case it struggles to be successful, because it is necessary to consider a significant quantity of dark matter anyway. However, MOND has been developed in a non-relativistic framework and its extension to the relativistic regime is not straightforward. In 2004, the work of Jacob Bekenstein [96] led to the development of the Tensor-Vector-Scalar (TeVeS) gravity theory, which is the first proposal for a relativistic theory of MOND. Despite the attention it received, TeVeS has not been able to explain the Bullet Cluster observations, as we mentioned in § 3.1.3, while the presence of dark matter is able to explain it very easily.

3.2 Dark matter candidates

The dark matter paradigm results very successful in explaining the observations of the Universe. It relies on the presence of a new type of collisionless matter, on top of the known baryonic matter, with very weak, if not inexistent, interactions with it. Unfortunately, the dark matter nature is still unknown. By the late 1980s, an increasing number of physicists became interested in the dark matter problem and many theories were proposed. Among them, the most popular is the one assuming dark matter to be made of one or more new particles, beyond the ones described by the Standard Model. Many proposals for possible particle candidates have been made in the literature, and we are going to review the most popular ones in the following sections.

Assuming the particle nature of dark matter, we can make a first classification on the basis on how the particles were produced and evolved in the early Universe. Indeed, we can have thermal relics, so particles in thermal equilibrium with the Standard Model in the early Universe, or non-thermal relics, so particles that were never in thermal equilibrium with the Standard Model. In the former scenario, dark matter particles can be categorized on the basis of their decoupling temperature:

- cold dark matter (CDM): the decoupling from radiation happens after becoming non-relativistic;
- hot dark matter (HDM): the decoupling from radiation happens while still relativistic;
- warm dark matter (WDM): it is an intermediate scenario between HDM and CDM.

This distinction allows us to make predictions on the structure formation of the Universe. Given a particle with mass m becomes non-relativistic when $T \ll m$, heavier particles will become non-relativistic before lighter ones, so that we can conclude HDM candidates are heavier than WDM and CDM candidates. The relativistic nature of the HDM particles at the time of decoupling translates in higher velocities with respect to WDM and CDM particles. For this reason, HDM particles will erase small-scale perturbations. The speed of dark matter is the thermal velocity, or the dispersion velocity of the particles it is made of. We define the free-streaming length λ_{fs} as the distance a particle travels before perturbations start to grow [97]. A higher value of λ_{fs} favors the formation of large structures, because particles would be too fast to collapse in small structures. This is the reason why, in the case of HDM, the structure formation is characterized by a top-down approach, with the formation of large scale structures first, undergoing fragmentation into smaller structures, and structure formation begins relatively late [98–101]. On the other hand, CDM and WDM will follow a bottom-up approach, with the formation of small-scale structures first, which merge into larger ones. This has also the effect of making the structure formation to begin earlier [102, 103]. Additionally, computing the Jeans mass, see eq. (B.55) will provide us with the minimum value of mass that a perturbation must have in order to grow (see [65, 104] and references therein):

$$M_J = \frac{4}{3}\pi\rho_{DM}(t)\left[\frac{\pi v_s^2(t)}{4G\,\bar{\rho}(t)}\right]^{3/2}, \tag{3.14}$$

where $\bar{\rho}(t)$ is the background density of the Universe. This translates in the following values for the different kinds of dark matter:

$$M_{\mathrm{min}} \approx \begin{cases} (10^5 \text{ to } 10^6)\, M_\odot & \text{CDM,} \\ 10^{16}\, M_\odot & \text{HDM,} \\ 10^{11}\, M_\odot & \text{WDM.} \end{cases} \tag{3.15}$$

The simulation of the top-down and bottom-up scenarios showed that the top-down approach in not compatible with observations of the large scale structures, which means the HDM scenario can be ruled out. The cosmological Big Bang model described by the ΛCDM theory, briefly mentioned in § 3.1.4, assumes the dark matter component of the Universe to be cold.

Next to the non-relativistic nature for dark matter particles, a good dark matter candidate must be:

- stable on cosmological scales: otherwise it would have decayed by now;
- neutral or *milli-charged*: if dark matter particles were charged, they would have interacted with the electromagnetic field, and this would have impacted the behavior of dark matter density fluctuations, modifying the CMB spectrum; it is possible to set an upper limit on the possible electric charge of dark matter, equivalent to $Q_{\mathrm{DM}} < 3.5 \times 10^{-7}$ e, for $m_{\mathrm{DM}} > 1$ GeV, and $Q_{\mathrm{DM}} < 4.0 \times 10^{-7}$ e, for $m_{\mathrm{DM}} < 1$ GeV [105];
- consistent with Big Bang Nucleosynthesis (BBN): the presence of dark matter particles would have affected the formation of light elements during BBN, and it is possible to impose limits on the dark matter energy density at the time of BBN [106].

3.2.1 Relic neutrinos

Unexpectedly, the Standard Model is able to provide us with a great thermal dark matter candidate: the neutrino. Neutrinos fulfill all the requirements a dark matter candidate must have: they are stable, neutral, and they interact weakly with other particles. Cosmological neutrinos are referred to as *relic neutrinos*, because they are the result of the decoupling from the primordial plasma (see § 3.3 for reference to the decoupling mechanism) and has formed what it is known as the Cosmic Neutrino Background [107]. Neutrinos decoupling happened when the temperature of the Universe was about $T_{\nu,\mathrm{dec}} \approx 1$ MeV, and they were relativistic at that time, so they are HDM candidates. Their nature as HDM already excludes them as good dark matter candidates, for the arguments on structure formation we discussed in the previous section. After decoupling, neutrinos were no more in thermal equilibrium with electrons and photons, and they continued to cool as relativistic particles until the global temperature dropped below the mass of the electron, so that they were no more part of the relativistic degrees of freedom. At that point, electrons and positrons annihilated, transferring their entropy to photons, which became hotter than neutrinos. Computing the effective degrees of freedom of the components in thermal equilibrium we have:

$$g_\star^{th}(m_e < T < T_{\nu,dec}) = 2 + \frac{7}{8}(2 \cdot 2) = \frac{11}{2}\,, \tag{3.16}$$

$$g_\star^{th}(T < m_e) = 2\,, \tag{3.17}$$

so that T_γ changed from $T_\gamma = T_\nu$ to

$$T_\gamma = \left(\frac{11}{4}\right)^{1/3} T_\nu\,. \tag{3.18}$$

We can now apply eq. (B.25) to compute $n_\nu(T_0)$. Finally, it is possible to obtain their relic density:

$$\Omega_\nu h^2 = \sum_{i \in \{e,\mu,\tau\}} \frac{m_i}{93\,\text{eV}}\,. \tag{3.19}$$

From the Planck experiment [108] it is possible to constrain the sum of neutrino masses, obtaining

$$\sum_{i \in \{e,\mu,\tau\}} m_i < 0.12\,\text{eV}\,, \tag{3.20}$$

so that their relic density results:

$$\Omega_\nu h^2 < 0.0013\,, \tag{3.21}$$

that is too low to account for dark matter relic density, see eq. (3.63) [20].

3.2.2 Sterile neutrinos

Standard Model neutrinos are too light to account for the whole dark matter relic density. However, it is possible to extend the Standard Model with the addition of new neutrinos, called sterile neutrinos ν_s, which may have larger mass as well as small interactions with the Standard Model particles. We already introduced sterile neutrinos when discussing the seesaw mechanism for the generation of neutrinos masses, in § 2.5.2. The introduction of right-handed sterile components next to the Standard Model left-handed neutrinos is a quite natural extension of the Standard Model. In 1994, Dodelson and Widrow [109] proposed sterile neutrinos with a keV mass scale to be good warm dark matter candidate. Differently from many other dark matter candidates, they were not in thermal equilibrium with the Standard Model in the early Universe, due to their feeble interactions. A promising search strategy for sterile neutrinos is the detection of the γ-ray line produced by the radiative loop-induced decay of the sterile neutrino into a photon and a Standard Model neutrino $\nu_2 \to \nu_1 + \gamma$ [110], where ν_1, ν_2 are mass eigenstates with $m_{\nu_1} < m_{\nu_2}$. The produced γ-ray line is at half of the ν_s mass.

3.2.3 Axions

Axions are related to the strong CP problem, briefly introduced in § 2.4, and related to the addition of the following CP-violating term to the QCD Lagrangian, from eq. (2.38),

$$\mathcal{L}_{QCD} \supset \vartheta \frac{g_s^2}{32\pi^2} G^b_{\mu\nu} \widetilde{G}^{b\mu\nu} . \tag{3.22}$$

The effects caused by this term (in particular on the neutron electric dipole moment) are not observed, so the value of ϑ must be very small, but there is no natural explanation in the Standard Model for it. In 1977 Roberto Peccei and Helen Quinn introduced an extension of the Standard Model where a new $U(1)$ global symmetry is spontaneously broken at the energy scale f_a. This effect makes possible to drive the value of ϑ to zero [24] naturally. The axion a is the Goldstone boson associated with the spontaneous breaking of the $U(1)$ symmetry, and we can write its interactions as:

$$\mathcal{L}_a = -\frac{g_s^2}{32\pi^2} \frac{a}{f_a} G^b_{\mu\nu} \widetilde{G}^{b\mu\nu} . \tag{3.23}$$

The axion mass is proportional to f_a^{-1}. Axions can be good dark matter candidates, they are light, stable and can interact weakly with other particles. In general, they are not thermal relics.

3.2.4 Supersymmetric particles

The MSSM has been briefly introduced in § 2.6.3, and it is able to provide interesting dark matter candidates. Indeed, the supersymmetric particle with the smaller mass, known as the LSP, is stable and represents one of the most promising candidates. Among the LSPs, the most popular are the sneutrino and the neutralino.

Sneutrino

Sneutrinos are the supersymmetric partners of the neutrinos. They are sfermions, and, if they are LSP, there are certain models in which they can be good dark matter candidates [111].

Neutralino

Neutralinos are four Majorana fermions, they are indicated by $\tilde{\chi}_i$, with $i \in \{1, 2, 3, 4\}$. In the MSSM, neutralinos are obtained as the mass eigenstates from the mixing of the zino, photino and the neutral higgsinos. In theories where R-parity is conserved, the lightest neutralino is stable and can be a good thermal dark matter candidate. The neutralino is an excellent example of a Weakly Interacting Massive Particle (WIMP), which will be examined in § 3.4.

3.2.5 Primordial black holes

Primordial Black Holes (PBH) are black holes that formed in the early Universe, due to the collapse of overdensities, generated during inflation. They can be good dark matter candidates, because they behave as non-baryonic matter, and, despite they are subjected to evaporation via Hawking radiation, they can survive until today. Indeed, PBH with an initial mass of $M_{\rm PBH} \gtrapprox 10^{15}$ g can be considered stable with respect to the age of the Universe. It is possible to detect PBHs, by exploiting their observable effects, for example [112]:

- their evaporation can be the source of γ and cosmic rays (CRs), which could be observed and that would modify the CMB spectra;
- they can be observed through the microlensing effect, when they pass in front of a star;
- gravitational waves detection from black holes mergers can be used to constrain the PBH abundance.

3.3 Deciphering Universe dynamics: the Boltzmann equation

Thermal equilibrium has been a key element in the description of the early Universe and its evolution. Different species were in thermal equilibrium with each other, until the progressive cooling of the Universe made them decouple and evolve independently. These phenomena are the building blocks on which the actual Universe took its shape. Thermal equilibrium is maintained as long as the thermalization processes are efficient enough with respect to the expansion of the Universe. These processes encompass a variety of interactions, including the scattering between different species and the annihilation or production of a species. Their efficiency can be quantified by the interaction rate γ, and parametrized as

$$\Gamma = n\sigma v \,, \tag{3.24}$$

where n is the number density of a certain species, σ is the interaction cross section and v is the relative velocity of the interacting particles. Conversely, the expansion of the Universe is quantified by the Hubble parameter H, defined in eq. (B.3). As long as the interaction rate exceeds the expansion rate, $\Gamma > H$, thermal equilibrium is maintained. In app. B we introduced the main concepts and basic equations of the equilibrium thermodynamics. In particular, during Universe expansion, the number density of a certain species decreases with the temperature, see eqs. (B.25) and (B.28), so there will be a time, known as decoupling, when $\Gamma < H$, meaning a species has decoupled from thermal equilibrium. Around and after decoupling, the description of the trend of the number density and energy of the species requires particular care.

In general, it is possible to follow closely the evolution of a species by solving the Boltzmann equation:

$$\mathbf{L}[f] = \mathbf{C}[f] \,, \tag{3.25}$$

where $f = f(E, t)$ is the phase-space density of the species, $\mathbf{L}$ is the Liouville operator and $\mathbf{C}$ is the collision operator, which takes into account the interactions between the species and the other components of the Universe. We integrate eq. (3.25) over the momentum space:

$$\frac{g}{(2\pi)^3} \int d^3p \, \mathbf{L}[f] = \frac{g}{(2\pi)^3} \int d^3p \, \mathbf{C}[f] \,, \tag{3.26}$$

and using the following definition of the Liouville operator

$$\mathbf{L}[f] = E \frac{\partial f}{\partial t} - H |\mathbf{p}|^2 \frac{df}{dE} \,, \tag{3.27}$$

and the definition of the number density in terms of $f(E, t)$, recalling eq. (B.16):

$$n = \frac{g}{(2\pi)^3} \int d^3p \, f(E, t) \,, \tag{3.28}$$

it is possible to obtain the following expression:

$$\frac{dn}{dt} + 3Hn = \frac{g}{(2\pi)^3} \int d^3p \, \frac{\mathbf{C}[f]}{E} \,. \tag{3.29}$$

The second member of eq. (3.29) can be expanded in a lengthy expression, assuming the process $\chi + a + b + \cdots \leftrightarrow i + j + \cdots$, focusing on the evolution of the particle χ:

$$\frac{g}{(2\pi)^3}\int dp_\chi \frac{\mathbf{C}[f]}{E_\chi} = -\int d\Pi_\chi\, d\Pi_a\, d\Pi_b \cdots d\Pi_i\, d\Pi_j \cdots \\ \times (2\pi)^4 \delta^4(p_\chi + p_a + p_b \cdots - p_i - p_j \cdots) \\ \times \Big[|\mathcal{M}|^2_{\chi+a+b+\cdots\to i+j+\cdots} f_a f_b \cdots f_\chi (1 \pm f_i)(1 \pm f_j) \cdots \\ - |\mathcal{M}|^2_{i+j+\cdots\to\chi+a+b+\cdots} f_i f_j \cdots (1 \pm f_a)(1 \pm f_b) \cdots (1 \pm f_\chi) \Big] , \tag{3.30}$$

where f_i, f_j, f_a, f_b, f_χ are the phase-space densities of the respective species, $\mathcal{M}$ is the matrix element of the process and the $+$ sign is for bosons, while $-$ is for fermions. The volume element $d\Pi$ is defined as:

$$d\Pi \doteq \frac{g}{(2\pi)^3} \frac{d^3 p}{2E} . \tag{3.31}$$

The conservation of energy and momentum is ensured by the presence of the δ function. We are not interested in the technicalities of the development of the collision operator beyond the form indicated in eq. (3.30). In general, it is possible to write the collision operator as a combination of a term $\mathbf{C}_{\text{el}}$ related to elastic scattering, and a term $\mathbf{C}_{\text{ann}}$ keeping into account annihilations. Elastic collisions are responsible for maintaining the kinetic equilibrium, while inelastic collisions keep the chemical equilibrium. In [113] it is possible to find the complete description of $\mathbf{C}_{\text{el}}$ and $\mathbf{C}_{\text{ann}}$.

Now we will focus on the computation of the relic abundance of the species χ, with number density n and mass m. When a species decouples from the thermal bath, its number density is no more described by the equilibrium distribution, namely eqs. (B.25) and (B.28), the species freezes-out and its relic density remains constant. For the canonical freeze-out, a number of approximating assumptions are usually applied, simplifying significantly eq. (3.29) and its numerical solution. The main assumption is the existence of the kinetic equilibrium between χ and the thermal bath (made by the Standard Model particles), so that the distribution of the species is proportional to the equilibrium one, $f \propto f_{\text{eq}}$. This assumption allows simplifying eq. (3.29) into an ordinary differential equation for the number density of χ, the well-known Zeldovich-Okun-Pikelner-Lee-Weinberg equation [114, 115]:

$$\frac{dn}{dt} + 3Hn = -\langle \sigma v \rangle \left(n^2 - n_{\text{eq}}^2 \right) , \tag{3.32}$$

where $\langle \sigma v \rangle$ is the thermally averaged cross-section at temperature T. In the non-relativistic regime, the dark matter particle phase-space density follows

Maxwell-Boltzmann statistics $f_{eq} \approx \exp\left(-E(p)/T\right)$ and $\langle\sigma v\rangle_T$ reads:

$$\langle\sigma v\rangle = \int_{4m^2}^{\infty} ds \frac{s\sqrt{s-4m^2}\, K_1(\sqrt{s}/T)\sigma v}{16\, T m^4 K_2^2(m/T)}, \tag{3.33}$$

where K_i are the modified Bessel functions of order i. It is convenient to introduce the dimensionless variable Y, called yield or comoving number density, defined as:

$$Y \doteq \frac{n}{s}, \tag{3.34}$$

where s is the entropy density of the Universe. Introducing the entropy allows us to factorize the time dependence of certain quantities, indeed, given entropy is conserved, the term sa^3 is constant. It is possible to rewrite both members of eq. (3.32) in terms of Y:

$$\frac{dn}{dt} + 3Hn = \frac{1}{a^3}\frac{d}{dt}\left(na^3\right) = \frac{1}{a^3}\frac{d}{dt}\left(Ysa^3\right) = s\frac{dY}{dt}, \tag{3.35}$$

$$\langle\sigma v\rangle\left(n^2 - n_{eq}^2\right) = \langle\sigma v\rangle s^2\left(Y^2 - Y_{eq}^2\right), \tag{3.36}$$

so that

$$\frac{dY}{dt} = -\langle\sigma v\rangle s\left(Y^2 - Y_{eq}^2\right). \tag{3.37}$$

We perform another substitution, introducing the dimensionless variable $x \doteq m/T$, which is better suited to keep track of the relativistic/non-relativistic nature of χ. Assuming the decoupling of χ happens in a radiation-dominated universe, we can write the Hubble parameter using eq. (B.14a):

$$H(x) = \frac{\dot{a}}{a} = \frac{1}{2t}, \tag{3.38}$$

while, using eq. (B.6a), with $k = 0$, $\rho_b \ll \rho_r$ and knowing $\rho_r \propto T^4$, as in eq. (B.26),

$$H = \frac{H(m)}{x^2}. \tag{3.39}$$

Finally, we obtain the Jacobian:

$$\frac{d}{dt} = \frac{H(m)}{x}\frac{d}{dx}. \tag{3.40}$$

It is important to point out that we considered an approximation in the previous steps. The exact dependence of ρ_r on T is given by:

$$\rho_r \propto g_\star(T) T^4 \tag{3.41}$$

while to obtain eq. (3.39) we implicitly assumed $g_\star(T)$ to be constant in the temperature range of interest. In reality, $g_\star(T)$ is not constant, but varies with the temperature on the basis of the different species that are in thermal equilibrium at that temperature. However, our approximation is valid in case we assume a temperature variation in a range in which $g_\star(T)$ may be considered constant, which is a usually the case. A similar discussion can be made for the entropy density s, in particular, it is possible to write:

$$s = \frac{s(m)}{x^3} \,. \tag{3.42}$$

Putting it all together, we obtain a simpler form of eq. (3.37):

$$\frac{dY}{dx} = -\frac{\lambda(x)}{x^2}\left(Y^2 - Y_{eq}^2\right) , \tag{3.43}$$

where $\lambda(x)$ is defined as:

$$\lambda(x) \doteq \frac{s(m)\langle\sigma v\rangle(x)}{H(m)} \,. \tag{3.44}$$

The parameter $\lambda(x)$ depends in general on T, because of the temperature dependence of the thermally averaged cross-section. In this form, the Boltzmann equation is a particular type of Riccati equation, no analytical solution is known, but it is possible to solve it numerically. However, we can draw some qualitative conclusions. The equilibrium yield Y_{eq} has the following behavior:

$$Y_{eq}(x) = \frac{45}{2} g_{eff} \frac{\zeta(3)}{g_{\star S}} \qquad \text{relativistic,} \tag{3.45}$$

$$Y_{eq}(x) = \frac{45}{2\pi^4}\sqrt{\frac{\pi}{8}}\frac{g}{g_{\star S}} x^{3/2}\exp(-x) \qquad \text{non-relativistic.} \tag{3.46}$$

When the particle becomes non-relativistic, its number density drops exponentially, because there is not enough energy in the thermal bath so that χ can be produced from the other particles. We can express the interaction rate Γ in terms of $\lambda(x)$:

$$\Gamma = \langle\sigma v\rangle n_{eq} = \frac{\langle\sigma v\rangle Y_{eq}\, s(m)}{x^3} = \lambda(x) Y_{eq} \,. \tag{3.47}$$

As the temperature becomes lower (x increases), Γ evolves as

$$\Gamma(x) \propto x^{-3} \qquad \text{relativistic,} \tag{3.48}$$

$$\Gamma(x) \propto x^{-3/2}\exp(-x) \qquad \text{non-relativistic,} \tag{3.49}$$

so it decreases in both scenarios. We can write eq. (3.43) in terms of Γ and H:

$$\frac{x}{Y_{eq}}\frac{dY}{dx} = -\frac{\Gamma}{H}\left(\frac{Y^2}{Y_{eq}^2} - 1\right). \tag{3.50}$$

The ratio Γ/H is called effectiveness of annihilations, and it is a measure of the efficiency of the annihilations with respect to the expansion of the Universe. When Γ/H is large, annihilations are efficient, thermal equilibrium is maintained and the left-hand side of eq. (3.50) is negligible with respect to the right-hand side, so that Y tracks the equilibrium density Y_{eq}. On the contrary, when Γ/H is small, annihilations are inefficient, the right-hand side of eq. (3.50) is negligible, so that Y remains constant and the species freezes-out. This roughly happens when:

$$\frac{\Gamma(x)}{H(x)} \approx 1 \Rightarrow x = x_f\,, \tag{3.51}$$

where x_f is the point of thermal decoupling and $T_f = m\,x_f$ is the freeze-out temperature. As a result, it follows that:

$$Y(x) \approx Y_{eq}(x) \quad \text{for } x < x_f\,, \tag{3.52}$$

$$Y(x) \approx Y_{eq}(x_f) \quad \text{for } x > x_f\,. \tag{3.53}$$

The freeze-out calculation is different for the different kinds of dark matter:

- HDM: freeze-out takes place while the species is still relativistic, implying $x_f < 1$. We can compute the final value of Y, which results $Y_\infty = Y_{eq}(x_f)$.
- CDM: freeze-out occurs when the species is non-relativistic. The equilibrium density of a non-relativistic species drops exponentially until freeze-out, according to eq. (3.53). When reaching freeze-out, $Y(x > x_f) = Y_{eq}(x_f)$ and, given the equilibrium density is still exponentially suppressed, $Y(x > x_f) \gg Y_{eq}(x)$. The Boltzmann equation can be written as:

  $$\frac{dY}{dx} = -\frac{\lambda}{x^2}Y^2\,, \tag{3.54}$$

  that can be simply integrated from x_f to $+\infty$. We can obtain a rough estimate of $Y(x > x_f)$ if we assume λ to be constant in x, that implies $\langle\sigma v\rangle(x) = \langle\sigma v\rangle_0$. So that

  $$Y(x > x_f) \approx \frac{x_f}{\lambda}\,, \tag{3.55}$$

  by assuming $Y(x_f) \gg Y(x > x')$. That means a larger λ translates into a smaller relic abundance, because of the direct proportionality between λ and the interaction rate Γ.

Now we want to focus on the case of a CDM candidate and we want to solve the Boltzmann equation numerically. For a cold relic, we expand the thermally averaged cross section in eq. (3.33) in the non-relativistic regime:

$$\langle \sigma v \rangle = a + b v^2 + \mathcal{O}(v^4)\,, \tag{3.56}$$

where a represents the s-wave contribution, and b is the p-wave one. Higher order contributions may be present, but they are suppressed by higher powers of v, and usually negligible. Given the non-relativistic velocity can be related to the temperature,

$$v = \sqrt{\frac{2T}{m}} = \sqrt{\frac{2}{x}}\,, \tag{3.57}$$

it is possible to write the $\langle \sigma v \rangle$ in terms of x:

$$\langle \sigma v \rangle = \langle \sigma v \rangle_0\, x^{-n}\,. \tag{3.58}$$

We can write eq. (3.43) making the dependence on x explicit:

$$\frac{dY}{dx} = -\frac{\lambda_0}{x^{n+2}}\left(Y^2 - Y_{eq}^2\right), \tag{3.59}$$

where λ_0 is defined as:

$$\lambda_0 \doteq \frac{s(m)\langle \sigma v \rangle_0}{H(m)}\,. \tag{3.60}$$

We know that before freeze-out $Y \approx Y_{eq}$, so we can impose the initial condition $Y(x = 1) = Y_{eq}(x = 1)$ and integrate from $x = 1$ to $x \gg x_f$. In fig. 3.4 we show several examples of solutions of the Boltzmann equation, comparing different cases of dark matter masses and annihilation cross sections. In all cases, we assumed $g = 2$ degrees of freedom, typical for a Majorana dark matter candidate, while $g_\star$ and $g_{\star S}$ depend on the temperature. It is possible to obtain an estimation for the freeze-out point x_f, by solving explicitly

$$\Gamma(x_f) = H(x_f)\,. \tag{3.61}$$

We can plug in the expressions for Γ and H in terms of x, using the eqs. (3.39), (3.42), (3.44), (3.46), (3.47), (3.58), (B.31) and (B.39), obtaining the following expression:

$$\sqrt{\frac{\pi}{8}} g m^3 \langle \sigma v \rangle_0\, x_f^{-3/2-n} \exp(-x_f) = \sqrt{\frac{8\pi G}{90}}\pi\sqrt{g_\star(x_f)}\,\frac{m^2}{x_f^2}\,, \tag{3.62}$$

which can be solved numerically. For simplicity, we assume s-wave only contributions ($n = 0$). In principle, the value of x_f depends on the choice of

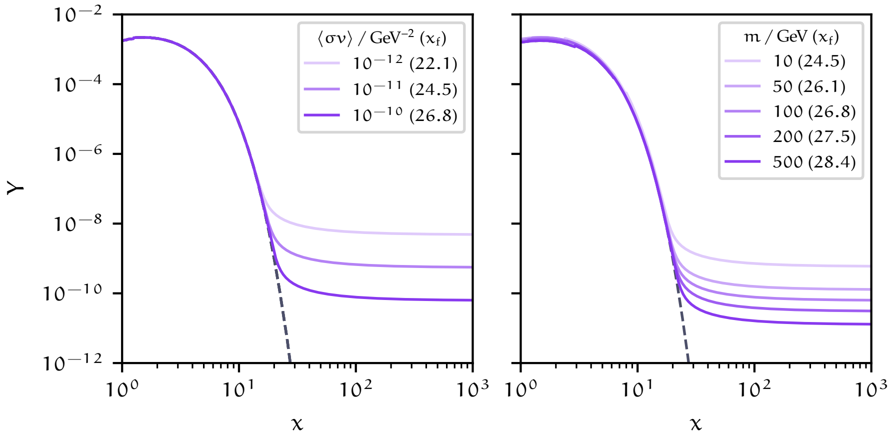

Figure 3.4: Numerical solutions for the Boltzmann equation, the different lines represent different cases of masses and cross sections. The gray dashed line represents the equilibrium yield Y_{eq}. The value of the freeze-out point x_f is indicated in parentheses for each case. LEFT PANEL: different values of the annihilation cross section $\langle\sigma v\rangle$, $m = 100\,\text{GeV}$. RIGHT PANEL: different values of the dark matter mass m, $\langle\sigma v\rangle = 10^{-10}\,\text{GeV}^{-2}$.

$\langle\sigma v\rangle$ and the mass m, but we can verify that it is practically insensitive to them if we choose values typical of a weakly coupled particle. In tab. 3.1, we list some values of x_f for typical masses and cross sections.

Table 3.1: Values of x_f for different masses and cross sections for a weak-scale coupled particle.

m / GeV	$\langle\sigma v\rangle$ / GeV^{-2}	x_f
10	10^{-9}	26.8
	10^{-10}	24.5
50	10^{-9}	28.4
	10^{-10}	26.1
100	10^{-9}	29.2
	10^{-10}	26.8
1000	10^{-9}	31.5
	10^{-10}	29.2

3.4 The miracle of WIMPs

In the previous chapter, we studied the dark matter freeze-out, showing that the comoving relic abundance after freeze-out remains constant. The Planck experiment recently performed the measurement of the relic density today [20]:

$$\Omega h^2|_{\text{Planck}} = 0.1200 \pm 0.0012\,. \tag{3.63}$$

This value makes possible to infer strong constraints on the parameter space of dark matter models. From a theoretical point of view, we can try to match the relic density value, by solving the Boltzmann equation as we have done in the previous section considering a CDM candidate interacting with the Standard Model with a magnitude compatible with the electroweak interaction, the so-called WIMP dark matter. To compute the abundance of our candidate today, we need to calculate $\rho_{\text{DM}}(T_0)$, recalling eqs. (B.8), (B.13b) and (B.29):

$$\begin{aligned}\rho_{\text{DM}}(T_0) = \rho_{\text{DM}}(T')\left(\frac{a'}{a_0}\right)^3 &= m\,Y(x')\,s(T')\left(\frac{a'}{a_0}\right)^3\\ &= m\,Y(x')\,\frac{g_{\star S}(T')}{g_{\star S}(T_0)}\,s(T_0)\left(\frac{a'T'}{a_0T_0}\right)^3,\end{aligned} \tag{3.64}$$

where the temperature T' is picked at a sufficiently late time after dark matter freeze-out, so that it is possible to assume $Y(x') \approx Y_\infty$. Following from the conservation of entropy, eq. (B.44), we have:

$$\left(\frac{a'T'}{a_0T_0}\right)^3 = \frac{g_{\star S}(T_0)}{g_{\star S}(T')}\,. \tag{3.65}$$

Finally, if we assume contributions to the cross section as coming only from s-wave, we can use the approximate solution in eq. (3.55) the relic density can be obtained from eq. (B.9)

$$\begin{aligned}\Omega_{DM}h^2 &\approx h^2\, m\, Y_\infty s_0 \frac{8\pi G}{3H_0^2} = h^2\, m\, x_f \frac{H(m)}{s(m)\langle\sigma v\rangle_0} s_0 \frac{8\pi G}{3H_0^2} \\ &\approx \frac{x_f}{\langle\sigma v\rangle_0}\sqrt{g_\star(m)}\left(\frac{8\pi G}{3}\right)^{3/2}\frac{\pi}{\sqrt{30}}\frac{T_0^3}{30}\frac{h^2}{H_0^2}\,,\end{aligned} \tag{3.66}$$

where we used the definition of the Hubble parameter and the following expression:

$$\frac{s(T_0)}{s(m)} = \underbrace{\frac{g_{\star S}(T_0)}{g_{\star S}(m)}}_{\approx\frac{3.91}{106.75}}\frac{T_0^3}{m^3} \approx \frac{1}{30}\frac{T_0^3}{m^3}\,. \tag{3.67}$$

We set $g_{\star S}(m) \approx 106.75$, corresponding to the scenario where all Standard Model particles are in thermal equilibrium, which is a good approximation when $m \gtrsim 10^2\,\text{GeV}$, consistent with the assumption of a weak-scale dark matter candidate. Indeed, it is possible to compute the value of the relativistic degrees of freedom today in the following way:

$$g_{\star S}(T_0) = g_{\star S}^{th}(T_0) + g_{\star S}^{dec}(T_0) = 2 + \frac{7}{8}\cdot 2\cdot 3\cdot\left(\frac{4}{11}\right) \approx 3.91\,, \tag{3.68a}$$

$$g_{\star}(T_0) = g_{\star}^{th}(T_0) + g_{\star}^{dec}(T_0) = 2 + \frac{7}{8}\cdot 2\cdot 3\cdot\left(\frac{4}{11}\right)^{4/3} \approx 3.36\,, \tag{3.68b}$$

where we used the fact that the thermal bath is made of only photons, while neutrinos are decoupled from it, despite being relativistic, so that their temperature follows eq. (3.18). Now we can substitute the real values of the constants in eq. (3.66), in particular*:

$$H_0 = 2.133\times 10^{-42}\,\text{GeV}\cdot h\,, \tag{3.69a}$$

$$M_{Pl} \doteq \frac{1}{\sqrt{8\pi G}} = 2.435\times 10^{18}\,\text{GeV}\,, \tag{3.69b}$$

$$T_0 = 2.726\,\text{K}\cdot k_B = 2.349\times 10^{-13}\,\text{GeV}\,. \tag{3.69c}$$

The relic density of a dark matter WIMP candidate is then given by:

$$\Omega_{DM}h^2 \approx 0.12\,\frac{x_f}{20}\sqrt{\frac{g_\star(m)}{100}}\,\frac{1.2\times 10^{-9}\,\text{GeV}^{-2}}{\langle\sigma v\rangle}\,, \tag{3.70}$$

*The constant M_{Pl} is known as (reduced) Planck mass, while k_B is the Boltzmann constant.

so, choosing a typical value for an electroweak cross section, and a freeze-out temperature compatible with a dark matter particle with a mass scale of the order of the weak scale, we obtain a value of the relic density compatible with observations. This is the so-called WIMP miracle. Moreover, the relic density depends (approximately) only on the thermally-averaged cross section:

$$\Omega_{DM} h^2 \underset{\approx}{\propto} \frac{1}{\langle \sigma v \rangle} \,. \tag{3.71}$$

3.5 Coannihilation

In the previous section, we studied the freeze-out of a dark matter candidate, implicitly assuming it was the only dark matter particle in the thermal bath. In a general scenario, this may not be the case, indeed, a plethora of new particles may be present in the thermal bath. This is an important point, and it lays the foundations of what happens in the case of rich dark sectors, characterized by many particles interacting with each other, under, possibly, a new dark force, while at the same time being able to communicate to the Standard Model with special mediators. Let us consider a set of new particles χ_i, with $i \in \{1, \ldots, N\}$, where we set the mass hierarchy such that, $m_{\chi_i} < m_{\chi_j}$, for any pair $i < j$. In such case, the dark matter candidate will be the lightest particle, χ_1, while the other particles will decay into it. The heavier particles χ_j, $j \in \{2, \ldots, N\}$ are known as coannihilating partners or coannihilators. When all these particles are in the thermal bath, the following processes are possible:

$$\chi_i \chi_j \leftrightarrow f f' \,, \tag{3.72a}$$

$$\chi_i f \leftrightarrow \chi_j f \,, \tag{3.72b}$$

$$\chi_j f \leftrightarrow \chi_j f f' \,, \tag{3.72c}$$

assuming $i < j$, and where f and f' are Standard Model particles. The first processes, eq. (3.72a), are known as coannihilation processes, the ones in eq. (3.72b) are the scattering processes, sometimes known also as conversions, while the latter in eq. (3.72c) are decays (and in principle inverse decays) of the coannihilators [116]. Coannihilator decays are usually fast, so that today we expect only the lightest particle to be present in the Universe. The presence of multiple processes in the thermal bath affects the freeze-out mechanism, both by opening new channels for dark matter depletion, or adding new sources in the form of the decay. In general, to perform the computation of the relic density, it will be necessary to write a set of N Boltzmann equations:

$$\dot{n}_i + 3Hn_i = -\sum_{j,f}\Big[\langle\sigma_{ij}v\rangle\big(n_i n_j - n_i^{eq} n_j^{eq}\big) \\ - \big(\langle\sigma'_{ij}v\rangle n_i n_f - \langle\sigma'_{ji}v\rangle n_j n_f\big) - \Gamma_{ij}\big(n_j - n_j^{eq}\big)\Big]\,, \tag{3.73}$$

where n_i is the number density of the species χ_i and n_i^{eq} is their equilibrium number density. We also define the following quantities, related to the processes in eq. (3.72):

$$\sigma_{ij} = \sigma(\chi_i\chi_j \leftrightarrow ff')\,, \tag{3.74a}$$
$$\sigma'_{ij} = \sigma(\chi_i f \leftrightarrow \chi_j f)\,, \tag{3.74b}$$
$$\Gamma_j = \Gamma(\chi_j f \leftrightarrow \chi_j ff')\,, \tag{3.74c}$$

The set of Boltzmann equations written in the form in eq. (3.73) keep into account any term that can cause a change in number density. Since all χ_j heavier than χ_1 will eventually decay into it, we can simplify the computation, by considering the total number density:

$$n = \sum_{i=1}^{N} n_i\,, \tag{3.75}$$

Additionally, it is possible to reduce eq. (3.73) to a single equation, according to some assumptions on the rates of the processes [116]. First, if conversion processes between the dark matter and the coannihilating partners are efficient during freeze-out, then the chemical equilibrium between the species is maintained, and each abundance tracks its equilibrium value:

$$\frac{n_i}{n_i^{eq}} \approx \frac{n_j}{n_j^{eq}}\,, \tag{3.76}$$

Using this approximation, it is possible to write a single Boltzmann equation for the total number density n:

$$\dot{n} + 3Hn = -\langle\sigma_{\mathrm{eff}}v\rangle\big(n^2 - n^{eq\,2}\big)\,, \tag{3.77}$$

where we define σ_{eff} as:

$$\sigma_{\mathrm{eff}} \doteq \sum_{i,j}\sigma_{ij}\frac{n_i^{eq} n_j^{eq}}{n^{eq\,2}}\,. \tag{3.78}$$

We can expand the previous term, obtaining:

$$\begin{aligned}\sigma_{\text{eff}} &= \sum_{i,j} \sigma_{ij} \frac{g_i g_j \left(\frac{m_{\chi_i}}{m_{\chi_1}}\right)^{3/2} \left(\frac{m_{\chi_j}}{m_{\chi_1}}\right)^{3/2} \exp\left(-\frac{m_{\chi_i}+m_{\chi_j}-2m_{\chi_1}}{T}\right)}{\left(\sum_{k=1}^{N} g_k \left(\frac{m_{\chi_k}}{m_{\chi_1}}\right)^{3/2} \exp\left(-\frac{m_{\chi_k}-m_{\chi_1}}{T}\right)\right)^2} \\ &= \sum_{i,j} \sigma_{ij} \frac{g_i g_j (1+\Delta_i)^{3/2} (1+\Delta_j)^{3/2} \exp\left(-x(\Delta_i+\Delta_j)\right)}{\left(\sum_{k=1}^{N} g_k (1+\Delta_k)^{3/2} \exp(-x\Delta_k)\right)^2} \\ &= \sum_{i,j} \sigma_{ij} \frac{g_i g_j}{g_{\text{eff}}^2} (1+\Delta_i)^{3/2} (1+\Delta_j)^{3/2} \exp\left(-x(\Delta_i+\Delta_j)\right),\end{aligned} \tag{3.79}$$

where $\Delta_i \doteq (m_{\chi_i} - m_{\chi_1})/m_{\chi_1}$, $x = m_{\chi_1}/T$ and

$$g_{\text{eff}} \doteq \sum_{k=1}^{N} g_k (1+\Delta_k)^{3/2} \exp(-x\Delta_k)\,. \tag{3.80}$$

The contribution of the heavier coannihilators depends on the mass difference with the dark matter candidate. Coannihilations are significant only in scenarios characterized by small mass differences, typically in the range $\Delta_i \lessapprox (10 \text{ to } 20)\,\%$, otherwise their contribution is exponentially suppressed, or it is also said Boltzmann-suppressed. An advantage of this scenario is that it allows us to write the Boltzmann equation neglecting the conversions terms, that are efficient and maintain the chemical equilibrium.

However, there are cases in which this approximation is not valid, and the chemical equilibrium is not maintained during freeze-out. This can be the scenario when the coupling between the dark matter and the coannihilators is very small. In such case, the chemical decoupling of the dark sector from the Standard Model happens after the chemical decoupling of the dark matter within the dark sector itself. While in the previous scenario, the freeze-out of the dark matter was only dependent on the annihilations shutting off, in this case the main processes determining the dark matter freeze-out are the conversions. This is known as the so-called conversion-driven freeze-out [117] or coscattering [118]. This is a scenario particularly relevant in models where dark matter self-annihilations are suppressed, while coannihilators annihilations are dominant, and coannihilators decays are forbidden or negligible.

3.6 Hunting for dark matter

The search of dark matter is a very active field of research, with many experiments looking for a variety of signals. Assuming the actual observed relic density comes from the freeze-out process, or from a similar mechanism, implies that dark matter can interact not only gravitationally. The interaction

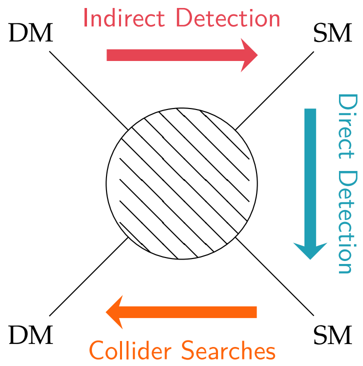

Figure 3.5: Graphical representation of the detection methods of dark matter (indicated by DM), involving interactions with the Standard Model (indicated by SM). The arrows go from the initial states to the final ones. Notice that the diagrams is an exemplification, and it always shows two initial states, while, in the case of indirect detection, also dark matter decays are relevant.

of dark matter with other particles is the key to perform its search. The main strategy is to look for any interactions with the Standard Model, either directly or indirectly, or to possibly produce dark matter. There are three main ways to search for dark matter:

- indirect detection: aims to study the products of dark matter annihilations or decay;
- direct detection: aims to detect dark matter elastic scattering off atomic nuclei or Standard Model's particles;
- collider searches: aims to produce dark matter particles in colliders or beam dump experiments.

Usually, these strategies are represented graphically in a diagram, where the arrows go from the initial states to the final ones, see fig. 3.5. The next sections will be dedicated to the description of each strategy, with a particular focus on indirect detection, which is the most studied in this dissertation.

3.7 Indirect detection

Indirect searches focus on detecting the products of dark matter annihilation or decay. After freeze-out, the dark matter relic density is constant, and annihilation processes are inefficient with respect to the expansion of the Universe. However, density perturbations make possible for dark matter to clump in structures with large amount of gravitational matter. These structures are called halos, and they are characterized by a large dark matter density, that can benefit the annihilation rate. Examples of halos can be found in galaxies, galaxy clusters, or dwarf galaxies, and, as also mentioned in § 3.1.4, they are also one of the main ingredients that allowed the formation of the large scale structures of the Universe, as we observe today. One feature of dark matter in halos is its velocity distribution, which is non-relativistic. Typical values within the Milky Way [119] and for similar galaxies are of the order of 10^{-3} c, while dwarf spheroidal galaxies (dSph) are expected to host even colder dark matter, $v \approx 10^{-5}$ c. This makes possible to set the center-of-mass energy of the annihilation process to be $\sqrt{s} \approx 2m_{\mathrm{DM}}$. The signals of indirect detection are stable or unstable Standard Model particles, undergoing hadronization and decay, producing a plethora of secondary particles, such as photons, neutrinos, electrons, positrons, antiprotons, nuclei and antinuclei. These can then reach the Earth, where they can be detected by experiments. Additionally, secondary interactions of the primary particles with the interstellar medium can also provide observable signatures. A prominent example is given by charged particles making inverse Compton scattering. In particular, the following are the main final state spectra typical of indirect detection:

- **photons:** photons can be produced by many sources, and their spectra can be divided in two main categories:
  - continuum: the spectrum is smooth and contains very few features, it is usually produced from annihilations into τ leptons, gauge bosons or combination of quarks. These particles can hadronize into neutral pions, which can naturally decay into photons, $\pi \to \gamma\gamma$. This signature produces a soft photon-rich continuum spectrum. Another possibility is the annihilation into leptonic channels, which produce photons through bremsstrahlung, or by final state radiation (FSR). The final spectrum will be hard and peaked towards the dark matter mass [120];
  - lines: the spectrum is characterized by sharp features, and it is usually produced by direct annihilations into $\gamma\gamma$ or γX, where X can be Z, h or a new neutral particle. These channels are very interesting, because the spectrum is characterized by monochromatic lines as a function of the dark matter mass, and this allows evading most of the astrophysical backgrounds. However, given in most models dark matter is electrically neutral, the direct annihilation into photons is loop-suppressed, and the cross section is very small, see chapter 5 for γ-lines phenomenology;
- **neutrinos:** dark matter can decay or annihilate into neutrinos. Though this channel is difficult to probe, there are many experiments looking for this signal, like for example ANTARES and IceCube experiments [121]. A promising strategy is to look for dark matter annihilation in the

Sun, so that neutrinos are the only particles to escape [122]. Moreover, neutrino production implies that gauge bosons can be radiated off from the interaction point, thus producing signatures typical of a hadronic channel, that can be investigated [123];

- **CRs:** dark matter annihilation in charged particles can produce CRs. This interests mainly electrons, positrons, antiprotons, antideuterons, nuclei and antinuclei that can be produced from the hadronization of quarks and gluons constituting the final states of annihilation or decay. CRs do not propagate in straight line, and they are subject to the magnetic fields of the astrophysical objects.

In the following, we will review the theory behind indirect detection, and we will describe the main experiments looking for dark matter signals. This section is partly based on [69, 71, 124, 125], while each experiment is referenced in the corresponding section.

3.7.1 Dark matter distribution

Signals from dark matter annihilation or decay depend strongly on the dark matter distribution in the Universe. Dark matter clusters in halos, which typically host substructures, such as subhalos, that can be very dense. We parametrize the dark matter density in a halo as $\rho(\mathbf{r})$, where $\mathbf{r}$ is the position vector. The term $\rho(\mathbf{r})$ is usually called density profile. Its measurement is not trivial, and it is usually performed by studying the kinematics of stars and gas in the halo, and by performing N-body simulations. For simplicity, the dark matter distribution is usually assumed to be spherically symmetric, and the density profile is parametrized as a function of the distance from the center of the halo, $r = |\mathbf{r}|$, so that $\rho(\mathbf{r}) = \rho(r)$. Today, we consider different density profiles:

- Navarro-Frenk-White (NFW) profile [126]:

$$\rho_{\mathrm{gNFW}}(r) = \rho_s \left(\frac{r}{r_s}\right)^{-\gamma} \left(1 + \frac{r}{r_s}\right)^{\gamma-3} , \tag{3.81}$$

where γ is linked to the *cuspiness* of the profile. Eq. (3.81) is sometimes called generalized NFW profile. The NFW profile is an example of a cuspy profile. The $\gamma = 1$ case corresponds to the canonical NFW profile.

$$\rho_{\mathrm{NFW}}(r) = \rho_s \left(\frac{r}{r_s}\right)^{-1} \left(1 + \frac{r}{r_s}\right)^{-2} ; \tag{3.82}$$

- Einasto profile [127]:

$$\rho_{\mathrm{Ein}}(r) = \rho_s \exp\left\{-\frac{2}{\alpha}\left[\left(\frac{r}{r_s}\right)^{\alpha} - 1\right]\right\}, \tag{3.83}$$

  characterized by the parameter α, which controls the curvature of the profile;

- Burkert profile [128]:

$$\rho_{\mathrm{Bur}}(r) = \rho_s \left(1 + \frac{r}{r_s}\right)^{-1} \left(1 + \frac{r^2}{r_s^2}\right)^{-1}. \tag{3.84}$$

  The Burkert profile is an example of a cored profile, meaning that it is characterized by a flatter density behavior.

- Isothermal profile [129]

$$\rho_{\mathrm{Iso}}(r) = \rho_s \left(1 + \frac{r}{r_s}\right)^{-1} \left[1 + \left(\frac{r}{r_s}\right)^2\right]^{-1}, \tag{3.85}$$

  which is another example of a cored profile.

The terms r_s and ρ_s are the scale radius and the scale density, respectively. In the case of Milky Way, the values of the free parameters can be read in [130, 131]. The scale density is usually fixed by the normalization:

$$\rho_\odot = \rho(r_\odot), \tag{3.86}$$

where $r_\odot \approx 8.12\,\mathrm{kpc}$ is the distance between the Sun and the galactic center, while $\rho_\odot \approx 0.39\,\mathrm{GeV\,cm^{-3}}$ is the local dark matter density [119, 130, 132].

3.7.2 Neutral particles

Photons and neutrinos are simple to modelize, because they travel mostly unperturbed from their production point to the Earth. It is possible to trace their sources on a 2-dimensional plane, while one can grasp the information on the distance from the redshift. We observe these sources as a function of the solid angle $\Delta\Omega$ in a certain time interval Δt. Our detector is equipped with an effective area A, and it will record the number of events ΔN with a certain energy ΔE in that interval. Let us suppose the signal arises from a volume ΔV, located at the spherical coordinates $\mathbf{r}' = (r', \vartheta, \varphi)$, with Earth at the origin. From the particle physics perspective, photons or neutrinos come from the annihilation or decay of a certain dark matter candidate, that, for simplicity, we assume to be a Majorana fermion[†]. Each annihilation/decay channel f produces

[†]For dark matter which is not self-conjugate, the next formulas will be characterized by an additional factor $1/2$.

a spectrum of photons or neutrinos dN^f/dE, proportionally to the branching ratio $\mathcal{B}_f$ of the channel under study. If there are no substantial change in the energy of photons or neutrinos from the source to the detector (e.g. due to redshift and absorption), it is possible to write the following expression that links the quantities mentioned so far:

$$\frac{\Delta N}{\Delta E\,\Delta t\,\Delta V} = \sum_f \mathcal{B}_f \frac{dN^f}{dE} \frac{A}{4\pi|\mathbf{r}'|^2} \begin{cases} \frac{1}{2}\langle\sigma v\rangle\, n^2(\mathbf{r}) & \text{annihilation,} \\ \frac{n(\mathbf{r})}{\tau} & \text{decay,} \end{cases} \tag{3.87}$$

where $\mathbf{r}$ is the coordinate of the annihilation point with respect to the dark matter halo center, $n(\mathbf{r})$ is the dark matter number density in that point, and τ is the lifetime of the dark matter particle. We can further simplify the expression, by introducing the dark matter density distribution $\rho(\mathbf{r}) = m\,n(\mathbf{r})$, valid for non-relativistic dark matter particles of mass m, and the flux of particles:

$$\Phi_\gamma \doteq \frac{dN}{dt}\,, \tag{3.88}$$

so that, in the limit of localized source, small-time and energy intervals, we can write:

$$\frac{\partial^2\Phi}{\partial E\,\partial V} = \sum_f \mathcal{B}_f \frac{dN^f}{dE} \frac{A}{4\pi|\mathbf{r}'|^2} \begin{cases} \frac{\langle\sigma v\rangle}{2m^2}\,\rho^2(\mathbf{r}) & \text{annihilation,} \\ \frac{1}{m\tau}\,\rho(\mathbf{r}) & \text{decay,} \end{cases} \tag{3.89}$$

It is easy to see that eq. (3.89) can be separated into a term that only depends on particle physics, involving the spectra, $\langle\sigma v\rangle$ or τ; and a term depending only on astrophysics, characterized by the dark matter density profile and the volume of observation. The latter part is more explicit if we integrate over the volume of observation, $dV = d^3r$, known also as region of interest (ROI):

$$\frac{d\Phi}{dE} = \sum_f \mathcal{B}_f \frac{dN^f}{dE} \frac{A}{4\pi} \begin{cases} \frac{\langle\sigma v\rangle}{2m^2} \int_{\mathrm{ROI}} \frac{d^3r'}{|\mathbf{r}'|^2}\,\rho^2(\mathbf{r}) & \text{annihilation,} \\ \frac{1}{m\tau} \int_{\mathrm{ROI}} \frac{d^3r'}{|\mathbf{r}'|^2}\,\rho(\mathbf{r}) & \text{decay,} \end{cases} \tag{3.90}$$

And we can highlight the two integrals, that are known as $\mathcal{J}$-factors[‡]:

$$\mathcal{J}_{\mathrm{ann}} \doteq \int_{\mathrm{ROI}} \frac{d^3r'}{|\mathbf{r}'|^2}\,\rho^2(\mathbf{r})\,, \tag{3.91a}$$

$$\mathcal{J}_{\mathrm{dec}} \doteq \int_{\mathrm{ROI}} \frac{d^3r'}{|\mathbf{r}'|^2}\,\rho(\mathbf{r})\,. \tag{3.91b}$$

[‡]Notice that $\mathcal{J}_{\mathrm{dec}}$ is also known with the name $\mathcal{D}$-factor in the literature.

The computation of the $\mathcal{J}$-factors is not trivial, and it depends on the particular region of observation of the experiment. App. C.1.1 contains a detailed description of the computation of the $\mathcal{J}$-factor for the galactic center, performing the integration explicitly. Here we will just give a brief overview of the geometrical aspect of the problem. The density profile is expressed as a function of the distance $\mathbf{r}$ from the center of our galaxy. However, the integration is performed from the point of view of the Earth, while the density profile is expressed in the target reference frame. The transformation between the two reference frames can be performed by the following change of variables, which invokes the use of the galactocentric coordinates (colongitude l and colatitude b):

$$|\mathbf{r}(\mathbf{r}')| = |\mathbf{r}(r', b, l)| = \sqrt{r'^2 + r_\odot^2 - 2r'r_\odot \cos(b)\cos(l)}\,, \tag{3.92}$$

where we identify r' as the line-of-sight. Other choices for the coordinate frame are possible (for example the spherical coordinates), and they depend on the specific ROI of the experiment.

The $\mathcal{J}$-factor is an indication of the interaction potential of the ROI under investigation, given it depends on the dark matter density profile, to the power of the number of dark matter particles we expect an interaction from. Subsequently, the larger the $\mathcal{J}$-factor, the more interesting is the target. Typical values for the $\mathcal{J}$-factor for the galactic center (without any mask on the galactic plane) are of the order $(10^{22}$ and $10^{23})$ GeV^2 cm^{-5} for the canonical NFW profile, with ROI of amplitude 3° and 16°, respectively. Other targets such as the dSph have smaller $\mathcal{J}$-factors, of the order 10^{20} GeV^2 cm^{-5}. However, for an efficient detection, it is not enough to maximize the $\mathcal{J}$-factor, and the astrophysical background is also important: the galactic center is a very bright region, and the astrophysical background is very high, while the dSph contain fewer stars and are very dim, so that the astrophysical background is very low. Finally, the computation performed so far depends on the assumption the dark matter profile is a smooth function, while in reality halos can contain substructures, that can greatly increase the local $\mathcal{J}$-factor.

The particle physics-related part is enclosed in the factor:

$$\mathcal{B}_f \frac{dN^f}{dE} \frac{A}{4\pi} \begin{cases} \dfrac{\langle \sigma v \rangle}{2m^2} & \text{annihilation,} \\ \dfrac{1}{m\tau} & \text{decay,} \end{cases} \tag{3.93}$$

These terms are model-dependent. They contain the velocity-averaged cross section $\langle \sigma v \rangle$, or the lifetime τ, and the spectra of the final state particles.

3.7.3 Particle spectra

The term dN^f/dE in eq. (3.93) expresses the spectrum of interest produced by the final states of the process labeled as f. Each process f contains a certain number of final states particles, kinematically accessible, possibly including new particles, further decaying to Standard Model ones. These particles can quickly decay and hadronize to stable particles, such as photons, neutrinos, electrons, positrons, antiprotons, antideuterons, nuclei and antinuclei.

The photon spectrum can be generated in different ways, depending on the final state particles. Quarks, gauge bosons and τ leptons constitute what are called the soft channels, they hadronize into neutral pions, further decaying into photons, $\pi^0 \to \gamma\gamma$. Another possibility is that the process f contains photons in the final states, such as in the case of the annihilation into $\gamma\gamma$, γZ, γh or, in general, γX. Indeed, this kind of processes are two-body processes, and the energy of the final states is fixed by the kinematics of the process [133–135]. They produce a monochromatic γ spectrum, made of different peaks, depending on the mass of the final state particles accompanying the photon. Hence, for this kind of process, the photon energy spectrum, $dN_\gamma^{\text{line}}/dE_\gamma$ in eq. (3.93), is a sharp spectral line [133–135]:

$$\frac{dN_\gamma^{\text{line}}}{dE_\gamma} = \delta(E_\gamma - E_\gamma^{\text{line}}) \times \begin{cases} 2 & \text{for } \gamma\gamma\,, \\ 1 & \text{for } \gamma X\,. \end{cases} \tag{3.94}$$

Accordingly,

$$E_\gamma^{\text{line}} = m_{\text{DM}}\,, \tag{3.95a}$$

for $\gamma\gamma$, and

$$E_\gamma^{\text{line}} = m_{\text{DM}}\left(1 - \frac{m_X^2}{m_{\text{DM}}^2}\right) \tag{3.95b}$$

for γX, where X is a Standard Model neutral or new particle with mass m_X. This characteristic shape allows for peak searches within the experimental data.

Finally, photon spectra receive a contribution from secondary emissions. These are produced by charged particles final states, and include i) inverse Compton scattering of interstellar photons, ii) bremsstrahlung, iii) synchrotron radiation when propagating in the magnetic field of an astrophysical object, iv) interactions with the interstellar medium, producing neutral pions that decay into photons.

For what concerns neutrinos, neutrino spectra can be produced by final states containing e.g. W^+W^-, $\mu^+\mu^-$ and $\tau^+\tau^-$. Given they travel from a far source to the Earth, they behave like in a long baseline experiment, so that their oscillations even out, and they can be detected with a flavor ratio of 1 : 1 : 1.

Finally, CR candidates protons and antiprotons can be produced by final states containing quarks, gauge bosons and τ leptons.

3.7.4 Cosmic rays

CRs can be produced by dark matter annihilation or decay, and they behave very differently from the neutral photons and neutrinos. Indeed, they are charged particles traveling through the galactic magnetic fields, and they are subject to many phenomena, such as deflection, diffusion and energy losses, that changes their propagation and, eventually, their final spectrum. CRs are very challenging to modelize and study, given the large uncertainties on the propagation parameters and on the astrophysical background. The propagation of CRs can be described by the following equation [136]:

$$\begin{aligned}\frac{\partial\psi(\mathbf{r},p,t)}{\partial t} &= Q(\mathbf{r},p) + \boldsymbol{\nabla}\cdot\left(D_{xx}\boldsymbol{\nabla}\psi - \boldsymbol{v}_c\psi\right) + \frac{\partial}{\partial p}\left[p^2 D_{pp}\frac{\partial}{\partial p}\left(\frac{\psi}{p^2}\right)\right] \\ &\quad - \frac{\partial}{\partial p}\left[\dot{p}\psi - \frac{p}{3}(\boldsymbol{\nabla}\cdot\boldsymbol{v}_c)\psi\right] - \frac{1}{\tau_f}\psi - \frac{1}{\tau_r}\psi\,, \end{aligned} \tag{3.96}$$

where $\psi(\mathbf{r},p,t)$ is the density of CR particles with a certain momentum p at the position $\mathbf{r}$. The various terms represent the following phenomena: i) Q is the source term, ii) D_{xx} is the diffusion coefficient, iii) $\boldsymbol{v}_c$ is the convection velocity, iv) D_{pp} is the diffusion reacceleration coefficient in momentum space, v) $\dot{p}$ is the momentum loss rate, vi) τ_f and τ_r are the time scales for fragmentation and radioactive decay, respectively. There exist public codes to modelize the CR propagation numerically, namely DRAGON [137, 138] and GALPROP [139–141]. Dark matter annihilation can provide a contribution to the CR flux, acting as a source term in eq. (3.96).

3.7.5 Indirect searches summary

In the following paragraphs, we will review the main experiments looking for dark matter signals in the framework of indirect detection. This is not meant to be an exhaustive list, rather a selection of the experiments and signatures relevant for this dissertation.

WIMP γ-ray searches

As we already mentioned, γ-rays represent an important channel for indirect detection. Given they travel undisturbed through the interstellar medium, it is possible to map the sources of the signal. For what concerns the targets, the Milky-Way galactic center is a very interesting region, because it is expected to host a large amount of dark matter, and it is very bright in γ-rays, containing a variety of large substructures, like a central black hole, supernovas remnants, neutron stars and pulsars. However, the brightness of the galactic center is also a disadvantage, because the astrophysical background is very high, and it may be difficult to disentangle the signal from it. Another promising target is represented by the dSph, which are dimmer, and they are expected to host a large amount of dark matter [142, 143]. The main experiments looking for γ-rays are:

- **Fermi-LAT** [144]: the Fermi Large Area Telescope is a space-based γ-ray telescope, sensitive to the energy range between 20 MeV and 1 TeV. It is wide enough to cover around 20 % of the sky, and it is equipped with a tracker, a calorimeter and an anti-coincidence detector.

- **HAWC** [145]: the High-Altitude Water Čerenkov Observatory is a ground-based γ-ray telescope located in Mexico at an altitude of 4100 m, sensitive to the energy range in between 300 GeV and few hundreds of TeV.

- **HESS** [146]: the High Energy Stereoscopic System is a ground-based γ-ray telescope located in Namibia. It is made of several imaging atmospheric Čerenkov telescope (IACT) arrays, and it is sensitive to the energy range between 30 GeV and 100 TeV.

- **MAGIC** [147]: the Major Atmospheric Gamma Imaging Čerenkov Telescope is a ground-based γ-ray telescope located in the Canary Islands. It is made of two telescopes, and it is sensitive to photons above 50 GeV.

- **VERITAS** [148]: the Very Energetic Radiation Imaging Telescope Array System is a ground-based γ-ray telescope located in Arizona. It is made of four telescopes, and it is sensitive to photons in the energy range between 85 GeV to 30 TeV.

One of the main results of γ-ray searches is the observation of the Milky Way dSph, that provides very stringent constraints on the dark matter annihilation cross section. This observation is on the continuum γ-ray spectrum and has been performed by Fermi-LAT [149], VERITAS [150], and MAGIC [151]. A common feature of ground-based telescopes is that they are sensitive to very-high energy photons, with respect to space-based telescope, like Fermi-LAT, being sensitive also in lower energy range.

Another important result is the observation of γ-lines from the galactic center. The Fermi-LAT [152, 153], HESS [154] and MAGIC [155] experiments released constraints on the dark matter annihilation cross section into $\gamma\gamma$. Line searches have also targeted dSph, and have been performed by HESS [156] and HAWC [157] experiments.

There are also many other planned, or currently taking data, experiments:

- **LHAASO** [158]: the Large High Altitude Air Shower Observatory operates in China. It is made of several air and water Čherenkov telescopes combined with huge water pools for observation. It began its activity in 2019. Its aim is to study γ-rays from tens of GeV to PeV.

- **GAMMA-400** [159]: it is a space-based γ-ray telescope, sensitive in the energy range between 20 MeV to several TeV.
- **CTA** [160]: the Čerenkov Telescope Array is the next generation ground-based observatory for gamma-ray astronomy at very-high energies. It is an array of more than 100 telescopes, located in both the northern (in La Palma, Spain) and in the southern (in Chile) hemispheres. It aims at detecting photons from 20 GeV to more than 300 TeV.

Cosmic Microwave Background

Dark matter annihilation or decay may inject energy into the thermal bath, resulting in a reionization of the Hydrogen, and in a distortion of the CMB spectrum [161–165]. This effect is particularly relevant for sub-GeV dark matter, and it can strongly constrain light dark matter characterized by s-wave annihilation [20]. This is relevant only for those models presenting a strong component of dark matter annihilation at late time, which is typically the case for models testable in the framework of indirect detection. Models with p-wave annihilation, or where dark matter self-annihilation is suppressed, can easily evade these constraints.

Neutrinos searches

Like photons, neutrinos are stable and travel undisturbed from their production point to the Earth. They require large volumes of water or ice to improve the statistics of the detection. In general, detection happens through the Čerenkov radiation produced in the detector medium as the neutrino passes through it. The main experiments looking for neutrinos are:

- **IceCube** [166]: it is a neutrino telescope located in Antarctica, exploiting the natural ice for neutrino interaction. It is instrumented with photomultipliers tubes to detect the Čerenkov light yielded by the interaction of neutrinos with the ice.
- **ANTARES** [167]: it is a water Čerenkov detector located in the Mediterranean Sea.
- **Super Kamiokande** [168]: situated in Japan, it is a water Čerenkov detector, made of a cylindrical tank of 50 kt of water, surrounded by photomultipliers. It performs measurements of atmospheric neutrinos, solar neutrinos and supernova neutrinos, and also acts as the far detector for the T2K experiment.

Moreover, planned upgrades of the previous experiments will be available in the near future:

- **KM3NeT** [169]: it is the next-generation neutrino telescope located in the Mediterranean Sea with a total volume of 1 km^3 or more.
- **Hyper Kamiokande** [170]: it is the next-generation of water Čerenkov detectors, and it will be made of 260 kt of water, surrounded by photomultipliers, with the aim of reaching twice the sensitivity of Super Kamiokande.

The mentioned experiments are sensitive to neutrino energies from $\mathcal{O}(\text{GeV})$ to $\mathcal{O}(\text{TeV})$. There are also experiments sensitive to lower energies, $\mathcal{O}(\text{MeV})$, which could be able to probe lighter dark matter candidates. The main ones are:

- **Borexino** [171]: it was a liquid scintillator detector placed at the Laboratori Nazionali del Gran Sasso in Italy, and it has performed several measurements in the field of solar neutrinos, succeeding into detecting the neutrinos originated by the carbon-nitrogen-oxygen cycle in the Sun [172–174].
- **KamLAND** [175]: the Kamioka Liquid Scintillator Antineutrino Detector is located in Japan, under Mt. Ikenoyama, close to Kamioka, and it is made of a liquid scintillator detector, used to reveal electron antineutrinos coming from nuclear reactions.
- **JUNO** [176]: the Jiangmen Underground Neutrino Observatory is a liquid scintillator detector under construction in China, and it is the next-generation multipurpose neutrino detector, capable of revealing neutrinos from different sources, including nuclear power plants, terrestrial and astrophysical sources.

Several other experiments are under construction, and will be available in the next decades, in particular for what concerns the detection of neutrinos from heavy dark matter, introduced in the next paragraph.

Heavy dark matter

Decay or annihilation of very heavy dark matter can produce Ultra-High Energy (UHE) neutrinos [177] or photons [178], that can be detected by neutrinos or γ-ray telescopes.

For what concerns neutrinos, when UHE neutrinos reach the Earth, they can be detected by the hadronic or electromagnetic showers that they create when interacting in a medium. Many new experiments will be available in the near future to collect these signals. In general, the showers originating from UHE neutrinos are characterized by emissions in the radio spectrum, a phenomenon known as the Askaryan effect. However, since the neutrino fluxes at these high energies are low, the experiments should be equipped with a large interaction volume, so that the main mediums that have been considered so far are air, water and ice. In the following we give a brief description of the main experiments at play in the next decades:

- **RNO-G** [179]: the Radio Neutrino Observatory in Greenland is a neutrino telescope exploiting an ice medium for neutrino interaction. UHE neutrinos can produce hadronic or electromagnetic showers inside the ice which can then be collected by the antennas equipped to each one of the 35 stations the experiment is made of.

- **IceCube-Gen2** [180, 181]: the next generation of the IceCube experiment is located in Antarctica, exploiting the natural ice for neutrino interaction. The detection of the showers relies on the radio array made of 200 stations.

- **GRAND** [182]: the Giant Radio Array for Neutrino Detection is a planned observatory sensitive to CRs, γ-rays and neutrinos. Its main strategy for neutrino detection focuses on Earth-skimming underground τ neutrinos: they are astrophysical ν_τ crossing the Earth medium at a very small angle with the surface, or passing through mountains. In this environment, neutrinos can interact with the medium by charged-current interaction and can produce τ leptons which can eventually decay outside the rock, producing an electromagnetic shower, detected by the large number of antennas foreseen in the design of GRAND.

UHE photons and CRs reaching the Earth's atmosphere will interact producing extensive air showers (EAS), generating cascades of charged particles that can leave traces in the detectors placed on the Earth's surface. Gamma-ray experiments usually employ one or more scintillation arrays or huge Čherenkov stations. The latter aim at detecting the Čherenkov light coming from the particles in the EAS traveling through the atmosphere, that is collected by photomultiplier arrays. One of the main obstacles for the measurement of γ-rays with ground-based telescopes is the high level of residual charged CR background. Unfortunately, EAS can not be distinguished by background charged CRs based solely on directional information.

The following decommitted experiments have placed several bounds on UHE photons:

- **CASA-MIA** [183]: the Chicago Air Shower Array-MIchigan Muon Array experiment was a surface array of scintillation counters located in Utah (USA), able to infer the properties of EAS. It was active until 1998. The main detection strategy relied on discriminating γ-ray primary showers from hadronic (or CR)-generated ones, by identifying muon-less or muon-poor events. This principle is based on the fact that muons originate mainly from charged pion and kaon decays which are abundant in a hadronic shower, while the muon content in an electromagnetic shower is mainly coming from photoproduction events whose interaction rate is suppressed with respect to nucleus-nucleus events.

- **KASCADE and KASCADE-GRANDE** [184]: the KArlsruhe Shower Core and Array DEtector was located at the Karlsruhe Institute of Technology (Germany) and operated until the end of 2012. It was made of three detector systems: a large field array, a muon tracking detector and a central detector. The experiment's aim was to measure the electromagnetic, muonic and hadronic components of EAS.

- **TA** [185]: the Telescope Array experiment operates in Utah (USA) since 2008, and it is made of a surface detector with plastic scintillators and three fluorescence detectors. It obtained limits on diffuse photon flux with energies greater than EeV.

- **PAO** [186]: the Pierre Auger Observatory is a surface detector array of Čherenkov stations, sensitive to the electromagnetic, muonic and hadronic EAS components. An additional fluoresce detector completes the setup to observe the longitudinal development of the shower. It operates in Argentina, and it performed a search for UHE photons with energies above EeV.

Indirect detection of a very heavy decaying dark matter is the main topic of chapter 7.

3.7.6 Recorded excesses

Indirect detection searches have reported some excesses in the data, fostering many interesting hypotheses whether they could be explained by adding a dark matter source on top of the known astrophysical phenomena.

Cosmic-ray antiprotons

Several collaborations have reported an excess in the AMS-02 antiprotons data [187], for energies around $(10 \text{ to } 20)$ GeV. The existence of this excess is still under debate [188–195]. The main issues are related to many systematic uncertainties affecting various aspects of the detector and of the analysis, namely the propagation model, the astrophysical sources model and the cross section for antiprotons production in the detector. However, it is interesting to note that it is possible to provide a dark matter explanation [188, 189, 191, 192].

Cosmic-ray positrons

The excess in CR positrons stems from the observation of a rise in the positron fraction, defined as the ratio between the flux of positrons and the sum of the fluxes of positrons and electrons, for energies above 10 GeV. The measurement was performed by PAMELA in 2008 [196], later confirmed by Fermi-LAT [197] and AMS-02 [198]. An explanation with dark matter theory is possible, if the dark matter candidate is sufficiently heavy, $m_{DM} \approx \mathcal{O}(100\,\text{GeV})$. In such case, its decays or annihilation in leptonic channels can provide a source of positrons able to explain the excess. However, this hypothesis requires the dark matter to not annihilate strongly in other channels, so to avoid constraints from antiprotons or photon searches.

Another possible explanation invoking conventional astrophysics involves the production of positrons from pulsars [199].

Fermi-LAT galactic center excess

One of the most prominent measured excesses is the one observed by Fermi-LAT in the galactic center [188, 200–215], and regarding an excess in the continuum γ-ray spectrum. This galactic center excess (GCE) has been detected using different kind of techniques and models of the γ-ray sky or of the interstellar emission. The excess is characterized by the shape of its spectral energy distribution (SED) peaked at $(1\text{ to }3)\,\text{GeV}$, and a high energy tail extending up to about 50 GeV. It is located within 10° from the galactic center, and its position coincides with the Milky Way dynamical center, and it is roughly spherically symmetric [214, 215].

Many speculations on the origin of the GCE have been proposed, and the dark matter hypothesis constitutes one of the most optimistic [188, 195, 207, 208, 211, 216–219]. Indeed, the GCE is compatible with a typical WIMP mass scale thermal relic, $m_{DM} \lessapprox 100\,\text{GeV}$, that can annihilate to quarks. The best fit annihilation channel is represented by $b\bar{b}$, with a dark matter mass around $(4\text{ to }50)\,\text{GeV}$. The GCE is compatible with a dark matter template characterized by a slightly cuspy NFW profile, with $\gamma = 1.1$ to 1.2 [214]. Observations on several dSph have been used to impose constraints on the dark matter interpretation of the GCE [142, 149, 195, 220–225]. In chapter 6 we will perform a fit of the GCE SED in the framework of a dark matter model.

Despite the dark matter interpretation is optimistic, other possible explanations have found a way in the debate on the origin of the GCE. The most promising one regards the existence of a faint population of millisecond pulsars, close to the galactic center [226, 227]. However, also this hypothesis has been recently discussed [228–231], and it is still under investigation. Other alternative hypotheses feature spinning neutron stars, or γ-rays sourced by high-energy CRs, see [232–235].

3.8 Direct detection

The first idea to exploit the interaction of dark matter with ordinary matter as a way of detection dates back to the 1980s [236]. The elastic scattering between a WIMP and a nucleus can make the latter recoil, producing different kind of signatures: energy deposition, ionization, or scintillation light. Direct detection experiments are designed to detect these signals, and they are usually located in underground facilities to reduce the background from CRs. They have reached unprecedented sensitivities in the last decades, and they strongly constrain the parameter space of WIMP models. In this section we will review the main aspects of direct detection, and we will discuss the main experiments and their results, following the reviews [72, 73, 237, 238]. The rate of dark matter nucleus scattering depends both on astrophysical and particle physics quantities.

3.8.1 Astrophysics: the dark matter velocity distribution

Direct detection experiments relies on the local dark matter density and its distribution around the Sun. The value of the local dark matter density is $\rho_\odot = (0.39 \pm 0.03)\,\mathrm{GeV\,cm^{-3}}$ [130, 132]. Another important ingredient is the velocity distribution of the dark matter particles in the halo. In this context, one usually considers the Standard Halo Model (SHM) [239], which modelizes the halo as smooth, isotropic and spherically symmetric. It also assumes a Maxwell-Boltzmann velocity distribution:

$$\tilde{f}(\boldsymbol{v}) = \frac{1}{N}\left(\frac{1}{\pi v_0^2}\right)^{3/2} \exp\left(-\frac{|\boldsymbol{v}|^2}{v_0^2}\right)\Theta(v_{\rm esc} - |\boldsymbol{v}|)\,, \tag{3.97}$$

in the dark matter frame (rest frame), with N being a normalization constant, while

$$v_0 = \sqrt{\frac{2}{3}}\sigma_v \tag{3.98}$$

is the most probable velocity, with σ_v being the velocity dispersion. The term Θ is the Heaviside step function. The distribution is truncated at the escape velocity $v_{\rm esc}$, beyond which the dark matter particles are not gravitationally bounded to the halo. The current assumed value for the escape velocity is $v_{\rm esc} = 544\,\mathrm{km\,s^{-1}}$ [240]. In the Earth's reference frame, the velocity distribution of dark matter particles is subject to a modulation, so that in the laboratory frame one could perform a boost on $\tilde{f}$:

$$f(\boldsymbol{v}, t) = \tilde{f}(\boldsymbol{v}_{\rm obs}(t) + \boldsymbol{v})\,, \tag{3.99}$$

where

$$\boldsymbol{v}_{\text{obs}}(t) = \boldsymbol{v}_{\odot} + \boldsymbol{v}_{\oplus}(t) \tag{3.100}$$

is the motion of the laboratory frame with respect to the rest frame, with $\boldsymbol{v}_{\odot}$ being the velocity of the Sun and $\boldsymbol{v}_{\oplus}$ the velocity of the Earth with respect to the Sun. In the SHM, one can write the velocities in play with respect to the so-called Local Standard of Rest (LSR), which is an imaginary point orbiting on a perfect circular path around the galactic center. The LSR moves at a velocity which is the average velocity of the stars in the solar neighborhood. Given the Maxwell-Boltzmann distribution, this velocity is exactly $\boldsymbol{v}_0$. Using a galactic coordinate frame[§], we have $\boldsymbol{v}_0 \approx (0,\ 235, 0)\,\text{km}\,\text{s}^{-1}$ [241–244]. In turn, one can write the Sun velocity in galactic coordinates [245]:

$$\boldsymbol{v}_{\odot} \approx \boldsymbol{v}_0 + (-11,\ 12, 7)\,\text{km}\,\text{s}^{-1}\,. \tag{3.101}$$

Finally, the Earth velocity can be written as:

$$\boldsymbol{v}_{\oplus}(t) \approx v_{\oplus} \cos(\vartheta) \cos\big(\omega(t - t_0)\big)\,, \tag{3.102}$$

because this term varies on a timescale of one year, due to the motion of the Earth around the Sun. So, $\omega = 2\pi/1\,\text{y}$, t_0 refers to the time so that $|\boldsymbol{v}_{\oplus}(t_0)|$ is maximum, while $\vartheta \approx 60°$ is the inclination angle between the Earth's orbit and the galactic plane, and $v_{\oplus} \approx 29.8\,\text{km}\,\text{h}^{-1}$.

3.8.2 Recoil energy and rate

From the particle physics point of view, the process happening in direct detection experiments is a dark matter elastic scattering off a nucleus. Kinematically, the process can be described assuming the target nucleus is at rest, due to the extremely low temperatures of the detector. The initial kinetic energy of the dark matter particle can be written in the non-relativistic limit as:

$$E_i = \frac{|\mathbf{p}|^2}{2m_{\text{DM}}}\,, \tag{3.103}$$

where $\mathbf{p} = m_{\text{DM}}\,\boldsymbol{v}$, with $\boldsymbol{v}$ being the dark matter velocity. During the collision, dark matter and nucleus $\mathcal{N}$ exchange the momentum $\mathbf{q}$, so that the final kinetic energy of the dark matter particle is:

$$E_f = \frac{|\mathbf{p} - \mathbf{q}|^2}{2m_{\text{DM}}} + \frac{|\mathbf{q}|^2}{2m_{\mathcal{N}}}\,. \tag{3.104}$$

[§]The galactic reference frame is a cylindrical frame centered in the galactic center and characterized by the coordinates $(r,\ \vartheta,\ z) = r\,\hat{\mathbf{r}} + \vartheta\,\hat{\boldsymbol{\vartheta}} + z\,\hat{\mathbf{z}}$, with $\hat{\mathbf{r}}$ pointing away from the galactic center, $\hat{\mathbf{z}}$ pointing to the galactic north and $\hat{\boldsymbol{\vartheta}} = \hat{\mathbf{r}} \times \hat{\mathbf{z}}$.

We define the recoil energy as:

$$E_R = \frac{|\mathbf{q}|^2}{2m_{\mathcal{N}}} = \frac{\mu^2 v^2}{m_{\mathcal{N}}}\left(1 - \cos(\vartheta)\right), \tag{3.105}$$

where μ is the reduced mass of the dark matter-nucleus system

$$\mu = \frac{m_{DM} m_{\mathcal{N}}}{m_{DM} + m_{\mathcal{N}}}, \tag{3.106}$$

and ϑ is the scattering angle in the center-of-mass frame. The recoil energy is the quantity that can be measured in the detector, and the detectors themselves are designed to be sensitive to a certain range of recoil energies. The maximum recoil energy for a WIMP-nucleus scattering can be computed from eq. (3.105):

$$E_R^{max} \approx 90\,\text{keV} \times \left(\frac{m_{DM}}{100\,\text{GeV}}\right)^2 \left(\frac{100\,\text{GeV}}{m_{\mathcal{N}}}\right) \left(\frac{v}{200\,\text{km}\,\text{s}^{-1}}\right). \tag{3.107}$$

So it is of the order $\mathcal{O}(100\,\text{keV})$, for the typical WIMP mass $m_{DM} = (10 \text{ to } 100)$ GeV.

In a detector of target mass M, composed of nuclei $\mathcal{N}$, the differential rate is:

$$\frac{dR}{dE_R} = \frac{\rho_\odot M}{m_{\mathcal{N}} m_{DM}} \int_{v_{min}}^{v_{esc}} d^3v\, |\mathbf{v}|\, f(\mathbf{v}, t) \frac{d\sigma}{dE_R}, \tag{3.108}$$

where $d\sigma/dE_R$ is the differential scattering cross section, while v_{min} is the minimum velocity required to have a recoil energy E_R:

$$v_{min} = \sqrt{\frac{E_R\, m_{\mathcal{N}}}{2\mu^2}}. \tag{3.109}$$

3.8.3 Cross sections

Dark matter scatters off the whole nucleus coherently, because the momentum exchange $|\mathbf{q}|$ is very small, so that dark matter can not resolve the internal structure of the nuclei. In this case, the common approximation is to consider a certain nucleus as the sum of the individual nucleons. However, this approach is a good approximation only in the case of light nuclei, because of the low number of nucleons. Direct detection experiments employ heavy nuclei, typically, because of the advantages of having higher cross sections and more interactions per unit time. The aforementioned approximation requires corrections, which are added as nuclear form factors F. In general, one could write the differential cross section term in eq. (3.108) including both a spin-independent (SI) and a spin-dependent (SD) term:

$$\frac{d\sigma}{dE_R} = \left(\frac{d\sigma}{dE_R}\right)_{SI} + \left(\frac{d\sigma}{dE_R}\right)_{SD}, \tag{3.110}$$

which can be cast in the following form:

$$\frac{d\sigma}{dE_R} = \frac{m_{\mathcal{N}}}{2\mu^2 v^2} \left[\sigma_0^{SI} F_{SI}^2 + \sigma_0^{SD} F_{SD}^2\right] . \tag{3.111}$$

The form factors embed the nuclear structure and the dependence on the momentum transfer in a single expression. The complexity of the nuclear structure makes the computation of the form factors a difficult task and an area of active research. One example of a form factor is the Helm form factor [246, 247]:

$$F(q) = \left(\frac{3j_1(qR_1)}{qR_1}\right)^2 \exp\left(-\frac{q^2 s^2}{2}\right), \tag{3.112}$$

where j_1 is the spherical Bessel function of the first kind, $R_1 \approx 1.25\,\mathrm{fm} \times A^{1/3}$ is the effective nuclear radius, with A the number of nucleons in the nucleus, and $s \approx 1$ fm is the nuclear *skin thickness*. The SI cross section is usually parametrized as:

$$\sigma_0^{SI} = \frac{4\mu^2}{\pi} \Big[Zf_p + (A - Z)f_n\Big]^2 , \tag{3.113}$$

where f_n, f_p are the WIMP couplings to neutrons and protons respectively, and Z is the atomic number. In the SD case we have:

$$\sigma_0^{SD} = \frac{32\mu^2 G_F^2}{\pi} \frac{J+1}{J} \Big(a_p \langle S_p \rangle + a_n \langle S_n \rangle\Big)^2 , \tag{3.114}$$

where a_p, a_n are the effective WIMP-nucleon couplings, $\langle S_p \rangle$, $\langle S_n \rangle$ are the average spin contributions of the nucleon and J is the nuclear spin.

3.8.4 Experimental searches

Elastic scattering of dark matter off nuclei relies on the detection of the small recoil energy deposited in the recoiling nucleus, this signature is known as nuclear recoil. The expected event rate is very low, and one of the main concerns is to increase the exposure of the detector and to keep the background as low as possible. Not only that, the detection requires anyway large periods of data-taking to build up enough statistics. Moreover, there are several sources of backgrounds that can mimic the signal, and they need to be carefully studied and reduced. One of the main background is represented by CRs, which can be reduced by placing the detector underground. Moreover, radioactivity of the detector components and of the material that are being used is another important source of background. In general, it is possible to shield the detector against external and natural radioactivity, while the internal radioactivity can be reduced by using radiopure materials and purification techniques¶. Another important background source is given from the coherent elastic neutrino-nucleus scattering (CEνNS) of astrophysical neutrinos, which can perfectly resemble the dark matter-nucleus scattering. This background is subject to many systematic uncertainties, mainly due to the poor knowledge of the neutrino fluxes. The effects of this background manifest themselves in a loss of experimental sensitivity to dark matter-nucleus scattering, making the parameter space region more challenging to probe. The shape of this background is known as neutrino fog [248–251]. This term officially replaces the previous neutrino floor, which was deemed inappropriate, because this background does not represent a hard limit, rather a region where detection is challenging, but that can be tackled by collecting more statistics.

One of the most promising techniques to detect nuclear recoils is the dual-phase time projection chamber, with Xe as target material. This technology is responsible for the most constraining bounds on the SI dark matter-nucleon cross section. The setup consists of a large volume of liquid Xe, which is the target material, and a smaller volume of gaseous Xe. When a particle hits the target Xe, a prompt scintillation signal, called S1, is produced along with ionization electrons. These electrons can either recombine with the parent ion, or they can be drifted in the gaseous Xe volume by an electric field, reaching the gaseous Xe phase, where they are extracted by another electric field, producing a second signal S2. This technology is currently used by the XENONnT, LZ and PandaX-II experiments. XENONnT [252] and LZ [253] recently released their first limits on SI (and SD) cross section, placing the most constraining bound at 30 GeV, excluding cross sections above $5.9 \times 10^{-48}\,\text{cm}^2$. Future experiments, like DARWIN [254] will be characterized by an even larger target mass (around 40 t), and they will be able to probe cross sections down to $1 \times 10^{-49}\,\text{cm}^2$.

Current experimental bounds and future sensitivities are shown in fig. 3.6.

¶An interesting anecdote on this: many experiments employ Ancient Roman lead ingots retrieved from 2000-year-old shipwrecks to shield the detectors. This is different from freshly mined lead, which has been exposed to CRs, rendering it slightly radioactive. In contrast, Ancient Roman lead, having rested undisturbed at the bottom of the sea for nearly two millennia, has been spared from CRs bombardment and constitutes a very clean material.

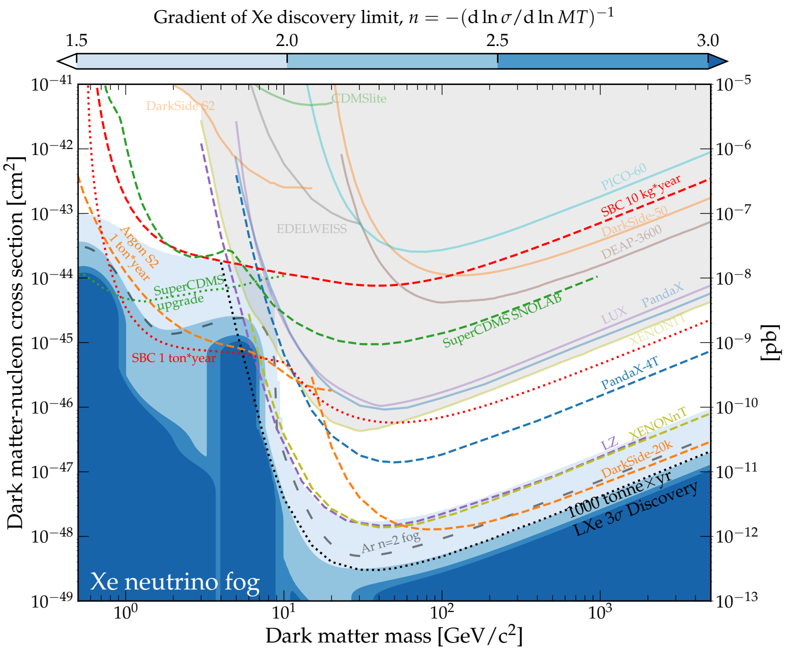

Figure 3.6: Summary of SI dark matter-nucleon scattering cross section parameter space. Experimental bounds are shown in solid lines [255–266], and they exclude the gray region. Sensitivities of future experiments are shown as 90 % CL upper limits in dashed lines. Notice that the latest LZ [253] and XENONnT [252] results are not included in this plot. The neutrino fog is shown in shadings of blue, and each n contour denotes a region where the cross section sensitivities require a 10^n increase in exposure. Figure from [238, fig. 1].

3.9 Collider searches

Colliders and particle accelerators are powerful tools to probe the existence of new particles. In particular, given WIMPs have interacted with the Standard Model in the past, it is possible to assume that they can be produced in particle collisions. If any dark matter is produced in colliders, it would then escape detection as a neutrino would do, because of the lack of any electromagnetic or color charge. In general, dark matter may be produced along with other particles, so that the key signature in collider searches is the presence of missing energy, $\not{E}_T$. Colliders have the great advantage of being able to measure many different kinematical variables, and their multipurpose detectors are able to reconstruct the kinematics of the dark matter production processes. Additionally, given dark matter interaction is expected to be weak, its production would require a lot of events, which implies the need of a high value of luminosity. Luminosity expresses the rate of events per unit time, and the higher it is, the higher will be the probability to obtain a dark matter event.

It is possible to tackle the problem of dark matter production in a model-dependent way. Knowing exactly the model under investigation would allow performing accurate analysis of the possible backgrounds and the choice of optimized kinematical cuts. If the dark matter is the lightest particle of a certain new physics model, colliders may be able to produce the heavier particles of the model, which would then decay to dark matter, producing extensive showers of different final states, accompanied by missing energy. An alternative would be to look for production of final states containing both a dark matter particle and at least one Standard Model particle, the so-called mono-X searches.

One of the most successful experiments is the LHC at CERN, which is a proton-proton collider. At the LHC, protons are accelerated to energies of 7 TeV, and they are made to collide in four points along the ring, where four large multipurpose detectors are located. ATLAS and CMS performed multiple searches for dark matter and for possible mediators between the dark matter and the Standard Model, see [267] for a review. Indeed, if dark matter couples to Standard Model h or Z, then it can be produced by the decay of these particles, and be part of the invisible decay width [268, 269]. Other searches looked for jet+$\not{E}_T$ [270, 271], γ+$\not{E}_T$ [272, 273], Z+$\not{E}_T$ [274, 275] or $\not{E}_T$+$h \to \gamma\gamma$ [276, 277]. Moreover, these experiments also looked for any hint of SUSY. The MSSM adds into play many more particles and degrees of freedom, each one with a certain decay pattern, presenting many possible final states that can be targeted. Some of them involve strongly-produced superpartners, like squarks and gluinos, with a variety of final states [278–283]. However, so far, no evidence for SUSY or dark matter has been found by LHC.

Chapter 4

Light dark sectors: the role of dark photon

> The story so far:
> In the beginning the Universe was created. This has made a lot of people very angry and been widely regarded as a bad move.
>
> *The Restaurant at the End of the Universe*
> Douglas Adams

In the previous chapters, we introduced the Standard Model of particle physics along with the most important inconsistencies affecting this theory. We studied the problem of neutrino masses, and the possibility to extend the Standard Model with new particles, realizing the seesaw Mechanism see § 2.5.2. Additionally, we characterized the dark matter problem, explaining that a new form of non-observable matter might exist to explain astrophysical observations. From a particle physics perspective, the addition of new particles is a valid solution to this problem, and WIMP-like dark matter candidates would provide a straightforward and elegant answer, see § 3.4. A common characteristic of beyond Standard Model particles is their *elusiveness*. These particles, if they exist, have not been detected so far. The non-observation can be explained assuming these new states are not charged under any Standard Model gauge group and might exist in secluded sectors that are mostly decoupled from the Standard Model itself, so that they are called *dark*, or *hidden*, sectors. Hidden sectors represent a compelling approach to the problems of Standard Model, since they can contain new gauge symmetries and new stable and feebly interacting particles, which can be promising dark matter candidates. Dark sectors can really shed light on the Standard Model problems, providing new prospects for model building and experimental searches. In particular, the connection between the dark sector and the Standard Model usually requires the presence of new mediators that couple to the two sectors [115, 284–286]. These mediators are usually called *portals* and can be new scalars (Higgs portal), heavy neutral leptons (neutrino portal), or new gauge bosons (vector portal). Experimental searches targeting the portals mediator offer a promising way to test the dark sector framework, and many efforts have been made in this direction [287–289].

In this chapter, we introduce the three portal connections that make dark sectors accessible from the Standard Model in § 4.1. In particular, we will focus on the dark photon Z', the vector portal mediator, in § 4.2. Model independent bounds on the dark photon will be discussed in § 4.3. A dark sector model featuring all three introduced portals will be presented in § 4.4. Finally, we will discuss the MiniBooNE LEE in the framework of a dark photon model in § 4.5.

4.1 The portal connections between dark sectors and the Standard Model

In the following we will introduce three renormalizable portals between a hidden sector and the Standard Model. In general, we will call these hidden sector models as dark sectors, applying the common convention, typically referring to below the electroweak scale sectors. However, in this section, we will not make any assumptions on the energy scale of the new states, so that the discussion will be valid for both low and high energy scenarios. Other kind of portals may exist, mainly involving other non-renormalizable interactions, see for example the axion-like particles coupling to photon.

4.1.1 The neutrino portal

The neutrino portal has already been introduced in § 2.5.1, as a way to generate neutrino masses in the Standard Model. It has been characterized in § 2.5.2 to couple the new right-handed sterile state N to the left-handed weak isospin doublet, in the same way as the Yukawa terms

$$\mathcal{L} \supset -(\overline{\mathbf{L}}\widetilde{H})Y\mathbf{N}\,, \tag{4.1}$$

where Y is the Yukawa matrix, and $\mathbf{N}$ might be a multiplet of sterile states. This has the same structure of the Yukawa terms, used to write Dirac mass terms for the Standard Model neutrinos, and introduced in eq. (2.39). Its components are also known as heavy neutral leptons (HNLs). The term $\overline{L_\alpha}\widetilde{H}$ is a Standard Model gauge singlet and can be coupled directly with other singlets. The inclusion of this term inside the Standard Model Lagrangian has the effect of inducing an off-diagonal term in the mass matrix. Off-diagonal terms allow the mixing between the Standard Model neutrinos and the new sterile states, and, ultimately, can be responsible for the generation of light neutrino masses. Additionally, it is also possible to write a Majorana mass term for each N_i, because they are sterile.

4.1.2 The scalar portal

As we just appreciated in the previous section, the combination of Standard Model components can result in a Standard Model singlet. These structures can then be used to build portal connections, using beyond Standard Model states, that are singlets under the Standard Model gauge groups. It is possible to build a singlet using the Standard Model Higgs doublet: $H^\dagger H$. This portal is known as the scalar portal or the Higgs portal. If we assume the existence of a new scalar state Φ, sterile under both the Standard Model and the dark sector, we can write the following portal connections:

$$\mathcal{L} \supset \lambda_{HH\Phi}(H^\dagger H)\Phi + \lambda_{HH\Phi\Phi}(H^\dagger H)\Phi^2 \,. \tag{4.2}$$

Alternatively, we can assume the existence of a new Abelian *dark* $U(1)_D$ gauge symmetry in the dark sector. Assuming the new scalar Φ is charged under this new symmetry, it would carry a dark charge Q_X. We assume no particles of the Standard Model are charged under it. In this case, the portal would be:

$$\mathcal{L} \supset \lambda_{H\Phi}(H^\dagger H)(\Phi^*\Phi) \,. \tag{4.3}$$

In this scenario, a mixing between the Higgs boson and the new scalar is generated, allowing the decay of the Higgs boson to the new scalar. Experimentally, this can be applied to constrain this kind of model with scalar mixing through invisible Higgs width searches. Given these kinds of bounds are usually quite strong, the portal coupling is generally small. Additionally, the portal is also responsible for the interaction between the new hidden scalar and the Standard Model massive fermions: the coupling is proportional to the fermion Yukawa coupling and the portal coupling, so that it is often suppressed.

4.1.3 The vector portal

We assume the existence of a new dark $U(1)_D$ symmetry in the dark sector. The gauge boson of this symmetry is X_μ, with field strength $X_{\mu\nu} = \partial_\mu X_\nu - \partial_\nu X_\mu$. It can couple, in general, with the hypercharge field strength $B_{\mu\nu}$:

$$\mathcal{L} \supset -\frac{\varepsilon}{2} B_{\mu\nu} X^{\mu\nu} \,, \tag{4.4}$$

where the parameter ε is known as kinetic mixing. Alternatively, in lower energetic scenarios, we can consider the coupling directly between $X_{\mu\nu}$ and the electromagnetic field strength tensor $F_{\mu\nu}$. The structure of eq. (4.4) allows the gauge bosons of the hypercharge group and the dark $U(1)_D$ to mix together, generating the mass states A_μ (photon), Z_μ (weak Z-boson), Z'_μ, the latter of them is known as the dark photon. The mixing allows the dark photon to couple to the neutral and electromagnetic currents, with a coupling proportional to the kinetic mixing. We will focus on the case of a massive dark photon. Among the possible mechanisms that can be responsible for generating its mass, we can either have a Stückelberg mechanism or the spontaneous symmetry breaking of a new scalar, charged under the new dark symmetry.

In general, the kinetic mixing parameter is expected to be sizable, unless forbidden by the existence of new symmetries. Despite that, no experimental observations for dark photons have been reported so far. It is possible to account for a smaller kinetic mixing by assuming that in an ultraviolet (UV) complete theory, new heavy states could be charged both under the Standard Model hypercharge and the new dark gauge group. In this case, we can compute the one-loop expectation for ε:

$$\varepsilon \approx \frac{g' g_D}{16\pi^2} \sum_i Q_i^Y Q_i^X \log\left(\frac{M_i^2}{\mu^2}\right) \approx \mathcal{O}\left(10^{-2} \text{ to } 10^{-3}\right) \tag{4.5}$$

with M_i and $Q_i^{\{Y,X\}}$ being the masses and charges of the new fermions running in the loop. We also define the renormalization scale μ, and the dark gauge coupling g_D, of the order of Standard Model couplings, and we further define:

$$\alpha_D \doteq \frac{g_D^2}{4\pi}\,. \tag{4.6}$$

Unfortunately, a kinetic mixing of this size has not been observed so far.

4.2 The dark photon

When studying the vector portal, we defined the dark photon as the gauge boson obtained after diagonalization of the gauge bosons mass matrix. Now we will introduce a minimal scenario of a model with a massive dark photon, where its mass is generated through the spontaneous symmetry breaking of a new scalar. In the following discussion, we focus on below the electroweak scale. We start by assuming the dark $U(1)_D$ symmetry with gauge boson X_μ. Additionally, we assume the existence of a scalar Φ, charged under the dark symmetry, with charge Q_X. This dark scalar is associated with a scalar potential $V(\Phi)$ and a scalar portal of the kind reported in eq. (4.3). Moreover, the dark scalar gets a VEV v_Φ, breaking the dark symmetry. The expansion of the field around the vacuum results in:

$$\Phi = \frac{1}{\sqrt{2}}(v_\Phi + \varphi)\,, \tag{4.7}$$

where we have fixed the unitary gauge, to get rid of the Goldstone bosons. The pattern of the dark symmetry breaking and its relation with the electroweak symmetry breaking will be further studied in § 4.4.1. We are interested in showing how the dark photon boson is defined and how the mass diagonalization is performed, therefore we limit ourselves into studying only the relevant terms of the Lagrangian:

$$\mathcal{L} \supset (\mathcal{D}_\mu H)^\dagger \mathcal{D}^\mu H + (\mathcal{D}_\mu \Phi)^\dagger \mathcal{D}^\mu \Phi - \frac{1}{4} B_{\mu\nu} B^{\mu\nu} - \frac{1}{4} W^a_{\mu\nu} W^{\mu\nu a} - \frac{1}{4} X_{\mu\nu} X^{\mu\nu} - \frac{s_\chi}{2} X_{\mu\nu} B^{\mu\nu} \,, \tag{4.8}$$

where the covariant derivative has the following general form:

$$\mathcal{D}_\mu = \partial_\mu - i\frac{g'}{2} Y B_\mu - i\frac{g}{2} \sigma^a W^a_\mu - i g_D Q_X X_\mu \,, \tag{4.9}$$

The kinetic term is clearly not diagonal, however, it must be placed in a diagonal form to be able to work with canonical propagators and Feynman rules. We perform the following field redefinition:

$$X'_\mu = X_\mu + s_\chi\, B_\mu \,, \tag{4.10a}$$
$$B'_\mu = c_\chi\, B_\mu \,, \tag{4.10b}$$

which is equivalent to the following non-unitary $GL(2,\mathbb{R})$ transformation, see [290]:

$$\begin{pmatrix} B_\mu \\ W_\mu \\ X_\mu \end{pmatrix} = \begin{pmatrix} \frac{1}{c_\chi} & 0 & 0 \\ 0 & 1 & 0 \\ -t_\chi & 0 & 1 \end{pmatrix} \begin{pmatrix} B'_\mu \\ W'_\mu \\ X'_\mu \end{pmatrix} \doteq \mathcal{R}(\chi) \begin{pmatrix} B'_\mu \\ W'_\mu \\ X'_\mu \end{pmatrix} . \tag{4.11}$$

The previous transformation allows diagonalizing the kinetic term:

$$\mathcal{L} \supset -\frac{1}{4} B'_{\mu\nu} B'^{\mu\nu} - \frac{1}{4} W'^a_{\mu\nu} W'^{\mu\nu a} - \frac{1}{4} X'_{\mu\nu} X'^{\mu\nu} \,. \tag{4.12}$$

Now we will focus on the scalars kinetic term. After electroweak symmetry breaking we obtain:

$$\begin{aligned}(\mathcal{D}_\mu H)^\dagger \mathcal{D}^\mu H = {} & \frac{1}{2}\partial_\mu h \partial^\mu h + \frac{g^2}{4} W^+_\mu W^{-\,\mu}(v_H^2 + 2v_H h + h^2) \\ & + \frac{g^2}{8} W^3_\mu W^{3\,\mu}(v_H^2 + 2v_H h + h^2) + \frac{g'^2}{8} B_\mu B^\mu (v_H^2 + 2v_H h + h^2) \\ & + \frac{g g'}{4} W^3_\mu B^\mu (v_H^2 + 2v_H h + h^2) \,,\end{aligned} \tag{4.13}$$

and after dark symmetry breaking:

$$(\mathcal{D}_\mu \Phi)^\dagger \mathcal{D}^\mu \Phi = \frac{1}{2}\partial_\mu \varphi \partial^\mu \varphi + \frac{g_D^2}{4} Q_X^2 X_\mu X^\mu (v_\varphi^2 + 2v_\varphi h + h^2) \,. \tag{4.14}$$

Eq. (4.13) contains the mass terms and the interactions with h and φ*. We can now collect the mass terms and write the mass matrix:

$$\mathcal{L} \supset \frac{1}{2}\begin{pmatrix} B_\mu & W_\mu & X_\mu \end{pmatrix} \begin{pmatrix} \frac{v_H^2}{4} g'^2 & -\frac{v_H^2}{4} g g' & 0 \\ -\frac{v_H^2}{4} g g' & \frac{v_H^2}{4} g^2 & 0 \\ 0 & 0 & v_\Phi^2 g_D^2 Q_X^2 \end{pmatrix} \begin{pmatrix} B^\mu \\ W^\mu \\ X^\mu \end{pmatrix} . \tag{4.15}$$

It is interesting to notice that the only mixing of the X_μ boson is given by the kinetic mixing, not by mass mixing terms. Performing the transformation in eq. (4.11) we obtain:

$$\begin{aligned}\mathcal{L} &\supset \frac{1}{2}\begin{pmatrix} B'_\mu & W'_\mu & X'_\mu \end{pmatrix} \mathcal{R}(\chi)^T \begin{pmatrix} \frac{v_H^2}{4} g'^2 & -\frac{v_H^2}{4} g g' & 0 \\ -\frac{v_H^2}{4} g g' & \frac{v_H^2}{4} g^2 & 0 \\ 0 & 0 & v_\Phi^2 g_D^2 Q_X^2 \end{pmatrix} \mathcal{R}(\chi) \begin{pmatrix} B'^\mu \\ W'^\mu \\ X'^\mu \end{pmatrix} \\ &= \frac{(m_Z^{SM})^2}{2}\begin{pmatrix} B'_\mu & W'_\mu & X'_\mu \end{pmatrix} \begin{pmatrix} \frac{s_w^2 + \mu^2 s_\chi}{c_\chi^2} & -\frac{c_w s_w}{c_\chi} & -\mu^2 Q_X^2 t_\chi \\ -\frac{c_w s_s}{c_\chi} & c_w^2 & 0 \\ -\mu^2 Q_X^2 t_\chi & 0 & \mu^2 Q_X^2 \end{pmatrix} \begin{pmatrix} B'^\mu \\ W'^\mu \\ X'^\mu \end{pmatrix} .\end{aligned} \tag{4.16}$$

where we defined:

$$s_w = \frac{g'}{\sqrt{g^2 + g'^2}} , \tag{4.17a}$$

$$c_w = \frac{g}{\sqrt{g^2 + g'^2}} , \tag{4.17b}$$

$$m_Z^{SM} = \frac{v_H}{2}\sqrt{g^2 + g'^2} , \tag{4.17c}$$

$$\mu = \frac{g_D v_\Phi}{m_Z^{SM}} . \tag{4.17d}$$

The diagonalization of the matrix is necessary to obtain the physical mass states of the gauge bosons. It is possible to proceed in steps. First, we perform the following transformation using the rotation matrices:

$$\begin{aligned} R_z(\vartheta_w)^T R_y(-\chi)^T &\begin{pmatrix} \frac{s_w^2 + \mu^2 s_\chi}{c_\chi^2} & -\frac{c_w s_w}{c_\chi} & -\mu^2 Q_X^2 t_\chi \\ -\frac{c_w s_s}{c_\chi} & c_w^2 & 0 \\ -\mu^2 Q_X^2 t_\chi & 0 & \mu^2 Q_X^2 \end{pmatrix} R_y(-\chi) R_z(\vartheta_w) \\ &= \begin{pmatrix} 0 & 0 & 0 \\ 0 & 1 & s_w t_\chi \\ 0 & s_w t_\chi & \frac{\mu^2}{c_\chi^2} + s_w^2 t_\chi^2 \end{pmatrix} . \end{aligned} \tag{4.18}$$

*As we will see in § 4.1.2, h and φ scalar mass states are a superposition of the h and φ that are contained in the expressions.

It is now clear that the first eigenvalue we have found is related to the physical state of the massless photon. The remaining sub-block can be diagonalized with a single rotation:

$$R_x(\beta)^T \begin{pmatrix} 0 & 0 & 0 \\ 0 & 1 & s_w\, t_X \\ 0 & s_w\, t_X & \frac{\mu^2}{c_X^2} + s_w^2\, t_X^2 \end{pmatrix} R_x(\beta) = \begin{pmatrix} 0 & 0 & 0 \\ 0 & \lambda_+ & 0 \\ 0 & 0 & \lambda_- \end{pmatrix}, \tag{4.19}$$

where the rotation angle is expressed by:

$$\tan(2\beta) = \frac{2\, s_X\, c_X}{c_X^2 - s_X^2 - \mu^2 Q_X^2}\,. \tag{4.20}$$

The eigenvalues are:

$$\lambda_+ = 1 + s_w\, t_X\, t_\beta\ , \tag{4.21a}$$

$$\lambda_- = 1 - \frac{s_w\, t_X}{t_\beta}\,, \tag{4.21b}$$

so that we can write the final mass terms for the gauge bosons as:

$$\mathcal{L} \supset= \frac{1}{2} \begin{pmatrix} A_\mu & Z_\mu & Z'_\mu \end{pmatrix} \begin{pmatrix} 0 & 0 & 0 \\ 0 & m_Z^2 & 0 \\ 0 & 0 & m_{Z'}^2 \end{pmatrix} \begin{pmatrix} A_\mu \\ Z_\mu \\ Z'^{\mu} \end{pmatrix}; \tag{4.22}$$

with

$$m_Z^2 = \left(m_Z^{SM}\right)^2 (1 + s_w\, t_X\, t_\beta)\,, \tag{4.23a}$$

$$m_{Z'}^2 = \left(m_Z^{SM}\right)^2 \left(1 - \frac{s_w\, t_X}{t_\beta}\right). \tag{4.23b}$$

Considering the transformations all together we obtain the relations expressing the original massless gauge bosons in the Lagrangian through the physical states:

$$B_\mu = c_w\, A_\mu - (s_w\, c_\beta + t_X\, s_\beta) Z_\mu + (s_w\, c_\beta - t_X\, c_\beta) Z'_\mu\,, \tag{4.24a}$$

$$W_\mu^3 = s_w\, A_\mu + c_w\, c_\beta\, Z_\mu - c_w\, s_\beta\, Z'_\mu\,, \tag{4.24b}$$

$$X_\mu = \frac{s_\beta}{c_X} Z_\mu + \frac{c_\beta}{c_X} Z'_\mu\,. \tag{4.24c}$$

Additionally, it is possible to express the Standard Model fields as functions of the new fields:

$$A_\mu^{SM} = A_\mu - t_X\, c_w\, s_\beta\, Z_\mu - t_X\, c_w\, c_\beta\, Z'_\mu\,, \tag{4.25a}$$

$$Z_\mu^{SM} = (c_\beta + t_X\, s_w\, s_\beta) Z_\mu - (s_\beta - t_X\, s_w\, c_\beta) Z'_\mu\,. \tag{4.25b}$$

Recalling the coupling of the photon and the Z boson in the Standard Model:

$$-\mathcal{L}_{\rm SM} \supset e\, A^{\rm SM}_\mu J^\mu_{\rm em} + \frac{g}{2\,c_W} Z^{\rm SM}_\mu J^\mu_{\rm nc}\,, \tag{4.26}$$

then we can use eq. (4.25) and write the following interaction Lagrangian:

$$\begin{aligned}
-\mathcal{L} \supset{}& e\, A_\mu J^\mu_{\rm em} \\
&+ Z_\mu \left[-e\, t_\chi\, c_W\, s_\beta\, J^\mu_{\rm em} + (c_\beta + t_\chi\, s_W\, s_\beta) \frac{g}{2\,c_W} J^\mu_{\rm nc} \right] \\
&+ Z'_\mu \left[-e\, t_\chi\, c_W\, c_\beta\, J^\mu_{\rm em} - (s_\beta - t_\chi\, s_W\, c_\beta) \frac{g}{2\,c_W} J^\mu_{\rm nc} \right].
\end{aligned} \tag{4.27}$$

Assuming the χ parameter to be small, translating in a smaller kinetic mixing, it is possible to define:

$$\varepsilon \doteq c_W\, t_\chi \approx c_W\, \chi\,. \tag{4.28}$$

Recalling also eq. (4.23), the interaction Lagrangian can be written as:

$$\begin{aligned}
-\mathcal{L} \supset{}& e\, A_\mu J^\mu_{\rm em} \\
&+ Z_\mu \left[-e\varepsilon\, s_\beta\, J^\mu_{\rm em} + c_\beta\, \frac{g}{2\,c_W} \frac{m_Z^2}{(m_Z^{\rm SM})^2} J^\mu_{\rm nc} \right] \\
&+ Z'_\mu \left[-e\varepsilon\, c_\beta\, J^\mu_{\rm em} - s_\beta\, \frac{g}{2\,c_W} \frac{m_{Z'}^2}{(m_Z^{\rm SM})^2} J^\mu_{\rm nc} \right].
\end{aligned} \tag{4.29}$$

The mixing realized with the vector portal makes possible for the new definition of the Z boson to couple to both Standard Model and the dark sector. Furthermore, we can explicitly write the fermion interaction Lagrangian obtaining the new fermion vertices, starting from:

$$\overline{\psi} i \not{D} \psi = \sum_f \overline{\psi}_f \left(\not{\partial} - i\frac{g}{2}\sigma^a \not{W}^a - i\frac{g'}{2} Y^f \not{B} - i g_D Q^f_X \not{X} \right) \psi_f\,, \tag{4.30}$$

assuming ψ_f, with $f \in \{ q_\upsilon, q_\delta, \ell_\alpha, \nu_\alpha \}$, with $\upsilon \in \{ u, c, t \}$ (u-like quarks), $\delta \in \{ d, s, b \}$ (d-like quarks), $\alpha \in \{ e, \mu, \tau \}$ (leptons). Notice that in this case we are not considering the existence of particles with dark charge Q_X[†]. By means of the Gell-Mann–Nishijima relation in eq. (2.6), it is possible to write

[†] A proper dark sector model with dark-charged particles will be considered in § 4.4; in particular § 4.4.2 will contain updated versions of the equations shown in the current section.

Table 4.1: The vector and axial-vector couplings of the Standard Model fermions with the Z and Z′ bosons, notice that $\frac{g}{2\,c_W} = \frac{e}{4\,s_W\,c_W}$.

		Vector	Axial-vector
Z_μ	ℓ_α	$c_V^\ell = \frac{g}{2\,c_W}\left[c_\beta\left(-1+4\,s_W^2\right)+3\,t_\chi\,s_W\,s_\beta\right]$	$c_A^\ell = -\frac{g}{2\,c_W}\left(c_\beta + s_\beta\,s_W\,t_\chi\right)$
	ν_α	$c_V^\nu = \frac{g}{2\,c_W}\left(c_\beta + t_\chi\,s_W\,s_\beta\right)$	$c_A^\nu = \frac{g}{2\,c_W}\left(c_\beta + t_\chi\,s_W\,s_\beta\right)$
	q_υ	$c_V^u = \frac{g}{2\,c_W}\left[c_\beta\left(1-\frac{8}{3}\,s_W^2\right)-\frac{5}{3}\,t_\chi\,s_W\,s_\beta\right]$	$c_A^u = \frac{g}{2\,c_W}\left(c_\beta + t_\chi\,s_W\,c_\beta\right)$
	q_δ	$c_V^d = \frac{g}{2\,c_W}\left[c_\beta\left(-1+\frac{4}{3}\,s_W^2\right)+\frac{1}{3}\,t_\chi\,s_W\,s_\beta\right]$	$c_A^d = -\frac{g}{2\,c_W}\left(c_\beta + t_\chi\,s_W\,s_\beta\right)$
Z'_μ	ℓ_α	$d_V^\ell = \frac{g}{2\,c_W}\left[3\,t_\chi\,s_W\,c_\beta - s_\beta\left(-1+4\,s_W^2\right)\right]$	$d_A^\ell = -\frac{g}{2\,c_W}\left(t_\chi\,s_W\,c_\beta - s_\beta\right)$
	ν_α	$d_V^\nu = \frac{g}{2\,c_W}\left(t_\chi\,s_W\,c_\beta - s_\beta\right)$	$d_A^\nu = \frac{g}{2\,c_W}\left(t_\chi\,s_W\,c_\beta - s_\beta\right)$
	q_υ	$d_V^u = -\frac{g}{2\,c_W}\left[\frac{5}{3}\,t_\chi\,s_W\,c_\beta + s_\beta\left(1-\frac{8}{3}\,s_W^2\right)\right]$	$d_A^u = \frac{g}{2\,c_W}\left(t_\chi\,s_W\,c_\beta - s_\beta\right)$
	q_δ	$d_V^d = \frac{g}{2\,c_W}\left[\frac{1}{3}\,t_\chi\,s_W\,c_\beta - s_\beta\left(-1+\frac{4}{3}\,s_W^2\right)\right]$	$d_A^d = -\frac{g}{2\,c_W}\left(t_\chi\,s_W\,c_\beta - s_\beta\right)$

the following interaction Lagrangians, first for the vector couplings:

$$
\begin{aligned}
-\mathcal{L}_V \supset \sum_f \overline{\psi}_f \gamma^\mu \Bigg\{ & A_\mu\left(eQ_e^f\right) \\
& + Z_\mu\left[\frac{e}{4\,s_W\,c_W}\left(c_\beta\left(4\,c_W^2\,Q_e^f - Y_L^f - Y_R^f\right) - t_\chi\,s_W\,s_\beta\left(Y_L^f + Y_R^f\right)\right)\right] \\
& + Z'_\mu\left[\frac{e}{4\,s_W\,c_W}\left(s_\beta\left(Y_L^f + Y_R^f - 4Q_e^f\,c_W^2\right) - t_\chi\,s_W\,c_\beta\left(Y_L^f + Y_R^f\right)\right)\right]\Bigg\}\psi_f\,,
\end{aligned}
\tag{4.31}
$$

and then for the axial-vector couplings

$$
\begin{aligned}
-\mathcal{L}_A \supset \sum_f \overline{\psi}_f \gamma^\mu \gamma^5 \Bigg\{ & Z_\mu\left[\frac{e}{4\,s_W\,c_W}\left(Y_R^f - Y_L^f\right)\left(c_\beta + t_\chi\,s_W\,s_\beta\right)\right] \\
& + Z'_\mu\left[\frac{e}{4\,s_W\,c_W}\left(Y_R^f - Y_L^f\right)\left(t_\chi\,s_W\,c_\beta - s_\beta\right)\right]\Bigg\}\psi_f\,,
\end{aligned}
\tag{4.32}
$$

So that the final interaction Lagrangian can be written as

$$
-\mathcal{L} \supset \overline{\psi}_f \gamma^\mu\left[\left(eQ_e^f\right)A_\mu + \left(c_V^f - c_A^f\gamma^5\right)Z_\mu + \left(d_V^f - d_A^f\gamma^5\right)Z'_\mu\right]\psi_f\,, \tag{4.33}
$$

where the coefficients are defined in tab. 4.1.

The dark photon here defined represents a realization of the vector and scalar portals introduced in § 4.1. Moreover, it constitutes the common base which many of the dark sector model that will be studied in this dissertation are based on. The dark photon is able to mediate interactions between the Standard Model and a hypothetical hidden sector, that could contain multiple generations of states. These states may or may not be charged under the new $U(1)_D$ dark symmetry. New states can then constitute possible dark matter candidates or may couple to the Standard Model through a neutrino portal, resulting in the possibility to explain neutrino masses. Moreover, the dark photon would be able to both decay invisibly into these new dark states and to decay visibly, thanks to the couplings to electromagnetic and neutral currents.

4.3 Model independent bounds

In this dissertation, we will consider dark photons with mass in the range from 10 MeV to 10 GeV and kinetic mixing of the order 10^{-4} to 0.1. Several model-independent constraints have been placed in this range of masses and kinetic mixing, mainly coming from colliders, and beam dump experiments [291–295]. Indeed, given the coupling of dark photons to the Standard Model, there is the possibility for it to decay to e^+e^- pairs, which can be searched for in colliders. We summarize the model independent constraints in fig. 4.1, while a more detailed discussion can be found in [287, 289, 296, 297]. This section is partially based on [4].

4.3.1 Visible resonance searches

Visible dark photon searches are one among the most common strategies for dark photon searches at colliders and beam dump experiments [304–306]. They exploit the fact that the dark photon can be produced on-shell, decaying into Standard Model particles, such as e^+e^-, $\pi^+\pi^-$ and $\pi^+\pi^-\pi^0$. The dark photon production cross section is proportional to $\varepsilon^2 \frac{\alpha_{em}}{\alpha_D}$. The inverse proportionality to α_D makes the dark photon resonance wider for large values of it, tampering the beam hunt search. Another strategy would be to search for virtual dark photon exchange processes, which would provide a constraint independent on the model details and branching ratios.

4.3.2 Deep-inelastic scattering

The features of a kinetic mixing portal manifest themselves also in deep-inelastic scattering (DIS) experiments. The direct coupling of dark photons to Standard Model fermions makes it possible for the dark photon to be exchanged in t-channel diagrams of charged leptons scattering on nuclei. This has the effect of modifying the parton distribution functions (PDFs) [307–310]. In 2020,

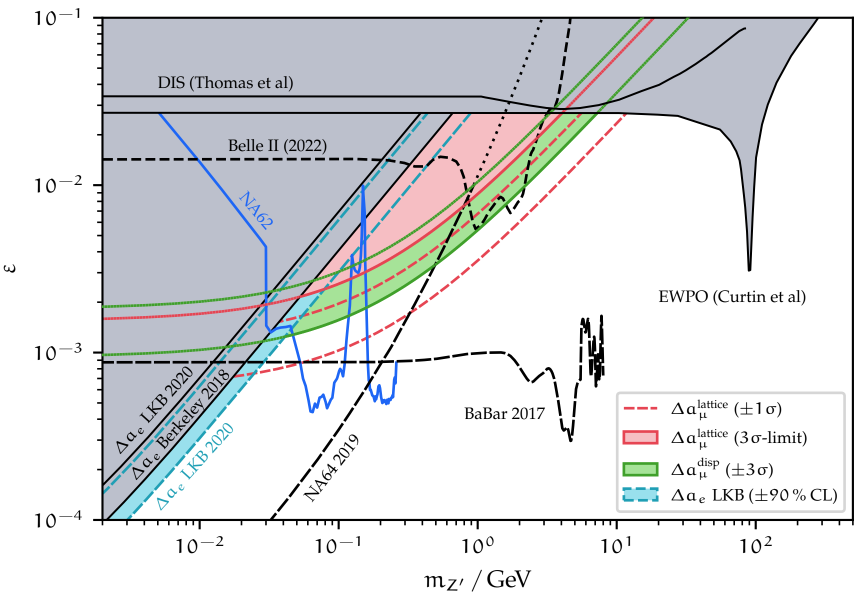

Figure 4.1: Model independent bounds on kinetic mixing ε and limits assuming invisible dark photon decays. Gray regions indicate limits independent on the decay channels of the dark photon. Blue solid lines indicate constraints from meson decays, $\pi^0 \to \gamma Z'$ and $K^+ \to \pi^+ Z'$, assuming Z' is invisible. Constraints from BaBar [298], NA64 [299], Belle-II [300] (recast, see text) are shown in dashed lines. The green region represents the preferred parameter space to explain $\Delta a_\mu^{\text{disp}}$ at $3\,\sigma$, while the constraints obtained from lattice results, $\Delta a_\mu^{\text{lattice}}$, are drawn in solid orange lines and dashed orange lines ($1\,\sigma$). Constraints coming from the anomalous magnetic moment of the electron, Δa_e, are shown in dashed black lines for what concerns the most recent measurements [301, 302], while the light blue region indicates the region of preference to explain the measurement of the α_{em} constant by the LKM group [303]. Adapted from [4, fig. 2].

for the first time, the work [307] set a limit on the kinetic mixing by fixing the PDFs to the best-fit values of the HERA measurement, finding $\varepsilon \lessapprox 0.015$ for $m_{Z'} \lessapprox 2\,\text{GeV}$ at 95 % CL. Later on, also the authors of [308] were successful in the same attempt, finding $\varepsilon \lessapprox 0.034$ for $m_{Z'} < 1\,\text{GeV}$ at 95 % CL.

4.3.3 Electroweak precision observables

The measurement of the electroweak precision observables (EWPO) have been used to perform a global fit on Standard Model parameters. This has been exploited to predict and constrain new quantities coming from new physics. The most important observable affected by the value of the kinetic mixing in this case is

$$m_Z^2 \approx m_{Z^0}^2 - \varepsilon^2 m_{Z'}^2 \,, \tag{4.34}$$

which is also responsible for the shift in the mass of the W boson. Boson W-mass measurements can be used to constraint the value of ε, as shown in [311], where the following bound has been found: $\varepsilon^2_{\text{EWPO}} < 7.3 \times 10^{-4}$ at 95 % CL for $m_{Z'} \ll 10\,\text{GeV}$. Recent developments in the W-mass searches have been obtained in [312], where the CDF collaboration reported a significant deviation from the previous measurements.

4.3.4 Meson decays

The production of dark photons in meson decays is a robust way to constrain the kinetic mixing [291]. Searches for invisible dark photons have been performed looking at the channels $\pi^0 \to \gamma Z'$ [313] and $K \to \pi Z'$, with Z' invisible [314]. The latter has been updated using the latest measurement of $K \to \pi\nu\bar{\nu}$ [315], obtained by NA64, including also the dedicated search for $\pi^0 \to \text{inv.}$ [316].

4.3.5 Anomalous magnetic moments of electron and muon

Consider a fermion ℓ with mass m_ℓ and electric charge q_ℓ moving in a magnetic field $\mathbf{B}$. Its motion is described by the Dirac equation. In the non-relativistic limit, the Hamiltonian is:

$$H = \frac{p^2}{2m_\ell} + V(r) + \frac{q_\ell}{2m_\ell}\mathbf{B} \cdot (\mathbf{L} + g_\ell \mathbf{S}) \,, \tag{4.35}$$

where $\mathbf{p}$ is the momentum, $V(r)$ is the potential, $\mathbf{L}$ is the orbital angular momentum and $\mathbf{S}$ is the spin. The coupling g_ℓ, sometimes known as g-factor in the case of the electron, represents the strength of the lepton's intrinsic *magnetic dipole moment* to the classical spin-orbit coupling. It is possible to define the

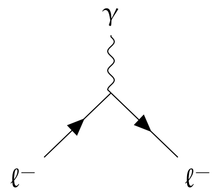

Figure 4.2: The tree-level photon-lepton coupling mediated by the intrinsic magnetic moment.

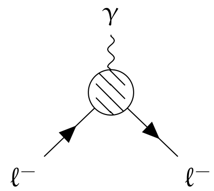

Figure 4.3: One-loop correction diagram to the lepton magnetic moment.

intrinsic magnetic dipole moment as the quantity:

$$\mu_\ell^s \doteq g_\ell \frac{q_\ell}{2m_\ell} \mathbf{S}\,, \tag{4.36}$$

while the orbital magnetic dipole moment is:

$$\mu_\ell^l \doteq \frac{q_\ell}{2m_\ell} \mathbf{L}\,. \tag{4.37}$$

This coupling plays a role in the diagram represented in fig. 4.2. One of the most important conclusions of the Dirac equation was the prediction of $g_\ell = 2$, in excellent agreement with data [317] in 1928. However, an important question arose in the following years, whether g_ℓ is exactly 2 or there may be quantum corrections that could modify its value slightly. This was motivated in part by the calculation of the hyperfine structure of hydrogen [318, 319], and obtained great attention after the development and understanding of the renormalization of QED. Schwinger advanced the hypothesis that an additional contribution from radiative corrections could predict an anomalous magnetic moment, which can be defined as

$$a_\ell \doteq \frac{g_\ell - 2}{2}\,, \tag{4.38}$$

and it is known also as $g_\ell - 2$ or $(g-2)_\ell$. Corrections to the magnetic moment must come from diagrams of the kind represented in fig. 4.3, and contributing to the process in fig. 4.2. The calculation, performed by Schwinger [320],

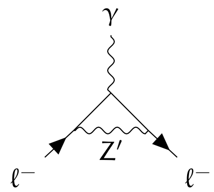

Figure 4.4: Dark photon one-loop correction to the lepton's anomalous magnetic moment.

Feynman [321] and Tomonaga [322] in 1948, resulted in the value:

$$a_\ell^{\text{1-loop}} = \frac{\alpha_{\text{em}}}{2\pi} \approx 0.001\,16\,, \tag{4.39}$$

which was in agreement with experiments [323]. The precision measurement of the leptons anomalous magnetic moments makes possible to derive model-independent constraints on ε. In particular, the dark photon enters the one-loop correction diagrams represented in fig. 4.3. The kinetic mixing between the gauge boson of the new $U(1)_D$ symmetry and the hypercharge boson allows the dark photon to couple to Standard Model states, thanks to the mixing with the Standard Model photon. This makes possible to realize the interaction diagram shown in fig. 4.4, which brings a correction to the lepton's anomalous magnetic moment. The correction to the value of a_ℓ is given by:

$$\Delta a_\ell^{Z'} = \frac{\alpha_{\text{em}}}{2\pi}\varepsilon^2 \int_0^1 dz \frac{2m_\ell^2 z(1-z)^2}{m_\ell^2(1-z)^2 + m_{Z'}^2 z^2}\,, \tag{4.40}$$

where ε is the kinetic mixing parameter, while $\Delta a_\ell \doteq a_\ell^{\text{exp}} - a_\ell^{\text{SM}}$, representing the deviation of the experimental measurement a_ℓ^{exp} from the theory prediction based on the Standard Model a_ℓ^{SM}. It is important to notice that the contribution expressed by eq. (4.40) comes with a positive sign.

Electron $(g-2)$

The electron a_e has been measured in 2008 [301] and later in 2022 with 2.2 times more precision [302]. The collaboration quoted the following value for g_e:

$$\frac{g_e}{2} = (100\,115\,965\,218\,059 \pm 13) \times 10^{-14}\,. \tag{4.41}$$

The theoretical prediction for a_e is given by [324], and it can be compared to the experimental estimation. However, the prediction is affected by the value of the fine structure constant α_{em}, which is not known with sufficient precision. The two leading measurements of α_{em} have been performed by a group in Berkeley [325], using ^{133}Ce atoms to reach an uncertainty of 120 ppm, and a by group in Paris [303], using a technique known as LKM to measure α_{em} lowering the precision to 81 ppm [303]. Nevertheless, the two measurements are in disagreement at more than $5\,\sigma$ with each other, showing that it is not possible to derive a meaningful bound. In this thesis, we followed a conservative approach, and we quoted the most stringent limit, which is the one coming from the Berkeley group [325]. Consequently, the deviation of the experimental measurement from the theoretical prediction is:

$$\Delta a_e = (-102 \pm 26) \times 10^{-14}\,. \tag{4.42}$$

The deviation has a negative sign. Given the dark photon contribution in eq. (4.40) has a positive sign, it would increase the significance of the measurement. The parameter space of the dark photon can be constrained by assuming that its contribution to Δa_e does not make the measurement to exceed $5\,\sigma$ significance.

In fig. 4.1, both limits coming from the two approaches for the calculations of the fine structure constant are shown, together with the region of preference that would explain the measurement of the Paris group [303]. In general, the bounds exclude the Δa_μ-explanation for dark photon masses below $m_{Z'} \approx 30\,\text{MeV}$.

Muon $(g-2)$

The muon anomalous magnetic moment is not affected by the uncertainties on α_{em}, because theoretical and experimental uncertainties on a_μ are much larger. Therefore, it is not subject to the ambiguities discussed for a_e and the enhancement due to the factor $a_\mu/a_e \approx m_\mu^2/m_e^2$ makes it more sensitive to new physics. The theoretical predictions for a_μ in the Standard Model (see [324, 326, 327] for a review) have differed from the experimental measurement at E821 at the Brookhaven National Laboratory (BNL) with a significance of $3.7\,\sigma$ [328–330],

$$a_\mu^{\text{BNL}} = (116\,592\,920 \pm 63) \times 10^{-11}\,. \tag{4.43}$$

Following the BNL measurement, a_μ has been measured at the Fermi National Accelerator Laboratory (FNAL) at the E989 experiment [331], using the data collected in 2018 (FNAL-I) [332] and later using the data collected until 2020 (FNAL-II) [333]. Both the FNAL measurement confirmed the central value of the BNL measurement, reporting:

$$a_\mu^{\text{FNAL-I}} = (116\,592\,040 \pm 54) \times 10^{-11}\,, \tag{4.44}$$

$$a_\mu^{\text{FNAL-II}} = (116\,592\,057 \pm 25) \times 10^{-11}\,, \tag{4.45}$$

where the error in parentheses is the sum in quadrature of systematical and statistical errors. The FNAL average is:

$$a_\mu^{\rm FNAL} = (116\,592\,055 \pm 24) \times 10^{-11}\,, \tag{4.46}$$

so that the current experimental world average is set to:

$$a_\mu^{\rm exp} = (116\,592\,059 \pm 22) \times 10^{-11}\,. \tag{4.47}$$

Eventually, the remaining three years of data collection are expected to improve the precision of the measurement by a factor of 2. Next generation experiments, like the J-PARC muon facility [334], will have the possibility to test this value using complementary techniques with lower muon momenta.

The Standard Model predictions are obtained by combining QED corrections up to 5 loops [335, 336], electroweak ($a_\mu^{\rm EW}$) corrections up to 2 loops [337, 338], and hadronic contributions including the hadronic vacuum polarization ($a_\mu^{\rm HVP}$) [339–344] and hadronic light-by-light scattering ($a_\mu^{\rm HLbL}$) diagrams [345–359]. The uncertainty is dominated by the $a_\mu^{\rm HVP}$ component. The two terms HPV and HLbL can be computed using either data-driven dispersive methods or lattice QCD calculations. In the former case, the hadronic contributions are obtained by integrating the cross section of $e^+e^- \to$ hadrons, using experimental measurements of the relevant quantities, like the R-ratio, while in the latter case, the hadronic contributions are obtained by computing the relevant correlation functions on the lattice. The data-driven calculation for $a_\mu^{\rm HVP}$ and $a_\mu^{\rm HLbL}$ converge on the prediction [324] (known as the *White Paper* estimation):

$$a_\mu^{\rm disp} = (116\,591\,810 \pm 43) \times 10^{-11}\,. \tag{4.48}$$

If the dispersive value holds, the tension between experiment and theory reaches 5.1 σ, where $\Delta a_\mu^{\rm disp} = a_\mu^{\rm disp} - a_\mu^{\rm exp}$ is

$$\Delta a_\mu^{\rm disp} = (249 \pm 48) \times 10^{-11}\,. \tag{4.49}$$

In principle, one could try to explain this discrepancy invoking hadronic uncertainties or deviation in the cross section $\sigma(e^+e^- \to \text{hadrons})$. Both the idea have been tested in the literature: hadronic uncertainties are not large enough to account for the deviation [360–362], while a discrepancy in the value of the cross section $\sigma(e^+e^- \to \text{hadrons})$ has been ruled out for e^+e^- center-of-mass energies of $\sqrt{s} > 0.7\,\text{GeV}$ [363]. The latter implies that, if any missed contribution exists, then it would be hiding in the $\pi^+\pi^-$ region [364]. Moreover, other sub-dominant channels measurements have been obtained by the BABAR, BESIII, CMD-3, and SND collaborations. Finally, it should not be excluded that new physics could be hiding in these data [365–368].

However, lattice calculations bring a different prediction for $a_\mu^{\rm HVP}$, which does not agree with the data-driven approach. In this context, the BMW collaboration [369] obtained a value for $a_\mu^{\rm HVP}$ with a 2.1 σ significant disagreement with the value obtained using the data-driven dispersive method of [324]. Using the BMW result for $a_\mu^{\rm HVP}$ brings the deviation between theory and the experimental average down to 1.5 σ,

$$\Delta a_\mu^{\rm lattice} = (107 \pm 69) \times 10^{-11} \,. \tag{4.50}$$

This result is currently under a careful scrutiny by the lattice community, and it is not clear whether there exist additional sources of systematic uncertainties, in particular for what concerns the discretization and finite-volume effects. Further consistency checks of the BMW result rely on the calculation of the separate pieces $a_\mu^{\rm SD}$ and $a_\mu^{\rm W}$, which are the contribution to $a_\mu^{\rm HVP}$ coming from respectively the short and intermediate time-distance regions. These terms are known as *Euclidean window observables* [370]. The data-driven dispersive method and the lattice calculations agree on the value of $a_\mu^{\rm SD}$, while the comparison with $a_\mu^{\rm W}$ results in a 3.8 σ significant tension with all lattice results [369–373]. This behavior suggests a possible disagreement with $e^+e^- \to$ hadrons data in the energy region $\sqrt{s} \approx (1 \text{ to } 3)$ GeV [374]. The 3 σ preference region for $\Delta a_\mu^{\rm disp}$ is shown as a green band in fig. 4.1, alongside the 1 σ preference band and the 3 σ exclusion limit from $\Delta a_\mu^{\rm lattice}$.

Recently, un update on the data-driven approach was released by the CMD-3 collaboration [375], showing new results on the cross section of $\pi^+\pi^-$, which turned out to be in tensions with all previous measurements used in [324], including measurements from CMD-2 and SND experiments. Surprisingly, the new measurement shows an agreement with the lattice calculations. However, this result is currently under investigation, and the origin of the discrepancy is not clear.

4.3.6 Belle-II

The Belle-II experiment is an e^+e^- collider located at the SuperKEKB accelerator in Tsukuba, Japan. It performed searches for $L_\mu - L_\tau$ gauge bosons, in collisions of the kind $e^+e^- \to \mu^+\mu^- Z'_{\mu-\tau}$, with dark photons emitted as FSR, and studying the missing energy carried by $Z'_{\mu-\tau}$. Differently, the analogous QED process $e^+e^- \to \mu^+\mu^-\gamma$ can be characterized by either initial state radiation (ISR) or FSR, and that applies also to $U(1)_D$ dark photons. The ISR and FSR components interfere, and may generate important charge asymmetries [376], which would modify the differential rate for a dark photon. However, it is possible to provide a simple estimate of the Belle-II limit on the kinetic mixing, if we neglect the interference term, and we add together the ISR and FSR pieces. This limit is shown in fig. 4.1 with an asterisk to emphasize the approximation in the recast method. A proper recast operation would require a dedicated study of the efficiencies.

4.4 An example of a dark sector model: the three-portal model

The presence of a new dark symmetry $U(1)_D$ makes possible to build an entire new sector of particles which are singlets under the Standard Model gauge groups, and charged under the dark symmetry, so that they can be secluded. Additionally, the dark sector can also contain states that are neutral under all gauge groups, and considered to be sterile. The only way to communicate through such a sector is with the portals introduced in § 4.1. These portals, together with the dark photon, are the main ingredients of the dark sector models that will be studied in this dissertation. In general, the new states making up the dark sector can be either be scalar or fermions. In this dissertation we will focus mainly on a fermionic dark sectors, whose components are known as heavy neutral fermions (HNFs). As we already mentioned, the presence of a neutrino portal allows these states to mix with the Standard Model neutrinos, and they are referred to as HNLs and labeled N_4, N_5, and so on. Furthermore, dark sectors of this kind offer a natural mechanism for generating dark matter candidates. The secluded nature of the dark sector means that the lightest HNF can be made stable easily (this would imply to remove any other interaction or portal that would allow for the dark particles to interact with the Standard Model) and be considered a dark matter candidate. In such case, conventionally, the lightest HNF is denoted as χ_1, while the heavier particles in the spectrum are labeled as χ_j with $j \in \{2, \ldots, n\}$.

In the following, we will introduce a dark sector model [377] that utilizes the three kind of portals previously introduced in § 4.1. The model is characterized by a spontaneously-broken $U(1)_D$ gauge symmetry and the presence of a neutrino portal allows it to provide a mechanism to generate neutrino masses. The new gauge symmetry is characterized by the scalar Φ and the phenomenology is equivalent to what has been presented in § 4.2: the gauge symmetry spontaneously breaks below the electroweak scale by the VEV of Φ, $v_\Phi = \mathcal{O}(500\,\text{MeV})$, and the dark gauge boson X_μ can mix with the Standard Model bosons B_μ and W^3_μ to produce the mass states A_μ, Z_μ and Z'_μ. Additionally, the model includes d vector-like dark fermions, $\boldsymbol{\nu}_D = \boldsymbol{\nu}_{D_L} + \boldsymbol{\nu}_{D_R}$, and n completely sterile states, $\boldsymbol{\nu}_N$. The scalar Φ and the dark fermions $\boldsymbol{\nu}_D$ have dark charge $Q_X = Q$, which guarantees the anomaly freedom of the model[‡]. In tab. 4.2 we show the new states and their quantum numbers. The full Lagrangian of the model

[‡]Independently on this feature, the next steps will be carried out assuming each fermion to have a dark charge in general different from the other fermions.

Table 4.2: The field content of the three-portal model, for $U(1)_Y$ and $U(1)_D$ we indicate the respective charges.

Field	$SU(3)_C \times SU(2)_L \times U(1)_Y \times U(1)_D$
ν_N	$(\mathbf{1}, \mathbf{1}, 0, 0)$
ν_{D_L}	$(\mathbf{1}, \mathbf{1}, 0, Q)$
ν_{D_R}	$(\mathbf{1}, \mathbf{1}, 0, Q)$
Φ	$(\mathbf{1}, \mathbf{1}, 0, Q)$

before symmetry breaking is given by:

$$\begin{aligned}\mathcal{L} \supset -\frac{1}{4}X_{\mu\nu}X^{\mu\nu} - \frac{\varepsilon}{2\,c_W}X_{\mu\nu}B^{\mu\nu} + (\mathcal{D}_\mu\Phi)^\dagger(\mathcal{D}^\mu\Phi)\\ - V(\Phi, H) + \overline{\boldsymbol{\nu}_N}i\partial\!\!\!/\boldsymbol{\nu}_N + \overline{\boldsymbol{\nu}_D}i\mathcal{D}\!\!\!\!/\,\boldsymbol{\nu}_D\\ - \Bigg[(\overline{\mathbf{L}}\widetilde{H})Y\boldsymbol{\nu}_N^c + \frac{1}{2}\boldsymbol{\nu}_N M_N \boldsymbol{\nu}_N^c + \overline{\boldsymbol{\nu}_D}M_X\boldsymbol{\nu}_D\\ + \overline{\boldsymbol{\nu}_N}(Y_L\boldsymbol{\nu}_{D_L}^c\Phi + Y_R\boldsymbol{\nu}_{D_R}\Phi^*) + \text{h.c.}\Bigg]\,. \end{aligned} \tag{4.51}$$

where, as introduced previously, $\widetilde{H} = i\sigma^2 H^*$, and $L_\alpha = \begin{pmatrix}\nu_{\alpha L}^T & \ell_{\alpha L}^T\end{pmatrix}^T$. Moreover, the covariant derivative can be written as in eq. (4.9), which we recall here for convenience:

$$\mathcal{D}_\mu = \partial_\mu - i\frac{g'}{2}YB_\mu - i\frac{g}{2}\sigma^a W_\mu^a - ig_D Q_X X_\mu\,, \tag{4.52}$$

The following terms are all matrices with different dimensions: Y $(3 \times n)$, M_N $(n \times n)$, M_X $(d \times d)$, Y_L and Y_R $(n \times d)$. The mixing between the Standard Model leptons and the dark sector fermions happens through the neutrino portal term, which connects the Standard Model fermions to the sterile states, and with the Yukawa-like terms of the kind $\overline{\boldsymbol{\nu}_N}Y_\times\boldsymbol{\nu}_{D_\times}\Phi$, connecting the dark-charged fermions to the Standard Model. The $\boldsymbol{\nu}_D$ states are commonly known as dark neutrinos, because they can mix with the Standard Model neutrinos to generate new physical states. Additionally, the scalar portal constitutes another bridge between the dark sector fermions and the Standard Model particles. As we will see in the next section, the Higgs doublet H and the new dark scalar Φ can mix together to generate two massive scalar states, one of them being the Standard Model Higgs boson.

4.4.1 The scalar portal

The scalar potential of the model is built on top of the Higgs potential introduced in eq. (2.4), and will contain terms related to the scalar Φ and the scalar portal term in eq. (4.3):

$$V(H,\Phi) = -\mu_H^2 H^\dagger H - \mu_\Phi^2 \Phi^*\Phi + \lambda_H (H^\dagger H)^2 + \lambda_\Phi (\Phi^*\Phi)^2 + \lambda_{H\Phi}(H^\dagger H)(\Phi^*\Phi)\,. \tag{4.53}$$

We choose to parametrize the scalar fields as:

$$H = \frac{1}{\sqrt{2}}\begin{pmatrix} G_1^+ + iG_2^+ \\ h + iG_3^0 \end{pmatrix}, \tag{4.54a}$$

$$\Phi = \frac{\varphi + iG_\varphi}{\sqrt{2}}, \tag{4.54b}$$

where h and φ are scalars, while G_i are the Goldstone bosons. For simplicity, we will assume the unitary gauge, so that the Goldstone bosons are effectively integrated out, and we can write:

$$H = \frac{1}{\sqrt{2}}\begin{pmatrix} 0 \\ h \end{pmatrix}, \tag{4.55a}$$

$$\Phi = \frac{\varphi}{\sqrt{2}}\,. \tag{4.55b}$$

After the electroweak symmetry breaking, both H and Φ get a VEV, respectively v_H and v_Φ, which are also responsible for minimizing the scalar potential:

$$v_H^2 = \frac{\lambda_\Phi\, m_H^2 - \lambda\, m_\Phi^2/2}{\lambda_H\lambda_\Phi - \lambda_{H\Phi}^2/4}\,. \tag{4.56a}$$

$$v_\Phi^2 = \frac{\lambda_H\, m_\Phi^2 - \lambda\, m_H^2/2}{\lambda_H\lambda_\Phi - \lambda_{H\Phi}^2/4}, \tag{4.56b}$$

Additionally, the new degrees of freedom around the minimum are found by the following transformations:

$$h \to h + v_H, \tag{4.57a}$$

$$\varphi \to \varphi + v_\Phi\,. \tag{4.57b}$$

The potential can be expanded in terms of the new definitions of the fields, obtaining:

$$\begin{aligned} V(H,\Phi) = {} & \lambda_\Phi v_\Phi^2 \varphi^2 + \lambda_H v_H^2 h^2 + \lambda_{H\Phi} v_\Phi v_H \varphi h \\ & + \frac{\lambda_{H\Phi}}{2} v_H \varphi^2 h + \frac{\lambda_{H\Phi}}{2} v_\Phi \varphi h^2 + \lambda_\Phi v_\Phi \varphi^3 + \lambda_H v_H h^3 \\ & + \frac{\lambda_\Phi}{4}\varphi^4 + \frac{\lambda_H}{4} h^4 + \frac{\lambda_{H\Phi}}{4}\varphi^2 h^2 + C\,, \end{aligned} \tag{4.58}$$

where C is a constant. Eq. (4.58) contains the mass terms of h and φ bosons. They can be reorganized into a mixing matrix:

$$
\begin{aligned}
V(H,\Phi) &= \begin{pmatrix} h & \varphi \end{pmatrix} \begin{pmatrix} \lambda_H v_H^2 & \frac{\lambda_{H\Phi}}{2} v_H v_\Phi \\ \frac{\lambda_{H\Phi}}{2} v_H v_\Phi & \lambda_\Phi v_\Phi^2 \end{pmatrix} \begin{pmatrix} h \\ \varphi \end{pmatrix} \\
&= \begin{pmatrix} h' & \varphi' \end{pmatrix} R(\vartheta) \begin{pmatrix} \lambda_H v_H^2 & \frac{\lambda_{H\Phi}}{2} v_H v_\Phi \\ \frac{\lambda_{H\Phi}}{2} v_H v_\Phi & \lambda_\Phi v_\Phi^2 \end{pmatrix} R(-\vartheta) \begin{pmatrix} h' \\ \varphi' \end{pmatrix},
\end{aligned}
\tag{4.59}
$$

where

$$
R(\vartheta) = \begin{pmatrix} \cos(\vartheta) & -\sin(\vartheta) \\ \sin(\vartheta) & \cos(\vartheta) \end{pmatrix}, \tag{4.60a}
$$

with

$$
\tan(2\vartheta) = \frac{\lambda_{H\Phi} v_H v_\Phi}{\lambda_H v_H^2 - \lambda_\Phi v_\Phi^2}, \tag{4.60b}
$$

$$
\sin(2\vartheta) = \frac{\lambda_{H\Phi} v_\Phi v_H}{\sqrt{(\lambda_\Phi v_\Phi^2 - \lambda_H v_H^2)^2 + \lambda_{H\Phi}^2 v_H^2 v_\Phi^2}}, \tag{4.60c}
$$

$$
\cos(2\vartheta) = \frac{\lambda_H v_H^2 - \lambda_\Phi v_\Phi^2}{\sqrt{(\lambda_\Phi v_\Phi^2 - \lambda_H v_H^2)^2 + \lambda_{H\Phi}^2 v_H^2 v_\Phi^2}}. \tag{4.60d}
$$

The masses of the physical fields are

$$
m_{\varphi',h'}^2 = \lambda_\Phi v_\Phi^2 + \lambda_H v_H^2 \pm \sqrt{\left(\lambda_\Phi v_\Phi^2 - \lambda_H v_H^2\right)^2 + \lambda_{H\Phi}^2 v_H^2 v_\Phi^2}\,. \tag{4.61}
$$

We have the physical states h' and φ', that are superpositions of the states h and φ. We can identify h' as the Standard Model Higgs boson.

4.4.2 The vector portal

The vector portal can be developed in the same way as it has been shown in § 4.1.3. The kinetic terms diagonalization makes possible to highlight the mixing among the gauge bosons and to get the expression of the kinetic Lagrangian, with the coupling between the photon, the new Z and Z′ bosons, in eq. (4.65). In this case, the model contains particles belonging to the dark sectors, charged under $U(1)_D$ with charge $Q_X = Q$. These new fields will be the building blocks for the dark current, that can be obtained by expanding the covariant derivative in eq. (4.52) within their kinetic terms. The kinetic Lagrangian can be written as:

$$
-\mathcal{L} \supset e\, A_\mu^{SM} J_{em}^\mu + \frac{g}{2\, c_w} Z_\mu^{SM} J_{nc}^\mu + g_D X_\mu J_X^\mu, \tag{4.62}
$$

where we now have the dark current J_X^μ coupling with the dark gauge boson X_μ, differently from eq. (4.26). Following the same computation carried out in § 4.1.3, we can obtain updated versions of eq. (4.29):

$$\begin{aligned}
-\mathcal{L} \supset\, & e\, A_\mu J^\mu_{em} \\
& + Z_\mu \left[-e\varepsilon\, s_\beta\, J^\mu_{em} + c_\beta\, \frac{g}{2\, c_w} \frac{m_Z^2}{\left(m_Z^{SM}\right)^2} J^\mu_{nc} + g_D \frac{s_\beta}{c_X} J^\mu_X \right] \\
& + Z'_\mu \left[-e\varepsilon\, c_\beta\, J^\mu_{em} - s_\beta\, \frac{g}{2\, c_w} \frac{m_{Z'}^2}{\left(m_Z^{SM}\right)^2} J^\mu_{nc} + g_D \frac{c_\beta}{c_X} J^\mu_X \right] .
\end{aligned} \tag{4.63}$$

And finally we can obtain the updated versions of eq. (4.31), namely the expression of the Lagrangian for the matter couplings, where now ψ_f includes also the dark fermions: $f \in \{ Q, L, e_R, \mu_R, \tau_R, \nu_{D_L}, \nu_{D_R} \}$.

$$\begin{aligned}
-\mathcal{L}_V \supset \sum_f \overline{\psi}_f \gamma^\mu \Bigg\{ & A_\mu \left(e Q_e^f\right) \\
& + Z_\mu \left[\frac{e}{4\, s_w\, c_w} \Big(c_\beta \left(4\, c_w^2\, Q_e^f - Y_L^f - Y_R^f\right) - t_X\, s_w\, s_\beta \left(Y_L^f + Y_R^f\right) \Big) + g_D Q_X^f \frac{s_\beta}{c_X} \right] \\
& + Z'_\mu \left[\frac{e}{4\, s_w\, c_w} \Big(s_\beta \left(Y_L^f + Y_R^f - 4 Q_e^f\, c_w^2\right) - t_X\, s_w\, c_\beta \left(Y_L^f + Y_R^f\right) \Big) + g_D Q_X^f \frac{c_\beta}{c_X} \right] \Bigg\} \psi_f ,
\end{aligned} \tag{4.64}$$

The expression of the axial-vector part of the Lagrangian, eq. (4.32), does not change because the new $U(1)_D$ interaction is not affected by the chirality. The final interaction Lagrangian can be written in the same way, that is, recalling eq. (4.33),

$$-\mathcal{L} \supset \sum_f \overline{\psi}_f \gamma^\mu \Big[\left(e Q_e^f\right) A_\mu + \left(c_V^f - c_A^f \gamma^5\right) Z_\mu + \left(d_V^f - d_A^f \gamma^5\right) Z'_\mu \Big] \psi_f , \tag{4.65}$$

where the coefficients for the Standard Model fermions are defined in tab. 4.1, while the ones for the dark fermions can be found in tab. 4.3. Notice that f labels generic fermions, including the dark fermions. Specifically, we can see $Q_X^{f \neq D_k} = 0\ \forall k \in \{1, \dots, d\}$[§].

The expression of the interaction Lagrangian shows that the dark photon Z' couples to both charged fermions and to particles having a non-zero dark charge Q_X. This means the dark photon can mediate between the Standard Model and a hypothetical dark sector made of particles charged under the new $U(1)_D$ gauge group. On the contrary, the Standard Model photon couples

[§] A note on the notation: the D in $\boldsymbol{\nu}_{D_L}$ or $\boldsymbol{\nu}_{D_R}$ is just a label for *dark*, while D_k with index k labels the dark-charged gauge states among all the neutral fermions. Similarly, $\nu_{D_L k}$ and $\nu_{D_R k}$ label each dark fermion separately.

Table 4.3: The vector and axial-vector couplings of the dark-charged fermions $f = D_k$, $k \in \{1, \ldots, d\}$ with the Z and Z′ bosons, notice that $\frac{g}{2c_W} = \frac{e}{4 s_W c_W}$.

		Vector	Axial-vector
Z_μ	$\nu_{D_L k}, \nu_{D_R k}$	$c_V^{D_k} = g_D Q_X^{D_k} \frac{s_\beta}{c_X}$	$c_A^{D_k} = 0$
Z'_μ	$\nu_{D_L k}, \nu_{D_R k}$	$d_V^{D_k} = g_D Q_X^{D_k} \frac{c_\beta}{c_X}$	$d_A^{D_k} = 0$

only to Standard Model charged fermion and has no interactions with the dark sector.

4.4.3 The neutrino portal and the neutrino mass basis

The neutrino portal opens up the possibility for the new dark and sterile fermions to mix with the Standard Model neutrinos. The mass Lagrangian is expressed by the following terms, from eq. (4.51):

$$-\mathcal{L}_M \supset \frac{1}{2}\boldsymbol{\nu}_N M_N \boldsymbol{\nu}_N^c + \overline{\boldsymbol{\nu}_D} M_X \boldsymbol{\nu}_D + (\overline{\mathbf{L}}\widetilde{H}) Y \boldsymbol{\nu}_N^c + \overline{\boldsymbol{\nu}_N}\, Y_L \boldsymbol{\nu}_{D_L}^c \Phi + \overline{\boldsymbol{\nu}_N}\, Y_R \boldsymbol{\nu}_{D_R} \Phi^* + \text{h.c.}\,. \tag{4.66}$$

The mass Lagrangian involves the following fields:

- $L_\alpha = \begin{pmatrix} \nu'^T_{\alpha L} & \ell'^T_{\alpha L} \end{pmatrix}^T$, $\alpha \in \{e, \mu, \tau\}$: the left-handed Standard Model weak-isospin doublet, with $\nu'_{\alpha L}$ being the left-handed Standard Model neutrinos;
- $\nu_{D_L k}, \nu_{D_R k}$, $k \in [1, d]$: the left and right-handed dark neutrinos;
- $\nu_{N r}$, $r \in [1, n]$: the left-handed sterile neutrinos, singlets under all the gauge groups.

We can consider the following basis for the neutrino fields, formed with only right-handed fields:

$$\boldsymbol{\nu}_f = \begin{pmatrix} \boldsymbol{\nu}'^c \\ \boldsymbol{\nu}_N^c \\ \boldsymbol{\nu}_{D_L}^c \\ \boldsymbol{\nu}_{D_R} \end{pmatrix}, \tag{4.67}$$

where $\boldsymbol{\nu}_f$ is made of $(3 + 2d + n)$ fields. After symmetry breaking, this basis makes possible to write the mass Lagrangian in a compact way:

$$\mathcal{L}_M \supset \frac{1}{2}\boldsymbol{\nu}_m^T \mathcal{C}^\dagger \mathbf{M} \boldsymbol{\nu}_m + \text{h.c.}\,, \tag{4.68}$$

where $\boldsymbol{\nu}_{\mathrm{m}}$ are the neutral leptons mass states, and we define the mass matrix $\mathbf{M}$ as:

$$\mathbf{M} = \begin{pmatrix} 0 & M_D & 0 & 0 \\ M_D^T & M_N & \Lambda_L & \Lambda_R \\ 0 & \Lambda_L^T & 0 & M_X \\ 0 & \Lambda_R^T & M_X^T & 0 \end{pmatrix}, \tag{4.69}$$

where the following definitions are assumed: the standard $3 \times n$ Dirac mass matrix is $M_D \doteq Y v_H/\sqrt{2}$, and the other two additional $n \times d$ Dirac mass matrices are $\Lambda_{L,R} \doteq Y_{L,R} v_\Phi/\sqrt{2}$. The $n \times n$ matrix M_N and the $d \times d$ matrix M_X are the Majorana mass matrix for the sterile neutrinos and the Dirac mass matrix for the dark neutrinos, respectively, already defined in eq. (4.66).

In order to find the mass basis, it is necessary to diagonalize the mass matrix $\mathbf{M}$. The diagonalization is performed by an unitary transformation, which can be written as the mixing matrix $\mathbf{U}$, defined in terms of sub-blocks:

$$\mathbf{U} \doteq \begin{pmatrix} U_\nu \\ U_N \\ U_{D_L} \\ U_{D_R} \end{pmatrix}, \tag{4.70}$$

where the sub-blocks are rectangular matrices: U_α has dimension $3 \times (3+n+2d)$, U_N has dimension $n \times (3+n+2d)$, U_{D_L} and U_{D_R} have both dimension $d \times (3+n+2d)$. The diagonalization results in:

$$\mathbf{M}_{\mathrm{diag}} = \mathbf{U}^T \mathbf{M} \mathbf{U}, \tag{4.71}$$

and the neutrino mass eigenstates given by:

$$\boldsymbol{\nu}_{\mathrm{m}} \doteq \begin{pmatrix} \boldsymbol{\nu} \\ \mathbf{N} \end{pmatrix} = \mathbf{U}^\dagger \boldsymbol{\nu}_{\mathrm{f}}. \tag{4.72}$$

where we define the mass eigenstates of the 3 Standard Model neutrinos $\boldsymbol{\nu}$ and the $(n+2d)$ HNLs $\mathbf{N}$.

Using the mixing matrix, we can obtain the expression of the interaction Lagrangian in the mass basis:

$$
\begin{aligned}
\mathcal{L} \supset\ & \sum_{\alpha} \overline{\nu}_{\alpha} \Big[\big(c_V^{\nu_\alpha} - c_A^{\nu_\alpha}\gamma^5\big)\gamma^\mu Z_\mu + \big(d_V^{\nu_\alpha} - d_A^{\nu_\alpha}\gamma^5\big)\gamma^\mu Z'_\mu \Big] \nu_\alpha \\
& + \sum_k \overline{\nu}_{D_L k} \Big[\big(c_V^{D_k} - c_A^{D_k}\gamma^5\big)\gamma^\mu Z_\mu + \big(d_V^{D_k} - d_A^{D_k}\gamma^5\big)\gamma^\mu Z'_\mu \Big] \nu_{D_L k} \\
& + \sum_k \overline{\nu}_{D_R k} \Big[\big(c_V^{D_k} - c_A^{D_k}\gamma^5\big)\gamma^\mu Z_\mu + \big(d_V^{D_k} - d_A^{D_k}\gamma^5\big)\gamma^\mu Z'_\mu \Big] \nu_{D_R k} \\
= & - \sum_{i,j=1}^{3+n+2d} \nu_{mi}^T \mathcal{C}^\dagger \Big\{ \sum_\alpha (U_\nu)_{\alpha i} (U_\nu^*)_{\alpha j} \\
& \qquad \times \Big[\big(c_V^{\nu_\alpha} - c_A^{\nu_\alpha}\gamma^5\big)\gamma^\mu Z_\mu + \big(d_V^{\nu_\alpha} - d_A^{\nu_\alpha}\gamma^5\big)\gamma^\mu Z'_\mu \Big] \\
& + \sum_k (U_{D_L})_{ki} (U_{D_L}^*)_{kj} \Big[\big(c_V^{D_k} - c_A^{D_k}\gamma^5\big)\gamma^\mu Z_\mu + \big(d_V^{D_k} - d_A^{D_k}\gamma^5\big)\gamma^\mu Z'_\mu \Big] \\
& + \sum_k (U_{D_R}^*)_{ki} (U_{D_R})_{kj} \Big[\big(c_V^{D_k} - c_A^{D_k}\gamma^5\big)\gamma^\mu Z_\mu + \big(d_V^{D_k} - d_A^{D_k}\gamma^5\big)\gamma^\mu Z'_\mu \Big] \Big\} \nu_{mj}^c \\
= & - \sum_{i,j=1}^{3+n+2d} \nu_{mi}^T \mathcal{C}^\dagger \Big\{ (U_\nu^\dagger U_\nu)_{ij}^* \big(c_V^\nu - c_A^\nu \gamma^5\big) \\
& + \sum_k \Big[(U_{D_L})_{ki} (U_{D_L}^*)_{kj} + (U_{D_R}^*)_{ki} (U_{D_R})_{kj} \Big] \big(c_V^{D_k} - c_A^{D_k}\gamma^5\big) \Big\} \gamma^\mu Z_\mu \nu_{mj}^c \\
& - \sum_{i,j=1}^{3+n+2d} \nu_{mi}^T \mathcal{C}^\dagger \Big\{ (U_\nu^\dagger U_\nu)_{ij}^* \big(d_V^\nu - d_A^\nu \gamma^5\big) \\
& + \sum_k \Big[(U_{D_L})_{ki} (U_{D_L}^*)_{kj} + (U_{D_R}^*)_{ki} (U_{D_R})_{kj} \Big] \big(d_V^{D_k} - d_A^{D_k}\gamma^5\big) \Big\} \gamma^\mu Z'_\mu \nu_{mj}^c \\
\doteq & - \sum_{i,j=1}^{3+n+2d} \nu_{mi}^T \mathcal{C}^\dagger \big(c_{ij} Z_\mu + d_{ij} Z'_\mu\big) \gamma^\mu \nu_{mj}^c \,.
\end{aligned}
\tag{4.73}
$$

We exploited the fact that $c_V^{\nu_\alpha} = c_V^\nu$, $c_A^{\nu_\alpha} = c_A^\nu$, $d_V^{\nu_\alpha} = d_V^\nu$, $d_A^{\nu_\alpha} = d_A^\nu$ $\forall \alpha$. The coefficients c_{ij} and d_{ij} are defined as follows:

$$
\begin{aligned}
c_{ij} = & \frac{g}{2\,c_w} (U_\nu^\dagger U_\nu)_{ij}^* \big(c_\beta + t_\chi\, s_w\, s_\beta\big) \\
& + g_D \sum_k Q_X^{D_k} \Big[(U_{D_L})_{ki} (U_{D_L}^*)_{kj} + (U_{D_R}^*)_{ki} (U_{D_R})_{kj} \Big] \frac{s_\beta}{c_\chi} \,,
\end{aligned}
\tag{4.74a}
$$

$$
\begin{aligned}
d_{ij} = & \frac{g}{2\,c_w} (U_\nu^\dagger U_\nu)_{ij}^* \big(t_\chi\, s_w\, c_\beta - s_\beta\big) \\
& + g_D \sum_k Q_X^{D_k} \Big[(U_{D_L})_{ki} (U_{D_L}^*)_{kj} + (U_{D_R}^*)_{ki} (U_{D_R})_{kj} \Big] \frac{c_\beta}{c_\chi} \,.
\end{aligned}
\tag{4.74b}
$$

If $Q_X^{D_k} = Q_X \, \forall k$, then they reduce to the following expressions:

$$c_{ij} = \frac{g}{2\,c_w}(U_\nu^\dagger U_\nu)^*_{ij}\left(c_\beta + t_X\, s_w\, s_\beta\right) + g_D Q_X \left[(U_{D_L}^\dagger U_{D_L})^*_{ij} + (U_{D_R}^\dagger U_{D_R})_{ij}\right]\frac{s_\beta}{c_X}\,, \tag{4.75a}$$

$$d_{ij} = \frac{g}{2\,c_w}(U_\nu^\dagger U_\nu)^*_{ij}\left(t_X\, s_w\, c_\beta - s_\beta\right) + g_D Q_X \left[(U_{D_L}^\dagger U_{D_L})^*_{ij} + (U_{D_R}^\dagger U_{D_R})_{ij}\right]\frac{c_\beta}{c_X}\,. \tag{4.75b}$$

4.5 A look at the MiniBooNE LEE from a dark sector point of view

In § 2.5.3 we observed that the current Standard Model is unable to account for the results of some neutrinos experiments. The MiniBooNE LLE is the prime example of such anomalies: the experiment recorded an excess of electron-like events with a significance of $4.8\,\sigma$. While the main Standard Model backgrounds are understood or are currently subject to investigation, there is still not a clear explanation for this phenomenon. In this section, we will give a hint on how a dark photon-based dark sector model could provide an interesting solution to the MiniBooNE anomaly. The presence of a neutrino portal and the introduction of a dark $U(1)_D$ symmetry featuring a dark photon make possible for the dark-charged HNLs making up the dark sector to decay to Standard Model particles. In particular, such decays can produce e^+e^- pairs in the final states: for e.g., the dark heavier HNFs can decay to the lighter ones, through a three-body decay mediated by either an on or off-shell dark photon, further decaying to e^+e^-. The e^+e^- pairs constitute a viable explanation for the MiniBooNE LEE. Indeed, the LEE can be mimicked by overlapping or highly asymmetric e^+e^- pairs, so that only one single electromagnetic shower can be resolved by the detector. In this case, the decaying HNLs can be produced via interaction of the beam neutrinos with the material inside or outside the MiniBooNE detector. This process is known as upscattering and allows producing short-lived HNLs that subsequently decay visibly inside the fiducial volume, according to the process [377, 378]:

$$\nu_\mu \mathcal{N} \to (N_j \to N_i Z'^{(*)} \to N_i e^+ e^-)\mathcal{N}\,, \tag{4.76}$$

where $\mathcal{N}$ is the target nucleus, N_i and N_j are the dark neutrinos (with $m_j > m_i$); the dark photon can be produced either on or off-shell. These kinds of models are known as $3+n$ models, where n is the number of HNLs.

This dark sector model will be featured in chapter 8, because the dark photon decay patterns to unstable HNLs, followed by their subsequent decays to e^+e^- pairs, is able to leave both invisible and visible signatures inside a detector. The same process would also produce a long-lived HNL or a neutrino along them.

The produced e^+e^- can shower inside the electromagnetic calorimeters, while the other particle produced along them would escape the detector, leaving a missing energy signature. This decay pattern allows relaxing most of the constraints placed on invisible dark photon decays, because most of the dark photon decays in this case will feature visible e^+e^- pairs, so that the whole event would be vetoed in the experimental selection. Furthermore, 3+1 and 3+2 dark sector models will be the subject of the experimental analysis presented in chapter 9. That analysis would provide the MicroBooNE experimental sensitivity to the e^+e^- pairs coming from dark photon upscattering to HNLs and their subsequent decay.

Part II

Phenomenology of dark matter models

Chapter 5

Loop-induced dark matter annihilation and γ-lines phenomenology

Life isn't just about passing on your genes. We can leave behind much more than just DNA. [...] That's what I live for. We need to pass the torch, and let our children read our messy and sad history by its light. We have all the magic of the digital age to do that with. [...] Building the future and keeping the past alive are one and the same thing.

—Solid Snake

Metal Gear 2: Sons of Liberty
Hideo Kojima

In § 3.7.3, we introduced the monochromatic line signature coming from dark matter annihilation into neutral final states containing a photon. In particular, we mentioned how line signatures are hardly mimicked by any astrophysical background. For this reason, they constitute a smoking-gun signal for indirect detection searches. However, the annihilation of dark matter into photons is a loop-induced process at leading order (LO), as in most models dark matter is assumed to be electrically neutral. This is different from what happens in neutrino lines, that usually can be produced at tree level see e.g. [379–382]. The loop-induced nature of the process makes the signal suppressed by a loop factor, but its experimental sensitivity is high, because of the sharp energy spectrum. As we already mentioned, current γ-ray telescopes, like Fermi-LAT [152] and HESS [154, 156], set strong constraints on this signal.

In renormalizable models, loop-induced processes are finite. However, their computation can be complicated, as it may require the evaluation of many different diagrams, on the basis of the model under consideration.

Numerical techniques are therefore needed to automatize the computation of the annihilation cross section and to obtain predictions within generic dark matter models.

This chapter will be dedicated to the study of γ-line signatures of different dark matter models, with the derivation of constraints on their parameter space, and the observation of the potential of this signal to establish the models under investigation. In this context, we will introduce the numerical tool MadDM v3.2, which allows automatizing the computation of loop-induced processes for indirect detection. The numerical tool MadDM is a plugin of MadGraph5_aMC@NLO [383, 384] with the focus on dark matter phenomenology. MadDM is model-agnostic, and it can be used to study the phenomenology of any dark matter model, provided in the UFO [385, 386] format, that, in the case of loop-induced processes, must be exported with next-to-leading order (NLO) information [387]. The new version of MadDM, v3.2, extends the indirect detection module of the previous version, MadDM v3.0 [388, 389]. At the time of writing, it is the only numerical tool with such capabilities. A discussion on the other available dark matter tools can be found in [390]. MicrOMEGAs [391–396] and DarkSUSY [397, 398] include expressions for the supersymmetric neutralino dark matter in the MSSM [399, 400], and the inert doublet model (IDM) [401]. Other tools provide results for specific simplified models [402–406], the next-to-MSSM [407–409], and Kaluza-Klein dark matter [410–412]. Many endeavors have been made into obtaining analytic expressions in a model-independent approach [413, 414], or utilizing effective field theory to integrate the photon out, reducing the loop process to an effective vertex [415–425].

The main features of MadDM v3.2 are:

- automatic generation and computation of loop-induced processes, using MadLoop [426], embedded in MG5_aMC [383] and already extensively used to compute QCD, electroweak corrections [427–430], and loop-induced processes [431, 432] in the framework of colliders;
- treatment of the line signature as a sharp spectral feature, with the possibility of including multiple lines;
- computation of the γ-lines respective fluxes for different dark matter density profiles (including the $\mathcal{J}$-factor computation) and exclusion limits from Fermi-LAT [152] and HESS [154, 156];
- possibility to compute loop-induced processes in the case of a continuum γ spectrum, e.g. annihilation into a pair of gluons, that can be constrained by the Fermi-LAT dSph analysis [221, 433].

Loop-induced processes can be relevant also when including higher-order corrections in the relic density computation [434–437], but this discussion is left for future work.

The chapter is organized as follows. The phenomenology of the γ-line signature and the implementation of the experimental constraints will be discussed in § 5.1. In § 5.2, the generation of one-loop processes within MadDM is discussed, with details on the UFO model files. Sec. 5.3 presents the study of two dark matter models, a top-philic t-channel model and the IDM, discussing the main constraints associated to the γ-line signature. A summary of the discussion can be found in § 5.4.

Further details and technicalities can be found in app. C. In app. C.1, we describe the implementation of automatic $\mathcal{J}$-factor computation and provide more information about the experimental data. In app. C.2 we describe the treatment of multiple line signatures within MadDM.

The chapter is entirely based on the following publication:

[1] Arina, C., Heisig, J., Maltoni, F., **DM**, Mattelaer, O., "Indirect dark-matter detection with MadDM v3.2 – Lines and Loops". *Eur. Phys. J. C* 83.3 (2023), p. 241. DOI: 10.1140/epjc/s10052-023-11377-2.

First, I was responsible of the development of MadDM and the release of the version 3.2. This part of the work involved the addition of a brand new module to MadDM, regarding the implementation of the phenomenological γ-line analysis, with the development of the algorithms and the concepts listed in app. C and § 5.2.2. After the release of the code, I was involved in the bug fixing and user support.
Second, I contributed to the realization of the phenomenological study presented in § 5.3. I performed the computation of the cross sections, of the γ-line bounds and I realized the final plots.
Part of this work is also based on my master thesis [60], from which I took part of the discussion contained in §§ 5.2.1 and 5.3.1. The phenomenology of the top-philic model has been updated.

5.1 Gamma-ray line phenomenology and constraints

In § 3.7.3 we discussed the main features of γ-ray lines, both from a theoretical and a phenomenological point of view. Monochromatic photon spectra are a smoking-gun signatures for dark matter indirect detection searches, because of the low astrophysical background associated to them. They can be generated by dark matter annihilation into a pair of photons, or a photon and another particle. However, given in most model, dark matter is assumed to be electrically neutral, no direct coupling to photons is possible, and the only way to produce γ-lines is via loop-induced processes, that are suppressed by a loop factor. We will recall now the main concepts, and we will discuss the implementation of the constraints in MadDM. The differential γ-ray flux from dark matter annihilation can be expressed from eq. (3.90) as:

$$\frac{d\Phi(E_\gamma)}{dE_\gamma} = \frac{1}{8\pi m_{DM}^2} \sum_i \langle\sigma v\rangle_i \frac{dN_\gamma^i}{dE_\gamma} \int_{ROI} d\Omega \int_{los} dr' \rho^2\left(\mathbf{r}(r', \Omega)\right), \tag{5.1}$$

where m_{DM} is the mass of the dark matter candidate. The particle physics information is encoded in the annihilation cross section $\langle\sigma v\rangle_i$, and the spectrum of photons per annihilation dN_γ^i/dE_γ. In the case of γ-lines, the latter is trivial, recalling eq. (3.94),

$$\frac{dN_\gamma^{line}}{dE_\gamma} = \delta(E_\gamma - E_\gamma^{line}) \times \begin{cases} 2 & \text{for } \gamma\gamma\,, \\ 1 & \text{for } \gamma X\,, \end{cases} \tag{5.2}$$

The astrophysical input is encoded in the $\mathcal{J}$-factor, from eq. (3.91a):

$$\mathcal{J} = \int_{ROI} d\Omega \int_{los} dr' \rho^2\left(\mathbf{r}(r', \Omega)\right), \tag{5.3}$$

where ρ represents the dark matter density profile, integrated over the experimental ROI, while r' represents the line-of-sight.

Despite the loop-suppression that γ-ray line processes suffer from, the sensitivities associated with them is high because of the low background contamination. Investigating the regions of the sky where the dark matter density is expected to be high allows maximizing the signal. The most promising target is the galactic center, where density profiles are expected to peak. However, both the continuum γ-ray background and the choice of a certain profile (because of its *cuspiness*) contribute to the final sensitivity of the analysis, that can be further maximized with the choice of an optimized ROI. Our analysis is based on the 95 % CL upper limits on the dark matter annihilation cross section into a pair of photons from the Fermi-LAT satellite [152] and the HESS telescope [154]. In particular, we will consider the exclusion bounds obtained by Fermi-LAT using 5.8 years of data [152]. The strongest bound reaches $\langle\sigma v\rangle_{\gamma\gamma}^{UL} \approx 2 \times 10^{-30}\,\mathrm{cm^3\,s^{-1}}$ for $m_{DM} \approx 1\,\mathrm{GeV}$ and $\langle\sigma v\rangle_{\gamma\gamma}^{UL} \approx 3 \times 10^{-28}\,\mathrm{cm^3\,s^{-1}}$ for $m_{DM} \approx 500\,\mathrm{GeV}$ for NFWc, the cuspiest dark matter density profile. The analysis takes into account four dark matter density profiles and associates an optimized ROI to each one of them. That is defined as a circular region centered on the galactic center, with a mask over the galactic plane, excluding longitudes further than 6° and latitudes smaller than 5°, because large dark matter signals are not expected in those regions and the photon emission is dominated by standard astrophysical sources. This leaves a 12° × 10° box centered on the galactic center. The ROIs are R3, R16, R41, and R90 (where the number indicates the opening angle over the galactic center), optimized for the contracted NFW (NFWc), eq. (3.81) with $\gamma = 1.3$, Einasto, eq. (3.83), canonical NFW, eq. (3.82), and isothermal, eq. (3.85), density profiles, respectively. In the case of isothermal profile (cored profile) the upper bound excludes annihilation cross-sections $\langle\sigma v\rangle^{\mathrm{UL}}_{\gamma\gamma} \approx 8\times10^{-29}\,\mathrm{cm^3\,s^{-1}}$ for $m_{\mathrm{DM}} = 1\,\mathrm{GeV}$ and $\langle\sigma v\rangle^{\mathrm{UL}}_{\gamma\gamma} \approx 3\times10^{-27}\,\mathrm{cm^3\,s^{-1}}$ for $m_{\mathrm{DM}} = 500\,\mathrm{GeV}$. The dependence on the dark matter density profile is sizable, using optimized ROIs mitigates the effect. Fermi-LAT data constrain dark matter masses in the range $(0.2$ to $500)\,\mathrm{GeV}$.

The HESS telescope has also surveyed the galactic center, releasing exclusion limits on γ-lines spectra for heavier dark matter than Fermi-LAT, namely above $300\,\mathrm{GeV}$ up to $70\,\mathrm{TeV}$ [154], using $254\,\mathrm{h}$ of live time observation data. The analysis is performed for the Einasto density profile and yields an upper limit of $\langle\sigma v\rangle^{\mathrm{UL}}_{\gamma\gamma} \approx 4\times10^{-28}\,\mathrm{cm^3\,s^{-1}}$ at $m_{\mathrm{DM}} = 500\,\mathrm{GeV}$ and $\langle\sigma v\rangle^{\mathrm{UL}}_{\gamma\gamma} \approx 2\times10^{-25}\,\mathrm{cm^3\,s^{-1}}$ at $m_{\mathrm{DM}} = 70\,\mathrm{TeV}$. Only the Einasto profile was considered in the analysis, with an optimized ROI, called R1, defined as a circular region centered on the galactic center, with the galactic plane masked at latitudes lower than $0.3°$. Limits for the NFW profile can also be obtained by rescaling $\langle\sigma v\rangle^{\mathrm{UL}}_{\gamma\gamma}$ obtained with the Einasto dark matter density profile by the appropriate $\mathcal{J}$-factor. Also for these exclusion limits, the choice of the dark matter density profile introduces large astrophysical uncertainties. This is known and common to all searches pointing towards the galactic center, a region where the determination of the spatial distribution of the dark matter is rather uncertain.

Other searches for γ-lines have been performed, but they are not considered in this analysis. Fermi-LAT released exclusion limits using 14 years of data [153], considering a circular region of interest of 30° around the galactic center, with a mask over the galactic plane, that leaves an opening over the galactic center. The two defined ROIs are called R5 and R0.6, and they are masked for latitudes smaller than $3°$ and $1°$, respectively, only in the region outside $5°$ and $0.6°$. However, the approach is different from the one used in the previous analysis, and the results are related to different ROIs and dark matter density profiles. Applying this analysis on top of the results we obtained yields larger uncertainty bands, due to the smaller set of density profiles and optimized ROIs that have been studied in the newer analysis, so that the newer bounds are not as strong as the ones obtained initially.
The MAGIC telescope surveyed the galactic center, collecting data for $223\,\mathrm{h}$ and releasing exclusion limits on γ-lines spectra for heavy dark matter, with mass above $900\,\mathrm{GeV}$ up to $100\,\mathrm{TeV}$ [155]. The collaboration performed the analysis for both the Einasto profile and for a cored Hernquist-Zhao profile [438, 439], and they quoted results obtained with an NFW and a Burkert profile, rescaling the results by the appropriate $\mathcal{J}$-factor. In this case the choice of different density profiles has a noticeable effect in modifying the exclusion bounds: the cored profiles are characterized by a lower amount of dark matter towards the galactic center, which inevitably suppresses the annihilation rate and the resulting fluxes. Also in this case, we decided to stay conservative, and we applied the exclusion limits provided by HESS, in the mass region of interest.

Note that γ-ray line searches have also been proposed in dSph, see e.g. [156, 157, 440], but we do not consider them in this analysis.

From the point of view of the MadDM implementation, exclusion limits are provided both as flux $\Phi(E_\gamma)$ bounds, translated into annihilation cross section $\langle\sigma v\rangle_{\gamma\gamma}$, as a function of m_{DM}, computed only for the $\gamma\gamma$ channel. Limits depends on the chosen dark matter density profile. We include a new command, see § 5.2.2, to generate all the possible $2 \to 2$ annihilation processes that involve at least one photon in the final state, further computing the corresponding fluxes. The fluxes are then compared with the exclusion limits, and the results are displayed in the output. On one hand, the program displays the cross section for each channel, together with the corresponding exclusion limits. It is possible to find $\langle\sigma v\rangle^{UL}_{\gamma X}$ for a generic final state γX, by performing a rescaling of $\langle\sigma v\rangle^{UL}_{\gamma X}$:

$$\langle\sigma v\rangle^{UL}_{\gamma X}(m_{DM}) = 2\left(\frac{m_{DM}}{E_\gamma}\right)^2 \langle\sigma v\rangle^{UL}_{\gamma\gamma}(E_\gamma)\,, \tag{5.4}$$

where E_γ is the position of the line, according to eq. (3.95b). In this case, we do the comparison *as it is*, we neither combine different channels (if their $E^{\rm line}_\gamma$ is equal within the experimental resolution) nor check the applicability of the experimental analysis (in case of multiple distinguishable lines; see below). On the other hand, we list all spectral lines as they would occur in the experimental analysis and display the respective fluxes together with the corresponding 95 % CL limits for both experiments. To this end, MadDM combines all channels whose peaks are sufficiently close in energy such that they are indistinguishable given the experimental resolution. This is, in particular, relevant for heavy dark matter, i.e. for $4m^2_{DM}/m^2_X \gg 1$. Experimental resolution depends on the experiment under consideration. Furthermore, (combined) spectral lines lacking a sufficient separation from each other question the applicability of the experimental limit-setting procedure and are flagged accordingly. The minimal separation and combination conditions (in terms of the experimental resolution) can be adjusted by the user. The merging procedure is detailed in app. C.2.

Another feature of this version of MadDM is the possibility to automatically compute the $\mathcal{J}$-factor. MadDM gives the possibility to choose the dark matter density profile and to set its parameters in the file `maddm_card.dat`. By default, it considers the Einasto profile. Moreover, it is possible to change the region of interest for the Fermi-LAT analysis, see app. C.1.2 for details. However, note that the cross section upper limits from Fermi-LAT are only displayed for the combination of ROI and profile chosen in the analysis. Similarly, the display of limits is omitted outside the energy range for which the analyses have been performed. Finally, we would like to mention that the user can easily implement other experiments e.g. for the computation of projected limits. A template experiment is provided with the code, see app. C.1.3 for details.

On top of the above results, MadDM computes an approximate likelihood from the predicted flux for two of the ROIs of the Fermi-LAT analysis, namely R3 and R16. In [211], a likelihood profile has been derived from the Fermi-LAT data as a function of the integrated flux in these ROIs. We utilize these results within MadDM. The likelihood functions extend the MadDM experimental module `ExpConstraints`.

5.2 Loop-induced processes in MadDM

5.2.1 The MadLoop interface

In this work, we are considering the MG5_aMC framework to present the automation of loop-induced computation. The computation of the amplitudes of a certain $2 \to n$ process is performed by considering the quantity:

$$d\sigma \propto \overline{\sum_{\substack{\text{spin}\\ \text{color}}} |\mathcal{A}|^2} \,. \tag{5.5}$$

At one-loop, the square amplitude can be expressed as:

$$|\mathcal{A}|^2 = \left|\mathcal{A}^{(n,0)} + \mathcal{A}^{(n,1)}\right|^2 = \left|\mathcal{A}^{(n,0)}\right|^2 + \left|\mathcal{A}^{(n,1)}\right|^2 + 2\mathcal{R}e\left\{\mathcal{A}^{(n,0)}\mathcal{A}^{(n,1)*}\right\}, \tag{5.6}$$

where the notation $\mathcal{A}^{(n,\ell)}$ indicates the amplitude of a $2 \to n$ process characterized by the presence of ℓ loops. The tree-level (or Born level) amplitude is $\left|\mathcal{A}^{(n,0)}\right|^2$, which is null in the case of loop-induced processes. This means that the leading order term is $\left|\mathcal{A}^{(n,1)}\right|^2$. This situation is different from the NLO computation with a non-zero Born amplitude. In that case, the leading order term is $\left|\mathcal{A}^{(n,0)}\right|^2$, while the NLO term is the interference term $2\mathcal{R}e\left\{\mathcal{A}^{(n,0)}\mathcal{A}^{(n,1)*}\right\}$, and $\left|\mathcal{A}^{(n,1)}\right|^2$ contributes already to the next-to-next-to-leading order. In general, the one-loop amplitude can be expressed as a sum over the contribution $\mathcal{C}$ given by the different Feynman diagrams participating in the process:

$$\mathcal{A}^{(n,1)} = \sum_{\text{diagrams}} \mathcal{C} \,. \tag{5.7}$$

This amplitude can be decomposed through the so-called integral reduction techniques, namely algorithms that allow expressing a loop amplitude as a linear combination of the scalar integrals and a rational term R. Examples of these techniques are: the tensor integral reduction (TIR, introduced by Passarino & Veltman [441]) or the Ossola, Papadopoulos, Pittau technique

(OPP), [442]. The one-loop amplitude can so be decomposed as:

$\mathcal{A}^{(n,1)} = \sum_i d_i(\mathcal{A}^{(n,1)}) \Big($ 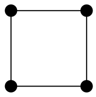 $\Big)_i + \sum_i c_i(\mathcal{A}^{(n,1)}) \Big($ 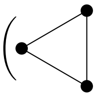 $\Big)_i$

$+ \sum_i b_i(\mathcal{A}^{(n,1)}) \Big($ 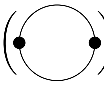 $\Big)_i + \sum_i a_i(\mathcal{A}^{(n,1)}) \Big($ 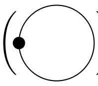 $\Big)_i + R(\mathcal{A}^{(n,1)}),$ (5.8)

where each diagram (in order: box, triangle, bubble, tadpole) shown is a one-loop (scalar) integral independent of $\mathcal{C}$. The linear combination of the scalar integrals is also known as the cut-constructible part of the amplitude. Using the dimensional regularization technique, the expression of the one-loop amplitude can be cast in d dimensions, where $d = 4 - 2\varepsilon$, with $\varepsilon \to 0$, to recover 4 dimensions. In d dimensions, the scalar integrals can be defined as:

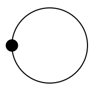

$$\doteq A_0(m) = \frac{(2\pi\mu)^{4-d}}{i\pi^2} \int d^d q \frac{1}{q^2 - m^2}, \tag{5.9}$$

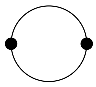

$$\doteq B_0(p, m_1, m_2) = \frac{(2\pi\mu)^{4-d}}{i\pi^2} \int d^d q \frac{1}{[q^2 - m_1^2][(q+p)^2 - m_2^2]}, \tag{5.10}$$

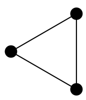

$$\begin{aligned} \doteq C_0(p_1, p_2, m_1, m_2, m_3) &= \frac{(2\pi\mu)^{4-d}}{i\pi^2} \\ &\times \int d^d q \frac{1}{[q^2 - m_1^2][(q+p_1)^2 - m_2^2][(q+p_1+p_2)^2 - m_3^2]}, \end{aligned} \tag{5.11}$$

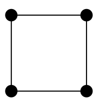

$$\begin{aligned} \doteq D_0(p_1, p_2, p_3, m_1, m_2, m_3, m_4) &= \frac{(2\pi\mu)^{4-d}}{i\pi^2} \\ &\times \int d^d q \frac{1}{\begin{aligned}&[q^2 - m_1^2][(q+p_1)^2 - m_2^2] \\ &\times [(q+p_1+p_2)^2 - m_3^2][(q+p_1+p_2+p_3)^2 - m_4^2]\end{aligned}}, \end{aligned} \tag{5.12}$$

where we assumed the 't Hooft-Veltman [443] conventions, and we dropped the $i\varepsilon$ prescription, while adding a normalization constant with the dimension of mass. The term $\mathcal{C}$ is decomposed in two steps. On one hand, one can express it as

$$\mathcal{C} = \mathcal{C}_{\text{non-}R_2} + R_2, \tag{5.13}$$

where R_2 is a rational term, part of the R term in eq. (5.8): this term arises from the ε part of the loop integral numerator. Subsequently, it is possible to decompose $\mathcal{C}_{\text{non-}R_2}$ as:

$$\mathcal{C}_{\text{non-}R_2} = \mathcal{C}_{cc} + R_1\,, \tag{5.14}$$

defined as the sum of the cut-constructible part $\mathcal{C}_{cc}$ and the rational term R_1. The rational term in eq. (5.8) is the sum of R_1 and R_2 contributions, while the cut-constructible part can be expressed as a linear combination of the scalar integrals. The R_1 term arises from the ε part of the loop integral denominator.

In general, loop computations require special attention to properly handle the aforementioned rational part. Thanks to the fact that the denominators have a simple and well-defined analytical structure, R_1 can always be systematically reconstructed in the loop evaluation procedure, when obtaining the cut-constructible part. On the other hand, the calculation of R_2 is more complex, but it can be performed analytically. In general, it is possible to demonstrate that the R_2 contribution can always be reconstructed as a tree-level amplitude, obtained with a set of Feynman rules, depending on the topology under exam [444]. The main feature of this new set of Feynman rules is that it is a finite set, that can be computed once and only once for each model, and added as external ingredients to the routines that are computing the integrals. This is the only external ingredient that can be provided, as, in general, loop-induced processes are finite, and they do not require counterterms.

Within MG5_aMC, the automation of one-loop processes is performed by the library MadLoop [426, 431]. As of today, computations of one-loop amplitudes can benefit from numerous tools and libraries, see [445] for a review. In this situation, MadLoop is able to generate all the Feynman diagrams contributing to the process, and to evaluate the numerator of them either as a complex number or as a polynomial in the loop-momenta. Subsequently, MadLoop invokes other tools to perform the reduction of the loop integrals, and to evaluate the rational terms: Collier [446], Ninja [447–449], CutTools [450] or IREGI [384] to decompose the loop either employing TIR or OPP. Finally, the library OneLoop [451] or QCDLoop [452] are used to return the finite part and the pole of the associated loop. MadLoop can switch among the aforementioned tools and algorithms, and it can find the most suitable for the specific computation.

The decomposition of $\mathcal{C}_{\text{non-}R_2}$ can be numerically challenging and sometimes it could cause numerical instabilities resulting in unreliable computations. MadLoop is able to assess the numerical stability of the final results, employing either an estimator provided by the algorithm itself, or by recomputing the same quantity after a boost or a rotation. If the result is not stable, MadLoop automatically switches to a different tool. The process is repeated until a stable result is obtained. If this is not possible, MadLoop tries to perform the computation in quadruple precision, supported by only Ninja and CutTools.

For what concerns the R_2 terms, we saw that they can be computed beforehand and provided as external input to the loop computation. Their computation is performed with the Mathematica packages FeynRules [453], FeynArts [454] and NLOCT [387]. Finally, they can be embedded in the resulting NLO UFO model. NLOCT is a specific software able to compute both R_2 terms and UV counterterms for a given model. To be more specific, the user has to implement the model in FeynRules by writing the Lagrangian in the appropriate form. Afterwards, it is renormalized within FeynRules. To enable electroweak loops, the flag `QCDonly` needs to be set to `False`. Feynman gauge should be used. The renormalized Lagrangian is then passed to FeynArts, which expresses the various interaction vertices in terms of their couplings and Lorentz structures. Subsequently, NLOCT is called to solve the renormalization conditions and compute the UV counterterms and the R_2 terms. The lists of the R_2 terms and UV counterterms are written on an external file by NLOCT, which must be imported in FeynRules to obtain the NLO UFO format of the model. Depending on the model, the file `.nlo` produced by NLOCT could be sizable, making the exporting of the model slow or unstable. It is advisable to make use of the `Assumptions` list when running NLOCT to specify the possible relations between the parameters of the model (for example by writing explicitly the relations among the particle masses of the Standard Model). Those relations will be used during the computation to shorten the analytical expressions of the UV and R_2 terms. It is possible to export a model using either the MS or $\overline{\text{MS}}$ renormalization schemes; the latter is recommended. Note that in the presence of unstable internal particles in the loop, the use of the complex mass scheme can improve numerical stability. It can be enabled by choosing `ComplexMass->True` in the `WriteCT` command, see [387] for details.

5.2.2 Generate loop-induced annihilation processes in MadDM

MadDM is equipped with a command to automatically generate all annihilation processes in final states involving at least one photon:

```
MadDM> generate indirect_spectral_features
```

More precisely, it generates all diagrams for the final states $\gamma\gamma$ and γX, where X includes the Z and h particles of the Standard Model as well as *all* additional beyond Standard Model particles, that are lighter than twice the dark matter mass and transform evenly under the assumed $\mathbb{Z}_2$ dark symmetry that stabilizes dark matter. Individual channels can be generated by explicitly specifying the final state, e.g.

```
MadDM> generate indirect_spectral_features a z
```

Besides the annihilation cross section, MadDM computes the fluxes and the experimental constraints as discussed in § 5.1.

Loop-induced annihilation into other final states may contribute to the continuum flux of cosmic messengers. A prominent example is annihilation into a pair of gluons, gg, that subsequently shower and hadronize. This channel can, for instance, become relevant in top-philic dark matter models, where dark matter couples only to the top quark at tree level, see e.g. [428, 455, 456]. In the absence of a tree-level diagram for the channel, MadDM automatically switches to the loop-induced mode. Hence, this annihilation channel is considered by executing the command:

```
MadDM> generate indirect_detection g g
```

It can also be computed together with tree-level diagrams:

```
MadDM> generate indirect_detection
MadDM> add indirect_detection g g
```

Here, the first line leads to the computation of all $2 \to 2$ tree-level annihilation processes. For more details about the existing syntax of MadDM see [388, 389]. After the computation of the annihilation cross section and generation of events, MadDM proceeds with the indirect detection analysis pipeline as introduced in [388]. The energy spectra are either obtained using Pythia [457] or the PPPC4DMID tables [458]. Subsequently, the energy spectra of all contributions (including tree-level contributions if present) are summed up to obtain the total fluxes at source and (if requested) near Earth. The corresponding γ-ray flux is confronted with constraints from Fermi-LAT observations of dSph [221].

5.3 Physics applications

To demonstrate the physics impact, in the following we apply the new features of MadDM to two beyond Standard Model scenarios and derive γ-ray line constraints on their model parameter space. We consider a simplified top-philic dark matter model and the IDM as illustrative examples.

5.3.1 Simplified top-philic dark matter model

In this scenario, the Standard Model is extended with a Majorana dark matter candidate, χ, and a colored top-philic scalar mediator, $\tilde{t}$. The former is a singlet under all Standard Model gauge interactions, while the latter has the same quantum numbers as the right-handed top quark. A $\mathbb{Z}_2$ symmetry is imposed: both of these particles are odd and the Standard Model particles are even. Choosing a mass hierarchy so that $m_\chi < m_{\tilde{t}}$ makes possible to stabilize χ, rendering it a proper dark matter candidate. The Lagrangian of the model can be written as:

$$\mathcal{L}_{\text{t-philic}} = \mathcal{D}_\mu \tilde{t} (\mathcal{D}^\mu \tilde{t})^\dagger - m_{\tilde{t}}^2 \tilde{t}^\dagger \tilde{t} + \overline{\chi}(i\not{\partial} - m_\chi)\chi + \lambda_\chi \tilde{t}\, \overline{t}\, P_L\, \chi + \text{h.c.}\,, \tag{5.15}$$

where λ_χ is the dark matter coupling. The two masses m_χ, $m_{\tilde{t}}$, and λ_χ are considered free parameters of the model. It is possible to recognize some similarities with the MSSM, indeed, for $\lambda_\chi^{\text{MSSM}} = \frac{2\sqrt{2}e}{3\cos(\vartheta_w)} \approx 0.33$, the model is equivalent to the MSSM in the limit where only the right-handed quark stop $\tilde{t}$ and a bino-like neutralino χ are light and, hence, phenomenologically relevant. However, the model can be also considered as a low energy limit of a non-supersymmetric scenario.

Such t-channel mediator or *charged-parent* models have been widely studied in the literature. In particular, an in-depth review of this specific model has been presented in [455]. Through thermal freeze-out, the model can explain the relic density in a wide range of masses with perturbative couplings. We will focus on the slice in parameter space with

$$\Delta m = m_{\tilde{t}} - m_\chi = m_t\,, \tag{5.16}$$

characterized by the smallest coupling around $m_\chi \gtrsim m_t$ where the annihilation into a pair of top-quarks opens up. The choice of this mass splitting also ensures that χ and $\tilde{t}$ are in chemical equilibrium during freeze-out. A lower mass splitting would make that assumption to break down: in that case the relic density would be governed by the so-called conversion-driven freeze-out [117], that we will not discuss, see § 3.5 for reference. That special regime is characterized by a higher rate of conversions, or coscatterings, like $\chi f \to \tilde{t} f$, with f any allowed Standard Model particle, leading the freeze-out.

In the case of standard freeze-out, the relic density depends on both annihilations and coannihilations. For small dark matter masses, coannihilations become Boltzmann suppressed during freeze-out and the three-body and loop-induced annihilation processes tWb and gg, respectively, are dominant [455]. The mass splitting is very important to guarantee the presence of the coannihilator in the thermal bath, keeping the Boltzmann suppression factor under control. The main diagrams regulating the relic density are shown in figs. 5.1–5.4. They include i) $2 \to 2$ annihilations and coannihilations, fig. 5.1; ii) $2 \to 3$ processes, fig. 5.2; iii) loop-induced annihilations, figs. 5.3 and 5.4, that may be relevant in certain parts of the parameter space. On the basis of the center-of-mass energy $\sqrt{s} \approx 2m_\chi$, so depending on m_χ, we have different processes:

- $m_\chi < m_t$: the relic density is characterized by the loop-induced process $\chi\chi \to gg$, fig. 5.4 with $\gamma, X \to g$ substitution, and by the $2 \to 3$ processes $\chi\chi \to W^+ b\bar{t}$, $\chi\chi \to W^- \bar{b} t$, fig. 5.2. In this mass range we can have also the 2-loop process $\chi\chi \to h \to f\bar{f}$, with f any massive kinematically allowed

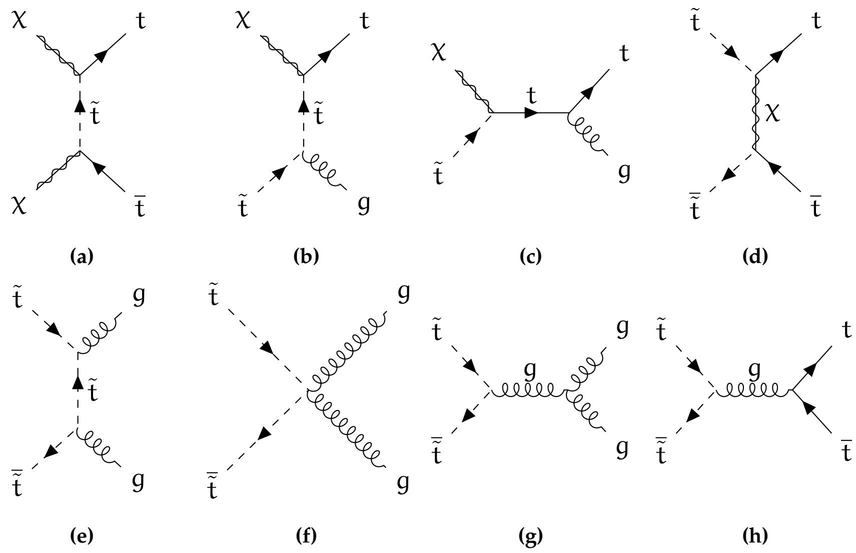

Figure 5.1: LO $2 \to 2$ annihilation and coannihilation diagrams for the simplified top-philic model.

Standard Model particle, fig. 5.3; which, despite being 2-loop-suppressed, it can have a sizable contribution on the Higgs resonance $m_\chi \approx m_h/2$;

- $m_\chi \geqslant m_t$: the annihilation into $t\bar{t}$, fig. 5.1a, kicks in and becomes the main annihilation process;
- the processes $\tilde{t}\bar{\tilde{t}} \to t\bar{t}$ and $\chi\tilde{t} \to tg$, in figs. 5.1b–5.1d and 5.1h, are always kinematically allowed, because of the chosen mass splitting in eq. (5.16), that guarantees $m_{\tilde{t}} > m_t$. However, the lower m_χ, the larger is the relative mass splitting between χ and $\tilde{t}$, meaning the coannihilation is less efficient because the abundance of the coannihilator partner in the thermal bath would be further suppressed;
- other coannihilation processes, such as $\tilde{t}\bar{\tilde{t}} \to gg$, figs. 5.1e–5.1g, depend solely on g_s, so they are an important contribution for low λ_χ.

We use the results on relic density computation performed by the authors of [455], adding the constraints coming from γ-lines.

We consider dark matter annihilations into $\gamma\gamma$, γZ, and γh, involving respectively 14, 14, and 6 diagrams, shown in fig. 5.4. We generate the NLO UFO model with FeynRules [453], FeynArts [454], and NLOCT [387], and compute the various processes. The computation of the $\gamma\gamma$ contribution has been performed in the literature for the first time in [459, 460] (see also [455, 461]). Our results agree with the ones from [455, 459].

The resulting constraints on the dark matter coupling, λ_χ, are shown in fig. 5.5. The green and blue lines denote the limits from Fermi-LAT and HESS,

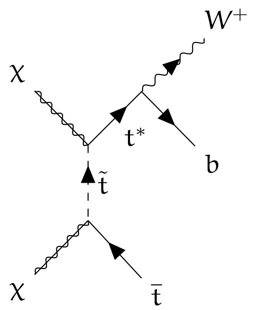

Figure 5.2: The $2 \to 3$ process $\chi\chi \to W^+ b\bar{t}$; the process $\chi\chi \to W^- \bar{b}t$ has the same topology.

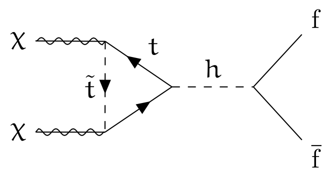

Figure 5.3: Higgs-mediated loop-induced annihilation in Standard Model massive particle f; this process is relevant only on the Higgs resonance, $m_\chi \approx m_h/2$.

respectively, assuming an Einasto profile. The corresponding shaded bands around them indicate the uncertainty from the density profile. Its lower and upper boundaries mark the limits assuming the NFWc and the isothermal profile, respectively. Notably, the band for the case of Fermi-LAT is considerably smaller as a result of optimized ROIs for the different profiles, see section § 5.1. The dot-dashed curve denotes the projection for CTA [462], taken from [463].

For $m_\chi \gtrsim 240$ GeV, the energy of the spectral lines arising from annihilation into γh and γZ are equal within the detector resolution of Fermi-LAT and hence combined for the limit setting. They are combined with $\gamma\gamma$ above $m_\chi \gtrsim 260$ GeV. However, the γh annihilation cross section is p-wave suppressed and hence negligible (the corresponding limit for the individual channel is far outside the displayed window). The limits arising from combinations of channels are drawn as solid lines.

For $m_\chi \lesssim 260$ GeV we display the limits for the individual channels; the dotted and dot-dashed lines correspond to $\gamma\gamma$ and γZ, respectively. However, in the range 110 GeV $\lesssim m_\chi \lesssim 260$ GeV, the peaks are not sufficiently separated while their integrated fluxes are of similar size questioning the validity of the limit-setting procedure in the Fermi-LAT analysis. This is indicated by the missing green band which is only shown in the ranges providing a reliable limit. Note that for $m_\chi \lesssim 110$ GeV it corresponds to the stronger limit (γZ).

Current limits only constrain the region below 110 GeV for the NFWc profile. Note that the region shown in the plot is challenged by direct detection experiments, see [455], and independent on astrophysical parameters, by LHC searches for supersymmetric top partners [279, 280, 282, 283]. Many searches for the neutralino-stop sector were performed in the literature, however, given the $\tilde{t}$ production depends only on its gauge interaction and not on λ_χ, these searches do not reference the strength of that coupling. An alternative is to consider searches for $\tilde{t}$ decays that do not involve other supersymmetric particles. We

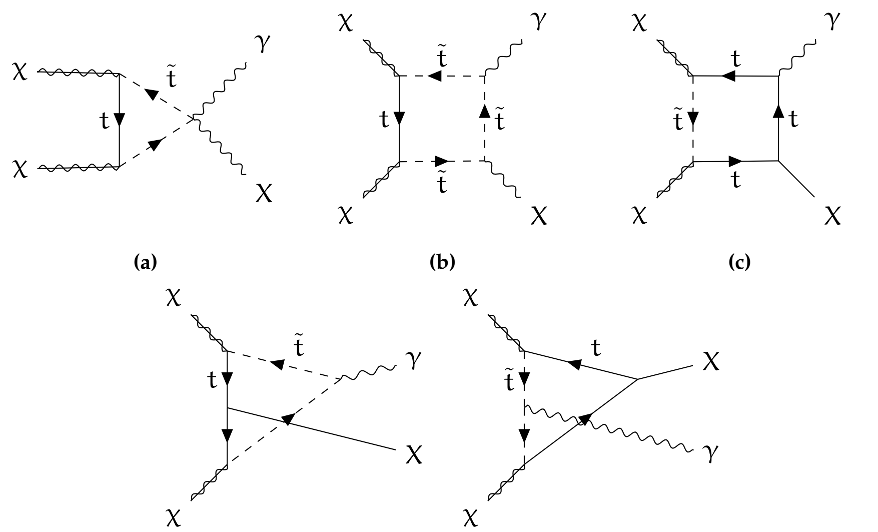

Figure 5.4: Loop-induced annihilation diagrams in γX (unitary gauge) for the simplified top-philic model; $X \in \{\gamma, Z, h\}$, except for the diagrams a and b, where the Higgs boson is not allowed in the final states. Notice that these diagrams are topologically equivalent to the ones describing the loop-induced annihilation into a pair of gluons $\chi\chi \to gg$, upon substitutions $\gamma, X \to g$.

have considered the LHC 13 TeV following analysis: CMS fully hadronic [464, 465], CMS single lepton [466], ATLAS fully hadronic [467], ATLAS single lepton [468] and ATLAS two leptons [469]. In [455], the authors have combined them and analyzed the resulting 95 % CL exclusion region on the parameters $(m_\chi, \Delta m)$. In this case we have taken the bounds for the mass splitting as in eq. (5.16), that results in the exclusion region $(56$ to $400)$ GeV in dark matter mass. However, for the considered slice $\Delta m \approx m_t$ the signal acceptance is subject to large uncertainties and, hence, this region is often blanked out in the experimental limits, see e.g. [282].

5.3.2 Inert doublet model

The IDM is built on top of the Standard Model by the addition of a new (*inert*) Higgs doublet, Φ, odd under an exact $\mathbb{Z}_2$ symmetry, stabilizing the lightest state. The Lagrangian of the model contains the following kinetic term:

$$\mathcal{L} \supset (\mathcal{D}_\mu \Phi)^\dagger \mathcal{D}^\mu \Phi \,, \tag{5.17}$$

where $\mathcal{D}_\mu = \partial_\mu - i\frac{g}{2} b_\mu^k \sigma^k - i\frac{g'}{2} B_\mu$, with b_μ^k $(k = 1, 2, 3)$, B_μ gauge bosons of $SU(2)_L \times U(1)_Y$. The term H is the Standard Model Higgs doublet. The $\mathbb{Z}_2$ odd parity of Φ implies that its VEV vanishes. In addition, the scalar potential

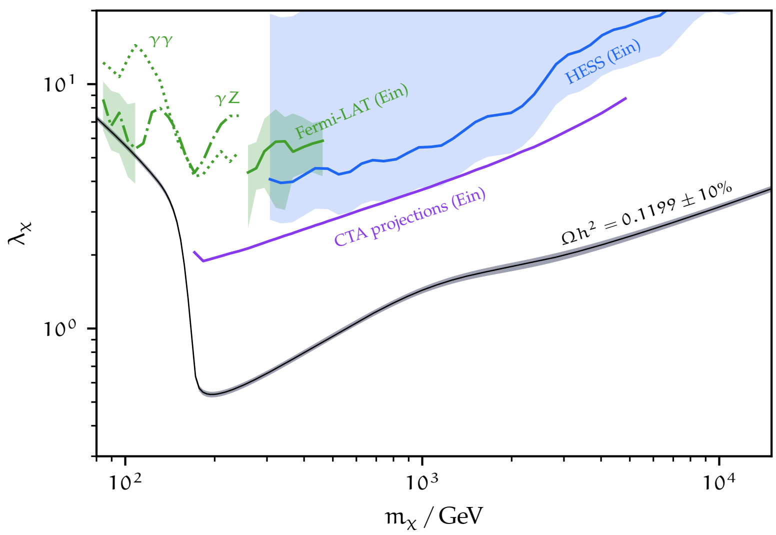

Figure 5.5: Parameter space for the top-philic model, including the constraints for loop-induced dark matter annihilation into monochromatic photons. The black solid curve (and shaded band around it) shows the dark matter coupling that yields the measured relic density, assuming $\Omega h^2 = 0.1199$ (with a 10 % uncertainty on the theory prediction), taken from [455]. The green (blue) curve denotes the Fermi-LAT (HESS) limits for the Einasto profile. The lower and upper boundaries of the shaded bands indicate the corresponding limits for the NFWc and Isothermal profile, respectively. The dotted and dot-dashed curves show the upper limits for the individual final states $\gamma\gamma$ and γZ, respectively, in the range where the signals are not combined (see text for details). The violet curve shows projections for CTA assuming the Einasto profile.

reads:

$$\begin{aligned} V = \mu_1^2\, H^\dagger H + \mu_2^2\, \Phi^\dagger \Phi + \lambda_1 (H^\dagger H)^2 + \lambda_2 (\Phi^\dagger \Phi)^2 \\ + \lambda_3 (H^\dagger H)^2 (\Phi^\dagger \Phi)^2 + \lambda_4 (H^\dagger \Phi)^2 + \frac{\lambda_5}{2} \left[(H^\dagger \Phi)^2 + \text{h.c.} \right] . \end{aligned} \tag{5.18}$$

Upon electroweak symmetry breaking we are left with the fields:

$$\Phi = \begin{pmatrix} h^+ \\ \frac{1}{\sqrt{2}}(h_0 + i a_0) \end{pmatrix} . \tag{5.19}$$

The model contains a total of five physical scalar states, with masses given by:

$$m_h^2 = \mu_1^2 + 3v_H^2\lambda_1 \,, \tag{5.20a}$$

$$m_{h^\pm}^2 = \mu_2^2 + \frac{v_H^2}{2}\lambda_3 \,, \tag{5.20b}$$

$$m_{h_0}^2 = \mu_2^2 + v_H^2\lambda_L \,, \tag{5.20c}$$

$$m_{a_0}^2 = \mu_2^2 + v_H^2\lambda_S \,, \tag{5.20d}$$

where we have defined the following constants:

$$\lambda_{\substack{L\\S}} = \frac{1}{2}(\lambda_3 + \lambda_4 \pm \lambda_5)\,. \tag{5.21}$$

We are left with five free parameters, after imposing $m_h \approx 125\,\mathrm{GeV}$. They are:

$$m_{h_0}\,, \quad m_{a_0}\,, \quad m_{h_\pm}\,, \quad \lambda_L\,, \quad \lambda_2\,. \tag{5.22}$$

The two neutral states are stable, because of the $\mathbb{Z}_2$ symmetry of the model. Either of them could be dark matter, we chose $m_{h_0} < m_{a_0}$ as the lightest particle, and, consequently, as the dark matter candidate. These parameters are subject to several theoretical and experimental constraints, see [470–472]:

- vacuum stability and perturbativity: they prevent the parameters λ_i to be large and impose several conditions between them;
- accelerators constraints: e.g. new physics searches at LEP-II [473, 474]; these constraints impose a lower bound on the masses of the heavier scalar states, in particular

$$m_{h^\pm} \gtrapprox m_W\,, \tag{5.23a}$$

$$m_{a_0} \gtrapprox 100\,\mathrm{GeV}\,; \tag{5.23b}$$

- EWPO: the new doublet Φ contributes to EWPO, which are subject to experimental constraints [475, 476].

Despite its simplicity, the IDM leads to a rich phenomenology. It provides a viable dark matter candidate in various regions of the parameter space, involving several regimes [116] of dark matter freeze-out: annihilation near a resonance, close to thresholds and coannihilation, seee.g. [477–480]. In particular, the relic density can be explained in several regions of the parameter space. The first region is characterized by $m_{h_0} \lessapprox m_W$. In this regime the annihilations proceed through interaction via Higgs portal-like processes $h_0h_0 \to h \to f\bar{f}\,/\,VV^*$ (where f is a Standard Model fermion and $V = W^\pm, Z$; the V^* denotes an off-shell gauge boson) or point-like interactions $h_0h_0 \to VV^*$. Given the high mass difference between h_0 and the other scalar states, due to

LEP-II bound in eq. (5.23), coannihilation is suppressed. Annihilations into virtual gauge bosons becomes more important the more the kinematic threshold is approached. Indeed, when we hit the region $m_{h_0} \gtrapprox m_W$, the annihilation into gauge bosons becomes a viable channel. That would be the dominant process, and it is efficient, so we would expect the dark matter abundance to drop. However, in this regime we observe a destructive interference with the annihilation diagrams into gauge bosons (which do not depend on λ_L) and the annihilation through Higgs exchange (which depends on λ_L). It is indeed possible to choose the coupling λ_L to balance the efficiency of the annihilation into gauge bosons. This mechanism can be applied until roughly 121 GeV, above which the dark matter density becomes underabundant.

The third region is for $m_{h_0} \gtrapprox 500\,\text{GeV}$. The dark matter abundance is given by an interplay of different mechanisms. We could have a cancellation between $h_0 h_0 \to VV$ diagrams and t-channel diagrams involving the heavier scalars $h^\pm$, a_0, which are efficient if the mass splitting satisfies $|m_{h_0} - m_{a_0/h^\pm}| \lessapprox 10\,\text{GeV}$. Moreover, we have contributions from Higgs exchange diagrams. Given the small mass splittings between h_0 and the other odd states, coannihilations are also important.

We can consider direct detection constraints: the tree-level spin independent WIMP-nucleon scattering cross section arises from Z and Higgs exchange diagrams [470]. The former is significant only for small mass splitting. The Higgs exchange diagrams depend on λ_L. That means large part of the parameter space will be wiped out and the only regions remaining are those related to low λ_L or high mass (where the constraints are weaker). In this context, we can identify a viable region where the relic density depends on the annihilations into virtual gauge bosons, which is efficient, but not too much in order to require cancellations. We are able to keep λ_L small, and direct detection constraints are under control: diagrams with massive gauge bosons in the loop [481] dominate the direct detection cross section; they are around an order of magnitude smaller than the current limits from LZ [253] and XENONnT [252]. This happens in the region around $m_{h_0} \approx 72\,\text{GeV}$, which would be the focus of our analysis. That region has been previously studied by some of the authors in [480]. This region is also interesting, because it can potentially explain the Fermi-LAT GCE, see § 3.7.6, when interpreted as a dark matter signal [480]. Another important feature is that it not only avoids direct detection bounds, but it is also unchallenged by current limits from the LHC [482]. Probing this region with γ-ray observations is therefore highly desirable. A final remark about the direct detection constraints regards the electroweak radiative corrections. Those are independent on λ_L and could provide a sizable contribution to the dark matter-nucleon scattering cross section, however, for the points in the studied region, the radiative corrections are of the order of $1.5 \times 10^{-48}\,\text{cm}^2$ [481], which is slightly outside current experimental sensitivity, but well in the reach of the future DARWIN.

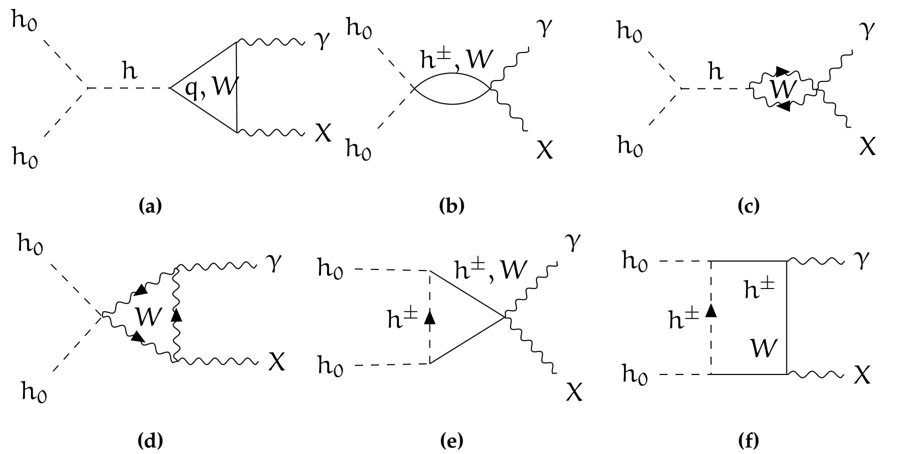

Figure 5.6: Subset of the loop-induced annihilation diagrams in γX, where $X = \{\gamma, Z\}$ (unitary gauge) for the IDM.

Again, we generate the NLO UFO model with FeynRules [453], FeynArts [454] and NLOCT [387]. The processes $h_0 h_0 \to \gamma\gamma$ and $h_0 h_0 \to \gamma Z$ involve 140 and 172 diagrams, respectively. Note that $h_0 h_0 \to \gamma h$ is forbidden due to charge-conjugation invariance (i.e. a generalization of Furry's theorem). The main diagrams are shown in fig. 5.6. The numerical computation of the cross sections performed by MadDM v3.2 agrees with the literature [401, 414]*.

The region of the parameter space we focus on has been studied by the authors of [480], who performed a scan over the parameter space, taking into account constraints from the relic density [483], electroweak precision observables [475, 476], new physics searches at LEP-II [473, 474], indirect detection searches for continuum γ-ray spectra from dSph [221] and theoretical requirements of unitarity, perturbativity and vacuum stability computed with 2HDMC [476]. The scan was performed with Multinest [484, 485] for efficient parameter sampling. We consider points within the $2\,\sigma$ region.

The resulting cross sections for $\langle\sigma v\rangle_{\gamma\gamma}$ and $\langle\sigma v\rangle_{\gamma Z}$ are shown in fig. 5.7 together with the corresponding limits from Fermi-LAT [152] and future projections for GAMMA-400 (2 years) as well as a combination of both observations (with 12 and 4 years observational time, respectively) [486]. Constraints assume the Einasto profile, while the shaded band around the Fermi-LAT limit illustrates the uncertainty due to the choice of the profile. The upper and lower boundary of the shaded band corresponds to the limit assuming the isothermal and NFWc profile, respectively. In the $\gamma\gamma$ channel, the current limits only constrain the considered region for the case of NFWc profile. For the Einasto profile, future observations are expected to provide sensitivity. In the case of

*The results exhibit a noticeable dependence on the choice of Standard Model parameters of the electroweak sector.

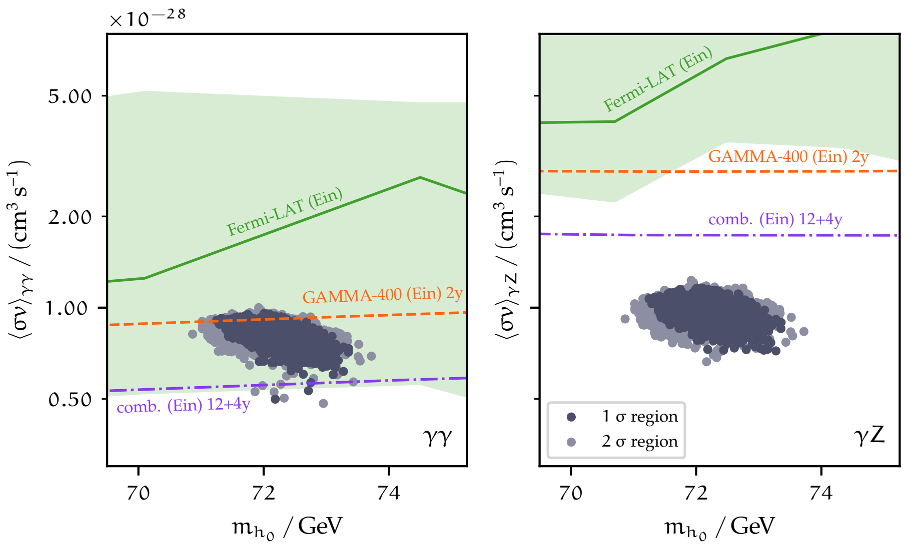

Figure 5.7: Cross section for the loop-induced dark matter annihilation into $\gamma\gamma$ (left panel) and γZ (right panel) for the allowed IDM parameter points explaining all of dark matter ($\Omega h^2 = 0.12$) in the range $(70$ to $75)$ GeV. Parameter points in the 1 σ and 2 σ regions are drawn in shades of gray. The green solid curve denotes the Fermi-LAT limit for the Einasto profile. The lower and upper boundary of the green shaded band shows the respective limits for NFWc and isothermal profile, respectively. The orange dotted and violet dot-dashed curves show projections for GAMMA-400 (2 years) and the combination of Fermi-LAT (12 years) and GAMMA-400 (4 years), respectively, both assuming the Einasto profile.

an excess in $\gamma\gamma$, the confirmation of a line-signal around $E_\gamma \approx 43$ GeV in γZ would be important to establish the model. However, the sensitivity of the combination of Fermi-LAT and GAMMA-400 (violet dot-dashed curve in the right panel) is still too low by about a factor of two to reach the expected signal originating from $\langle \sigma v \rangle_{\gamma Z}$.

5.4 Summary

Gamma-ray lines are striking signatures of direct dark matter annihilation into photons in galactic halos. Additionally, they can complement continuum γ-ray emission from dark matter. Searches for γ-rays is particularly relevant, given the presence of unexplained excesses in the γ-ray flux, like the Fermi-LAT GCE.

One of the main feature of $\gamma\gamma$ or γX final states is that they are loop-induced processes, assuming electrically neutral dark matter. The computation of the cross section in this case is challenging, because it requires the evaluation of one-loop diagrams. This work has been accompanied by the release of MadDM v3.2, which is equipped with a new framework to automatize the study of loop-induced processes, from the computation of the cross section to the phenomenological study, for any dark matter model provided in the NLO UFO format. MadDM utilizes MadLoop and interfaces with MadGraph to perform the loop-induced computation automatically, using a broad range of other tools and algorithms under the hood. Furthermore, MadDM has been extended to include the complete study of γ-lines phenomenology: it computes the integrated fluxes and applies experimental constraints from Fermi-LAT and HESS to the model. It also includes the automatic computation of the $\mathcal{J}$-factor for a variety of dark matter density profiles and ROIs, providing the user with the necessary flexibility for comprehensive dark matter studies.

In this chapter, we applied MadDM v3.2 to two relevant physics scenarios, showing also the potential of γ-lines searches. First, we studied a simplified top-philic dark matter model, made of a single dark matter candidate interacting with the Standard Model through a colored scalar mediator. The relic density depends on coannihilations and $2 \to 2$ annihilations. However, the latter are suppressed for dark matter lighter than the top-quark, while loop-induced processes become important and consequently require large dark matter couplings to reproduce the correct value of relic density. This also enhances the strength of the γ-line signals relative to the continuum emission for indirect detection. However, current line searches from Fermi-LAT only constrain the region of dark matter masses below roughly 110 GeV. In the parameter space under consideration it was possible to show another capability of MadDM, namely the analysis of the γ-line spectrum. MadDM is able to merge the different γ-lines according to the given experimental resolution. For instance, for the channels $\gamma\gamma$ and γZ, this happens above $m_{\rm DM} = 260$ GeV in the case of the Fermi-LAT constraints, while their signals could be merged for the entire reported range for the current HESS and projected CTA limits. Nevertheless, the model remains unchallenged by these limits.

The second model we considered is the IDM. Its rich phenomenology provides a viable dark matter candidate in several regions of the parameter space. We focused on a viable region where $71\,\text{GeV} \lessapprox m_{\rm DM} \lessapprox 74\,\text{GeV}$ that yields the measured relic density without any particular tuning of the involved parameters, while at the same time compatible with most of the constraints existing on this model. In this region, the relic density depends on annihilation into WW^*, ZZ^* due to the Standard Model gauge interactions. Furthermore, this region provides a good fit to the Fermi-LAT galactic center excess and is currently not challenged by direct detection or collider searches. We found that current limits from γ-line observation constrain the scenario for the very cuspy NFWc profile while future observations by GAMMA-400 and Fermi-LAT are expected to probe it for a slightly broader range of dark matter profiles. An intriguing possibility is the observation of two peaks, from $\gamma\gamma$ and γZ which are well separated in the considered parameter region. However, the γZ signal still appears out-of-reach according to the above-mentioned projections.

This latest release marks the initial step towards the integration of automated loop-level computations in MadDM. With current CMB data achieving relic density measurements below the percent precision level, the importance of higher-order corrections in theoretical predictions has grown, calling for automated computational tools. While MadGraph5_aMC@NLO provides a suitable framework for this endeavor, the efficient computation of thermally averaged cross sections at NLO demands further investigation, which is left for future work. Another upcoming enhancement in MadDM is focused on generic one-loop computations of direct detection cross sections, phenomenologically significant across various dark matter models. Notably, in the two physics scenarios explored in this chapter, the primary contribution to dark matter scattering off nuclei arises from loop-induced processes.

Chapter 6

Dark matter on the Higgs resonance

A wizard is never late, nor is he early,
he arrives precisely when he means to.
—Gandalf

The Lord of the Rings: The Fellowship of the Ring
Directed by PETER JACKSON
Based on a character from J. R. R. TOLKIEN

In chapter 3, we have introduced the dark matter puzzle. We introduced the main cosmological observations that can be explained with dark matter, and we studied the freeze-out mechanism and the WIMP dark matter candidate, which is able to explain the dark matter relic density with very few assumptions. Moreover, we explained the main search strategies for dark matter: indirect detection, direct detection and collider searches.

Regarding indirect detection, in chapter 5, we studied the importance of the γ-ray channel. The discovery of excesses in the γ-ray spectrum fostered several speculations regarding a possible dark matter interpretation. The GCE is certainly the most famous example [188, 200–215], and a possible explanation in terms of dark matter annihilation has been extensively studied in the literature [188, 195, 207, 208, 211, 216–219]. In addition to the galactic center, also dSph are a promising target. Remarkably, a combined experimental analysis of dSph samples [195, 225], or single objects [487], have recorded a $1\,\sigma$ to $3\,\sigma$ excess in the data, which could be tackled with a dark matter explanation. Furthermore, also CRs present excesses [187–195] that could be expressed by a dark matter interpretation [188, 189, 191, 192].

From the point of view of direct detection, dark matter nucleon scattering has reached an impressive sensitivity to the WIMP-nucleon cross section and the discovery potential of LZ [253] and XENONnT [252] is constantly improving. Their sensitivity is expected to reach the neutrino fog in the next decade, while next generation direct detection experiments will be able to improve their limits of about a factor of 10.

Finally, collider searches at LHC are studying dark matter through several different techniques, involving its production and the observation of final state signals [488].

In this chapter we put all these pieces together, and we perform a detailed study of one among the simplest dark matter model: the singlet scalar Higgs portal model (SHP). The SHP model is one of the simplest extensions of the Standard Model, including a single scalar dark matter candidate coupled to the Higgs boson through a Higgs portal interaction. It can provide a meaningful explanation of dark matter in our Universe [489–497]. It has been extensively studied in the literature and large parts of its parameter space are already excluded by direct detection and collider constraints. However, the Higgs resonant region, $m_{DM} \approx m_h/2$, is still viable [498, 499] and constitutes a great target to probe phenomenologically: a WIMP candidate of that mass scale has the potential of explaining both the GCE and the antiprotons excess mentioned above. The objective of the chapter is to perform a phenomenological study of the SHP model, combining the signals from the different cosmic messengers (γ, $\overline{p}$), with the constraints from direct detection (LZ) and collider searches (ATLAS, CMS), looking for any compatibility between the best fit regions and the major bounds. On top of this, we compute the relic density of the model, characterized by a resonant annihilation mechanism, leading to early kinetic decoupling. This phenomenon affects the freeze-out process and will be studied in details [113, 500].

The chapter is organized as follows. In § 6.1, we introduce the SHP model, and we compute the main observables and cross sections. Sec. 6.2 is dedicated to the study of the relic density, impacted by the kinetic equilibrium breaking down. Collider and direct detection constraints are examined in §§ 6.3 and 6.4, respectively, while indirect detection is presented in § 6.5, where analysis of γ and $\overline{p}$ constraints are discussed. Finally, in § 6.6 we combine all the constraints, and we discuss the viable parameter space and the implications for the model. We conclude in § 6.7.

The chapter is entirely based on the following publication:

[2] Di Mauro, M., Arina, C., Fornengo, N., Heisig, J., **DM,** "Dark matter in the Higgs resonance region". *Phys. Rev. D* 108.9 (2023), p. 095008. DOI: 10.1103/PhysRevD.108.095008.

My main contribution was in the study of the model and its features, understanding the trends of the different observables and of the spectra. The SHP was also presented in my master thesis [60], and I was already confident with this model. I provided technical support in the calculation of the spectra and of the various constraints with MadDM, MadGraph and Pythia. I participated in the discussion of the results, but I did not realize any of the plots shown, directly.

The study presented in this chapter is accompanied by the release of the Python package SingletScalar_DM available on GitHub [501], enabling the calculation of the dark matter spectra, relic density, as well as direct detection and collider constraints within the model. I helped in the development of the package, providing technical support, suggestions, writing the documentation, and taking care of the webpage of the repository.

6.1 Singlet scalar Higgs portal model

6.1.1 Overview

The SHP is one of the simplest extensions of the Standard Model [489]. It includes a singlet scalar dark matter candidate S, coupling to the Standard Model with a scalar portal of the same form as the one shown in eq. (4.2). The interaction is renormalizable, S is singlet under all Standard Model gauge groups and the model respects a $\mathbb{Z}_2$ symmetry. Under this symmetry, all particles except S are assumed to be even, while S is odd ($S \to -S$). In this way, the stability of the dark matter candidate is guaranteed (incidentally forbidding any Lagrangian terms proportional to an odd power of the S field). Extensive studies of the model have been performed in the literature [490–497]. The Lagrangian reads:

$$\mathcal{L} \supset \frac{1}{2}\partial_\mu S \partial^\mu S - \frac{1}{2}\mu_S^2 S^2 - \frac{1}{4}\lambda_S S^4 - \frac{1}{2}\lambda_{HS} H^\dagger H S^2 \,, \tag{6.1}$$

where H is the Standard Model Higgs doublet and μ_S, λ_S, and λ_{HS} are free parameters. After spontaneous symmetry breaking, the Lagrangian in eq. (6.1) becomes:

$$\mathcal{L} \supset \frac{1}{2}\partial_\mu S \partial^\mu S - \frac{1}{2}m_S^2 S^2 - \frac{1}{4}\lambda_S S^4 - \frac{1}{4}\lambda_{HS} h^2 S^2 - \frac{1}{2}v_H \lambda_{HS} h S^2 \,, \tag{6.2}$$

where h is the Higgs field, and we defined the mass of S as $m_S^2 = \mu_s^2 + 1/2\, v_H^2 \lambda_{HS}$. It is worth to notice that μ and λ_S deal with the S-sector only, while λ_{HS} regards the interaction between the Standard Model and S. Additionally, the quartic coupling λ_S has an important role in the stability of the electroweak vacuum, which should be bounded from below, so that [491]:

$$\lambda_S > 0 \,, \tag{6.3a}$$

$$\lambda_S \lambda_H > \lambda_{HS}^2 \quad \text{if } \lambda_{HS} < 0 \,, \tag{6.3b}$$

where λ_H is the quartic coupling of the Higgs field. Moreover, S does not take a VEV, because it is protected by the $\mathbb{Z}_2$ symmetry, so that $\mu > 0$.

In this context, the quartic coupling λ_S does not play any role in the phenomenology of the model, and it is highly unconstrained (but it cannot be chosen too large to not violate the perturbative regime). The phenomenology

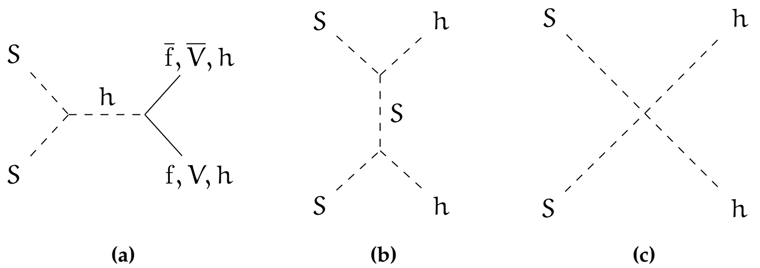

Figure 6.1: Tree-level annihilation Feynman diagrams of the SHP model. The symbol f refers to any charged fermions, while V refers to either $W^{\pm}$, Z. The diagram b includes also the u-channel.

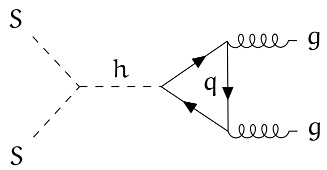

Figure 6.2: Feynman diagram for the loop-induced annihilation $SS \to gg$. The symbol q stands for quarks.

is solely governed by the last two interaction terms in eq. (6.2). These terms are responsible for the annihilation of S into Standard Model particles through the Higgs portal. Annihilation processes are crucial for the thermalization and freeze-out of S, which ultimately determines the dark matter relic density, while they are the main ingredients for indirect detection searches. Additionally, Higgs boson can decay to a pair of S particles, which can be searched in colliders through missing energy signals. Finally, the same coupling generates S scattering off quarks, which can be probed in direct detection experiments. The relevant diagrams for S annihilation are shown in figs. 6.1 and 6.2. Tree-level s-channel annihilation is possible either into fermions, gauge bosons or Higgs bosons. The loop-induced annihilation into a pair of gluons is also possible, and also the annihilation into $\gamma\gamma$, γZ and γh is allowed, but it is subdominant, and it will not be considered here.

6.1.2 Annihilation cross section

In this section we will list the expressions for the annihilation cross section of the SHP model. For indirect detection and thermal decoupling, the main observable to consider is the velocity-averaged annihilation cross section $\langle \sigma v \rangle$. In the case of dark matter particles annihilating into a pair of Standard Model particles, as given by the diagram in fig. 6.1a, we can write, excluding the hh

final state [502]:

$$\sigma v = \frac{2\lambda_{HS}^2 v_H^2}{\sqrt{s}} |D_h(s)|^2 \Gamma_{h\to i}(\sqrt{s}) \,, \tag{6.4}$$

where $\Gamma_{h\to i}(\sqrt{s})$ is the partial decay width into the state i of the Standard Model Higgs boson evaluated at energy $\sqrt{s}$. This is a very convenient expression, since it depends on the Higgs width, which is a well-known quantity, with many theoretical and experimental results available in the literature [503]. The Higgs propagator $D_h(s)$ is defined as:

$$|D_h(s)|^2 = \frac{1}{\left(s - m_h^2\right)^2 + m_h^2 \Gamma_h^2} \,. \tag{6.5}$$

The term Γ_h is the total Higgs width for the Standard Model Higgs boson, taking into account every kinematically allowed partial decay widths, including the invisible Higgs width $\Gamma_{h,\text{inv}}$. We adopt the following theoretical predictions for the former: $\Gamma_{h,\text{SM}} = 4.1$ MeV [503]. The invisible width can be computed at tree level as:

$$\Gamma_{h,\text{inv}} = \frac{\lambda_{HS}^2 v_H^2}{32\pi m_h} \sqrt{1 - \frac{4m_S^2}{m_h^2}} \,, \tag{6.6}$$

where m_h is the Higgs boson mass, with value $m_h = 125$ GeV as recently measured by ATLAS [504]. The propagator expression in eq. (6.5) is written according to the fixed-width prescription, which is a good approximation for the Higgs boson, since its width is a slowly varying function of the energy. However, on the resonance region we are interested in, this approximation is not valid, because the invisible decay channel opens up and Γ_h acquires a strong dependence on s [505]. This can be taken into account by substituting m_h with $\sqrt{s}$ in eq. (6.6).

The cross sections in the SHP are s-wave over most of the parameter space, and they do not depend on the velocity. A slight velocity dependence is present in the resonance region, however, this dependence is relevant only for velocities higher than the typical dark matter velocity in the galactic halo, which we assumed to be $10^{-3}c$, and it contributes only for around 1 %, so we neglected it. The annihilation cross section for all the possible annihilation channels is provided in [506]. In the following, we will discuss only the LO cross sections on the basis of m_S and λ_{HS}. In fig. 6.3, we show the features of the velocity-averaged annihilation cross section on the basis of the dark matter masses, expliciting the dependence on λ_{HS} and the contribution of the different final states to the total. First, annihilation into a pair of fermions reads:

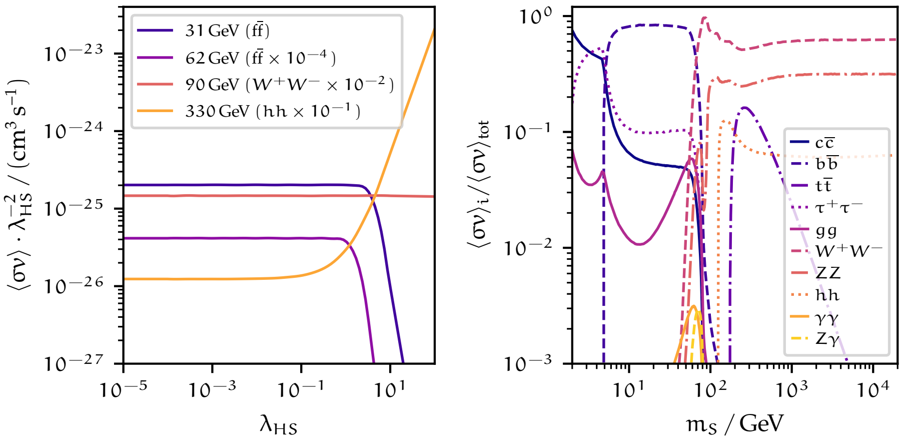

Figure 6.3: LEFT PANEL: annihilation cross section normalized by λ_{HS}^2 as a function of the coupling parameter λ_{HS} for four different values of m_S. For $m_S = 31\,\text{GeV}$ and $m_S = 62\,\text{GeV}$, $\langle \sigma v \rangle$ is dominated by the $f\bar{f}$ final state; for $m_S = 90\,\text{GeV}$ is dominated by the $W^\pm$ channel, while for $m_S = 330\,\text{GeV}$ the largest contribution comes from the Higgs production. RIGHT PANEL: ratio between the annihilation cross section for the different channels $\langle \sigma v \rangle_i$ with respect to the total $\langle \sigma v \rangle_{tot}$ as a function of the dark matter mass, computed for a fixed $\lambda_{HS} = 0.01$. Adapted from [2, fig. 3].

$$\sigma = \frac{\lambda_{HS}^2 m_f^2 N_c (s - 4m_f^2)^{3/2}}{8\pi s \sqrt{s - 4m_S^2}\left[(s - m_h^2)^2 + \Gamma_h^2 m_h^2\right]}, \tag{6.7}$$

where $N_c = 3$ for quarks, $N_c = 1$ for leptons, and m_f is the fermion mass. Referring to fig. 6.3 left, we can see the features of the cross section in different regimes of mass and couplings. Considering $m_S < m_h/2$, the cross section gets its main contribution from annihilation into a pair of fermions, see fig. 6.3 right for the branching ratios, and we can identify two regimes:

- $\lambda_{HS} < 0.01$; the invisible $h \to SS$ channel, despite being kinematically available, is negligible and Γ_h can be approximately considered to be constant;
- $\lambda_{HS} > 0.01$: Γ_h gets an increasingly higher contribution on the basis of λ_{HS}, though making the dependence of the kind $\langle \sigma v \rangle \propto \lambda_{HS}^2/(1 + k\lambda_{HS}^4)$, see eq. (6.6). It is interesting to notice that the second term in the denominator is suppressed unless λ_{HS} acquires non-perturbative values.

The cross section into vector bosons has the following expression:

$$\sigma = \frac{\lambda_{HS}^2 \sqrt{s - 4m_V^2}\,(s^2 - 4m_V^2 s + 12 m_V^4)}{16\pi s \sqrt{s - 4m_S^2}\left[(s - m_h^2)^2 + \Gamma_h^2 m_h^2\right]}, \tag{6.8}$$

where V stands for $W^\pm$ and Z. Most of the contributions from these processes are in the $m_S > m_h/2$ region, see fig. 6.3 right, where Γ_h is constant ($h \to SS$ is not available kinematically). So, we see that for $m_S = 90\,\mathrm{GeV}$, this channel scales always as λ_{HS}^2.

Lastly, the cross section for annihilation into a pair of Higgs bosons can be written as the following expression, using the non-relativistic limit (justified because of the low velocity dark matter is assumed to have in the galactic halo), $s \to 4m_S^2$:

$$\sigma = \frac{\lambda_{HS}^2 \sqrt{1-\frac{m_h^2}{m_S^2}}\left[m_h^4 - 4m_S^4 + 2\lambda_{HS} v_H^2 (4m_S^2 - m_h^2)\right]^2}{64\pi m_S^2 (m_h^4 - 6m_h^2 m_S^2 + 8m_S^4)^2} \,. \tag{6.9}$$

In this case, the cross section scales as λ_{HS}^2 when $\lambda_{HS} < 0.1$. Larger couplings would make the polynomial term in the numerator to become more relevant than all the other terms, and modifying the scaling to λ_{HS}^4. This is shown in fig. 6.3 left for the case of $m_S = 330\,\mathrm{GeV}$, dominated by the annihilation into Higgs bosons.

Below the resonance, it is important to take into account the annihilation into a pair of gluons. This is a loop-induced process, and its contribution accounts for at most 7 % of the total cross section for $m_S \approx 60\,\mathrm{GeV}$. Differently, annihilations into $\gamma\gamma$, γZ and γh contribute at few ‰.

In this work, we calculated the annihilation cross sections with MadDM [1, 388, 507, 508], using the UFO implementation of the SHP model and exploiting the functionalities of MadDM to link with Pythia [509] for hadronization and showering*.

Another important channel is the contribution from off-shell gauge or Higgs bosons. This is relevant for $W^\pm$ and Z final states, while it has a minor effect for h boson. Below the on-shell production thresholds, processes such as $SS \to W^{\pm *} W^{\mp(*)}$ and $SS \to Z^* Z^{(*)}$ may be allowed. We calculated the cross section into the four-body diagram where both final states bosons are produced off-shell, eventually decaying into fermions f:

$$SS \to h \to V^* V'^* \to 4f \,, \tag{6.10}$$

where V and V' stand for $W^\pm$ or Z.

Fig. 6.3 right shows the relative contribution of each annihilation channel to the total cross section with fixed $\lambda_{HS} = 0.01$. For very small S masses, the annihilation happens predominantly into $c\bar{c}$ quarks and $\tau^+\tau^-$ leptons. Instead, for $m_S = (5 \text{ to } 50)\,\mathrm{GeV}$ the main contribution comes from $b\bar{b}$ annihilation. Finally, for large dark matter masses the main channels are the one with gauge and Higgs bosons. The effect of the off-shell contribution of the gauge bosons is particularly relevant for the annihilation involving $W^\pm$ bosons, which becomes

*We used MadDM v3.2 on top of MadGraph v2.9.9 (LTS) and Pythia v8.3.

the main channel even below the on-shell production threshold $m_S < m_W$. For dark matter masses above 5 GeV, the contribution of $\tau^+\tau^-$ annihilation is larger than $c\bar{c}$. This may seem to be counter-intuitive since, from eq. (6.7), the cross sections for the two channels are $\sigma(c\bar{c}) \propto 3m_c^2$ and $\sigma(\tau^+\tau^-) \propto m_\tau^2$. Accordingly, one may expect $\sigma(c\bar{c})/\sigma(\tau^+\tau^-) = 3m_c^2/m_\tau^2 > 1$. However, taking into account the running quark masses in our calculation, we find $m_c \leqslant 1$ GeV [510] for $m_S \geqslant 3$ GeV, which leads to $\sigma(c\bar{c}) < \sigma(\tau^+\tau^-)$.

6.1.3 Source energy spectra

Energy spectra from dark matter annihilation are important for indirect detection searches. They are obtained using MadDM to generate events for each final state, and then linking its output to Pythia for hadronization and showering. All channels previously discussed are included in the computation of the spectra. We included FSR contributions and electroweak emissions of weak gauge bosons off fermions, using Pythia settings. Differently from the ready-to-use spectra contained in the PPPC4DMID package [458], we included the contribution of off-shell $W^\pm$ and Z, and we took into account the polarization of them. The latter impact is particularly relevant for the antiprotons spectra.

We compute the dark matter spectra for masses between 2 GeV and 20 TeV generating 10^6 events per point. For $m_S > 110$ GeV we vary λ_{HS} between 10^{-2} and 10.

6.2 Relic density

In § 3.3 we studied the evolution of the dark matter number density in the early Universe and the freeze-out mechanism. This process is governed by the Boltzmann equation, eq. (3.25), which we repeat here for convenience:

$$\mathbf{L}[f] = \mathbf{C}[f] \,. \tag{6.11}$$

Usually, it is safe to assume that the dark matter particles are in kinetic equilibrium with the Standard Model particles, i.e. the elastic scattering processes are fast enough to keep the dark matter particles in thermal equilibrium. This involves the assumptions that the distribution of S particles is proportional to the thermal one: $f_S \propto f_{S,\mathrm{eq}}$. In such case, it is possible to further simplify the Boltzmann equation, obtaining

$$\frac{dn}{dt} + 3Hn = -\langle\sigma v\rangle\left(n^2 - n_{\mathrm{eq}}^2\right) , \tag{6.12}$$

where n is the dark matter number density, n_{eq} is the equilibrium number density, H is the Hubble parameter and $\langle\sigma v\rangle$ is the thermally-averaged annihilation cross section. As soon as the Universe cools down, the dark matter particles become non-relativistic, its equilibrium density drops until the annihilation rate becomes smaller than the Hubble rate. The particle freezes-out and the number density remains constant. The value of the dark matter relic abundance has been measured by the Planck experiment [20] and constitutes one of the main constraints on dark matter models. In this section, we study the relic density of the SHP model showing that the assumption of kinetic equilibrium breaks down in the resonance region, discussing its impact on the relic density calculation.

Kinetic equilibrium holds when the elastic scattering processes are fast enough to guarantee efficient momentum exchange between the particles of the thermal bath, and they are usually orders of magnitude larger than the annihilation processes that initiate chemical decoupling. This can be justified given the large number density of light Standard Model particles dark matter can scatter off in the thermal bath. Indeed, during chemical decoupling, dark matter number density is Boltzman suppressed, so that also kinetic equilibrium is not maintained and the particle freezes-out. However, in the resonance region, annihilation processes are enhanced because of the resonant s-channel Higgs boson exchange, while t-channel scattering processes are not. This means elastic scattering processes are suppressed compared to annihilation, and kinetic equilibrium can break down during chemical freeze-out [113]. This is also justified by the fact that the main contribution to scattering processes comes from Higgs boson coupling to light particles, which is proportional to their light masses. Subsequently, it is not possible to use approximate solutions of the Boltzmann equation, but it is necessary to solve the full version of it, including the elastic collision term.

We compute the relic density of S, $\Omega_S h^2$, in the two scenarios described above:

- `fBE`: solving the full Boltzmann equation, eq. (6.11);
- `nBE`: solving the simplified eq. (6.12), i.e., assuming kinetic equilibrium during freeze-out.

This computation has been performed in [113], where a discrepancy of up to two orders of magnitude between the two cases has been found. The authors of [113] released the code DRAKE [500], to compute the relic density in these scenarios. We relied on DRAKE to perform this computation, obtaining results for both `fBE` and `nBE` models.

The freeze-out temperature in this case is around few GeV, which is close to the region where the QCD phase transition takes place. After the QCD phase transition, quarks become confined in baryons and mesons, and the elastic scattering processes are suppressed. Accordingly, we considered two different physics models, which are implemented in the DRAKE code and studied in [113]. These are extreme scenarios to evaluate the impact of the

QCD phase transition on the relic density, and they are intended to bracket the uncertainties:

- $\mathtt{QCD}_A$: elastic scattering is maximized, and all quarks are free and present in the plasma (according to their equilibrium abundance) down to temperatures of $T_c = 154\,\text{MeV}$;
- $\mathtt{QCD}_B$: elastic scattering is minimized, only light quarks (u, d, s) can contribute, and we considered temperatures above $4T_c \approx 400\,\text{MeV}$.

The temperature threshold is important to ensure that hadronization effects are negligible.

Additionally, for the sake of comparison of different tools, we also compute $\Omega_S h^2$ in the approximate scenario (nBE) using MicrOMEGAs [391–396], which ships an implementation of the SHP model. Both DRAKE and MicrOMEGAs take into account the off-shell contributions of $W^{\pm}$ and Z gauge bosons, and the contribution coming from loop-induced annihilation into gluons. We show the computation of the fBE model in the $\mathtt{QCD}_B$ scenario with DRAKE. The first consideration we can do regards the resonance region: for $m_S \approx m_h/2$, the value of λ_{HS} decreases very quickly. This can be explained with the resonant enhancement of the annihilation cross section for this particular parameter choice. As a result, the correct value of the relic abundance necessarily requires a very small value of the coupling λ_{HS}. Fig. 6.4 left shows the parameter space λ_{HS} vs m_S with the relic density lines accounting for a fraction (from 1 to 100) % of the measured value of the relic abundance obtained by the Planck experiment, $\Omega_{DM}h^2$. Fig. 6.4 right shows the same parameter space with the relic density lines corresponding to $\Omega_{DM}h^2$. Each line has been computed with either a different tool or different assumptions: we show MicrOMEGAs (only nBE model) and DRAKE (for fBE model with both $\mathtt{QCD}_A$ and $\mathtt{QCD}_B$ assumptions). As expected, we observe a large discrepancy between the nBE and fBE models, accounting for a factor between 0.5 and 2, in the whole range of dark matter masses (50 to 67) GeV, with maximal difference around 57 GeV and minimal on the Higgs pole. The difference between the $\mathtt{QCD}_A$ and $\mathtt{QCD}_B$ assumptions is maximal in the range (55 to 60) GeV, where it is at the level of (40 to 50) %. This region (also highlighted in the plot) represents the uncertainty due to the QCD phase transition.

Further corrections to the annihilation cross section can be considered, and can be relevant on the resonance region. When on the resonance, the center-of-mass energy of the annihilation process is close to the SS threshold. As we briefly mentioned in § 6.1.2, this can potentially have an effect on the Higgs width, modifying the annihilation cross section. The approximation of fixed-width calculation breaks down and the computation of the relic density requires a running-width description [505]. However, this effect is relevant only for $\lambda_{HS} > 0.3$ in the region $|m_S - m_h/2| \approx 0.1\,\text{GeV}$. So, despite this

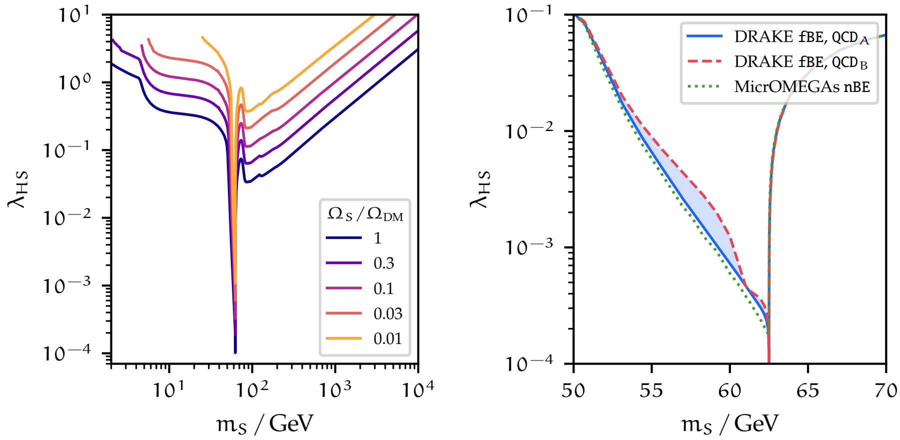

Figure 6.4: LEFT PANEL: relic density lines in the λ_{HS} vs m_S parameter space, reproducing the measured value of $\Omega_S h^2$ within a fraction (from 1 to 100) % of the measured value of the relic abundance obtained by the Planck experiment, $\Omega_{DM} h^2$. Here $\Omega_S h^2$ is computed solving the full Boltzmann equation taking into account both the elastic and annihilation collision operators (model fBE with QCD_B in DRAKE). RIGHT PANEL: comparison between the different approaches of computing the relic density, considering the results obtained by solving the Boltzmann equation with both MicrOMEGAs and DRAKE, see eq. (6.11). The MicrOMEGAs line accounts only for the annihilation processes (nBE); the DRAKE lines always assume fBE for the two extreme QCD phase transition choices, QCD_A and QCD_B. Adapted from [2, fig. 5].

phenomenon being relevant for collider searches, it is perfectly negligible for the computation of the relic density, since, on the resonance region, the coupling λ_{HS} is required to be very small. This is true even for the scenarios in which S constitutes a subdominant fraction of dark matter considered in § 6.6. We also neglect thermal corrections to the Higgs width and virtual corrections to the annihilation into an on-shell Higgs, which have recently been computed in [511].

Finally, we mention an alternative mechanism to generate the dark matter density within the model, namely the freeze-in mechanism [512–514]. For very small (or *feeble*) Higgs-portal couplings, dark matter may never thermalize with the Standard Model bath. In order to explain the relic density in this scenario, couplings of the order of $\lambda_{HS} \approx 10^{-12}$ to 10^{-11} for $m_S = (50 \text{ to } 70)\,\text{GeV}$ are required. Another assumption is that an initial abundance of dark matter is present in the early Universe, which could have been generated from processes taking place during reheating. However, the inefficient annihilation processes in this regime makes it difficult to dilute this initial abundance. Furthermore, the annihilation rate is way below the typical signal detectable in astroparticle data, like the GCE. This case is not studied in this work.

6.3 Collider searches

Collider constraints are independent of cosmological assumptions and can provide a robust probe of the model. The main observable is the invisible branching ratio of the Higgs boson, $\mathcal{B}_{h,\text{inv}}$, taking into account possible decays of h into an SS pair. For $m_S < m_h/2$, the dark matter candidate contributes directly to $\Gamma_{h,\text{inv}}$, and it is possible to derive constraints on the parameter space, by employing the limits derived experimentally. The invisible branching ratio is:

$$\mathcal{B}_{h,\text{inv}} = \frac{\Gamma_{h,\text{inv}}}{\Gamma_{h,\text{inv}} + \Gamma_{h,\text{SM}}} \,. \tag{6.13}$$

The latest 95 % CL upper limits on $\mathcal{B}_{h,\text{inv}}$ are 0.13 [268] (ATLAS, preliminary) and 0.19 [269] (CMS, published). However, in the resonant region, $m_S \approx m_h/2$, contributions from off-shell Higgs boson production are important. For this reason, we follow the method presented in [505] to reinterpret the experimental results. Additionally, the total Higgs boson decay width can become a rapidly varying function of the invariant mass, given the opening of the decay channel $h \to SS$, so that it is not possible to use the fixed-width approximation. We start by factorizing the Higgs boson production and decay channels, expressing the cross section for dark matter pair production at the LHC as:

$$\sigma(pp \to SS) = \int \frac{ds}{\pi}\, \sigma_h(s)\, |D_h(s)|^2 \,\sqrt{s}\, \Gamma_{h,\text{inv}}(s)\, \Theta(s - 4m_S^2)\,, \tag{6.14}$$

where $\sigma_h(s)$ is the Higgs boson production cross section for an (off-shell) Higgs boson with invariant mass $\sqrt{s}$. In order to generalize this expression for any dark matter mass, we can consider S to be produced by a generic on-shell Standard Model-Higgs-like scalar φ with mass m_φ, so that $\sigma_h(s = m_\varphi^2) = \sigma_\varphi(m_\varphi)$. Constraints on this scalar have been derived in [268], where the 95 % CL upper limit on the product between the cross section and the invisible branching ratio has been reported. From this result, we can derive the upper limit on the coupling λ_{HS} as a function of the dark matter mass m_S, using eq. (6.14), and the running width approximation, i.e. replacing $m_h \to \sqrt{s}$ in eq. (6.6), see [505, app. A] for further details. The cross section $\sigma_\varphi(m_\varphi)$ is taken from [503, 515]. Fig. 6.5 shows our results as the 95 % CL upper limit on λ_{HS} as a function of m_S. When $m_S < m_h/2$, the result is equivalent to the one obtained in [268]. This study also updates the results of [505] with the latest results from the ATLAS experiment [268], improving the limits by a factor of about 2.5 with respect to [269]. We also report the projected limits for the HL-LHC and HE-LHC at (14 and 27) TeV, respectively, taken from [505].

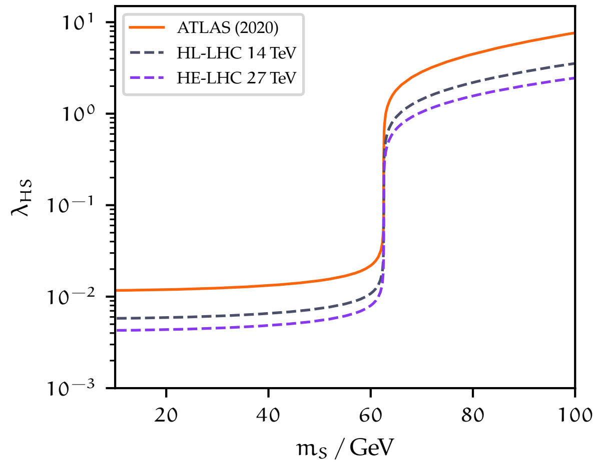

Figure 6.5: The 95 % CL upper limits for the parameter λ_{HS} as a function of the dark matter mass m_S. We show the constraints obtained from a reinterpretation of the ATLAS search in [268] and the projected limits for the HL-LHC and HE-LHC at (14 and 27) TeV, respectively, taken from [505]. Adapted from [2, fig. 6].

6.4 Direct detection

Direct detection can provide strong constraints on the dark matter parameter space. In the case of SHP model, the scattering cross section depends only on the spin-independent part. At the moment of writing, the tightest constraints on spin-independent cross section has been released by the XENONnT [252] and LZ [253] experiments. They constrain σ_{SI} at the level of 10^{-47} cm^2 for dark matter masses of the order of $\mathcal{O}$(few 10 GeV), and they are supposed to reach a sensitivity of around 10^{-48} cm^2 for similar mass scales. The spin-independent cross-section in the framework of the SHP model is [502]:

$$\sigma_{SI} = \frac{\lambda_{HS}^2}{4\pi m_h^4} \frac{m_N^4 f_N^2}{(m_S + m_N)^2}\,, \tag{6.15}$$

where m_N is the nucleon mass. The term f_N parametrizes the Higgs-nucleon interaction:

$$f_N = \sum_q f_q = \sum_q \frac{m_q}{m_N} \langle N|\bar{q}q|N\rangle\,, \tag{6.16}$$

where the sum is made over all quark flavors q with mass m_q. Usually, one adopts the typical value of $f_N \approx 0.3$ [502].

The computation of the direct detection rates has been performed using both MadDM and MicrOMEGAs. The main difference between the code

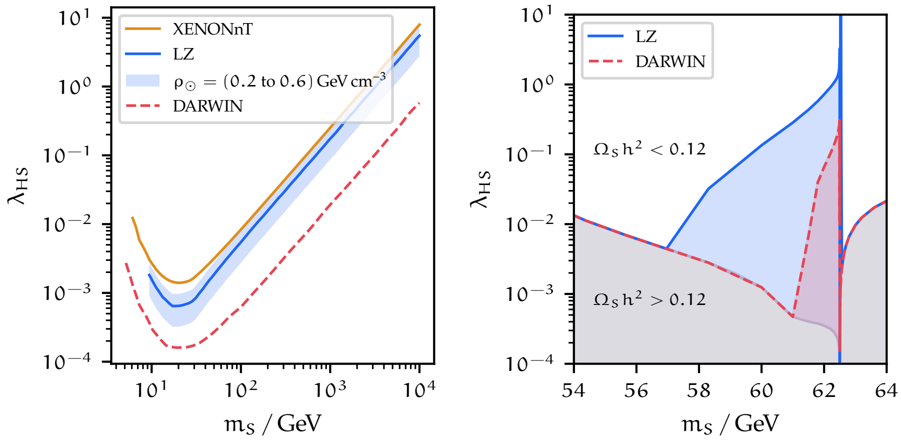

Figure 6.6: LEFT PANEL: the 90 % CL upper limits for the parameter λ_{HS} as a function of the dark matter mass m_S obtained with direct detection experiments. We recast the exclusion limits of LZ [253] and XENONnT [252], along with the projected sensitivity for the future experiment DARWIN [254], for the SHP model. The light blue region represents the uncertainty of the upper limit induced by the uncertainty on the local dark matter density $\rho_{\odot}$, varied in the range (0.2 to 0.6) GeV cm^{-3}. RIGHT PANEL: same as left panel but with the constraints rescaled on the basis of the actual value of $\Omega_S h^2$ following the assumption that the dark matter might be underabundant or overabundant, i.e., by using eq. (6.19). We show the allowed region obtained using the upper limits from the LZ experiment [253] (blue region) and the projected sensitivity for the future DARWIN experiment [254] (red region). We also show the combination of λ_{HS} and m_S that provides the correct relic abundance, and we display the region where the particle S is overabundant with a gray region. Adapted from [2, fig. 7].

is the inclusion of the QCD corrections and the higher twist operators in MicrOMEGAs[†], which makes its results larger than the ones obtained with MadDM by a factor of 5 %.

The upper limits on the parameter space of interests are shown in fig. 6.6. In fig. 6.6 left we show the computed upper limits for data from LZ [253] and XENONnT [252] experiments. These limits are characterized by uncertainties on the local dark matter density profile and the velocity distribution. The former are dominant for dark matter masses above 10 GeV [516], while the latter are dominant for lower masses, so we can neglect them given the parameter space of interest is around the Higgs resonance. The dark matter density is varied in the range (0.2 to 0.6) GeV cm^{-3} [517–520], and this uncertainty is shown as a light blue band in fig. 6.6 left. Future projections by DARWIN [254] are also included, which will improve the limits by nearly a factor of 4.

[†]We verified that turning off the running of the QCD coupling in MicrOMEGAs (setting the variable `qcdNLO=1` in the script `directDet.c`), and turning off the contributions from higher twist operators (setting `Twist2On=0`), the two codes give results compatible within 1 % between each other.

A second consideration regards the relic abundance of the dark matter candidate. The direct detection rate dR/dE is proportional to the local dark matter density $\rho_\odot$. If the dark matter candidate does not make up the entire dark matter relic density, the local dark matter density of S is lower, thus the direct detection limits should be rescaled accordingly. The scaling of the local dark matter density in this case can be parametrized as:

$$\rho_\odot(S) = \xi\, \rho_\odot\,, \tag{6.17}$$

assuming that there is no difference in how the particle S and the other dark matter components cluster in the Galaxy, where ξ is defined as

$$\xi = \frac{\Omega_S h^2}{\Omega_{DM} h^2}\,. \tag{6.18}$$

As a consequence, the upper limits on σ_{SI} associated to S can be computed as the parameter space of m_S, λ_{HS}, satisfying the condition:

$$\xi \cdot \sigma_{SI}(m_S, \lambda_{HS}) \leqslant \sigma^{UL}_{exp}\,, \tag{6.19}$$

where σ^{UL}_{exp} is the 90 % CL upper limit of the experiment under consideration. In fig. 6.6 right we show the results, considering the effect of S making up a fraction of the total dark matter relic density. For LZ upper limit, only m_S values in the range in the range (57 to 62.51) GeV are allowed. Additionally, the DARWIN projections are also shown in the same way, with the only remaining available region around $m_S = 61\,\text{GeV} - m_h/2$. We notice that constraints can be relaxed in this case.

6.5 Indirect detection

Indirect detection is a powerful tool to probe dark matter models. It surveys regions of the sky where the dark matter density is expected to be large, such as the galactic center, dSphs and galaxy clusters, looking for a signal of dark matter annihilation. The main observable is the flux of astrophysical particles, such as γ-rays, neutrinos, antiprotons, positrons and antinuclei. Current experiments can detect astrophysical neutrinos for energies above 1 TeV with quite low statistics [521], making them not suitable for our objectives. For what concerns photons, we focus on the γ-rays detected by Fermi-LAT: the GCE data [214, 215] and the analysis of dSph [195, 225]. CRs are also an interesting probe, but they are affected by large uncertainties in the propagation model. We will only consider antiprotons, since the SHP model predicts large hadronic production for these particles, with respect to positrons. Finally, antinuclei will not be treated in this work, because of the lack of experimental data, and upper limits are much weaker than other probes [522].

6.5.1 The γ-rays from the galactic center and dwarf galaxies

The model

The γ-ray emission from dark matter annihilation includes two components: the prompt and the secondary emission. The former refers to the direct production of γ-rays through an intermediate annihilation channel, while the latter is relevant only for leptonic annihilation channels, and it is due to the inverse Compton scattering of leptons produced from the prompt emission on the interstellar radiation fields photons. The prompt emission is theoretically calculated as follows, see also eq. (3.90) for reference:

$$\frac{\partial^2 N}{\partial E\, \partial\Omega} = \frac{1}{2}\frac{r_\odot}{4\pi}\left(\frac{\rho_\odot}{m_S}\right)^2 \mathcal{J} \times \langle\sigma v\rangle \sum_f \frac{\langle\sigma v\rangle_f}{\langle\sigma v\rangle}\frac{dN_\gamma^f}{dE}\,, \tag{6.20}$$

where $\rho_\odot$ is the local dark matter density, and $r_\odot$ is the distance of the Earth from the center of the Galaxy. We use $r_\odot = 8.12\,\mathrm{kpc}$, as measured recently in [119]. The term $\mathcal{J}$ is the usual geometrical factor, already discussed in § 3.7.2:

$$\mathcal{J} = \frac{1}{\Delta\Omega}\int_{\Delta\Omega} d\Omega \int_{\mathrm{los}} \frac{dl}{r_\odot}\frac{\rho^2\big(\mathbf{r}(l,\Omega)\big)}{\rho_\odot^2}\,. \tag{6.21}$$

which differs by eq. (3.91a) only for the normalization. The γ-ray spectra are encoded in the term dN_γ^f/dE, which depends on the specific annihilation channel f, characterized by the branching ratio $\langle\sigma v\rangle_f/\langle\sigma v\rangle$.

The secondary emission of γ-rays depends on the presence of leptonic channels, i.e. e^+e^-, $\mu^+\mu^-$ and $\tau^+\tau^-$, producing γ-rays by inverse Compton scattering. This contribution is relevant in the galactic center region, where the starlight and dust densities are much higher than the local ones [523]. Inverse Compton scattering contributes only for the energies below 1 GeV, for m_S from $(10$ to $100)$ GeV, which is the most interesting region in our analysis. Despite that, given the uncertainties on the GCE flux are very large for these energies, and the significance for detection is small, we decide to neglect this contribution and the secondary emission of γ-rays.

An important source of uncertainty is the dark matter distribution in the galactic center, namely the dark matter density profile. To estimate this uncertainty, we consider the approach applied in [195], where the authors tackled the problem using two factors. The first one are the data on the rotation curve of the galaxy, able to constrain the dark matter density beyond a few kpc from the galactic center. The second one are the GCE data, which fix the density shape between about 0.1 and few kpc under the assumption that the GCE is originated by dark matter annihilation. Using this strategy, it is possible to identify three models, labeled as MIN, MED MAX, to bracket the uncertainty on the geometrical factor. The variation of $\mathcal{J}$ value between the MIN and MAX models is about a factor of 7. Instead, for what concerns dSph, the uncertainty

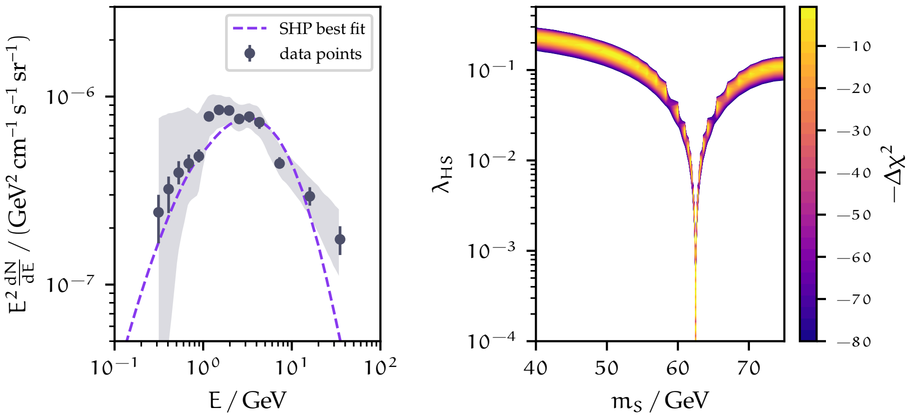

Figure 6.7: LEFT PANEL: SDE best-fit for dark matter in the SHP model to the GCE found in [215]. Data are shown with the statistical and systematic errors with a gray band, with the 3 σ uncertainty band on the best-fit in light blue. RIGHT PANEL: contour plot for the $-\Delta\chi^2$ defined as $-(\chi^2(m_S, \lambda_{HS}) - \chi^2_{min})$, where χ^2_{min} is the χ^2 of the best fit. Adapted from [2, fig. 8].

on $\mathcal{J}$ is included directly in the analysis of the γ-ray data from these objects. In that case, this parameter is treated as a nuisance parameter of the likelihood fit, see [195, 225] for more details.

Results

The first result is the fit to the GCE data found in [214, 215]. We keep into account statistical and systematic uncertainties, due to the choice of the galactic interstellar emission model. The parameters m_S and $\langle\sigma v\rangle$ are free parameters of the fit. Fig. 6.7 left shows the result of the fit to the data found in [215], which gives the best-fit values for the dark matter parameters: $m_S = (58 \pm 6)$ GeV and $\langle\sigma v\rangle = (2.4 \pm 0.4) \times 10^{-26}$ cm^3 s^{-1}. The best-fit value for the coupling parameter is between 0.03 to 0.18. The range is quite wide because the best-fit masses are very close to the Higgs resonance, where $\langle\sigma v\rangle$ increases dramatically, so that the required coupling decreases. This behavior can be seen in fig. 6.7 right, where we show the χ^2 profile as a function of the parameters m_S and λ_{HS}. Around $m_S \approx 50$ GeV, the best-fit of the coupling is approximately from $(1 \text{ to } 2) \times 10^{-2}$, while close to the resonance the best fit coupling decreases to values of the order $(1 \text{ to } 2) \times 10^{-4}$. Above the resonance region, $m_S \approx (70 \text{ to } 80)$ GeV, the best-fit of the coupling increases to values of the order $\mathcal{O}(0.1)$. As we briefly introduced in the previous section, we can identify an uncertainty in the $\mathcal{J}$ factor on the basis of the MIN, MED and MAX models. Given the γ-ray flux is proportional to $\mathcal{J}$, this translates into an uncertainty in the best-fit of the coupling λ_{HS}. The variation of $\mathcal{J}$ can indeed be reabsorbed by an opposite variation of the annihilation cross section, so that the best-fit of λ_{HS} is affected by an uncertainty of a factor of $\sqrt{7} \approx 2.6$.

For what concerns constraints from dSph, we use the results of [195, 225]. In [195], the authors have analyzed 48 dSph, both classical and ultrafaint, using 11 years of data and assuming that the objects are pointlike (i.e. smaller than the Fermi-LAT point-spread function). In [225], 12 years of data in the direction of 22 dSph have been analyzed considering a spatial extended template for the dark matter flux. We also analyzed the γ-ray constraints coming from dSphs. No clear detection has been found in either cases. The data released can be used to build a χ^2 profile as a function of the parameters m_S and $\langle\sigma v\rangle$, similarly to what has been done for the GCE. The peak of the signal is located at masses around $(50 \text{ to } 300)$ GeV and $\langle\sigma v\rangle \approx (0.4 \text{ to } 6) \times 10^{-26}\,\text{cm}^3\,\text{s}^{-1}$.

6.5.2 Antiproton flux

The differential production rate of $\overline{p}$ per volume, time and energy reads:

$$Q(E, \mathbf{r}) = \left(\frac{\rho(\mathbf{r})}{\rho_\odot}\right)^2 \sum_i \frac{\langle\sigma v\rangle_i}{\langle\sigma v\rangle} \frac{dN^i_{\overline{p}}}{dE}, \tag{6.22}$$

where $dN^i_{\overline{p}}/dE$ is the spectrum of $\overline{p}$ produced from dark matter particle interactions, and it depends on the specific annihilation channel assumed and labeled with i. Additionally, CR protons and nuclei scattering on the interstellar matter can generate a background of astrophysical antimatter.

Calculating the flux of secondary dark matter antiprotons requires calibrating the galactic propagation parameters so that the spectra of primary particles match AMS-02 observations. In [524], the authors have performed a fit over 7 years of AMS-02 data [525], complementing them with low-energy data for protons and helium from the Voyager satellite [526]. Their fit regards proton, helium and antiproton-to-proton ratio datasets, and the propagation model used includes diffusion (parametrized by a smoothly broken power-law in terms of the particle rigidity), reacceleration, energy losses, secondary production/fragmentation processes, and solar modulation, modeled as a force field approximation, see [524] for further details. We compute the χ^2 profile as a function of m_S and λ_{HS}, adding a possible dark matter contribution to the antiproton source spectra. The analysis of [524] has been followed up with [527]. In that work, the authors have tested two models, labeled as INJ.BRK and DIFF.BRK on the basis of the injection and diffusion coefficients. The former describes the injection spectra of the primary CRs with a broken power law using different slopes for p and He. The diffusion coefficient is modeled as a broken power law with a single break. In the latter model, instead, spectra are parametrized with a single power law, while the diffusion coefficient has both a low and a high-energy break. Possible correlations in the data [194] were also studied, and a separate analysis was performed for them.

We considered both models in our analysis. The DIFF.BRK model excludes the hypothesis for a dark matter contribution below 100 GeV, allowing us to impose strong constraints on the SHP model parameter space. The INJ.BRK model, instead, results in a very slight modification of our constraints. These cases will be further discussed in § 6.6.3.

6.6 Combined results from direct, indirect, collider searches and cosmology

6.6.1 The S particle as dominant dark matter component

In this section, we combine the results found previously using γ-ray and $\overline{p}$ cosmic data, collider, direct detection constraints and cosmological measurements. We first combine the results from γ-ray and $\overline{p}$ flux data by summing the χ^2 profile defined as a function of the parameters m_S and λ_{HS}. The best-fit region is shown in fig. 6.8 along with constraints from collider, direct detection and relic density. We assume that S makes up 100 % of the total dark matter relic density. This assumption enters the calculations of indirect and direct detection constraints. The green band shows the coupling providing the relic density through thermal freeze-out. The intersections between the best-fit contour region and the green band indicates the regions where the SHP model is able to simultaneously describe astroparticle data and relic density. Observing fig. 6.8 top left, we can find a first intersection for $m_S = (63 \text{ to } 69)\,\text{GeV}$ and $\lambda_{HS} = (2 \text{ to } 6) \times 10^{-2}$, but it is ruled out by direct detection constraints. There is a second intersection for dark matter masses such that $m_S \approx m_h/2 - (10 \text{ to } 20)\,\text{MeV}$ and $\lambda_{HS} \approx (1.4 \text{ to } 1.7) \times 10^{-4}$, which is also compatible with both direct detection and collider constraints. In this region the GCE is fitted with a reduced χ^2 of about 0.8. These results are valid with the assumption of the MED model for the description of the galactic center dark matter density. To take into account the uncertainties on the dark matter density profile, discussed in § 6.5.1, we also consider the MIN and MAX models, shown in figs. 6.8 bottom left and 6.8 bottom right, respectively. We observe that a change in the density has little effect on the best-fit region, and the conclusions drawn above remains valid. A region close to the resonance fitting both cosmic data and relic density, while being compatible with direct detection and collider constraints still exists. Only the coupling λ_{HS} fitting the cosmic data changes, and it is now in the range 1.2×10^{-4} to 2.0×10^{-4}.

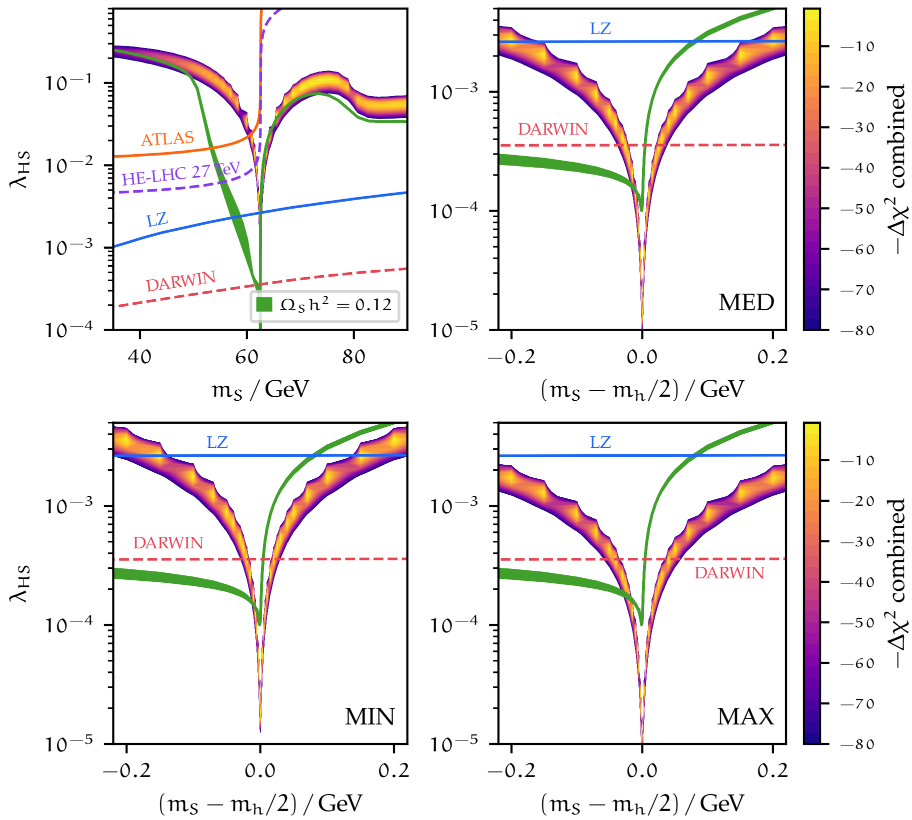

Figure 6.8: TOP LEFT PANEL: contour regions obtained with a combined fit to cosmic particle flux data (GCE, dSphs and antiprotons), assuming the MED model for the dark matter density in the galactic center. We also show the upper limits on λ_{HS} obtained from ATLAS data [268] (orange line) and the HE-LHC projections for 27 TeV [505] (violet dashed line). Direct detection upper limits refer to LZ data [253] (blue line) and projections to DARWIN (red dashed line). We also report the region of the parameter space compatible with the observed dark matter relic abundance via thermal freeze-out (green region) in case of the model fBE, including the uncertainty coming from the different choice of the QCD phase transition model. TOP RIGHT PANEL: same as in top left panel, but for the region around the resonance $m_S \approx m_h/2$. BOTTOM LEFT PANEL: same as in top right panel, but for the MIN model. BOTTOM RIGHT PANEL: same as in top right panel, but for the MAX model. Adapted from [2, figs. 9, 10].

6.6.2 The S particle as subdominant dark matter component

In this section, we discuss the possibility that the S particle is not the dominant component of dark matter density. This means we will consider the same parameter space, but allowing for configurations so that the S particle makes up only a fraction of the total dark matter relic density. Namely, $\Omega_S h^2$ will be set to account for a fraction (from 1 to 100) % of $\Omega_{DM} h^2$, meaning the parameter ξ will vary in the range 0.01 to 1. This configuration implies that the relic density line, and the constraints coming from direct detection experiments, will be rescaled accordingly. Additionally, also the cosmic particle fluxes would be rescaled, and the best-fit regions may change. If the S particle constitutes a fraction ξ of the dark matter relic abundance, according to eq. (6.18), the dark matter galactic density should be rescaled by ξ. The geometrical factor $\mathcal{J}$ is proportional to ρ^2. This implies that $\mathcal{J} \propto \xi^2$. Since $\Phi \propto \mathcal{J}\langle\sigma v\rangle \propto \xi^2\langle\sigma v\rangle$, to obtain the same flux, $\langle\sigma v\rangle$ has to increase for decreasing ξ according to $\langle\sigma v\rangle \propto \xi^{-2}$. Since $\langle\sigma v\rangle$, in turn, scales with λ_{HS}^2, for $\lambda_{HS} < 0.1$ (see fig. 6.3 left), we can just rescale λ_{HS} of the combined fit to the cosmic particle flux data shown in the previous subsection by $1/\xi$. In fig. 6.9, we show the results for the combined analysis for $\xi = 0.3,\ 0.1,\ 0.03$ and 0.01. Also in this case, any intersection between the cosmic flux data fit and the relic density band is searched for and compared to the other constraints. When $\xi = 0.3$ (S makes up 30 % of total dark matter density) we obtain a compatibility region for masses $m_S \approx m_h/2$ and $\lambda_{HS} = (2.3 \text{ to } 2.7) \times 10^{-4}$, which is consistent with the direct detection upper limits. We can find a second intersection for $m_S \approx m_h/2 + 0.20\,\text{GeV}$ and $\lambda_{HS} = (0.8 \text{ to } 1.8) \times 10^{-2}$, which is, however, excluded by LZ constraints. For ξ smaller than about 20 %, also the higher mass region of compatibility between cosmic data and relic abundance becomes consistent with direct detection upper limits. This is visible in fig. 6.9 for the case with $\xi = 0.1$ where there is still a region of compatibility at about $m_S \approx m_h/2$ and $\lambda_{HS} \approx 3 \times 10^{-4}$, while the second one is at $m_S \approx m_h/2 + 0.05\,\text{GeV}$ and $\lambda_{HS} \approx (0.5 \text{ to } 1.2) \times 10^{-2}$. The smaller the value of ξ, the closer the high mass compatibility region is to the right side of $m_S \approx m_h/2$ while at the same time requiring smaller values of λ_{HS}. For $\xi < 0.02$ the two regions merge. This can be seen in fig. 6.10, where the two intersections between the best-fit regions of the cosmic particle flux data and the relic density (corresponding to the aforementioned intersections) are reported in a λ_{HS} vs ξ plot. The intersection between the two bands implies that they merged. For values of ξ smaller than 1 % there is no region of the parameter space for which the best-fit from cosmic data is compatible with the relic density calculation.

In summary, if $\xi \geqslant 0.20$ the only region fitting the cosmic data and compatible with the relic density and direct detection constraints is for $m_S \approx m_h/2$ with values of λ_{HS} of the order of $(1.5 \text{ to } 4) \times 10^{-4}$. Instead, if $\xi = 0.01$ to 0.20, also slightly larger m_S values are allowed, around $m_S \approx m_h/2 + 0.05\,\text{GeV}$, while

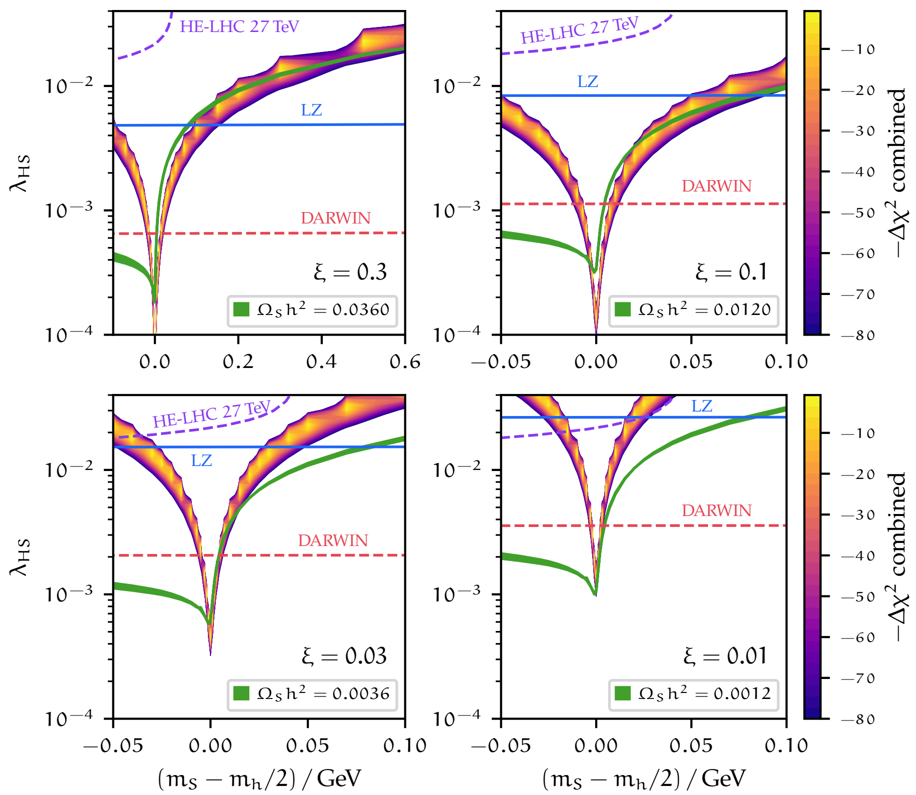

Figure 6.9: Same as in fig. 6.8 top right but for various values of the ξ parameter, as labeled in the different frames. Adapted from [2, fig. 11].

the coupling can be as large as 10^{-2}. The projected sensitivity of DARWIN is shown in figs. 6.9 and 6.10 as the red dot-dashed curves. While the region with $m_S \lessapprox m_h/2$ and smaller coupling remains out-of-reach for direct detection experiments in the foreseeable future, the region with $m_S \gtrapprox m_h/2$ (orange shaded area) can be probed with the sensitivity of DARWIN. The results presented in this section are consistent with the ones reported in [211].

In fig. 6.11 we show the best-fit region for cosmic data, while rescaling all other astrophysical signals according to the value of ξ, obtained by the relic density computation for each point of the parameter space. The gray region refers to $\Omega_S h^2 > 0.12$, i.e. S is overabundant, and it is excluded. Above that region, $\xi < 1$, and ξ decreases towards larger λ_{HS}. The blue shaded region is excluded by direct detection constraints from LZ. Collider constraints, independent on ξ, are shown as a black solid line. The sudden drop of the best-fit region for $m_S \approx 50\,\mathrm{GeV}$ in fig. 6.11 left is due to the fact that $\xi < 1$ in that region, the flux is rescaled accordingly, and the best-fit region changes.

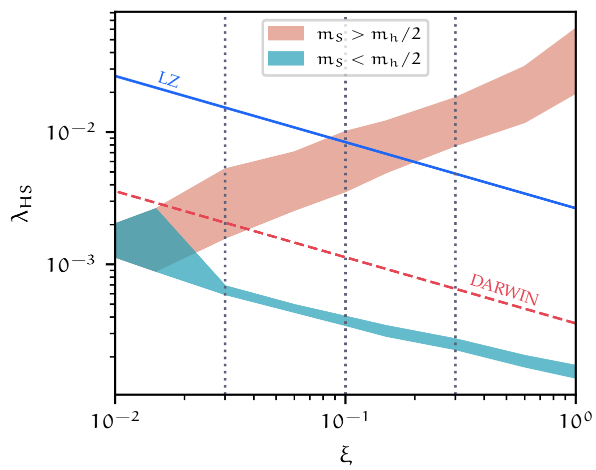

Figure 6.10: Best-fit regions of the combined cosmic particle flux data compatible with thermal freeze-out (corresponding to the intersections of the green and color-shaded bands in the plots of fig. 6.9) in the λ_{HS} vs ξ plane. The orange (teal green) shaded bands denote the regions where m_S is slightly larger (smaller) than $m_h/2$. We also report the upper limits from direct detection by LZ (blue solid line) and the future prospects for DARWIN (red dashed line). The gray dotted lines mark the values of ξ shown in fig. 6.9. Adapted from [2, fig. 13].

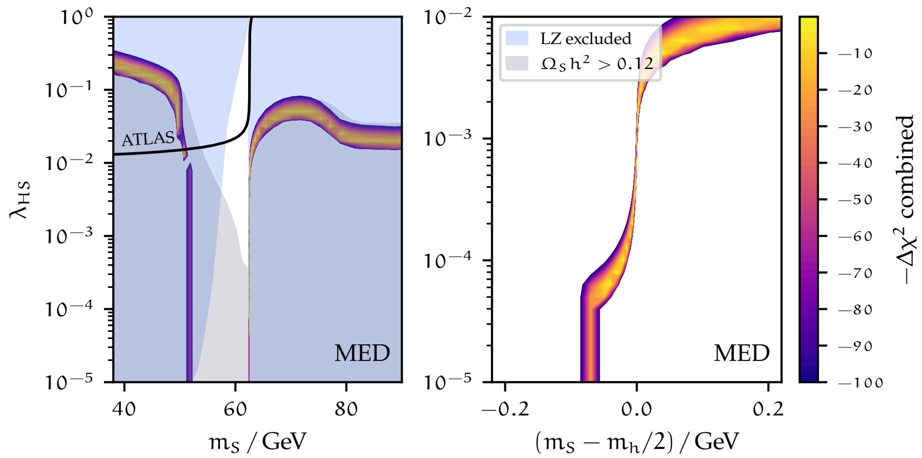

Figure 6.11: Same as in figs. 6.8 top left and 6.8 top right but rescaling, in each point of the parameter space, all predicted astrophysical signals (for direct and indirect detection) according to the dark matter fraction ξ, as it is predicted from the relic density computation. The gray shaded region denotes the parameter space characterized by $\Omega_S h^2 > 0.12$ ($\xi > 1$). The blue shaded region shows the region excluded by the direct detection constraints from LZ data. Adapted from [2, fig. 12].

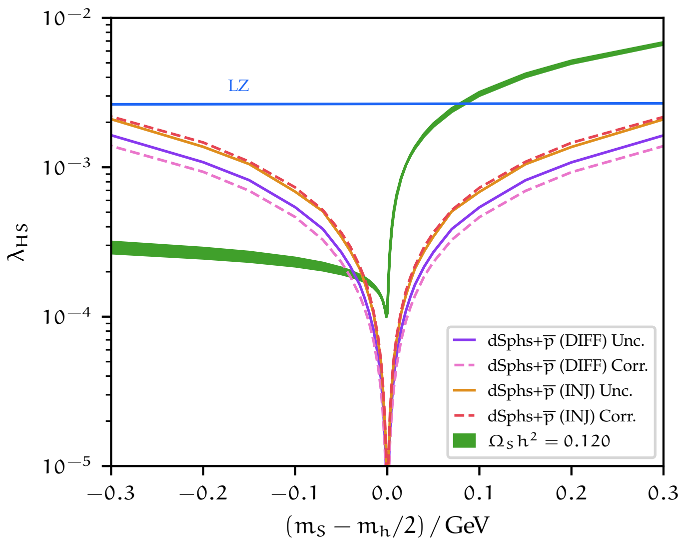

Figure 6.12: Same as in fig. 6.8 top right but with the upper limits derived from CR antiprotons flux data from AMS-02, with different assumptions on the propagation setup. In particular the model labeled as DIFF (INJ) stands for the model DIFF.BRK (INJ.BRK) in [527]. Moreover, the cases labeled as “Unc.” and “Corr.” refer to uncorrelated and correlated uncertainties, respectively. Adapted from [2, fig. 14].

6.6.3 Results without the GCE and upper limits from cosmic antiprotons

Despite the optimistic hypothesis of the GCE to be originated from dark matter, there are other possible astrophysical explanations, see also § 3.7.6. The most famous states the GCE is due to a population of millisecond pulsars located in the galactic bulge [226, 227, 528, 529]. If this is the case, it is possible to constrain the dark matter contribution to the GCE [530]. Additionally, the analysis of a possible dark matter contribution to the CR flux of antiprotons have not found any signal, and upper limits on the annihilation cross section has been imposed in [527] with the DIFF.BRK model.

In this section, we report the results of our analysis assuming that the dark matter is not responsible for the GCE. In this case, we can draw upper limits on the parameter space of the SHP model. We take into account the results obtained by [527], while, unfortunately, the results of [530] are not available for the SHP model.

In fig. 6.12, we show the results obtained with a combined analysis of dSphs, as presented in § 6.5.1, and with antiprotons, following the results published in [527]. We considered both DIFF.BRK and INJ.BRK models, with and without taking into account correlations between data points, showing the 95 % CL upper limits on λ_{HS}. The relic density regions above the upper limits are excluded, and in this case the remaining available parameter space is for $m_S \lessapprox m_h/2 - 0.05\,\text{GeV}$, where λ_{HS} is approximately in the range $(2.5$ to $3.5) \times 10^{-4}$.

6.7 Summary

In this chapter, we studied the SHP model, providing updated results on the parameter space, and combining data from indirect and direct detection, colliders, and dark matter relic density. The SHP is a simple extension of the Standard Model, where a new scalar particle S is added, that can communicate to the Standard Model through the Higgs portal. We pinpointed the parameter space allowed by constraints as well as an explanation of the long-standing Fermi-LAT GCE measurement. The constraints on the model from current data leaves only two available regions of the parameter space: one is the resonance region $m_S \approx m_h/2$, and the other one is the high-mass region $m_S \gtrapprox 3\,\text{TeV}$. The latter will be probed in the next future by direct detection experiments, like DARWIN. The former is characterized by very small couplings able to match the measured relic density while being out-of-reach for any direct detection and collider experiment in the foreseeable future. Indirect detection, though, have the potential of probing this region.

The first step of our analysis was to fit the GCE with the SHP model, which gave a best-fit region around the resonance. Subsequently, we used both the data from the GCE, dSph and antiprotons, and we performed a combined fit, narrowing down the parameter space in the resonance region. We utilized recent results from [214, 215, 524] based on 11 years of Fermi-LAT data and 7 years of AMS-02 data, respectively, thereby improving over previous results obtained within the model.

We compared these results with the relic density of the models. The computation of this observable required special care, because the resonance region is characterized by a large enhancement of the annihilation cross section with respect to scattering processes, leading the kinetic equilibrium hypothesis to break down.

It is possible to identify two regions fitting the cosmic data while predicting the correct relic density: one slightly below and one just above $m_h/2$. The latter is excluded by direct detection due to the large coupling required. Additionally, we studied the possibility the S particle is not the dominant component of dark matter density. In this case, the best-fit regions, the relic density and the direct detection constraints are rescaled accordingly. Due to the different scaling of indirect and direct detection rates with the dark matter fraction, the latter subregion becomes allowed for a fraction of 10 % or less. Both subregions provide good fits down to a dark matter fraction of 1 % below which the relic density and the indirect detection signals become incompatible. The required coupling is of the order of 10^{-4} to 10^{-2}, which is extremely hard to probe with future experiments. Unfortunately, HE-LHC at 27 TeV will not be able to test the model in the laboratory. However, the DARWIN experiment is expected to reach a sensitivity which will be enough to probe the subregion with $m_S \gtrapprox m_h/2$ and coupling $\lambda_{HS} \gtrapprox 2 \times 10^{-3}$.

Chapter 7

Phenomenology of superheavy decaying dark matter from string theory

I'm not gonna run away, I never go back on my word! That's my nindō: my ninja way!

—Naruto Uzumaki

Naruto
Masashi Kishimoto

In chapter 3 we introduced the WIMP dark matter candidate as a straightforward, optimistic, solution to the dark matter problem. WIMP dark matter is a well-motivated theory, and it received a lot of attention in the previous chapters, 5 and 6. There, we introduced several dark matter models able to provide a proper dark matter description assuming a WIMP-like candidate. However, the WIMP paradigm is not the only possible solution to the dark matter problem, and the lack of a positive signal in indirect, direct or collider searches, have fostered many speculations regarding the existence of dark matter candidates much lighter or much heavier than the typical WIMP scale. In this chapter we will focus on the latter possibility.

Very heavy (superheavy) dark matter of mass scales larger than 100 TeV can easily evade the main constraints from direct detection and colliders, because those experiments have not enough sensitivity to those mass regions. Indirect detection may be the only framework able to probe such heavy dark matter candidates, however, standard dark matter annihilation in this case is also suppressed, given the signal scales as the number density squared, $n_{\rm DM}^2$, which is in turn suppressed due to the high mass. An alternative possibility is to consider decaying dark matter, so that indirect detection signal would scale as $n_{\rm DM}$. This hypothesis brings many other issues in the dark matter phenomenology: an unstable dark matter candidate must be characterized by a sufficiently long lifetime, namely orders of magnitude longer than the age of the Universe [177, 178, 531–547]. This, in turn, translates into having a very small decay rate, representing a challenge for the model building point of view, which ends up to be characterized by the fine-tuning of very tiny couplings in order to achieve that. On the other hand, the symmetries protecting the stability of the dark matter candidate forbids its decay, so that one must invoke higher-energy effects able to break them (e.g. string theory or quantum gravity). Finally, superheavy dark matter is characterized by an overproduction of relic density [548] through normal freeze-out, so that new mechanisms are required to explain the relic abundance.

The objective of this chapter is to investigate the phenomenology of superheavy decaying dark matter, addressing both its relic abundance and indirect detection constraints. From a model building point of view, we will consider a string theory-motivated model, characterized by a high scale SUSY breaking. The LSP of the theory will be the dark matter candidate, protected by R-parity. The relic abundance will be obtained through a non-thermal production mechanism, involving one or more epochs of early matter domination (EMD), driven by string moduli. This would yield the correct abundance for a dark matter candidate of mass scale of order $(10^{10}$ to $10^{11})$ GeV. Additionally, tiny RPV couplings can also be generated by exponentially suppressed non-perturbative terms induced by istantons, making the dark matter unstable and with a long lifetime.

Phenomenologically, the model resembles a MSSM with RPV couplings and a bino-like LSP. Dark matter can decay through RPV terms into three or two-body decays to Standard Model particles. The decay products can produce energetic showers of γ and ν, which can be detected by current and future experiments, further imposing bounds on dark matter mass and lifetimes, translating into bounds into the string coupling. The tightest bounds on dark matter lifetime happen to be in the $(10^9$ to $10^{11})$ GeV mass range, while the string coupling is constrained by an upper limit of $\mathcal{O}(0.1)$, ensuring the perturbative regime.

The chapter is organized as follows. In § 7.1 we introduce the string theory motivated model, naturally yielding a SUSY model with a superheavy dark matter candidate. Specifically, Sec. 7.1.3 will cover the RPV terms that make the dark matter unstable. In § 7.2 we discuss the current and future experiments that can constrain this type of dark matter, by detection of energetic γ and ν fluxes. The computation of the three-body spectra coming from the decays relies on specific tools and techniques which are discussed in § 7.3. In § 7.4 we discuss the model-independent γ-ray and ν bounds on superheavy decaying dark matter into three-body final states, as well as the sensitivity of future experiments. A summary of the main results is presented in § 7.5.

The chapter is entirely based on the following publication:

[3] Allahverdi, R., Arina, C., Chianese, M., Cicoli, M., Maltoni, F., **DM**, Osiński, J. K., "Phenomenology of superheavy decaying dark matter from string theory". *JHEP* 02 (2024), p. 192. DOI: 10.1007/JHEP02(2024)192.

My main contribution was in the calculation of the two and three-body shower spectra from dark matter decay. Given the dark matter mass scale of interest, two-body electroweak-corrected shower spectra are obtained by HDMSpectra. Concerning the three-body decay spectra, I developed a code that performs the convolution of the two-body spectra with the three-body phase space, coming from the decay processes, generated in MadGraph. I describe the procedure in § 7.3. The final spectra have been used to obtain the constraints discussed in § 7.4. I participated in the discussion regarding the objective of the work, the model phenomenology, and the interpretation of the results. The physics model under investigation was proposed by some of my coauthors, working in string theory [549].

7.1 Superheavy dark matter from string theory

String theory is a promising candidate for a theory that can unify gravity with the other fundamental interactions. Though, its definition requires the existence of extra dimensions. The usual 4-dimensional physics can be then recovered with a procedure called string compactification. This procedure consists in curling up the extra dimensions into a compact manifold.

7.1.1 Generic features of 4-dimensional string models

Low-energy 4-dimensional string models have been studied in details recently, in particular for what concerns type IIB frameworks, characterized by a better handling of module stabilization. These models have several features. On one hand, they are characterized by a (statistical) preference for high SUSY breaking scale [550–552], and high inflationary scale [553, 554], mainly as a consequence on the matching of the amplitude of the primordial density perturbations. Another important feature is the moduli domination: moduli are new scalar fields with gravitational couplings to matter. They parametrize the shape and size of extra dimensions in string theory, and they behave as matter in the Universe. During the evolution of the Universe, moduli fields may undergo a period of oscillation around their energy minima, which were displaced due to inflation. The energy stored in these oscillations can act as a source for the creation of non-relativistic particles, initiating the so-called EMD phases, that can alter the standard thermal history of the Universe. The decay of the moduli can dilute any dark matter production that took place before that [549, 555–560].

Finally, these models are able to reproduce the MSSM with RPV. This can be realized by considering a compactification of D7-branes wrapping 4-cycles in the internal manifold, whose size can be linked to the Standard Model gauge couplings values [561]. The RPV terms are induced by non-perturbative effects like instantons. This will first generate a discrete $\mathbb{Z}_2$ symmetry identified with the R-parity [562] and secondly inducing tiny RPV couplings, exponentially suppressed, because proportional to $\exp(-S_{\text{inst}}) \ll 1$, where S_{inst} is the instanton action [563].

7.1.2 The string theory model

The features of 4-dimensional compactifications described in § 7.1.1 can give rise to a superheavy decaying dark matter scenario. In [549] a model with high scale SUSY breaking and dilution from moduli domination can reproduce the correct relic abundance for a 10^{10} GeV dark matter candidate.

The model under investigation involves three moduli fields: φ, σ, ρ. The modulus σ drives the inflation [564, 565]. Both σ and ρ are wrapped by D7-branes, respectively by a hidden sector stack and an MSSM stack, while φ is shifted from its minimum by the amount $Y_\varphi = \varphi_0/M_{\text{Pl}}$ (where $M_{\text{Pl}} \approx 10^{18}$ GeV is the Planck scale), and it drives and EMD epoch after the end of inflation [566]. The moduli break SUSY, generating non-zero gravitino mass $m_{3/2} \approx M_{\text{Pl}}/\mathcal{V} \ll M_{\text{Pl}}$, where $\mathcal{V}$ is the extradimensional volume in units of string length. Their interactions with MSSM induces soft SUSY breaking terms, proportional to $m_{3/2}$, so that the mass spectrum at the scale $M_{\text{Pl}}/\mathcal{V}^{2/3}$ (called Kaluza-Klein scale) is:

$$m_\varphi \approx m_{3/2}\sqrt{\frac{m_{3/2}}{M_{\text{Pl}}}} \ll m_0 = \frac{m_{3/2}}{\sqrt{2}} \approx M_{1/2} = m_{3/2} \approx m_\sigma \approx m_\rho\,, \tag{7.1}$$

where SUSY scalars have common mass m_0 and gaugino masses are $M_{1/2}$. The gravitino mass is fixed to 10^{10} GeV by the requirement of reproducing density perturbations during inflation, and this corresponds to a volume of $\mathcal{V} \approx 10^6$ GeV, which is also the typical mass scale of SUSY particles and of the moduli σ and ρ. The modulus φ is much lighter, $m_\varphi \approx 10^7$ GeV.

The dilution of the dark matter candidate, namely the LSP of the MSSM, is due to the decay of the moduli fields. In particular, the main contributions come from the σ and φ decays, while the ρ decay is negligible (it would decay when it is not dominating the energy density). However, σ decays mainly into hidden sectors, hence the production rate of MSSM particles, including the LSP, from inflaton decay is very small [549]. On the other hand, φ is much lighter than any superpartner, so its decays can not produce dark matter particles. However, they contribute to the dilution of the dark matter particles produced by the inflaton decays. To get the final dark matter abundance it is necessary to redshift, during the radiation-dominated epoch, from σ-decay to φ-domination and, finally, to φ-decay, during the matter-dominated era, obtaining a final expression for n_{DM} [549] that should match the observed value [20]:

$$\left(\frac{n_X}{s}\right)_{\text{obs}} \approx 4.2 \times 10^{-10}\left(\frac{1\,\text{GeV}}{m_{\text{DM}}}\right), \tag{7.2}$$

where s is the entropy density. It is possible to obtain a match for $m_{\text{DM}} \approx 10^{10}\,\text{GeV}$, [549].

The last step consists in performing the one-loop renormalization-group equation (RGE) evolution of gaugino masses and Standard Model couplings, to obtain the mass spectrum of the MSSM particles. The evolution is performed from the Kaluza-Klein scale down to the mass scale of the modulus $m_\varphi \approx 10^7\,\text{GeV}$, with initial conditions $M_{1/2} = m_{3/2} = 10^{10}\,\text{GeV}$, $m_0 = m_{3/2}/\sqrt{2}$, and the gauge couplings given by their approximate unification value $g_a = 0.7$. In this case, the heaviest particle is the gluino, while the LSP is the bino.

7.1.3 Decaying dark matter and three-body decay spectra

One of the main feature of this model-building procedure is that the resulting MSSM model contains RPV terms. We introduced the RPV terms in § 2.6.3, they have the feature of making the LSP unstable. The superpotential of the MSSM with RPV terms is given by [58, 59], recalling eq. (2.77):

$$W_{\text{RPV}} = \lambda LLE^c + \lambda' LQD^c + \lambda'' U^c D^c D^c \,, \tag{7.3}$$

where the coupling constants λ, λ' and λ'' are dimensionless. The explicit expression of each term is given in eq. (2.78). The RPV terms allows the sfermions to decay into two fermions. This, in addition to the existence of the neutralino-sfermion-fermion vertex in the MSSM, allows the neutralino, $\tilde{\chi}_0$, to decay into three fermions. In this case, the Feynman diagrams of neutralino decays are depicted in fig. 7.1.

The neutralino, being the LSP, can be a viable dark matter candidate. In the model under investigation, $\tilde{\chi}_0$ is mostly made of bino eigenstates, and it is possible to write the decay rates for the three RPV terms as [59]

$$\Gamma^{LLE}_{\tilde{\chi}_0} = \lambda^2_{ijk} \frac{\alpha_{\text{em}}(m^2_{\tilde{\chi}_0})}{128\pi^2} \frac{m^5_{\tilde{\chi}_0}}{m^4_{\tilde{f}}} \,, \tag{7.4a}$$

$$\Gamma^{LQD}_{\tilde{\chi}_0} = \lambda'^2_{ijk} \frac{3\alpha_{\text{em}}(m^2_{\tilde{\chi}_0})}{128\pi^2} \frac{m^5_{\tilde{\chi}_0}}{m^4_{\tilde{f}}} \,, \tag{7.4b}$$

$$\Gamma^{UDD}_{\tilde{\chi}_0} = \lambda''^2_{ijk} \frac{3\alpha_{\text{em}}(m^2_{\tilde{\chi}_0})}{64\pi^2} \frac{m^5_{\tilde{\chi}_0}}{m^4_{\tilde{f}}} \,, \tag{7.4c}$$

where α_{em} is computed at the scale of the dark matter mass. All sfermions are considered to be degenerate in mass and heavier than the neutralino. Eqs. (7.4b) and (7.4c) are characterized by a color factor of N_C and $N_C!$, respectively, because they involve quarks in the final states.

An important remark is that, in order for the neutralino to be a viable dark matter candidate, its lifetime should be larger than the age of the Universe, namely $\tau_{\tilde{\chi}_0} \gtrsim 10^{26}\,\text{s}$, to be compatible with current bounds on decaying dark

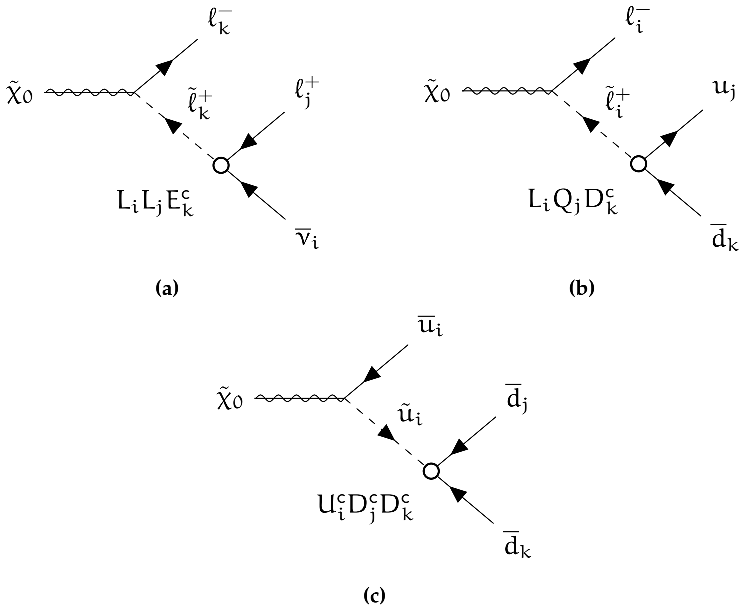

Figure 7.1: Feynman diagrams illustrating the decay of the $\tilde{\chi}_0$ into three Standard Model fermions, mediated by a sfermion $\tilde{f}$. The RPV vertex is highlighted by an empty dot.

matter [177, 178, 531–544]. This requires the RPV couplings to be very small, in the case of LLE term, for $m_{\tilde{\chi}_0} = m_{\tilde{f}} = 10^{10}$ GeV, we find $\lambda_{ijk} \lessapprox 10^{-26}$. It may be difficult to justify such small couplings, however, in string theory, the RPV terms are induced by instantons, and they get the form $\lambda_{ijk} \propto \exp(-S_{\text{inst}})$, where the instanton action can be described in terms of the inverse of the string coupling g_S, $S_{\text{inst}} \sim 2\pi/g_S$. Therefore, we expect:

$$\lambda_{ijk} \sim \exp(-2\pi/g_S)\,, \tag{7.5}$$

which, for values of the string coupling that keep the effective field theory in the perturbative regime, would give indeed $\lambda_{ijk} \approx \exp(-20\pi) \lessapprox 5 \times 10^{-28}$.

7.2 Astrophysical signatures of superheavy decaying dark matter

Superheavy dark matter particles distributed in galactic and extra-galactic structures can decay into ordinary matter by producing UHE particles. Here we focus on UHE neutrino and γ-ray fluxes produced by dark matter decays. UHE charged CRs are also an interesting probe for dark matter decay. However, their understanding is subject to larger astrophysical uncertainties, because of their propagation in the galaxy, with respect to neutrinos and γ-rays which trace the source. Our analysis on neutrino and γ-ray data is based on [177, 178] which we refer the reader to for further details.

7.2.1 Theoretical astrophysical fluxes

Dark matter decay can produce energetic γ-ray and neutrino fluxes from both galactic and extra-galactic sources. Extra-galactic production is, however, expected to be subdominant, due to absorption by $\gamma\gamma$ scattering at high energies and high redshift, and can be safely neglected. Additionally, any secondary production in the form of inverse Compton scattering of electrons and positrons contributes only to γ-ray energies $E_\gamma \lessapprox 10^5$ TeV, and therefore can be neglected in our analysis based on UHE γ-rays. Hence, the dominant component at $E_\gamma \gtrapprox 10^5$ TeV is the prompt galactic emission which gives the following expected flux:

$$\frac{\partial^2\Phi_\gamma}{\partial E_\gamma\,\partial\Omega} = \frac{1}{4\pi m_{DM}\tau_{DM}}\frac{dN_\gamma}{dE_\gamma}\int_0^{+\infty} dr'\,\rho\big(\mathbf{r}(r',b,l)\big)\exp\left[-\tau_{\gamma\gamma}(E_\gamma,r',b,l)\right], \tag{7.6}$$

where $\tau_{\gamma\gamma}$ represents the total optical depth of photons to $\gamma\gamma$ collisions, $\rho(\mathbf{r})$ is the dark matter density profile, usually assumed to be an NFW profile, see eq. (3.82). The optical depth takes into account the photon pair production from the interaction of the γ-rays with CMB radiation, starlight and infrared light (see [178, 531] for details on its computation). The former is homogeneous and thermally defined by the CMB temperature ($\approx 2.348\times 10^4$ eV). For the latter two, the photon density depends on the spatial information in the Milky Way, so we take the results from the GALPROP code [139–141].

Current UHE γ-ray observatories place bounds on the diffuse γ-ray flux, which can be linked to the integral γ-ray flux, averaged over the field of view of each experiment Ω_{exp} (see [532, tab. I, supplementary]), and taking the following expression:

$$\Phi_\gamma^{DM}(E_\gamma) = \frac{1}{\Omega_{exp}}\int_{E_\gamma}^{+\infty} dE'_\gamma\int_{\Omega_{exp}} d\Omega\,\frac{\partial^2\Phi_\gamma}{\partial E'_\gamma\,\partial\Omega}, \tag{7.7}$$

Contrarily to γ-rays, neutrinos travel unimpeded and the neutrino flux from dark matter decays has both a galactic and extra-galactic component. The first one is given by:

$$\frac{\partial^2\Phi^{gal}_{\nu_\alpha+\bar\nu_\alpha}}{\partial E_\nu\,\partial\Omega} = \frac{1}{4\pi m_{DM}\tau_{DM}}\frac{dN_\alpha}{dE_\nu}\int_0^{+\infty} dr'\,\rho\big(\mathbf{r}(r',b,l)\big), \tag{7.8}$$

where α is the flavor of the (anti)neutrino considered. The important feature of extra-galactic neutrinos is that their absorption in the intergalactic medium is negligible. Hence, they produce a sizable flux that can be written as:

$$\frac{\partial^2 \Phi^{\text{ex-gal}}_{\nu_\alpha+\bar{\nu}_\alpha}}{\partial E_\nu\, \partial\Omega} = \frac{\Omega_{\rm DM}\, \rho_c}{4\pi m_{\rm DM} \tau_{\rm DM}} \int_0^{+\infty} \frac{dz}{H(z)} \frac{dN_\alpha}{dE'_\nu}\bigg|_{E'_\nu = E_\nu(1+z)}, \tag{7.9}$$

where H is the Hubble parameter, ρ_c is the critical density and $\Omega_{\rm DM}$ is the dark matter relic density, according to the latest Planck data [20]. This flux depends on the cosmological redshift z.

Both galactic and extra-galactic neutrinos reach the Earth after having traveled long distances. They oscillate during their propagation, so that the final detected flux is a combination of the three flavor eigenstates. This feature is taken into account by summing the fluxes of each flavor neutrino in a total flux. Additionally, the directional information is lost, as experiments are sensitive to the average angular distribution. We keep that into account by performing an integration over the solid angle. As a result, the total combined flux is:

$$\frac{d\Phi^{\rm DM}_{3\nu}}{dE_\nu} = \sum_\alpha \int_{4\pi} d\Omega \left[\frac{\partial^2 \Phi^{\text{gal}}_{\nu_\alpha+\bar{\nu}_\alpha}}{\partial E_\nu\, \partial\Omega} + \frac{\partial^2 \Phi^{\text{ex-gal}}_{\nu_\alpha+\bar{\nu}_\alpha}}{\partial E_\nu\, \partial\Omega} \right]. \tag{7.10}$$

Considering the angle-averaged flux means to neglect neutrino flux anisotropies which are particularly relevant for galactic neutrinos in the direction of the galactic center. This implies that the combined flux expressed by eq. (7.10) allows us to understand only the flux normalization, staying conservative on the angular distribution.

The neutrino and γ-ray fluxes in eqs. (7.6), (7.8) and (7.9) depend on the energy spectrum, $\partial N_{\nu,\gamma}/\partial E_{\nu,\gamma}$, that denotes the energy distribution of neutrinos and photons deriving from the three-body or two-body dark matter decays. This is a central feature that needs to be carefully evaluated to have proper estimates of the sensitivity of current and future experiments. We will discuss how we properly compute this quantity in § 7.3, after having introduced the experimental neutrino and γ-ray probes, as well as the corresponding statistical approach we adopt to compute the limits on the dark matter lifetime $\tau_{\rm DM}$ for different dark matter masses $m_{\rm DM}$.

7.2.2 Future neutrino telescopes

Superheavy decaying dark matter offers a natural source of neutrinos that can propagate through the galaxy and reach the Earth. Future-generations neutrino telescopes will be able to detect UHE neutrinos, providing a powerful probe for superheavy dark matter searches. The main experiments have been described in § 3.7.5, where we refer the reader for further details. In the following analysis, we will consider the sensitivities from the following experiments: RNO-G, IceCube-Gen2 and GRAND (with two different configurations with 10k and 200k radio antennas). Given a dark matter candidate of mass $m_{\rm DM}$

and lifetime τ_{DM}, we can compute the expected number of neutrino events in a given telescope, assuming an observation period of $T_{obs} = 3\,y$:

$$N_\nu^{DM} = T_{obs} \int_0^{E_{max}} dE_\nu \frac{d\Phi_{3\nu}^{DM}}{dE_\nu} A_{eff}(E_\nu)\,, \tag{7.11}$$

where $E_{max} = m_{DM}/2$ is the maximum neutrino energy achieved in the dark matter decay. The neutrino flux from dark matter decay has been previously defined in eq. (7.10), while we label the effective area of the experiment with A_{eff}. The latter can be defined through the flux sensitivity $S(E_\nu)$, which is the quantity provided by the experimental collaborations, and the observation time:

$$A_{eff}(E_\nu) = \frac{2.44\,E_\nu}{4\pi \log(10) S(E_\nu) T_{obs}}\,, \tag{7.12}$$

where 2.44 is the number of neutrino events for each energy decade.

Following [177], we will consider two main contributions (taken from [182]) to the UHE neutrino flux coming from astrophysical sources (on top of the dark matter-produced neutrino flux):

- **cosmogenic neutrinos**: they originate from collisions between high-energy CRs and the CMB. Their contribution to the flux of UHE neutrinos is affected by important theoretical uncertainties and, to be conservative, we will consider the most optimistic estimate on this contribution in order to obtain the weakest limits on dark matter;

- **pulsar neutrinos**: the extreme astrophysical environment of newborn pulsars might give rise to one of the highest UHE neutrino fluxes.

Such astrophysical models predict the observation of a certain number of astrophysical neutrino events, N_ν^{astro}, which can be computed from the neutrino flux through an equation analogous to eq. (7.11). Hence, it is possible to obtain conservative limits on dark matter lifetime by assuming the observation of N_ν^{obs} neutrino events, which translates into considering the following test statistic:

$$TS(m_{DM}, \tau_{DM}) = \begin{cases} 0 & \text{for } N_\nu^{DM} < N_\nu^{obs}\,, \\ -2\log\left(\dfrac{\mathcal{L}(N_\nu^{obs} \mid N_\nu^{DM})}{\mathcal{L}(N_\nu^{obs} \mid N_\nu^{obs})}\right) & \text{for } N_\nu^{DM} \geqslant N_\nu^{obs}\,, \end{cases} \tag{7.13}$$

with N_ν^{obs} being a Poissonian stochastic variable with mean N_ν^{astro}, and the likelihood $\mathcal{L}$ is assumed to be a Poisson distribution. According to these statistical arguments [567], we can place future bounds on the dark matter lifetime τ_{DM} at 95 % CL by taking $TS(m_{DM}, \tau_{DM}) = 2.71$. The idea behind the statistical analysis is that, according to astrophysical models, one expects to observe a certain number of events from neutrino sources, N_ν^{astro}, which depends on several uncertainties on the specifications of the models assumed. This number is then set as the mean value of a Poissonian distribution, used to perform a Monte-Carlo (MC) simulation to generate the number of observed events. Finally, this number is compared to the expected number of events from dark matter decay, N_ν^{DM}, and used to draw lower bounds on the dark matter lifetime. Indeed, if N_ν^{DM} exceeds N_ν^{astro}, then it is possible to constrain the values of dark matter mass and lifetime producing this excess of events. In this context, choosing a model so that $N_\nu^{\mathrm{astro}} = 0$ means that the experiments are not expected to observe any event in the time window considered. This means we can impose stronger bounds on any dark matter flux, excluding higher values of dark matter lifetime.

7.2.3 Current γ-ray experiments

The main signature produced by UHE γ-rays when they reach the Earth are EAS, made of cascades of charged particles. This signature has been studied by many experiments in the past, that have placed bounds on the UHE γ-ray diffuse flux above 10^5 GeV (see [178, fig. 1]). In the present study, we focus on the following current and decommissioned experiments: KASKADE, KASKADE-GRANDE, CASA-MIA, TA, PAO, which have been briefly discussed in § 3.7.5.

Given the upper bounds on the angle-averaged integral γ-ray flux from each experiment, we compute the limits on dark matter by simply performing a χ^2 analysis using the test statistic:

$$\mathrm{TS}(m_{\mathrm{DM}}, \tau_{\mathrm{DM}}) = \sum_i \left[\frac{\Phi_\gamma^{\mathrm{DM}}(E_{\gamma,i}) - \Phi_{\gamma,i}^{\mathrm{data}}}{\sigma_i} \right]^2 , \tag{7.14}$$

where the index i runs over the experimental energy bins, $\Phi_\gamma^{\mathrm{DM}}$ is the expected γ-ray flux expected from dark matter, while $\Phi_\gamma^{\mathrm{data}} = 0$, corresponding to the definition of upper limit (no observation of photons), and σ_i is the corresponding standard deviation at 68 % CL of each data point. The limits on the dark matter lifetime at 95 % CL can be obtained by taking $\mathrm{TS} = 2.76$, a threshold value deriving from the constraints that the γ-ray measurements cannot be negative [178].

7.3 Methodology and energy spectra

The computation of the decay processes and the event generation has been performed with MadGraph5_aMC@NLO [383, 384], using the RPVMSSM UFO model [568] publicly available in the FeynRules [385, 453] database, and based on [59, 569]. The user can choose the appropriate SUSY mass spectrum. As previously discussed in § 7.1.2, the SUSY spectrum is characterized by gauginos

Table 7.1: Three-body neutralino final states induced by the RPV vertices in eq. (7.3). The indices i, j, k label the fermion generations.

	Couplings (channel)		
	λ_{ijk} (LLE)	λ'_{ijk} (LQD)	λ''_{ijk} (UDD)
$\tilde{\chi}_0$	$\ell_i^+ \overline{\nu}_j \ell_k^-$, $\ell_i^- \nu_j \ell_k^+$, $\overline{\nu}_i \ell_j^+ \ell_k^-$, $\overline{\nu}_i \ell_j^- \ell_k^+$	$\ell_i^+ \overline{u}_j d_k$, $\ell_i^- u_j \overline{d}_k$, $\overline{\nu}_i \overline{d}_j d_k$, $\nu_i d_j \overline{d}_k$	$\overline{u}_i \overline{d}_j \overline{d}_k$, $u_i d_j d_k$

and sfermions with the same mass scale, corresponding to the gravitino mass. This feature can be exploited to optimize the event generation, discarding the contribution of the irrelevant decay matrix elements, and setting all SUSY particles that do not participate in the decay to a heavier mass scale.

The kinematics of the final states is fixed for a two-body decay, while it is not for a three-body final state. In this case, the energy distribution of the final state particles of the hard process requires a proper simulation, which has been done with MadGraph. The possible final states for neutralino decay are shown in tab. 7.1. For the computation of the hard process spectra, we have considered the three RPV vertices separately, in order to study the impact of each one of them on the final results.

The LLE vertex gives rise to three leptons of different flavors in the final state, one of them always being a neutrino such as $\tilde{\chi}_0 \to \mu^+ e^- \nu_\tau$, $\tilde{\chi}_0 \to e^+ e^- \nu_\mu$ and so on, with a total of 36 different final states. In the case of the LQD vertex, the final states are characterized by one lepton and two quarks, such as $\tilde{\chi}_0 \to e^- u \, \overline{d}$, $\tilde{\chi}_0 \to \overline{\nu}_e \, s \, \overline{d}$, for a total of 108 final states. Finally, the UDD vertex gives rise to 18 final states with different combinations of quarks, e.g. $\tilde{\chi}_0 \to u \, s \, b$, $\tilde{\chi}_0 \to \overline{b} \, \overline{t} \, \overline{s}$. We generated about 10^6 events for each vertex.

In the following discussion, we will assume χ to be a generic dark matter particle. The final states obtained from the hard processes of the three-body neutralino decay are highly energetic, given the large mass scale of the dark matter under consideration, $m_\chi \approx 10^{10}$ GeV.

Every final state will generate a shower, producing a cascade of new particles. Given the high energy of the process, it is important to properly include electroweak corrections that affect the final energy spectra of neutrinos and γ-rays (for a discussion, see [123, 570]). Notice that the electroweak evolution is collinear, and therefore local. Hence, given the mother particle and its energy, it is enough to perform the evolution. This can be done consistently using the electroweak corrections obtained with the tool HDMSpectra [570].

HDMSpectra provides electroweak-corrected spectra for γ, ν's and protons originating from the two-body annihilation (or decay) of a generic dark matter particle into two particles f, $\bar{f}'$, for energies up to 10^{19} GeV:*

$$\chi\,\chi \to f\,\bar{f}' \to \text{ shower}\,, \tag{7.15}$$

for which the hard spectrum is highly peaked. However, in our case we need to compute the spectra for a three-body decay process, distributed accordingly to a continuum of energies, hence a convolution operation between the hard spectra and HDMSpectra results is necessary. We proceed as follows. For each RPV vertex, we sum over all the neutralino three-body decay processes, getting P different particles overall:

$$\left.\begin{array}{ll} \tilde{\chi}_0 & \to e^+ e^- \nu_\mu \\ \tilde{\chi}_0 & \to \mu^+ e^- \nu_\tau \\ \tilde{\chi}_0 & \to \dots \end{array}\right\} \quad \Rightarrow \quad p_1 \dots p_P\,. \tag{7.16}$$

The convolution operation requires us to consider each p_i, compute the electroweak shower spectra with HDMSpectra and sum over every particle. To avoid doing that for each event, we bin the particles in the hard spectra and do a convolution. This is possible assuming that the particles belonging to each bin in the hard spectra have the same energy, equal to the mid-value of the bin. This is true if the binning scheme is fine enough to have very small bins, which is realized by taking 1000 bins in our case. The convolution is made by considering that each binned particle is coming from a *fake* two-body annihilation with a proper center-of-mass energy to match the energy of the bin. The result will be the electroweak-corrected spectra coming from the three-body decay of the neutralino.

More precisely, the hard process spectrum generated by MadGraph is stored in an event file in the Les Houces Event (LHE) format [571], containing the different generated processes and kinematics for each event. This file can be parsed to extract the hard spectra of the final states. Each hard spectrum of the particle p_i, with $i \in [1, P]$, is a one-dimensional histogram with M bins in the variable $x = E/m_{\tilde{\chi}_0}$, where E is the energy of the particle p_i. Each bin j, with $j \in [1, M]$, of the hard spectrum of the particle p_i will contain n_{ij} particles, and we have:

$$\sum_{i=1}^{P} \sum_{j=1}^{M} n_{ij} = D\,, \tag{7.17}$$

*In the case of decay, HDMSpectra simulates the process $\chi \to f\bar{f}'$. Using annihilation or decay is equivalent in the procedure we followed, and in our case we preferred to use annihilation because the energy is sampled over $x = E/m_\chi$ instead of $x = 2E/m_\chi$ used in decay, which would introduce several factors of 2 in the following steps.

where D is the total number of generated events for the decays in eq. (7.16). Furthermore, the histogram is normalized according to D, so that:

$$\frac{n_{ij}}{D} = w_{ij}\,, \tag{7.18a}$$

$$\sum_{i=1}^{P}\sum_{j=1}^{M} w_{ij} = 1\,. \tag{7.18b}$$

The term w_{ij} is the probability that the three-body decay of χ will yield the particle p_i with energy fraction x_j (belonging to the j-th bin).

Then we need to compute the shower spectrum for each one of the three-body decays. Every particle p_i coming from the decay will produce a shower, generating several different particles:

$$p_i \to s_1 \dots s_H\,, \tag{7.19}$$

where H is the number of different particles types generated (γ, ν's, ...), each one being a state s_k, with $k \in [1, H]$. We remark that the process written in eq. (7.19) happens for each particle in the histogram of p_i, while every bin j is associated to the weight w_{ij} and contains particles $(p_i)_j$ with energy $E_j = x_j m_{\tilde{\chi}_0}$. For each bin j, we run HDMSpectra simulating the following process:

$$\chi_j\chi_j \to (p_i)_j(\overline{p}_i)_j \to s_1 \dots s_H\,, \tag{7.20}$$

where χ_j is a *fake* dark matter with a mass consistent with the energy of the particles $(p_i)_j$:

$$m_{\chi_j} = x_j m_{\tilde{\chi}_0} = E_j\,. \tag{7.21}$$

Because HDMSpectra samples its output on the basis of m_χ, according to the binned variable $y_j = E/m_{\chi_j}$, we substitute:

$$y_j = \frac{E}{m_{\chi_j}} = x\,\frac{m_{\tilde{\chi}_0}}{E_j}\,, \tag{7.22}$$

to have results in terms of the main binned variable x. HDMSpectra returns the values of $\left(dN_k/dy_j\right)_i$, which represents the electroweak-corrected spectra of the final state s_k, as coming from the shower of the hard spectrum particle p_i with energy E_j. This spectrum should be rescaled appropriately:

$$\left(\frac{dN_k}{dx}\right)_{ij} = \left(\frac{dy_j}{dx}\right)_{ij}\left(\frac{dN_k}{dy_j}\right)_i = \frac{m_{\tilde{\chi}_0}}{E_j}\left(\frac{dN_k}{dy_j}\right)_i\,, \tag{7.23}$$

for every bin j of the particle p_i hard spectrum and then for any particle p_i of the decay processes. The total spectrum of the particle s_k is eventually given by

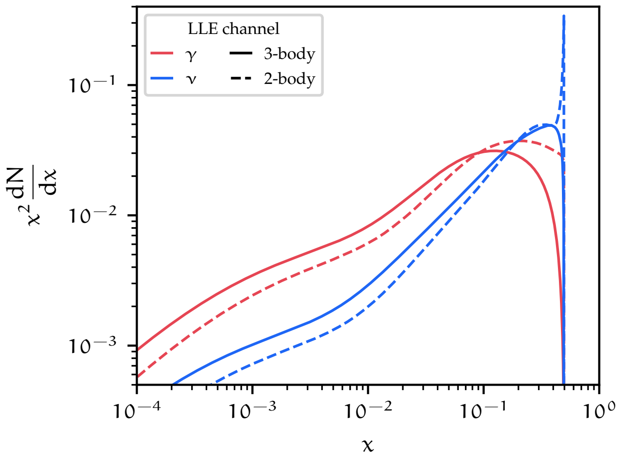

Figure 7.2: Comparison between the shower spectra in γ (red) and ν (blue, averaged over the three flavors) for three (solid lines) and two-body (dashed lines) decay patterns, both with $m = 10^{10}$ GeV and decaying via the LLE vertex.

summing all the contributions for each bin j and for each particle p_i, weighting each contribution on the basis of the probability w_{ij} discussed before:

$$\frac{dN_k}{dx} = \sum_{i=1}^{P}\sum_{j=1}^{M} w_{ij}\left(\frac{dN_k}{dx}\right)_{ij}. \tag{7.24}$$

In fig. 7.2 we show a comparison between the shower spectra in photons and neutrinos, coming from the three and two-body decay patterns for the LLE channel, fixing $m = 10^{10}$ GeV. As expected, the three-body decay spectra are shallower and peaked towards lower x with respect to the case of the two-body decay spectra.

7.4 Neutrino and γ-ray bounds for three-body decays

In this section we will study the lower bounds on dark matter lifetime for dark matter masses in the range (from 10^7 to 10^{15}) GeV, regarding neutralino dark matter. The computation is done according to the statistical procedure discussed in § 7.2, and it is based on the spectra computed in § 7.3. We will consider the case of a neutralino dark matter, where the possible decay processes are those listed in tab. 7.1. As we mentioned before, we will consider the three RPV vertices separately, studying their impact on the constraints one at a time, additionally assuming that each coupling is independent on the particle flavor. The couplings LLE, LQD and UDD give rise to 36, 108 and 18 different final

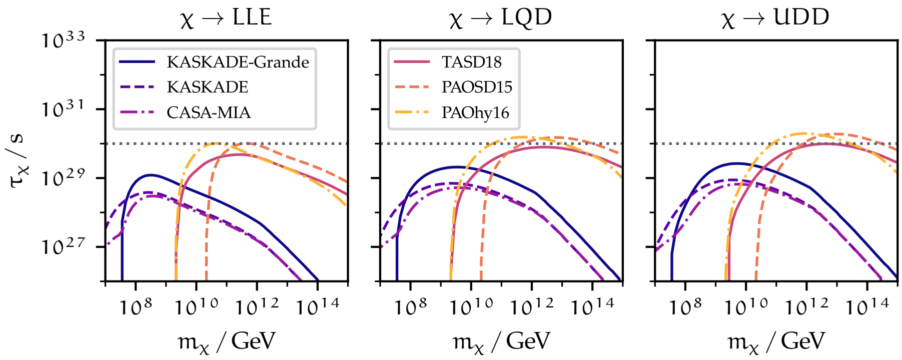

Figure 7.3: Current γ-ray limits on dark matter lifetime as a function of the dark matter mass for different experiments (indicated by different lines styles and colors) in the case of a dark matter candidate with a three-body decay pattern, assuming each RPV decay channel separately, for each plot, one at a time, see tab. 7.1: LLE (left), LQD (center), and UDD (right). The horizontal dotted line acts as a reference. Adapted from [3, fig. 4].

states, respectively, and each final state has the same branching ratio as the others. We assume χ to be a generic dark matter candidate undergoing a three-body decay with the pattern described by the RPV channels. Indeed, the bounds are model-independent and depend only on the three-body decay pattern, not on the nature of the dark matter itself, which may also not be a neutralino.

The bounds obtained with current γ-ray data and future projections for ν data are reported in figs. 7.3 and 7.4, for the three decay channels. Fig. 7.3 is characterized by several bounds, one for each experiment, reported with different line styles, according to the legend. Fig. 7.4 shows the bounds obtained with the future neutrino telescopes RNO-G and IceCube-Gen2, while the results from GRAND10k and GRAND200k are reported in separate panels, for clarity. In this latter case, bounds are shown as bands, where the width of the band is due to the uncertainty on the observations, leading to a different number of expected neutrino events. The higher bound is obtained by assuming zero neutrino events, while the lower bound refers to the expected astrophysical pulsar and cosmogenic neutrinos, both cases considered after three years of data-taking. The former provides a stronger constraint, as expected. For both figures, the shape of the bounds is related to the experimental sensitivities of each experiment: each one of them is sensitive to a certain energy range, so this can be translated to an interval of dark matter masses that can be probed. Across the different channels, the bounds are similar, with the quark-rich channels somewhat more constraining than the others, with peaks slightly higher than 10^{30} s, in the case of γ-rays. The situation is reversed for neutrinos, where the LLE channel is the most constraining one, with peaks of approximately 10^{30} s.

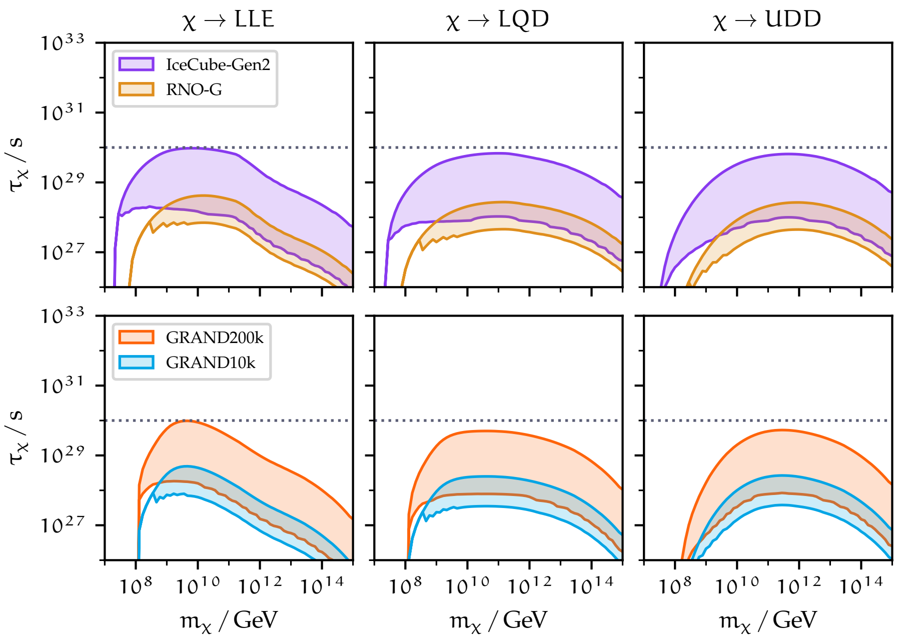

Figure 7.4: Projections for neutrino limits on dark matter lifetime as a function of the dark matter mass for different future neutrino telescopes in the case of a dark matter candidate with a three-body decay pattern, assuming each RPV decay channel separately, for each plot, one at a time, see tab. 7.1: LLE (left), LQD (center), and UDD (right). The bands cover the uncertainty on the astrophysical neutrino, flux which leads to a different expected number of detected neutrino events after three years of observation, with the upper bound being referred to zero neutrino events (null observation). The horizontal dotted line acts as a reference. Adapted from [3, fig. 5].

Fig. 7.5 presents a comparison between γ-rays and neutrinos constraints. We consider a combination of all γ experiments, while we consider only the zero neutrino observation sensitivity expected for IceCube-Gen2 after three years of data-taking. The three RPV vertices are shown with different line styles. Future neutrino experiments will be able to fill the gap left by current γ-ray constraints, providing a stronger and complementary bound for dark matter masses in the range $(10^8$ to $10^{11})$ GeV. In particular, the LLE channel brings an improvement for a larger mass range, because of its leptophilic nature. The pure hadronic channels LQD and UDD have a lower impact on neutrino data, given the different energy injection into UHE photons and neutrinos for the various decay channels. The analysis presented is independent on angular dark matter anisotropy and spectral features, because it stems from angle-averaged and energy-integrated quantities.

All the previous bounds are model-agnostic, and refer just to the case of a generic model, where the dark matter candidate can decay in the final

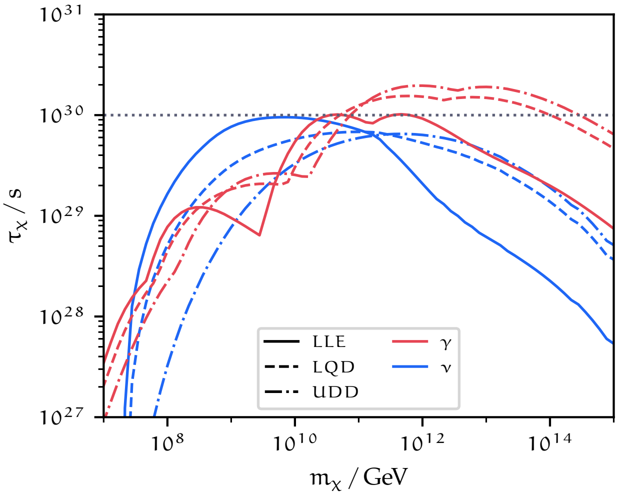

Figure 7.5: Comparison between the combined γ-ray constraints (red lines) and the IceCube-Gen2 projections after three years of data taking with no detected neutrino events (blue lines), on dark matter lifetime in the case of a dark matter candidate with a three-body decay pattern. The solid, dashed and dot-dashed lines refer to the LLE, LQD, UDD channels, respectively. Adapted from [3, fig. 6].

states listed in tab. 7.1. However, considering the specific string model under investigation, it is possible to recast the constraints on dark matter lifetimes into bounds on the RPV coupling λ, using eqs. (7.4a)–(7.4c), and, ultimately, on the string coupling g_S, by the means of eq. (7.5). This computation depends on the value of other quantities, such as the mass of the mediator and the RGE running of α_{em} at the energy scale $Q \approx 10^{10}$ GeV. From the RGE running, we can compute the mass of the neutralino dark matter to be $m_{\tilde{\chi}_0} = 7.3 \times 10^9$ GeV, while the averaged masses of the mediators are $m_{\tilde{f}} = (8.0 \times 10^9,\ 9.1 \times 10^9$ and $9.9 \times 10^9)$ GeV, for LLE, LQD and UDD, respectively. The fine-structure constant is $\alpha_{em}(m^2_{\tilde{\chi}_0}) = 0.01172$. The constraints on the three RPV couplings are shown in fig. 7.6, for the three decay channels separately, as a function of the neutralino dark matter mass $m_{\tilde{\chi}_0}$. Photons and neutrinos are shown with different line styles and colors. The neutrino bound is referred to the strongest bound that can be placed with future neutrino observations assuming zero neutrino events. The values expected for the dark matter mass and the string couplings are marked with thin black lines.

Finally, in fig. 7.7, these bounds are translated into g_S constraints. In the plot, we show the string coupling as a function of the ratio between the mediator and the dark matter mass, for the three RPV channels separately. The dark matter mass is fixed to $m_{\tilde{\chi}_0} = 7.3 \times 10^9$ GeV, corresponding to the value obtained via RGE running. The vertical lines mark the values of the mediator mass, as obtained from the RGE running. For the dark matter mass predicted by the

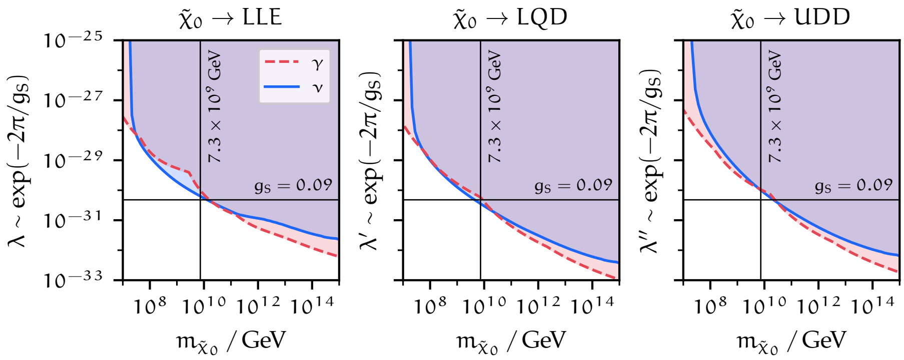

Figure 7.6: Upper bounds on the LLE (left), LQD (center) and UDD (right) couplings from current gamma-ray (red dashed lines) and future neutrino (blue solid lines) data, as a function of the neutralino dark matter mass. For the three cases, the mediator mass is fixed according to the RGE running (see the main text). The thin black lines display a benchmark value for the string coupling $g_S = 0.09$ and the model prediction for $m_{\tilde{\chi}_0}$. Adapted from [3, fig. 7].

model, g_S is constrained to be $g_S \lessapprox 0.1$, which implies that the string coupling has a value compatible to the perturbative regime of the low-energy effective field theory. In the following, we discuss an important remark on the value of g_S. In string compactification the string coupling is determined dynamically by the VEV of the dilaton. The dilaton is a scalar field in string theory, which can be stabilized by using background fluxes. However, the choice of the fluxes is not unique, so that it is possible to have a landscape of string vacua (defined as sets of values for the moduli fields, including the dilaton and compactification parameters), which can exhibit an approximately uniform distribution of the string coupling values [551, 552, 572, 573]. Therefore, one could think that the constraint $\lambda \lessapprox 10^{-30} \doteq \overline{\lambda}$ from fig. 7.6 might leave only a very sparse region of the landscape, but this is not true, given the exponential dependence of λ with g_S, see eq. (7.5). One can verify that the distribution of λ is not uniform, but goes as $o(\log \lambda)$. Subsequently, the increase in the number of vacua, for $\lambda \gtrapprox \overline{\lambda}$, is milder than logarithmic. This implies the region with $\lambda \lessapprox \overline{\lambda}$ is not sparse, because it can still contain several vacua in agreement with current data, that can be probed by future observations.

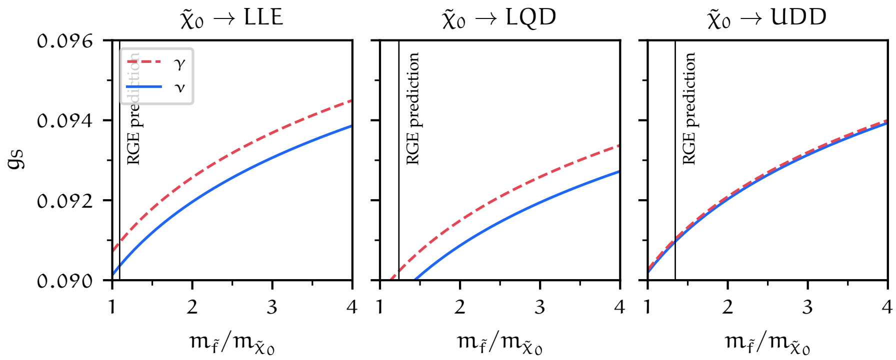

Figure 7.7: Upper bounds on the string coupling g_S as a function of the mass ratio $m_{\tilde{f}}/m_{\tilde{\chi}_0}$ with $m_{\tilde{\chi}_0} = 7.3 \times 10^9$ GeV. The different panels correspond to the different RPV couplings of the model: LLE (left), LQD (center) and UDD (right). Red dashed lines (blue solid lines) refer to the current γ-ray (future neutrino) limits. The vertical thin black lines display the model prediction for the mass ratio. Adapted from [3, fig. 8].

7.5 Summary

In this chapter we studied the impact of the decay of a superheavy dark matter candidate on the neutrino and γ-ray spectra. We considered a model coming from string theory, characterized by generic features of string constructions, namely high scale SUSY breaking and moduli stabilization, yielding one or more EMD epochs. This framework allowed us to obtain a model resembling the MSSM with RPV couplings, in which one can obtain the correct dark matter abundance assuming a superheavy dark matter candidate with mass scale around $(10^{10}$ to $10^{11})$ GeV [549]. The tiny RPV couplings are generated naturally by non-perturbative effects due to istantons and make the dark matter unstable, but with a lifetime longer than the age of the Universe.

We derived the SUSY mass spectrum using RGE evolution, finding that the LSP is a mostly-bino neutralino, representing the dark matter candidate. RPV couplings make the neutralino to decay into three-body final states. We followed a model-independent approach, computing the energy spectra of the final states, taking into account electroweak corrections (relevant for the mass scales at play), and obtaining neutrinos and γ-rays spectra. The spectra were used to draw constraints on the dark matter lifetime, using current γ-ray data and neutrino projections from future experiments. The most stringent bound on the lifetime is $\tau_{\rm DM} \gtrapprox 10^{30}$ s for $m_{\rm DM} \approx (10^9$ to $10^{11})$ GeV. There is a mild dependence on the specific decay channel. Additionally, these limits can be translated into upper bounds on the string coupling, resulting in $g_S \lessapprox 0.1$, which is a value consistent with the effective field theory to be in the perturbative regime.

Superheavy dark matter can evade very easily constraints coming from direct detection and colliders, so indirect detection is, so far, the only way these models can be probed. These results provide an explicit example of how indirect detection is able to constrain such models. Additionally, the model under investigation may be extended to include right-handed neutrinos, possibly addressing the neutrinos mass issue. These high energy right-handed neutrinos could provide an explanation to the anomalous events reported by IceCube and ANITA [574].

Part III

Dark photons and dark sectors

Chapter 8

Semi-visible dark photons below the GeV scale

Now I see. You're Jealous. You're jealous of humans, aren't you? According to you, humans are supposed to be a lot weaker than Homunculi. And yet, even if they get discouraged after being beaten, and even if they get close to falling down after losing their paths, they continue to get up and fight. Everyone around them helps them get back up. And you're envious of that.

—Edward Elric

Fullmetal Alchemist
HIROMU ARAKAWA

In chapter 4 we discussed the role of the dark photon as a vector portal mediator in dark sectors, giving a hint on its phenomenology and the main searches and constraints characterizing it. The vector portal with kinetically-mixed dark photon constitutes an interesting scenario that can be realized in many different ways, and it is a natural starting point for the study of dark sectors. The one-loop expectation for the kinetic mixing parameter ε, discussed in eq. (4.5), is of the order $\mathcal{O}(10^{-2} \text{ to } 10^{-3})$. This range of values is already strongly constrained, suggesting scenarios with smaller dark couplings or a higher-order origin for ε [575]. So far, experimental searches for dark photons have focused on the fully visible and fully invisible decay channels, which are the simplest and most predictive scenarios [298, 305, 576, 577]. In this chapter we will focus on particular realizations of dark photon-mediated dark sectors models, where the dark photon can decay *semi-visibly*, i.e. to both visible and invisible particles. This approach makes possible to avoid most of the laboratory constraints while at the same time to remain compatible with the naive one-loop estimation of ε. Nonetheless, the geometry of the detector in consideration and its experimental resolution can still lead to an invisible dark photon signature. The switch to a paradigm with semi-visible dark photons makes possible to reinterpret the experimental results of the past and current experiments, and to propose new strategies for future searches. In particular, searches for GeV-scale invisible dark photons from e^+e^- colliders and beam dump experiments [285, 294, 295, 578–581] can be recast according to the new semi-visible model. In this chapter we will focus on reinterpreting the constraints coming from BaBar [298] and NA64 experiments [299, 577, 582, 583].

Additionally, semi-visible dark photons constitute a viable explanation for the anomalous magnetic moment of the muon, introduced already in § 4.3.5. In particular, the discrepancy can be explained by a light dark photon with a mass of $m_{Z'} \lessapprox 3\,\text{GeV}$ and a kinetic mixing parameter of $\varepsilon \approx 10^{-3}$ to 10^{-2} [291, 584]. Although current constraints on fully visible or invisible dark photons exclude this possibility, they can be relaxed in case of semi-visible dark photons with mass in the range $m_{Z'} \approx (0.6 \text{ to } 1)\,\text{GeV}$. While this possibility has already been studied in minimal models [585–587], in this chapter we will move away from that picture and consider new models with different features. In particular, we will consider dark sector models below the GeV scale, containing multiple HNFs with mass of the order $\mathcal{O}(100\,\text{MeV})$, studying both a dark matter interpretation and the possibility for seesaw neutrino mass models. The former involves the presence of dark photon-mediated dark matter coannihilations (ensured by the presence of off-diagonal couplings between the dark photon and the HNFs, thanks to the conservation of charge-conjugation symmetry C), while the latter yields interesting predictions for neutrino experiments [377].

Finally, we will study some of the possible detection strategies for these models, highlighting the signatures of semi-visible dark photons. In this framework, future searches for monophoton-like events at Belle-II and the possibility to adapt current invisible-Z' searches to the missing energy signature of dark photon decay events are a great opportunity to explore the parameter space of these models.

The chapter is organized as follows. We discuss several semi-visible dark photon models in § 8.1, including their HNF spectra and the interaction vertices with the dark photon. Sec. 8.2 details the recasting procedure that we applied to reinterpret the constraints coming from BaBar and NA64. Results are presented in § 8.3. In § 8.4 we discuss the features of dark matter and HNL models in the context of semi-visible dark photons, reviewing the possible detection strategies. We summarize the main results in § 8.5.

The chapter is entirely based on the following publication:

[4] Abdullahi, A. M., Hostert, M., **DM**, Pascoli, S., “Semi-Visible Dark Photon Phenomenology at the GeV Scale”. *Phys. Rev. D* 108.1 (2023), p. 015032. DOI: 10.1103/PhysRevD.108.015032,

where I was mainly involved in the reinterpretation of the NA64 bounds, discussed in § 8.2, and in the production of the final plots in § 8.3. In particular, I developed a simulation of the NA64 detector in order to recast the bounds in

[299, 583]. The simulation allowed us to get the recast bounds for all the models considered in the paper. Additionally, this work made possible to strengthen an important collaboration with the NA64 experimental group. Their expertise helped us to improve our simulation and to better understand the experimental constraints. Moreover, our approach to the reinterpretation of the NA64 bounds was used as a starting point for a companion paper:

[6] Mongillo, M., Abdullahi, A., Oberhauser, B. B., Crivelli, P., Hostert, M., **DM**, Bueno, L. M., Pascoli, S., "Constraining light thermal inelastic dark matter with NA64". *Eur. Phys. J. C* 83.5 (2023), p. 391. DOI: 10.1140/epjc/s10052-023-11536-5,

where we studied the sensitivity of NA64 experiment to semi-visible dark photons, posing the basis for a future experimental search. Finally, I also worked to refine and improve the BaBar simulation. Sec. 8.1 and 8.4 have been adapted from [4].

8.1 Semi-visible dark photons

Dark photon models can be obtained by introducing a $U(1)_D$ *dark* gauge symmetry, using the same approach applied in § 4.1.3, where the new gauge boson X_μ with field strength $X_{\mu\nu}$ kinetically mixes with the hypercharge gauge boson. The general Lagrangian can be written as

$$\mathcal{L} = \mathcal{L}_{SM} - \frac{\varepsilon}{2\,c_w} X_{\mu\nu} B^{\mu\nu} - \frac{1}{4} X_{\mu\nu} X^{\mu\nu} + g_D X_\mu J^\mu_d + \frac{m_X^2}{2} X_\mu X^\mu \,, \tag{8.1}$$

where J^μ_D is the dark current containing new degrees of freedom of the model, made by new fermions or scalars. In this section, we stay agnostic for what concerns the origin of the dark photon mass. In general, it is possible to consider a dark Higgs mechanism, like in § 4.4, at the expenses of introducing additional assumptions, or we can assume a Stückelberg mass [588]. The next step is the diagonalization of the gauge kinetic term, in the same fashion as explained in § 4.2, yielding the dark photon mass eigenstate Z' with mass $m_{Z'} \approx m_X$, coupling to both the Standard Model electromagnetic current and the Standard Model weak neutral current,

$$\begin{aligned}\mathcal{L} \supset Z'_\mu \left(g_D J^\mu_D - e\varepsilon J^\mu_{EM} - \varepsilon\, t_w \frac{m^2_{Z'}}{m^2_Z} \frac{g}{2\,c_w} J^\mu_{NC} \right) \\ + Z_\mu \left(\frac{g}{2\,c_w} J^\mu_{NC} + g_D\, t_w\, \varepsilon J^\mu_D \right) + \mathcal{O}(\varepsilon^2)\,. \end{aligned} \tag{8.2}$$

Let us now explore the particle composition of the dark sector. A semi-visible dark photon is characterized by a decay pattern involving dark particles that subsequently decay into Standard Model particles with missing energy. In § 8.2

we will see how these features make possible to avoid most of the constraints coming from laboratory experiments. The simplest choice would be to add a dark complex scalar Φ, charged under $U(1)_D$. The resulting dark current can be expressed as $J^\mu_D = \Phi^* i\overleftrightarrow{\partial}^\mu \Phi$, and the interactions of the dark photon would always occur between the real components of Φ, φ_1 and φ_2, because of the hermiticity of the Lagrangian. Additionally, adding a soft breaking term $\mu\Phi^\dagger\Phi$ would induce a mass splitting between the real components of Φ, φ_1 and φ_2, and the dark photon would decay semi-visibly through $Z' \to \varphi_1(\varphi_2 \to \varphi_1 e^+ e^-)$. The same model can be realized with dark fermions, but the half-integer spin introduces a more intricate structure. In this chapter, we will consider models with n dark fermions, where the dark current can be written as

$$J^\mu_D = \sum_{i,j=1}^{n} V_{ij}\overline{\psi}_i \gamma^\mu \psi_j\,, \tag{8.3}$$

with V_{ij} representing the model-dependent coupling vertices. The vertices are constrained by the dark charge conservation, $\sum_{i,j}^n |V_{ij}|^2 \leqslant \sum_i^n |Q_i|$, where Q_i is the dark charge of the i-th fermion. Similar to the scalar case, these interactions would lead to semi-visible decays of the dark photon, because they are off-diagonal in the i and j fermion indices (if dark fermions are Majorana particles), as discussed in [589]. In this context, we focus specifically on a fermionic dark sector with the couplings defined in eq. (8.3). HNFs will be denoted with ψ_i with $i \in \{1, \dots, n\}$ and heavier HNFs ψ_j, with $j \in \{2, \dots, n\}$, are expected to decay in cascades down to the lightest HNF, emitting two charged particles at each step. We will consider the dark photon to be heavier than all the HNFs, to that their decay process is a three-body decay, characterized by an off-shell dark photon. Additionally, we will assume that decays into three HNFs are kinematically forbidden. One of the prominent example of such models is the inelastic Dark Matter model (iDM) [585, 586], where the dark photon can decay into two HNFs, one of which is stable and constitutes the dark matter candidate, while the other is heavier and short-lived. In this study, we extend this concept to more complex dark sectors.

In the following sections, we will study the fermionic content of the dark sector models under investigation. We start from the case of two Majorana HNFs, as for the iDM. Subsequently, following [377], we extend the model to include three HNFs, organized into either a pseudo-Dirac pair and one Majorana HNF, or three Majorana HNFs, according to the choice of parameters. While the former option resembles the iDM model, the latter is more versatile and can accommodate the neutrino mass model of [377]. Finally, we present the scenario featuring four Majorana HNFs, along to its limit of two Dirac particles, recently examined in [590]. A common requirement for all these models is the suppression of the dark photon decay to two ψ_1 states, because it will contribute to its invisible branching ratio, already significantly constrained by missing energy searches. Introducing a C-symmetry, see § 8.1.1 can help into meeting this request effectively.

Tab. 8.1 summarizes the models considered in this chapter, their HNF spectra and the interaction vertices with the dark photon.

Table 8.1: A summary of the benchmark models considered. We outline the HNF spectra and the interaction vertices with the dark photon, Z'. Blue lines indicate C-even states, and pink lines C-odd states. Pseudo-Dirac states with negligible mass splitting are denoted by two opposite C lines close together. The vertex matrices are defined in the basis $(A_1, A_2, \dots)$, with $A \in \{\psi, \Psi, N\}$, where the mixing angles are small $\alpha, \beta \ll 1$, and the entries denoted by $\times$ are arbitrary. States with mixed-color have no definite C property. Adapted from [4, fig. 1].

Theory model	HNF spectrum C-even C-odd	Z' coupling matrix $(A_1, A_2, \dots)$ basis $A \in \{\psi, \Psi, N\}$
Benchmarks 1 iDM 2 Majorana	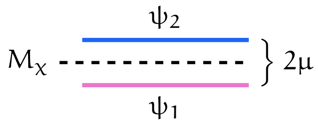	$\begin{pmatrix} 0 & 1 \\ 1 & 0 \end{pmatrix}$
Benchmarks 2 mixed-iDM 1 Dirac, 1 Majorana	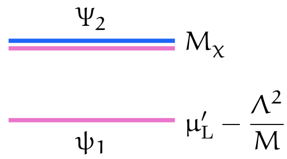	$\begin{pmatrix} 0 & \alpha \\ \alpha & 1 \end{pmatrix}$
Benchmarks 3 i2DM 2 Dirac	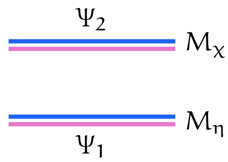	$\begin{pmatrix} \beta^2 & \beta \\ \beta & 1 \end{pmatrix}$
Benchmarks 4 3 Majorana	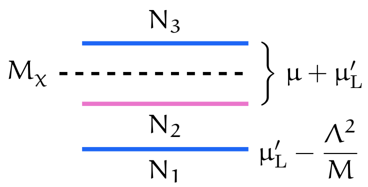	$\begin{pmatrix} 0 & \times & 0 \\ \times & 0 & \times \\ 0 & \times & 0 \end{pmatrix}$
Benchmarks 5 3 Majorana	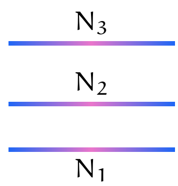	$\begin{pmatrix} \times & \times & \times \\ \times & \times & \times \\ \times & \times & \times \end{pmatrix}$

8.1.1 Two HNFs

One of the simplest models that can be considered is characterized by two Majorana HNFs. As usual, we introduce the dark symmetry $U(1)_D$ and the particle content in the interaction basis is made of χ_L and χ_R fermions with dark charges Q_L, and Q_R, respectively. The Lagrangian for the dark sector can be written as

$$\begin{aligned}\mathcal{L}_\chi = \overline{\chi_L} i(\partial\!\!\!/ - i g_D Q_L X\!\!\!/)\chi_L + \overline{\chi_R^c} i(\partial\!\!\!/ + i g_D Q_R X\!\!\!/)\chi_R^c \\ + \frac{1}{2}\begin{pmatrix}\chi_L^T & \chi_R^{cT}\end{pmatrix} \mathcal{C}^\dagger \begin{pmatrix}\mu_L & M_\chi \\ M_\chi & \mu_R\end{pmatrix}\begin{pmatrix}\chi_L \\ \chi_R^c\end{pmatrix} + \text{h.c.}\,,\end{aligned} \tag{8.4}$$

where the Majorana masses μ_L and μ_R are defined as:

$$\mu_L \doteq Y_L v_\Phi\,, \tag{8.5a}$$

$$\mu_R \doteq Y_R v_\Phi\,. \tag{8.5b}$$

These two terms break the $U(1)_D$ softly, and they can be generated by the VEV of dark Higgs Φ_2 with $Q_{\Phi_2} = 2Q_{L,R}$. The mass matrix M is complex and symmetric, and can be diagonalized by a unitary matrix U: $\text{diag}(m_1, m_2) = UMU$, where $U = R(\vartheta)\,\text{diag}(e^{i\delta}, 1)$ with $R(\vartheta)$ the rotation matrix of the angle

$$\tan(2\vartheta) = \frac{M_\chi}{\Delta\mu}\,. \tag{8.6}$$

Additionally, we define $\Delta\mu = (\mu_R - \mu_L)/2$ and $\mu = (\mu_L + \mu_R)/2$. The conservation of CP is ensured when the Majorana phase is $\delta = 0, \pi/2$. The dark current can then be written in terms of the Majorana mass eigenstates, ψ_1 and ψ_2,

$$\begin{aligned}J_D^\mu = \frac{Q_A - Q_V\cos(2\vartheta)}{2}\overline{\psi_2}\gamma^\mu\gamma^5\psi_2 + \frac{Q_A + Q_V\cos(2\vartheta)}{2}\overline{\psi_1}\gamma^\mu\gamma^5\psi_1 \\ + iQ_V\sin(2\vartheta)\sin(\delta)\,\overline{\psi_2}\gamma^\mu\psi_1 + Q_V\sin(2\vartheta)\cos(\delta)\,\overline{\psi_2}\gamma^\mu\gamma^5\psi_1\,,\end{aligned} \tag{8.7}$$

where $Q_V \doteq (Q_L + Q_R)/2$ and $Q_A \doteq (Q_L - Q_R)/2$. Imposing $Q_L = Q_R$ ($Q_A = 0$) fixes gauge anomaly cancellation.

The C symmetry

We can easily see that imposing $\Delta\mu \to 0$, the mixing angle ϑ is maximal, so that the couplings between the dark photon and the mass eigenstates are only off-diagonal. This can be understood thanks to a C symmetry. The action of this symmetry happens through the U_C operator, that on Weyl fermions has the following effect:

$$U_C\,\chi_{wL}\,U_C^{-1} = \eta_C\,\psi_{wR}^c\,, \tag{8.8a}$$
$$U_C\,\chi_{wR}\,U_C^{-1} = \eta_C\,\psi_{wL}^c\,, \tag{8.8b}$$

where $\psi_{wL}^c = -i\sigma^2\psi_{wR}^{*T}$ (charge conjugation on the Weyl fermions) and we choose the phase factor $\eta_C = +1$, for simplicity. In the case of a Dirac fermion, the C operation is achieved by charge conjugating the field

$$\chi = \begin{pmatrix} \zeta_w \\ -i\sigma^2\,\xi_w^* \end{pmatrix} \mapsto \chi^c = \begin{pmatrix} \xi_w \\ -i\sigma^2\,\zeta_w^* \end{pmatrix}\,. \tag{8.9}$$

The C symmetry is satisfied in case the Lagrangian is invariant under the exchange $\xi_w \leftrightarrow \zeta_w$ (i.e., $\chi_L \leftrightarrow \chi_R^c$).

The left-handed fermions,

$$\chi_+ = \frac{\chi_L + \chi_R^c}{\sqrt{2}}\,, \tag{8.10a}$$
$$\chi_- = e^{i\delta}\left(\frac{\chi_L - \chi_R^c}{\sqrt{2}}\right), \tag{8.10b}$$

are the C eigenbasis, with δ being the same Majorana phase as before. The dark photon has $C(Z'_\mu) = -1$, and the C-parity of each fermion can be set to $C(\chi_\pm) = \pm 1$ without loss of generality. We can rewrite the Lagrangian in eq. (8.4) in this basis:

$$\mathcal{L}_\chi = \overline{\chi_+} i\partial\!\!\!/ \chi_+ + \overline{\chi_-} i\partial\!\!\!/ \chi_- + g_D Z'_\mu\left[\frac{Q_A}{2}\left(\overline{\chi_+}\gamma^\mu\gamma^5\chi_+ + \overline{\chi_-}\gamma^\mu\gamma^5\chi_-\right) + iQ_V\overline{\chi_+}\gamma^\mu\chi_-\right]$$
$$-\frac{1}{2}\begin{pmatrix}\overline{\chi_-^c} & \overline{\chi_+^c}\end{pmatrix}\begin{pmatrix} M_\chi - \mu & i\Delta\mu \\ i\Delta\mu & M_\chi + \mu \end{pmatrix}\begin{pmatrix}\chi_- \\ \chi_+\end{pmatrix} + \text{h.c.}\,, \tag{8.11}$$

where $\varphi \to \pi/2$, so that the mass terms are positive for $M_\chi > \mu$. This shows also that the two fermions have opposite CP parities. For $\Delta\mu \to 0$ we obtain the physical mass basis. The only parameters breaking the C-symmetry in this model are $\Delta\mu$ and Q_A.

In the C-symmetric limit, $\chi_\pm$ behaves like the components of a pseudo-Dirac particle with a mass gap 2μ. Moreover, in the same limit, interactions with the dark photon are off-diagonal, while we can also conclude that interactions with a C-even dark Higgs would be purely diagonal. Such dark Higgs may be part of the spectrum, and in this case we will consider it to be heavier than Z'_μ and with negligible mixing with the Standard Model Higgs.

This C-symmetry can not be preserved in the Standard Model, because of the different hypercharges of left and right-handed fermions. So, we can consider the breaking of C to be stronger in the Standard Model than in the dark sector. Alternatively, if there are two C symmetries in the theory, C_{SM} in the Standard Model, and C_{DS} in the dark sector, then the conservation of C_{DS}, but not C_{SM}, would forbid kinetic mixing, $F^{\mu\nu}X_{\mu\nu} \xrightarrow{C_{DS}} -F^{\mu\nu}X_{\mu\nu}$.

Inelastic Dark Matter

The iDM model [591, 592] is a particular realization of the model described above, where the dark sector is made of two HNFs, ψ_1 and ψ_2, with equal dark charges $Q_L = Q_R = 1$, in the C-symmetric limit. This implies $Q_A = 0$, so that we are anomaly-free, and $Q_V = 1$. Additionally, we take $\varphi = \pi/2$, and the Lagrangian reads:

$$J^{\mu}_{iDM} = i\overline{\psi}_2\gamma^{\mu}\psi_1 + \text{h.c.}\,. \tag{8.12}$$

There are five free parameters in the model:

$$m_1\,, \quad \Delta_{21}\,, \quad r\,, \quad \alpha_D\,, \quad \varepsilon\,, \tag{8.13}$$

with the following definitions:

$$\Delta_{21} \doteq \frac{m_2 - m_1}{m_1}\,, \tag{8.14a}$$

$$r \doteq \frac{m_1}{m_{Z'}}\,, \tag{8.14b}$$

$$\alpha_D \doteq \frac{g_D^2}{4\pi}\,. \tag{8.14c}$$

The model has an interesting phenomenology, because of the possibility to provide a good dark matter candidate and an unstable coannihilating partner, that can be searched for through its displaced decays in collider experiments [593–596]. While historically, the model was proposed as an explanation of the DAMA observation, given the energy threshold for direct detection, as induced by the mass splitting Δ_{21}, varies between Sodium-Iodine and Xenon experiments [591].

The presence of an additional scalar field would make possible to realize ψ_1 self-interactions and, in case of mixing of this scalar with the Standard Model Higgs boson, direct annihilation to Standard Model fermions. However, the mixing with the Higgs induces couplings smaller than the Higgs's Yukawa couplings, so that annihilations are suppressed by fermion masses, on top of Higgs mixing parameters. The latter must be sufficiently small for the scalar contribution to self-annihilations to be sub-dominant with respect to the exponentially suppressed Z'-mediated coannihilations. Additionally, the dark Higgs is assumed to be heavier than the HNFs.

The main Feynman diagram for this model are represented in fig. 8.1. Each dark photon produced can only be accompanied by a single semi-visible decay, $\psi_2 \to \psi_1 f^+ f^-$, with f a Standard Model particle. However, this is not enough

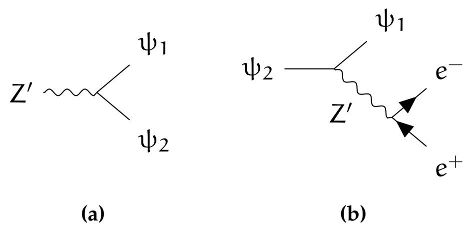

Figure 8.1: Feynman diagrams for the iDM model. The dark photon Z' can decay into two HNFs, ψ_1 and ψ_2, with a subsequent decay of ψ_2 into ψ_1 and a pair of charged leptons.

to provide a strong relaxation of the invisible dark photon bounds, and the explanation of Δa_μ in this model is in tension with invisible dark photon limits, as we will show in § 8.3. Indeed, even small losses of acceptance in the detector can lead to a missed e^+e^- pair. With this limitation in mind, we consider new models where multiple unstable fermions accompany dark photon production. There are two ways to achieve this: i) in models where ψ_2 can be produced in pairs, $Z' \to \psi_2\psi_2$, and ii) in models of three or more HNFs, where the dark photon couples predominantly to the heaviest and most short-lived states, e.g. $Z' \to \psi_3\psi_2$. These possibilities will be explored in the following sections: we will consider models with three and four Weyl fermions, which will reduce to three distinguishable states in the spectrum. This allows for better compatibility between the Δa_μ anomaly and a dark photon explanation. We will prove this in § 8.3 with a detailed analysis.

8.1.2 Three HNFs

The two-HNFs model can be extended to include three HNFs, by adding a sterile Weyl fermion η_L. The new particle content will be made of χ_L, χ_R, and η_L, with dark charges $Q_L = Q_R = 1$ and $Q_\eta = 0$. The Lagrangian is given by

$$\mathcal{L}_{\text{3-HNF}} = \mathcal{L}_\chi + \overline{\eta_L} i\partial\!\!\!/ \eta_L - \left[\frac{\mu_L'}{2}\overline{\eta_L^c}\eta_L + \Lambda_L \overline{\eta_L^c}\chi_L + \Lambda_R \overline{\eta_L^c}\chi_R^c + \text{h.c.}\right]. \tag{8.15}$$

This model is a simplified version of the three-portal model discussed in § 4.4. The dark symmetry $U(1)_D$ is broken by the mixing terms: they can be generated via a dark scalar Φ_1 with dark charge $Q_{\Phi_1} = 1$, while the Majorana masses can be generated through an additional dark Higgs Φ_2 with dark charge $Q_{\Phi_2} = 2$. In this case, the mixing terms are defined as $\Lambda_{L,R} \doteq Y_{L,R}\, v_{\Phi_1}/\sqrt{2}$, where $Y_{L,R}$ are the Yukawa couplings.

The phenomenology of the sterile fermion η_L can be challenging: given it is neutral, it can couple to the Standard Model lepton doublets through the Yukawa coupling $\overline{L}\widetilde{H}\eta_L^c$, making possible to realize a neutrino portal like the one discussed in § 4.1.1. This term would be essential to generate light neutrino masses, while it would give small corrections to the HNFs masses. A separate discussion on the importance of this term can be found in § 8.1.4. However, the term will have little to no impact on collider and fixed-target phenomenology, given the smallness of the neutrino Yukawa coupling. Another important effect of this term is that it would allow the lightest HNF to decay into Standard Model neutrinos, making it unstable and preventing it from being a dark matter candidate. To ensure the stability of the lightest HNF, we forbid this term by charging η_L and all dark fermions under a dark parity, e.g. $\mathbb{Z}_2$ symmetry. On a separate note, the dark parity can also be attributed to the conservation of lepton number if $L(\eta_L) = 0$, which forbids the neutrino Yukawa coupling [597].

Now we want to write the dark sector mass matrix. We utilize the dark fermion basis studied in eq. (8.10b), χ_+ and χ_-, setting the Majorana phases in order to conserve CP. In this case, the mass terms are positive when $M_\chi > \mu$ and the mass Lagrangian is:

$$-\mathcal{L}_{\text{3-HNF}} \supset \frac{1}{2}\begin{pmatrix}\overline{\eta_L^c} & \overline{\chi_-^c} & \overline{\chi_+^c}\end{pmatrix}\begin{pmatrix}\mu_L' & \Delta\Lambda & \Lambda \\ \Delta\Lambda & M_\chi - \mu & \Delta\mu \\ \Lambda & \Delta\mu & M_\chi + \mu\end{pmatrix}\begin{pmatrix}\eta_L \\ \chi_- \\ \chi_+\end{pmatrix} + \text{h.c.}\,, \tag{8.16}$$

where $\Lambda \doteq (\Lambda_L + \Lambda_R)/\sqrt{2}$ and $\Delta\Lambda \doteq (\Lambda_R - \Lambda_L)/\sqrt{2}$. The C symmetry in the χ sector in preserved in the limit $\Delta\mu = \Delta\Lambda = 0$. The model realized in this case is very similar to the two HNFs model, with the difference that χ_+ can mix with a sterile state, while χ_- decouples. This is also a consequence of the C symmetry, because $C(\eta_L) = +1$, so that only the C-even fermion can mix with η_L. As we will see, the spectrum can consist of one Dirac and one Majorana particle or three Majorana states.

A single rotation in the C-even sector leads to the mass basis,

$$\psi_1 = c_\alpha\, \eta_L + s_\alpha\, \chi_+\,, \tag{8.17a}$$

$$\psi_2 = \chi_-\,, \tag{8.17b}$$

$$\psi_3 = -\, s_\alpha\, \eta_L + c_\alpha\, \chi_+\,, \tag{8.17c}$$

where the masses of the three states are:

$$m_1 = \mu_L' - M\frac{\sin^2(\alpha)}{\cos(2\alpha)}\,, \tag{8.18a}$$

$$m_2 = M_\chi - \mu\,, \tag{8.18b}$$

$$m_3 = \mu_L' + M\frac{\cos^2(\alpha)}{\cos(2\alpha)}\,, \tag{8.18c}$$

with $\tan(2\alpha) = 2\Lambda/M$ and $M = M_\chi + \mu - \mu_L'$. If $\tan(2\alpha) \ll 1$, a seesaw mechanism is in place, and ψ_2 and ψ_3 form a pseudo-Dirac pair. The other scenario, with $\tan(2\alpha) \gg 1$, does not preserve the pseudo-Dirac limit. The mass splittings in that case are given by $m_3 - m_1 \approx M + 2\Lambda^2/M$ and $m_3 - m_2 \approx 2\mu + \Lambda^2/M$.

In the C symmetric case, the dark current is also fully off-diagonal and is given by

$$J^{\mu}_{\text{3-HNF}} \supset s_\alpha\, \overline{\psi}_2 \gamma^\mu \psi_1 + c_\alpha\, \overline{\psi}_2 \gamma^\mu \psi_3 + \text{h.c.}\,. \tag{8.19}$$

The pseudo-Dirac pair and the dark photon coupling is mediated by the α mixing angle, so that a larger angle implies a stronger coupling. The lightest HNF ψ_1 is the dark matter candidate predicted by this model, and its relic abundance is set exclusively through coannihilation with the heavier partners. Similarly to the iDM model, this mechanism allows evading constraints from the CMB and direct detection experiments. Below, we highlight the two types of phenomenological models that can be derived from eq. (8.15) above.

Mixed-inelastic Dark Matter

In the mixed-inelastic Dark Matter (mixed-iDM) scenario, we consider the limit where one of the Weyl fermions is mostly a Majorana fermion, while the other two states form a mostly-dark pseudo-Dirac pair. In this setup, the lighter and mostly-sterile Majorana fermion constitutes a dark matter candidate, while the pseudo-Dirac fermion acts as the coannihilator. Notably, the C symmetry forbids the self-annihilation of dark matter via Z' interactions, and so, the CMB bounds are not applicable.

The dark current, characterized by the Majorana state ψ_1 and the pseudo-Dirac state Ψ_2, takes the following form:

$$J^{\mu}_{\text{mixed-iDM}} \supset s_\alpha\, \overline{\Psi}_2 \gamma^\mu \psi_1 + c_\alpha\, \overline{\Psi}_2 \gamma^\mu \Psi_2 + \text{h.c.}\,, \tag{8.20}$$

and so this model is fully characterized by the parameters in eq. (8.13) and the mixing angle α. An important remark in order to effectively use this model is that the Majorana states ψ_2 and ψ_3 in the pseudo-Dirac state Ψ_2 must be coherent, allowing their treatment as a singular Dirac particle. The dark matter hypothesis is strongly dependent on the choice of the mass splitting Δ_{21}, which must be small enough to prevent the Boltzmann suppression of the coannihilation rate, while the parameter Δ_{32} plays a marginal role in this scenario. In this context, we can define M_X and Λ in terms of $\tan(2\alpha)$ and Δ_{21}, as follows:

$$m_1 \approx \mu_L' - \frac{1}{4}\mu\,\Delta_{21}\tan^2(2\alpha)\,, \tag{8.21a}$$

$$m_2 = \mu_L'(1+\Delta_{21})\,, \tag{8.21b}$$

$$m_3 \approx \mu_L'(1+\Delta_{21}) + \frac{1}{4}\mu\,\Delta_{21}\tan^2(2\alpha)\,, \tag{8.21c}$$

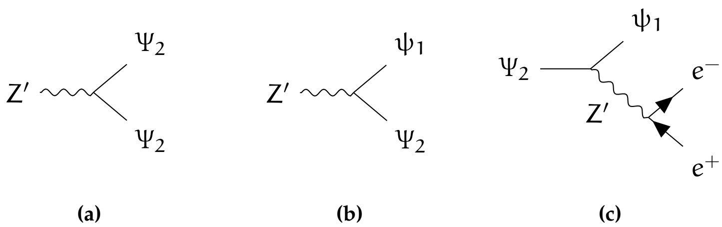

Figure 8.2: Feynman diagrams for the mixed-iDM model. The dark photon Z' can decay into two HNFs, ψ_1 and Ψ_2, with a subsequent decay of Ψ_2 into ψ_1 and a pair of charged leptons. Additionally, differently from the iDM model, Z' can also decay in a pair of Ψ_2 states, greatly enhancing the production rate of e^+e^-.

valid for $\mu < M_X$. Additionally, the mass splitting between the pseudo-Dirac pair is given by:

$$\Delta_{32} = \frac{1}{4}\frac{\mu}{\mu'_L}\frac{\Delta_{21}}{1+\Delta_{21}}\tan^2(2\alpha)\,, \tag{8.22}$$

and it is small under the condition of $\tan^2(2\alpha) \ll 1$. For $\mu'_L = \mu = 0$, the mass splitting between the pseudo-Dirac pair results $\Delta_{32} \propto \alpha^2$, so that in the limit $\alpha \to 0$, we recover an exact Dirac state. In summary, the smallness of the mixing angle ensures the mass splitting Δ_{32} is negligible and the pseudo-Dirac pair is, effectively, a Dirac particle. The decay of the heavier state $\psi_3 \to \psi_2 + \ldots$ is proportional to $\Delta_{32}^5 \propto \alpha^{10}$, and so suppressed under the condition discussed above, so that it can be safely neglected.

The main Feynman diagrams for this model are represented in fig. 8.2.

Three Majorana fermions

In this second scenario, we relax the constraints on $\alpha \ll 1$ and the C symmetry. This allows for a more general mass spectrum, where the three HNFs are Majorana fermions N_k, $k \in \{1, 2, 3\}$, and no pseudo-Dirac pair is present. The main feature of this model is that the semi-visible decay rates of N_3 and N_2 are enhanced, while the on-diagonal couplings in the dark sector are suppressed.

In principle, on the basis of the mass hierarchy of the three HNFs, it would be possible to have heavier states decaying into multiple lighter HNFs, e.g. into three N_1. In this study, we will not consider this possibility, and we will kinematically forbid such decays, because they would lead to a large invisible branching ratio of the dark photon, in case N_1 is stable or long-lived.

The main Feynman diagrams for this model are represented in fig. 8.3.

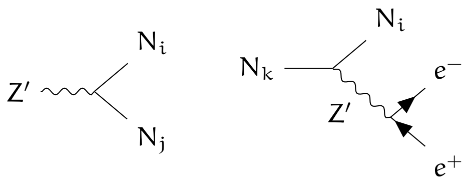

(a) **(b)**

Figure 8.3: Feynman diagrams for the three Majorana fermions model. On the basis of the values of the mixing matrix, some of the channels may be suppressed. In general, the dark photon Z' can decay into any pair of two HNFs, and each heavier state can decay in chain to lighter states. Other processes, like $N_3 \to N_1 N_1 N_1$ that would increase the invisible branching ratio of the dark photon, are kinematically forbidden.

8.1.3 Four HNFs

We can increase the fermionic content of the models so far discussed and obtain a 2-Dirac fermion picture. The HNFs are now χ, charged under $U(1)_D$, and a sterile η. The new Lagrangian reads:

$$
\begin{aligned}
\mathcal{L} = \mathcal{L}_\chi + \bar{\eta} i \partial\!\!\!/ \eta - M_\eta \bar{\eta}\eta - \Bigg[& \frac{\mu'_R}{2} \overline{\eta_R} \eta_R^c + \Lambda'_L \overline{\eta_R} \chi_L + \Lambda'_R \overline{\eta_R} \chi_R^c \\
& + \frac{\mu'_L}{2} \overline{\eta_L^c} \eta_L + \Lambda_L \overline{\eta_L^c} \chi_L + \Lambda_R \overline{\eta_L^c} \chi_R^c + \text{h.c.} \Bigg] ,
\end{aligned}
\tag{8.23}
$$

where again, Yukawa couplings between the sterile fermions and the Standard Model neutrinos have been neglected, see § 8.1.2. Imposing the C symmetry, we find $\Lambda_L = \Lambda'_R$ and $\Lambda_L = \Lambda'_R$. The mass matrix in the C eigenbasis is:

$$
\begin{aligned}
-\mathcal{L}_{\text{4-HNF}} \supset & \frac{1}{2} \begin{pmatrix} \overline{\eta_-^c} & \overline{\eta_+^c} & \overline{\chi_-^c} & \overline{\chi_+^c} \end{pmatrix} \\
& \times \begin{pmatrix} M_\eta - \mu' & 0 & \Lambda_- & 0 \\ 0 & M_\eta + \mu' & 0 & \Lambda_+ \\ \Lambda_- & 0 & M_\chi - \mu & 0 \\ 0 & \Lambda_+ & 0 & M_\chi + \mu \end{pmatrix} \begin{pmatrix} \eta_- \\ \eta_+ \\ \chi_- \\ \chi_+ \end{pmatrix} + \text{h.c.} ,
\end{aligned}
\tag{8.24}
$$

where $\Lambda_\pm \doteq (\Lambda'_L + \Lambda_R)/2 \pm (\Lambda_L + \Lambda'_R)/2$. The C-even and C-odd sectors decouple from each other. To write the particle spectrum, we can define the mixing angle β and consider two commuting rotation transformations, such that $\tan(2\beta_\pm) = 2\Lambda_\pm / \Delta_\pm$, where $\Delta_\pm \doteq \pm(M_\chi - M_\eta) + \mu - \mu'$,

$$\psi_1 = c_{\beta_-} \eta_- + s_{\beta_-} \chi_- , \tag{8.25a}$$

$$\psi_2 = c_{\beta_+} \eta_+ + s_{\beta_+} \chi_+ , \tag{8.25b}$$

$$\psi_3 = s_{\beta_-} \chi_- - c_{\beta_-} \eta_- , \tag{8.25c}$$

$$\psi_4 = s_{\beta_+} \eta_+ - c_{\beta_+} \chi_+ , \tag{8.25d}$$

with the masses given by:

$$m_1 = M_\eta - \mu' + \Delta_- \frac{\sin^2(\beta_-)}{\cos(2\beta_-)}, \tag{8.26a}$$

$$m_2 = M_\eta + \mu' - \Delta_+ \frac{\sin^2(\beta_+)}{\cos(2\beta_+)}, \tag{8.26b}$$

$$m_3 = M_\chi - \mu - \Delta_- \frac{\sin^2(\beta_-)}{\cos(2\beta_-)}, \tag{8.26c}$$

$$m_4 = M_\chi + \mu + \Delta_+ \frac{\sin^2(\beta_+)}{\cos(2\beta_+)}. \tag{8.26d}$$

When μ, μ', $\Lambda \ll M_\chi$, M_η, the spectrum is composed of two pseudo-Dirac particles, split by the $U(1)_D$-breaking terms. In the following, we will study the scenario where $\mu = \mu' = 0$ and $\Delta_+ = -\Delta_- \doteq \Delta$. The mass splitting between the Dirac pairs is now:

$$\Delta_{43} \approx \Delta_{12} \approx \Delta(\beta_+^2 - \beta_-^2), \tag{8.27}$$

which is small for small mixing angles and vanishes when $\beta_+ = \beta_-$. In this case, the mass spectrum is composed of two Dirac pairs, and can be achieved in two ways: i) $\Lambda_+ = -\Lambda_-$ ($\Lambda'_L = \Lambda_R = 0$), or ii) $\Lambda_+ = \Lambda_-$ ($\Lambda_L = \Lambda'_R = 0$).

Expressed in terms of the mass eigenstates, the dark current is given by

$$\begin{aligned} J^\mu_X = {} & c_{\beta_+} c_{\beta_-} \overline{\psi}_4 \gamma^\mu \psi_3 + s_{\beta_+} c_{\beta_-} \overline{\psi}_4 \gamma^\mu \psi_1 \\ & + s_{\beta_-} c_{\beta_+} \overline{\psi}_3 \gamma^\mu \psi_2 + s_{\beta_+} s_{\beta_-} \overline{\psi}_2 \gamma^\mu \psi_1 + \text{h.c.}, \end{aligned} \tag{8.28}$$

where interactions occur exclusively between C-even and C-odd states. The dark photon coupling is stronger for the heaviest pseudo-Dirac pair. Decays such as $\psi_{4,2} \to \psi_{3,1} + \ldots$ are suppressed compared to the dominant $\psi_{4,3} \to \psi_{1,2} + \ldots$ by factors of $(\beta_+^2 - \beta_-^2)^5 \beta_\pm^2$.

To sum up, under the C symmetric limit, a pair of pseudo-Dirac particles emerges, each separated by a small gap proportional to $\Delta(\beta_+^2 - \beta_-^2)$, where β_+ and β_- denote the mixing angles in the C-even and C-odd sectors, respectively. Individual splittings only become relevant for large mixings and vanish precisely when $\beta_+ = \beta_-$.

Inelastic Dirac Dark Matter

The inelastic Dirac Dark Matter (i2DM) model is a variation of the iDM model, where we consider two Dirac HNFs in the spectrum. This model can be obtained by the 4 HNFs scenario just described, in the exact Dirac limit, $\beta_+ = \beta_-$. The dark matter candidate is the lightest, mostly-neutral, fermion Ψ_1,

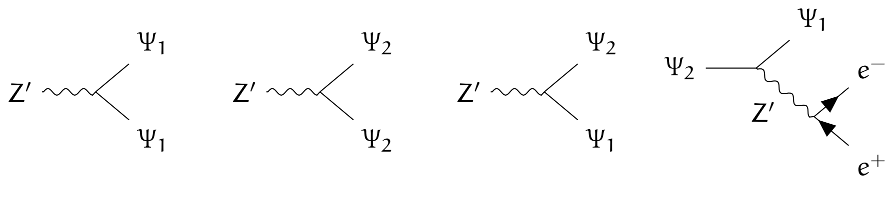

Figure 8.4: Feynman diagrams for the i2DM model. The dark photon Z' can decay into any pair of HNFs, with a subsequent decay of Ψ_2 into Ψ_1 and a pair of charged leptons. This means that, differently from the mixed-iDM model, Z' can decay into a pair of the lightest Ψ_1 states, opening the possibility for Ψ_1 self-interactions, which are crucial for the evaluation of the CMB bounds.

while the heavier, mostly-dark, fermion Ψ_2 plays the role of the coannihilator:

$$\mathcal{J}^{\mu}_{\text{i2DM}} = s_\beta^2\, \overline{\Psi}_1 \gamma^\mu \Psi_1 + s_\beta\, c_\beta \left(\overline{\Psi}_2 \gamma^\mu \Psi_1 + \text{h.c.} \right) + c_\beta^2\, \overline{\Psi}_2 \Psi_2\,. \tag{8.29}$$

The self-interactions of the dark matter candidate are suppressed by s_β^2. The relic density is typically set by the self-annihilation of the heavy partner, $\Psi_2\Psi_2 \to f^+ f^-$, and coscattering, $\Psi_2\Psi_2 \leftrightarrow \Psi_{2,1}\Psi_1$ and $\Psi_2 f \leftrightarrow \Psi_1 f$ [590]. Differently from the mixed-iDM scenario, the off-diagonal interactions between the dark matter and its coannihilator are suppressed with respect to the self-interactions of the coannihilator, Ψ_2, and in this model there are also dark matter self-annihilation that, despite being suppressed, make the model subject to CMB limits. The phenomenology is fully determined by the parameters in eq. (8.13), in addition to β. The idea of a sterile dark matter candidate coannihilating with a heavier partner has already been studied in context of models with two Majorana fermions [598].

Concerning accelerator phenomenology, the main signature of missing energy accompanied by e^+e^- pairs depends on the dark photon branching ratios, which can be approximately parametrized by $(1 : \beta^2 : \beta^4)$ for decays into $(\Psi_2\Psi_2, \Psi_2\Psi_1, \Psi_1\Psi_1)$ final states. Given $Z' \to \Psi_2\Psi_2$ dominates, a large number of events will contain two semi-visible particles, further enhancing the visible energy in the final states and allowing to relax the constraints on kinetic mixing from dark photon searches. The presence of more visible final states enhances the prospects for discovery.

The main Feynman diagrams for this model are represented in fig. 8.4.

8.1.4 Mixing with light neutrinos

Secluded dark sectors may be characterized by different kind of portals. In particular, the vector portal we have considered so far is not the only possibility. In § 4.1.1, we discussed the possibility of a neutrino portal, where sterile fermions mix with the Standard Model leptonic doublet through Yukawa couplings. This has very important consequences for the phenomenology of the model, because it can make possible to generate light neutrino masses, while the lightest HNF is no longer stable and decays to neutrinos. Conventionally, the HNFs are called HNLs in this scenario. To recover a stable dark matter candidate in this case, it is necessary to invoke an additional symmetry, like $\mathbb{Z}_2$, which distinguishes the HNLs from the light neutrinos, forbidding the neutrino portal interaction. This is what has been done for the model described in § 8.1.2.

In this section, we will discuss the presence of a neutrino portal in the models introduced before, and the phenomenological consequences of this choice. The most obvious choice is to introduce the neutrino portal in models with multiple HNFs, where the neutral fermions η are free to mix with the Standard Model neutrinos. For the model in § 8.1.2, one can add the following Yukawa interaction:

$$\mathcal{L} = \mathcal{L}_{\text{3-HNF}} - \sum_{\alpha=e,\mu,\tau} \left(y_\alpha \overline{L_\alpha} \widetilde{H} \eta_L^c + \text{h.c.} \right), \tag{8.30}$$

where L_α is the $SU(2)$ leptonic doublet of the Standard Model, and we have the usual definition $\widetilde{H} = i\sigma_2 H^*$. The HNFs mix among themselves and, as mentioned before, they are called HNLs, $N_i \doteq \psi_i$. This particular model resembles the one discussed in § 4.4 [377], with the addition of a dark scalar Φ with $Q_\Phi = 1$. In this case, considering the values for kinetic mixing and $m_{Z'}$ used in this chapter, the lightest HNL, N_4, will decay via $N_4 \to \nu \ell^+ \ell^-$ or $N_4 \to \nu \pi^+ \pi^-$. However, due to the smallness of the mixing, the decay width is suppressed and the HNL is long-lived ($c\tau_{N_4} \gg 1\,\text{m}$), so that it constitutes missing energy in e^+e^- colliders and fixed-target experiments. For a review of the phenomenology of HNLs, see [599].

As we mentioned previously, an important phenomenological consequence of this portal is the possibility of generating light neutrino masses, and there have been multiple studies in the literature about a GeV-scale seesaw mechanism as the origin of the observed neutrino masses and mixing angles [600–608]. For a review of this topic, see [287] and references therein.

Moreover, the lepton number has an interesting role in these scenarios. If one wants to make the Yukawa term lepton number conserving, then η_L should be charged under L. However, in this scenario, the Majorana mass term μ_L' would break the lepton number symmetry by two units. The situation is different in the dark sector, where it is possible to charge χ_L and χ_R arbitrarily, and lepton number conservation will depend on this charge assignment: it will be broken by $\Lambda_{L,R}$, M_χ and $\mu_{L,R}$, or by Λ_L and $\mu_{L,R}$, for $L(\chi_L) = L(\chi_R^c) = 0$, $L(\chi_L) = L(\chi_R^c) = 1$ or $L(\chi_L) = -L(\chi_R^c) = 1$, respectively. Both $\Lambda_{L,R}$ and $\mu_{L,R}$ terms also break $U(1)_D$ by one and two units, respectively, and can arise once multiple scalars, carrying $U(1)_D$ charges, develop a VEV. In the most minimal case of one scalar Φ with dark charge $Q_\Phi = 1$, either of the resulting Λ_L, or Λ_R, term breaks the lepton number explicitly by 2 units. Let us consider a simple case, where all new fields are neutral under the lepton number symmetry: in this case, the lepton number violating term is the Yukawa coupling itself, which would naturally explain its smallness. A seesaw mechanism is in place: for negligible μ_L' and $\Lambda_{L,R} \ll M_\chi$, we have $m_1 \approx \Lambda^2/M$, $m_2 \approx m_3 = M$, and it is possible to write a one-generation estimate for light neutrino masses:

$$m_\nu \approx \frac{y^2 v_H^2}{\Lambda^2} M \,. \tag{8.31}$$

Given the scale of dark symmetry breaking is smaller than the electroweak scale, there may be additional contributions coming from loops, especially if μ_L' is large [609].

In the following, we will study the case with four HNFs. Adding the Yukawa interactions to the Lagrangian, we obtain:

$$\mathcal{L} = \mathcal{L}_{\text{4-HNF}} - \sum_{\alpha=e,\mu,\tau} \left(y_\alpha \overline{L_\alpha} \widetilde{H} \eta_R + y'_\alpha \overline{L_\alpha} \widetilde{H} \eta_L^c + \text{h.c.} \right) . \tag{8.32}$$

One option is not to charge either of $\eta_{L,R}$ implying that both Yukawa couplings are suppressed being lepton number violating, or it is possible to charge both and forbid one of the Yukawa couplings. The same applies also to the dark sector, where the different charge assignments can make some of the terms in the Lagrangian forbidden or naturally small. In this section, we highlight one interesting case, where $L(\chi_L) = L(\chi_R) = 1$, phenomenologically equivalent to the case $L(\chi_L) = L(\chi_R) = -1$. This choice is compatible with the C-symmetry discussed earlier in order to avoid diagonal dark photon vertices and forbids the terms Λ_R' and Λ_L. We notice, that in this case, the lightest neutrino mass is zero as it is protected by the accidental lepton number symmetry.

8.2 Reinterpreting constraints on invisible Z'

Searches for invisibly decaying dark photons at e^+e^- colliders and fixed-target experiments provide the strongest constraints on models of semi-visible dark photons. At collider experiments, the dark photon is produced directly alongside ISR in the $e^+e^- \to \gamma Z'$ process. Prompt decays of Z' to a pair of HNFs, $Z' \to \psi_i \psi_j$, in which the HNFs are: i) long-lived and decay outside the detector, or ii) short-lived and decay inside to $\psi_i \to \psi_j \, \ell^+ \ell^-$, with final state lepton pairs whose energies fall below detector thresholds, would appear identical to a monophoton signature accompanied by missing $\not{E}_T$. The strongest bound of this kind is obtained by the BaBar experiment, excluding explanations of $(g-2)_\mu$ with invisibly decaying dark photons [298]. Dark photons can also be produced in bremsstrahlung events at fixed-target experiments such as NA64 [299, 577, 583]. In this type of experiment, the dark photon signature

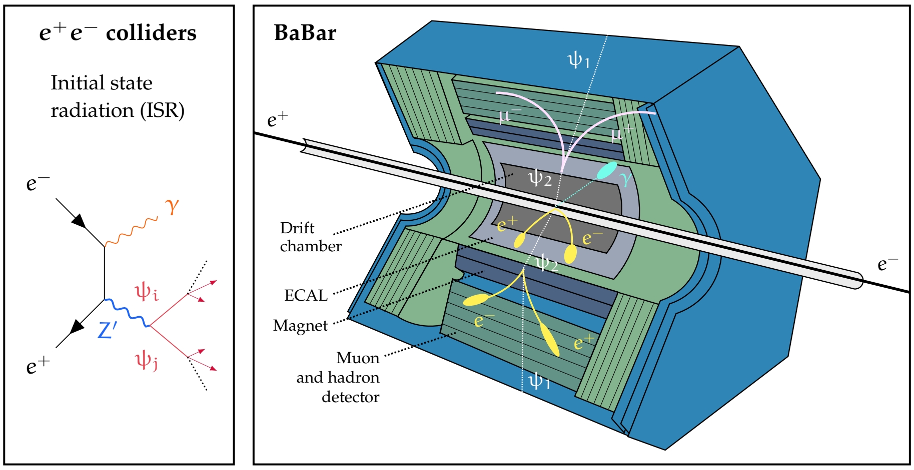

Figure 8.5: The signatures of semi-visible dark photons at e^+e^- colliders. LEFT PANEL: production of a dark photon in association with an ISR photon, $e^+e^- \to \gamma Z'$. RIGHT PANEL: an inner view of the BaBar detector with the displaced, semi-visible decay of the HNFs into charged lepton pairs. In this example, the decay cascade is $Z' \to (\psi_2 \to \psi_1\mu^+\mu^-)(\psi_3 \to \psi_2 e^+e^- \to \psi_1 e^+e^-e^+e^-)$, where ψ_3 decayed promptly. Adapted from [4, fig. 3].

constitutes a large amount of missing energy in the primary electron beam that scatters on the target. Below we discuss the reinterpretation of these two leading constraints on the parameter space of the models discussed in § 8.1. In the following, the vector x represents the set of free model parameters, $x = (\varepsilon, m_{Z'}, \Delta_{21}, \dots)$, that have been varied in the analysis performed.

8.2.1 BaBar monophoton search

Based on the PEP-II asymmetric e^+e^- collider at the Stanford Linear Accelerator Center (SLAC National Accelerator Laboratory), the BaBar experiment searched for single photons accompanied by missing energy and momentum in the process $e^+e^- \to \gamma Z'$. The search was conducted in the 53 fb^{-1} dataset collected between 2007-2008 at the center-of-mass energies $\Upsilon(2S)$, $\Upsilon(3S)$ and $\Upsilon(4S)$. The components of the BaBar detector relevant for our analysis are a charged-particle-tracking system provided by a five-layer, double-sided silicon vertex tracker (SVT) and 40-layer drift chamber (DCH); an electromagnetic calorimeter (ECAL) of 6580 CsI(Tl) crystals. These systems are all contained within a 1.5 T superconducting solenoid magnet. Beyond the superconducting coil is located an instrumented flux return (IFR) barrel that provides muon and neutral hadron identification. An illustration of the detector and the HNF signatures is shown in fig. 8.5.

Event generation

Using our own MC event generator, we simulate the production of dark photons at BaBar in the process $e^+e^- \to \gamma Z'$ at a center-of-mass energy $\sqrt{s} \approx 10\,\text{GeV}$. We boost and rotate to the laboratory frame, considering that the e^+e^- collision frame is itself already boosted with respect to the laboratory by $\beta_z \approx 0.5$. In the laboratory frame, we take the z-direction to be aligned with the direction of e^+e^- collision. The experiment employs a primary selection cut on the photon angle to suppress Standard Model backgrounds, $|\cos(\vartheta^*_\gamma)| < 0.6$. To a good approximation, the Z' decay to HNF pairs is prompt upon production. However, the HNF can travel before decaying, and the distance traveled is modeled by random sampling an exponential distribution according to its decay width. We simulate the decays $Z' \to e^+e^-$, $\mu^+\mu^-$, and $\pi^+\pi^-$ according to their differential decay rates, taking into account the differences in the decay kinematics of Majorana and Dirac particles. As the original analysis searched for single photons and vetoed additional activity in the detector above a certain energy, we introduced a set of veto criteria to dispense those events that would not have passed the event selection.

Monophoton selection

An $e^+e^- \to \gamma Z'$ event passing the initial monophoton selection is vetoed if, anywhere along the decay chain, a charged particle is produced in an instrumented region of the detector, i.e., within the SVT, DCH, ECAL, or IFR regions, and satisfies both of the following conditions:

1. for e^+e^- pairs with angular separation $\vartheta_{\text{sep}} > 10°$, the energy of each electron exceeds BaBar's energy threshold to resolve charged particle tracks, $E_\pm > 100\,\text{MeV}$. For overlapping e^+e^- pairs with $\vartheta_{\text{sep}} < 10°$, we require $(E_+ + E_-) > 100\,\text{MeV}$;

2. the polar angles, ϑ_{pol}, of the electrons individually, or as a pair, are sufficiently wide that the electrons do not escape along the beam pipeline, $17° < \vartheta_{\text{pol}} < 142°$.

The criteria above amount to a statement that all HNF decays that occur inside the detector and produce charged lepton final states that leave visible tracks are vetoed.

The threshold is assumed to be a step function with 100 % detection efficiency above $E_{\text{threshold}}$ and 0 % below it. Realistically, the final state leptons can escape detection even if their energy is large, as leptons can escape between the active materials in the detector. This effect requires a more detailed description of the geometry and particle propagation model, which is beyond the capabilities of our simulation. Nevertheless, we expect this will not significantly change our conclusions, as the leptons are always produced in pairs and follow bent trajectories due to the magnetic field, especially at low energies.

Recasting the bound

To derive their bound, BaBar assumed an invisibly decaying dark photon:

$$\sigma^{\text{BaBar}}_{e^+e^-\to\gamma+\text{inv.}}(x) = \sigma_{e^+e^-\to\gamma Z'}(x) \times \mathcal{B}(Z' \to \text{inv.})\,, \tag{8.33}$$

with $\mathcal{B}(Z' \to \text{inv.}) = 1$. To reinterpret the bound for a semi-visible dark photon, we introduce a factor P^{inv} that accounts for the probability that decays of semi-visible dark photons produced alongside ISR appear invisible and contribute to the monophoton dataset:

$$\sigma^{\text{BaBar}}_{e^+e^-\to\gamma+\text{inv.}}(x) = \sigma_{e^+e^-\to\gamma X}(x) \times P^{\text{inv}}(x)\,, \tag{8.34}$$

where X is the semi-visible dark photon. From eq. (8.33) and eq. (8.34), we may obtain the relation:

$$\varepsilon^{\text{BaBar}} = \varepsilon\, g_D \sqrt{P^{\text{inv}}(x)}\,, \tag{8.35}$$

where $\varepsilon^{\text{BaBar}}$ is the bound on the kinetic mixing parameter obtained by BaBar. We may define the function P^{inv} as follows

$$P^{\text{inv}}(x) = 1 - P^{\text{veto}}(x) = 1 - \frac{N^{\text{veto}}(x)}{N(x)}\,, \tag{8.36}$$

with N being the total number of events that pass the initial monophoton selection, and N^{veto} the subset of events that are vetoed according to the criteria set out above. To recast BaBar's monophoton limit, we solve eq. (8.35) for ε at each value of x. The function P^{inv} contains all model dependencies, including the HNF masses and any mixing parameters. The results of our recast are given in § 8.3 for all benchmark points of interest.

Relation with Belle-II limits

Because of the similar geometries of BaBar and Belle-II, we do not include Belle-II limits, see § 4.3.6 in our recast analyses: a strong relaxation of BaBar would lead to a similar effect in Belle-II, which is, in addition, a more hermetic detector.

8.2.2 NA64 dark photon searches

The fixed-target experiment NA64 searches for dark sector particles at the CERN Super Proton Synchrotron, employing a 100 GeV electron beam. The main search strategy relies on the fact that invisible dark photons can carry away a large amount of missing energy in hard electron-nucleus bremsstrahlung

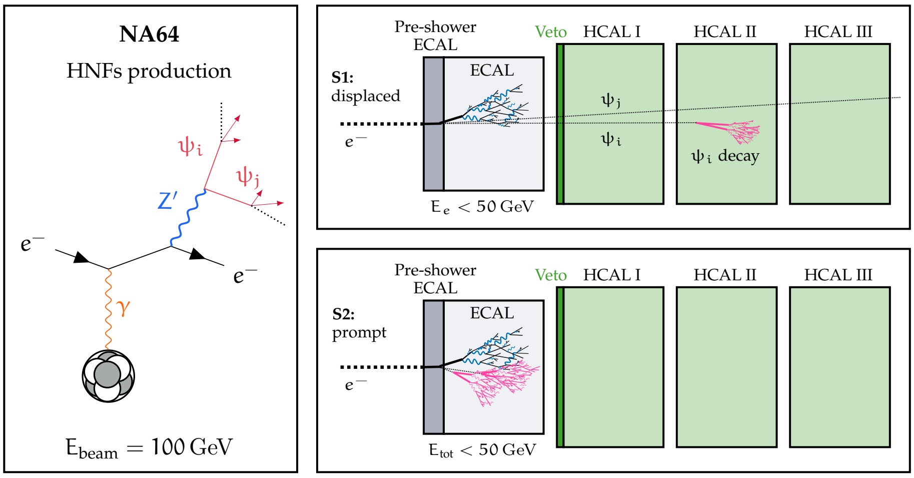

Figure 8.6: The signatures of semi-visible dark photons at the NA64 experiment. **LEFT PANEL:** production process of the HNFs. **TOP RIGHT PANEL:** the first kind of signature with a displaced vertex already considered in [583]. **BOTTOM RIGHT PANEL:** the prompt decay signature that NA64 can use to constrain regions of parameter space where the HNFs are promptly decaying. Image not in scale. Adapted from [4, fig. 5].

events [295, 299, 577, 580, 582],

$$e^- \mathcal{N} \to e^- \mathcal{N} Z' , \quad Z' \to \text{ inv.}, \tag{8.37}$$

where $\mathcal{N}$ is the target nucleus in the fixed target. Like in monophoton searches, the bremsstrahlung signal is proportional to ε^2.

The main parts of the detector relevant to our analysis are:

- the ECAL, which also works as the active beam dump, made of Pb+Sc layers, with an average photon conversion length of $X_0 = 1.175$ cm;
- a large high-efficiency veto counter downstream of the ECAL;
- a hadronic calorimeter (HCAL), made of three different modules.

The search for invisible decays of Z' [299] was conducted on the total sample of electrons on target (EOT) collected during the period 2016–2018, $n_{EOT} = 2.74 \times 10^{11}$.

NA64 also searched for semi-visible dark photon decays assuming the iDM model [583]. In this search, they considered the same data collected in the period 2016–2018, performing a recast-based analysis resembling that of their search for axion-like particles [610], targeting visible final states coming from the dark photon decay chain and putting a model-dependent constraint on the kinetic mixing parameter.

Event generation

We simulated the production of dark photons and the detection of e^+e^- pairs in the NA64 detector with a fast MC generator. From a comparison of the sensitivity curves with the limits obtained in [6], we find that our projections are comparable to the limits obtained using a proper GEANT4 detector simulation, with minor discrepancies that can be attributed to the complete description of the detector geometry, shower development, and energy collection within the different detectors. The complete GEANT4 detector simulation, along with a discussion of the latest NA64 constraints on several semi-visible dark photon models, can be found in [6].

We simulate bremsstrahlung events, producing a Z' with an electron beam at energy $E_{\text{beam}} = 100\,\text{GeV}$. We consider the electron beam energy to be unaffected by any energy losses happening when entering the ECAL, so that E_{beam} can be considered constant. The beam is considered to impact the ECAL at coordinates $x = y = z = 0$. The energy of the Z' is distributed according to the following formula, obtained by applying the improved Weizsäcker–Williams (IWW) approximation [611]:

$$\frac{d\sigma}{dx} \propto \left(m_{Z'}^2 \frac{1-x}{x} + m_e^2 x \right)^{-1} \left(1 - x + \frac{x^2}{3} \right), \tag{8.38}$$

where $x = E_{Z'}/E_{\text{beam}}$, and the Z' is in the z direction. After radiating a Z', the beam electron (or main electron) will have energy $E_e = E_{\text{beam}} - E_{Z'}$, and will shower inside the ECAL completely. The Z' decays promptly into a pair of HNFs, which are boosted and rotated to the lab frame according to the Z' energy. Each HNF will then decay according to its decay modes. The simulation automatically handles the decay of the secondary HNFs in the same way. The lightest HNF from each model is considered stable with respect to the size of the detector. We assume a simplified shower development model for the e^+e^- pairs produced inside the ECAL. The energy loss can be computed with an exponential law:

$$\frac{dE}{dz} = -\frac{E}{X_0} \Rightarrow \Delta E(z) = E(z) - E_0 = E_0 \left[1 - \exp\left(-\frac{z - z_0}{X_0} \right) \right], \tag{8.39}$$

where z_0 is the production point of the pair. For pairs detected inside the HCAL, we assumed each pair is able to shower completely inside it. Given the high energies of the Z', the e^+e^- pairs are highly boosted and collimated. We may then treat each pair as a single particle with energy $E(z_0) = E_{e^+}(z_0) + E_{e^-}(z_0)$.

Each event is made of invisible final states (the stable HNFs) and visible energy (the e^+e^- pairs):

$$e^- \mathcal{N} \to e^- \mathcal{N} Z' , \tag{8.40}$$

$$Z' \to (\psi_i \to (\psi_k \to \dots)\, e^+e^-)(\psi_j \to (\psi_l \to \dots)\, e^+e^-) . \tag{8.41}$$

We check the visible energy collected in each event against the veto criteria applied to the different regions of the detector to see if the event is recorded as signal for the experiment.

Semi-visible selection (S1)

This signature corresponds to the one employed by NA64 to study semi-visible dark photon decays in the framework of the iDM model [583]. In this work, we recast the invisible dark photon limits also to the more complex models presented in § 8.1.

The following selection criteria were applied, according to the expected signal yield coming from this model, relying on the decay of the heaviest HNF $\psi_i = \psi_2$ or ψ_3 into a single e^+e^- pair:

1. ψ_i is expected to decay inside the HCAL: in particular, the analysis targets a fiducial HCAL volume composed by the last two modules of the HCAL detector in which a consistent amount of energy coming from a single e^+e^- pair is expected to be detected;

2. events with any other activity happening before the fiducial HCAL volume are vetoed;

3. events with more than one visible decay vertex in the fiducial HCAL volume are vetoed.

Additionally, in case ψ_i decays beyond the HCAL, no other significant energy deposits are expected in the full detector, and the event resembles an invisible dark photon event.

This proposed analysis is tailored to the iDM model, focusing in particular in the parameter space where the ψ_2 lifetime is comparable to the size of the detector. It rapidly loses sensitivity in the high mass region where ψ_2 decays promptly. Other models involving large mass splittings between HNFs are also characterized by a shorter lifetime, due to $c\tau \propto \Delta^{-5}$, so this search will also be less sensitive to the high mass region.

Invisible selection (S2)

The analysis focused on detecting invisible decays of Z' by constraining the amount of visible energy collected. The set of energy cuts relies on the search strategy applied by the NA64 experiment to detect dark photon events containing missing energy, while limiting the possible background [299]:

1. **pre-shower ECAL.** The total energy collected in the first layers of the ECAL should be compatible with the deposit expected for a primary electron.

2. **ECAL.** The total energy collected, E_{ECAL}, including both the main electron and the e^+e^- pairs, is compared against the missing energy threshold chosen by the experiment:

$$E_{ECAL} > 50\,\text{GeV}\,. \tag{8.42}$$

3. **Veto counter.** We do not expect any activity in the veto, in order to record an invisible event. In the case of semi-visible dark photon models, a particle can reach the veto in two cases:

   - if they are produced inside the ECAL, they can shower until its end, releasing the remaining energy in the veto;
   - if they are produced between the end of the ECAL and the veto, they will release their energy inside the veto.

   We further assume that if a particle happens to reach the veto, it is able to release all of its energy inside it. This can be justified by the fact that the imposed veto threshold is sufficiently low that even the softest e^+e^- pairs we expect to produce would be able to trigger an event. Moreover, the thickness of the veto counter is large enough to guarantee a consistent energy deposit by the e^+e^- pairs.

4. **HCAL**: For an invisible event, no activity is expected inside the HCAL. Particles created between the veto and the HCAL or in the empty space between the three HCAL modules will be intercepted by the HCAL, eventually. The HCAL detector of NA64 is sufficiently long so that we can assume that any pair created inside it has enough space to shower completely, depositing its entire energy inside the HCAL. This approximation does not apply only to the small number of particles created at the very end of the HCAL.

It should be noted that in performing the recast of the invisible selection, we have assumed that NA64 is not able to distinguish the e^+e^- showers due to short-lived HNF decays in the ECAL from the main electron beam. We assume that the total energy deposition in the ECAL for these cases is the aggregate of the e^+e^- energy and beam electron energy. Given the NA64 sensitivity to these prompt decays has not been previously studied, we take this recast constraint as a projection of NA64's potential sensitivity to decays of this kind. The latest constraints from NA64 [6] tackle this region and show good agreement with our projections.

Recasting the bound

The derivation of the recast bound is done similarly to the BaBar simulation. We start by considering the bound obtained by the invisible dark photon search performed in [299], which we call $\varepsilon^{\mathrm{NA64}}$. In addition, we extrapolated the bound above 1 GeV, through a 2-degree polynomial fit. Our toy MC yields the probability of obtaining an invisible event assuming the semi-visible dark photon decay P^{inv}. The recast bound can be found by solving the following equation, which matches eq. (8.35) discussed for the BaBar recast, with x being the set of model parameters:

$$\varepsilon^{\mathrm{NA64}} = \varepsilon\, g_D \sqrt{P^{\mathrm{inv}}(x)}\,. \tag{8.43}$$

8.2.3 Other limits from beam dumps

In addition to BaBar and NA64, other beam dump experiments have searched for dark sector particles. We considered E137 and NuCal limits, that were recast in the literature in the context of iDM models in [585, 595, 612]. We did not perform simulations of these experiments, but we rescaled the upper and lower bounds on the basis of few assumptions. In the small coupling regime, corresponding to the upper bound, the rate of decay-in-flight is proportional to the product between the number of particles produced and the decay rate into the signal channels we are interested on, namely $\psi_i \to \psi_j \ell^+\ell^-$. The reinterpretation of the bounds is done by matching our models' production and detection rates with the ones coming from the iDM model. For models with more than one HNF, namely the mixed-iDM or i2DM models, more productions channels for ψ_2 are available than in the original study, for example pair production in meson decays or bremsstrahlung. To account for this effect, we multiply the signal rate by the respective Z' vertices and the corresponding long-lived particle decay rate. For example, considering the recast from iDM to mixed-iDM or i2DM, we take

$$\frac{\varepsilon^4_{\mathrm{iDM}}}{\varepsilon^4_{\mathrm{new}}} = \frac{\alpha_D^{\mathrm{new}}}{\alpha_D^{\mathrm{iDM}}} \sum_{i\geqslant j} |V_{ij}|^2 \frac{\widehat{\Gamma}^{\mathrm{new}}_{\psi_i\to\psi_{i-1}e^+e^-} + \widehat{\Gamma}^{\mathrm{new}}_{\psi_j\to\psi_{j-1}e^+e^-}}{\widehat{\Gamma}^{\mathrm{iDM}}_{\psi_2\to\psi_1 e^+e^-}}\,, \tag{8.44}$$

where $\widehat{\Gamma}$ are the decay rates where all the coupling prefactors have been removed. In this case, the prefactor $\alpha_D|V_{ij}|^2$ takes care of rescaling the production of different dark states at the source or target, and the decay rate ratios account for the different mass splitting and mediator masses. There are some assumptions involved in this procedure, namely i) effects of the mass splitting on the kinematics have not been taken into account, ii) decay cascades have been neglected, iii) the decay of the HNFs is dominated by the decay into the closest lighter HNF, so that processes like $\psi_i \to \psi_{i-2}e^+e^-$ have been neglected.

Table 8.2: The benchmark models for semi-visible dark photons used in this chapter. The type of model considered is indicated in the second column. We define $r \doteq m_1/m_{Z'}$ and $\Delta_{ij} \doteq (m_i - m_j)/m_j$. The dark photon coupling vertices V_{ij} can be found in eq. (8.3). Adapted from [4, tab. I].

BP	model	r	Δ_{21}	Δ_{32}	α_D	V_{11}	V_{21}	V_{22}	V_{31}	V_{32}	V_{33}
								$/10^{-2}$			
1a	iDM	1/3	0.5		0.5	0	1	0	0	0	0
1b	iDM[585]	1/3	0.4		0.1	0	1	0	0	0	0
2a	mixed-iDM	1/3	0.3		0.5	0	$s_\alpha\, c_\alpha$	c_α^2		$(\alpha = 8°)$	
2b	mixed-iDM	1/3	0.3		0.5	0	$s_\alpha\, c_\alpha$	c_α^2		$(\alpha = 4°)$	
3a	i2DM	1/3	0.4		0.5	s_β^2	$s_\beta\, c_\beta$	c_β^2		$(\beta = 8.6°)$	
3b	i2DM	1/3	0.4		0.5	s_β^2	$s_\beta\, c_\beta$	c_β^2		$(\beta = 4.6°)$	
3c	i2DM	1/3	0.4		0.5	s_β^2	$s_\beta\, c_\beta$	c_β^2		$(\beta = 2.3°)$	
3d	i2DM	1/3	0.4		0.5	s_β^2	$s_\beta\, c_\beta$	c_β^2		$(\beta = 1.1°)$	
4a	3 HNFs[377]	0.11	2.44	0.54	0.3	0	3.9	0	0	99	0
4b	3 HNFs[377]	0.16	2.44	0.54	0.3	0	3.9	0	0	99	0
4c	3 HNFs[377]	0.15	0.85	0.77	0.3	0	0.10	0	0	99	0
5	3 HNFs[377]	0.16	0.573	0.586	0.3	0.40	7.8	8.3	2.8	98	69

The lower bound recast, corresponding to the upper line, is done by matching the total lifetimes of the lightest unstable particles of the original bound to the one in our models. This corresponds to the simple relation: $\widehat{\Gamma}_{\psi_2}^{\text{new}} = \widehat{\Gamma}_{\psi_2}^{\text{iDM}}$. This is an approximate solution, nevertheless, the lower-limit regime is characterized by a large number of particles produced, while the probability of an unstable state decaying within the detector is exponentially suppressed. For E137 (scatter), the recast is similar to eq. (8.44), but we rescale the scattering rate of dark particles instead, neglecting differences in mass splitting.

8.3 Results

We study the dark sector models presented in § 8.1, implementing the recast limits of BaBar and NA64. As the parameter space is very large, we fix representative values for the gauge coupling g_D and the masses of the HNFs, parametrized in terms of $m_1/m_{Z'}$ (known as r in the literature) and Δ_{ij}. We take α_D to be in the range from 0.1 to 0.5 as we are interested in the fast decays of the HNFs while maintaining perturbativity. Except for the 3 HNF models, we fix the mass ratio r to be 1/3 for most of the benchmarks, a standard value in the literature. The values Δ_{ij} have been set to minimize the lifetime of the HNFs and maximize the amount of visible energy deposited by their decay products in the BaBar and NA64 detectors. The benchmark points, along with the values of their parameters, are summarized in tab. 8.2.

The constraints from NA64 are labeled according to the dark photon signature.

- **NA64 (S1)** (solid line): described in [583], a model-dependent search for iDM was performed in the context of the semi-visible dark photon signature of the model.
- **NA64 proj. (S2)** (dash-dotted line): described in [299], this bound is on invisible dark photon decays. Our recast expresses the potential future sensitivity of the experiment towards a dedicated semi-visible dark photon search, showing the capability to constrain the parameter space in a model-independent way.

We also show the model-dependent bounds from NuCal [595, 613, 614], E137 (scatter) [585, 595, 612], and the model-independent limits discussed in § 4.3. Notice that the bounds from meson decays assumes the dark photon to be invisible, so they would be modified in the case of the semi-visible models of interest. However, we follow the aggressive strategy of showing these limits without modifications in all our plots.

In addition, for benchmarks BP1, BP2, and BP3, the lightest HNF can be a dark matter candidate. In this case, we compute the relic density of the model, which needs to be characterized by a small value of Δ_{ij}, to minimize the Boltzmann suppression of coannihilations.

8.3.1 Inelastic Dark Matter (BP1a, b)

The results for the iDM benchmarks are shown in fig. 8.7, expressed in the ε vs $m_{Z'}$ plane. In BP1a, we see a significant relaxation of the NA64 and BaBar bounds, with a sizable Δa_μ preference region now open. Due to a large dark sector coupling, $\alpha_D = 0.5$, the decay rates of the HNFs are enhanced, allowing for more semi-visible events in the detectors. Benchmark BP1b corresponds to the choice of parameters used in [585]. Assuming the lightest HNF, ψ_1, is a dark matter candidate, we find that the correct dark matter abundance can be achieved in both benchmarks BP1a and BP1b.

In BP1b we find a much less significant relaxation of the bounds compared to BP1a, leaving very little open parameter space for a Δa_μ explanation. In particular, we find the BaBar bound to be much more constraining than in [585]. This is predominantly due to the difference in selection criteria used in the two analyses. In [585], an energy cut of 60 MeV is applied to charged particles produced in semi-visible Z' decays. In this work, we take the larger value of 100 MeV, corresponding to the energy threshold used in the experimental analyses to veto additional tracks in the BaBar drift chamber [298, 615]. The impact of the higher energy threshold is to veto a greater proportion of the semi-visible decays, leading to a stronger constraint from BaBar. In addition, we cut on the polar angle of the charged lepton pairs, which allows us to exclude events where leptons are produced in the direction of the beam pipeline. We find the fraction of these pipeline events to be small and that the relative strength of the BaBar bound is predominantly a consequence of the energy threshold. In contrast to the more conservative analysis of [586], in which a threshold energy of 150 MeV is taken, a very tiny region of preference for Δa_μ remains open at the 2σ level for $m_{Z'} \approx (300 \text{ to } 500)$ MeV.

In both BP1a and BP1b, we find that a search for promptly decaying HNFs at NA64, with signatures of the type S2, can cover the newly open Δa_μ parameter space, see also [6]. This region of parameter space is also accessible to other lower-energy e^+e^- colliders, including KLOE/KLOE-2 [616, 617] and BES-III [618].

In the BaBar signal selection, events with charged tracks above 100 MeV were vetoed, justifying our choice for the energy threshold [298]. However, the probability of detection of such low-energy tracks may not be exactly 1, setting an effective energy threshold. Therefore, our hard requirement on the energy of leptons is an important source of uncertainty. In fig. 8.8, we show the effects of changing this value on the BaBar limits for the iDM model in BP1a and BP1b. Increasing the energy threshold makes it more difficult to veto events, leading to a stronger bound. For a threshold larger than 250 MeV, BaBar would cover the entire parameter space allowed by Δa_μ in the case of BP1a, while a threshold of 150 MeV is already sufficient to rule it out completely in BP1b. We note, however, that thresholds exceeding 200 MeV are likely unrealistic as the probability of missing such tracks within the inner BaBar detectors is very small.

To understand whether it is possible to accommodate the different constraints and the relic density, we can inspect the parameter space in α_D vs $m_{Z'}$ and Δ_{21} vs $m_{Z'}$, shown respectively in fig. 8.9 and in fig. 8.10. In fig. 8.9, we fix the value of ε to that required to explain Δa_μ, and we vary α_D and $m_{Z'}$.
Increasing α_D affects the lifetime of ψ_2, making them short-lived and allowing their decays to happen inside the detector, increasing the amount of semi-visible events that can be identified. Both scenarios are strongly constrained by BaBar, NA64, E137, and NuCal, and only a small part of the parameter space is allowed, as shown in fig. 8.9 top. That region is also able to accommodate the dark matter relic density. The two scenarios differ only by the value of the mass splitting Δ_{21}: fig. 8.9 bottom is characterized by a lower value. Decreasing Δ_{21} means that the two HNFs become more degenerate and the lifetime of ψ_2 increases, becoming larger than the size of the detector. This effect reduces the amount of ψ_2 decays happening inside the detector and makes the bound more constraining. The parameter space in fig. 8.9 bottom is indeed entirely constrained.
In fig. 8.10 we fix the value of ε to that required to explain Δa_μ, and we vary Δ_{21} and $m_{Z'}$. In this case, the E137 constraint shown with a thin gray line has been extrapolated at large Δ_{21} value. As discussed previously, decreasing Δ_{21} makes

most of the ψ_2 decays to happen outside the detector. No semi-visible event would be detected in this case, and the bound would resemble the original invisible Z' bound, covering the region in which ε can explain $(g-2)_\mu$. In this case, the NA64 (S1) constraint follows a similar trend as for the BaBar constraint, becoming weaker for larger mass splitting. In the case of NA64 (S2), at large $m_{Z'}$, the experiment loses sensitivity, and the bound becomes naturally weaker, independently of the value of Δ_{21}. This corresponds to the loss of sensitivity in the original invisible bound posed by NA64, caused by a lack of event rate.

Nevertheless, increasing the mass splitting between the two HNFs to accommodate the constraints affects the dark matter relic abundance of ψ_1. A larger mass splitting increases the Boltzmann suppression of ψ_2 number density in the early universe, depleting it faster and suppressing the coannihilation contribution to the cross section. This results in an overabundant scenario, which can be controlled only assuming secluded annihilations within the dark sector, and it is expressed by the parameter space above the relic density line in fig. 8.10. The smaller α_D value in BP1b translates into a shift of the relic density line towards lower Δ_{21}, because of its effect in decreasing the coannihilation cross section. A smaller Δ_{21} ensures a smaller Boltzmann suppression of ψ_2 number density and a larger coannihilation cross section.

It is interesting to notice that the projections shown by the NA64 (S2) line could constrain the free parameter space left in most of the discussed scenarios. The search for promptly decaying HNFs in the detector can address whether this minimal model can simultaneously explain Δa_μ and dark matter.

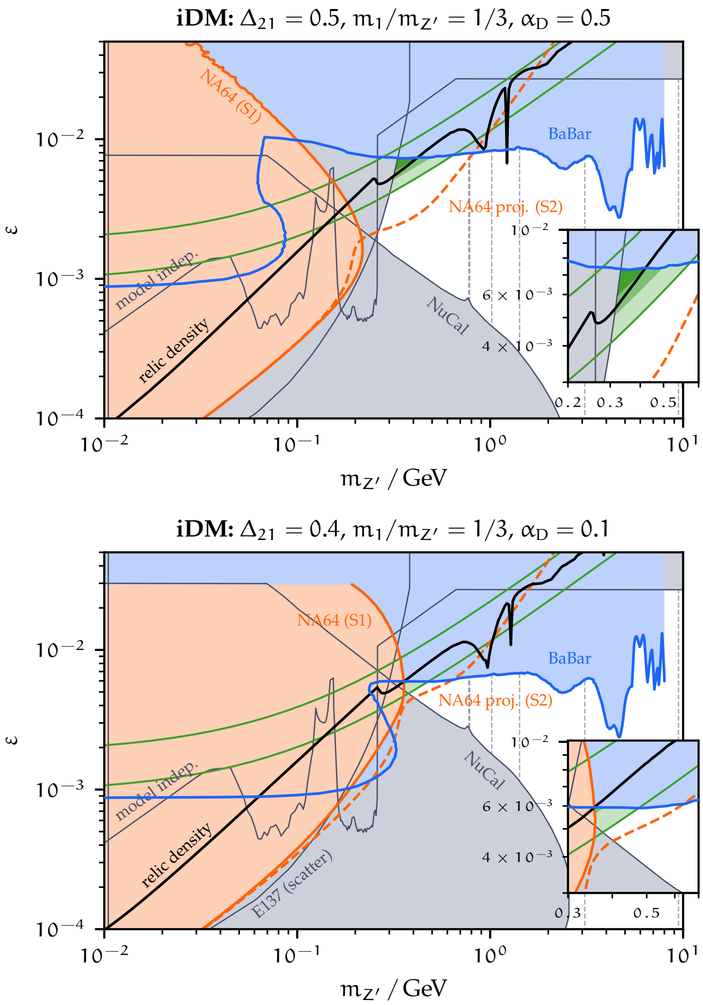

Figure 8.7: The kinetic mixing ε as a function of the dark photon mass $m_{Z'}$ for BP1a (top) and BP1b (bottom), corresponding to the iDM model. We show the Δa_μ-preferred 1, 2, and 3 σ regions in shades of green. The recast constraints from BaBar and NA64 are shown in blue and orange, respectively. The NA64 curves show the recast constraints using the dedicated semi-visible search (solid line), corresponding to those derived using displaced decays (S1 in fig. 8.6), and the projected sensitivity (dashed line) of a search for invisible and promptly-decaying particles (S2 in fig. 8.6). Assuming the lightest HNF to be dark matter, the relic density line is shown in black. Other constraints from $(g-2)_e$, EWPO, DIS, and NA62 are shown with thin gray lines and light gray regions and are referred to as model independent constraints (see § 4.3). The constraint imposed by NuCal and E137 (scatter) are shown with the same style. The masses of vector meson resonances are shown as vertical gray dashed lines.

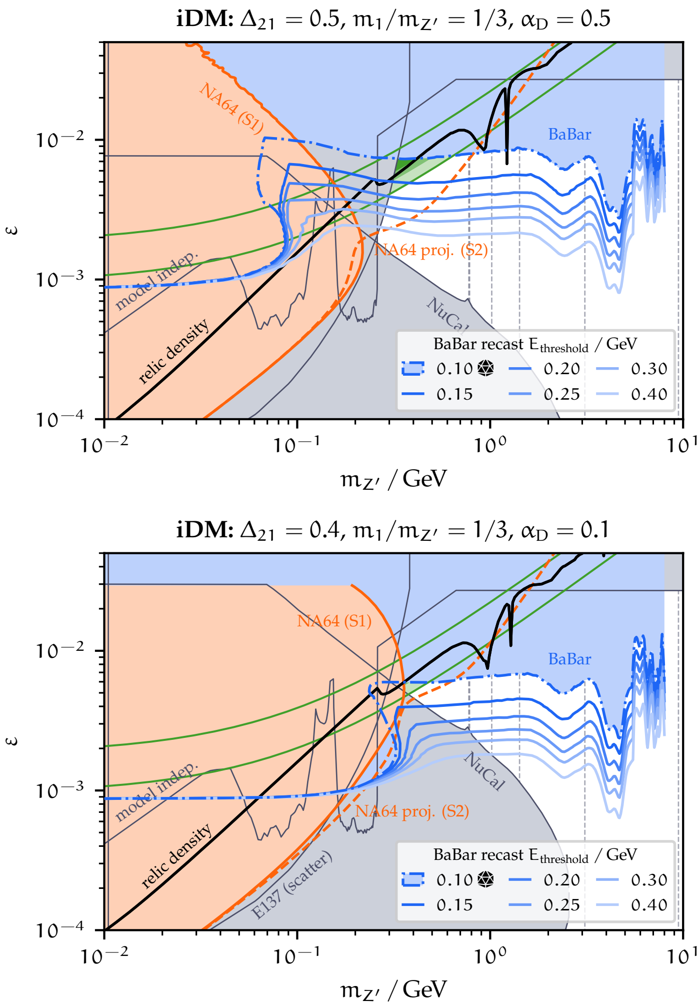

Figure 8.8: Same as fig. 8.7, with the addition of multiple BaBar recast bounds, obtained under different assumptions for the energy threshold for the e^+e^- tracks. The different energy thresholds are represented by shades of blue with the adopted values shown in the legend. The threshold chosen for the analysis performed in this work is marked with a ✪ symbol.

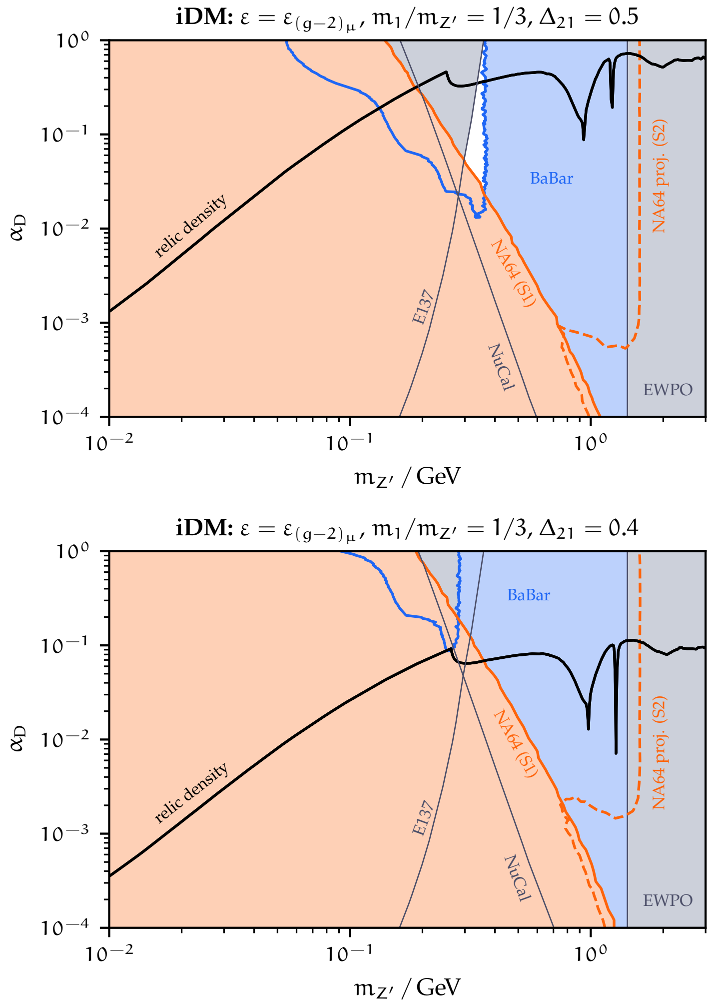

Figure 8.9: Parameter space of α_D vs $m_{Z'}$ for the iDM model, fixing ε to the value needed to explain the Δa_μ, $\varepsilon = \varepsilon_{(g-2)_\mu}$. The mass splitting is fixed at $\Delta_{21} = 0.5$ (top) and $\Delta_{21} = 0.4$ (bottom). The constraints are shown with the same style used in fig. 8.7.

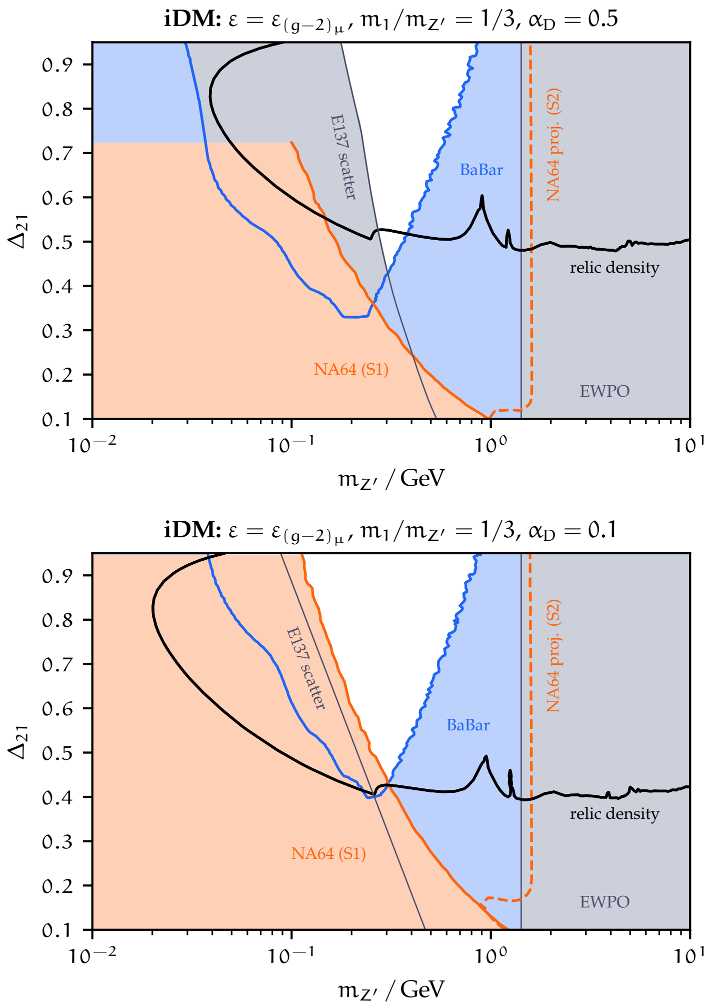

Figure 8.10: Parameter space of Δ_{21} vs $m_{Z'}$ for the iDM model, fixing ε to the value needed to explain the Δa_μ, $\varepsilon = \varepsilon_{(g-2)_\mu}$. The dark coupling is fixed at $\alpha_D = 0.5$ (top) and $\alpha_D = 0.1$ (bottom). The constraints are shown with the same style used in fig. 8.7.

8.3.2 Mixed-inelastic Dark Matter (BP2a, b)

We show the constraints for the mixed-iDM model in fig. 8.11, expressed as ε vs $m_{Z'}$ constraints. This model main feature, which is also expected in BP3, is an enhanced Z' decay branching ratio into $\Psi_2\Psi_2$. The branching ratio to $\Psi_2\psi_1$ is suppressed by the mixing angle α, and the one into two $\psi_1\psi_1$ is forbidden by the C symmetry. Because most dark photon events come accompanied by two unstable particles, the additional energy deposition is missed even less often, relaxing the bounds further.

The relic density of ψ_1 for this model depends strongly on the efficiency of coannihilations and coscattering processes. In the realization shown in fig. 8.11, we find that a simultaneous explanation of Δa_μ and dark matter relic density, along with the constraints discussed, can be achieved in the region $0.9\,\mathrm{GeV} \lessapprox m_{Z'} \lessapprox 1.2\,\mathrm{GeV}$ for BP2a. In the case of BP2b, the coannihilation processes are inefficient due to the smaller α, so that ψ_1 is overabundant in the region of parameter space that can explain Δa_μ.

Additionally, we report an analysis on the Δ_{21} and α parameters, showing the constraints in the Δ_{21} vs α plane in fig. 8.12, fixing the mass of the dark photon to $m_{Z'} = 1,\ 1.25$ and $2\,\mathrm{GeV}$ and $\varepsilon = 0.01, 0.02$ and $\varepsilon_{(g-2)}$. For some combinations of the parameters, the NA64 constraints are not present because they are too weak, given the efficient relaxation that this model can provide. The dependence on the angle α is expressed by the branching ratio: a larger value favors a larger branching ratio to the $\Psi_2\psi_1$ channel, with respect to $\Psi_2\Psi_2$; it has the effect of decreasing the amount of visible energy, and ultimately the possibility to detect a semi-visible event. On the contrary, a smaller α affects the decay rate of Ψ_2, suppressing its decay, and recovering the original invisible bound. The behavior of the constraints is similar to BP1 for what concerns Δ_{21} dependence: a larger Δ_{21} means a shorter Ψ_2 lifetime, and the energy of its decay is released inside the detector. On the other hand, a lower Δ_{21} resembles the case of fully invisible dark photon decays, as the lifetime becomes larger than the size of the detector.

The relic density lines in fig. 8.12 identify the overabundant regions, corresponding to high Δ_{21} and low α. In that case, coannihilation and coscattering processes become too inefficient. For small Δ_{21}, the choice of mixing angle does not have a strong impact, as coscattering remains efficient for longer, and the self-annihilations of Ψ_2 set the relic abundance of ψ_1. For large α the dependence on Δ_{21} on the relic density is relaxed: the enhanced coscattering ratio obtained with a larger α allows affording a larger Δ_{21} value before ending up in an underabundant scenario. The kink present in the dark matter relic density for $m_{Z'} = 1\,\mathrm{GeV}$ is due to the presence of a resonance region, that can be observed also in fig. 8.13. In that figure we show the trend of the relic density line for different choice of the parameters of the model, along with the $3\,\sigma$ region accounting for the Δa_μ explanation.

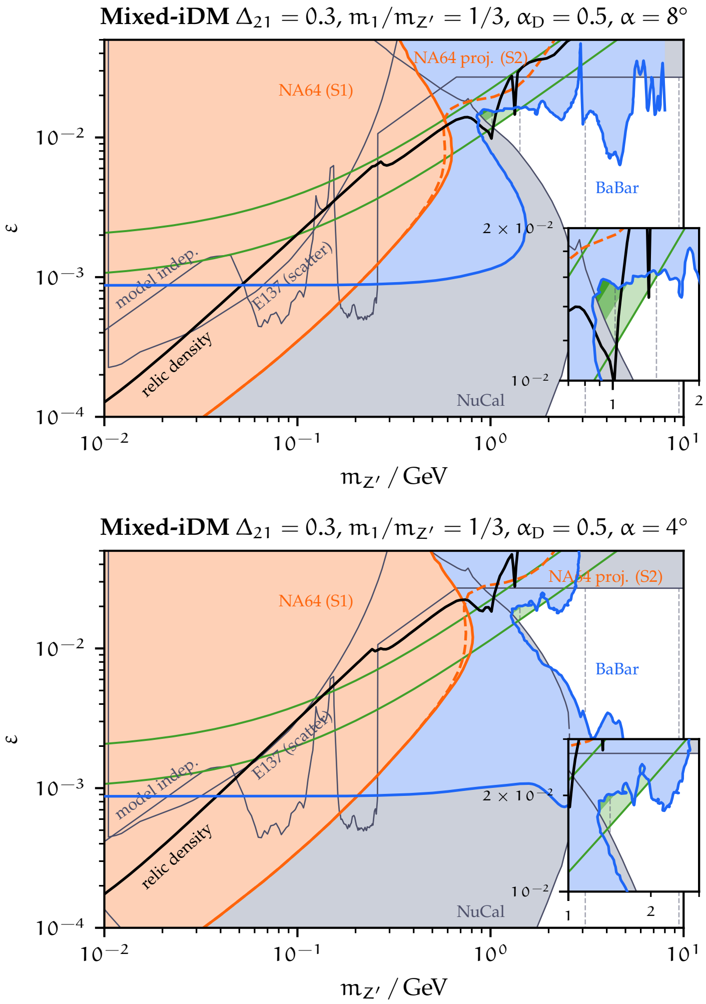

Figure 8.11: Same as fig. 8.7 but for BP2a (top) and BP2b (bottom), corresponding to the mixed-iDM model. The two panels represent two different realizations of the model, obtained by varying the α mixing angle.

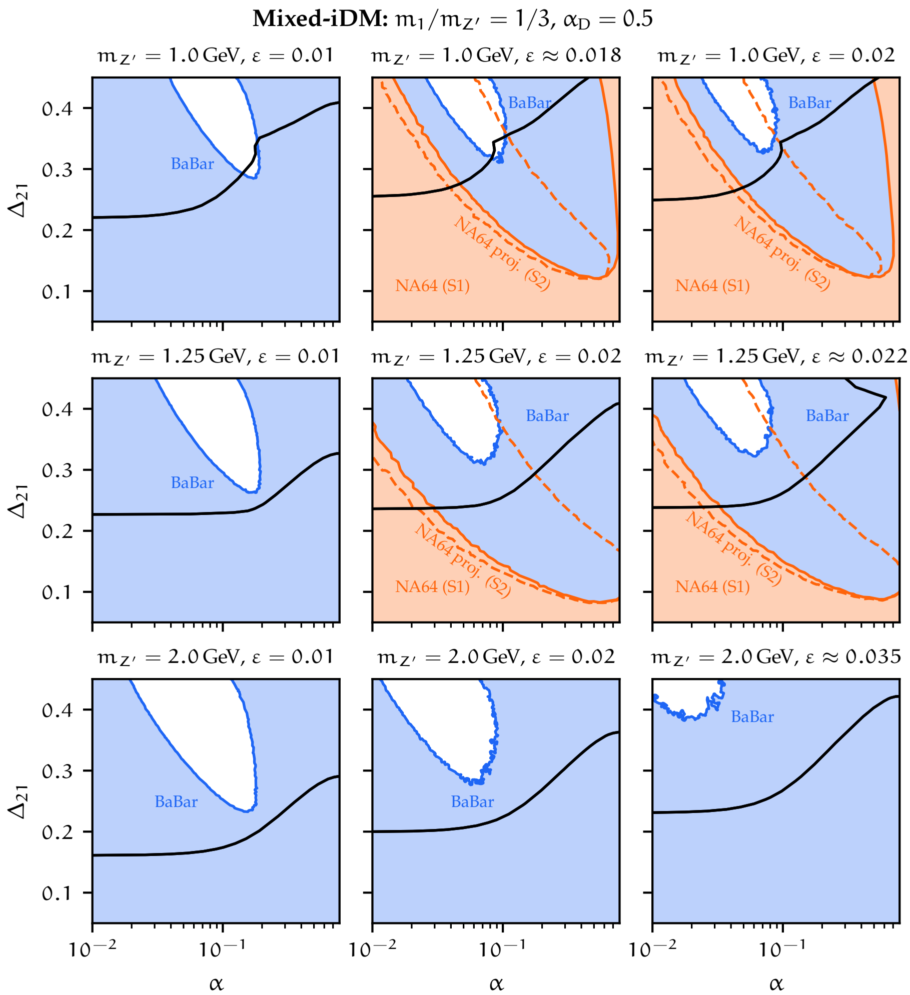

Figure 8.12: Parameter space of the mixed-iDM in the plane Δ_{21} vs the mixing angle α. The parameter $m_{Z'}$ has been fixed to 1, 1.25 and 2 GeV (column-wise), while the kinetic mixing ε has been chosen among 0.01, 0.02 and $\varepsilon_{(g-2)_\mu}$ (row-wise), corresponding to the central value of the Δa_μ explanation. BaBar and NA64 recast bounds are shown with the same style used in fig. 8.7.

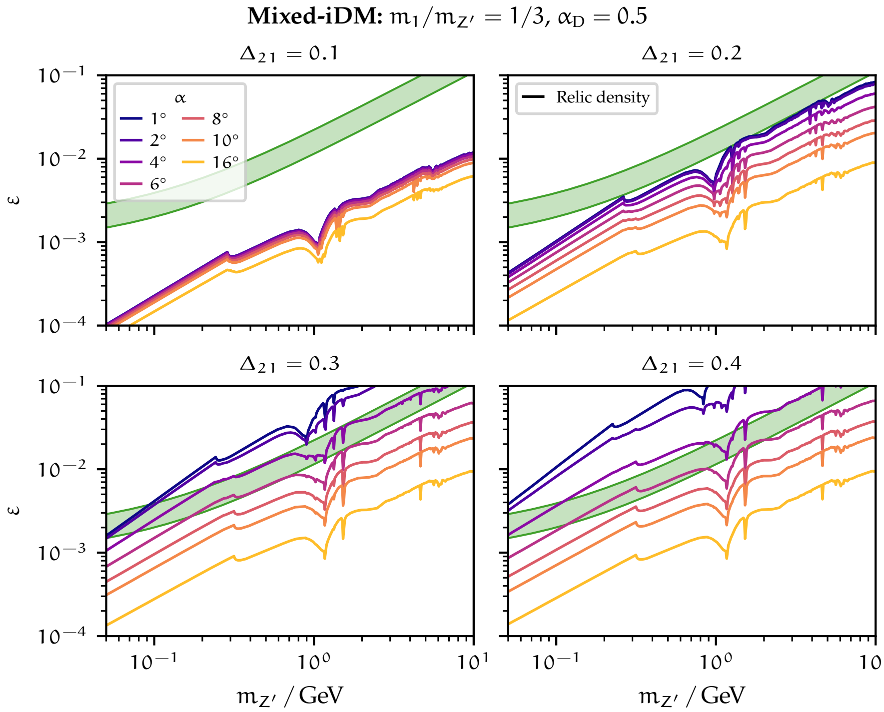

Figure 8.13: The relic density (solid lines) in the parameter space for the mixed-iDM model in the plane of kinetic mixing ε vs dark photon mass $m_{Z'}$ for fixed values of $\alpha_D = 0.5$, $r = m_1/m_{Z'} = 1/3$, and Δ_{21}. CMB limits are not applicable as the dark matter self-annihilation $\psi_1\psi_1 \to f^+f^-$ is forbidden in the C symmetric limit. The Δa_μ 3σ preferred region is shown as a green band. Adapted from [4, fig. 12].

8.3.3 Inelastic Dirac Dark Matter (BP3a–d)

We show the constraints for the i2DM model in figs. 8.14 and 8.15, expressed as ε vs $m_{Z'}$ constraints. Similarly to the previous model, the constraints are relaxed, and a new region of the parameter space opens up. This model is characterized by an enhanced dark photon decay rate to the channel $\Psi_2\Psi_2$ as it happens in the case of the mixed-iDM model. The rate into the channels $\Psi_2\Psi_1$ and $\Psi_1\Psi_1$ is suppressed by respectively a factor β and β^2. Differently from the mixed-iDM case, this model allows for dark photon decays to $\Psi_1\Psi_1$ channel. A larger branching ratio to the heaviest HNF increases the possibility to detect a semi-visible event in the detector, given the larger abundance of those particles releasing e^+e^- pairs after their decay.

The relic density of Ψ_1 for this model depends on the efficiency of coannihilation and coscattering processes. The main difference with respect to the previous model is that it is not possible to evade the CMB bounds, because of the possibility for the dark matter candidate Ψ_1 to annihilate through the vertex $\Psi_1\Psi_1$. Even though this vertex is suppressed, it can have a sizable contribution to late time annihilations, injecting additional energy into the CMB. In the realizations shown in figs. 8.14 and 8.15, we find that, despite the relaxation of the main constraints, the CMB bounds are unavoidable and can exclude large parts of the parameter space, with the only exception being the choice of a small β parameter, as represented by benchmarks BP3c and BP3d. This choice corresponds to suppress further the channels $\Psi_2\Psi_1$ and $\Psi_1\Psi_1$. However, it has an impact on the relic abundance of Ψ_1, because it suppresses the contributions of coscatterings and annihilations, resulting in an overabundant scenario, which can be set under control only assuming secluded annihilations within the dark sector.

Additionally, the relic density depends also on Δ_{21}, because that parameter affects the Boltzmann suppression of $\Psi_2\Psi_1$ coannihilations. It is interesting to understand the interplay of Δ_{21} and β for the different constraints. In fig. 8.16, the bounds are shown in a Δ_{21} vs β plane, fixing the mass of the dark photon to $m_{Z'} = 1,\ 1.25$ and $2\,\text{GeV}$ and $\varepsilon = 0.01, 0.02$ and $\varepsilon_{(g-2)}$. We can draw similar conclusions as the ones discussed for the mixed-iDM model in fig. 8.12, with the difference that the x-axis now represents the parameter β. In addition, the CMB constraints are shown: their exclusion region corresponds to large β values, because of the enhancement of $\Psi_1\Psi_1$ annihilation rate. Regarding the relic density, we can draw a similar conclusion as for benchmarks BP2a and BP2b. The overabundant region corresponds to large Δ_{21} and low β, due to both inefficient coannihilations and suppressed Ψ_1 self-annihilations. However, the dependence on β is stronger due to the presence of Ψ_1 self-annihilations, which can dominate over coannihilations in depleting the dark matter density. For this reason, the relic density is underabundant for large β independently on the value of Δ_{21}: the coannihilator does not play a crucial role anymore in the determination of the dark matter relic density. Nevertheless, the small regions in which dark matter density is underabundant and compatible with other constraints are excluded by the CMB bounds. The trend of the relic density for different choice of the parameters of the model, and the interplay with CMB limits, is shown in fig. 8.17, along with the $3\,\sigma$ region accounting for the Δa_μ explanation.

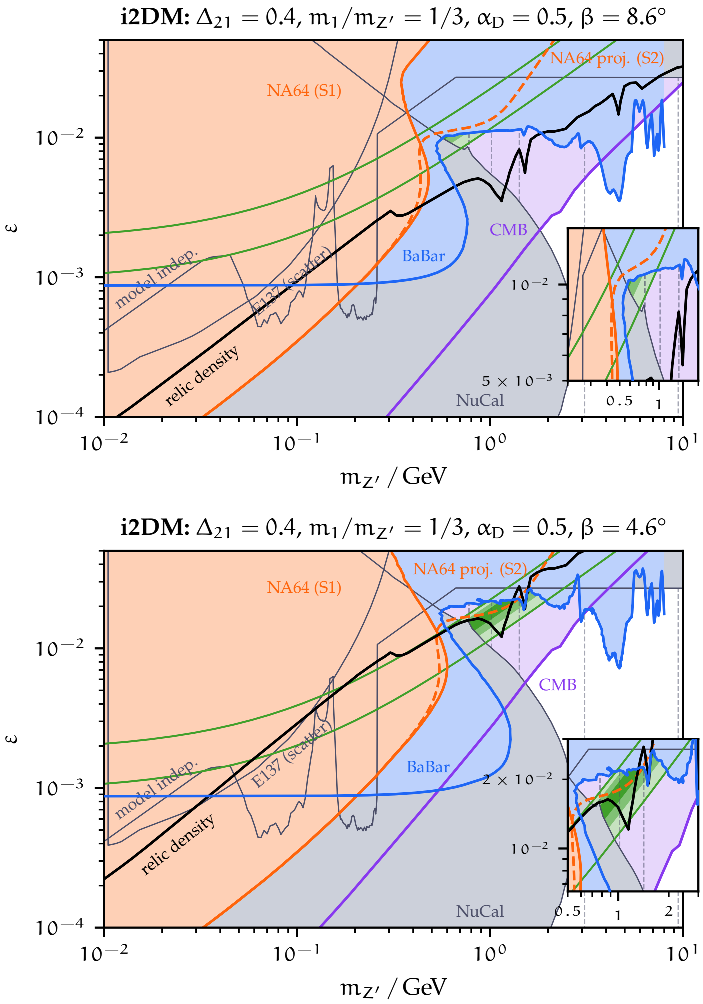

Figure 8.14: Same as fig. 8.7, but for BP3a (top) and BP3b (bottom), corresponding to the i2DM model. The panels represent the same choice of parameters, varying solely the mixing angle, β.

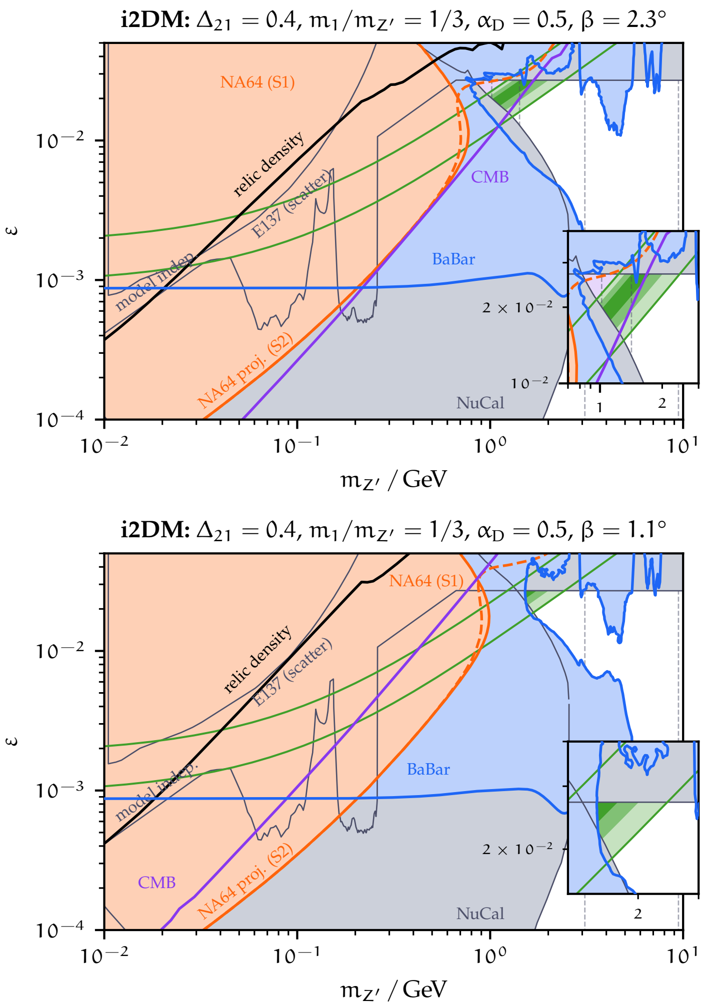

Figure 8.15: Same as fig. 8.14, but for BP3c (top) and BP3d (bottom).

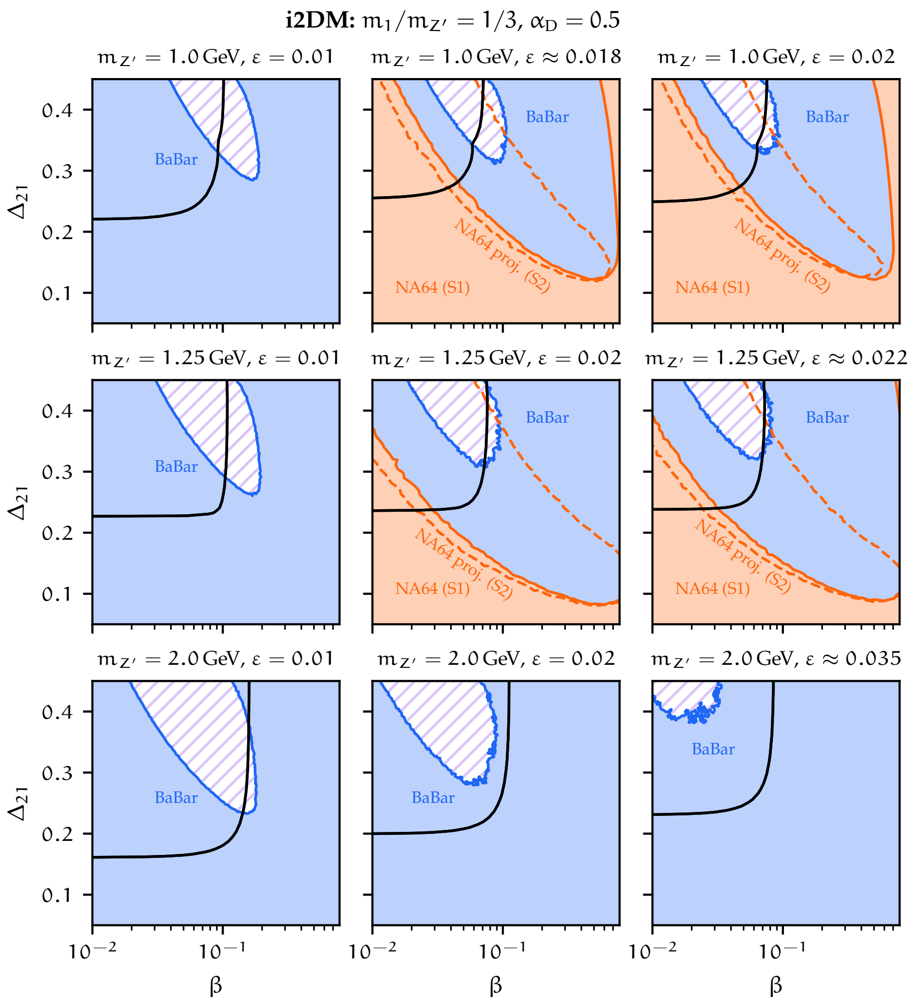

Figure 8.16: Same as fig. 8.7 but for BP3, corresponding to the i2DM model. The parameter space is shown as a function of Δ_{21} and the mixing angle β. The region hatched in violet is excluded by CMB limits, providing a full exclusion of these slices of parameter space.

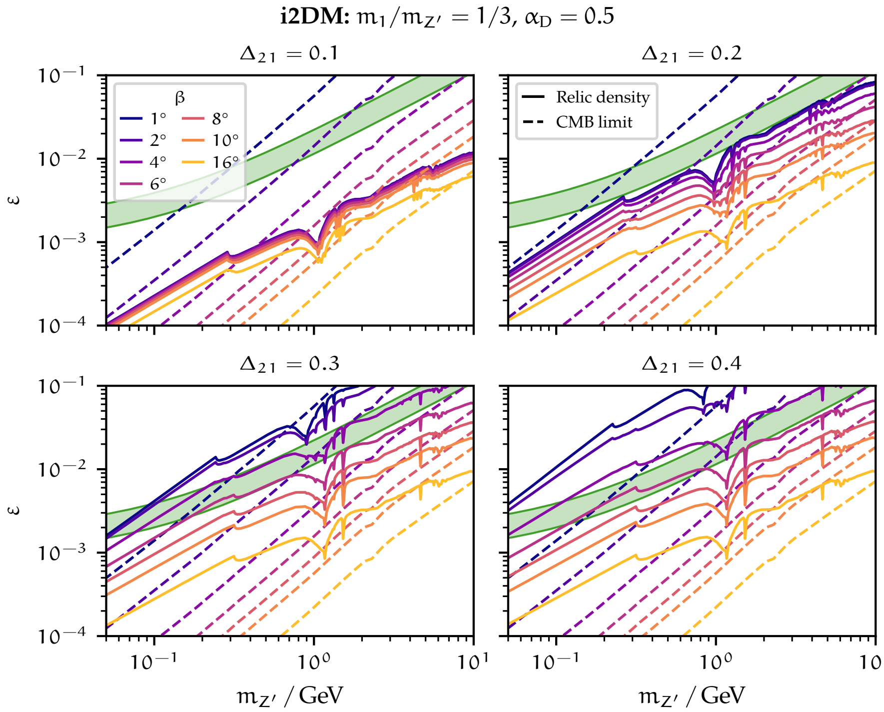

Figure 8.17: The relic density (solid lines) and CMB limits (dashed lines) in the parameter space of i2DM in the plane of kinetic mixing ε vs dark photon mass $m_{Z'}$ for fixed values of $\alpha_D = 0.5$, $r = m_1/m_{Z'} = 1/3$, and Δ_{21}. Each curve corresponds to a different value of the mixing angle β. The CMB limits exclude large values of ε. The Δa_μ 3σ preferred region is shown as a green band. Adapted from [4, fig. 15].

8.3.4 Three HNFs (BP4a–c, BP5)

We show the constraints for the three HNFs models in figs. 8.18 and 8.19, expressed as ε vs $m_{Z'}$ constraints. Similarly to the previous cases, the constraints coming from both BaBar and NA64 are relaxed, and a new region of the parameter space opens up. All benchmarks are characterized by having three HNFs, and by a sizable V_{32} coupling, which enhances the dark photon decay rate to N_3N_2 final states. Furthermore, the produced HNFs can promptly decay, releasing e^+e^- pairs in the detectors. The presence of a new fermion, and the enhanced annihilation rate to the heaviest HNFs make it possible to have a larger number of e^+e^- pairs, and, consequently, a larger probability of detecting a semi-visible event. The main difference between the models is that BP4a–c are characterized by only off-diagonal couplings, with the only possible decay chains being:

$$Z' \to (N_2 \to N_1 e^+ e^-)\,(N_3 \to (N_2 \to N_1 e^+ e^-) e^+ e^-)\,, \tag{8.45a}$$

$$Z' \to (N_2 \to N_1 e^+ e^-) N_1\,, \tag{8.45b}$$

Differently, BP5 allows for any possible coupling among the HNFs.

The downward shift of the BaBar bound happening between BP4a and BP4b benchmarks is due to the different values assumed by the parameter $r = m_1/m_{Z'}$. This parameter affects both the HNF lifetime and the Z' branching ratios. The HNF lifetime depends on r according to $c\tau \approx r^{-5}$, so a larger value would imply a shorter lifetime, translating into a more relaxed bound, because of the larger fraction of events releasing energy inside the instrumented regions of the detector. However, as it can be observed, the bound becomes stronger from BP4a to BP4b, even with a larger r. The new value modifies the branching ratio of the dark photon decay and forbids the channel $Z' \to N_3N_2$, because of kinematical reasons:

$$m_{Z'} > m_2 + m_3 \Rightarrow r < \frac{1}{(\Delta_{32}+2)(\Delta_{21}+1)} \approx 0.116\,, \tag{8.46}$$

which is satisfied for BP4a, but not for BP4b. Being the decay to the two heavy HNFs forbidden means a lower rate of e^+e^- pairs production, because Z' can decay only to N_2N_1, and only N_2 can decay further.

The constraints show that the NA64 (S2) projected bound has the capability of excluding new regions of the parameter space, demonstrating the capability of the experiment to be sensitive to promptly decaying HNFs.

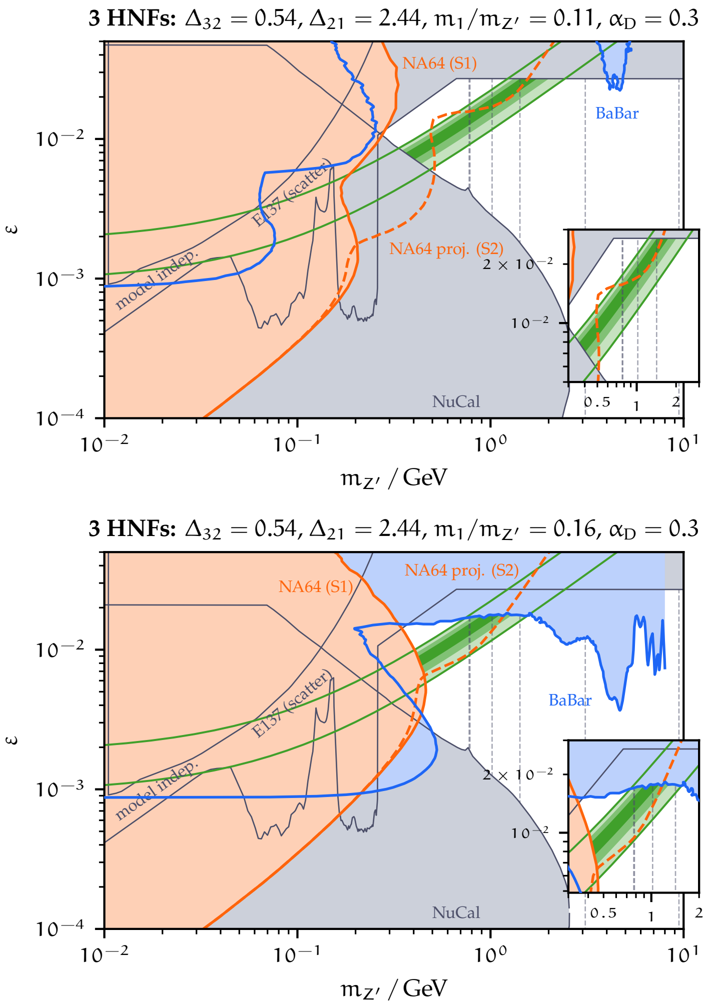

Figure 8.18: Same as fig. 8.7 but for BP4a (top), BP4b (bottom), corresponding to the models with 3 HNFs.

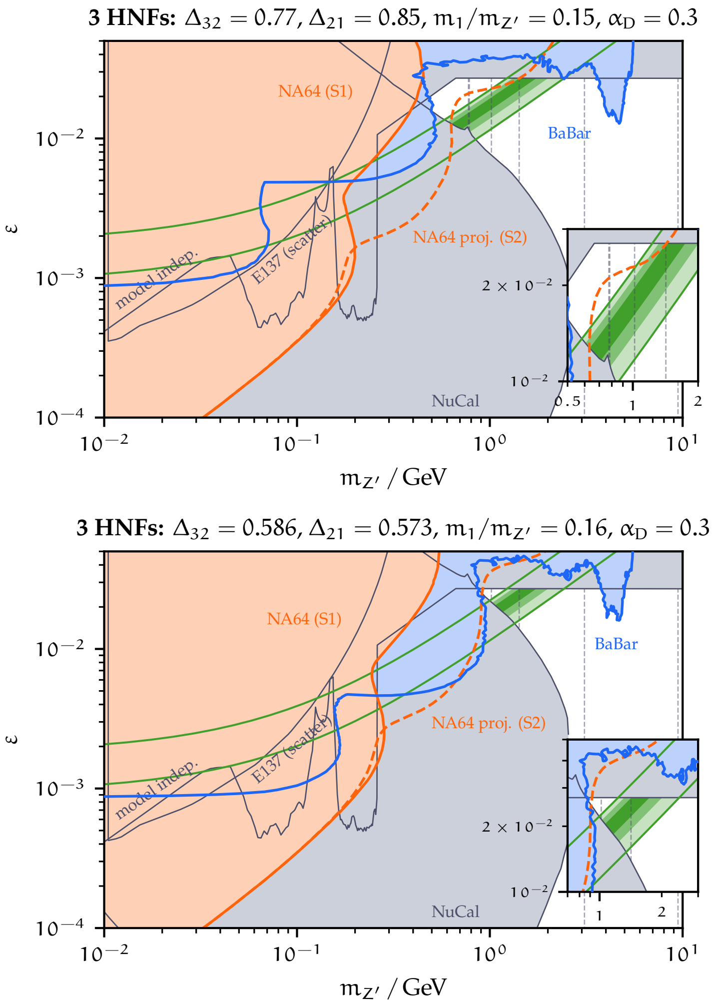

Figure 8.19: Same as fig. 8.18, but for BP4c (top) and BP5 (bottom).

8.4 Prospects and constraints on HNL and dark matter interpretations

In this section, we will indicate the HNFs generically with ψ_i, $i \in \{1, 2, 3\}$, independently on the model considered, where ψ_1 is the lightest HNF.

8.4.1 HNFs as dark matter candidates

As we previously mentioned when discussing the different models, the lightest HNF can be a dark matter candidate. The presence of a $U(1)_D$ symmetry makes possible to seclude the dark sector from the Standard Model, and, consequently, to have the lightest HNF to be stable. However, for the mass range we are considering, the self-interaction cross section of Dirac dark matter candidates is s-wave, unsuppressed by velocity, but excluded by CMB data. Differently, Majorana fermions or scalar particles are characterized by a p-wave velocity-suppressed self-annihilation cross section, which can evade CMB constraints, but it is characterized by a long-lived dark photon, constrained by invisible dark photon searches and practically preventing any Δa_μ explanation. A solution for this would be to guarantee self-annihilation near the Z' resonance, $r = m_1/m_{Z'} \lessapprox 1/2$, which can significantly enhance cross sections, but the resulting mass spectrum would leave no room for semi-visible, promptly-decaying fermions. In this framework, the most natural possibility to achieve the correct relic abundance while also avoiding the main constraints is to consider coannihilations of the lightest HNF with a heavier partner, $\psi_1\psi_{2,3} \to Z'^* \to f^+f^-$. The coannihilation cross section of opposite C states, ψ_i and ψ_j, is given by

$$\sigma v(\psi_i\psi_j \to f^+f^-) = 8\pi\alpha_D\alpha\varepsilon^2|V_{ij}|^2 \frac{\left(2\Delta_{ij}^2 m_j^2 + m_f^2\right)}{\left(4\Delta_{ij}^2 m_j^2 - m_{Z'}^2\right)^2 + m_{Z'}^2\Gamma_{Z'}^2} \times \sqrt{1 - \frac{m_f^2}{\Delta_{ij}^2 m_j^2}} + \mathcal{O}(v^2)\,. \tag{8.47}$$

Just like the self-annihilation of Dirac fermions, the cross section is velocity unsuppressed. Nevertheless, the Boltzmann suppression factor of the coannihilator and its decay impact significantly late time coannihilations, evading naturally the CMB constraints. To calculate the dark matter relic density of ψ_1 in our benchmarks, we assume that all dark sector fermions are in chemical equilibrium at the time of freeze-out, and employ the formalism of [116]. We find good agreement with the literature on iDM [581, 586] and i2DM [590]. We find a 50 % disagreement with the relic curves of [593] for $m_1 \gtrapprox 100$ MeV.

Direct detection

Direct detection experiments have reached impressive sensitivity to dark matter-nucleon scattering cross section. They would be able to provide strong evidence for the dark matter nature of the HNFs. However, the iDM and mixed-iDM models are characterized by *inelastic* nucleon scattering interactions, where the dark matter scatters off nuclei producing its heavier partner. Such tree-level interactions are kinematically suppressed by the mass splitting between the two HNFs, which only the largest dark matter velocities can overcome, having enough kinetic energy. This makes the direct detection prospects for these models very challenging as the only available elastic processes left are loop-induced.

In the case of kinetic mixing, the scalar-current dominates, $c_S^q(\overline{\chi}\chi)(\overline{q}q)$ [619]. In terms of coupling to nucleons,

$$\sigma_{\chi N}^{\text{1-loop}} = \frac{\left(c_1^N \mu_N\right)^2}{\pi}\,, \tag{8.48}$$

where μ_N is the reduced mass of the dark matter particle χ and the nucleon N, while c_1^N is the loop-induced dark matter-nucleon coupling. The matching to nucleon currents gives [620]

$$c_1^N = 4\frac{\alpha_D \alpha_{em} \varepsilon^2}{m_{Z'}^4} m_\chi F_3(r^2) \sum_q F_S^{q/N} Q_q^2 \sum_i |V_{1i}|^2\,, \tag{8.49}$$

where Q_q is the quark electric charge, $r = m_\chi/m_{Z'}$, $F_3(x)$ is the loop function from [619], and $F_S^{q/N}(Q^2)$ the nucleon scalar form factors. It is possible to give a naive estimation of the elastic dark matter-nucleon scattering cross section at a typical point of the parameter space, assuming the values of the form factors at $Q^2 = 0$, so that $F_S^{q/p}(0) \approx F_S^{q/n}(0) \approx (15, 35, 40)$ MeV for $q = (u, d, s)$:

$$\sigma_{\chi N}^{\text{1-loop}} \approx 1.4 \times 10^{-3}\,\text{pb} \times \left(\frac{\alpha_D}{0.3}\right)^2 \left(\frac{\varepsilon}{10^{-2}}\right)^4\,, \tag{8.50}$$

where $m_{Z'} = 3m_\chi = 1\,\text{GeV}$ and $\sum_i |V_{1i}|^2 = 1$. Unfortunately, current experiments are not sensitive to such small cross sections. In this mass region, only CRESST-III (2019) [255] provides the leading limits on elastic dark matter-nucleus scattering using nuclear recoils, and they are two orders of magnitude above our estimate. In the near future, the SuperCDMS experiment at SNO-LAB [621, 622] may be able to reach the needed sensitivity to probe this parameter space.

A more promising avenue in sub-GeV dark matter direct detection is the Migdal effect, which received great attention in recent years [623]. This method relies on the ionization of the target nucleus by the dark matter, which subsequently de-excites emitting an electron. The inelastic kinematics of the process and the magnitude of the energy deposition makes it ideal to perform sub-GeV dark matter direct detection [624–627]. This method has been used by the LUX [628], SENSEI [629], XENON1T [630], and DarkSide-50 [631] collaborations to set limits in our mass region of interest. The best constraints come from DarkSide-50, where $\sigma_{\chi N} \lesssim 0.1\,\text{pb}$ at $m_\chi = 300\,\text{MeV}$ at 90 % CL.

Another possibility is to perform direct detection for dark matter-electron scattering. Also in this case, iDM and mixed-iDM models are affected by the same loop-suppression as for dark matter-nucleon scattering, given the absence of elastic processes at tree-level. However, in the i2DM model, direct detection is sensitive to the mixing-angle-suppressed elastic scattering of $\chi \equiv \Psi_1$ on electrons. For a heavy dark photon, the total cross section is

$$\begin{aligned} \sigma_e &= \frac{16\pi \sin^4(\beta)\alpha_D \alpha_{em} \varepsilon^2 \mu_e^2}{m_{Z'}^4} \\ &\approx 4 \times 10^{-7}\,\text{pb} \times \left(\frac{\sin(\beta)}{0.14}\right)^4 \left(\frac{\alpha_D}{0.3}\right) \left(\frac{\varepsilon^2}{10^{-2}}\right) \left(\frac{1\,\text{GeV}}{m_{Z'}}\right)^4, \end{aligned} \tag{8.51}$$

The leading limits in this parameter space are from XENON1T [632, 633], PandaX-II [634], and SENSEI [629]. At $m_\chi \approx 100\,\text{MeV}$, XENON1T constrains $\sigma_e \lesssim 10^{-4}\,\text{pb}$, which is still orders of magnitude above our estimates for $\beta = 8°$.

One more possibility for direct detection is to search for a boosted dark matter population [635–638]. Indeed, the interaction of dark matter background with energetic CRs may results in the upscattering $\chi \to \psi_{2,3,...}$ with the heavier partners, and their subsequent decay to fast dark matter particles. This CR-boosted dark matter population can then be searched for in direct detection and neutrino experiments. Limits on this scenario have been derived in [639, 640] using XENON1T data, but they are still too weak to constrain our parameter space, in all models of interest. A first solution may be to employ large neutrino detectors, that can improve the general sensitivity, thanks to their large mass and excellent detector performance [636]. However, a thorough study is needed to assess the features of boosted dark matter and its flux in our models, to understand the testability via this strategy.

Cosmic Microwave Background

Precision measurements of the CMB impose strong constraints on HNFs models. In scenarios where dark matter can self-annihilate or decay to charged particles at the time of recombination, the energy injection into the Standard Model plasma can alter the CMB power spectrum. The resulting hydrogen reionization can delay the formation of the CMB [161–165]. Latest Planck data [20] specifically exclude light and thermally produced dark matter candidate with s-wave annihilations for the sub-GeV region. Models with coannihilating dark matter candidates, like iDM and mixed-iDM, and models with p-wave annihilations, like those featuring a Majorana dark matter candidate, remain largely unconstrained by these CMB limits.

Among the models we consider, only i2DM is subject to CMB constraints. This is primarily due to the presence of a light Dirac dark matter candidate, which can undergo velocity-unsuppressed self-annihilations, despite them being suppressed by the fourth power of the small mixing angle β. The self-annihilation cross section to charged leptons in the i2DM model has the same shape as in eq. (8.47), upon substitution of $\Delta_{ij} \to m_1$ and $V_{ij} \to \beta^2$. In fig. 8.17 we show the curves achieving the correct relic density for the i2DM model, for different values of β, with comparison with the CMB limits. Notably, for the typical lifetimes and mass splittings considered in this study, late-time annihilations involving $\psi_2, \psi_3, \ldots$ can be safely neglected.

8.4.2 HNFs as HNLs

The HNL interpretation within our models introduces distinctive phenomenological consequences. Mixing with active neutrinos, emerging by the Yukawa coupling after symmetry breaking, leads to specific decay patterns for the HNLs. Heavier HNLs predominantly decay into lighter HNLs and dark photons, three lighter HNLs, or HNLs and dilepton pairs, depending on the kinematics. In our case, the latter case is preferred, so that we focus on a specific mass hierarchy, that will also allow us to evade constraints from experiments like BaBar. The inclusion of a light dark photon enhances both HNL scattering and decays compared to standard scenarios. Experimental tests primarily involve peak searches and visible decays. The former employs the emission of HNL from a pion or kaon decay, leading to the formation of a small peak in the charged lepton spectrum at a lower energy. Relying on solely meson kinematics, these constraints can be strong, especially in the sub-GeV mass region [641]. Similarly, for strong HNL coupling to the τ lepton, peak searches in τ and D decays, such as the recent BaBar analysis [642], provide strong limits. Nonetheless, events featuring very fast decays may be vetoed by the requirement of no additional charged particles, weakening the bounds in certain regions of parameter space. A more detailed discussion of the potential impact on peak searches is available in [377].

The production of HNLs can happen via different channels. On one hand, GeV-scale HNLs are produced thanks to a beam of protons impinging on a target, with further production of a large amount of mesons, subsequently decaying and producing HNLs via mixing. These particles can travel long distance before decaying and being revealed in dedicated experiments. The rate of the decay process is indeed $\Gamma^{Z'}_{N_4 \to \nu e^+ e^-} \gg \Gamma^{W,Z}_{N_4 \to \mathrm{SM}}$, where Γ^X is the decay rate mediated by the particle X, due to kinetic mixing requirements. If N_4 is long-lived with respect to the baseline of the experiment L, $c\tau^{\mathrm{lab}} > L$, then the bounds become stronger because of the rate scaling as $\Gamma^{Z'}_{N_4 \to \nu e^+ e^-}/L$. On the contrary, very short-lived N_4 particles, so that $c\tau_4^{lab} \ll d$, where d is the distance between the source and the detector, do not reach the detector at all, and they are not constrained. Constraints on the mixing parameters rely on experiments such as T2K [643] and MicroBooNE [644] (see also PS191 limits [645–647]) for U_{e4} and $U_{\mu4}$; CHARM [648–651], NOMAD [652], and LEP [653–655] for $U_{\tau4}$.

Alternatively, HNLs production can happen via neutrino beam upscattering in the detector. Advantages of this approach feature the significantly larger upscattering cross section with respect to the standard one and shorter decay lengths. This setup has the potential of yielding distinctive signatures in short-baseline neutrino experiments, such as the SBN program at Fermilab, as well as near detectors in long-baseline accelerator neutrino experiments like T2K, NoVA, and DUNE. A very interesting signature is represented by e^+e^- pairs signature from HNLs decays induced by neutrino upscattering in the MiniBooNE experiment. This signature has the potential of explaining the MiniBooNE LEE [7, 377], see also § 2.5.3 and chapter 9. The produced HNLs can decay into a dilepton pair mimicking an electron neutrino scattering. This occurs when the two leptons are very collimated or one of them is not reconstructed being too soft [656]. The success of this explanation crucially hinges on the large values of kinetic mixing permitted in our models. Specifically, to account for the anomalous excess in MiniBooNE, HNLs must decay within the detector's typical size of a few meters. Achieving decay lengths $\tau_N \ll 1$ m is unattainable in the standard HNL scenario and necessitates the presence of light dark photons and substantial kinetic mixing.

8.4.3 Prospects for detection

In this subsection, we discuss future prospects for the detection of semi-visible dark photons and HNFs.

Low-energy e^+e^- colliders

Direct tests of the parameter space of the model presented can be performed with dedicated semi-visible search at BaBar, KLOE, BES-III, and Belle-II e^+e^- colliders. In particular, experiments like KLOE and BES-III ran with center-of-mass energies close to the dark photon mass, significantly enhancing their prospects for direct production of HNFs. These searches can be divided into two categories:

- *on-shell production of dark photon through ISR*, $e^+e^- \to Z'\gamma$: many invisible particles are produced in the final states, and it is not possible to reconstruct the dark photon mass based only on visible energy, but the ISR topology features an energy imbalance in the photon-dark photon center-of-mass system, that makes possible to highlight a resonance in $M_X^2 = s - 2E_\gamma\sqrt{s}$ after having isolated the photon, shedding light on the value of the dark photon mass. A sensitivity study on this approach has been performed for Belle-II in the case of the iDM model [586, 587], while for the case of mixed-iDM and i2DM, results are expected to be even better given the presence of multiple HNFs decays;

- *production via s-channel through off-shell dark photons*, $e^+e^- \to Z' \to \psi_i\psi_j$: the production cross section depends on the dark coupling α_D, and it can be large when $\alpha_D \gg \alpha_{em}$ [377, 657]. From the point of view of the kinematics, this process yields two back-to-back HNFs that further decay to dilepton pairs and missing energy. The main feature of the visible products is that they are not back-to-back, because of the presence of missing energy. Additionally, in case of production of the heaviest state ψ_3 and its decay chain $\psi_3 \to \psi_2 \to \psi_1$, a third, lower energetic dilepton pair could be visible, with the two primary decay vertices and the collision point on the same line. Sensitivity studies for this channel have been performed for the iDM model in [657], finding that Belle-II has the potential of covering open regions of the parameter space, which incidentally correspond to the parameter space favoring a Δa_μ explanation, namely $\varepsilon < 10^{-3}$ and $m_{Z'} \gtrapprox 500\,\mathrm{MeV}$.

In both strategies, it would be possible to reconstruct the dilepton invariant mass $m_{\ell\ell}$, which is a powerful tool to constrain the mass splittings between the HNFs, with the relation $m_{\ell\ell} < \Delta_{ij} m_j$. Additionally, displaced vertices would help to isolate the different HNFs decay cascades.

Current datasets may be used to shed light on semi-visible dark photons in short-term. Prime examples are the visible Z' searches performed by KLOE/KLOE-2 [616, 617] and BES-III [618]. Dilepton invariant mass distributions can be searched for on top of the smooth backgrounds and the following channels are a promising starting point: i) $e^+e^- \to \gamma(X \to \ell^+\ell^-)$ [305, 616, 658, 659], ii) $\varphi \to \eta(X \to e^+e^-)$ [304, 660], iii) $e^+e^- \to (X \to \ell^+\ell^-)X_{\mathrm{inv}}$ [661], and iv) $e^+e^- \to (X \to \ell^+\ell^-)(Y \to (X \to \ell^+\ell^-)(X \to \ell^+\ell^-))$ [662], where X and Y are some fully visible resonances.

Couplings to the Z boson

Kinetic mixing dark photon models feature the Z-boson coupling to the dark sector, shown in eq. (4.63), which can be used on top of the Z' coupling to electromagnetic current. Assuming large kinetic mixing, the Z boson can decay into HNFs with the following branching ratios:

$$\mathcal{B}(Z \to \psi_i\psi_j) \approx \tau_Z \frac{|V_{ij}|^2 G_F m_Z^3}{12\sqrt{2}\pi}\left(\frac{2 g_D\, s_w\, \varepsilon}{g}\right)^2 \approx |V_{ij}|^2 \times 10^{-7} \times \left(\frac{\alpha_D}{0.1}\right)\left(\frac{\varepsilon}{10^{-2}}\right)^2, \tag{8.52}$$

where we neglected the small mass of the HNFs. We can immediately see that the branching ratio is very small, evading invisible Z width constraints.

However, searches for HNLs accompanied by lepton jets have been performed at LEP [653–655], namely looking for a single HNL decaying to leptons or quarks, produced alongside a neutrino, $Z \to N\nu$. Such decay pattern can be mimicked efficiently in models of semi-visible dark photons, where the dark photon decays to HNFs, $Z' \to \psi_2\psi_1$, followed by prompt ψ_2 decay with ψ_1 being missing energy. Parameters like the mass splitting would act in modifying the dilepton energy.

Neutrino experiments

A promising strategy to study semi-visible dark photon models within neutrino experiments depend on the kind of model assumed.

In the case of a dark matter interpretation of the HNFs, they can be produced through meson decays and bremsstrahlung at the target. The stable dark matter candidate can travel the whole distance to the detector, where it can coherently interact with the nucleus $\mathcal{N}$ and produce its coannihilation partners [595, 612, 663],

$$\psi_1\,\mathcal{N} \to (\psi_{2,3,\ldots} \to \psi_1\ell^+\ell^-)\,\mathcal{N}\,. \tag{8.53}$$

Displaced dileptons are then produced from the decays of the unstable coannihilator. Experiments like MINERνA, the near detector of T2K, ND280 [664, 665], and finally DUNE and Hyper-Kamiokande [666, 667] can look for the displaced vertex of this process. Other experiments like IceCube and KM3NeT can search for the so-called double-bang signature: dark matter particles can be produced in the atmosphere, upscatter via DIS, and the subsequent coannihilator decay would be sufficiently displaced to give two separated signals in the same time window, see [668, 669] where this process was studied in the context of HNLs, but can be adapted to dark matter particles. Coannihilators particles can also be produced at the target alongside ψ_1. If they are short-lived, their decay would contribute to the flux of ψ_1. However, for small mass splitting, they will be long-lived, and high energy beam dump experiments like CHARM and NuCAL [595] can constrain them, while forward or surface detectors at the LHC [670] can search for them.

The iDM model received attention in this framework and a sensitivity study in the context of the SBN program at Fermilab has been performed [663]. The BNB has unique features to probe these kinds of models efficiently: its three Liquid Argon detectors are sensitive to dark matter produced both in the BNB itself and in the off-axis NuMI beam, and it can run off-target, directing the proton straight into the beam dump, minimizing the flux of neutrinos going through the detector, avoiding the magnetic horns.

If we consider an HNL interpretation, the lightest HNF is not stable and can decay in-flight to Standard Model neutrinos, through charged-current, neutral current or dark photon interaction, making it a good target for neutrino experiments. For the models considered in this chapter, the value of $\alpha_D \varepsilon^2$ is sufficiently large so that N_4 decays would be dominated by dark photon exchange, so that branching ratios into $\psi_i \to \nu_{1,2,3}\, \ell^+\ell^-$ would be the largest. The T2K experiment released the strongest limits on this signature [643]. Noticeably, the dark photon contribution to the decay rate of N_4 and the enhancement of the decay-in-flight event rate opens new possibilities for the parameter space of the model, already constrained by cosmological and laboratory-based limits on N_4 mixing with active neutrinos [646].

In the HNL interpretation, dark photon-mediated neutrino upscattering in the detector or with the dirt can produce HNLs, which then decay, see § 8.4.2:

$$\nu_\alpha\, \mathcal{N} \to (N_i \to N_j \ell^+\ell^-)\, \mathcal{N}\,. \tag{8.54}$$

The event rate is proportional to the mixing between the HNLs and active neutrinos. Given most of the flux at accelerator and atmospheric experiments is composed of ν_μ and $\bar{\nu}_\mu$, the mixing with the muon flavor is the most relevant in this case. Any evidence of this process would be a smoking gun for the HNL interpretation of the HNFs.

Kaon factories

Kaon decays are a powerful tool to probe the parameter space of semi-visible dark photons and HNFs, either i) through direct production of dark photons, or ii) through direct production of HNFs. The production of dark photons happens through kinetic mixing, via $K \to \pi\, Z'$ and $K^+ \to \ell^+ \nu_\ell\, Z'$ processes, see § 4.3, and can subsequently decay semi-visibly into multi-lepton final states [671]. This production method is suppressed by $m_{Z'}^2/m_K^2$ and its constraining power are limited, see fig. 4.1. A more promising avenue is the direct production of HNLs through their mixing with the electron or muon flavor. The experiment NA62 can probe the production and decay products of HNLs, with a three-track search setup, looking at processes like:

$$K^+ \to \ell_\alpha^+ (N_i \to N_j\, \ell_\beta^+ \ell_\beta^-)\,, \tag{8.55}$$

where $\alpha, \beta \in \{e, \mu\}$. It is possible to reconstruct the HNL mass through the observables: $m_{N_i}^2 \approx (p_K - p_{\ell_\alpha})^2$ and $m_{N_j}^2 = (p_K - p_{\ell_\alpha} - p_{\ell_\beta^+} - p_{\ell_\beta^-})^2$. The event rate depends on $|U_{\alpha N_i}|^2$ only, and any additional HNLs decay would provide new lepton tracks independently on the rate. Moreover, the NA62 experiment can identify displaced vertices for HNL proper lifetimes as short as $c\tau_0 \approx 10\,\text{ps}$ due to its vertex resolution of $\mathcal{O}(10\,\text{cm})$.

Future fixed target experiments

The fixed-target Light Dark Matter eXperiment (LDMX) at SLAC National Accelerator Laboratory [672–674] employs a next-generation setup to search for semi-visible signatures. It is made of an electron beam of approximately (4 to 16) GeV impinging on a thin target, with a large detector (ECAL and HCAL) downstream. It will be focused on searches for bremsstrahlung-produced dark sector particles, like in the NA64 experiment, namely exploiting the process $e^- \mathcal{N} \to e^- Z' \mathcal{N}$. However, its search strategy will be based on the missing-momentum technique, and it will measure both the energy and the transverse momentum of the recoiling electron. Given the primary electron will not shower until reaching the ECAL, any additional produced e^+e^-, $\mu^+\mu^-$, and $\pi^+\pi^-$ pairs coming from prompt decays of semi-visible Z' would provide a striking signature in the experiment. The lower energetic beam of LDMX makes possible to probe a wider parameter space in the HNF lifetime, compared to NA64, while its enhanced tracking capabilities will make possible to observe additional tracks together with the recoiling electron.

8.5 Summary

In this chapter we studied the semi-visible dark photon models. The simple extension of the Standard Model through the vector portal and a new dark symmetry $U(1)_D$ makes possible to build models with non-trivial phenomenology and particle content. Semi-visible dark photons can arise in such scenarios, where the dark photon mediates a dark sector made of HNFs with the Standard Model. The lightest HNF can be made stable and constitutes a dark matter candidate. Alternatively, HNFs mixing with Standard Model neutrinos can realize scenarios in which the lightest HNF is unstable and decays to neutrinos with long lifetime.

The models we considered in this chapter are characterized by a dark photon mediator and a dark sector made of multiple HNFs ψ_i. We discussed the phenomenology of these models, highlighting that the semi-visible dark photon paradigm is a viable solution to evade most of the constraints coming from invisible and visible dark photon searches. In this context, it is essential to forbid the dark photon invisible branching ratio, namely $Z' \to \psi_1\psi_1$, strongly constrained by BaBar and NA64, in favor of off-diagonal interactions $Z' \to \psi_i\psi_j$ in i and j indices. This request can be realized by introducing a charge-conjugation symmetry C in the dark sector. We then considered the popular iDM model, along with simple extensions:

- the mixed-iDM model, where a mostly-sterile Majorana dark matter candidate ψ_1 interacts with a mostly-dark and heavier Dirac fermion, Ψ_2, through a small mixing α;

- a three fermion model, with three Majorana fermions and a pronounced mass hierarchy;
- the i2DM model, representing the Dirac limit of a four Weyl fermions scenario [590], where a dark charged Dirac state mixes with a sterile Dirac fermion, the dark matter candidate has self-interactions, suppressed by the mixing angle β.

The main feature of semi-visible Z' is that its decays to lighter HNFs is followed by their subsequent decay to both visible and invisible states: $\psi_i \to \psi_j \ell^+\ell^-$ or $\psi_i \to \psi_j \pi^+\pi^-$. For large couplings and kinetic mixing, HNFs decays are prompt and can leave visible signatures in particle detectors. The presence of visible particles and missing energy within the detector vetoes these semi-visible decays, modifying existing constraints on invisible dark photons. Assessing the constraints relaxation requires a dedicated recasting of the existing experimental results, which we performed in the case of BaBar and NA64 experiments by developing a custom simulation. We find a significant modification of the bounds on kinetic mixing, opening up new regions of the parameter space around $m_{Z'} \approx (0.3 \text{ to } 1.3)\,\text{GeV}$ and with values of $\varepsilon \approx \mathcal{O}(10^{-3} \text{ to } 10^{-2})$. Incidentally, the same parameter space region is favored by the Δa_μ discrepancy (considering the dispersive approach), which can be explained by a semi-visible dark photon. For both iDM, mixed-iDM and i2DM models, we also discussed the possibility of the lightest HNF to constitute a thermal dark matter candidate. In this context, we highlighted the need to forbid ψ_1 self-annihilation, strongly constrained by CMB measurements. Indeed, in the case of i2DM model, those constraints are powerful enough to exclude the entire Δa_μ region, despite the mixing angle suppression.

Focusing in particular on the NA64 experiment, it should be noted that the current experimental setup can be sensitive to semi-visible dark photon decays. Indeed, aggregating the additional energy coming from any e^+e^- pairs produced by the short-lived HNFs to the energy of the primary electron beam in the ECAL, it is possible to probe the missing energy carried away by stable or long-lived HNFs. Our sensitivity curves show that this new signal definition could cover most of the open $\Delta a_\mu^{\text{disp}}$ parameter space in an iDM model. In this context, the NA64 collaboration pursued the possibility of detecting semi-visible dark photons, and a dedicated sensitivity study on iDM and i2DM models was presented in [6], where a sophisticated detector simulation has been used. Our projections resulted to be in good agreement with that.

Other experimental searches at e^+e^- colliders can be performed to probe the parameter space of semi-visible dark photons. Prime examples are BaBar, KLOE/KLOE-II and BES-III, which can search for semi-visible dark photons already in their current data. Moreover, the coupling of the dark current to Z boson may be able to give additional constraints, coming from LEP data. In the next future, the most important contribution to these searches may come from the Belle-II experiment, which will be able to improve the BaBar results, thanks to its better hermeticity. Dedicated searches for semi-visible dark photons would be essential to establish these models.

One of the most important questions that experimental results would be able to shed light on is whether the HNFs are dark matter or HNLs. For the parameter space under consideration, a thermal dark matter solution is feasible only by assuming inelastic dark matter models and a coannihilation-based freeze-out. However, this solution makes difficult to probe the parameter space with direct detection experiments, due to the large mass splittings between dark matter and its coannihilating partners. In this context, boosted dark matter from CRs may revive this possibility, additionally allowing to probe the same parameter space with neutrino detectors. Alternatively, in case of HNLs, the presence of mixing with active neutrinos would lead to distinctive signatures, like decay-in-flight, neutrino upscattering, and direct production in kaon decays.

The framework of GeV-scale semi-visible dark photons is a rich playground for new physics searches at low-energy experiments. Additionally, the scenarios we discussed represent one last chance for the dark photon interpretation of the Δa_μ discrepancy, already strongly constrained by visible and invisible dark photon searches. Semi-visible dark photon models are within reach of current and future experiments, and they may offer insights into whether nature prefers a rich and complex dark sector.

Chapter 9

Search for dark sector-produced e^+e^- pairs in MicroBooNE

> You want my treasure? You can have it!
> I left everything I gathered together in
> one place. Now you just have to find it.
> —Gol D. Roger
>
> *One Piece*
> Eiichiro Oda

The long-standing experimental anomalies recorded by neutrino experiments have motivated extensive research for new physics beyond the Standard Model. In particular, the very well known MiniBooNE LEE, already discussed in § 2.5.3, has been the subject of many theoretical interpretations. Several signatures have been proposed to explain the excess: the MiniBooNE detector is unable to distinguish between electrons and photons, so that signals coming from different final states can be all misidentified as electronic-like events and make up for the excess. In general, final states of single-e^-, single-γ, and collimated or highly asymmetric e^+e^- and $\gamma\gamma$ pairs can be considered as possible explanations of the LEE. These signatures can be generated either within or beyond the Standard Model.

From a theoretical point of view, the most popular explanation of the MiniBooNE excess comes from sterile neutrino oscillations. This scenario features a new sterile neutrino, N, mixing with the active neutrinos. This model resembles exactly the type-I seesaw model discussed in § 2.5.2. From cosmological constraints [20], it is possible to set an approximate scale for the mass of the fourth neutrino mass eigenstate, $m_4 \approx 1\,\text{eV}$. The MiniBooNE collaboration performed a fit to a two-neutrino oscillation model, finding a best-fit value of [41]:

$$\Delta m^2 = 0.0043\,\text{eV}^2\,, \tag{9.1a}$$

$$\sin^2(2\vartheta) = 0.807\,. \tag{9.1b}$$

This explanation, however, is in tension with the first results of the MicroBooNE experiment about ν_e interactions to be at the origin of the LEE [50–53], already discussed in § 2.5.3. Indeed, the MicroBooNE experiment was built with the aim of investigating the MiniBooNE LEE: its LArTPC detector makes it possible to separate electrons from photons. Its first results have shown that explanations of the LEE using either only the Standard Model radiative Δ background or ν_e interactions are unlikely [47, 50–53].

However, this conclusion gave rise to several speculations whether this result definitely excludes sterile neutrino oscillations as the origin of the LEE. In particular, the MicroBooNE analysis prefers a model-agnostic approach, using a fixed energy template for the LEE data. The choice of a constant template crucially underestimates possible systematic uncertainties and correlations in the MiniBooNE background prediction. Moreover, specific models providing good fits to the MiniBooNE data may not be representable by this template. The 3+1 sterile neutrino oscillation model has since been studied according to this new picture, and it has been shown that it could still be a viable explanation of the LEE [43, 675].

Another popular explanation can be found in dark sector models. In this chapter we will study the sensitivity of the MicroBooNE experiment to a dark sector model able to explain the MiniBooNE LEE, through production of e^+e^- pairs. This model is practically the same dark photon model as the one previously discussed in § 4.4, where we introduce a new dark gauge symmetry $U(1)_D$ whose gauge boson kinetically mixes with the Standard Model hypercharge group, giving origin to the dark photon. In this case, the signature that can be used to explain the LEE is the production of e^+e^- pairs, misidentified as a single-e^- event. This possibility was briefly introduced in § 4.5. The dark photon can mediate the neutrino upscattering to HNLs in the beam of the MiniBooNE experiment. The HNLs can then decay to produce boosted e^+e^- pairs, which can be either overlapping or very energy asymmetric, so that they can be misidentified as a single electron in the MiniBooNE detector. Among the possible realizations of the three-portal model of § 4.4, we will focus on 3+1 and 3+2 models, where respectively one and two dark HNLs are added to the Standard Model particle content.

In this chapter we perform a Pandora-based, multi-topological analysis in MicroBooNE, with the aim of constraining the parameter space of the dark sector models that could provide a solution to the MiniBooNE LEE, while simultaneously delimiting the broader theoretical landscape of such models. The analysis will be targeted on several topologies that can contribute to the e^+e^- signal, instead of using just the $1\gamma0p$ topology, as done previously. Moreover, the analysis will make use of the validated tools and techniques developed in the context of the MicroBooNE experiment, as well as the experience gained in the previous analyses performed, e.g. the radiative Δ decay search [47]. Finally, despite the dark sector models considered have an extensive parameter space, the analysis aim is to cover a wide part of it, in order to provide a general overview of the sensitivity of the MicroBooNE experiment to this kind of models. In particular for the last remark, a full simulation of the MicroBooNE detector for each parameter space point is not feasible, given the large amount of free parameters of the theory, so we developed a reweighting method to predict the final reconstructed spectra in MicroBooNE in a fast and efficient way. In this context, the event generation is also performed with a fast MC simulation, leveraging the recent tool DarkNews [5], developed for the purpose of event generation in neutrino experiments.

The chapter is organized as follows. In § 9.1 we introduce the analysis and its main features, focusing on the assumed theoretical model in § 9.1.1 and on the specific goals in § 9.1.3. Sec. 9.2 is dedicated to the description of the event generation and the reweighting method, with emphasis on the main features and challenges. In § 9.3 we describe the event selection and the main analysis cuts, while § 9.4 is dedicated to the description of the systematic uncertainties. We present the sensitivities curves we obtained in § 9.5. Finally, § 9.6 summarizes the results and discusses the future prospects.

The chapter is based on an ongoing work, which will be published in the near future. Most of the information presented here can be found in an internal technical note:

[676] Abdullahi, A. M., Guanqun, G., Zink, J. H., Hostert, M., Karagiorgi, G., **DM**, Pascoli, S., Ross-Lonergan, M., *Pandora based search for exotic* e^+e^- *production due to new "Dark Sector" physics in the Booster Neutrino Beam*. Tech. rep. MicroBooNE Collaboration and MoU with MicroBooNE, 2023.

This work was carried out in collaboration with the MicroBooNE experimental group, according to a *Memorandum of Understanding* (MoU) agreement. My contribution to this work was mainly focused on the development of the reweighting method, and on performing the event generation, presented in § 9.2. The experimental parts, shown in §§ 9.2.4, 9.2.6, 9.3 and 9.4, were developed and realized by the experimental colleagues, including the running of the analysis itself and the realization of the sensitivity plots in § 9.5. Discussions on the analysis goals, the models and the parameter space to study, § 9.1, were carried out all together.

Part of this work was carried out abroad, at the Columbia University in the City of New York, where part of my collaborators are based, under the supervision of Prof. Georgia Karagiorgi.

The code developed for the reweighting method is still under closed source, and it will be released as an open source tool in the near future. This tool leverages the DarkNews event generator, which is already open source and available as a public Python package:

[5] Abdullahi, A. M., Hoefken Zink, J., Hostert, M., **DM**, Pascoli, S., "DarkNews: A Python-based event generator for heavy neutral lepton

production in neutrino-nucleus scattering". *Comput. Phys. Commun.* 297 (2024), p. 109075. DOI: 10.1016/j.cpc.2023.109075.

I was also responsible for a small contribution to DarkNews, where I designed the main interface to interact with the generator and its broad range of parameters and options.

9.1 Analysis overview

9.1.1 The model

The model we consider is an extension of the Standard Model featuring i) a new dark $U(1)_D$ symmetry, whose gauge boson kinetically mixes with the Standard Model hypercharge gauge boson; ii) n HNLs, interacting through the new dark force and mixing with the Standard Model neutrinos. After diagonalization of the kinetic and mass terms, the model presents a massive dark photon Z' and five neutral leptons, where N_h, $h \in \{4, 5\}$, (with $m_4 < m_5$) are the heaviest and mostly dark ones, while ν_k, $k \in \{1, 2, 3\}$, are the massive states of the Standard Model neutrinos. Dark photon mass generation can be indeed achieved either through spontaneous $U(1)_D$ symmetry breaking, or assuming a Stückelberg mechanism. The model can be considered a realization of the three-portal model discussed in § 4.4, where the heaviest HNLs N_r, $r > 5$, and the dark scalar Φ are decoupled entirely and are not interesting phenomenologically, so that only $(3 + 2)$ states are important. The interaction Lagrangian can be written as:

$$\mathcal{L} \supset \frac{m_{Z'}^2}{2} Z'_\mu Z'^\mu - e\varepsilon Z'_\mu J^\mu_{\mathrm{EM}} + g_D Z'_\mu J^\mu_D \,, \tag{9.2}$$

where, as usual, we define ε as the kinetic mixing, g_D as the dark gauge coupling of $U(1)_D$, and J^μ_{EM} and J^μ_D as the electromagnetic and dark currents, respectively. The dark current can be expressed in general terms on the basis of the neutral lepton mass states, according to a particular realization of eqs. (4.73) and (4.74b):

$$J^\mu_D = \sum_{\psi_{i,j} \in \{\nu_r, N_h\}} V_{ij} \overline{\psi}_i \gamma^\mu \psi_j \,. \tag{9.3}$$

The interaction vertices V_{ij} are determined by the mixing matrix $\mathbf{U}$ between the mass and flavor eigenstates of the neutral fermions. To describe the mixing matrix, we use the same parametrization already introduced in eq. (4.70), and we isolate the blocks:

$$\mathbf{U} \doteq \begin{pmatrix} U_\nu \\ U_D \end{pmatrix} \,. \tag{9.4}$$

We can write V_{ij} in the following way:

$$V_{ij} = \sum_{h=4}^{5} Q_X^{D_h} \mathbf{U}_{hi} \mathbf{U}^*_{hj} = \sum_{d=1}^{2} Q_X^d (U_D)_{di} (U_D)^*_{dj} \,, \tag{9.5}$$

with d running the generations of dark states, each one with dark charge Q_X^d; for consistency $D_h = d$, with $d \in \{1, 2\}$. We follow the same formalism applied in [664], assuming $Q_X^d = 1$ for each dark state and $|V_{ij}| \leqslant 1$ for each interaction vertex, due to mixing matrix unitarity. This model is a $(3+2)$ upscattering model, where the main theoretical parameters are:

- $m_{Z'}$: the dark photon mass, typically $\mathcal{O}(1 \text{ to } 2000)$ MeV;
- m_5: the mass of the heaviest HNL N_5, typically $\mathcal{O}(1 \text{ to } 1000)$ MeV;
- the mass splitting

$$\Delta \doteq \frac{m_5 - m_4}{m_4} \tag{9.6}$$

  between the heaviest and the lightest HNLs, typically more interesting phenomenologically than the absolute value of m_4;
- ε: the kinetic mixing parameter, usually fixed to a reasonable representative value $\varepsilon = 8 \times 10^{-4}$.

Other important parameters to be discussed are the mixing parameters and the interaction vertices between the massive neutrino states. The upscattering process happening in this model is:

$$\hat{\nu}_\mu \, \mathcal{N} \to (N_h \to \nu_j e^+ e^-) \, \mathcal{N} \,, \tag{9.7}$$

where $\mathcal{N}$ is the target nucleus, $\hat{\nu}_\mu$ is the coherent superposition of massive neutrinos states,

$$|\hat{\nu}_\mu\rangle = \frac{\sum_{k=1}^{3} (U_\nu)_{\mu k} |\nu_k\rangle}{\sqrt{\sum_{k=1}^{3} |(U_\nu)_{\mu k}|^2}} \,, \tag{9.8}$$

produced in the incident neutrino beam, and the heavier HNLs N_h decays to a massive neutrino state and an e^+e^- pair. Notice that the ν_μ neutrinos in the beam are obtained from charged pions decays, and they are superposition of only the states kinematically allowed: that is the reason only massive ν_k are considered, while the heaviest states N_h are not. Additionally, the final superposition in this case requires a proper orthonormalization, which is achieved through the coefficient at the denominator.

In this $(3+2)$ model, the upscattering coupling is defined as $V_{\alpha h}$, $\alpha \in \{e, \mu, \tau\}$, which represents the vertex coupling between the flavor Standard

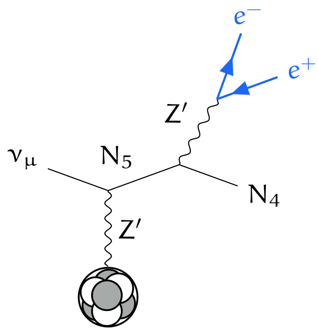

Figure 9.1: The upscattering diagram for the $(3+2)$ model under investigation.

Model neutrino α in the beam with the massive HNL state N_h. The upscattering diagram is shown in fig. 9.1. Notice that this is different from V_{ij}, which is the mixing matrix element of the interaction vertex between the i-th and j-th massive neutrino states. To define $V_{\alpha h}$, we start from the expression of the matrix element of the coherent neutrino scattering:

$$\mathcal{M}^{Z'}_{\text{ups}} = \frac{e\varepsilon g_D}{q^2 - m^2_{Z'}} \ell_\mu \langle \mathcal{N} | J^\mu_{\text{EM}} | \mathcal{N} \rangle \,, \tag{9.9}$$

where q is the momentum transfer, ℓ_μ is the leptonic current, and $\langle \mathcal{N} | J^\mu_{\text{EM}} | \mathcal{N} \rangle$ is the elastic electromagnetic transition of the target nucleus $\mathcal{N}$. The leptonic current can be written as:

$$\begin{aligned}
\ell^\mu &= \langle N_h | J^\mu_D | \widehat{\nu}_\mu \rangle \\
&= \left\langle N_h \middle| \sum_{i,j=1}^{5} V_{ij} \overline{\nu}_i \gamma^\mu \nu_j \middle| \widehat{\nu}_\mu \right\rangle \\
&= \frac{\sum_{k=1}^{3} (U_\nu)_{\alpha k} \sum_{i,j=1}^{5} V_{ij} \langle N_h | \overline{\nu}_i \gamma^\mu \nu_j | \nu_k \rangle}{\sqrt{\sum_{k=1}^{3} |(U_\nu)_{\mu k}|^2}} \\
&= \frac{\sum_{k=1}^{3} (U_\nu)_{\alpha k} V_{hk} \langle N_h | \overline{\nu}_h \gamma^\mu \nu_k | \nu_k \rangle}{\sqrt{\sum_{k=1}^{3} |(U_\nu)_{\alpha k}|^2}} \\
&\doteq V_{\alpha h} \langle N_h | \overline{\nu}_h \gamma^\mu \nu_k | \nu_k \rangle \,,
\end{aligned} \tag{9.10}$$

We can now write the relevant expression for the upscattering coupling

$$\begin{aligned}
V_{\alpha h} &\doteq \frac{\sum_{k=1}^{3}(U_\nu)_{\alpha k} V_{hk}}{\sqrt{\sum_{k=1}^{3}|(U_\nu)_{\alpha k}|}} \\
&= \sum_{d=1}^{2} \frac{(U_D)_{dh}\left[(U_\nu)_{\alpha 1}(U_D)^*_{d1} + (U_\nu)_{\alpha 2}(U_D)^*_{d2} + (U_\nu)_{\alpha 3}(U_D)^*_{d3}\right]}{\sqrt{|(U_\nu)_{\alpha 1}|^2 + |(U_\nu)_{\alpha 2}|^2 + |(U_\nu)_{\alpha 3}|^2}} \\
&= \sum_{r=4}^{5} \mathbf{U}_{rh} \frac{\mathbf{U}_{\alpha 1}\mathbf{U}^*_{r1} + \mathbf{U}_{\alpha 2}\mathbf{U}^*_{r2} + \mathbf{U}_{\alpha 3}\mathbf{U}^*_{r3}}{\sqrt{1 - |(U_\nu)_{\alpha 4}|^2 - |(U_\nu)_{\alpha 5}|^2}} \\
&= \sum_{r=4}^{5} \mathbf{U}_{rh} \frac{-\mathbf{U}_{\alpha 4}\mathbf{U}^*_{r4} - \mathbf{U}_{\alpha 5}\mathbf{U}^*_{r5}}{\sqrt{1 - |(U_\nu)_{\alpha 4}|^2 - |(U_\nu)_{\alpha 5}|^2}} \\
&= -\sum_{d=1}^{2} (U_D)_{dh} \frac{(U_\nu)_{\alpha 4}(U_D)^*_{d4} + (U_\nu)_{\alpha 5}(U_D)^*_{d5}}{\sqrt{1 - |(U_\nu)_{\alpha 4}|^2 - |(U_\nu)_{\alpha 5}|^2}}\,,
\end{aligned} \tag{9.11}$$

where we used the unitarity relations for the matrix $\mathbf{U}$:

$$\sum_{i=1}^{5} \mathbf{U}_{\alpha i}\mathbf{U}^*_{ri} = \delta_{\mu r}\,, \tag{9.12}$$

with $r \in \{e, \mu, \tau, 4, 5\}$*. In our scenario, we consider only the upscattering coupling $V_{\mu h}$, given the MicroBooNE beam is almost entirely formed by ν_μ. For simplicity, we define the shorter notations: $U_{\mu i} \doteq (U_\nu)_{\mu i}$ and $U_{Di} \doteq (U_D)_{di}$, independently on the index d (distinguishing between the two matrix elements is not phenomenologically relevant). Furthermore, we will always assume:

$$|U_{\mu 4}| = |U_{\mu 5}|\,, \tag{9.13a}$$

$$|U_{D4}| = |U_{D5}| = \frac{1}{\sqrt{2}}\,, \tag{9.13b}$$

with this choice of values, it is easy to see that

$$1 = |U_{D4}|^2 + |U_{D5}|^2 = 1 - \sum_{i=1}^{3} |U_{Di}|^2 \Rightarrow \sum_{i=1}^{3} |U_{Di}|^2 = 0\,, \tag{9.14}$$

*With this choice of index, it is easy to demonstrate that a certain element of $\mathbf{U}$ can be written as

$$\mathbf{U}_{ri} = \begin{cases} (U_\nu)_{ri} & \text{if } r \in \{e, \mu, \tau\} \\ (U_D)_{(r-3)i} & \text{if } r \in \{4, 5\} \end{cases}$$

according to the definition in eq. (9.4).

Table 9.1: The four benchmark scenarios considered in the analysis. They are divided into $(3+2)$-like and $(3+1)$-like on the basis of the Δ value: a very large Δ value makes the lightest HNL N_4 decoupled from the other states, so that the model is effectively a $(3+1)$ one. Additionally, one can separate the cases for a light or heavy dark photon, which would make the HNLs decay with an on-shell or off-shell Z', respectively.

	Light Z' $m_{Z'} \approx 30\,\text{MeV}$ $m_5 > m_{Z'} + m_4$	Heavy Z' $m_{Z'} \approx 1.5\,\text{GeV}$ $m_5 < m_{Z'} + m_4$
$(3+1)$-like $\Delta \gg 1$	A	B
$(3+2)$-like $\Delta < 1$	C	D

meaning that we are neglecting contributions from small mixing angles. Additionally, this makes $|V_{\mu 4(5)}|$ directly proportional to $|U_{\mu 4(5)}|$. A thorough analysis of the phenomenology of this model in the context of the MiniBooNE LEE can be found in [7]. For some values of the mass splitting, the heaviest HNL can decay invisibly via $N_5 \to N_4 N_4 N_4$. This decay will not produce any visible signal in the detector and, to properly explore the full parameter space of the model, we can forbid that by suppressing the dark photon couplings $|V_{4i}|, |V_{44}| \ll e\varepsilon$. This assumption may be explained by invoking the presence of a C-symmetry in the dark sector, phenomenologically equivalent in the one discussed previously for semi-visible dark photons in § 8.1.1. Light neutrinos and N_4 are C-odd ($C = -1$), so they cannot interact with each other via the C-odd dark photon. On the other hand, N_5 is C-even ($C = 1$). The presence of this conserved C-symmetry makes possible to forbid direct interactions between N_4 and light neutrinos, while keeping the N_5 interactions unconstrained.

This model has a large parameter space, made of more than six free parameters, and it is useful to define a set of benchmark points to be used in the analysis. These benchmarks have been chosen to cover the main representative cases of the model, and they are summarized in tab. 9.1. A first distinction can be performed on the basis of the $m_{Z'}$ value: a light dark photon allows the HNLs to decay to a physically on-shell Z', while a heavy dark photon makes the HNLs decay to an off-shell Z'. In the former case, the full decay pattern of the HNLs is made of two prompt subsequent two-body decays, and the HNLs lifetime will be in general short. The latter case will be characterized by a single three-body decay, and the HNLs lifetime will be longer. Additionally, the value of Δ plays an important role setting the relative kinematical importance of the two HNLs. A very large value of Δ makes the mass of N_4 to become phenomenologically irrelevant, so that the model can be considered to be a $(3+1)$ model, where the scattering involves only one single HNL. On the other hand, a value of $\Delta < 1$ makes N_4 to play an increasingly important kinematical

Table 9.2: The parameters of the four benchmark points. For all benchmarks, $g_D = 2$, $|U_{D4}|^2 = |U_{D5}|^2 = 1/2$. The N_{evt} row refers to the raw MC entries, while N_{TPC} is the number of events expected in the active TPC for combined ν_μ and $\overline{\nu}_\mu$ that pass the TPC reconstruction cuts.

	A	B	C	D
$m_{Z'}$ / MeV	30	1250	30	1250
m_5 / MeV	150	150	150	150
m_4 / MeV	0	0	107	107
ε	10^{-3}	3×10^{-3}	10^{-3}	10^{-2}
$\lvert U_{\mu 4}\rvert^2$	10^{-10}	10^{-7}	10^{-10}	10^{-7}
$\lvert U_{\mu 5}\rvert^2$	10^{-10}	10^{-5}	10^{-10}	10^{-5}
N_{evt}	46 313	46 718	46 276	46 672
N_{TPC}	147.3	221.7	147.3	2516.4
$c\tau_5$ / cm	5.3×10^{-13}	17.46	5.1×10^{-12}	103.08

role in the scattering, and the model is a $(3+2)$ one. The parameters' values for the four benchmark points are summarized in tab. 9.2.

This dark photon model, in the parameter space under consideration, including the benchmark points just described, is characterized by a large dominant contribution from the coherent scattering. However, there is also a non-zero contribution from incoherent scattering. In this first generation analysis, we are neglecting entirely the incoherent contribution to the signal. The reason is that, differently from the NC Δ radiative search, where the MC simulation was carried out with the GENIE generator, in this case the simulation is performed with the DarkNews generator, that does not have the same hadronic treatment that GENIE has. Including incoherent scattering events would inject several new sources of background events, because of their hadronic component, so that comparing these DarkNews-generated events with the GENIE backgrounds would be inconsistent, and it would be difficult to be confident in their validity. The choice to consider only coherent contributions has also the effect of making most of the events forward, because neutrinos exchange very little momentum with the nucleus during the upscattering process.

9.1.2 The DarkNews event generator

The model is simulated through the DarkNews generator [5], which is a fast MC event generator for neutrino experiments, available publicly as a Python package on GitHub [677] and PyPI [678]. The DarkNews generator is able to generate events for several beyond the Standard Model scenarios, including the three-portal model. It is able to handle the production and decay of the HNLs via both vector, scalar mediators and transition magnetic moments.

The generator has been used to simulate events for a large chunk of the full parameter space of the model considered. The output files in the `HEPevt` file format [679] can be directly used as input for the LArSoft software package [680–683], which is the standard simulation and reconstruction framework for the MicroBooNE experiment.

9.1.3 Goals and methods

The main goals of the analysis can be summarized in:

- **based on NC Δ single-photon tools**: the analysis is based on the same tools developed for the first generation NC Δ radiative search, which are already validated and well understood;
- **multi-topology analysis**: the analysis is based on several topologies, all contributing to the e^+e^- signal, instead of just the $1\gamma0p$ one, which is the only one considered in the NC Δ radiative analysis; the multiple topology feature greatly improves Pandora efficiencies;
- **broad search (reweighting method)**: the analysis is based on a reweighting method, which allows obtaining the reconstructed spectra in MicroBooNE, without the need of a full detector simulation for each point of the parameter space, allowing us to cover a wide range of parameters of interests.

To achieve these goals, the analysis can be broken into the following steps, that will be discussed in the following sections:

1. **reweighting method**: develop a reweighting method to predict the MicroBooNE reconstructed spectra in a fast and efficient way for any point in the parameter space;
2. **analysis selection**: develop an event selection based on the original NC Δ radiative search, and apply it on representative model points, that will be passed to the MicroBooNE detector simulation;
3. **validation**: both the reweighting scheme and the analysis selection will be validated on fake data and open data or sidebands, respectively;
4. **sensitivities**: the analysis will be performed on the full parameter space, and the sensitivities curves will be extracted;
5. **unblinding**: the analysis will be unblinded on the data, and the results will be compared with the sensitivities to obtain bounds on the parameter space.

At the current stage, unblinding is yet to be performed.

9.2 Generating model predictions

Simulating the theoretical model in the MicroBooNE detector is a time-consuming task, due to the heavy computational cost that a full detector simulation requires. In particular, the full MicroBooNE simulation and reconstruction chain can be divided into the following steps:

1. **event generation**: performed with DarkNews;
2. **Geant4**: propagation of particles through the detector;
3. **DetSim**: simulation of drift and readout;
4. **Reco1**: reconstruction of the 2-dimensional event on the wire planes;
5. **Reco2**: Pandora pattern recognition and reconstruction of the 3-dimensional event in the TPC;
6. **nTuple Vertexing**: additional second shower scan and output condensing.

The entire simulation chain requires about (12 to 48) h for 25 000 MC events. This makes the simulation of the full parameter space of the model unfeasible, given the large number of free parameters. To overcome this issue, we developed a reweighting method: only few points are passed to the full simulation chain, and the remaining points are obtained through a reweighting of the former ones on the basis of truth-level observables. Generating the reweighting scheme is a fast process, because it only requires truth-level information. The reweighting method can be summarized in the following steps:

1. generate a large sample of e^+e^- signal from a set of representative points in the parameter space with DarkNews, in order to sufficiently cover the phase space; these points will make up the master benchmark point $\mathcal{M}$;
2. pass $\mathcal{M}$ through the full reconstruction chain described above;
3. perform the analysis on $\mathcal{M}$, and select only events satisfying the analysis cut, $\mathcal{M}_{\text{pass}}$;
4. reweight $\mathcal{M}_{\text{pass}}$.

9.2.1 The master benchmark

The four representative points, summarized in tab. 9.2 provide a good coverage of the main features of the parameter space of the theoretical model under investigation. Around 50 000 events were generated for each point in the active TPC volume of MicroBooNE and were passed through the MicroBooNE reconstruction chain. The combination of these points makes the master benchmark point $\mathcal{M}$. In fig. 9.2, we show some truth-level distributions of some observables of the four benchmark points.

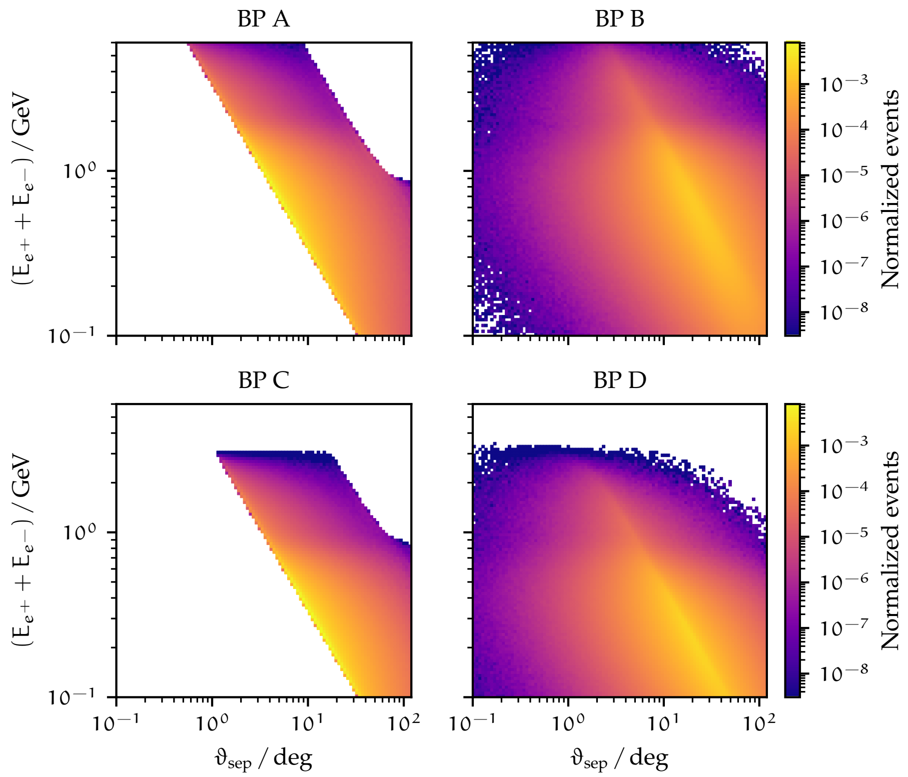

Figure 9.2: Some truth-level 2-dimensional distributions for the benchmark points considered. The x axis shows the separation angle between e^+ and e^-, while on the y axis there is the total energy of the e^+e^- pair. Events have been generated only in the MicroBooNE TPC.

9.2.2 Building the reweighting map

The reweighting map is built on the basis of the truth-level information of the events generated for a certain parameter space point. In general, an e^+e^- pair can be described by six kinematical independent variables. We observed that it is not necessary to reweight on all six variables, and that we obtain good agreement if we reweight on three kinematical variables and one geometrical variable. The reweighting framework developed is general, and allows for any number of variables to be reweighted on. In this case, we chose the following:

- E_{sum}: the total energy of the e^+e^- pair;
- ϑ_{sep}: the opening angle between e^+ and e^-;
- $|E_{asy}|$: the absolute energy asymmetry between e^+ and e^-,

$$|E_{asy}| \doteq \frac{|E_{e^+} - E_{e^-}|}{E_{sum}}; \tag{9.15}$$

Table 9.3: The binning scheme used for the reweighting map.

Variable	Bins	Left edge	Right edge	Notes
E_{sum}	20	0 GeV	2 GeV	+1 bin of overflow
ϑ_{sep}	20	$0°$	$180°$	
$\lvert E_{asy} \rvert$	10	0	1	
z_{decay}	10	From front to back face of the active TPC volume		

Listing 9.1: Procedure to obtain the reweighted spectra for a target point, starting from the reconstructed MicroBooNE spectra of the master benchmark.

```
procedure ReweightTarget(mapMasterPath, mapTargetPath, evtMasterRecoPath)
    rwMapMaster ← Read(mapMasterPath);                                    ▷ Read files
    rwMapTarget ← Read(mapTargetPath);
    evtsMasterReco ← Read(evtMasterRecoPath);
    for event in evtsMasterReco, do                       ▷ Loop over recostructed events
        bin ← rwMapMaster.GetBin(event);                   ▷ Get the bin event belongs to
        recoWtMaster ← event.weight;
        recoWtTarget ← recoWtMaster × rwMapTarget[bin] / rwMapMaster[bin];
    end for
    return recoWtTarget;
end procedure
```

- z_{decay}: the z-coordinate of N_5 decay vertex in the detector.

The reweighting map is built as a multidimensional histogram, describing the distributions of each observable in a certain binning scheme. The binning scheme is chosen to be fine enough to capture the features of the distributions, but not too fine to avoid overfitting. In general, a finer binning scheme would allow a better description of the features of each distribution, but it would also require a larger number of events to be generated, which would make the reweighting map too computationally expensive and each file to be of a non-negligible size on disk. In this case, our binning scheme contains a total of approximately 10^5 total bins, non-uniformly distributed in order to better describe the distribution features. The binning scheme is summarized in tab. 9.3.

The reweighting map is built for both the master benchmark and for each target point in the parameter space that we want to reweight to. To estimate the model in reconstructed space and apply the reweighting map, it is necessary to loop over the observables in the master benchmark, obtain the corresponding bin in the chosen binning scheme and reweight the reconstructed spectra by multiplying them by the ratio between the two maps in the bin considered. The procedure is contained in the listing 9.1.

9.2.3 Decay filter

Events generated by DarkNews contains the kinematics of the upscattering process, including the kinematics of the e^+e^- pairs. However, events are not propagated or simulated within a detector, they are events at truth-level, where the scattering point is generated uniformly in the full TPC volume. Nonetheless, DarkNews includes the information on the decay width $c\tau_5$ of the HNLs, so that it is possible to perform a simulation of their decay inside the MicroBooNE active TPC volume afterward. To model HNLs decays inside the detector, it is possible to consider the HNL propagation direction from its momentum, and mark the decay vertex at a distance $c\tau_5$ from the scattering point. However, this procedure is computationally wasteful, especially for long HNL lifetimes, most events would likely happen outside the active TPC volume, and achieving a large event statistics would require to generate a great number of events, see fig. 9.3 top. To overcome this issue, we developed a decay filter. The decay filter is a procedure that, given a certain HNL lifetime, generates a decay vertex inside the active TPC volume, with a probability that is proportional to the HNL decay probability. In summary, it generates a new weight w_d for each event, corresponding to the probability of the HNL decay to happen inside the active TPC volume, and multiplies it to the original event weight. The application of the decay filter is shown in fig. 9.3 bottom. Considering the HNL decay vertex corresponding to the point O and the direction of the HNL momentum to cross the TPC active volume in the points A and B, the decay filter would first assign a random position x between A and B:

$$x = |\overline{OA}| + (|\overline{OB}| - |\overline{OA}|) \cdot u \,, \tag{9.16}$$

where $u \sim U(0,1)$. Finally, it would yield the following weight:

$$w_d = \begin{cases} \exp\left(-\dfrac{x}{c\tau_5}\right) & \text{if } \exists\, A, B \\ 0 & \text{if } \nexists\, A, B \end{cases} \tag{9.17}$$

Indeed, if the HNL momentum direction does not cross the active TPC volume, neither A nor B points exist, and the decay weight is set to zero, rejecting the event.

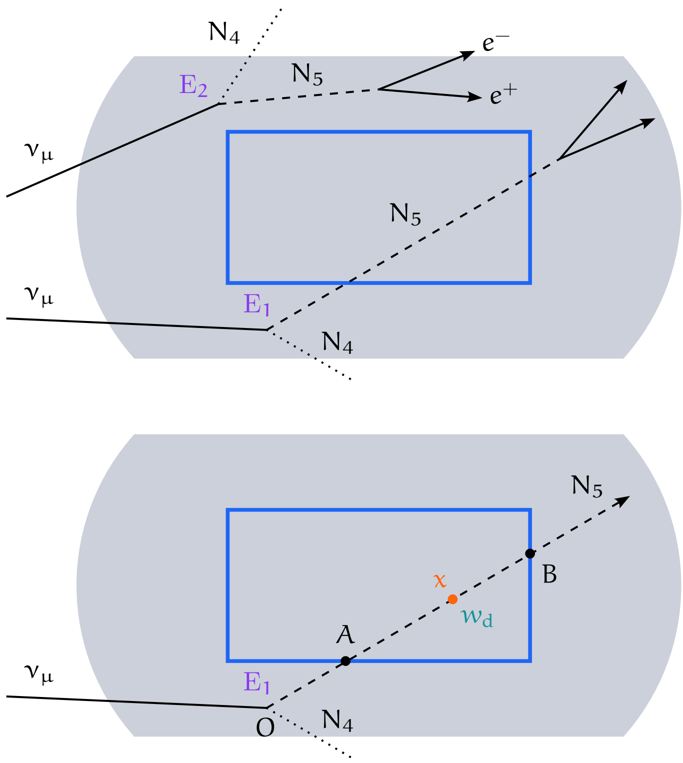

Figure 9.3: A graphical depiction of the decay filter procedure. In gray, we show the MicroBooNE TPC, while the blue rectangle represents the active TPC volume. **TOP PANEL:** the main issue associated with the realization of a simple decay simulation: events like E_1 in the picture, with long lifetime, would be rejected because they would decay outside the active volume. **BOTTOM PANEL:** the same example, but after the application of the decay filter: the event E_1 would be accepted, and the weight w_d would be associated to it. However, events like E_2 in the top panel would always be rejected, because their direction would never cross the active volume and they would always decay outside of it. The decay filter will assign a weight $w_d = 0$ to these events.

Lifetime reweighting

A second important function of the decay filter is to perform a reweighting on the HNL lifetime. The parameter space of the model is very broad, but only some parameters have an effect into modifying the kinematics of each upscattering event. These are the HNLs and dark photon masses, namely m_5, Δ and $m_{Z'}$. Other parameters, like the mixings $U_{\mu 4}$ and $U_{\mu 5}$, as well as ε, only affect the HNL lifetime, without changing the events' kinematics. This means that generating events for same values of m_5, Δ, $m_{Z'}$, while varying only $U_{\mu 4}$, $U_{\mu 5}$, ε would be computationally wasteful, because e^+e^- kinematics, which regulates the map's weights, would be substantially the same. The main difference would be the HNL lifetime, which would affect the distribution of the events decaying in the active TPC volume. It is possible to recycle the same events, and reweight them on the basis of the HNL lifetime, after performing the decay filter. This procedure would allow us to cut off approximately a factor of 50 in the number of total MC generations. The main step in this procedure involves running the decay filter multiple times, with a different HNL lifetime each time and building a two-dimensional array of weights, where the first dimension is the event index, and the second dimension is the lifetime. That array is saved separately from the main events at truth-level, and it is used to obtain the reweighting map for a certain HNL lifetime. The main advantage of this approach is that it makes the MC generation independent of parameters like $U_{\mu 4}$, $U_{\mu 5}$, ε, allowing to perform a parameter space scan only over the parameters changing the events' kinematics. Obtaining the new set of weights for a certain combination of those parameters requires just to compute the lifetime they yield, interpolate the decay filter weights $\boldsymbol{w}_\mathrm{d}$ over the lifetime values and multiply it by the original weights $\boldsymbol{w}_\mathrm{truth}$, so that the final weights after lifetime reweight can be expressed as the item by item product between the two sets of weights:

$$w^i_{c\tau} = w^i_\mathrm{truth} \cdot w^i_\mathrm{d}\,, \tag{9.18}$$

for $i \in [0, N_\mathrm{evt})$, where N_evt is the number of events in the sample. The procedure is summarized in listings 9.2 and 9.3.

9.2.4 Other reweighted quantities

Flux

The MC generation with DarkNews was run only simulating ν_μ upscattering and neglecting the contribution from $\overline{\nu}_\mu$. However, the BNB beam consists of both ν_μ and $\overline{\nu}_\mu$, with contributions of around 94 % and 6 %, respectively. Instead of generating a new set of events for $\overline{\nu}_\mu$, we decided to reweight the ν_μ events on the basis of the flux, as a function of the true neutrino energy. The

Listing 9.2: Procedure showing the usage of the decay filter on MC events generated for a certain point in the parameter space.

```
procedure GetLifetimeMap(evts, lifetimes, lifetimeMapPath)
    lifetimeMap ← EmptyMap();                          ▷ Initialize empty map
    for event in events, do                            ▷ Loop over events
        for lifetime in lifetimes, do                  ▷ Loop over lifetimes
            w ← DecayFilter(event, lifetime);          ▷ Apply decay filter
            lifetimeMap[event][lifetime] ← w;
        end for
    end for
    lifetimeMap.lifetimes ← lifetimes;                 ▷ Save lifetimes as attributes
    Write(lifetimeMap, lifetimeMapPath);               ▷ Save lifetime map to disk
end procedure
```

Listing 9.3: Procedure showing the reweighting based on the lifetime.

```
procedure ReweightByLifetime(evts, lifetimeMapPath, lifetime)
    lifetimeMap ← Read(lifetimeMapPath);               ▷ Read lifetime map
    lifetimes ← lifetimeMap.lifetimes;
    newWeights ← [];
    for i ← 0, Length(events), do                      ▷ Loop over events
        weights ← lifetimeMap[i];
        wtLifetime ← Interpolate(lifetimes, weights, lifetime);  ▷ Interpolate weights
        newWeights[i] ← events[i].weight × wtLifetime;
    end for
    return newWeights;
end procedure
```

new set of weights, computed event-by-event is given by:

$$w^{i}_{\text{flux}} = 1 + \frac{\Phi_{\overline{\nu}_\mu}(E^i_\nu)}{\Phi_{\nu_\mu}(E^i_\nu)}\,, \tag{9.19}$$

where $i \in [0, N_{\text{evt}})$.

Cross section and POT

The parameter space grid was generated with fixed values of $U_{\mu 5}$, ε and POTs, in general different to the ones used for the benchmark points. Cross section and POTs were rescaled accordingly on the basis of the different values, with the factors w_σ, w_{POT}.

9.2.5 Reweighting summary

To perform a broad analysis of the parameter space, it is necessary to obtain the reconstructed spectra for a large number of points. The full simulation chain is computationally expensive, and it is not feasible to run it for each point in the parameter space, so we developed a reweighting method, which allows reweighting the events from a master benchmark point, that has been passed through the full reconstruction chain. This method allows us to obtain the reconstructed spectra for any point in the parameter space, without the need of a full detector simulation. The reweighting map is built on the basis of the truth-level information of the events generated for a certain parameter space point, and the MC generation is performed with DarkNews. In summary, the following steps make up the final algorithm to obtain the final MicroBooNE reconstructed spectra for a generic point of the parameter space:

1. for the master benchmark point $\mathcal{M}$:
   (a) generate a large set of e^+e^- events with DarkNews for a master benchmark point;
   (b) pass these events through the full MicroBooNE reconstruction chain and obtain the final reconstructed spectra;
   (c) select a set of observables and a binning scheme and build the reweighting map for the master benchmark point, using the truth-level events;
2. perform a scan of the parameter space following a grid of $m_{Z'}$, m_5, Δ parameters:
   (a) generate a set of e^+e^- events with DarkNews for each point in the grid;
   (b) pre-calculate the observables needed to build the reweighting map for each point in the grid;
   (c) pre-calculate the decay filter weights for each point in the grid, using 60 representative values of $c\tau_5$ (from 10^{-10} to 10^8) cm;
3. for each target point $\mathcal{T}(m_{Z'}, m_5, \Delta, \varepsilon, U_{\mu4}, U_{\mu5}, \dots)$ in the grid:
   (a) calculate the proper lifetime $c\tau_5$ according to the set of parameters and compute the decay filter weights $\boldsymbol{w}_d$;
   (b) build the reweighting map where the final set of weights is

$$w^i_{\mathcal{T}} = w^i_{\text{truth}} \cdot w^i_{c\tau} \cdot w^i_{\text{flux}} \cdot w_\sigma \cdot w_{\text{POT}}\,; \qquad (9.20)$$

   for $i \in [0, N_{\text{evt}})$;

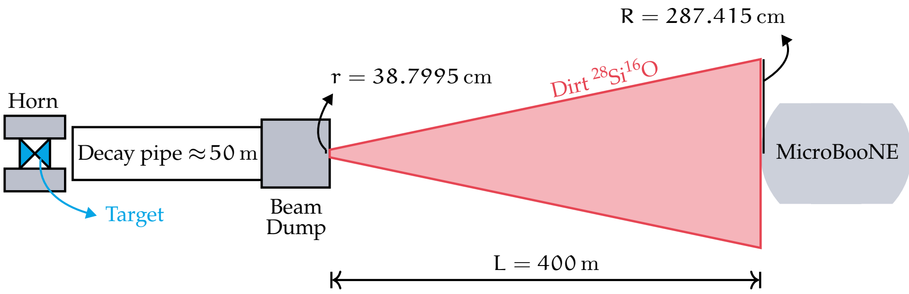

Figure 9.4: The dirt model used in the analysis. Adapted from [676].

(c) apply the reweighting map, by looping over the master benchmark reconstructed events, and reweighting them by the ratio of the maps weights in the bin they belong to:

$$w^{i}_{\mathcal{T},\text{reco}} = w^{i}_{\mathcal{M},\text{reco}} \cdot \frac{w^{i}_{\mathcal{T}}}{w^{i}_{\mathcal{M}}}\,. \tag{9.21}$$

9.2.6 Modeling the dirt upscattering signal

Before reaching the detector, neutrinos of the BNB beam go through the material surrounding the experiment, and they can interact with it. The material surrounding the MicroBooNE detector is composed of rock, concrete, steel and other components, and it will be referred as *dirt*. Neutrinos upscattering with the dirt can produce a signal that is then detected in the TPC. These events are included in the analysis, and they are generated at truth-level by the DarkNews generator, which is equipped with a dirt model. Furthermore, their treatment is then equivalent to the one applied for events generated inside the TPC, they go through the same reconstruction chain, and they are reweighted according to the same principles. The same decay filter is applied, ensuring that only events intersecting the active TPC volume are considered.

The dirt model used is made as a large truncated cone preceding the TPC, consisting of soil (46.7 % ^{28}Si and 53.3 % ^{16}O) with a density of 2.15 g cm^{-3}. The minor radius is taken to be 38.7995 cm, while the major radius is 287.415 cm, and the length of the cone is 400 m. This corresponds to a total mass of 8579.28 t. The dirt model is shown in fig. 9.4. Choosing a cone model allows the generation to be computationally more efficient, while still providing a good approximation of the dirt region, given the forward nature of the events.

In general, dirt is a source of background events in a Standard Model-only analysis. Processes happening in dirt are dominated by π^0 production and subsequent decay to a photons pair, with one of the photons entering the detector. Because the radiation length of π^0-produced photons is $\mathcal{O}(14\,\text{cm})$, only events happening in the dirt directly surrounding the detector, namely (1 to 2) m around the cryostat, are relevant to properly modelize this background.

This region is too small to contribute to the upscattering signal, while the entire dirt region from the decay pipe onward allows for a build up of the upscattering signal, potentially producing a flux of dark neutrinos, with a small fraction decaying inside the active TPC volume.

9.3 Analysis selection

9.3.1 Development

The selection is based on the same concepts developed for the NC Δ radiative analysis, but it is extended to include more topologies. The main idea is to use several Boosted Decision Trees (BDTs), each designed to target a specific background. All BDTs are rejection BDTs, making use of the XtremeGradient-Boosting (XGBoost) algorithm [684], meaning that they are trained to reject background events, while keeping signal events. If they yield a low score, it means the event looks like the background they are targeted to reject. The main difference with respect to the NC Δ radiative analysis is that the BDTs are trained over all topologies simultaneously, instead of just the $1\gamma0\text{p}$ and $1\gamma1\text{p}$ ones. We chose the four following BDTs:

- **Cosmic**: trained on real off-beam cosmic data, to suppress cosmic background;
- **CC** ν_e: focused on rejecting true intrinsic ν_e in the beam;
- **NC** π^0: NC π^0 events are the major background of the analysis, due to $\pi^0 \to \gamma\gamma$, where one photon shower is missed, similarly to what has been studied for the NC Δ search;
- **CC** ν_μ: this is a *catch-all* BDT, with the aim of rejecting all BNB-induced backgrounds, not covered by the above BDTs, including mainly CC ν_μ events with or without a final state π^0.

BDTs were trained with both MC data and real data (for the cosmic BDT), and they were validated on real BNB data, in order to ensure the MC simulation is well compatible with the data. However, cosmic data are the majority of events and a simple comparison of the MC+cosmic with BNB data would be misleading, given it would mostly be a data-to-data comparison. To avoid this scenario, a cut on a single variable, neutrino slice score, is applied. This variable is a score placed by Pandora to rank how cosmic-like (low score) or neutrino-like (high score) an event appears. This cut, placed on 0.2, allows reducing the cosmic events domination, yielding an *MC-rich* data sample, making the BDTs validation more meaningful. The data-to-MC validation has been performed on Open 5e19 Run1 data, and all tested observables show a good agreement with the data, meaning that the MC simulation is able to

Table 9.4: The final selection cuts.

BDT	Cut
Cosmic	> 0.997
CC ν_e	> 0.905
NC π^0	> 0.722
CC ν_μ	> 0.988

faithfully describe reality. The OPEN 5E19 RUN1 data is a small (approximately 5 %) data set that is unblinded, in order to perform a preliminary validation of our MC.

A note on the NC π^0 selection

The primary background of this search is the NC π^0 events, where one of the two photons is missed or mis-reconstructed. To constrain it, we used the same strategy applied in the NC Δ radiative analysis, namely to use a two-shower NC π^0 selection to constrain the large cross-section uncertainty on this background. The main differences with the original search are the larger amount of data available, due to an increase in POT number and a larger efficiency to select $2\gamma 0p$. One of the main issues in using this constraint is the fact that e^+e^- can be selected as $2\gamma Xp$ events, so that some signal events can enhance the background rate. We obtained an efficiency of around 0.09 % for mis-classified e^+e^- pairs in NC $1\pi^0$ $2\gamma 1p$ and 2.53 % for NC $1\pi^0$ $2\gamma 0p$. The latter may be important on the total number of events. We estimated that around 12 events on a total prediction of 861.6 Standard Model events for this background would be mis-classified e^+e^- pairs. We decided to neglect this contribution and to use the NC π^0 constraint as it is, without any correction.

9.3.2 Final selection

The final selection is obtained by choosing a set of cuts on the BDT scores. An event passes the selection if it satisfies simultaneously the cuts described in tab. 9.4. The distribution of the BDT scores, with a comparison with OPEN 5E9 RUN1 data, is shown in fig. 9.5. These cuts were optimized to maximize (efficiency $\times$ purity) of the new physics signal for a representative master benchmark point.

The analysis validation was performed using the OPEN 5E19 RUN1 dataset. Results in fig. 9.6 show the various steps of the application of the different selections to the data.

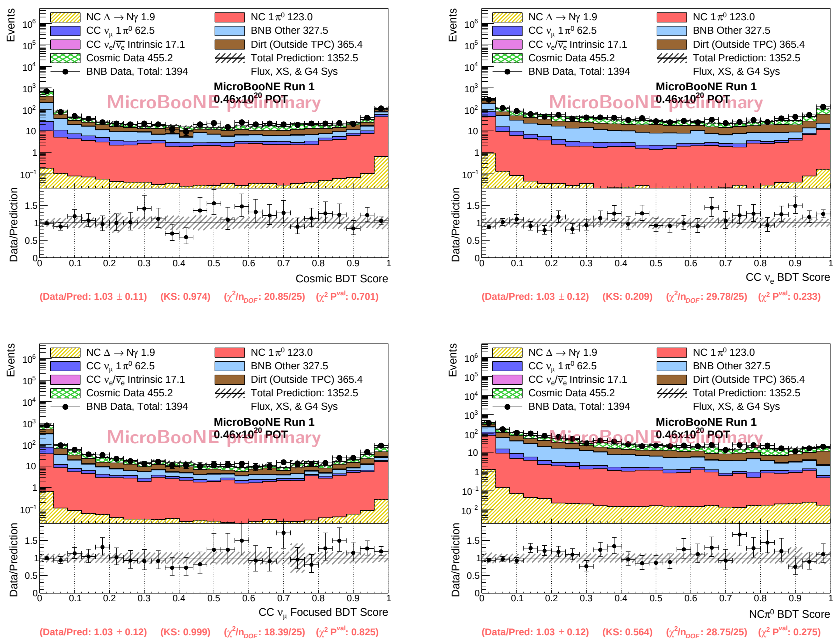

Figure 9.5: The BDT scores distributions for the final selection compared to the Open 5e9 Run1 data, with an *MC-rich* sample. Low scores correspond to background-like events, while high scores correspond to signal-like events. Figure from [676].

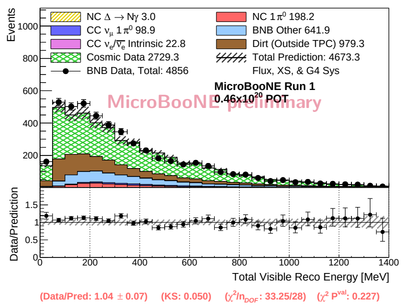

(a) Topological selection.

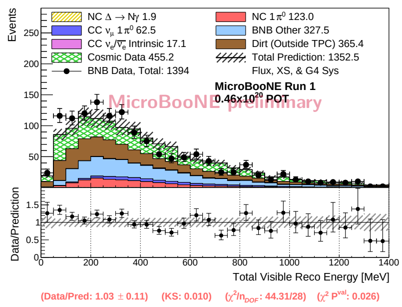

(b) *MC-rich* stage: cut on neutrino slice score.

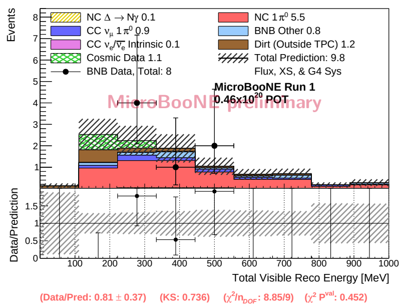

(c) All BDT cuts except NC π^0 BDT cut.

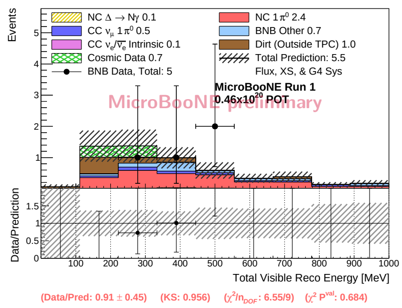

(d) Final selection with all BDT cuts applied.

Figure 9.6: The analysis validation on the Open 5e19 Run1 dataset, shown for the total visible reconstructed energy. MC is compared with data across all steps of the analysis selection, detailed as above. Figure from [676].

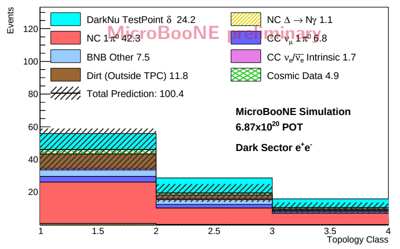

(a) Topology class (1: $1\gamma0p$, 2: $1\gamma1p$, 3: $2\gamma0p$).

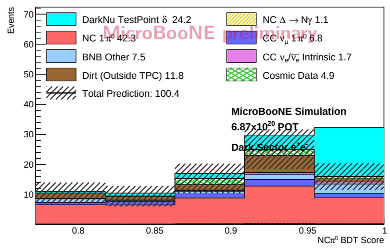

(b) NC π^0 BDT score.

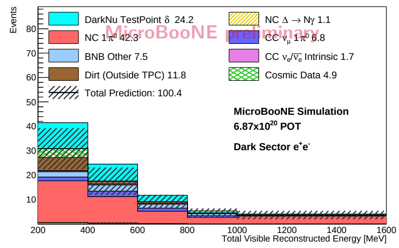

(c) Reconstructed visible energy.

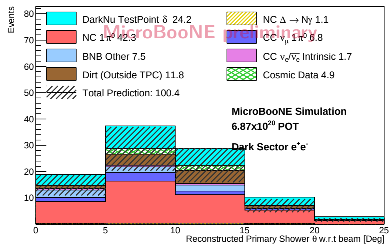

(d) Angle between the primary shower and the neutrino beam.

Figure 9.7: Final predicted spectra for Run1–3 data and 6.87×10^{20} POT exposure, for the four mentioned observables. Predictions include flux, cross section and Geant4 systematics only. The signal contribution from the test point δ is shown in light blue for shape comparison. Figure from [676].

9.3.3 Predictions

If we consider the total amount of POT, we can scale up the results of the previous section to obtain the predictions for the final selection. In fig. 9.7, we show the expected rates for the reconstructed topology, NC π^0 BDT score, reconstructed visible energy and angle between the primary shower and the neutrino beam. Additionally, we add the signal contribution from a representative test point (called δ in this case) of the parameter space of the model under investigation, for shape comparison. Note that this is a simulation scaled to the expected POT exposure reached for the Run1–3 data.

9.3.4 Efficiencies

Moving to a multi-topological selection allows us to obtain a final efficiency significantly higher than the NC Δ radiative search. The overall efficiency of the developed analysis is 21.38 %, with individual efficiencies varying in the range (10 to 30) %, and accounting for a (5 to 10) % increase on the first generation NC Δ search efficiencies. In particular, the analysis performs best for very forward e^+e^- events, $\vartheta_{beam} < 20°$, and energies (from 300 to 800) MeV, with opening angle $\vartheta_{sep} < 10°$.

9.4 Systematic uncertainties

There are three categories of systematics for background events:

- **intrinsic MC statistical uncertainty**: due to finite nature of MC, leaving a large uncertainty on distant bins and large samples;
- **re-weightable systematics**: they do not require new MC samples, but their effect on new samples can be computed through reweighting, and they involve flux, cross section (GENIE) and GEANT4 systematics;
- **detector systematics**: they include Wire Modification Systematics, Light Yield Related Systematics, Space Charge Effect Systematics and Recombination Model Systematics.

Notice that cross section systematics are relevant only for backgrounds and represent the largest source of uncertainty. For what concerns the signal, the total systematic uncertainty on the 1-bin signal e^+e^- master benchmark is approximately 11 %.

A separate consideration must be made for the dirt-generated signal events. It is necessary to include additional sources of systematics in this case, to cover potential discrepancies due to how the dirt is modeled:

- uncertainties in MicroBooNE flux scaling: the simple scaling applied of $1/R^2$, with R the distance from the TPC, is accurate for short distance, while for SBND-like distances $\mathcal{O}(100\,\mathrm{m})$ one should expect a shift of approximately 3 % [48], which we applied as an additional flux systematic;
- uncertainty in decay position of mesons inside the decay pipe: it has an effect on the flux of neutrinos and its estimation was based on observing the flux deviations by repeating the event generation fixing the parent meson decay on the furthest possible distance, namely the BNB target; we obtained an uncertainty of 1.3 %;
- uncertainties in the dirt composition: the dirt model is based on the composition of the soil surrounding the detector; recent sampling of it showed that its density can vary on the basis of water and mineral content, so that we set the following central value in DARKNEWS, $(2.15\pm0.15)\,\mathrm{g\,cm^{-3}}$, including an uncertainty of 7 % to cover the extreme cases;
- soil content composition: in DARKNEWS it is assumed to be entirely made of SiO_2, while, in reality, the distribution of elements from recent sampling shows the following weight distribution:

- O_2: 55.03 %;
- Si: 22.85 %;
- Ca: 6.05 %;
- Al: 5.51 %;
- C: 3.32 %;
- Fe: 2.91 %;
- Mg: 2.09 %;
- H: 1.23 %;
- K: 0.52 %;
- Na: 0.40 %;

accounting for nearly 1.5 % shift in the flux.

In summary, the signal from dirt systematics amounts to approximately 7.87 % uncertainty, to be added on top of the standard MicroBooNE flux uncertainty of approximately 7 %.

9.5 Sensitivities

In this analysis, the choice of the parameter space to investigate was made on the basis of the compatibility with the MiniBooNE LEE. We will use the results provided by a scan on the phase space reported in [7, fig. 7], where a fit of the MiniBooNE LEE data was performed. The fit was realized on MiniBooNE E_ν^{CCQE} spectra, in joint neutrino and antineutrino modes. In particular, the following parameters were chosen:

- m_5: smooth variable (from 0.01 to 1) GeV;
- $|U_{\mu 4}|^2 = |U_{\mu 5}|^2$: smooth variables from 10^{-1} to 10^{-11};
- Δ: varied in the list 0.3, 0.5, 1.0 and 3.0;
- $m_{Z'}$: varied in the list (0.03, 0.06, 0.10, 0.20, 0.80 and 1.24) GeV;
- $\varepsilon = 8 \times 10^{-4}$: fixed.

Sensitivities are computed and shown in figs. 9.8 and 9.9 as 95 % CL exclusion limits on the parameter space. These bounds are calculated using the Wilks Theorem with 2 d.o.f., one separate exclusion for each pair $(\Delta, m_{Z'})$. Best fit regions are shown as $3\,\sigma$ contours in $|U_{\mu 5}|$ vs m_5 plots, and each panel of figs. 9.8 and 9.9 corresponds to a different value of Δ, from nearly-degenerate to hierarchical HNL masses. Higher values of Δ open up the decay phase space, making N_5 shorter-lived, additionally making possible to release more energy in the e^+e^- pairs, so that the fit can be performed better for more regions of the parameter space. Additional model-independent exclusion bounds on heavy neutrinos provided by other experiments [685] are shown. The left-hand side of each plot is characterized by N_5 decay through off-shell Z' with long lifetime. Most events are produced in the dirt and travels to the detector. Lifetime decreases with increasing m_5, given the strong dependence $c\tau_5 \propto m_{Z'}^4 m_5^{-5}$, so that more events can decay inside the detector and a lower upscattering coupling is required to balance the number of events. The downward trend stops when N_5 becomes too short-lived to reach the detector and the dirt contribution is suppressed: the best fit regions stay constant for higher values of m_5. In the same way, $m_{Z'}$ affects the lifetime, so that higher values of $m_{Z'}$ correspond to longer lifetimes and a higher coupling is required to match the number of events. The transition from an off-shell to an on-shell regime can be computed by imposing the condition to have an on-shell decay:

$$m_5 - m_4 > m_{Z'} \Rightarrow m_5 - \frac{m_5}{\Delta + 1} > m_{Z'} \Rightarrow m_5 > \frac{\Delta + 1}{\Delta} m_{Z'} \,. \tag{9.22}$$

In general, smaller values of Δ are disfavored, because of the less energy that it is possible to release in the e^+e^- pairs, while higher values of $m_{Z'}$ are disfavored because of the longer lifetime. High values of Δ are also characterized by the opening of different decay channels, like $N_5 \to N_4N_4N_4$ ($\Delta > 2$) or $N_5 \to N_4N_4\nu$ ($1 < \Delta < 2$), but these channels are forbidden following the assumptions of a C-symmetry, see § 9.1.1.

Sensitivity curves show that the current analysis can provide strong constraints on the model, potentially excluding the MiniBooNE LEE explanation for a relevant part of its parameter space. In general, the analysis is sensitive to low mass $m_{Z'}$ across the whole parameter space, while for higher $m_{Z'}$, results improve for larger values of Δ. For low Δ, large values of m_Z' are difficult to probe.

The mixing angle values shown would provide too large contributions to the Standard Model neutrino masses from the HNLs. It is possible to prevent this consequence in several ways [287]. One possibility is to impose an approximate lepton number symmetry [686], similarly to what happens in extensions of the type-I seesaw models, such as e.g. inverse seesaw [687–689], which respect a $B - \overline{L}$ symmetry ($\overline{L}$ is the generalization of the Standard Model lepton number L for the new particles introduced). A protecting symmetry of this kind allows systematic cancellations of the contributions to the neutrino masses, so that they can be kept small, without any fine-tuning. Additionally, extensions of the model under investigation with multiple HNLs can be considered, where new contributions to the neutrino masses can also provide ad hoc cancellations. However, in such scenarios, the absence of a protecting symmetry would require a certain degree of fine-tuning.

Another important consideration regards the cosmological constraints, in particular for what concerns the BBN bounds [690, 691], that can be relevant for the parameter space under investigation. That is because, in general, HNLs that are in thermal equilibrium in the early Universe can become non-relativistic and decay during or after BBN, altering the formation of light elements and the cosmological history after BBN. In the context of the dark sector model under investigation, where $m_5 > 10\,\mathrm{MeV}$, the HNLs decay very fast, as soon as they become non-relativistic, so that they do not affect the BBN. However, in case one considers masses around and below $(3 \text{ to } 4)\,\mathrm{MeV}$, the HNLs would become non-relativistic during neutrino decoupling, so that their decay would influence the temperature of the neutrino bath (for neutrinophilic HNLs), or of the electrons-photons plasma (for electrophilic HNLs). In that scenario, BBN bounds would apply, and they would be similar to the constraints of neutrinophilic or electrophilic dark matter [692], depending on the branching ratio of the related decay channels, which ultimately depends on the Δ parameter (some combinations of m_5 and Δ can make the decay to e^+e^- kinematically inaccessible). In that mass region, one should be more careful and do a dedicated study to understand the impact of the BBN bounds on the parameter space.

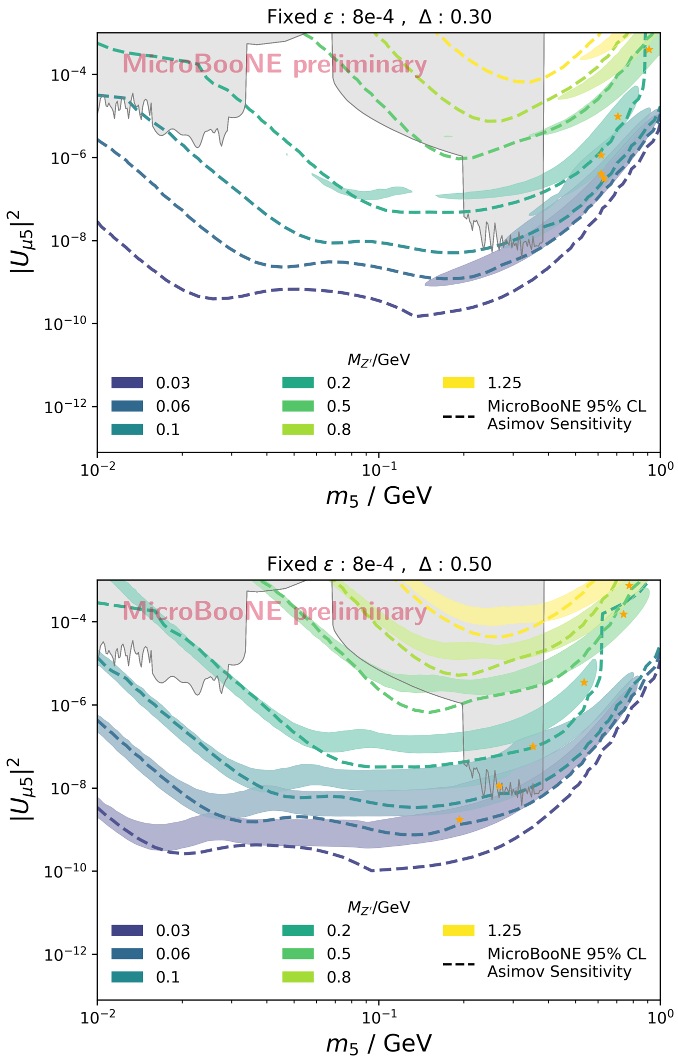

Figure 9.8: The 95 % CL exclusion limits on the parameter space relevant for the MiniBooNE LEE fit. Plots are shown as $|U_{\mu 5}|^2$ vs m_5, with the results related to different values of $m_{Z'}$ shown with the colors indicated in the legend. Sensitivities are plotted as dashed lines in the same color applied to the $m_{Z'}$ values they are associated to. Panels are characterized by $\Delta = 0.3$ (top) and $\Delta = 0.5$ (bottom). Each colored region is the 3 σ allowed region for the MiniBooNE LEE fit, and it is taken directly from [7, fig. 7], the best fit points are indicated with ★. Gray regions indicate model-independent exclusion bounds on heavy neutrinos provided by other experiments [685]. Figure from [676].

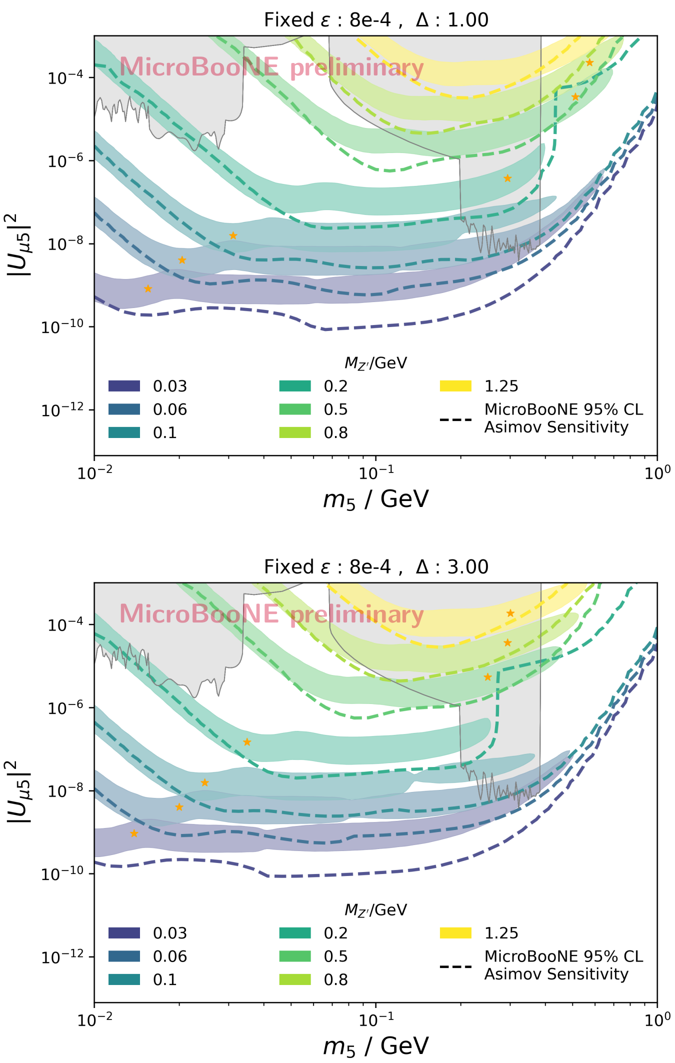

Figure 9.9: Same as fig. 9.8, for $\Delta = 1.0$ (top) and $\Delta = 3.0$ (bottom).

9.6 Summary

In this chapter we presented a new analysis for the MicroBooNE experiment, based on the search for e^+e^- pairs produced by the upscattering of a heavy neutrino in the BNB beam. The analysis is a PANDORA based, multi-topology search on the parameter space of dark sectors $(3+2)$ models, with the aim of testing the MiniBooNE LEE explanation. The dark sector model is characterized by a new $U(1)_D$ gauge symmetry, with a new massive gauge boson Z', and heavy neutrinos N_4, N_5, with mass m_4, m_5, mixing with the active neutrinos. This model is able to provide a fit to the MiniBooNE LEE data, while being compatible with the main experimental constraints [7]. The dark sector explanation of the MiniBooNE LEE is very popular, and it is timely to consider the possibility of a confirmation or a rejection of this hypothesis. The MicroBooNE experiment, equipped with LArTPC technology, is a natural candidate to perform this search, given its excellent reconstruction capabilities, able to distinguish electrons from photons, differently from MiniBooNE. Many signatures can mimic the MiniBooNE LEE, and e^+e^- pairs are one of them. This signature can be easily produced in dark sector models, and it is the objective of the presented analysis. The analysis is based on the original NC Δ radiative search performed by MicroBooNE and aims to utilize the same tools and techniques, with the addition of a multi-topology approach, to target the e^+e^- pairs.

The dark sector model under investigation is based on the fact that heavy neutrinos can be produced by upscattering of the neutrinos in the BNB beam with either the Ar in the TPC or the dirt surrounding the detector. Heavy neutrinos can then decay inside the detector, through an either on-shell or off-shell Z', producing e^+e^- pairs. If the pairs are sufficiently overlapped or energy asymmetric, they can be reconstructed as a single shower. The analysis is targeted to reconstruct several topologies of the e^+e^- pairs, namely $1\gamma0p$, $1\gamma1p$ and $2\gamma0p$.

The parameter space of the model considered is characterized by various parameters, and a full scan of it, including a simulation of the full MicroBooNE reconstruction chain, is not feasible. For this reason, a reweighting method to approximate the final reconstructed spectra in MicroBooNE has been developed. The method is based on the usage of a master benchmark point, for which a full simulation is performed, and a reweighting map is built. Any other point of the parameter space can be simply generated at truth-level and its approximated reconstructed spectra can be obtained by reweighting the master benchmark events. The reweighting tool leverages the event generator DARKNEWS, that has been used as the main event generator for the analysis. This method has been validated on dedicated test points and performs well for the purpose of the analysis. The reweighting method allows reweighting the parameter space points based both on the values of the main models parameters, but also on the basis of the lifetime of each point. For this reason, a decay filter was built and embedded into the reweighting map generation, to both ensure that only events happening inside the fiducial volume of the detector are considered, and to perform a lifetime reweighting, practically recomputing the weights of each event after the decay simulation on the basis of the new lifetime.

The core of the analysis is the selection, based on the use of several BDTs, each trained to reject a particular kind of background events. Using OPEN 5E19 RUN1 data, the BDTs have been trained and validated, and final selection cuts have been chosen to confidently reject the background. Systematic uncertainties were evaluated and included in the analysis.

Finally, a sensitivity study was performed, a scan over the parameter space of interest was realized, and results were compared with the best fit regions of the MiniBooNE LEE fit [7]. The results show that this analysis has the potential of probing the MiniBooNE LEE explanation for a relevant part of the parameter space of the dark sector model under investigation, potentially excluding it.

The analysis has been presented in its final form, and it is currently under review by the MicroBooNE collaboration, so that the final step of data unblinding can be performed.

Chapter 10

Conclusions

Black Mage: "We came to the frozen a*****e of the planet like Sarda said. What I wanna know is, where's the crappy item of great power we were promised, 'cause I don't see it. If it's something lame and immaterial like 'friendship' or 'trust', I'll have to cut his face off."
Red Mage: "Yeah, I don't need a quest to teach me the importance of faking friendship."

8-Bit Theater #536 - Savvy Customers
BRIAN CLEVINGER

The incredible success of the Standard Model of particle physics clashes with the numerous experimental evidences of new physics beyond it. The most prominent example is the dark matter problem, one of the most compelling issues in modern physics. Dark matter constitutes most of the matter content of the Universe, and many hypotheses have been made to explain its nature, with the most promising being that it is made of one or more unknown particles. The theoretical landscape of dark matter models is vast and experimental searches are ongoing in the whole world, trying to unveil the nature of dark matter or imposing stringent bounds on its main observables. In this scenario it is important to establish a connection between the theoretical models and the experimental searches, in the form of a phenomenological study of the main observables of the dark matter models, within the most promising experimental signatures.

In chapter 5, we looked at the striking signatures of γ-lines coming from direct annihilation of dark matter into photons. We considered two dark matter models, a top-philic model with a single dark matter candidate interacting with a colored scalar mediator, and the inert doublet model (IDM). Direct annihilation of dark matter into photons is a loop-induced process, and we relied on MadDM v3.2 for its computation. MadDM is also able to perform a phenomenological study of this signal, by computing the expected flux on the integrated region of interest, and imposing bounds on the basis of γ-line searches on the galactic center from Fermi-LAT and HESS experiments. These searches constrain the top-philic model below 110 GeV. For the IDM model, we considered the parameter space with a dark matter candidate in the mass range roughly (from 71 to 74) GeV. Current limits from Fermi-LAT constrain this scenario for very cuspy dark matter density profiles, while projections for Fermi-LAT and GAMMA-400 experiments can probe the same region for a broader range of dark matter profiles.

We then studied the singlet scalar Higgs portal model (SHP) in chapter 6, constituted by a scalar dark matter candidate interacting with the Higgs boson. The model is already constrained, except for the resonance region, where the dark matter mass is half of the Higgs boson mass, and allowed couplings are very small due to the resonance enhancement of the annihilation cross section. We studied the phenomenology of the model on two sides. On one hand, we computed the relic density, and implemented the constraints from direct detection and collider searches. On the other hand, we performed a combined fit using the data from the Fermi-LAT galactic center excess (GCE), dwarf spheroidal galaxies and antiprotons data. We found a region of the parameter space with dark matter mass slightly below the resonance, where the model predicts the correct relic density, is able to fit the cosmic data, and it is unconstrained by current experiments, while being in the sensitivity range of the future DARWIN experiment.

In chapter 7, we considered a superheavy dark matter candidate with mass scale of the order 10^{10} GeV, coming from a string theory model. The dark matter candidate is unstable and can decay into three fermions, through an off-shell mediator. We studied the γ-ray and neutrino spectra, simulating the showering of the dark matter decay products and keeping into account the electroweak corrections, significant for the mass range under investigation. We imposed constraints on the dark matter lifetime, with the strongest bound of $\tau_{\mathrm{DM}} \gtrapprox 10^{30}$ s for $m_{\mathrm{DM}} \approx (10^9 \text{ to } 10^{11})$ GeV. Additionally, we translated these bounds into constraints on the string coupling constant, obtaining $g_S \lessapprox 0.1$, a value consistent with the perturbative regime.

Despite the variety of dark matter models, no experimental evidence has been found so far. The elusiveness of beyond Standard Model physics may be explained by assuming new particles and interactions to be part of a dark (hidden) sector, mostly secluded from the Standard Model, if not for the presence of specific mediators, the so-called portal interactions. Portal interactions make possible to link the dark sector to the Standard Model, and they are based on different particle mediators, so that we can have the scalar, vector and neutrino portals. These couplings can be searched for in experiments, and they can be used to constrain the parameter space of dark sector models. Another motivation to consider dark sectors is that they provide a framework to develop theories solving other issues of the Standard Model, like the neutrino masses problem. In this thesis we focused on (light) dark sectors based mainly on the vector portal, where a new $U(1)_D$ dark symmetry is added, with a new gauge boson, the dark photon, kinetically mixed with the Standard Model photon.

Dark photons can be searched for in experiments, and the kinetic mixing coupling makes them able to be produced in electron colliders (like BaBar) or in fixed-target experiments (like NA64). The dark photon can decay both into visible final states (Standard Model particles) or invisible ones (dark sector particles), and searches for both signatures have been performed. In chapter 8, we considered a hybrid scenario, where the dark photon decays both into invisible states and e^+e^- pairs, that can be searched for in experiments. This new paradigm of semi-visible decays can relax the constraints on invisible dark photon decays, that must be updated accordingly. We considered different dark sector models, with a dark photon mediator in addition to heavy neutral fermions (HNFs) making up the dark sector: inelastic Dark Matter (iDM), mixed-iDM and inelastic Dirac dark matter. We also considered models with a neutrino portal, where the HNFs can also couple to neutrinos. To perform a phenomenological study of these models, we implemented a simple detector simulation for both BaBar and NA64 experiments, and we recast the bounds on invisible dark photon searches. We then discussed the parameter space of the models in light of existing constraints, highlighting also the regions where the dark photon can contribute to the magnetic moment of the muon, solving the discrepancy between the experimental measurement and the Standard Model prediction. The relaxation of the constraints due to the semi-visible nature of the dark photon decay makes possible to open new regions of the parameter space, providing a target for further experimental searches, in particular for BaBar, NA64, Belle-II and KLOE.

Finally, in chapter 9, we presented a new analysis for the MicroBooNE experiment, aimed at studying the e^+e^- pairs produced in the framework of a dark sector model with a dark photon mediator. The motivations of this analysis are twofold. On one hand, dark sectors are a promising framework to explain the anomalies in neutrino physics, like the MiniBooNE low-energy excess (LEE). On the other hand, these models can produce visible signatures in MicroBooNE: heavy neutrinos part of the dark sector can be produced through upscattering in the Booster Neutrino Beam and further decay into lighter states with e^+e^- pairs, that can be detected as a single shower if sufficiently overlapped or very energy asymmetric. In particular, we focused on the parameter space of a specific dark sector model able to accommodate the MiniBooNE LEE. The analysis follows the same approach of the neutral current Δ radiative search performed by MicroBooNE, but it employs multiple topologies to target e^+e^- pairs, namely $1\gamma0p$, $1\gamma1p$ and $2\gamma0p$. To efficiently study the full parameter space, we implemented a reweighting method, used to approximate the final reconstructed spectra in MicroBooNE. This tool is used to convert the reconstructed MicroBooNE spectra, obtained from a set of master benchmark points, to the reconstructed spectra of another parameter space point, on the basis of the truth-level distribution, that are very fast to generate. The analysis selection was developed on the basis of several boosted decision trees, that were trained and validated on open data. Selection cuts and systematic uncertainties were studied, and the expected sensitivity was computed. The results show that the analysis is able to probe a large portion of the parameter space of the dark sector model.

The existence of dark matter, the detection of anomalies in the neutrino sector and the puzzle of neutrino masses are certainly few of the most compelling challenges in contemporary physics. These topics have been guiding the global theoretical and experimental research for several decades. This thesis has delved into the intricate realm of dark matter and light dark sectors, offering theoretical insights and experimental perspectives. We learned that photons can carry a lot of information to unveil the nature of dark matter. Photon lines from dark matter annihilation in the galactic center are a striking signature that can be searched for in experiments. Future searches by Fermi-LAT, HESS, GAMMA-400 and CTA will provide strong exclusion bounds on the parameter space of dark matter models. On the other hand, the continuum spectrum of photons is responsible for the Fermi-LAT GCE, which can be fit exceptionally well in the picture of annihilating dark matter. In this context, the SHP model on the Higgs resonance region is able to fit it along with other astrophysical data and predict the correct relic density, while being unchallenged by current direct detection and collider constraints. If dark matter hides within such a simple model, its discovery is close, since the parameter space can be probed by the future DARWIN experiment. Indirect detection does not stop at photons, and neutrinos can also be used to search for dark matter. Future searches by experiments like IceCube-Gen2, RNO and GRAND will be able to probe the parameter space of superheavy decaying dark matter, imposing strong bounds on its lifetime, and constraining the parameter space of theoretical models.

From a theoretical point of view, the problem of dark matter can be tackled with light dark sectors models, which provide a diverse array of possibilities to extend the Standard Model of particle physics. Dark photons are a promising framework to build light dark sectors containing several HNFs that can also mix with neutrinos. In particular, semi-visible dark photon models are an interesting paradigm, where the dark photon can decay both into invisible states and e^+e^- pairs, allowing to lift the major constraints on the dark photon parameter space, and providing a target for future experimental searches by BaBar, NA64 and Belle-II. Additionally, these e^+e^- pairs can be searched for in the MicroBooNE experiment. This signal is able to explain the MiniBooNE LEE, and it is timely to perform a dedicated search in MicroBooNE, with the aim of establishing these dark sector models.

Ongoing experimental efforts continue to push the boundaries of our knowledge, aiming to unveil the mysteries concealed within dark matter and neutrinos. The theoretical input is essential to guide the experimental searches, and the phenomenological study of light dark sectors is a crucial step to establish a connection between the two. Physics is entering a groundbreaking era, pushing the boundaries of the Standard Model with unprecedented precision while exploring the realms of new physics at the highest energies. The future is full of exciting prospects.

Appendix A

Notation

In this appendix we list the notation used in the thesis. Notice that the identity and null matrices are indicated with $\mathbb{1}$ and 0, respectively. Their dimension is clear from the context.

A.1 Field theory

A.1.1 Metric tensor

The metric tensor is indicated with $g_{\mu\nu}$. We use the *west-coast*, or *mostly minus*, convention:

$$g_{\mu\nu} = \mathrm{diag}(1, -1, -1, -1)\,. \tag{A.1}$$

A.1.2 Pauli matrices

The Pauli matrices are indicated with σ^i, with $i \in \{1, 2, 3\}$, and they are defined as:

$$\sigma^1 = \begin{pmatrix} 0 & 1 \\ 1 & 0 \end{pmatrix}\,, \tag{A.2a}$$

$$\sigma^2 = \begin{pmatrix} 0 & -i \\ i & 0 \end{pmatrix}\,, \tag{A.2b}$$

$$\sigma^3 = \begin{pmatrix} 1 & 0 \\ 0 & -1 \end{pmatrix}\,. \tag{A.2c}$$

We also use the following *tensor-like* notation:

$$\sigma^\mu \doteq (\mathbb{1}, \boldsymbol{\sigma})\,, \tag{A.3a}$$

$$\overline{\sigma}^\mu \doteq (\mathbb{1}, -\boldsymbol{\sigma})\,. \tag{A.3b}$$

A.1.3 Dirac matrices

We use the Dirac representation in the chiral basis for the γ matrices:

$$\gamma^{\mu} = \begin{pmatrix} 0 & \sigma^{\mu} \\ \overline{\sigma}^{\mu} & 0 \end{pmatrix} . \tag{A.4}$$

The γ^{μ} matrices satisfy the Clifford algebra:

$$\{\gamma^{\mu}, \gamma^{\nu}\} = 2g^{\mu\nu}\mathbb{1} . \tag{A.5}$$

The γ^5 matrix is defined as:

$$\gamma^5 \doteq -i\gamma^0\gamma^1\gamma^2\gamma^3 = \begin{pmatrix} \mathbb{1} & 0 \\ 0 & -\mathbb{1} \end{pmatrix} , \tag{A.6}$$

and it satisfies:

$$\{\gamma^{\mu}, \gamma^5\} = 0 . \tag{A.7}$$

We have the following properties under complex conjugation:

$$\gamma^{\mu\dagger} = \gamma^0\gamma^{\mu}\gamma^0 , \tag{A.8a}$$

$$\gamma^{5\dagger} = \gamma^5 . \tag{A.8b}$$

A.1.4 Spinors

Dirac spinors are indicated by ψ. Weyl spinors are indicated with the subscript "w", like ψ_{w}. Chirality is indicated with subscripts L and R, and a left-handed Weyl spinor is indicated with ψ_{wL}. So we have:

$$\psi = \begin{pmatrix} \psi_{\mathrm{wL}} \\ \psi_{\mathrm{wR}} \end{pmatrix} . \tag{A.9}$$

The Lagrangian of a massive Dirac spinor is:

$$\mathcal{L} = \overline{\psi}(i\gamma^{\mu}\partial_{\mu} - m)\psi . \tag{A.10}$$

And the Dirac conjugate is:

$$\overline{\psi} \doteq \psi^{\dagger}\gamma^0 . \tag{A.11}$$

The chirality projectors are defined as:

$$P_L \doteq \frac{1+\gamma^5}{2} = \begin{pmatrix} \mathbb{1} & 0 \\ 0 & 0 \end{pmatrix}, \tag{A.12a}$$

$$P_R \doteq \frac{1-\gamma^5}{2} = \begin{pmatrix} 0 & 0 \\ 0 & \mathbb{1} \end{pmatrix}, \tag{A.12b}$$

$$\tag{A.12c}$$

satisfying the following properties:

$$P^{\dagger}_{\substack{L\\R}} = P_{\substack{L\\R}}, \tag{A.13a}$$

$$P^{2}_{\substack{L\\R}} = P_{\substack{L\\R}}, \tag{A.13b}$$

$$P_L\, P_R = P_R\, P_L = 0\,, \tag{A.13c}$$

$$P_L + P_R = \mathbb{1}\,. \tag{A.13d}$$

We can use the following shorthand notation for chiral Dirac spinors:

$$\psi_L \doteq P_L\,\psi = \begin{pmatrix} \psi_{wL} \\ 0 \end{pmatrix}, \tag{A.14a}$$

$$\psi_R \doteq P_R\,\psi = \begin{pmatrix} 0 \\ \psi_{wR}\,. \end{pmatrix} \tag{A.14b}$$

A.1.5 Charge conjugation

The charge conjugation operator is indicated with $\mathcal{C}$. Its action on a Dirac spinor is:

$$\psi^c \doteq \mathcal{C}\overline{\psi}^{\mathsf{T}}, \tag{A.15}$$

The definition of $\mathcal{C}$ is:

$$\mathcal{C} \doteq -i\gamma^2\gamma^0\,. \tag{A.16}$$

with the following properties:

$$\mathcal{C}^{\mathsf{T}} = -\mathcal{C}\,, \tag{A.17a}$$

$$\mathcal{C}^{-1} = -\mathcal{C}\,, \tag{A.17b}$$

$$\mathcal{C}^{\dagger} = -\mathcal{C}\,, \tag{A.17c}$$

$$\mathcal{C}^{*} = \mathcal{C}\,, \tag{A.17d}$$

$$\mathcal{C}^{\dagger}\mathcal{C} = \mathbb{1}\,, \tag{A.17e}$$

$$\mathcal{C}^{2} = -\mathbb{1}\,. \tag{A.17f}$$

A.1.6 Standard Model fields and indices

Each Standard Model field is linked to a certain particle. In general, we use the convention so that the name of the field is the same as the name of the particle, and this is always clear from the context. This is a slight abuse of notation, given a particle is a state generated by the field itself through the field expansion in construction and destruction operators.

For fields presenting multiple generations or multiple components, the situation is a little bit more tricky, because indices stack up. In general, we will use both the notation where a field has the same name of the particle it refers to, and the one where a field is indicated by ψ_p, where p is the name of the particle, only in the case of fermion fields. Usually, we avoid writing generation indices explicitly, in favor of the vector notation, such that

$$\mathbf{u} = \begin{pmatrix} \psi_u \\ \psi_c \\ \psi_t \end{pmatrix} , \tag{A.18a}$$

$$\mathbf{d} = \begin{pmatrix} \psi_d \\ \psi_s \\ \psi_b \end{pmatrix} , \tag{A.18b}$$

$$\boldsymbol{\ell} = \begin{pmatrix} \psi_e \\ \psi_\mu \\ \psi_\tau \end{pmatrix} , \tag{A.18c}$$

where ψ_f is the quantum field of the particle f. Notice that f may include also the weak isospin doublets, such as $\mathbf{L}$ or $\mathbf{Q}$, for which the vector notation can be used as well, where each component is a different generation doublet.

In the case of beyond Standard Model fields, such as dark or sterile HNFs, or HNLs, we usually write the following vectors

$$\boldsymbol{\nu}_D = \begin{pmatrix} \nu_{D1} \\ \vdots \\ \nu_{Dd} \end{pmatrix} , \tag{A.19a}$$

$$\boldsymbol{\nu}_N = \begin{pmatrix} \nu_{N1} \\ \vdots \\ \nu_{Nn} \end{pmatrix} , \tag{A.19b}$$

$$\mathbf{N} = \begin{pmatrix} N_1 \\ \vdots \\ N_{n'} \end{pmatrix} , \tag{A.19c}$$

where d, n and n' are the number of the components, introduced for each field.

When expanding vectors explicitly, we use the generation index. Usually, we just employ Latin indices i, $j \in \{1, 2, 3\}$ to mark the generation, unless we are dealing with leptons, in which case we may also use the *flavor* index $\alpha \in \{e, \mu, \tau\}$. We assume the flavor index can be used also as a matrix index (formally, this implies the assumption of a bijective map between the Latin numeric and the flavor indices). This means the following expressions for the lepton masses (after electroweak symmetry breaking) are equivalent:

$$\mathcal{L} \supset -\frac{v}{\sqrt{2}} Y_\ell^{ij} \overline{\ell_{iL}} \ell_{jL} + \text{h.c.}\,, \tag{A.20}$$

$$\mathcal{L} \supset -\frac{v}{\sqrt{2}} Y_\ell^{\alpha\alpha'} \overline{\ell_{\alpha L}} \ell_{\alpha' L} + \text{h.c.}\,. \tag{A.21}$$

The definition of the $SU(2)_L$ doublets follows the same logic.

Finally, when specified, primed fields are used to indicate flavor states, while unprimed fields are used to indicate mass states.

A.2 Abbreviations

Any abbreviation used in the thesis is always defined in advance. The only exceptions are the abbreviations listed in this section.

Shorter notations are used for the trigonometric functions:

- $c_\vartheta \doteq \cos(\vartheta)$;
- $s_\vartheta \doteq \sin(\vartheta)$;
- $t_\vartheta \doteq \tan(\vartheta)$.

Moreover, an upright "w" as a subscript of each function indicates the *weak* (Weinberg) angle, e.g. $s_\mathrm{w} \doteq \sin(\vartheta_\mathrm{w})$.

Additionally, in general the subscript *zero* is used to label either quantities measured *today*, e.g. $a_0 = a(t_0)$, or the zeroth-order expansion, depending on the context. Several other abbreviations are used in subscripts, but they are trivial and clear from the context.

A.3 Units

If not explicitly specified, natural units are assumed: $c = 1$, $\hbar = 1$.

Typesetting of units and measurements in this thesis follows the regulations of the *National Institute of Standards and Technology* (NIST) [693].

Appendix B

A brief review of cosmology

In this appendix, we will introduce the main concepts of cosmology used in the thesis and summarized from [60, § 2]. A more complete treatment of the topics can be found in books, for example [64, 65].

B.1 The Friedmann equations

The Universe observed at large scales, namely larger than 10 Mpc, is well described by the Cosmological Principle: it is both homogeneous and isotropic. We can write the Einstein's equations:

$$R_{\mu\nu} - \frac{1}{2} g_{\mu\nu} R + \Lambda g_{\mu\nu} = 8\pi G T_{\mu\nu} \,, \tag{B.1}$$

where $R_{\mu\nu}$ is the Ricci tensor, R is the Ricci scalar, Λ is the cosmological constant, $g_{\mu\nu}$ is the space-time metric and $T_{\mu\nu}$ is the energy-momentum tensor. Their solution yields the Friedmann-Lemaître-Robertson-Walker metric:

$$ds^2 = dt^2 - a(t)^2 \left(\frac{dr^2}{1 - kr^2} + r^2 d\vartheta^2 + r^2 \sin^2(\vartheta) d\varphi^2 \right), \tag{B.2}$$

where r, ϑ, φ are the spherical coordinates and $a(t)$ is the scale factor. The factor k is called curvature and can take the possible values: 1 for a close Universe, 0 for a flat Universe and -1 for an open Universe. We can define the Hubble parameter:

$$H(t) \doteq \frac{\dot{a}(t)}{a(t)} \,, \tag{B.3}$$

its value depends on time. Today we have [20]:

$$H_0 = (67.36 \pm 0.54)\,\mathrm{km\,s^{-1}\,Mpc^{-1}} \approx h \cdot 100\,\mathrm{km\,s^{-1}\,Mpc^{-1}} \,, \tag{B.4}$$

where the dimensionless parameter $h = 0.6736 \pm 0.0054$.

The components of the energy-momentum tensor mean the following: T^{00} is the energy density; T^{0j} is the energy flux across the spatial surface where x_j, $j \in \{1, 2, 3\}$, is constant; T^{i0} is the density of i^{th} component of momentum; T^{ij} is the i^{th} component of momentum flux across the spatial-surface so that x_j is constant. Normal momentum flux T^{ij}, with $i = j$, causes normal stress on the fluid element and the others T^{ij}, with $i \neq j$, cause shear stress. We can consider the approximation of perfect fluid (an idealized model of fluids characterized by no viscosity or heat conduction) and study the energy-momentum tensor in a comoving frame with it. Since heat conduction is null, there is no energy flux, so $T^{0j} = 0$. The absence of viscosity implies that there are not shear stresses $T^{ij} = 0$, with $i \neq j$. Further, isotropy implies that spatial components must be equal, so that $T^{ij} \propto \delta^{ij}$. That means we can cast the energy-momentum tensor in a simple, diagonal form:

$$T^{\mu\nu} = \mathrm{diag}(\rho, -P, -P, -P)\,, \tag{B.5}$$

where ρ is the energy density and P is the pressure, that characterizes normal stresses.

The dynamical equations describing the evolution of the scale factor $a(t)$ can be found solving eq. (B.1), assuming the metric eq. (B.2), yielding the Friedmann equations:

$$\dot{a}^2 + k = \frac{8}{3}\pi G \rho a^2\,, \tag{B.6a}$$

$$\ddot{a} = -\frac{4}{3}(\rho + 3P)a\,, \tag{B.6b}$$

From eq. (B.6a) we obtain

$$1 + \frac{k}{H(t)^2 a(t)^2} = \rho(t)\frac{8\pi G}{3H(t)^2}\,, \tag{B.7}$$

where we define the critical density:

$$\rho_c(t) \doteq \frac{3H(t)^2}{8\pi G}\,, \tag{B.8}$$

and consequently we introduce the dimensionless density parameter as the ratio

$$\Omega(t) \doteq \frac{\rho(t)}{\rho_c(t)}\,. \tag{B.9}$$

B.2 Composition of the Universe

The energy-momentum tensor satisfies the continuity equation $\nabla_\mu T^{\mu\nu} = 0$, where ∇_μ is the covariant derivative. Considering the $\nu = 0$ component we obtain the conservation of energy:

$$\frac{\partial \rho}{\partial t} + 3\frac{\dot{a}}{a}(\rho + P) = 0\,. \tag{B.10}$$

In general we can specify an equation of state for each component of the Universe in the form:

$$P = w\rho\,, \tag{B.11}$$

where w is a constant, with value:

- $w = 0$, for non-relativistic matter (dust). We have $P = nk_BT = \rho k_BT/m$ (k_B is the Boltzmann constant), but for non-relativistic species (see app. B.3) $T \ll m$, so that $P \approx 0$;
- $w = 1/3$, for radiation, because radiation pressure can be expressed as $P = \rho/3$;
- $w = -1$, for dark energy. Today observations show that the expansion of the Universe is accelerated, and this is incompatible with a dust-dominated Universe. The simplest way to take it into account is to assume the presence of Dark Energy, implemented via the celebrated cosmological constant, characterized by $P = -\rho$.

We can integrate eq. (B.10) obtaining

$$\rho \propto a^{-3(1+w)}\,, \tag{B.12}$$

and so we can write the different trend of the components through time:

$$\rho_r \propto a^{-4}\,, \tag{B.13a}$$
$$\rho_m \propto a^{-3}\,, \tag{B.13b}$$
$$\rho_\Lambda \propto a^{0}\,. \tag{B.13c}$$

The different dependence of the constituents of the Universe on the scale factor a implies that the Universe has evolved through different phases. In particular, there was an instant, called equivalence, in which the energy density of the radiation component was equal to the energy density of the matter component. We can also compute the time dependence of $a(t)$, obtaining:

$$a \propto t^{1/2} \quad \text{radiation epoch,} \tag{B.14a}$$
$$a \propto t^{2/3} \quad \text{matter epoch.} \tag{B.14b}$$

The density parameter is given by considering all the contributions of the different components the Universe is made of:

$$\Omega = \sum_{i \in \{\text{components}\}} \Omega_i\,. \tag{B.15}$$

B.3 Equilibrium thermodynamics

The history of the Universe is a history of cooling. If we consider the actual temperature of the Universe, we have $T_0 = 2.73\,\mathrm{K}$, that is the temperature of the CMB radiation. However, going backwards in time, in the early Universe, temperature was higher than now. Universe is made of different species, that are characterized by a mass m and a temperature T. In the early Universe, the sizable interaction strength of the Standard Model gauge groups implies that species were in thermal equilibrium, so there were processes (e.g. elastic scatterings between particles) maintaining the species thermalized. If these processes are faster than the rate of the expansion of the Universe, they are efficient and keep the species in equilibrium. Considering a weakly interacting gas of particles with g internal degrees of freedom, we can compute the expression of the number density n, the energy density ρ and the pressure P at thermal equilibrium,

$$n = \frac{g}{(2\pi)^3} \int f(\mathbf{p})\, d^3p\,, \tag{B.16}$$

$$\rho = \frac{g}{(2\pi)^3} \int f(\mathbf{p}) E(\mathbf{p})\, d^3p\,, \tag{B.17}$$

$$P = \frac{g}{(2\pi)^3} \int \frac{|\mathbf{p}|^2}{3E(\mathbf{p})} f(\mathbf{p})\, d^3p\,, \tag{B.18}$$

where $f(\mathbf{p})$ is the phase space distribution function (occupancy function) and the energy is given by $E(\mathbf{p})^2 = |\mathbf{p}|^2 + m^2$. When particles exchange energy and momentum efficiently, the system is in kinetic equilibrium, and the function $f(\mathbf{p})$ is the Fermi-Dirac (FD) or the Bose-Einstein (BE) distribution function, respectively for fermions and bosons:

$$f_{\substack{FD\\BE}}(\mathbf{p}) = \left[\exp\left(\frac{E(\mathbf{p}) - \mu}{T}\right) \pm 1\right]^{-1}\,, \tag{B.19}$$

where μ is the chemical potential. The following process

$$a + b \rightleftharpoons c + d\,, \tag{B.20}$$

is in chemical equilibrium if the forward and backward reactions are in equilibrium, so the chemical potentials are linked by the following equivalence:

$$\mu_a + \mu_b = \mu_c + \mu_d\,. \tag{B.21}$$

Introducing the parameter $x \doteq m/T$, making the change of variable $\xi = p/T$, considering spherical coordinates and dropping the chemical potential (because at early time is assumed to be small) we rewrite eqs. (B.16)–(B.18):

$$n = \frac{g}{2\pi^2} T^3 \int_0^{+\infty} \frac{\xi^2}{\exp\left(\sqrt{\xi^2 + x^2}\right) \pm 1} \, d\xi \,, \tag{B.22}$$

$$\rho = \frac{g}{2\pi^2} T^4 \int_0^{+\infty} \frac{\xi^2 \sqrt{\xi^2 + x^2}}{\exp\left(\sqrt{\xi^2 + x^2}\right) \pm 1} \, d\xi \,, \tag{B.23}$$

$$P = \frac{g}{6\pi^2} T^4 \int_0^{+\infty} \frac{\xi^4}{\sqrt{\xi^2 + x^2}\left[\exp\left(\sqrt{\xi^2 + x^2}\right) \pm 1\right]} \, d\xi \,, \tag{B.24}$$

Consider a certain species χ with mass m. It is possible to consider the relativistic and non-relativistic scenarios to cast eqs. (B.22)–(B.24) in a simpler form:

- relativistic case: $T \gg m$ ($x \ll 1$), the species contribute to the energy density of the radiation component of the Universe and χ can be produced by the other species in the thermal bath,

$$n = \begin{cases} \dfrac{\zeta(3)}{\pi^2} g T^3 & \text{bosons,} \\ \dfrac{3}{4} \dfrac{\zeta(3)}{\pi^2} g T^3 & \text{fermions,} \end{cases} \tag{B.25}$$

$$\rho = \begin{cases} \dfrac{\pi^2}{30} g T^4 & \text{bosons,} \\ \dfrac{7}{8} \dfrac{\pi^2}{30} g T^4 & \text{fermions,} \end{cases} \tag{B.26}$$

$$P = \frac{\rho}{3} \,; \tag{B.27}$$

- non-relativistic case: $T \ll m$ ($x \gg 1$), χ can not be produced by the other species in the thermal bath (that do not have enough energy),

$$n = g \left(\frac{mT}{2\pi} \right)^{3/2} \exp\left(-\frac{m}{T} \right) , \tag{B.28}$$

and at lowest order we can consider $E(\mathbf{p}) \approx m$ and so energy density is equal to the mass density,

$$\rho = mn \,, \tag{B.29}$$

while, considering the equation of state for a perfect gas we have,

$$P = nT \,, \tag{B.30}$$

and, by mean of $m \gg T$, we have $P \ll \rho$, so a non-relativistic gas of particles acts like pressureless dust.

Departures from the thermal equilibrium are possible and constitutes one of the main event characterizing the evolution of the Universe. The decoupling of a certain species happens when the rate of the expansion of the Universe is faster than the rate of the processes that maintain the species in thermal equilibrium. In summary, the key events that happened to the various species during the evolution of the Universe are:

- the transition from being relativistic to being non-relativistic;
- the decoupling: the processes that kept the species thermalized within each other becomes inefficient, because their rate is lower than the expansion rate of the Universe.

We can compute the total radiation energy density ρ_r by simply summing eq. (B.26) over the relativistic species,

$$\rho_r(T) = \sum_i \rho_i(T) = \frac{\pi^2}{30} g_\star(T) T^4 \,, \tag{B.31}$$

where $g_\star(T)$ is the effective number of degrees of freedom at a certain temperature T. It has two contributions:

$$g_\star(T) = g_\star^{\text{th}}(T) + g_\star^{\text{dec}}(T) \tag{B.32}$$

- species that are relativistic and in thermal equilibrium with radiation:

$$g_\star^{\text{th}}(T) = \sum_{i \in \{\text{bosons}\}} g_i + \frac{7}{8} \sum_{i \in \{\text{fermions}\}} g_i \,, \tag{B.33}$$

  there is no dependence on the temperature, because all the species are in thermal equilibrium and have the same temperature T;

- species that are relativistic but also decoupled from the cosmological fluid, so are not in thermal equilibrium with the other species:

$$g_\star^{\text{dec}}(T) = \sum_{i \in \{\text{bosons}\}} g_i \left(\frac{T_i}{T}\right)^4 + \frac{7}{8} \sum_{i \in \{\text{fermions}\}} g_i \left(\frac{T_i}{T}\right)^4 \,, \tag{B.34}$$

  and we see the dependence on the temperature of the species.

If we consider T larger than the top quark mass, every particle of the Standard Model is relativistic, so we have:

$$\begin{aligned} g_\star(T) = &\underbrace{2}_{\gamma} + \underbrace{3 \cdot 3}_{W^\pm, Z} + \underbrace{8 \cdot 2}_{g} + \underbrace{1}_{h} + \frac{7}{8} \Big(\underbrace{6 \cdot 2 \cdot 3 \cdot 2}_{q_i, \overline{q}_i \forall i \in \{\text{colors}\}} + \underbrace{3 \cdot 2 \cdot 2}_{e^\pm, \mu^\pm, \tau^\pm} + \underbrace{3 \cdot 2}_{\nu_e, \nu_\mu, \nu_\tau} \Big) \\ = &\, 106.75 \,, \end{aligned} \tag{B.35}$$

where we assumed three massless neutrino species.

B.4 Entropy

We can consider the expansion of the Universe as adiabatic, so we have the conservation of entropy. By the Second Law of Thermodynamics we have

$$T\,dS = dU + P\,dV\,, \tag{B.36}$$

with $U = \rho V$, so we obtain

$$dS = d\left(\frac{\rho + P}{T}V\right). \tag{B.37}$$

We can define the entropy per comoving volume,

$$s \doteq \frac{S}{V} = \frac{\rho + P}{T}\,, \tag{B.38}$$

that is conserved in thermal equilibrium. Now we can compute the total entropy per comoving volume, that is dominated by the relativistic species, as we have done in eq. (B.31), obtaining

$$s = \sum_i \frac{\rho_i + P_i}{T_i} = \frac{2\pi^2}{45} g_{\star S}(T) T^3\,, \tag{B.39}$$

where $g_{\star S}(T)$ is the effective number of degrees of freedom in Entropy at a certain temperature T, and it has two contributions:

$$g_{\star S}(T) = g_{\star S}^{th}(T) + g_{\star S}^{dec}(T) \tag{B.40}$$

- species in thermal equilibrium:

$$g_{\star S}^{th}(T) = \sum_{i\in\{\text{bosons}\}} g_i + \frac{7}{8} \sum_{i\in\{\text{fermions}\}} g_i = g_{\star}^{th}(T)\,, \tag{B.41}$$

- species that are decoupled:

$$g_{\star S}^{dec}(T) = \sum_{i\in\{\text{bosons}\}} g_i \left(\frac{T_i}{T}\right)^3 + \frac{7}{8} \sum_{i\in\{\text{fermions}\}} g_i \left(\frac{T_i}{T}\right)^3. \tag{B.42}$$

Furthermore, S is conserved:

$$S = sV \propto s a^3 \propto g_{\star S}(T) T^3 a^3\,. \tag{B.43}$$

Inverting the above expression we have

$$T \propto {g_{\star S}}^{-1/3} a^{-1} \,. \tag{B.44}$$

Whenever a species becomes non-relativistic, $g_{\star S}$ drops, while the temperature of the thermal bath T raises, according to eq. (B.44). This happens because of the conservation of entropy: when a species becomes non-relativistic, its entropy is transferred to the other species in the thermal bath.

B.5 Structure formation

The observations of our Universe on large scales suggest that it is both homogeneous and isotropic. However, on small scales it is very lumpy, the density of galaxies is about 10^5 times the average density of the Universe, and the density of a cluster of galaxies is about 10^2 to 10^3 times the average density of the Universe. These structures represent density perturbations in the actual Universe. We can define a density perturbation as

$$\delta \doteq \frac{\delta\rho}{\overline{\rho}} = \frac{\rho - \overline{\rho}}{\overline{\rho}} \,. \tag{B.45}$$

Today we can measure perturbations of the order $\delta \approx 10^2$, while at the time of the CMB they were of the order

$$\frac{\Delta T}{T} \lessapprox 10^{-5} \,. \tag{B.46}$$

How could the Universe get from a smooth situation with $\delta \approx 10^{-5}$ to a lumpy situation with $\delta \approx 10^2$? Cosmologists think that at the basis of the growth of perturbations we can find the gravitational instabilities, that carried the evolution of small inhomogeneities into the larger ones we can observe today. Density perturbations have a different growth rate on the basis of the composition of the Universe. Focusing on matter density perturbations in the presence of a gravitational field, we can write the following differential equation:

$$\ddot{\delta}_k + 2H\dot{\delta}_k + 4\pi G\rho_0 \left(\frac{k^2}{k_J^2} - 1 \right) \delta_k = 0 \,, \tag{B.47}$$

called Jeans equation, where $\delta_k(t) \doteq \hat{\delta}(t, \mathbf{k})$ is the Fourier transform of $\delta(t, \mathbf{x})$,

$$\delta(t, \mathbf{x}) = \int \frac{d^3k}{(2\pi)^3} \hat{\delta}(t, \mathbf{k}) \exp(-i\mathbf{k} \cdot \mathbf{x}) \,, \tag{B.48}$$

and k_J is the Jeans wavenumber, defined as

$$k_J = \frac{4\pi G \rho_0 a^2}{v_s^2}\,, \tag{B.49}$$

with v_s being the (adiabatic) sound speed,

$$v_s^2 = \left(\frac{\partial P}{\partial \rho}\right)_S\,. \tag{B.50}$$

The Jeans wavenumber separates the gravitationally stable and unstable modes. In particular, only perturbations such that $k \ll k_J$ can grow. Solving eq. (B.47) in that case, we obtain that in a matter-dominated Universe, matter perturbations grow as:

$$\delta_k \propto t^{2/3}\,. \tag{B.51}$$

However, considering a radiation-dominated epoch, the solutions of eq. (B.47) have the following form:

$$\delta_k \propto A + B\log(t)\,, \tag{B.52}$$

where A and B are constants. This means matter perturbations growth is damped. That happens because in a radiation-dominated epoch, the expansion rate is faster than it would be in a matter-dominated one, and the growth of perturbation is moderated. Finally, the matter perturbations can grow only in a matter-dominated Universe. However before the decoupling, matter is strongly coupled to radiation, which implies a large sound speed $c/\sqrt{3}$, that contributes to wipe out the perturbations.

Is it possible to cast k_J in another form, by introducing the Jeans length,

$$\lambda_J \doteq \frac{2\pi}{k_J}\,. \tag{B.53}$$

In this case the condition for growing perturbations is $\lambda \gg \lambda_J$. In general the Jeans length has the following form:

$$\lambda_J \propto \frac{v_s}{\sqrt{\rho}}\,. \tag{B.54}$$

As we see, the sound speed opposes to the gravitational collapse, because faster perturbations dissipate easily, resulting in a large value of the Jeans length. On the other hand a larger density makes the collapse easier, because the gravitational field is stronger. Next to the Jeans length, we can define the Jeans mass. It is the mass contained in a sphere of radius λ_J,

$$M_J \propto \rho\lambda_J^3\,. \tag{B.55}$$

The propagation of a perturbation of mass M is possible if $M > M_J$.

Appendix C

MadDM v3.2

C.1 Astrophysics of γ-ray lines

C.1.1 The $\mathcal{J}$-factor computation

In this section, we describe how the $\mathcal{J}$-factor is computed within MadDM. For simplicity, we will consider the case of the galactic center $\mathcal{J}$-factor. We describe only the scenario of the annihilation $\mathcal{J}$-factor, but the same procedure can be applied to the decay $\mathcal{J}$-factor. By definition, eq. (3.91a), the $\mathcal{J}$-factor is:

$$\mathcal{J} = \int_{\mathrm{ROI}} \frac{d^3 r'}{|\mathbf{r}'|^2}\, \rho^2(\mathbf{r})\,. \tag{C.1}$$

In general, the integration region is very complicated because of the presence of a mask over some region of the galactic plane. The mask ensures the exclusion of background regions and known sources. The integral is usually computed over the solid angle Ω, and the line-of-sight r', which are parametrized by $\mathbf{r}'$. This term is expressed in the reference frame of the Sun, while $\mathbf{r}$ is in the reference frame of the galactic center.

The choice of different parametrizations of the ROI can make the computation easier. In the most general scenario, the integration region is defined as follows:

$$\begin{aligned} \mathrm{ROI} = \Bigg\{ (x, y, z) \,\Bigg|\, & x^2 + y^2 + z^2 \leqslant R^2 \cap |y| \geqslant x \tan\left(\frac{\lambda}{2}\right) \\ & \cap\, x^2 + y^2 \geqslant z^2 \tan^2\left(\frac{\pi}{2} - \frac{\beta}{2}\right) \\ & \cap\, |x| \tan\left(\frac{\alpha_1}{2}\right) \leqslant \sqrt{z^2 + y^2} \leqslant |x| \tan\left(\frac{\alpha_2}{2}\right) \Bigg\}\,. \end{aligned} \tag{C.2}$$

The full computation has been implemented inside MadDM, and it gives the user a lot of freedom in the choice of the geometrical shape of the ROI. On one hand, it allows one to mask the galactic plane up to a latitude β and down to a galactic longitude λ. On the other hand, it allows for a circular mask around the galactic center with an opening angle $\alpha_1 \in [0, \alpha_2]$. The outer opening angle of the ROI is denoted by $\alpha_2 \in [0, \pi]$. Both masks can be defined at the same time, creating different shapes, as detailed in fig. C.1.

The integration required to compute the $\mathcal{J}$-factor is done in two steps:

1. computation without assuming the mask: this means to perform the integration over the conic region C detailed as follows, obtaining $\mathcal{J}_C$,

$$C = \left\{ (x, y, z) \,\middle|\, x^2 + y^2 + z^2 \leqslant R^2 \right. \\ \left. \cap\, |x| \tan\left(\frac{\alpha_1}{2}\right) \leqslant \sqrt{z^2 + y^2} \leqslant |x| \tan\left(\frac{\alpha_2}{2}\right) \right\}; \tag{C.3}$$

2. computation of the mask: this requires to perform the integration over the region M detailed as follows, obtaining $\mathcal{J}_M$,

$$M = \left\{ (x, y, z) \,\middle|\, x^2 + y^2 + z^2 \leqslant R^2 \cap |y| \geqslant x \tan\left(\frac{\lambda}{2}\right) \right. \\ \cap\, x^2 + y^2 \geqslant z^2 \tan^2\left(\frac{\pi}{2} - \frac{\beta}{2}\right) \\ \left. \cap\, |x| \tan\left(\frac{\alpha_1}{2}\right) \leqslant \sqrt{z^2 + y^2} \leqslant |x| \tan\left(\frac{\alpha_2}{2}\right) \right\}. \tag{C.4}$$

Both C and M regions have been defined so that the circular mask due to α_1 angle covering the galactic center has been excluded in both. This is done to avoid to perform the integration in the center, which usually is a singularity for most of the density profiles. The value of the $\mathcal{J}$-factor is given by:

$$\mathcal{J} = \mathcal{J}_C - \mathcal{J}_M \tag{C.5}$$

Here, we assume that the integration cone is centered around the x axis.

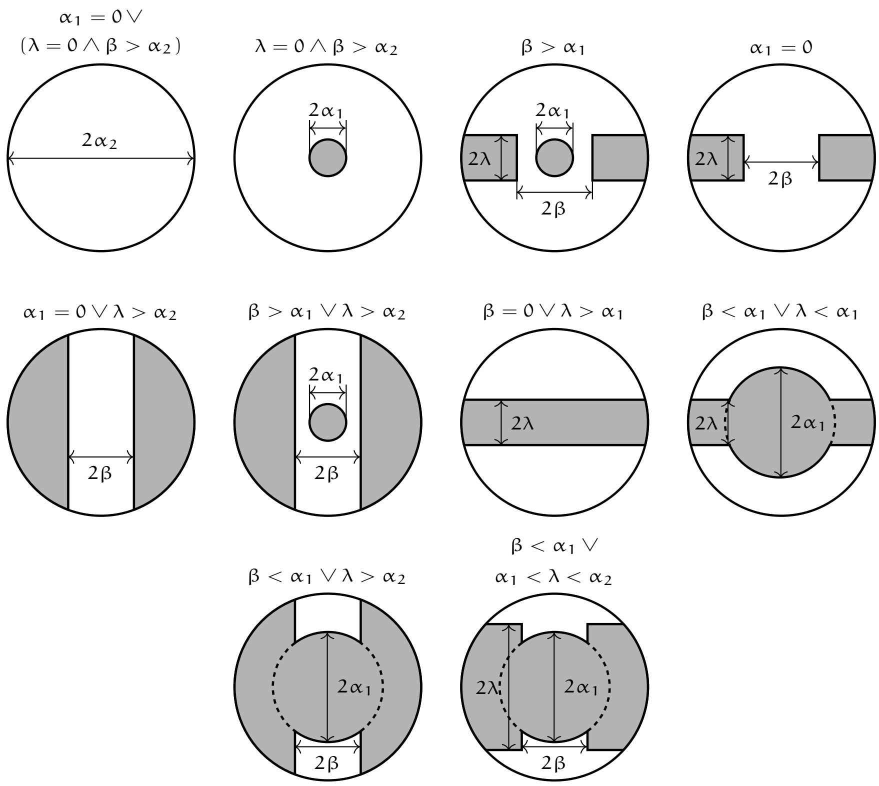

(a) Parameter `strategy` set to `normal`.

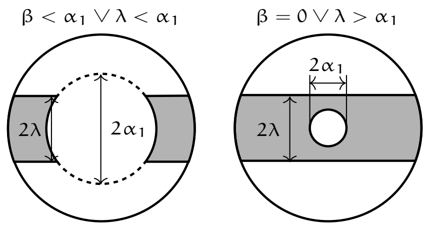

(b) Parameter `strategy` set to `inverted`.

Figure C.1: The 2-dimensional projections on the galactic center of the integration region A defined in the $\mathcal{J}$-factor integral. The shaded regions represent the mask. The `strategy` parameter can be set to select the way the integration is performed, according to the particular mask shape to consider.

Computation of the $\mathcal{J}$-factor without the mask

We use spherical coordinates to perform the computation: $\vartheta \in [0, \pi]$ and $\varphi \in [0, 2\pi]$:

$$x = r' \cos(\vartheta)\,, \tag{C.6a}$$
$$y = r' \sin(\vartheta) \sin(\varphi)\,, \tag{C.6b}$$
$$z = r' \sin(\vartheta) \cos(\varphi)\,, \tag{C.6c}$$

with Jacobian $|J| = r'^2 \cos(\vartheta)$. With this frame we need to compute the following integral:

$$\mathcal{J}_C = \iiint_{C(r',\vartheta,\varphi)} dr'\, d\vartheta\, d\varphi\; \cos(\vartheta) \rho^2\big(\mathbf{r}(r', \vartheta, \varphi)\big)\,, \tag{C.7}$$

where it is possible to express $\mathbf{r}$ as a function of the integration parameters, following geometrical arguments:

$$|\mathbf{r}(r', \vartheta)| = \sqrt{r'^2 + r_\odot^2 - 2r' r_\odot \cos(\vartheta)}\,. \tag{C.8}$$

The density profile functions are spherically symmetric, so they do not depend on the angle φ, and they depend only on the module of $\mathbf{r}$. Moreover, it is always possible to factorize the integrand function in the following way:

$$\mathcal{J}_C(x', \vartheta) = \cos(\vartheta) \rho_s^2\, \rho_{un}\Big(\sqrt{x^2 + x_\odot^2 - 2x x_\odot \cos(\vartheta)}\Big)\,, \tag{C.9}$$

where ρ_{un} is the un-normalized version of the density profile function, and we have performed the following substitutions:

$$x \doteq \frac{r'}{r_s}\,, \tag{C.10a}$$
$$x_\odot \doteq \frac{r_\odot}{r_s}\,, \tag{C.10b}$$
$$dx = \frac{dr'}{r_s}\,, \tag{C.10c}$$

so that eq. (C.7) becomes:

$$\mathcal{J}_C = 4\pi \rho_s^2 r_s \iint_{C(r',\vartheta)} dx\, d\vartheta\; \cos(\vartheta) \rho_{un}^2\Big(\sqrt{x^2 + x_\odot^2 - 2x x_\odot \cos\vartheta}\Big)\,. \tag{C.11}$$

We can now solve the inequalities of the integration region eq. (C.3):

$$0 \leqslant r' \leqslant R\,, \tag{C.12a}$$
$$\frac{\alpha_1}{2} \leqslant \vartheta \leqslant -\frac{\alpha_1}{2}\,. \tag{C.12b}$$

The final cone integral in the limit $R \to +\infty$ is defined as

$$\mathcal{J}_C(\alpha_1, \alpha_2) = 4\pi\rho_s^2 r_s \int_{-\alpha_1/2}^{\alpha_2/2} d\vartheta\, \cos(\vartheta) \int_0^{+\infty} dx\, \rho_{un}^2\big(r(x,\vartheta)\big)\,, \tag{C.13}$$

where

$$r(x,\vartheta) = \sqrt{x^2 + x_\odot^2 - 2xx_\odot \cos(\vartheta)}\,. \tag{C.14}$$

Computation of the $\mathcal{J}$-factor mask

We use galactic coordinates to perform the computation: colongitude $l \in [-\pi, \pi]$ and colatitude $b \in [-\pi/2, \pi/2]$. For definiteness, the galactic coordinates are:

$$x = r' \cos(b) \cos(l)\,, \tag{C.15a}$$

$$y = r' \cos(b) \sin(l)\,, \tag{C.15b}$$

$$z = r' \sin(b)\,, \tag{C.15c}$$

with Jacobian $|J| = r'^2 \cos(b)$. In this frame we need to compute the following integral:

$$\mathcal{J}_M = \iiint_{M(r',b,l)} dr'\, db\, dl\, \cos(b)\rho^2\big(\mathbf{r}(r',b,l)\big)\,, \tag{C.16}$$

and following the same approach applied previously, it is possible to express $\mathbf{r}$ as a function of the integration parameters, according to geometrical arguments:

$$|\mathbf{r}(r',b,l)| = \sqrt{r'^2 + r_\odot^2 - 2r'r_\odot \cos(b)\cos(l)}\,. \tag{C.17}$$

The density profile functions are spherically symmetric, so they depend only on the module of $\mathbf{r}$. Moreover, it is always possible to factorize the integrand function in the following way:

$$\mathcal{J}_M(x',b,l) = \cos(b)\rho_s^2\, \rho_{un}\Big(\sqrt{x^2 + x_\odot^2 - 2xx_\odot \cos(b)\cos(l)}\Big)\,, \tag{C.18}$$

where we performed the same substitutions as in eq. (C.10), so that eq. (C.16) becomes:

$$\mathcal{J}_M = \rho_s^2 r_s \iiint_{M(x,b,l)} dx\, db\, dl\, \cos(b)\rho_{un}^2\Big(\sqrt{x^2 + x_\odot^2 - 2xx_\odot \cos(b)\cos(l)}\Big)\,. \tag{C.19}$$

We start by solving the three inequalities of the integration region in eq. (C.4):

$$0 \leqslant r' \leqslant R\,, \tag{C.20a}$$

$$-\frac{\pi}{2} \leqslant l \leqslant -\frac{\lambda}{2} \lor \frac{\lambda}{2} \leqslant l \leqslant \frac{\pi}{2}\,, \tag{C.20b}$$

$$-\frac{\beta}{2} \leqslant b \leqslant \frac{\beta}{2}\,. \tag{C.20c}$$

While the solution of the last inequality of eq. (C.4) results in:

$$\sin^2(l) \gtreqless \cos^2\left(\frac{\alpha_i}{2}\right)\left(\tan^2\left(\frac{\alpha_i}{2}\right) - \tan^2(b)\right) \doteq f(\alpha_i, b)\,, \tag{C.21}$$

with $i \in \{1, 2\}$; we have $f(\alpha_i, b) \geqslant 0 \Rightarrow -\alpha_i/2 \leqslant b \leqslant \alpha_i/2$.

Solutions for l The solutions obtained so far are:

- $\sin^2(l) \geqslant f(\alpha_1, b)$:

$$\begin{cases} l \leqslant -l'(\alpha_1, b) \lor l \geqslant l'(\alpha_1, b) \\ -\dfrac{\alpha_1}{2} \leqslant b \leqslant \dfrac{\alpha_1}{2} \end{cases} \lor \begin{cases} \forall\, l \\ b < -\dfrac{\alpha_1}{2} \lor b > \dfrac{\alpha_1}{2} \end{cases} \tag{C.22}$$

- $\sin^2(l) \leqslant f(\alpha_2, b)$:

$$\begin{cases} -l'(\alpha_2, b) \leqslant l \leqslant l'(\alpha_2, b) \\ -\dfrac{\alpha_2}{2} \leqslant b \leqslant \dfrac{\alpha_2}{2} \end{cases} \lor \begin{cases} \nexists\, l \\ b < -\dfrac{\alpha_2}{2} \lor b > \dfrac{\alpha_2}{2} \end{cases} \tag{C.23}$$

with the term $l'(\alpha_i, b)$ defined as

$$l'(\alpha_i, b) \doteq \arcsin\left(\left|\cos\left(\frac{\alpha_i}{2}\right)\right|\sqrt{\tan^2\left(\frac{\alpha_i}{2}\right) - \tan^2(b)}\right). \tag{C.24}$$

We have $l'(\alpha_1, b) \leqslant l'(\alpha_2, b) \Leftrightarrow \alpha_1 \leqslant \alpha_2$, which is always true under our hypothesis.

Subsequently, we need to simultaneously solve the following system of equations.

$$\begin{cases} \text{eq. (C.20b)} \\ \text{eq. (C.22)} \\ \text{eq. (C.23)} \end{cases} \tag{C.25}$$

but prior to that, we need to study the behavior of $l'(\alpha_i, b)$ with respect to $\lambda/2$. Therefore, we impose the following condition:

$$\left|l'(\alpha_i, b)\right| \gtrless \frac{\lambda}{2} \Rightarrow \left|\arcsin\left(\left|\cos\left(\frac{\alpha_i}{2}\right)\right|\sqrt{\tan^2\left(\frac{\alpha_i}{2}\right) - \tan^2(b)}\right)\right| \gtrless \frac{\lambda}{2}, \tag{C.26}$$

implying

- $\left|l'(\alpha_i, b)\right| \geqslant \frac{\lambda}{2}$*:

$$\begin{cases} \lambda \leqslant \alpha_i \\ -b'(\alpha_i) \leqslant b \leqslant b'(\alpha_i) \end{cases} \vee \quad \begin{cases} \lambda > \alpha_i \\ \nexists\, b \end{cases} \tag{C.27}$$

- $\left|l'(\alpha_i, b)\right| < \frac{\lambda}{2}$:

$$\begin{cases} \lambda \leqslant \alpha_i \\ b'(\alpha_i) \leqslant b \leqslant \frac{\pi}{2} \vee -\frac{\pi}{2} \leqslant b \leqslant -b'(\alpha_i) \end{cases} \vee \quad \begin{cases} \lambda > \alpha_i \\ \forall\, b \end{cases} \tag{C.28}$$

with the term $b'(\alpha_i)$ defined as:

$$b'(\alpha_i) \doteq \arctan\left(\frac{1}{\left|\cos\left(\frac{\alpha_i}{2}\right)\right|}\sqrt{\sin^2\left(\frac{\alpha_i}{2}\right) - \sin^2\left(\frac{\lambda}{2}\right)}\right). \tag{C.29}$$

First, assume the conditions for $i = 2$:

$$\left|l'(\alpha_2, b)\right| \geqslant \frac{\lambda}{2}, \tag{C.30a}$$

$$-\frac{\alpha_2}{2} \leqslant b \leqslant \frac{\alpha_2}{2}, \tag{C.30b}$$

which implies a non-zero integration region for l and, further, eq. (C.27). Indeed, eq. (C.25) has no solution for l if eq. (C.30a) is not satisfied, because eqs. (C.20b) and (C.23) solutions do not intersect anywhere.

In the case of $i = 1$, there are different cases to take into account, obtained by considering the various conditions on b in eqs. (C.22) and (C.23):

- if $\left|l'(\alpha_1, b)\right| < \frac{\lambda}{2}$:

$$\text{eq. (C.25)} \Rightarrow \; -l'(\alpha_2, b) \leqslant l \leqslant -\frac{\lambda}{2} \vee \frac{\lambda}{2} \leqslant l \leqslant l'(\alpha_2, b), \tag{C.31}$$

$$\text{if } -\frac{\alpha_1}{2} \leqslant b \leqslant \frac{\alpha_1}{2};$$

*The resolution of these equations requires imposing the following condition on the argument of the square root: $\sin^2\left(\frac{\alpha_i}{2}\right) - \sin^2\left(\frac{\lambda}{2}\right) \geqslant 0 \Rightarrow \lambda \leqslant \alpha_i$.

- if $\left|l'(\alpha_1, b)\right| \geqslant \frac{\lambda}{2}$:

$$\text{eq. (C.25)} \Rightarrow \; -l'(\alpha_2, b) \leqslant l \leqslant -l'(\alpha_1, b) \vee l'(\alpha_1, b) \leqslant l \leqslant l'(\alpha_2, b)\,, \quad \text{if } -\frac{\alpha_1}{2} \leqslant b \leqslant \frac{\alpha_1}{2}\,; \tag{C.32}$$

- independently on $l'(\alpha_1, b)$ and $\frac{\lambda}{2}$, but according to b:

$$\text{eq. (C.25)} \Rightarrow \; -l'(\alpha_2, b) \leqslant l \leqslant -\frac{\lambda}{2} \vee \frac{\lambda}{2} \leqslant l \leqslant l'(\alpha_2, b)\,, \quad \text{if } -\frac{\alpha_2}{2} \leqslant b \leqslant -\frac{\alpha_1}{2} \vee \frac{\alpha_1}{2} \leqslant b \leqslant \frac{\alpha_2}{2}\,. \tag{C.33}$$

Solutions for b It is possible to conclude that $0 \leqslant b'(\alpha_1) \leqslant \alpha_1/2$ when $\lambda \leqslant \alpha_1$. That is the only relevant case to take into account under the conditions existing on $b'(\alpha_1)$. In the same way, $0 \leqslant b'(\alpha_2) \leqslant \alpha_2/2$ when $\lambda \leqslant \alpha_2$, for $b'(\alpha_1)$.

The input parameters for the computation of the $\mathcal{J}$-factor are β, λ, α_1 and α_2, so the solution of the integral needs to be expressed on the basis of those parameters:

- we have a first condition from eq. (C.20c);
- in order to have a non-empty integration region for l, we need to assume eq. (C.23) with:

$$-\frac{\alpha_2}{2} \leqslant b \leqslant \frac{\alpha_2}{2}\,, \tag{C.34}$$

  and also $\left|l'(\alpha_2, b)\right| \geqslant \frac{\lambda}{2}$, which further implies $\lambda \leqslant \alpha_2$ to have a non-zero integration region for b, with the additional condition:

$$-b'(\alpha_2) \leqslant b \leqslant b'(\alpha_2)\,. \tag{C.35}$$

The final integration region can be expressed as in the following (remember that $\alpha_1 \leqslant \alpha_2$, $b'(\alpha_i) \leqslant \alpha_i$ for $\lambda \leqslant \alpha_i$ and $b'(\alpha_1) \leqslant b'(\alpha_2)$):

- for $\lambda > \alpha_1$, from eqs. (C.27) and (C.28) we have a non-zero integration region over b if $\left|l'(\alpha_1, b)\right| < \frac{\lambda}{2}$, which further requires eq. (C.31), resulting in the following system of inequalities:

$$\begin{cases} -\frac{\beta}{2} \leqslant b \leqslant \frac{\beta}{2} \\ -\frac{\alpha_2}{2} \leqslant b \leqslant \frac{\alpha_2}{2} \\ -b'(\alpha_2) \leqslant b \leqslant b'(\alpha_2) \\ -\frac{\alpha_1}{2} \leqslant b \leqslant \frac{\alpha_1}{2} \end{cases} \tag{C.36}$$

the solution of which is

$$-B_3 \leqslant b \leqslant B_3 \,, \tag{C.37}$$

with the definition:

$$B_3 \doteq \min\left\{\frac{\beta}{2},\, \frac{\alpha_1}{2},\, b'(\alpha_2)\right\}. \tag{C.38}$$

- for $\lambda \leqslant \alpha_1$ we have different cases on the basis of:
  - if $\left|l'(\alpha_1, b)\right| \geqslant \frac{\lambda}{2}$: from eqs. (C.27) and (C.32) we have the following system of inequalities:

$$\begin{cases} -\frac{\beta}{2} \leqslant b \leqslant \frac{\beta}{2} \\ -\frac{\alpha_2}{2} \leqslant b \leqslant \frac{\alpha_2}{2} \\ -b'(\alpha_2) \leqslant b \leqslant b'(\alpha_2) \\ -\frac{\alpha_1}{2} \leqslant b \leqslant \frac{\alpha_1}{2} \\ -b'(\alpha_1) \leqslant b \leqslant b'(\alpha_1) \end{cases} \tag{C.39}$$

    the solution of which is

$$-B_1 \leqslant b \leqslant B_1 \,, \tag{C.40}$$

    with the definition

$$B_1 \doteq \min\left\{\frac{\beta}{2},\, b'(\alpha_1)\right\}. \tag{C.41}$$

- if $\left|l'(\alpha_1, b)\right| < \frac{\lambda}{2}$: from eqs. (C.28) and (C.31) we have the following system of inequalities:

$$\begin{cases} -\dfrac{\beta}{2} \leqslant b \leqslant \dfrac{\beta}{2} \\ -\dfrac{\alpha_2}{2} \leqslant b \leqslant \dfrac{\alpha_2}{2} \\ -b'(\alpha_2) \leqslant b \leqslant b'(\alpha_2) \\ -\dfrac{\alpha_1}{2} \leqslant b \leqslant \dfrac{\alpha_1}{2} \\ -\dfrac{\pi}{2} \leqslant b \leqslant -b'(\alpha_1) \vee b'(\alpha_1) \leqslant b \leqslant \dfrac{\pi}{2} \end{cases} \tag{C.42}$$

  the solution of which is

$$\begin{cases} -B_3 \leqslant b \leqslant -b'(\alpha_1) \vee b'(\alpha_1) \leqslant b \leqslant B_3 & \text{if } \dfrac{\beta}{2} \geqslant b'(\alpha_1) \\ \nexists\, b & \text{if } \dfrac{\beta}{2} < b'(\alpha_1) \end{cases} \tag{C.43}$$

- independently on λ and α_1, we can also have eq. (C.33), resulting in the following system of inequalities:

$$\begin{cases} -\dfrac{\beta}{2} \leqslant b \leqslant \dfrac{\beta}{2} \\ -\dfrac{\alpha_2}{2} \leqslant b \leqslant \dfrac{\alpha_2}{2} \\ -b'(\alpha_2) \leqslant b \leqslant b'(\alpha_2) \\ -\dfrac{\alpha_2}{2} \leqslant b \leqslant -\dfrac{\alpha_1}{2} \vee \dfrac{\alpha_1}{2} \leqslant b \leqslant \dfrac{\alpha_2}{2} \end{cases} \tag{C.44}$$

  the solution of which is

$$\begin{cases} -B_2 \leqslant b \leqslant -\dfrac{\alpha_1}{2} \vee \dfrac{\alpha_1}{2} \leqslant b \leqslant B_2 & \text{if } \beta \geqslant \alpha_1 \wedge b'(\alpha_2) \geqslant \dfrac{\alpha_1}{2} \\ \nexists\, b & \text{otherwise} \end{cases} \tag{C.45}$$

  with the definition

$$B_2 \doteq \min\left\{\frac{\beta}{2},\, b'(\alpha_2)\right\}. \tag{C.46}$$

Integration regions Considering both the solutions for l and b, we find the integration regions summarized in tab. C.1. The conditions $\left|l'(\alpha_1, b)\right| \gtrless \frac{\lambda}{2}$ are understood by assuming the related values of b in eqs. (C.27) and (C.28) ensuring their validity.

Moreover, each interval is symmetric with respect to zero. Recalling eq. (C.18), it is possible to show that it is an even function in b and l, in other

Table C.1: The integration regions on the basis of the input parameters.

Condition	b-region	l-region
$\alpha_1 \leqslant \lambda \leqslant \alpha_2$	$-B_3 \leqslant b \leqslant B_3$	$-l'(\alpha_2, b) \leqslant l \leqslant -\frac{\lambda}{2}$ $\frac{\lambda}{2} \leqslant l \leqslant l'(\alpha_2, b)$
$\lambda \leqslant \alpha_1$	$-B_1 \leqslant b \leqslant B_1$	$-l'(\alpha_2, b) \leqslant l \leqslant -l'(\alpha_1, b)$ $l'(\alpha_1, b) \leqslant l \leqslant l'(\alpha_2, b)$
$\lambda \leqslant \alpha_1$ $\frac{\beta}{2} \geqslant b'(\alpha_1)$	$-B_3 \leqslant b \leqslant -b'(\alpha_1)$ $b'(\alpha_1) \leqslant b \leqslant B_3$	$-l'(\alpha_2, b) \leqslant l \leqslant -\frac{\lambda}{2}$ $\frac{\lambda}{2} \leqslant l \leqslant l'(\alpha_2, b)$
$\beta \geqslant \alpha_1$ $b'(\alpha_2) \geqslant \frac{\alpha_1}{2}$	$-B_2 \leqslant b \leqslant -\frac{\alpha_1}{2}$ $\frac{\alpha_1}{2} \leqslant b \leqslant B_2$	$-l'(\alpha_2, b) \leqslant l \leqslant -\frac{\lambda}{2}$ $\frac{\lambda}{2} \leqslant l \leqslant l'(\alpha_2, b)$

words:

$$\mathcal{J}_M(x, -b, l) = \mathcal{J}_M(x, b, -l) = \mathcal{J}_M(x, b, l)\,. \tag{C.47}$$

The final mask integral in the limit $R \to +\infty$ is:

$$\begin{aligned}
\mathcal{J}_M(\alpha_1, \alpha_2, \beta, \lambda) = 4\rho_s^2 r_s \Theta(\alpha_2 - \lambda) \Bigg(& \Theta(\lambda - \alpha_1) \int_0^{B_3} db \int_{\lambda/2}^{l'(\alpha_2, b)} dl \\
& + \Theta(\alpha_1 - \lambda) \int_0^{B_1} db \int_{l'(\alpha_1, b)}^{l'(\alpha_2, b)} dl \\
& + \Theta(\alpha_1 - \lambda) \Theta\left(\frac{\beta}{2} - b'(\alpha_1)\right) \int_{b'(\alpha_1)}^{B_3} db \int_{\lambda/2}^{l'(\alpha_2, b)} dl \\
& + \Theta(\beta - \alpha_1) \Theta\left(b'(\alpha_2) - \frac{\alpha_1}{2}\right) \int_{\alpha_1/2}^{B_2} db \int_{\lambda/2}^{l'(\alpha_2, b)} dl \Bigg) \\
& \times \int_0^{+\infty} dx \cos(b)\, \rho_{un}^2\big(r(x, b, l)\big)\,,
\end{aligned} \tag{C.48}$$

with

$$l'(\alpha_i, b) \doteq \arcsin\left(\left|\cos\left(\frac{\alpha_i}{2}\right)\right| \sqrt{\tan^2\left(\frac{\alpha_i}{2}\right) - \tan^2(b)}\right), \tag{C.49}$$

$$b'(\alpha_i) \doteq \arctan\left(\frac{1}{|\cos(\frac{\alpha_i}{2})|} \sqrt{\sin^2\left(\frac{\alpha_i}{2}\right) - \sin^2\left(\frac{\lambda}{2}\right)}\right), \tag{C.50}$$

$$B_1 \doteq \min\left\{\frac{\beta}{2}, b'(\alpha_1)\right\}, \tag{C.51}$$

$$B_2 \doteq \min\left\{\frac{\beta}{2}, b'(\alpha_2)\right\}, \tag{C.52}$$

$$B_3 \doteq \min\left\{\frac{\beta}{2}, \frac{\alpha_1}{2}, b'(\alpha_2)\right\}, \tag{C.53}$$

$$r(x, b, l) = \sqrt{x^2 + x_\odot^2 - 2xx_\odot \cos(b)\cos(l)}\,. \tag{C.54}$$

C.1.2 $\mathcal{J}$-factor density profiles in MadDM

We have included four dark matter density profiles in MadDM, specified in eq. (3.81) (gNFW), eq. (3.83) (Einasto), eq. (3.84) (Burkert) and eq. (3.85) (isothermal). These dark matter profiles are all normalized at the Sun position, the normalization is given by the value of the scale radius r_s and by the scale density ρ_s. The latter is not a free parameter and is automatically computed once the user has fixed $\rho_\odot$, $r_\odot$ and r_s. The dark matter density profile and the scale radius can be changed by the user by editing the file `maddm_card.dat` or via the launch interface, for example:

```
MadDM> set profile nfw
MadDM> set r_s 25
```

These commands change the dark matter density profile from its default Einasto to NFW with (which corresponds to gNFW with $\gamma = 1$) and the scale radius to 25 kpc (the default value is $r_s = 20$ kpc). The default values for the measured energy density at the Sun position and the Sun's distance from the galactic center are $\rho_\odot = 0.4\,\text{GeV}\,\text{cm}^{-3}$ and $r_\odot = 8.5$ kpc, respectively, following the choice of the Fermi-LAT collaboration. Note that these parameters are not contained in the standard `maddm_card.dat`. The change of these parameters requires enabling the full mode via typing `update to_full` directly after entering the launch interface of MadDM. An example of the file `maddm_card.dat` in full mode is given in listing C.1. However, in the given example, MadDM computes the value of ρ_s that corresponds to the default $\rho_\odot$, $r_\odot$ and to $r_s = 25$ kpc.

For NFWg, the inner slope parameter γ is free. Users can change it by typing:

```
MadDM> set profile gnfw
MadDM> set gamma 1.3
```

This choice corresponds to NFWc density profile. Considering the Einasto profile, the slope α is a free parameter and can be set by

```
MadDM> set profile einasto
MadDM> set alpha 0.2
```

which changes α from its default value 0.17 to 0.2.

Listing C.1: Example of the content of `maddm_card.dat` associated with the new parameters introduced in MadDM v3.2 and related to γ-line signatures, including the extended set of parameters (full mode).

```
# setting for DM velocity
   2e-05     = vave_indirect_cont  # average velocity of DM for continuum searches (default: Fermi-LAT dSph searches)
   0.00075   = vave_indirect_line  # average velocity of DM for line searches (default: GC line search analysis)

# PPPC4DMID_ep settings for dm halo profile, propagation method and halo function
# --------------------
# Line analysis
# --------------------

# choice of the dark matter density profile
   einasto   = profile ! gnfw, einasto, nfw, isothermal, burkert

# profile common parameters
   20.0      = r_s # kpc

# gnfw specific parameters
   1.3       = gamma

# einasto specific parameters
   0.17      = alpha

# profile normalisation parameters
   8.5       = r_sun # kpc
   0.4       = rho_sun # GeV cm^-3

# specify a ROI for Fermi-LAT 2015
# set default to use the ROI for which your profile is optimized
   default   = roi_fermi_2015 ! default, R3, R16, R41, R90

# number of FWHM to take as the minimum energy separation between peaks to consider them well separated
   5.0       = n_fwhm_separation

# minimum ratio between peaks' heights to have one of them significantly higher than the other
   10.0      = peak_height_factor

# toggle line experiments on/off
   on        = toggle_fermi_2015
   on        = toggle_hess_2018

### Template line experiment
# in the following you are able to specify the parameters for an experiment of your choice
# - toggle it on/off
```

Listing C.1 (cont.): Example of the content of `maddm_card.dat` associated with the new parameters introduced in MadDM v3.2 and related to γ-line signatures, including the extended set of parameters (full mode).

```
   off            = toggle_template_line_experiment
# - name and arxiv (only for reference purpose)
   TEMPLATE_name  = template_line_experiment_name
   TEMPLATE_arxiv = template_line_experiment_arxiv
# - you can specify up to 1 ROI (in deg) and a profile associated to it (with the various parameters as seen above)
   1.0            = template_line_experiment_roi
   einasto        = template_line_experiment_profile
   20.0           = template_line_experiment_r_s
#  - gnfw parameter gamma
   1.3            = template_line_experiment_gamma
#  - einasto parameter alpha
   0.17           = template_line_experiment_alpha
# - specify the parameters of the mask (angles are in deg), refer to MadDM v3.2 documentation
   0.0            = template_line_experiment_mask_latitude    # angle 'beta' : mask P, if abs(latitude(P)) < beta
   180.0          = template_line_experiment_mask_longitude   # angle 'lambda' : mask P, if abs(longitude(P)) > lambda
   0.0            = template_line_experiment_mask_inner_angle # angle 'alpha_1': mask P, if abs(arctan(P.y/P.x)) < alpha_1/2
# - energy resolution: this is a percent value to be multiplied by the energy of the peak
   10.0           = template_line_experiment_energy_resolution
# - detection range in GeV
   0.0            = template_line_experiment_detection_range_min
   1000000.0      = template_line_experiment_detection_range_max
# - constraints file name: to be placed in $MADDM_PATH/ExpData/, must be 3 columns, lines starting with '#' will be considered as comments
#   DM mass (GeV), <sigmav> (cm^3 s^-1), flux (cm^-2 s^-1)
   None           = template_line_experiment_constraints_file
```

C.1.3 Details on experimental data

In general, the user can set the ROI for a given experiment. Concretely, the experimental bounds are derived for a ROI which is optimized for a certain dark matter density profile. In the case of Fermi-LAT there are four ROIs:

1. R3 associated with NFWc
2. R16 associated with Einasto
3. R41 associated with NFW
4. R90 associated with isothermal

For HESS, only one ROI is defined, namely R1. While the user is free to choose any of the four ROIs of the Fermi-LAT analysis by the variable `roi_fermi_2015` in the file `maddm_card.dat`, we recommend choosing the ROI associated with the dark matter density profile considered. This can automatically be achieved by setting the above parameter to `default`[†]. Note that if a ROI is chosen that

[†]For the Burkert profile, the R90 is chosen by default.

is not optimized for the considered profile, MadDM raises a warning. If the user only chooses the ROI without specifying the dark matter density profile, MadDM automatically chooses the profile for which it was optimized. Note further that the approximate Fermi-LAT likelihood and p-value computations are only performed if the user chooses the R3 or R16 ROI.

The experimental data is stored in the directory `$MG5_PATH/PLUGIN/maddm/ExpData`. It contains the respective data files for the Fermi-LAT and HESS analyses:

- `Fermi_2015_lines_R3_NFWcontracted.dat`;
- `Fermi_2015_lines_R16_Einasto.dat`;
- `Fermi_2015_lines_R41_NFW.dat`;
- `Fermi_2015_lines_R90_Isothermal.dat`;
- `HESS_2018_lines_R1_Einasto.dat`.

Each file contains the parameters of the density profile, the corresponding $\mathcal{J}$-factor, the ROI and the 95 % CL upper limits on $\langle\sigma v\rangle_{\gamma\gamma}$ and the flux in the 120 (60) energy bins considered by Fermi-LAT (HESS).

In addition to the implemented constraints from Fermi-LAT and HESS, we allow the user to consider further experimental data in the analysis pipeline. To this end, we have included a template experiment. It can, for instance, be used to compute the projected limits for future observations. The associated parameters are among the extended set of parameters accessible in `maddm_card.dat` in the full mode. The respective block is shown in listing C.1 below line 40. The relevant parameters are (* is a wildcard):

- `name`, `arxiv`: specify the name and (if applicable) the arXiv number of the analysis (optional);
- `roi`, `profile`: it is possible to specify the ROI (i.e. α_2 in degrees) and the dark matter density profile associated to it (the user can choose between the same profiles as for the main `profile` parameter discussed above);
- `r_s`, `gamma`, `alpha`: these are the profile parameters to be specified for the default dark matter density profile chosen as in the point above;
- `mask_*` parameters: allow the user to specify a mask, according to fig. C.1, where `mask_latitude` is λ, `mask_longitude` is β and `mask_inner_angle` is α_1; they are all expressed in degrees;
- `energy_resolution`: the relative energy resolution of the experiment in percentage; taken to be constant over the detection range;
- `detection_range_*` parameters: allow the user to specify the minimum (`min`) and maximum (`max`) energy range of the experiment (in GeV);

- `constraints_file`: additionally, the user can provide the (projected) constraints of the experiment via a data file in the same format as e.g. `Fermi_2015_lines_R90_Isothermal.dat`. The file should be included in the directory `\$MG5_PATH/PLUGIN/maddm/ExpData` of MadDM. It should contain three columns: dark matter mass (in GeV), $\langle\sigma v\rangle_{\gamma\gamma}$ upper limits (in $\mathrm{cm}^3\,\mathrm{s}^{-1}$) and $\Phi_{\gamma\gamma}$ upper limits (in $\mathrm{cm}^{-2}\,\mathrm{s}^{-1}$).

To enable the template experiment, the parameter `toggle_template_line_experiment` has to be set to `on`. In this case, MadDM considers it in the same way as the constraints from Fermi-LAT and HESS. Note that the dark matter density profile associated with the template experiment is supposed to be the one for which the cross section upper limit has been derived (if provided by the user). The density profile considered for the J-factor computation within MadDM remains the one specified through the parameter `profile` in `maddm_card.dat`. However, if the two profiles differ, a warning is raised.

Note that it is also possible to switch the Fermi-LAT and HESS analysis `on`/`off`. When switched `off` the respective experiment is not considered in the analysis pipeline.

C.2 Merging algorithm for multiple lines features

In the presence of multiple spectral lines, the application of experimental constraints (performed under the assumption of a single γ-ray line signal) requires particular attention. In the following, we provide details on the implemented merging algorithm for multiple spectral lines that are close in energy. Furthermore, we discuss the considered criteria for the applicability of the experimental analyses in this case.

Due to the non-relativistic nature of cold dark matter, the width of the γ-ray line signal is expected to be very small. In particular, it is assumed to be small compared to the experimental energy resolution. In the experimental measurement, the sharp peak, eq. (3.94), is hence smeared. We approximate it by a Gaussian,

$$\frac{d\Phi_{\mathrm{exp}}(E)}{dE} \propto \frac{\Phi}{\sigma\sqrt{2\pi}} \exp\left(-\frac{1}{2}\frac{(E-E_\gamma)^2}{\sigma^2}\right), \tag{C.55}$$

where σ corresponds to the experimental resolution, related to the full width at half maximum (FWHM) by $\mathrm{FWHM} = 2\sqrt{2\ln 2}\,\sigma$. The resolution of Fermi-LAT is reported in [152]. We consider the EDISP3 energy resolution, associated with the best energy reconstruction estimator. It ranges from approximately 10 % at 300 MeV down to 5.5 % at 500 GeV. Note that the width of each bin corresponds to the energy resolution (68 % containment) for that bin following EDISP3. The HESS telescope has a resolution in energy of 11 % above 300 GeV [154].

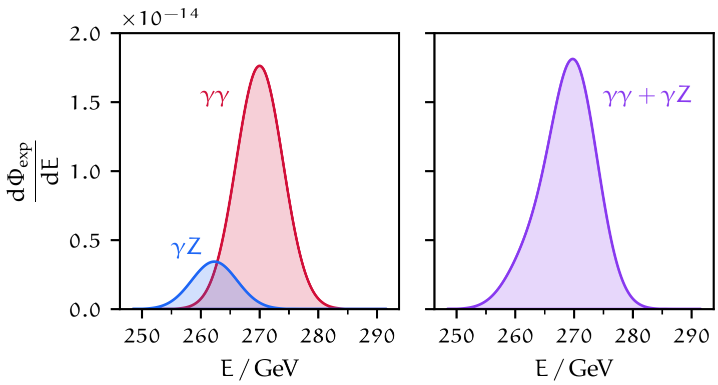

Figure C.2: Graphical example of the merging algorithm. **LEFT PANEL:** the $\gamma\gamma$ and γZ peaks are shown separately. **RIGHT PANEL:** the peak obtained after the merge is shown. This is a real-case scenario of the top-philic model introduced in § 5.3.1 for $m_\chi = 270\,\text{GeV}$, considered within the Fermi-LAT experiment for the R41 ROI.

The merging algorithm follows an iterative process. In each iteration, it considers all possible pairs of spectral lines (called peaks in the following) and selects the pair that is closest in energy, i.e. for which

$$s_{ab} = \frac{|E_a - E_b|}{\min\left(\mathrm{FWHM}_a, \mathrm{FWHM}_b\right)}, \tag{C.56}$$

is minimal, where a, b index the peaks and FWHM_a is the FWHM of peak a. If $s_{ab} < 1$, the Gaussian signals, eq. (C.55), of the peaks are summed and considered as a single (merged) peak. The iterative process is pursued with the set of merged and remaining unmerged peaks until no merging is possible anymore (under the above criterion). An example (taken from a real-case scenario) of a merging of two peaks is shown in fig. C.2.

The set of peaks obtained after merging represents the signal as potentially being observed by the experiment. However, if the signal still contains multiple peaks, the application of the experimental constraints to each of them is, in general, questionable as the limit-setting procedure has been performed under the hypothesis of a single peak. Similar issues can arise if a merged peak has become too broad. We address these concerns by introducing the following criteria the peaks have to satisfy. First, we require the FWHM of any merged peak to be smaller than $1.5 \times \mathrm{FWHM}(E_\star)$ corresponding to the experimental resolution at its peak energy $E_\star$. Secondly, we require a minimal separation between the (merged) peaks. Note that the separation criterion is bypassed for a large hierarchy between the corresponding fluxes of the peaks, i.e. if the ratio of fluxes (each normalized to the upper limit at the corresponding energy) is larger than a certain reference value, the largest peak is considered to be a line.

Bibliography

[1] C. Arina et al. "Indirect dark-matter detection with MadDM v3.2 – Lines and Loops". *Eur. Phys. J. C* 83.3 (2023), p. 241. doi: 10.1140/epjc/s10052-023-11377-2. arXiv: 2107.04598 [hep-ph].

[2] M. Di Mauro et al. "Dark matter in the Higgs resonance region". *Phys. Rev. D* 108.9 (2023), p. 095008. doi: 10.1103/PhysRevD.108.095008. arXiv: 2305.11937 [hep-ph].

[3] R. Allahverdi et al. "Phenomenology of superheavy decaying dark matter from string theory". *JHEP* 02 (2024), p. 192. doi: 10.1007/JHEP02(2024)192. arXiv: 2312.00136 [hep-ph].

[4] A. M. Abdullahi et al. "Semi-Visible Dark Photon Phenomenology at the GeV Scale". *Phys. Rev. D* 108.1 (2023), p. 015032. doi: 10.1103/PhysRevD.108.015032. arXiv: 2302.05410 [hep-ph].

[5] A. M. Abdullahi et al. "DarkNews: A Python-based event generator for heavy neutral lepton production in neutrino-nucleus scattering". *Comput. Phys. Commun.* 297 (2024), p. 109075. doi: 10.1016/j.cpc.2023.109075. arXiv: 2207.04137 [hep-ph].

[6] M. Mongillo et al. "Constraining light thermal inelastic dark matter with NA64". *Eur. Phys. J. C* 83.5 (2023), p. 391. doi: 10.1140/epjc/s10052-023-11536-5. arXiv: 2302.05414 [hep-ph].

[7] A. M. Abdullahi et al. "A panorama of new-physics explanations to the MiniBooNE excess" (Aug. 2023). arXiv: 2308.02543 [hep-ph].

[8] G. Aad et al. "Observation of a new particle in the search for the Standard Model Higgs boson with the ATLAS detector at the LHC". *Phys. Lett. B* 716 (2012), pp. 1–29. doi: 10.1016/j.physletb.2012.08.020. arXiv: 1207.7214 [hep-ex].

[9] S. Chatrchyan et al. "Observation of a New Boson at a Mass of 125 GeV with the CMS Experiment at the LHC". *Phys. Lett. B* 716 (2012), pp. 30–61. doi: 10.1016/j.physletb.2012.08.021. arXiv: 1207.7235 [hep-ex].

[10] F. Englert and R. Brout. "Broken Symmetry and the Mass of Gauge Vector Mesons". *Phys. Rev. Lett.* 13 (1964). Ed. by J. C. Taylor, pp. 321–323. doi: 10.1103/PhysRevLett.13.321.

[11] G. S. Guralnik, C. R. Hagen, and T. W. B. Kibble. "Global Conservation Laws and Massless Particles". *Phys. Rev. Lett.* 13 (1964). Ed. by J. C. Taylor, pp. 585–587. doi: 10.1103/PhysRevLett.13.585.

[12] P. W. Higgs. “Broken symmetries, massless particles and gauge fields”. *Phys. Lett.* 12 (1964), pp. 132–133. DOI: 10.1016/0031-9163(64)91136-9.

[13] P. W. Higgs. “Broken Symmetries and the Masses of Gauge Bosons”. *Phys. Rev. Lett.* 13 (1964). Ed. by J. C. Taylor, pp. 508–509. DOI: 10.1103/PhysRevLett.13.508.

[14] N. Cabibbo. “Unitary Symmetry and Leptonic Decays”. *Phys. Rev. Lett.* 10 (1963), pp. 531–533. DOI: 10.1103/PhysRevLett.10.531.

[15] M. Kobayashi and T. Maskawa. “CP Violation in the Renormalizable Theory of Weak Interaction”. *Prog. Theor. Phys.* 49 (1973), pp. 652–657. DOI: 10.1143/PTP.49.652.

[16] Q. R. Ahmad et al. “Measurement of the rate of $\nu_e + d \to p + p + e^-$ interactions produced by ^{8}B solar neutrinos at the Sudbury Neutrino Observatory”. *Phys. Rev. Lett.* 87 (2001), p. 071301. DOI: 10.1103/PhysRevLett.87.071301. arXiv: nucl-ex/0106015.

[17] Q. R. Ahmad et al. “Direct evidence for neutrino flavor transformation from neutral current interactions in the Sudbury Neutrino Observatory”. *Phys. Rev. Lett.* 89 (2002), p. 011301. DOI: 10.1103/PhysRevLett.89.011301. arXiv: nucl-ex/0204008.

[18] Y. Fukuda et al. “Evidence for oscillation of atmospheric neutrinos”. *Phys. Rev. Lett.* 81 (1998), pp. 1562–1567. DOI: 10.1103/PhysRevLett.81.1562. arXiv: hep-ex/9807003.

[19] V. C. Rubin and W. K. Ford Jr. “Rotation of the Andromeda Nebula from a Spectroscopic Survey of Emission Regions”. *Astrophys. J.* 159 (1970), pp. 379–403. DOI: 10.1086/150317.

[20] N. Aghanim et al. “Planck 2018 results. VI. Cosmological parameters”. *Astron. Astrophys.* 641 (2020). [Erratum: Astron.Astrophys. 652, C4 (2021)], A6. DOI: 10.1051/0004-6361/201833910. arXiv: 1807.06209 [astro-ph.CO].

[21] H.-Y. Cheng. “The Strong CP Problem Revisited”. *Phys. Rept.* 158 (1988), p. 1. DOI: 10.1016/0370-1573(88)90135-4.

[22] F. D. Steffen. “Dark Matter Candidates - Axions, Neutralinos, Gravitinos, and Axinos”. *Eur. Phys. J. C* 59 (2009), pp. 557–588. DOI: 10.1140/epjc/s10052-008-0830-0. arXiv: 0811.3347 [hep-ph].

[23] C. A. Baker et al. “An Improved experimental limit on the electric dipole moment of the neutron”. *Phys. Rev. Lett.* 97 (2006), p. 131801. DOI: 10.1103/PhysRevLett.97.131801. arXiv: hep-ex/0602020.

[24] R. D. Peccei and H. R. Quinn. “CP Conservation in the Presence of Instantons”. *Phys. Rev. Lett.* 38 (1977), pp. 1440–1443. DOI: 10.1103/PhysRevLett.38.1440.

[25] B. Pontecorvo. “Mesonium and anti-mesonium”. *Sov. Phys. JETP* 6 (1957), p. 429.

[26] B. Pontecorvo. "Inverse beta processes and nonconservation of lepton charge". *Zh. Eksp. Teor. Fiz.* 34 (1957), p. 247.

[27] Z. Maki, M. Nakagawa, and S. Sakata. "Remarks on the unified model of elementary particles". *Prog. Theor. Phys.* 28 (1962), pp. 870–880. DOI: 10.1143/PTP.28.870.

[28] R. Davis Jr., D. S. Harmer, and K. C. Hoffman. "Search for neutrinos from the sun". *Phys. Rev. Lett.* 20 (1968), pp. 1205–1209. DOI: 10.1103/PhysRevLett.20.1205.

[29] T. J. Haines et al. "Calculation of Atmospheric Neutrino Induced Backgrounds in a Nucleon Decay Search". *Phys. Rev. Lett.* 57 (1986), pp. 1986–1989. DOI: 10.1103/PhysRevLett.57.1986.

[30] M. Nakahata et al. "Atmospheric Neutrino Background and Pion Nuclear Effect for Kamioka Nucleon Decay Experiment". *J. Phys. Soc. Jap.* 55 (1986), p. 3786. DOI: 10.1143/JPSJ.55.3786.

[31] S. Weinberg. "Baryon and Lepton Nonconserving Processes". *Phys. Rev. Lett.* 43 (1979), pp. 1566–1570. DOI: 10.1103/PhysRevLett.43.1566.

[32] C. Athanassopoulos et al. "Evidence for neutrino oscillations from muon decay at rest". *Phys. Rev. C* 54 (1996), pp. 2685–2708. DOI: 10.1103/PhysRevC.54.2685. arXiv: nucl-ex/9605001.

[33] C. Athanassopoulos et al. "Evidence for anti-muon-neutrino —> anti-electron-neutrino oscillations from the LSND experiment at LAMPF". *Phys. Rev. Lett.* 77 (1996), pp. 3082–3085. DOI: 10.1103/PhysRevLett.77.3082. arXiv: nucl-ex/9605003.

[34] C. Athanassopoulos et al. "Evidence for nu(mu) —> nu(e) neutrino oscillations from LSND". *Phys. Rev. Lett.* 81 (1998), pp. 1774–1777. DOI: 10.1103/PhysRevLett.81.1774. arXiv: nucl-ex/9709006.

[35] C. Athanassopoulos et al. "Evidence for muon-neutrino —> electron-neutrino oscillations from pion decay in flight neutrinos". *Phys. Rev. C* 58 (1998), pp. 2489–2511. DOI: 10.1103/PhysRevC.58.2489. arXiv: nucl-ex/9706006.

[36] A. Aguilar et al. "Evidence for neutrino oscillations from the observation of $\bar{\nu}_e$ appearance in a $\bar{\nu}_\mu$ beam". *Phys. Rev. D* 64 (2001), p. 112007. DOI: 10.1103/PhysRevD.64.112007. arXiv: hep-ex/0104049.

[37] A. A. Aguilar-Arevalo et al. "A Search for Electron Neutrino Appearance at the $\Delta m^2 \sim 1 eV^2$ Scale". *Phys. Rev. Lett.* 98 (2007), p. 231801. DOI: 10.1103/PhysRevLett.98.231801. arXiv: 0704.1500 [hep-ex].

[38] A. A. Aguilar-Arevalo et al. "Unexplained Excess of Electron-Like Events From a 1-GeV Neutrino Beam". *Phys. Rev. Lett.* 102 (2009), p. 101802. DOI: 10.1103/PhysRevLett.102.101802. arXiv: 0812.2243 [hep-ex].

[39] A. A. Aguilar-Arevalo et al. “Event Excess in the MiniBooNE Search for $\bar{\nu}_\mu \to \bar{\nu}_e$ Oscillations”. *Phys. Rev. Lett.* 105 (2010), p. 181801. DOI: 10.1103/PhysRevLett.105.181801. arXiv: 1007.1150 [hep-ex].

[40] A. A. Aguilar-Arevalo et al. “Improved Search for $\bar{\nu}_\mu \to \bar{\nu}_e$ Oscillations in the MiniBooNE Experiment”. *Phys. Rev. Lett.* 110 (2013), p. 161801. DOI: 10.1103/PhysRevLett.110.161801. arXiv: 1303.2588 [hep-ex].

[41] A. A. Aguilar-Arevalo et al. “Significant Excess of ElectronLike Events in the MiniBooNE Short-Baseline Neutrino Experiment”. *Phys. Rev. Lett.* 121.22 (2018), p. 221801. DOI: 10.1103/PhysRevLett.121.221801. arXiv: 1805.12028 [hep-ex].

[42] A. A. Aguilar-Arevalo et al. “Updated MiniBooNE neutrino oscillation results with increased data and new background studies”. *Phys. Rev. D* 103.5 (2021), p. 052002. DOI: 10.1103/PhysRevD.103.052002. arXiv: 2006.16883 [hep-ex].

[43] A. A. Aguilar-Arevalo et al. “MiniBooNE and MicroBooNE Combined Fit to a 3+1 Sterile Neutrino Scenario”. *Phys. Rev. Lett.* 129.20 (2022), p. 201801. DOI: 10.1103/PhysRevLett.129.201801. arXiv: 2201.01724 [hep-ex].

[44] G. Cheng et al. “Measurement of K^+ production cross section by 8 GeV protons using high energy neutrino interactions in the SciBooNE detector”. *Phys. Rev. D* 84 (2011), p. 012009. DOI: 10.1103/PhysRevD.84.012009. arXiv: 1105.2871 [hep-ex].

[45] A. A. Aguilar-Arevalo et al. “First Observation of Coherent π^0 Production in Neutrino Nucleus Interactions with $E_\nu < 2$ GeV”. *Phys. Lett. B* 664 (2008), pp. 41–46. DOI: 10.1016/j.physletb.2008.05.006. arXiv: 0803.3423 [hep-ex].

[46] A. A. Aguilar-Arevalo et al. “Measurement of ν_μ and $\bar{\nu}_\mu$ induced neutral current single π^0 production cross sections on mineral oil at $E_\nu \sim \mathcal{O}(1\text{GeV})$”. *Phys. Rev. D* 81 (2010), p. 013005. DOI: 10.1103/PhysRevD.81.013005. arXiv: 0911.2063 [hep-ex].

[47] P. Abratenko et al. “Search for Neutrino-Induced Neutral-Current Δ Radiative Decay in MicroBooNE and a First Test of the MiniBooNE Low Energy Excess under a Single-Photon Hypothesis”. *Phys. Rev. Lett.* 128 (2022), p. 111801. DOI: 10.1103/PhysRevLett.128.111801. arXiv: 2110.00409 [hep-ex].

[48] R. Acciarri et al. “A Proposal for a Three Detector Short-Baseline Neutrino Oscillation Program in the Fermilab Booster Neutrino Beam” (Mar. 2015). arXiv: 1503.01520 [physics.ins-det].

[49] P. A. Machado, O. Palamara, and D. W. Schmitz. “The Short-Baseline Neutrino Program at Fermilab”. *Ann. Rev. Nucl. Part. Sci.* 69 (2019),

pp. 363–387. DOI: 10.1146/annurev-nucl-101917-020949. arXiv: 1903.04608 [hep-ex].

[50] P. Abratenko et al. “Search for an Excess of Electron Neutrino Interactions in MicroBooNE Using Multiple Final-State Topologies”. *Phys. Rev. Lett.* 128.24 (2022), p. 241801. DOI: 10.1103/PhysRevLett.128.241801. arXiv: 2110.14054 [hep-ex].

[51] P. Abratenko et al. “Search for an anomalous excess of charged-current quasielastic νe interactions with the MicroBooNE experiment using Deep-Learning-based reconstruction”. *Phys. Rev. D* 105.11 (2022), p. 112003. DOI: 10.1103/PhysRevD.105.112003. arXiv: 2110.14080 [hep-ex].

[52] P. Abratenko et al. “Search for an anomalous excess of charged-current νe interactions without pions in the final state with the MicroBooNE experiment”. *Phys. Rev. D* 105.11 (2022), p. 112004. DOI: 10.1103/PhysRevD.105.112004. arXiv: 2110.14065 [hep-ex].

[53] P. Abratenko et al. “Search for an anomalous excess of inclusive charged-current ν_e interactions in the MicroBooNE experiment using Wire-Cell reconstruction”. *Phys. Rev. D* 105.11 (2022), p. 112005. DOI: 10.1103/PhysRevD.105.112005. arXiv: 2110.13978 [hep-ex].

[54] J.-L. Gervais and B. Sakita. “Field Theory Interpretation of Supergauges in Dual Models”. *Nucl. Phys. B* 34 (1971). Ed. by K. Kikkawa, M. Virasoro, and S. R. Wadia, pp. 632–639. DOI: 10.1016/0550-3213(71)90351-8.

[55] Y. A. Golfand and E. P. Likhtman. “Extension of the Algebra of Poincare Group Generators and Violation of p Invariance”. *JETP Lett.* 13 (1971). Ed. by A. Salam and E. Sezgin, pp. 323–326. DOI: 10.1142/9789814542340_0001.

[56] D. V. Volkov and V. P. Akulov. “Possible universal neutrino interaction”. *JETP Lett.* 16 (1972). Ed. by J. Wess and V. P. Akulov, pp. 438–440.

[57] J. Wess and B. Zumino. “Supergauge Transformations in Four-Dimensions”. *Nucl. Phys. B* 70 (1974). Ed. by A. Salam and E. Sezgin, pp. 39–50. DOI: 10.1016/0550-3213(74)90355-1.

[58] S. Dawson. “R-Parity Breaking in Supersymmetric Theories”. *Nucl. Phys. B* 261 (1985), pp. 297–318. DOI: 10.1016/0550-3213(85)90577-2.

[59] R. Barbier et al. “R-parity violating supersymmetry”. *Phys. Rept.* 420 (2005), pp. 1–202. DOI: 10.1016/j.physrep.2005.08.006. arXiv: hep-ph/0406039.

[60] D. Massaro. “Loop-induced annihilation of dark matter”. Laurea Magistrale. Alma Mater Studiorum - Università di Bologna, 2019. URL: http://amslaurea.unibo.it/19428/.

[61] J. Einasto. “Dark Matter”. Jan. 2009. arXiv: 0901.0632 [astro-ph.CO].

[62] G. Bertone and D. Hooper. “History of dark matter”. *Rev. Mod. Phys.* 90.4 (2018), p. 045002. DOI: 10.1103/RevModPhys.90.045002. arXiv: 1605.04909 [astro-ph.CO].

[63] S. van den Bergh. “The Early history of dark matter”. *Publ. Astron. Soc. Pac.* 111 (1999), p. 657. DOI: 10.1086/316369. arXiv: astro-ph/9904251.

[64] E. W. Kolb and M. S. Turner. *The Early Universe*. Vol. 69. 1990. ISBN: 978-0-201-62674-2. DOI: 10.1201/9780429492860.

[65] P. Coles and F. Lucchin. *"Cosmology". "The Origin and Evolution of Cosmic Structure"*. 2nd ed. "John Wiley & Sons, Ltd", 2002. ISBN: 9780471489092.

[66] M. Bauer and T. Plehn. *Yet Another Introduction to Dark Matter: The Particle Physics Approach*. Vol. 959. Lecture Notes in Physics. Springer, 2019. DOI: 10.1007/978-3-030-16234-4. arXiv: 1705.01987 [hep-ph].

[67] F. Tanedo. “Defense Against the Dark Arts Notes on dark matter and particle physics Flip Tanedo”. URL: https://api.semanticscholar.org/CorpusID:15584524.

[68] M. Cirelli. “Indirect Searches for Dark Matter: a status review”. *Pramana* 79 (2012). Ed. by R. Godbole and N. K. Mondal, pp. 1021–1043. DOI: 10.1007/s12043-012-0419-x. arXiv: 1202.1454 [hep-ph].

[69] J. M. Gaskins. “A review of indirect searches for particle dark matter”. *Contemp. Phys.* 57.4 (2016), pp. 496–525. DOI: 10.1080/00107514.2016.1175160. arXiv: 1604.00014 [astro-ph.HE].

[70] J. Conrad and O. Reimer. “Indirect dark matter searches in gamma and cosmic rays”. *Nature Phys.* 13.3 (2017), pp. 224–231. DOI: 10.1038/nphys4049. arXiv: 1705.11165 [astro-ph.HE].

[71] T. R. Slatyer. “Indirect Detection of Dark Matter”. *Theoretical Advanced Study Institute in Elementary Particle Physics: Anticipating the Next Discoveries in Particle Physics*. 2018, pp. 297–353. DOI: 10.1142/9789813233348_0005. arXiv: 1710.05137 [hep-ph].

[72] M. Klasen, M. Pohl, and G. Sigl. “Indirect and direct search for dark matter”. *Prog. Part. Nucl. Phys.* 85 (2015), pp. 1–32. DOI: 10.1016/j.ppnp.2015.07.001. arXiv: 1507.03800 [hep-ph].

[73] K. Freese, M. Lisanti, and C. Savage. “Colloquium: Annual modulation of dark matter”. *Rev. Mod. Phys.* 85 (2013), pp. 1561–1581. DOI: 10.1103/RevModPhys.85.1561. arXiv: 1209.3339 [astro-ph.CO].

[74] F. Zwicky. “Die Rotverschiebung von extragalaktischen Nebeln”. *Helv. Phys. Acta* 6 (1933), pp. 110–127. DOI: 10.1007/s10714-008-0707-4.

[75] L. Kelvin. *Baltimore Lectures on Molecular Dynamics and the Wave Theory of Light*. Cambridge University Press, 1884. DOI: 10.1017/CBO9780511694523.

[76] S. Smith. "The Mass of the Virgo Cluster". *Astrophys. J.* 83 (1936), pp. 23–30. DOI: 10.1086/143697.

[77] E. Holmberg. "A Study of Double and Multiple Galaxies Together with Inquiries into some General Metagalactic Problems". *Annals of the Observatory of Lund* 6 (Jan. 1937), pp. 1–173.

[78] T. Page. "Radial Velocities and Masses of Double Galaxies." *Astrophys. J.* 116 (July 1952), p. 63. DOI: 10.1086/145593.

[79] G. C. Mc Vittie. "Problems of Extragalactic Research" (Aug. 12–12, 1961). Ed. by G. C. Mc Vittie. Santa Barbara, CA, USA: The Mac Millan Company, 1962.

[80] H. W. Babcock. "The rotation of the Andromeda Nebula". *Lick Obs. Bull.* 498 (Jan. 1939), pp. 41–51. DOI: 10.5479/ADS/bib/1939LicOB.19.41B.

[81] J. H. Oort. "Some Problems Concerning the Structure and Dynamics of the Galactic System and the Elliptical Nebulae NGC 3115 and 4494." *Astrophys. J.* 91 (Apr. 1940), p. 273. DOI: 10.1086/144167.

[82] H. C. van de Hulst, E. Raimond, and H. van Woerden. "Rotation and density distribution of the Andromeda nebula derived from observations of the 21-cm line". *Bulletin Astronomical Institute of the Netherlands* 14 (Nov. 1957), p. 1.

[83] M. S. Roberts. "A High-Resolution 21-CM Hydrogen-Line Survey of the Andromeda Nebula". *Astrophys. J.* 144 (May 1966), p. 639. DOI: 10.1086/148645.

[84] K. C. Freeman. "On the disks of spiral and SO Galaxies". *Astrophys. J.* 160 (1970), p. 811. DOI: 10.1086/150474.

[85] D. H. Rogstad and G. S. Shostak. "Gross Properties of Five Scd Galaxies as Determined from 21-CENTIMETER Observations". *Astrophys. J.* 176 (Sept. 1972), p. 315. DOI: 10.1086/151636.

[86] J. Wambsganss. "Gravitational lensing in astronomy". *Living Rev. Rel.* 1 (1998), p. 12. DOI: 10.12942/lrr-1998-12. arXiv: astro-ph/9812021.

[87] H. Hoekstra, H. K. C. Yee, and M. D. Gladders. "Properties of galaxy dark matter halos from weak lensing". *Astrophys. J.* 606 (2004), pp. 67–77. DOI: 10.1086/382726. arXiv: astro-ph/0306515.

[88] R. Massey, T. Kitching, and J. Richard. "The dark matter of gravitational lensing". *Rept. Prog. Phys.* 73 (2010), p. 086901. DOI: 10.1088/0034-4885/73/8/086901. arXiv: 1001.1739 [astro-ph.CO].

[89] European Space Agency (ESA). *The Bullet Cluster*. Image source: X-ray: NASA/CXC/CfA/M.Markevitch, Optical and lensing map:

NASA/STScI, Magellan/U.Arizona/D.Clowe, Lensing map: ESO WFI. July 2007. URL: https://www.esa.int/ESA_Multimedia/Images/2007/07/The_Bullet_Cluster2.

[90] D. Clowe, A. Gonzalez, and M. Markevitch. "Weak lensing mass reconstruction of the interacting cluster 1E0657-558: Direct evidence for the existence of dark matter". *Astrophys. J.* 604 (2004), pp. 596–603. DOI: 10.1086/381970. arXiv: astro-ph/0312273.

[91] M. Milgrom. "A Modification of the Newtonian dynamics as a possible alternative to the hidden mass hypothesis". *Astrophys. J.* 270 (1983), pp. 365–370. DOI: 10.1086/161130.

[92] M. Milgrom. "A Modification of the Newtonian dynamics: Implications for galaxies". *Astrophys. J.* 270 (1983), pp. 371–383. DOI: 10.1086/161131.

[93] M. Milgrom. "A modification of the Newtonian dynamics: implications for galaxy systems". *Astrophys. J.* 270 (1983), pp. 384–389. DOI: 10.1086/161132.

[94] M. Milgrom and R. H. Sanders. "MOND predictions of halo phenomenology in disc galaxies". *Mon. Not. Roy. Astron. Soc.* 357 (2005), pp. 45–48. DOI: 10.1111/j.1365-2966.2004.08578.x. arXiv: astro-ph/0406487.

[95] M. Milgrom and R. H. Sanders. "MOND rotation curves of very low mass spiral galaxies". *Astrophys. J. Lett.* 658 (2007), p. L17. DOI: 10.1086/513695. arXiv: astro-ph/0611494.

[96] J. D. Bekenstein. "Relativistic gravitation theory for the MOND paradigm". *Phys. Rev. D* 70 (2004). [Erratum: Phys.Rev.D 71, 069901 (2005)], p. 083509. DOI: 10.1103/PhysRevD.70.083509. arXiv: astro-ph/0403694.

[97] A. Schneider, R. E. Smith, and D. Reed. "Halo Mass Function and the Free Streaming Scale". *Mon. Not. Roy. Astron. Soc.* 433 (2013), p. 1573. DOI: 10.1093/mnras/stt829. arXiv: 1303.0839 [astro-ph.CO].

[98] J. R. Bond, A. S. Szalay, and M. S. Turner. "Formation of Galaxies in a Gravitino Dominated Universe". *Phys. Rev. Lett.* 48 (1982), p. 1636. DOI: 10.1103/PhysRevLett.48.1636.

[99] P. J. E. Peebles. "PRIMEVAL ADIABATIC PERTURBATIONS: EFFECT OF MASSIVE NEUTRINOS". *Astrophys. J.* 258 (1982), pp. 415–424. DOI: 10.1086/160094.

[100] J. R. Bond and A. S. Szalay. "The Collisionless Damping of Density Fluctuations in an Expanding Universe". *Astrophys. J.* 274 (1983), pp. 443–468. DOI: 10.1086/161460.

[101] S. D. M. White, C. S. Frenk, and M. Davis. "Clustering in a Neutrino Dominated Universe". *Astrophys. J. Lett.* 274 (1983). Ed. by M. A. Srednicki, pp. L1–L5. DOI: 10.1086/184139.

[102] S. D. M. White et al. “Clusters, filaments, and voids in a universe dominated by cold dark matter”. *Astrophys. J.* 313 (1987), pp. 505–516. DOI: 10.1086/164990.

[103] A. L. Melott et al. “CLUSTER ANALYSIS OF THE NONLINEAR EVOLUTION OF LARGE SCALE STRUCTURE IN AN AXION / GRAVITINO / PHOTINO DOMINATED UNIVERSE”. *Phys. Rev. Lett.* 51 (1983), pp. 935–938. DOI: 10.1103/PhysRevLett.51.935.

[104] G. R. Blumenthal et al. “Formation of Galaxies and Large Scale Structure with Cold Dark Matter”. *Nature* 311 (1984). Ed. by M. A. Srednicki, pp. 517–525. DOI: 10.1038/311517a0.

[105] S. D. McDermott, H.-B. Yu, and K. M. Zurek. “Turning off the Lights: How Dark is Dark Matter?” *Phys. Rev. D* 83 (2011), p. 063509. DOI: 10.1103/PhysRevD.83.063509. arXiv: 1011.2907 [hep-ph].

[106] P. F. Depta et al. “BBN constraints on the annihilation of MeV-scale dark matter”. *JCAP* 04 (2019), p. 029. DOI: 10.1088/1475-7516/2019/04/029. arXiv: 1901.06944 [hep-ph].

[107] A. S. Szalay and G. Marx. “Neutrino rest mass from cosmology”. *Astron. Astrophys.* 49 (1976), pp. 437–441.

[108] N. Aghanim et al. “Planck 2018 results. I. Overview and the cosmological legacy of Planck”. *Astron. Astrophys.* 641 (2020), A1. DOI: 10.1051/0004-6361/201833880. arXiv: 1807.06205 [astro-ph.CO].

[109] S. Dodelson and L. M. Widrow. “Sterile-neutrinos as dark matter”. *Phys. Rev. Lett.* 72 (1994), pp. 17–20. DOI: 10.1103/PhysRevLett.72.17. arXiv: hep-ph/9303287.

[110] P. B. Pal and L. Wolfenstein. “Radiative Decays of Massive Neutrinos”. *Phys. Rev. D* 25 (1982), p. 766. DOI: 10.1103/PhysRevD.25.766.

[111] D. E. Lopez-Fogliani, A. D. Perez, and R. R. de Austri. “Dark matter candidates in the NMSSM with RH neutrino superfields”. *JCAP* 04 (2021), p. 067. DOI: 10.1088/1475-7516/2021/04/067. arXiv: 2102.08986 [hep-ph].

[112] P. Villanueva-Domingo, O. Mena, and S. Palomares-Ruiz. “A brief review on primordial black holes as dark matter”. *Front. Astron. Space Sci.* 8 (2021), p. 87. DOI: 10.3389/fspas.2021.681084. arXiv: 2103.12087 [astro-ph.CO].

[113] T. Binder et al. “Early kinetic decoupling of dark matter: when the standard way of calculating the thermal relic density fails”. *Phys. Rev. D* 96.11 (2017). [Erratum: Phys.Rev.D 101, 099901 (2020)], p. 115010. DOI: 10.1103/PhysRevD.96.115010. arXiv: 1706.07433 [astro-ph.CO].

[114] Y. B. Zel’dovich, L. B. Okun’, and S. B. Pikel’ner. “QUARKS: ASTROPHYSICAL AND PHYSICOCHEMICAL ASPECTS”. *Sov. Phys. Usp.*

8.5 (May 1966), p. 702. DOI: 10.1070/PU1966v008n05ABEH003030. URL: https://dx.doi.org/10.1070/PU1966v008n05ABEH003030.

[115] B. W. Lee and S. Weinberg. "Cosmological Lower Bound on Heavy Neutrino Masses". *Phys. Rev. Lett.* 39 (1977). Ed. by M. A. Srednicki, pp. 165–168. DOI: 10.1103/PhysRevLett.39.165.

[116] K. Griest and D. Seckel. "Three exceptions in the calculation of relic abundances". *Phys. Rev. D* 43 (1991), pp. 3191–3203. DOI: 10.1103/PhysRevD.43.3191.

[117] M. Garny et al. "Coannihilation without chemical equilibrium". *Phys. Rev. D* 96.10 (2017), p. 103521. DOI: 10.1103/PhysRevD.96.103521. arXiv: 1705.09292 [hep-ph].

[118] R. T. D'Agnolo, D. Pappadopulo, and J. T. Ruderman. "Fourth Exception in the Calculation of Relic Abundances". *Phys. Rev. Lett.* 119.6 (2017), p. 061102. DOI: 10.1103/PhysRevLett.119.061102. arXiv: 1705.08450 [hep-ph].

[119] A.-C. Eilers et al. "The Circular Velocity Curve of the Milky Way from 5 to 25 kpc". *Astrophys. J.* 871.1 (2019), p. 120. DOI: 10.3847/1538-4357/aaf648.

[120] A. Birkedal et al. "Robust gamma ray signature of WIMP dark matter" (July 2005). arXiv: hep-ph/0507194.

[121] A. Albert et al. "Combined search for neutrinos from dark matter self-annihilation in the Galactic Center with ANTARES and IceCube". *Phys. Rev. D* 102.8 (2020), p. 082002. DOI: 10.1103/PhysRevD.102.082002. arXiv: 2003.06614 [astro-ph.HE].

[122] P. Baratella et al. "PPPC 4 DMν: a Poor Particle Physicist Cookbook for Neutrinos from Dark Matter annihilations in the Sun". *JCAP* 03 (2014), p. 053. DOI: 10.1088/1475-7516/2014/03/053. arXiv: 1312.6408 [hep-ph].

[123] P. Ciafaloni et al. "Weak Corrections are Relevant for Dark Matter Indirect Detection". *JCAP* 03 (2011), p. 019. DOI: 10.1088/1475-7516/2011/03/019. arXiv: 1009.0224 [hep-ph].

[124] M. Lisanti. "Lectures on Dark Matter Physics". *Theoretical Advanced Study Institute in Elementary Particle Physics: New Frontiers in Fields and Strings*. 2017, pp. 399–446. DOI: 10.1142/9789813149441_0007. arXiv: 1603.03797 [hep-ph].

[125] T. R. Slatyer. "Les Houches Lectures on Indirect Detection of Dark Matter". *SciPost Phys. Lect. Notes* 53 (2022), p. 1. DOI: 10.21468/SciPostPhysLectNotes.53. arXiv: 2109.02696 [hep-ph].

[126] J. F. Navarro, C. S. Frenk, and S. D. M. White. "The Structure of cold dark matter halos". *Astrophys. J.* 462 (1996), pp. 563–575. DOI: 10.1086/177173. arXiv: astro-ph/9508025.

[127] J. Einasto. “О ПОСТРОЕНИИ СОСТАВНОй МОДЕЛИ ГАЛАКТИКИ И ОПРЕДЕЛЕНИИ СИСТЕМЫ ГАЛАКТИЧЕСКИХ ПАРАМЕТРОВ”. *Trudy Astrofizicheskogo Instituta Alma-Ata* 5 (1965), pp. 87–100.

[128] A. Burkert. “The Structure of dark matter halos in dwarf galaxies”. *Astrophys. J. Lett.* 447 (1995), p. L25. DOI: 10.1086/309560. arXiv: astro-ph/9504041.

[129] J. Binney and S. Tremaine. *Galactic Dynamics: Second Edition*. 2008.

[130] R. Catena and P. Ullio. “A novel determination of the local dark matter density”. *JCAP* 08 (2010), p. 004. DOI: 10.1088/1475-7516/2010/08/004. arXiv: 0907.0018 [astro-ph.CO].

[131] M. Fornasa and A. M. Green. “Self-consistent phase-space distribution function for the anisotropic dark matter halo of the Milky Way”. *Phys. Rev. D* 89.6 (2014), p. 063531. DOI: 10.1103/PhysRevD.89.063531. arXiv: 1311.5477 [astro-ph.CO].

[132] J. I. Read. “The Local Dark Matter Density”. *J. Phys. G* 41 (2014), p. 063101. DOI: 10.1088/0954-3899/41/6/063101. arXiv: 1404.1938 [astro-ph.GA].

[133] M. Mateo. “Dwarf galaxies of the Local Group”. *Ann. Rev. Astron. Astrophys.* 36 (1998), pp. 435–506. DOI: 10.1146/annurev.astro.36.1.435. arXiv: astro-ph/9810070.

[134] D. R. Weisz et al. “The ACS Nearby Galaxy Survey Treasury VIII. The Global Star Formation Histories of 60 Dwarf Galaxies in the Local Volume”. *Astrophys. J.* 739 (2011), p. 5. DOI: 10.1088/0004-637X/739/1/5. arXiv: 1101.1093 [astro-ph.CO].

[135] T. M. Brown et al. “The Primeval Populations of the Ultra-Faint Dwarf Galaxies”. *Astrophys. J. Lett.* 753 (2012), p. L21. DOI: 10.1088/2041-8205/753/1/L21. arXiv: 1206.0941 [astro-ph.CO].

[136] B. D’Ettorre Piazzoli et al. “Chapter 4 Cosmic-Ray Physics”. *Chin. Phys. C* 46.3 (2022), p. 030004. DOI: 10.1088/1674-1137/ac3faa.

[137] G. Di Bernardo et al. “Unified interpretation of cosmic-ray nuclei and antiproton recent measurements”. *Astropart. Phys.* 34 (2010), pp. 274–283. DOI: 10.1016/j.astropartphys.2010.08.006. arXiv: 0909.4548 [astro-ph.HE].

[138] C. Evoli et al. “Cosmic-ray propagation with DRAGON2: I. numerical solver and astrophysical ingredients”. *JCAP* 02 (2017), p. 015. DOI: 10.1088/1475-7516/2017/02/015. arXiv: 1607.07886 [astro-ph.HE].

[139] I. V. Moskalenko and A. W. Strong. “Production and propagation of cosmic ray positrons and electrons”. *Astrophys. J.* 493 (1998), pp. 694–707. DOI: 10.1086/305152. arXiv: astro-ph/9710124.

[140] A. W. Strong and I. V. Moskalenko. “Propagation of cosmic-ray nucleons in the galaxy”. *Astrophys. J.* 509 (1998), pp. 212–228. DOI: 10.1086/306470. arXiv: astro-ph/9807150.

[141] *The GALPROP code for cosmic-ray transport and diffuse emission production*. URL: https://galprop.stanford.edu/ (visited on Jan. 31, 2024).

[142] A. A. Abdo et al. "Observations of Milky Way Dwarf Spheroidal galaxies with the Fermi-LAT detector and constraints on Dark Matter models". *Astrophys. J.* 712 (2010), pp. 147–158. DOI: 10.1088/0004-637X/712/1/147. arXiv: 1001.4531 [astro-ph.CO].

[143] A. Geringer-Sameth et al. "Astrophysical explanations of suspected dark matter signals in dwarf galaxies" (July 2018). arXiv: 1807.08740 [astro-ph.HE].

[144] M. Ackermann et al. "The Fermi Large Area Telescope On Orbit: Event Classification, Instrument Response Functions, and Calibration". *Astrophys. J. Suppl.* 203 (2012), p. 4. DOI: 10.1088/0067-0049/203/1/4. arXiv: 1206.1896 [astro-ph.IM].

[145] A. U. Abeysekara et al. "Observation of the Crab Nebula with the HAWC Gamma-Ray Observatory". *Astrophys. J.* 843.1 (2017), p. 39. DOI: 10.3847/1538-4357/aa7555. arXiv: 1701.01778 [astro-ph.HE].

[146] F. Aharonian et al. "Observations of the Crab Nebula with H.E.S.S". *Astron. Astrophys.* 457 (2006), pp. 899–915. DOI: 10.1051/0004-6361:20065351. arXiv: astro-ph/0607333.

[147] J. Sitarek et al. "Physics performance of the upgraded MAGIC telescopes obtained with Crab Nebula data". *33rd International Cosmic Ray Conference*. Aug. 2013, p. 0074. arXiv: 1308.0141 [astro-ph.IM].

[148] N. Park. "Performance of the VERITAS experiment". *PoS* ICRC2015 (2016), p. 771. DOI: 10.22323/1.236.0771. arXiv: 1508.07070 [astro-ph.IM].

[149] M. Ackermann et al. "Searching for Dark Matter Annihilation from Milky Way Dwarf Spheroidal Galaxies with Six Years of Fermi Large Area Telescope Data". *Phys. Rev. Lett.* 115.23 (2015), p. 231301. DOI: 10.1103/PhysRevLett.115.231301. arXiv: 1503.02641 [astro-ph.HE].

[150] B. Zitzer. "A Search for Dark Matter from Dwarf Galaxies using VERITAS". *PoS* ICRC2015 (2016), p. 1225. DOI: 10.22323/1.236.1225. arXiv: 1509.01105 [astro-ph.HE].

[151] M. L. Ahnen et al. "Limits to Dark Matter Annihilation Cross-Section from a Combined Analysis of MAGIC and Fermi-LAT Observations of Dwarf Satellite Galaxies". *JCAP* 02 (2016), p. 039. DOI: 10.1088/1475-7516/2016/02/039. arXiv: 1601.06590 [astro-ph.HE].

[152] M. Ackermann et al. "Updated search for spectral lines from Galactic dark matter interactions with pass 8 data from the Fermi Large Area Telescope". *Phys. Rev. D* 91.12 (2015), p. 122002. DOI: 10.1103/PhysRevD.91.122002. arXiv: 1506.00013 [astro-ph.HE].

[153] J. W. Foster et al. “Search for dark matter lines at the Galactic Center with 14 years of Fermi data”. *Phys. Rev. D* 107.10 (2023), p. 103047. DOI: 10.1103/PhysRevD.107.103047. arXiv: 2212.07435 [hep-ph].

[154] H. Abdallah et al. “Search for γ-Ray Line Signals from Dark Matter Annihilations in the Inner Galactic Halo from 10 Years of Observations with H.E.S.S.” *Phys. Rev. Lett.* 120.20 (2018), p. 201101. DOI: 10.1103/PhysRevLett.120.201101. arXiv: 1805.05741 [astro-ph.HE].

[155] H. Abe et al. “Search for Gamma-Ray Spectral Lines from Dark Matter Annihilation up to 100 TeV toward the Galactic Center with MAGIC”. *Phys. Rev. Lett.* 130.6 (2023), p. 061002. DOI: 10.1103/PhysRevLett.130.061002. arXiv: 2212.10527 [astro-ph.HE].

[156] H. Abdalla et al. “Searches for gamma-ray lines and ’pure WIMP’ spectra from Dark Matter annihilations in dwarf galaxies with H.E.S.S”. *JCAP* 11 (2018), p. 037. DOI: 10.1088/1475-7516/2018/11/037. arXiv: 1810.00995 [astro-ph.HE].

[157] A. Albert et al. “Search for gamma-ray spectral lines from dark matter annihilation in dwarf galaxies with the High-Altitude Water Cherenkov observatory”. *Phys. Rev. D* 101.10 (2020), p. 103001. DOI: 10.1103/PhysRevD.101.103001. arXiv: 1912.05632 [astro-ph.HE].

[158] A. Neronov and D. Semikoz. “LHAASO telescope sensitivity to diffuse gamma-ray signals from the Galaxy”. *Phys. Rev. D* 102.4 (2020), p. 043025. DOI: 10.1103/PhysRevD.102.043025. arXiv: 2001.11881 [astro-ph.HE].

[159] N. P. Topchiev et al. “Gamma- and Cosmic-Ray observations with the GAMMA-400 Gamma-Ray telescope”. *Adv. Space Res.* 70 (2022), pp. 2773–2793. DOI: 10.1016/j.asr.2022.01.036. arXiv: 2108.12609 [astro-ph.IM].

[160] B. S. Acharya et al. “Introducing the CTA concept”. *Astropart. Phys.* 43 (2013), pp. 3–18. DOI: 10.1016/j.astropartphys.2013.01.007.

[161] T. R. Slatyer, N. Padmanabhan, and D. P. Finkbeiner. “CMB Constraints on WIMP Annihilation: Energy Absorption During the Recombination Epoch”. *Phys. Rev. D* 80 (2009), p. 043526. DOI: 10.1103/PhysRevD.80.043526. arXiv: 0906.1197 [astro-ph.CO].

[162] M. S. Madhavacheril, N. Sehgal, and T. R. Slatyer. “Current Dark Matter Annihilation Constraints from CMB and Low-Redshift Data”. *Phys. Rev. D* 89 (2014), p. 103508. DOI: 10.1103/PhysRevD.89.103508. arXiv: 1310.3815 [astro-ph.CO].

[163] T. R. Slatyer. “Indirect dark matter signatures in the cosmic dark ages. I. Generalizing the bound on s-wave dark matter annihilation from Planck results”. *Phys. Rev. D* 93.2 (2016), p. 023527. DOI: 10.1103/PhysRevD.93.023527. arXiv: 1506.03811 [hep-ph].

[164] T. R. Slatyer. "Indirect Dark Matter Signatures in the Cosmic Dark Ages II. Ionization, Heating and Photon Production from Arbitrary Energy Injections". *Phys. Rev. D* 93.2 (2016), p. 023521. DOI: 10.1103/PhysRevD.93.023521. arXiv: 1506.03812 [astro-ph.CO].

[165] H. Liu, T. R. Slatyer, and J. Zavala. "Contributions to cosmic reionization from dark matter annihilation and decay". *Phys. Rev. D* 94.6 (2016), p. 063507. DOI: 10.1103/PhysRevD.94.063507. arXiv: 1604.02457 [astro-ph.CO].

[166] A. Achterberg et al. "First Year Performance of The IceCube Neutrino Telescope". *Astropart. Phys.* 26 (2006), pp. 155–173. DOI: 10.1016/j.astropartphys.2006.06.007. arXiv: astro-ph/0604450.

[167] M. Ageron et al. "ANTARES: the first undersea neutrino telescope". *Nucl. Instrum. Meth. A* 656 (2011), pp. 11–38. DOI: 10.1016/j.nima.2011.06.103. arXiv: 1104.1607 [astro-ph.IM].

[168] Y. Fukuda et al. "The Super-Kamiokande detector". *Nucl. Instrum. Meth. A* 501 (2003). Ed. by V. A. Ilyin, V. V. Korenkov, and D. Perret-Gallix, pp. 418–462. DOI: 10.1016/S0168-9002(03)00425-X.

[169] U. F. Katz. "KM3NeT: Towards a km**3 Mediterranean Neutrino Telescope". *Nucl. Instrum. Meth. A* 567 (2006). Ed. by E. Migneco et al., pp. 457–461. DOI: 10.1016/j.nima.2006.05.235. arXiv: astro-ph/0606068.

[170] K. Abe et al. "Letter of Intent: The Hyper-Kamiokande Experiment — Detector Design and Physics Potential —" (Sept. 2011). arXiv: 1109.3262 [hep-ex].

[171] G. Bellini et al. "Study of solar and other unknown anti-neutrino fluxes with Borexino at LNGS". *Phys. Lett. B* 696 (2011), pp. 191–196. DOI: 10.1016/j.physletb.2010.12.030. arXiv: 1010.0029 [hep-ex].

[172] M. Agostini et al. "Experimental evidence of neutrinos produced in the CNO fusion cycle in the Sun". *Nature* 587 (2020), pp. 577–582. DOI: 10.1038/s41586-020-2934-0. arXiv: 2006.15115 [hep-ex].

[173] S. Appel et al. "Improved Measurement of Solar Neutrinos from the Carbon-Nitrogen-Oxygen Cycle by Borexino and Its Implications for the Standard Solar Model". *Phys. Rev. Lett.* 129.25 (2022), p. 252701. DOI: 10.1103/PhysRevLett.129.252701. arXiv: 2205.15975 [hep-ex].

[174] D. Basilico et al. "Final results of Borexino on CNO solar neutrinos". *Phys. Rev. D* 108.10 (2023), p. 102005. DOI: 10.1103/PhysRevD.108.102005. arXiv: 2307.14636 [hep-ex].

[175] A. Gando et al. "A study of extraterrestrial antineutrino sources with the KamLAND detector". *Astrophys. J.* 745 (2012), p. 193. DOI: 10.1088/0004-637X/745/2/193. arXiv: 1105.3516 [astro-ph.HE].

[176] F. An et al. "Neutrino Physics with JUNO". *J. Phys. G* 43.3 (2016), p. 030401. DOI: 10.1088/0954-3899/43/3/030401. arXiv: 1507.05613 [physics.ins-det].

[177] M. Chianese et al. "Heavy decaying dark matter at future neutrino radio telescopes". *JCAP* 05 (2021), p. 074. DOI: 10.1088/1475-7516/2021/05/074. arXiv: 2103.03254 [hep-ph].

[178] M. Chianese et al. "Constraints on heavy decaying dark matter with current gamma-ray measurements". *JCAP* 11 (2021), p. 035. DOI: 10.1088/1475-7516/2021/11/035. arXiv: 2108.01678 [hep-ph].

[179] J. A. Aguilar et al. "Design and Sensitivity of the Radio Neutrino Observatory in Greenland (RNO-G)". *JINST* 16.03 (2021). [Erratum: JINST 18, E03001 (2023)], P03025. DOI: 10.1088/1748-0221/16/03/P03025. arXiv: 2010.12279 [astro-ph.IM].

[180] M. G. Aartsen et al. "Neutrino astronomy with the next generation IceCube Neutrino Observatory" (Nov. 2019). arXiv: 1911.02561 [astro-ph.HE].

[181] M. G. Aartsen et al. "IceCube-Gen2: the window to the extreme Universe". *J. Phys. G* 48.6 (2021), p. 060501. DOI: 10.1088/1361-6471/abbd48. arXiv: 2008.04323 [astro-ph.HE].

[182] J. Álvarez-Muñiz et al. "The Giant Radio Array for Neutrino Detection (GRAND): Science and Design". *Sci. China Phys. Mech. Astron.* 63.1 (2020), p. 219501. DOI: 10.1007/s11433-018-9385-7. arXiv: 1810.09994 [astro-ph.HE].

[183] M. C. Chantell et al. "Limits on the isotropic diffuse flux of ultrahigh-energy gamma radiation". *Phys. Rev. Lett.* 79 (1997), pp. 1805–1808. DOI: 10.1103/PhysRevLett.79.1805. arXiv: astro-ph/9705246.

[184] W. D. Apel et al. "KASCADE-Grande Limits on the Isotropic Diffuse Gamma-Ray Flux between 100 TeV and 1 EeV". *Astrophys. J.* 848.1 (2017), p. 1. DOI: 10.3847/1538-4357/aa8bb7. arXiv: 1710.02889 [astro-ph.HE].

[185] R. U. Abbasi et al. "Constraints on the diffuse photon flux with energies above 10^{18} eV using the surface detector of the Telescope Array experiment". *Astropart. Phys.* 110 (2019), pp. 8–14. DOI: 10.1016/j.astropartphys.2019.03.003. arXiv: 1811.03920 [astro-ph.HE].

[186] A. Aab et al. "Search for photons with energies above 10^{18} eV using the hybrid detector of the Pierre Auger Observatory". *JCAP* 04 (2017). [Erratum: JCAP 09, E02 (2020)], p. 009. DOI: 10.1088/1475-7516/2017/04/009. arXiv: 1612.01517 [astro-ph.HE].

[187] M. Aguilar et al. "Antiproton Flux, Antiproton-to-Proton Flux Ratio, and Properties of Elementary Particle Fluxes in Primary Cosmic Rays Measured with the Alpha Magnetic Spectrometer on the International

Space Station". *Phys. Rev. Lett.* 117.9 (2016), p. 091103. DOI: 10.1103/PhysRevLett.117.091103.

[188] A. Cuoco et al. "Probing dark matter annihilation in the Galaxy with antiprotons and gamma rays". *JCAP* 10 (2017), p. 053. DOI: 10.1088/1475-7516/2017/10/053. arXiv: 1704.08258 [astro-ph.HE].

[189] M.-Y. Cui et al. "Possible dark matter annihilation signal in the AMS-02 antiproton data". *Phys. Rev. Lett.* 118.19 (2017), p. 191101. DOI: 10.1103/PhysRevLett.118.191101. arXiv: 1610.03840 [astro-ph.HE].

[190] A. Cuoco, M. Krämer, and M. Korsmeier. "Novel Dark Matter Constraints from Antiprotons in Light of AMS-02". *Phys. Rev. Lett.* 118.19 (2017), p. 191102. DOI: 10.1103/PhysRevLett.118.191102. arXiv: 1610.03071 [astro-ph.HE].

[191] A. Cuoco et al. "Scrutinizing the evidence for dark matter in cosmic-ray antiprotons". *Phys. Rev. D* 99.10 (2019), p. 103014. DOI: 10.1103/PhysRevD.99.103014. arXiv: 1903.01472 [astro-ph.HE].

[192] I. Cholis, T. Linden, and D. Hooper. "A Robust Excess in the Cosmic-Ray Antiproton Spectrum: Implications for Annihilating Dark Matter". *Phys. Rev. D* 99.10 (2019), p. 103026. DOI: 10.1103/PhysRevD.99.103026. arXiv: 1903.02549 [astro-ph.HE].

[193] A. Reinert and M. W. Winkler. "A Precision Search for WIMPs with Charged Cosmic Rays". *JCAP* 01 (2018), p. 055. DOI: 10.1088/1475-7516/2018/01/055. arXiv: 1712.00002 [astro-ph.HE].

[194] J. Heisig, M. Korsmeier, and M. W. Winkler. "Dark matter or correlated errors: Systematics of the AMS-02 antiproton excess". *Phys. Rev. Res.* 2.4 (2020), p. 043017. DOI: 10.1103/PhysRevResearch.2.043017. arXiv: 2005.04237 [astro-ph.HE].

[195] M. Di Mauro and M. W. Winkler. "Multimessenger constraints on the dark matter interpretation of the Fermi-LAT Galactic center excess". *Phys. Rev. D* 103.12 (2021), p. 123005. DOI: 10.1103/PhysRevD.103.123005. arXiv: 2101.11027 [astro-ph.HE].

[196] O. Adriani et al. "An anomalous positron abundance in cosmic rays with energies 1.5-100 GeV". *Nature* 458 (2009), pp. 607–609. DOI: 10.1038/nature07942. arXiv: 0810.4995 [astro-ph].

[197] M. Ackermann et al. "Measurement of separate cosmic-ray electron and positron spectra with the Fermi Large Area Telescope". *Phys. Rev. Lett.* 108 (2012), p. 011103. DOI: 10.1103/PhysRevLett.108.011103. arXiv: 1109.0521 [astro-ph.HE].

[198] M. Aguilar et al. "First Result from the Alpha Magnetic Spectrometer on the International Space Station: Precision Measurement of the Positron Fraction in Primary Cosmic Rays of 0.5–350 GeV". *Phys. Rev. Lett.* 110 (2013), p. 141102. DOI: 10.1103/PhysRevLett.110.141102.

[199] D. Hooper et al. "HAWC Observations Strongly Favor Pulsar Interpretations of the Cosmic-Ray Positron Excess". *Phys. Rev. D* 96.10 (2017), p. 103013. DOI: 10.1103/PhysRevD.96.103013. arXiv: 1702.08436 [astro-ph.HE].

[200] L. Goodenough and D. Hooper. "Possible Evidence For Dark Matter Annihilation In The Inner Milky Way From The Fermi Gamma Ray Space Telescope" (Oct. 2009). arXiv: 0910.2998 [hep-ph].

[201] D. Hooper and L. Goodenough. "Dark Matter Annihilation in The Galactic Center As Seen by the Fermi Gamma Ray Space Telescope". *Phys. Lett. B* 697 (2011), pp. 412–428. DOI: 10.1016/j.physletb.2011.02.029. arXiv: 1010.2752 [hep-ph].

[202] A. Boyarsky, D. Malyshev, and O. Ruchayskiy. "A comment on the emission from the Galactic Center as seen by the Fermi telescope". *Phys. Lett. B* 705 (2011), pp. 165–169. DOI: 10.1016/j.physletb.2011.10.014. arXiv: 1012.5839 [hep-ph].

[203] D. Hooper and T. Linden. "On The Origin Of The Gamma Rays From The Galactic Center". *Phys. Rev. D* 84 (2011), p. 123005. DOI: 10.1103/PhysRevD.84.123005. arXiv: 1110.0006 [astro-ph.HE].

[204] K. N. Abazajian and M. Kaplinghat. "Detection of a Gamma-Ray Source in the Galactic Center Consistent with Extended Emission from Dark Matter Annihilation and Concentrated Astrophysical Emission". *Phys. Rev. D* 86 (2012). [Erratum: Phys.Rev.D 87, 129902 (2013)], p. 083511. DOI: 10.1103/PhysRevD.86.083511. arXiv: 1207.6047 [astro-ph.HE].

[205] C. Gordon and O. Macias. "Dark Matter and Pulsar Model Constraints from Galactic Center Fermi-LAT Gamma Ray Observations". *Phys. Rev. D* 88.8 (2013). [Erratum: Phys.Rev.D 89, 049901 (2014)], p. 083521. DOI: 10.1103/PhysRevD.88.083521. arXiv: 1306.5725 [astro-ph.HE].

[206] K. N. Abazajian et al. "Astrophysical and Dark Matter Interpretations of Extended Gamma-Ray Emission from the Galactic Center". *Phys. Rev. D* 90.2 (2014), p. 023526. DOI: 10.1103/PhysRevD.90.023526. arXiv: 1402.4090 [astro-ph.HE].

[207] T. Daylan et al. "The characterization of the gamma-ray signal from the central Milky Way: A case for annihilating dark matter". *Phys. Dark Univ.* 12 (2016), pp. 1–23. DOI: 10.1016/j.dark.2015.12.005. arXiv: 1402.6703 [astro-ph.HE].

[208] F. Calore et al. "A Tale of Tails: Dark Matter Interpretations of the Fermi GeV Excess in Light of Background Model Systematics". *Phys. Rev. D* 91.6 (2015), p. 063003. DOI: 10.1103/PhysRevD.91.063003. arXiv: 1411.4647 [hep-ph].

[209] F. Calore, I. Cholis, and C. Weniger. "Background Model Systematics for the Fermi GeV Excess". *JCAP* 03 (2015), p. 038. DOI: 10.1088/1475-7516/2015/03/038. arXiv: 1409.0042 [astro-ph.CO].

[210] M. Ajello et al. "Fermi-LAT Observations of High-Energy γ-Ray Emission Toward the Galactic Center". *Astrophys. J.* 819.1 (2016), p. 44. DOI: 10.3847/0004-637X/819/1/44. arXiv: 1511.02938 [astro-ph.HE].

[211] A. Cuoco et al. "A global fit of the γ-ray galactic center excess within the scalar singlet Higgs portal model". *JCAP* 06 (2016), p. 050. DOI: 10.1088/1475-7516/2016/06/050. arXiv: 1603.08228 [hep-ph].

[212] M. Ackermann et al. "The Fermi Galactic Center GeV Excess and Implications for Dark Matter". *Astrophys. J.* 840.1 (2017), p. 43. DOI: 10.3847/1538-4357/aa6cab. arXiv: 1704.03910 [astro-ph.HE].

[213] M. Di Mauro et al. "Search for γ-ray emission from dark matter particle interactions from Andromeda and Triangulum Galaxies with the Fermi Large Area Telescope". *Phys. Rev. D* 99.12 (2019), p. 123027. DOI: 10.1103/PhysRevD.99.123027. arXiv: 1904.10977 [astro-ph.HE].

[214] M. Di Mauro. "Characteristics of the Galactic Center excess measured with 11 years of Fermi-LAT data". *Phys. Rev. D* 103.6 (2021), p. 063029. DOI: 10.1103/PhysRevD.103.063029. arXiv: 2101.04694 [astro-ph.HE].

[215] I. Cholis et al. "Return of the templates: Revisiting the Galactic Center excess with multimessenger observations". *Phys. Rev. D* 105.10 (2022), p. 103023. DOI: 10.1103/PhysRevD.105.103023. arXiv: 2112.09706 [astro-ph.HE].

[216] N. Okada and O. Seto. "Gamma ray emission in Fermi bubbles and Higgs portal dark matter". *Phys. Rev. D* 89.4 (2014), p. 043525. DOI: 10.1103/PhysRevD.89.043525. arXiv: 1310.5991 [hep-ph].

[217] P. Agrawal et al. "WIMPs at the Galactic Center". *JCAP* 05 (2015), p. 011. DOI: 10.1088/1475-7516/2015/05/011. arXiv: 1411.2592 [hep-ph].

[218] T. Mondal and T. Basak. "Class of Higgs-portal Dark Matter models in the light of gamma-ray excess from Galactic center". *Phys. Lett. B* 744 (2015), pp. 208–212. DOI: 10.1016/j.physletb.2015.03.055. arXiv: 1405.4877 [hep-ph].

[219] M. Duerr, P. Fileviez Pérez, and J. Smirnov. "Gamma-Ray Excess and the Minimal Dark Matter Model". *JHEP* 06 (2016), p. 008. DOI: 10.1007/JHEP06(2016)008. arXiv: 1510.07562 [hep-ph].

[220] A. Lopez et al. "Fermi/LAT observations of Dwarf Galaxies highly constrain a Dark Matter Interpretation of Excess Positrons seen in

AMS-02, HEAT, and PAMELA". *JCAP* 03 (2016), p. 033. DOI: 10.1088/1475-7516/2016/03/033. arXiv: 1501.01618 [astro-ph.CO].

[221] A. Albert et al. "Searching for Dark Matter Annihilation in Recently Discovered Milky Way Satellites with Fermi-LAT". *Astrophys. J.* 834.2 (2017), p. 110. DOI: 10.3847/1538-4357/834/2/110. arXiv: 1611.03184 [astro-ph.HE].

[222] F. Calore, P. D. Serpico, and B. Zaldivar. "Dark matter constraints from dwarf galaxies: a data-driven analysis". *JCAP* 10 (2018), p. 029. DOI: 10.1088/1475-7516/2018/10/029. arXiv: 1803.05508 [astro-ph.HE].

[223] S. Hoof, A. Geringer-Sameth, and R. Trotta. "A Global Analysis of Dark Matter Signals from 27 Dwarf Spheroidal Galaxies using 11 Years of Fermi-LAT Observations". *JCAP* 02 (2020), p. 012. DOI: 10.1088/1475-7516/2020/02/012. arXiv: 1812.06986 [astro-ph.CO].

[224] A. B. Pace and L. E. Strigari. "Scaling Relations for Dark Matter Annihilation and Decay Profiles in Dwarf Spheroidal Galaxies". *Mon. Not. Roy. Astron. Soc.* 482.3 (2019), pp. 3480–3496. DOI: 10.1093/mnras/sty2839. arXiv: 1802.06811 [astro-ph.GA].

[225] M. Di Mauro, M. Stref, and F. Calore. "Investigating the effect of Milky Way dwarf spheroidal galaxies extension on dark matter searches with Fermi-LAT data". *Phys. Rev. D* 106.12 (2022), p. 123032. DOI: 10.1103/PhysRevD.106.123032. arXiv: 2212.06850 [astro-ph.HE].

[226] R. Bartels, S. Krishnamurthy, and C. Weniger. "Strong support for the millisecond pulsar origin of the Galactic center GeV excess". *Phys. Rev. Lett.* 116.5 (2016), p. 051102. DOI: 10.1103/PhysRevLett.116.051102. arXiv: 1506.05104 [astro-ph.HE].

[227] S. K. Lee et al. "Evidence for Unresolved γ-Ray Point Sources in the Inner Galaxy". *Phys. Rev. Lett.* 116.5 (2016), p. 051103. DOI: 10.1103/PhysRevLett.116.051103. arXiv: 1506.05124 [astro-ph.HE].

[228] R. K. Leane and T. R. Slatyer. "Revival of the Dark Matter Hypothesis for the Galactic Center Gamma-Ray Excess". *Phys. Rev. Lett.* 123.24 (2019), p. 241101. DOI: 10.1103/PhysRevLett.123.241101. arXiv: 1904.08430 [astro-ph.HE].

[229] L. J. Chang et al. "Characterizing the nature of the unresolved point sources in the Galactic Center: An assessment of systematic uncertainties". *Phys. Rev. D* 101.2 (2020), p. 023014. DOI: 10.1103/PhysRevD.101.023014. arXiv: 1908.10874 [astro-ph.CO].

[230] M. Buschmann et al. "Foreground Mismodeling and the Point Source Explanation of the Fermi Galactic Center Excess". *Phys. Rev. D* 102.2 (2020), p. 023023. DOI: 10.1103/PhysRevD.102.023023. arXiv: 2002.12373 [astro-ph.HE].

[231] F. List et al. “The GCE in a New Light: Disentangling the γ-ray Sky with Bayesian Graph Convolutional Neural Networks”. *Phys. Rev. Lett.* 125 (2020), p. 241102. DOI: 10.1103/PhysRevLett.125.241102. arXiv: 2006.12504 [astro-ph.HE].

[232] E. Carlson and S. Profumo. “Cosmic Ray Protons in the Inner Galaxy and the Galactic Center Gamma-Ray Excess”. *Phys. Rev. D* 90.2 (2014), p. 023015. DOI: 10.1103/PhysRevD.90.023015. arXiv: 1405.7685 [astro-ph.HE].

[233] J. Petrović, P. D. Serpico, and G. Zaharijaš. “Galactic Center gamma-ray ”excess” from an active past of the Galactic Centre?” *JCAP* 10 (2014), p. 052. DOI: 10.1088/1475-7516/2014/10/052. arXiv: 1405.7928 [astro-ph.HE].

[234] I. Cholis et al. “The Galactic Center GeV Excess from a Series of Leptonic Cosmic-Ray Outbursts”. *JCAP* 12 (2015), p. 005. DOI: 10.1088/1475-7516/2015/12/005. arXiv: 1506.05119 [astro-ph.HE].

[235] D. Gaggero et al. “Towards a realistic astrophysical interpretation of the gamma-ray Galactic center excess”. *JCAP* 12 (2015), p. 056. DOI: 10.1088/1475-7516-2015-12-056. arXiv: 1507.06129 [astro-ph.HE].

[236] M. W. Goodman and E. Witten. “Detectability of Certain Dark Matter Candidates”. *Phys. Rev. D* 31 (1985). Ed. by M. A. Srednicki, p. 3059. DOI: 10.1103/PhysRevD.31.3059.

[237] J. Cooley. “Dark Matter direct detection of classical WIMPs”. *SciPost Phys. Lect. Notes* 55 (2022), p. 1. DOI: 10.21468/SciPostPhysLectNotes.55. arXiv: 2110.02359 [hep-ph].

[238] D. S. Akerib et al. “Snowmass2021 Cosmic Frontier Dark Matter Direct Detection to the Neutrino Fog”. *Snowmass 2021*. Mar. 2022. arXiv: 2203.08084 [hep-ex].

[239] K. Freese, J. A. Frieman, and A. Gould. “Signal Modulation in Cold Dark Matter Detection”. *Phys. Rev. D* 37 (1988), pp. 3388–3405. DOI: 10.1103/PhysRevD.37.3388.

[240] M. C. Smith et al. “The RAVE Survey: Constraining the Local Galactic Escape Speed”. *Mon. Not. Roy. Astron. Soc.* 379 (2007), pp. 755–772. DOI: 10.1111/j.1365-2966.2007.11964.x. arXiv: astro-ph/0611671.

[241] F. J. Kerr and D. Lynden-Bell. “Review of galactic constants”. *Mon. Not. Roy. Astron. Soc.* 221.4 (1986), pp. 1023–1038. DOI: 10.1093/mnras/221.4.1023.

[242] M. J. Reid et al. “Trigonometric Parallaxes of Massive Star Forming Regions: VI. Galactic Structure, Fundamental Parameters and Non-Circular Motions”. *Astrophys. J.* 700 (2009), pp. 137–148. DOI: 10.1088/0004-637X/700/1/137. arXiv: 0902.3913 [astro-ph.GA].

[243] P. J. McMillan and J. J. Binney. "The uncertainty in Galactic parameters". *Mon. Not. Roy. Astron. Soc.* 402 (2010), p. 934. DOI: 10.1111/j.1365-2966.2009.15932.x. arXiv: 0907.4685 [astro-ph.GA].

[244] J. Bovy, D. W. Hogg, and H.-W. Rix. "Galactic masers and the Milky Way circular velocity". *Astrophys. J.* 704 (2009), pp. 1704–1709. DOI: 10.1088/0004-637X/704/2/1704. arXiv: 0907.5423 [astro-ph.GA].

[245] R. Schoenrich, J. Binney, and W. Dehnen. "Local Kinematics and the Local Standard of Rest". *Mon. Not. Roy. Astron. Soc.* 403 (2010), p. 1829. DOI: 10.1111/j.1365-2966.2010.16253.x. arXiv: 0912.3693 [astro-ph.GA].

[246] R. H. Helm. "Inelastic and Elastic Scattering of 187-Mev Electrons from Selected Even-Even Nuclei". *Phys. Rev.* 104 (1956), pp. 1466–1475. DOI: 10.1103/PhysRev.104.1466.

[247] G. Duda, A. Kemper, and P. Gondolo. "Model Independent Form Factors for Spin Independent Neutralino-Nucleon Scattering from Elastic Electron Scattering Data". *JCAP* 04 (2007), p. 012. DOI: 10.1088/1475-7516/2007/04/012. arXiv: hep-ph/0608035.

[248] C. A. J. O'Hare. "New Definition of the Neutrino Floor for Direct Dark Matter Searches". *Phys. Rev. Lett.* 127.25 (2021), p. 251802. DOI: 10.1103/PhysRevLett.127.251802. arXiv: 2109.03116 [hep-ph].

[249] J. Billard, L. Strigari, and E. Figueroa-Feliciano. "Implication of neutrino backgrounds on the reach of next generation dark matter direct detection experiments". *Phys. Rev. D* 89.2 (2014), p. 023524. DOI: 10.1103/PhysRevD.89.023524. arXiv: 1307.5458 [hep-ph].

[250] G. B. Gelmini, V. Takhistov, and S. J. Witte. "Casting a Wide Signal Net with Future Direct Dark Matter Detection Experiments". *JCAP* 07 (2018). [Erratum: JCAP 02, E02 (2019)], p. 009. DOI: 10.1088/1475-7516/2018/07/009. arXiv: 1804.01638 [hep-ph].

[251] C. A. J. O'Hare. "Can we overcome the neutrino floor at high masses?" *Phys. Rev. D* 102.6 (2020), p. 063024. DOI: 10.1103/PhysRevD.102.063024. arXiv: 2002.07499 [astro-ph.CO].

[252] E. Aprile et al. "First Dark Matter Search with Nuclear Recoils from the XENONnT Experiment". *Phys. Rev. Lett.* 131.4 (2023), p. 041003. DOI: 10.1103/PhysRevLett.131.041003. arXiv: 2303.14729 [hep-ex].

[253] J. Aalbers et al. "First Dark Matter Search Results from the LUX-ZEPLIN (LZ) Experiment". *Phys. Rev. Lett.* 131.4 (2023), p. 041002. DOI: 10.1103/PhysRevLett.131.041002. arXiv: 2207.03764 [hep-ex].

[254] J. Aalbers et al. "DARWIN: towards the ultimate dark matter detector". *JCAP* 11 (2016), p. 017. DOI: 10.1088/1475-7516/2016/11/017. arXiv: 1606.07001 [astro-ph.IM].

[255] A. H. Abdelhameed et al. "First results from the CRESST-III low-mass dark matter program". *Phys. Rev. D* 100.10 (2019), p. 102002. DOI: 10.1103/PhysRevD.100.102002. arXiv: 1904.00498 [astro-ph.CO].

[256] P. Agnes et al. "Low-Mass Dark Matter Search with the DarkSide-50 Experiment". *Phys. Rev. Lett.* 121.8 (2018), p. 081307. DOI: 10.1103/PhysRevLett.121.081307. arXiv: 1802.06994 [astro-ph.HE].

[257] P. Agnes et al. "DarkSide-50 532-day Dark Matter Search with Low-Radioactivity Argon". *Phys. Rev. D* 98.10 (2018), p. 102006. DOI: 10.1103/PhysRevD.98.102006. arXiv: 1802.07198 [astro-ph.CO].

[258] R. Ajaj et al. "Search for dark matter with a 231-day exposure of liquid argon using DEAP-3600 at SNOLAB". *Phys. Rev. D* 100.2 (2019), p. 022004. DOI: 10.1103/PhysRevD.100.022004. arXiv: 1902.04048 [astro-ph.CO].

[259] L. Hehn et al. "Improved EDELWEISS-III sensitivity for low-mass WIMPs using a profile likelihood approach". *Eur. Phys. J. C* 76.10 (2016), p. 548. DOI: 10.1140/epjc/s10052-016-4388-y. arXiv: 1607.03367 [astro-ph.CO].

[260] D. S. Akerib et al. "Results from a search for dark matter in the complete LUX exposure". *Phys. Rev. Lett.* 118.2 (2017), p. 021303. DOI: 10.1103/PhysRevLett.118.021303. arXiv: 1608.07648 [astro-ph.CO].

[261] X. Cui et al. "Dark Matter Results From 54-Ton-Day Exposure of PandaX-II Experiment". *Phys. Rev. Lett.* 119.18 (2017), p. 181302. DOI: 10.1103/PhysRevLett.119.181302. arXiv: 1708.06917 [astro-ph.CO].

[262] C. Amole et al. "Dark Matter Search Results from the PICO-60 C_3F_8 Bubble Chamber". *Phys. Rev. Lett.* 118.25 (2017), p. 251301. DOI: 10.1103/PhysRevLett.118.251301. arXiv: 1702.07666 [astro-ph.CO].

[263] R. Agnese et al. "Search for Low-Mass Dark Matter with CDMSlite Using a Profile Likelihood Fit". *Phys. Rev. D* 99.6 (2019), p. 062001. DOI: 10.1103/PhysRevD.99.062001. arXiv: 1808.09098 [astro-ph.CO].

[264] R. Agnese et al. "Results from the Super Cryogenic Dark Matter Search Experiment at Soudan". *Phys. Rev. Lett.* 120.6 (2018), p. 061802. DOI: 10.1103/PhysRevLett.120.061802. arXiv: 1708.08869 [hep-ex].

[265] E. Aprile et al. "Dark Matter Search Results from a One Ton-Year Exposure of XENON1T". *Phys. Rev. Lett.* 121.11 (2018), p. 111302. DOI: 10.1103/PhysRevLett.121.111302. arXiv: 1805.12562 [astro-ph.CO].

[266] E. Aprile et al. "Search for Coherent Elastic Scattering of Solar ^{8}B Neutrinos in the XENON1T Dark Matter Experiment". *Phys. Rev. Lett.* 126 (2021), p. 091301. DOI: 10.1103/PhysRevLett.126.091301. arXiv: 2012.02846 [hep-ex].

[267] A. Boveia and C. Doglioni. “Dark Matter Searches at Colliders”. *Ann. Rev. Nucl. Part. Sci.* 68 (2018), pp. 429–459. DOI: 10.1146/annurev-nucl-101917-021008. arXiv: 1810.12238 [hep-ex].

[268] “Search for invisible Higgs boson decays with vector boson fusion signatures with the ATLAS detector using an integrated luminosity of 139 fb^{-1}” (Apr. 2020).

[269] A. M. Sirunyan et al. “Search for invisible decays of a Higgs boson produced through vector boson fusion in proton-proton collisions at $\sqrt{s} = 13$ TeV”. *Phys. Lett. B* 793 (2019), pp. 520–551. DOI: 10.1016/j.physletb.2019.04.025. arXiv: 1809.05937 [hep-ex].

[270] M. Aaboud et al. “Search for dark matter and other new phenomena in events with an energetic jet and large missing transverse momentum using the ATLAS detector”. *JHEP* 01 (2018), p. 126. DOI: 10.1007/JHEP01(2018)126. arXiv: 1711.03301 [hep-ex].

[271] A. M. Sirunyan et al. “Search for new physics in final states with an energetic jet or a hadronically decaying W or Z boson and transverse momentum imbalance at $\sqrt{s} = 13$ TeV”. *Phys. Rev. D* 97.9 (2018), p. 092005. DOI: 10.1103/PhysRevD.97.092005. arXiv: 1712.02345 [hep-ex].

[272] M. Aaboud et al. “Search for dark matter at $\sqrt{s} = 13$ TeV in final states containing an energetic photon and large missing transverse momentum with the ATLAS detector”. *Eur. Phys. J. C* 77.6 (2017), p. 393. DOI: 10.1140/epjc/s10052-017-4965-8. arXiv: 1704.03848 [hep-ex].

[273] “Search for new physics in final states with a single photon plus missing transverse momentum in proton-proton collisions at $\sqrt{s} =$ 13 TeV using 2016 data” (2018).

[274] M. Aaboud et al. “Search for an invisibly decaying Higgs boson or dark matter candidates produced in association with a Z boson in pp collisions at $\sqrt{s} = 13$ TeV with the ATLAS detector”. *Phys. Lett. B* 776 (2018), pp. 318–337. DOI: 10.1016/j.physletb.2017.11.049. arXiv: 1708.09624 [hep-ex].

[275] A. M. Sirunyan et al. “Search for new physics in events with a leptonically decaying Z boson and a large transverse momentum imbalance in proton–proton collisions at $\sqrt{s} = 13$ TeV”. *Eur. Phys. J. C* 78.4 (2018), p. 291. DOI: 10.1140/epjc/s10052-018-5740-1. arXiv: 1711.00431 [hep-ex].

[276] M. Aaboud et al. “Search for dark matter in association with a Higgs boson decaying to two photons at $\sqrt{s} = 13$ TeV with the ATLAS detector”. *Phys. Rev. D* 96.11 (2017), p. 112004. DOI: 10.1103/PhysRevD.96.112004. arXiv: 1706.03948 [hep-ex].

[277] A. M. Sirunyan et al. “Search for dark matter produced in association with a Higgs boson decaying to $\gamma\gamma$ or $\tau^+\tau^-$ at $\sqrt{s} = 13$ TeV”. *JHEP* 09 (2018), p. 046. DOI: 10.1007/JHEP09(2018)046. arXiv: 1806.04771 [hep-ex].

[278] M. Aaboud et al. “Search for squarks and gluinos in events with an isolated lepton, jets, and missing transverse momentum at $\sqrt{s} = 13$ TeV with the ATLAS detector”. *Phys. Rev. D* 96.11 (2017), p. 112010. DOI: 10.1103/PhysRevD.96.112010. arXiv: 1708.08232 [hep-ex].

[279] G. Aad et al. “Search for new phenomena with top quark pairs in final states with one lepton, jets, and missing transverse momentum in pp collisions at $\sqrt{s} = 13$ TeV with the ATLAS detector”. *JHEP* 04 (2021), p. 174. DOI: 10.1007/JHEP04(2021)174. arXiv: 2012.03799 [hep-ex].

[280] G. Aad et al. “Search for new phenomena in events with two opposite-charge leptons, jets and missing transverse momentum in pp collisions at $\sqrt{s} = 13$ TeV with the ATLAS detector”. *JHEP* 04 (2021), p. 165. DOI: 10.1007/JHEP04(2021)165. arXiv: 2102.01444 [hep-ex].

[281] A. M. Sirunyan et al. “Search for supersymmetry in events with at least one photon, missing transverse momentum, and large transverse event activity in proton-proton collisions at $\sqrt{s} = 13$ TeV”. *JHEP* 12 (2017), p. 142. DOI: 10.1007/JHEP12(2017)142. arXiv: 1707.06193 [hep-ex].

[282] A. M. Sirunyan et al. “Search for top squark pair production using dilepton final states in pp collision data collected at $\sqrt{s} = 13$ TeV”. *Eur. Phys. J. C* 81.1 (2021), p. 3. DOI: 10.1140/epjc/s10052-020-08701-5. arXiv: 2008.05936 [hep-ex].

[283] A. M. Sirunyan et al. “Search for top squark production in fully-hadronic final states in proton-proton collisions at $\sqrt{s} = 13$ TeV”. *Phys. Rev. D* 104.5 (2021), p. 052001. DOI: 10.1103/PhysRevD.104.052001. arXiv: 2103.01290 [hep-ex].

[284] M. I. Vysotsky, A. D. Dolgov, and Y. B. Zeldovich. “Cosmological Restriction on Neutral Lepton Masses”. *JETP Lett.* 26 (1977). Ed. by M. A. Srednicki, pp. 188–190.

[285] C. Boehm and P. Fayet. “Scalar dark matter candidates”. *Nucl. Phys. B* 683 (2004), pp. 219–263. DOI: 10.1016/j.nuclphysb.2004.01.015. arXiv: hep-ph/0305261.

[286] M. Pospelov, A. Ritz, and M. B. Voloshin. “Secluded WIMP Dark Matter”. *Phys. Lett. B* 662 (2008), pp. 53–61. DOI: 10.1016/j.physletb.2008.02.052. arXiv: 0711.4866 [hep-ph].

[287] P. Agrawal et al. “Feebly-interacting particles: FIPs 2020 workshop report”. *Eur. Phys. J. C* 81.11 (2021), p. 1015. DOI: 10.1140/epjc/s10052-021-09703-7. arXiv: 2102.12143 [hep-ph].

[288] S. Gori et al. "Dark Sector Physics at High-Intensity Experiments" (Sept. 2022). arXiv: 2209.04671 [hep-ph].

[289] B. Batell et al. "Exploring Dark Sector Portals with High Intensity Experiments". *Snowmass 2021*. July 2022. arXiv: 2207.06905 [hep-ph].

[290] K. S. Babu, C. F. Kolda, and J. March-Russell. "Implications of generalized Z - Z-prime mixing". *Phys. Rev. D* 57 (1998), pp. 6788–6792. DOI: 10.1103/PhysRevD.57.6788. arXiv: hep-ph/9710441.

[291] M. Pospelov. "Secluded U(1) below the weak scale". *Phys. Rev. D* 80 (2009), p. 095002. DOI: 10.1103/PhysRevD.80.095002. arXiv: 0811.1030 [hep-ph].

[292] B. Batell, M. Pospelov, and A. Ritz. "Probing a Secluded U(1) at B-factories". *Phys. Rev. D* 79 (2009), p. 115008. DOI: 10.1103/PhysRevD.79.115008. arXiv: 0903.0363 [hep-ph].

[293] B. Batell, M. Pospelov, and A. Ritz. "Exploring Portals to a Hidden Sector Through Fixed Targets". *Phys. Rev. D* 80 (2009), p. 095024. DOI: 10.1103/PhysRevD.80.095024. arXiv: 0906.5614 [hep-ph].

[294] R. Essig et al. "Constraining Light Dark Matter with Low-Energy e^+e^- Colliders". *JHEP* 11 (2013), p. 167. DOI: 10.1007/JHEP11(2013)167. arXiv: 1309.5084 [hep-ph].

[295] E. Izaguirre et al. "Testing GeV-Scale Dark Matter with Fixed-Target Missing Momentum Experiments". *Phys. Rev. D* 91.9 (2015), p. 094026. DOI: 10.1103/PhysRevD.91.094026. arXiv: 1411.1404 [hep-ph].

[296] M. Fabbrichesi, E. Gabrielli, and G. Lanfranchi. "The Dark Photon" (May 2020). DOI: 10.1007/978-3-030-62519-1. arXiv: 2005.01515 [hep-ph].

[297] M. Graham, C. Hearty, and M. Williams. "Searches for Dark Photons at Accelerators". *Ann. Rev. Nucl. Part. Sci.* 71 (2021), pp. 37–58. DOI: 10.1146/annurev-nucl-110320-051823. arXiv: 2104.10280 [hep-ph].

[298] J. P. Lees et al. "Search for Invisible Decays of a Dark Photon Produced in e^+e^- Collisions at BaBar". *Phys. Rev. Lett.* 119.13 (2017), p. 131804. DOI: 10.1103/PhysRevLett.119.131804. arXiv: 1702.03327 [hep-ex].

[299] D. Banerjee et al. "Dark matter search in missing energy events with NA64". *Phys. Rev. Lett.* 123.12 (2019), p. 121801. DOI: 10.1103/PhysRevLett.123.121801. arXiv: 1906.00176 [hep-ex].

[300] I. Adachi et al. "Search for an Invisible Z′ in a Final State with Two Muons and Missing Energy at Belle II". *Phys. Rev. Lett.* 130.23 (2023), p. 231801. DOI: 10.1103/PhysRevLett.130.231801. arXiv: 2212.03066 [hep-ex].

[301] D. Hanneke, S. Fogwell, and G. Gabrielse. "New Measurement of the Electron Magnetic Moment and the Fine Structure Constant".

Phys. Rev. Lett. 100 (2008), p. 120801. DOI: 10.1103/PhysRevLett.100.120801. arXiv: 0801.1134 [physics.atom-ph].

[302] X. Fan et al. "Measurement of the Electron Magnetic Moment". *Phys. Rev. Lett.* 130.7 (2023), p. 071801. DOI: 10.1103/PhysRevLett.130.071801. arXiv: 2209.13084 [physics.atom-ph].

[303] L. Morel et al. "Determination of the fine-structure constant with an accuracy of 81 parts per trillion". *Nature* 588.7836 (2020), pp. 61–65. DOI: 10.1038/s41586-020-2964-7.

[304] D. Babusci et al. "Limit on the production of a light vector gauge boson in phi meson decays with the KLOE detector". *Phys. Lett. B* 720 (2013), pp. 111–115. DOI: 10.1016/j.physletb.2013.01.067. arXiv: 1210.3927 [hep-ex].

[305] J. P. Lees et al. "Search for a Dark Photon in e^+e^- Collisions at BaBar". *Phys. Rev. Lett.* 113.20 (2014), p. 201801. DOI: 10.1103/PhysRevLett.113.201801. arXiv: 1406.2980 [hep-ex].

[306] R. Aaij et al. "Search for Dark Photons Produced in 13 TeV pp Collisions". *Phys. Rev. Lett.* 120.6 (2018), p. 061801. DOI: 10.1103/PhysRevLett.120.061801. arXiv: 1710.02867 [hep-ex].

[307] G. D. Kribs, D. McKeen, and N. Raj. "Breaking up the Proton: An Affair with Dark Forces". *Phys. Rev. Lett.* 126.1 (2021), p. 011801. DOI: 10.1103/PhysRevLett.126.011801. arXiv: 2007.15655 [hep-ph].

[308] A. W. Thomas, X. G. Wang, and A. G. Williams. "Constraints on the dark photon from deep inelastic scattering". *Phys. Rev. D* 105.3 (2022), p. L031901. DOI: 10.1103/PhysRevD.105.L031901. arXiv: 2111.05664 [hep-ph].

[309] A. W. Thomas, X. Wang, and A. G. Williams. "Sensitivity of Parity-Violating Electron Scattering to a Dark Photon". *Phys. Rev. Lett.* 129.1 (2022), p. 011807. DOI: 10.1103/PhysRevLett.129.011807. arXiv: 2201.06760 [hep-ph].

[310] M. McCullough, J. Moore, and M. Ubiali. "The dark side of the proton". *JHEP* 08 (2022), p. 019. DOI: 10.1007/JHEP08(2022)019. arXiv: 2203.12628 [hep-ph].

[311] D. Curtin et al. "Illuminating Dark Photons with High-Energy Colliders". *JHEP* 02 (2015), p. 157. DOI: 10.1007/JHEP02(2015)157. arXiv: 1412.0018 [hep-ph].

[312] T. Aaltonen et al. "High-precision measurement of the *W* boson mass with the CDF II detector". *Science* 376.6589 (2022), pp. 170–176. DOI: 10.1126/science.abk1781.

[313] E. Cortina Gil et al. "Search for production of an invisible dark photon in π^0 decays". *JHEP* 05 (2019), p. 182. DOI: 10.1007/JHEP05(2019)182. arXiv: 1903.08767 [hep-ex].

[314] A. V. Artamonov et al. “Study of the decay $K^+ \to \pi^+\nu\bar{\nu}$ in the momentum region $140 < P_\pi < 199$ MeV/c”. *Phys. Rev. D* 79 (2009), p. 092004. DOI: 10.1103/PhysRevD.79.092004. arXiv: 0903.0030 [hep-ex].

[315] E. Cortina Gil et al. “Search for a feebly interacting particle X in the decay $K^+ \to \pi^+ X$”. *JHEP* 03 (2021), p. 058. DOI: 10.1007/JHEP03(2021)058. arXiv: 2011.11329 [hep-ex].

[316] E. Cortina Gil et al. “Search for π^0 decays to invisible particles”. *JHEP* 02 (2021), p. 201. DOI: 10.1007/JHEP02(2021)201. arXiv: 2010.07644 [hep-ex].

[317] P. A. M. Dirac. “The Quantum theory of electron. 2.” *Proc. Roy. Soc. Lond. A* 118 (1928), p. 351. DOI: 10.1098/rspa.1928.0056.

[318] D. E. Nagle, R. S. Julian, and J. R. Zacharias. “The Hyperfine Structure of Atomic Hydrogen and Deuterium”. *Phys. Rev.* 72 (1947), pp. 971–971. DOI: 10.1103/PhysRev.72.971.

[319] J. E. Nafe, E. B. Nelson, and I. I. Rabi. “The Hyperfine Structure of Atomic Hydrogen and Deuterium”. *Phys. Rev.* 71 (1947), pp. 914–915. DOI: 10.1103/PhysRev.71.914.

[320] J. S. Schwinger. “On Quantum electrodynamics and the magnetic moment of the electron”. *Phys. Rev.* 73 (1948), pp. 416–417. DOI: 10.1103/PhysRev.73.416.

[321] R. P. Feynman. “Space-time approach to nonrelativistic quantum mechanics”. *Rev. Mod. Phys.* 20 (1948), pp. 367–387. DOI: 10.1103/RevModPhys.20.367.

[322] S. Tomonaga. “On a relativistically invariant formulation of the quantum theory of wave fields”. *Prog. Theor. Phys.* 1 (1946), pp. 27–42. DOI: 10.1143/PTP.1.27.

[323] P. Kusch and H. M. Foley. “The Magnetic Moment of the Electron”. *Phys. Rev.* 74.3 (1948), p. 250. DOI: 10.1103/PhysRev.74.250.

[324] T. Aoyama et al. “The anomalous magnetic moment of the muon in the Standard Model”. *Phys. Rept.* 887 (2020), pp. 1–166. DOI: 10.1016/j.physrep.2020.07.006. arXiv: 2006.04822 [hep-ph].

[325] R. H. Parker et al. “Measurement of the fine-structure constant as a test of the Standard Model”. *Science* 360 (2018), p. 191. DOI: 10.1126/science.aap7706. arXiv: 1812.04130 [physics.atom-ph].

[326] F. Jegerlehner and A. Nyffeler. “The Muon g-2”. *Phys. Rept.* 477 (2009), pp. 1–110. DOI: 10.1016/j.physrep.2009.04.003. arXiv: 0902.3360 [hep-ph].

[327] J. P. Miller et al. “Muon (g-2): Experiment and Theory”. *Ann. Rev. Nucl. Part. Sci.* 62 (2012), pp. 237–264. DOI: 10.1146/annurev-nucl-031312-120340.

[328] G. W. Bennett et al. "Measurement of the positive muon anomalous magnetic moment to 0.7 ppm". *Phys. Rev. Lett.* 89 (2002). [Erratum: Phys.Rev.Lett. 89, 129903 (2002)], p. 101804. DOI: 10.1103/PhysRevLett.89.101804. arXiv: hep-ex/0208001.

[329] G. W. Bennett et al. "Measurement of the negative muon anomalous magnetic moment to 0.7 ppm". *Phys. Rev. Lett.* 92 (2004), p. 161802. DOI: 10.1103/PhysRevLett.92.161802. arXiv: hep-ex/0401008.

[330] G. W. Bennett et al. "Final Report of the Muon E821 Anomalous Magnetic Moment Measurement at BNL". *Phys. Rev. D* 73 (2006), p. 072003. DOI: 10.1103/PhysRevD.73.072003. arXiv: hep-ex/0602035.

[331] J. Grange et al. "Muon (g-2) Technical Design Report" (Jan. 2015). arXiv: 1501.06858 [physics.ins-det].

[332] B. Abi et al. "Measurement of the Positive Muon Anomalous Magnetic Moment to 0.46 ppm". *Phys. Rev. Lett.* 126.14 (2021), p. 141801. DOI: 10.1103/PhysRevLett.126.141801. arXiv: 2104.03281 [hep-ex].

[333] D. P. Aguillard et al. "Measurement of the Positive Muon Anomalous Magnetic Moment to 0.20 ppm". *Phys. Rev. Lett.* 131.16 (2023), p. 161802. DOI: 10.1103/PhysRevLett.131.161802. arXiv: 2308.06230 [hep-ex].

[334] M. Abe et al. "A New Approach for Measuring the Muon Anomalous Magnetic Moment and Electric Dipole Moment". *PTEP* 2019.5 (2019), p. 053C02. DOI: 10.1093/ptep/ptz030. arXiv: 1901.03047 [physics.ins-det].

[335] T. Aoyama et al. "Complete Tenth-Order QED Contribution to the Muon g-2". *Phys. Rev. Lett.* 109 (2012), p. 111808. DOI: 10.1103/PhysRevLett.109.111808. arXiv: 1205.5370 [hep-ph].

[336] T. Aoyama, T. Kinoshita, and M. Nio. "Theory of the Anomalous Magnetic Moment of the Electron". *Atoms* 7.1 (2019), p. 28. DOI: 10.3390/atoms7010028.

[337] A. Czarnecki, W. J. Marciano, and A. Vainshtein. "Refinements in electroweak contributions to the muon anomalous magnetic moment". *Phys. Rev. D* 67 (2003). [Erratum: Phys.Rev.D 73, 119901 (2006)], p. 073006. DOI: 10.1103/PhysRevD.67.073006. arXiv: hep-ph/0212229.

[338] C. Gnendiger, D. Stöckinger, and H. Stöckinger-Kim. "The electroweak contributions to $(g-2)_\mu$ after the Higgs boson mass measurement". *Phys. Rev. D* 88 (2013), p. 053005. DOI: 10.1103/PhysRevD.88.053005. arXiv: 1306.5546 [hep-ph].

[339] A. Kurz et al. "Hadronic contribution to the muon anomalous magnetic moment to next-to-next-to-leading order". *Phys. Lett. B* 734

(2014), pp. 144–147. DOI: 10.1016/j.physletb.2014.05.043. arXiv: 1403.6400 [hep-ph].

[340] A. Keshavarzi, D. Nomura, and T. Teubner. "$g-2$ of charged leptons, $\alpha(M_Z^2)$, and the hyperfine splitting of muonium". *Phys. Rev. D* 101.1 (2020), p. 014029. DOI: 10.1103/PhysRevD.101.014029. arXiv: 1911.00367 [hep-ph].

[341] M. Davier et al. "A new evaluation of the hadronic vacuum polarisation contributions to the muon anomalous magnetic moment and to $\mathbf{ff}(\mathbf{m_Z^2})$". *Eur. Phys. J. C* 80.3 (2020). [Erratum: Eur.Phys.J.C 80, 410 (2020)], p. 241. DOI: 10.1140/epjc/s10052-020-7792-2. arXiv: 1908.00921 [hep-ph].

[342] M. Hoferichter, B.-L. Hoid, and B. Kubis. "Three-pion contribution to hadronic vacuum polarization". *JHEP* 08 (2019), p. 137. DOI: 10.1007/JHEP08(2019)137. arXiv: 1907.01556 [hep-ph].

[343] G. Colangelo, M. Hoferichter, and P. Stoffer. "Two-pion contribution to hadronic vacuum polarization". *JHEP* 02 (2019), p. 006. DOI: 10.1007/JHEP02(2019)006. arXiv: 1810.00007 [hep-ph].

[344] A. Keshavarzi, D. Nomura, and T. Teubner. "Muon $g-2$ and $\alpha(M_Z^2)$: a new data-based analysis". *Phys. Rev. D* 97.11 (2018), p. 114025. DOI: 10.1103/PhysRevD.97.114025. arXiv: 1802.02995 [hep-ph].

[345] K. Melnikov and A. Vainshtein. "Hadronic light-by-light scattering contribution to the muon anomalous magnetic moment revisited". *Phys. Rev. D* 70 (2004), p. 113006. DOI: 10.1103/PhysRevD.70.113006. arXiv: hep-ph/0312226.

[346] P. Masjuan and P. Sanchez-Puertas. "Pseudoscalar-pole contribution to the $(g_\mu-2)$: a rational approach". *Phys. Rev. D* 95.5 (2017), p. 054026. DOI: 10.1103/PhysRevD.95.054026. arXiv: 1701.05829 [hep-ph].

[347] G. Colangelo et al. "Dispersion relation for hadronic light-by-light scattering: two-pion contributions". *JHEP* 04 (2017), p. 161. DOI: 10.1007/JHEP04(2017)161. arXiv: 1702.07347 [hep-ph].

[348] M. Hoferichter et al. "Dispersion relation for hadronic light-by-light scattering: pion pole". *JHEP* 10 (2018), p. 141. DOI: 10.1007/JHEP10(2018)141. arXiv: 1808.04823 [hep-ph].

[349] A. Gérardin, H. B. Meyer, and A. Nyffeler. "Lattice calculation of the pion transition form factor with $N_f = 2+1$ Wilson quarks". *Phys. Rev. D* 100.3 (2019), p. 034520. DOI: 10.1103/PhysRevD.100.034520. arXiv: 1903.09471 [hep-lat].

[350] J. Bijnens, N. Hermansson-Truedsson, and A. Rodríguez-Sánchez. "Short-distance constraints for the HLbL contribution to the muon anomalous magnetic moment". *Phys. Lett. B* 798 (2019), p. 134994. DOI: 10.1016/j.physletb.2019.134994. arXiv: 1908.03331 [hep-ph].

[351] G. Colangelo et al. “Longitudinal short-distance constraints for the hadronic light-by-light contribution to $(g-2)_\mu$ with large-N_c Regge models”. *JHEP* 03 (2020), p. 101. DOI: 10.1007/JHEP03(2020)101. arXiv: 1910.13432 [hep-ph].

[352] V. Pauk and M. Vanderhaeghen. “Single meson contributions to the muon‘s anomalous magnetic moment”. *Eur. Phys. J. C* 74.8 (2014), p. 3008. DOI: 10.1140/epjc/s10052-014-3008-y. arXiv: 1401.0832 [hep-ph].

[353] I. Danilkin and M. Vanderhaeghen. “Light-by-light scattering sum rules in light of new data”. *Phys. Rev. D* 95.1 (2017), p. 014019. DOI: 10.1103/PhysRevD.95.014019. arXiv: 1611.04646 [hep-ph].

[354] F. Jegerlehner. *The Anomalous Magnetic Moment of the Muon*. Vol. 274. Cham: Springer, 2017. DOI: 10.1007/978-3-319-63577-4.

[355] M. Knecht et al. “Scalar meson contributions to a μ from hadronic light-by-light scattering”. *Phys. Lett. B* 787 (2018), pp. 111–123. DOI: 10.1016/j.physletb.2018.10.048. arXiv: 1808.03848 [hep-ph].

[356] G. Eichmann, C. S. Fischer, and R. Williams. “Kaon-box contribution to the anomalous magnetic moment of the muon”. *Phys. Rev. D* 101.5 (2020), p. 054015. DOI: 10.1103/PhysRevD.101.054015. arXiv: 1910.06795 [hep-ph].

[357] P. Roig and P. Sanchez-Puertas. “Axial-vector exchange contribution to the hadronic light-by-light piece of the muon anomalous magnetic moment”. *Phys. Rev. D* 101.7 (2020), p. 074019. DOI: 10.1103/PhysRevD.101.074019. arXiv: 1910.02881 [hep-ph].

[358] T. Blum et al. “Hadronic Light-by-Light Scattering Contribution to the Muon Anomalous Magnetic Moment from Lattice QCD”. *Phys. Rev. Lett.* 124.13 (2020), p. 132002. DOI: 10.1103/PhysRevLett.124.132002. arXiv: 1911.08123 [hep-lat].

[359] G. Colangelo et al. “Remarks on higher-order hadronic corrections to the muon $g-2$”. *Phys. Lett. B* 735 (2014), pp. 90–91. DOI: 10.1016/j.physletb.2014.06.012. arXiv: 1403.7512 [hep-ph].

[360] M. Passera, W. J. Marciano, and A. Sirlin. “The Muon g-2 and the bounds on the Higgs boson mass”. *Phys. Rev. D* 78 (2008), p. 013009. DOI: 10.1103/PhysRevD.78.013009. arXiv: 0804.1142 [hep-ph].

[361] A. Crivellin et al. “Hadronic Vacuum Polarization: $(g-2)_\mu$ versus Global Electroweak Fits”. *Phys. Rev. Lett.* 125.9 (2020), p. 091801. DOI: 10.1103/PhysRevLett.125.091801. arXiv: 2003.04886 [hep-ph].

[362] E. de Rafael. “Constraints between $\Delta\alpha_{\mathrm{had}}(M_Z^2)$ and $(g_\mu-2)_{\mathrm{HVP}}$”. *Phys. Rev. D* 102.5 (2020), p. 056025. DOI: 10.1103/PhysRevD.102.056025. arXiv: 2006.13880 [hep-ph].

[363] A. Keshavarzi et al. "Muon $g-2$ and $\Delta\alpha$ connection". *Phys. Rev. D* 102.3 (2020), p. 033002. DOI: 10.1103/PhysRevD.102.033002. arXiv: 2006.12666 [hep-ph].

[364] G. Colangelo, M. Hoferichter, and P. Stoffer. "Constraints on the two-pion contribution to hadronic vacuum polarization". *Phys. Lett. B* 814 (2021), p. 136073. DOI: 10.1016/j.physletb.2021.136073. arXiv: 2010.07943 [hep-ph].

[365] L. Darmé, G. Grilli di Cortona, and E. Nardi. "The muon $g-2$ anomaly confronts new physics in $e^{\pm}$ and $\mu^{\pm}$ final states scattering". *JHEP* 06 (2022), p. 122. DOI: 10.1007/JHEP06(2022)122. arXiv: 2112.09139 [hep-ph].

[366] L. Di Luzio et al. "New physics behind the new muon g-2 puzzle?" *Phys. Lett. B* 829 (2022), p. 137037. DOI: 10.1016/j.physletb.2022.137037. arXiv: 2112.08312 [hep-ph].

[367] A. Crivellin and M. Hoferichter. "Width effects of broad new resonances in loop observables and application to $(g-2)_{\mu}$". *Phys. Rev. D* 108.1 (2023), p. 013005. DOI: 10.1103/PhysRevD.108.013005. arXiv: 2211.12516 [hep-ph].

[368] L. Darmé, G. Grilli di Cortona, and E. Nardi. "Indirect new physics effects on σhad confront the (g-2)μ window discrepancies and the CMD-3 result". *Phys. Rev. D* 108.9 (2023), p. 095056. DOI: 10.1103/PhysRevD.108.095056. arXiv: 2212.03877 [hep-ph].

[369] S. Borsanyi et al. "Leading hadronic contribution to the muon magnetic moment from lattice QCD". *Nature* 593.7857 (2021), pp. 51–55. DOI: 10.1038/s41586-021-03418-1. arXiv: 2002.12347 [hep-lat].

[370] M. Cè et al. "Window observable for the hadronic vacuum polarization contribution to the muon g-2 from lattice QCD". *Phys. Rev. D* 106.11 (2022), p. 114502. DOI: 10.1103/PhysRevD.106.114502. arXiv: 2206.06582 [hep-lat].

[371] C. Alexandrou et al. "Lattice calculation of the short and intermediate time-distance hadronic vacuum polarization contributions to the muon magnetic moment using twisted-mass fermions". *Phys. Rev. D* 107.7 (2023), p. 074506. DOI: 10.1103/PhysRevD.107.074506. arXiv: 2206.15084 [hep-lat].

[372] T. Blum et al. "Update of Euclidean windows of the hadronic vacuum polarization". *Phys. Rev. D* 108.5 (2023), p. 054507. DOI: 10.1103/PhysRevD.108.054507. arXiv: 2301.08696 [hep-lat].

[373] G. Gagliardi et al. "Time windows of the muon HVP from twisted-mass lattice QCD". *PoS* LATTICE2022 (2023), p. 310. DOI: 10.22323/1.430.0310. arXiv: 2212.09340 [hep-lat].

[374] G. Colangelo et al. "Data-driven evaluations of Euclidean windows to scrutinize hadronic vacuum polarization". *Phys. Lett. B* 833 (2022),

p. 137313. DOI: 10.1016/j.physletb.2022.137313. arXiv: 2205.12963 [hep-ph].

[375] F. V. Ignatov et al. "Measurement of the $e^+e^- \to \pi^+\pi^-$ cross section from threshold to 1.2 GeV with the CMD-3 detector" (Feb. 2023). arXiv: 2302.08834 [hep-ex].

[376] J. P. Lees et al. "Measurement of initial-state–final-state radiation interference in the processes $e^+e^- \to \mu^+\mu^-\gamma$ and $e^+e^- \to \pi^+\pi^-\gamma$". *Phys. Rev. D* 92.7 (2015), p. 072015. DOI: 10.1103/PhysRevD.92.072015. arXiv: 1508.04008 [hep-ex].

[377] A. Abdullahi, M. Hostert, and S. Pascoli. "A dark seesaw solution to low energy anomalies: MiniBooNE, the muon $(g-2)$, and BaBar". *Phys. Lett. B* 820 (2021), p. 136531. DOI: 10.1016/j.physletb.2021.136531. arXiv: 2007.11813 [hep-ph].

[378] P. Ballett, M. Hostert, and S. Pascoli. "Dark Neutrinos and a Three Portal Connection to the Standard Model". *Phys. Rev. D* 101.11 (2020), p. 115025. DOI: 10.1103/PhysRevD.101.115025. arXiv: 1903.07589 [hep-ph].

[379] M. Lindner, A. Merle, and V. Niro. "Enhancing Dark Matter Annihilation into Neutrinos". *Phys. Rev. D* 82 (2010), p. 123529. DOI: 10.1103/PhysRevD.82.123529. arXiv: 1005.3116 [hep-ph].

[380] Y. Farzan. "Flavoring Monochromatic Neutrino Flux from Dark Matter Annihilation". *JHEP* 02 (2012), p. 091. DOI: 10.1007/JHEP02(2012)091. arXiv: 1111.1063 [hep-ph].

[381] C. Arina, S. Kulkarni, and J. Silk. "Monochromatic neutrino lines from sneutrino dark matter". *Phys. Rev. D* 92.8 (2015), p. 083519. DOI: 10.1103/PhysRevD.92.083519. arXiv: 1506.08202 [astro-ph.HE].

[382] C. El Aisati et al. "Prospects for discovering a neutrino line induced by dark matter annihilation". *JCAP* 10 (2017), p. 021. DOI: 10.1088/1475-7516/2017/10/021. arXiv: 1706.06600 [hep-ph].

[383] J. Alwall et al. "MadGraph 5 : Going Beyond". *JHEP* 06 (2011), p. 128. DOI: 10.1007/JHEP06(2011)128. arXiv: 1106.0522 [hep-ph].

[384] J. Alwall et al. "The automated computation of tree-level and next-to-leading order differential cross sections, and their matching to parton shower simulations". *JHEP* 07 (2014), p. 079. DOI: 10.1007/JHEP07(2014)079. arXiv: 1405.0301 [hep-ph].

[385] C. Degrande et al. "UFO - The Universal FeynRules Output". *Comput. Phys. Commun.* 183 (2012), pp. 1201–1214. DOI: 10.1016/j.cpc.2012.01.022. arXiv: 1108.2040 [hep-ph].

[386] L. Darmé et al. "UFO 2.0: the 'Universal Feynman Output' format". *Eur. Phys. J. C* 83.7 (2023), p. 631. DOI: 10.1140/epjc/s10052-023-11780-9. arXiv: 2304.09883 [hep-ph].

[387] C. Degrande. "Automatic evaluation of UV and R2 terms for beyond the Standard Model Lagrangians: a proof-of-principle". *Comput. Phys. Commun.* 197 (2015), pp. 239–262. DOI: 10.1016/j.cpc.2015.08.015. arXiv: 1406.3030 [hep-ph].

[388] F. Ambrogi et al. "MadDM v.3.0: a Comprehensive Tool for Dark Matter Studies". *Phys. Dark Univ.* 24 (2019), p. 100249. DOI: 10.1016/j.dark.2018.11.009. arXiv: 1804.00044 [hep-ph].

[389] C. Arina et al. "Studying dark matter with MadDM 3.1: a short user guide". *PoS* TOOLS2020 (2021), p. 009. DOI: 10.22323/1.392.0009. arXiv: 2012.09016 [hep-ph].

[390] C. Arina. "Review on Dark Matter Tools". *PoS* TOOLS2020 (2021), p. 001. DOI: 10.22323/1.392.0001. arXiv: 2012.09462 [hep-ph].

[391] G. Belanger et al. "MicrOMEGAs 2.0: A Program to calculate the relic density of dark matter in a generic model". *Comput. Phys. Commun.* 176 (2007), pp. 367–382. DOI: 10.1016/j.cpc.2006.11.008. arXiv: hep-ph/0607059.

[392] G. Belanger et al. "micrOMEGAs_3: A program for calculating dark matter observables". *Comput. Phys. Commun.* 185 (2014), pp. 960–985. DOI: 10.1016/j.cpc.2013.10.016. arXiv: 1305.0237 [hep-ph].

[393] D. Barducci et al. "Collider limits on new physics within micrOMEGAs_4.3". *Comput. Phys. Commun.* 222 (2018), pp. 327–338. DOI: 10.1016/j.cpc.2017.08.028. arXiv: 1606.03834 [hep-ph].

[394] G. Bélanger et al. "micrOMEGAs5.0 : Freeze-in". *Comput. Phys. Commun.* 231 (2018), pp. 173–186. DOI: 10.1016/j.cpc.2018.04.027. arXiv: 1801.03509 [hep-ph].

[395] G. Belanger, A. Mjallal, and A. Pukhov. "Recasting direct detection limits within micrOMEGAs and implication for non-standard Dark Matter scenarios". *Eur. Phys. J. C* 81.3 (2021), p. 239. DOI: 10.1140/epjc/s10052-021-09012-z. arXiv: 2003.08621 [hep-ph].

[396] G. Alguero et al. "Co-scattering in micrOMEGAs: A case study for the singlet-triplet dark matter model". *SciPost Phys.* 13 (2022), p. 124. DOI: 10.21468/SciPostPhys.13.6.124. arXiv: 2207.10536 [hep-ph].

[397] T. Bringmann et al. "DarkSUSY 6 : An Advanced Tool to Compute Dark Matter Properties Numerically". *JCAP* 07 (2018), p. 033. DOI: 10.1088/1475-7516/2018/07/033. arXiv: 1802.03399 [hep-ph].

[398] P. Gondolo et al. "DarkSUSY: Computing supersymmetric dark matter properties numerically". *JCAP* 07 (2004), p. 008. DOI: 10.1088/1475-7516/2004/07/008. arXiv: astro-ph/0406204.

[399] L. Bergstrom and P. Ullio. "Full one loop calculation of neutralino annihilation into two photons". *Nucl. Phys. B* 504 (1997), pp. 27–44. DOI: 10.1016/S0550-3213(97)00530-0. arXiv: hep-ph/9706232.

[400] Z. Bern, P. Gondolo, and M. Perelstein. "Neutralino annihilation into two photons". *Phys. Lett. B* 411 (1997), pp. 86–96. DOI: 10.1016/S0370-2693(97)00990-8. arXiv: hep-ph/9706538.

[401] M. Gustafsson et al. "Significant Gamma Lines from Inert Higgs Dark Matter". *Phys. Rev. Lett.* 99 (2007), p. 041301. DOI: 10.1103/PhysRevLett.99.041301. arXiv: astro-ph/0703512.

[402] K.-Y. Choi and O. Seto. "A Dirac right-handed sneutrino dark matter and its signature in the gamma-ray lines". *Phys. Rev. D* 86 (2012). [Erratum: Phys.Rev.D 86, 089904 (2012)], p. 043515. DOI: 10.1103/PhysRevD.86.043515. arXiv: 1205.3276 [hep-ph].

[403] N. Weiner and I. Yavin. "How Dark Are Majorana WIMPs? Signals from MiDM and Rayleigh Dark Matter". *Phys. Rev. D* 86 (2012), p. 075021. DOI: 10.1103/PhysRevD.86.075021. arXiv: 1206.2910 [hep-ph].

[404] S. Tulin, H.-B. Yu, and K. M. Zurek. "Three Exceptions for Thermal Dark Matter with Enhanced Annihilation to $\gamma\gamma$". *Phys. Rev. D* 87.3 (2013), p. 036011. DOI: 10.1103/PhysRevD.87.036011. arXiv: 1208.0009 [hep-ph].

[405] F. Giacchino, L. Lopez-Honorez, and M. H. G. Tytgat. "Bremsstrahlung and Gamma Ray Lines in 3 Scenarios of Dark Matter Annihilation". *JCAP* 08 (2014), p. 046. DOI: 10.1088/1475-7516/2014/08/046. arXiv: 1405.6921 [hep-ph].

[406] A. Ibarra et al. "Sharp Gamma-ray Spectral Features from Scalar Dark Matter Annihilations". *Phys. Rev. D* 90.4 (2014), p. 043526. DOI: 10.1103/PhysRevD.90.043526. arXiv: 1405.6917 [hep-ph].

[407] G. Chalons and A. Semenov. "Loop-induced photon spectral lines from neutralino annihilation in the NMSSM". *JHEP* 12 (2011), p. 055. DOI: 10.1007/JHEP12(2011)055. arXiv: 1110.2064 [hep-ph].

[408] G. Chalons, M. J. Dolan, and C. McCabe. "Neutralino dark matter and the Fermi gamma-ray lines". *JCAP* 02 (2013), p. 016. DOI: 10.1088/1475-7516/2013/02/016. arXiv: 1211.5154 [hep-ph].

[409] D. G. Cerdeno, M. Peiro, and S. Robles. "Enhanced lines and box-shaped features in the gamma-ray spectrum from annihilating dark matter in the NMSSM". *JCAP* 04 (2016), p. 011. DOI: 10.1088/1475-7516/2016/04/011. arXiv: 1507.08974 [hep-ph].

[410] C. B. Jackson et al. "Higgs in Space!" *JCAP* 04 (2010), p. 004. DOI: 10.1088/1475-7516/2010/04/004. arXiv: 0912.0004 [hep-ph].

[411] G. Bertone et al. "The WIMP Forest: Indirect Detection of a Chiral Square". *Phys. Rev. D* 80 (2009), p. 023512. DOI: 10.1103/PhysRevD.80.023512. arXiv: 0904.1442 [astro-ph.HE].

[412] C. Arina et al. "Enhanced Line Signals from Annihilating Kaluza-Klein Dark Matter". *Phys. Rev. D* 90.8 (2014), p. 083506. DOI: 10.1103/PhysRevD.90.083506. arXiv: 1409.0007 [hep-ph].

[413] A. Ibarra, M. Totzauer, and S. Wild. "Higher order dark matter annihilations in the Sun and implications for IceCube". *JCAP* 04 (2014), p. 012. DOI: 10.1088/1475-7516/2014/04/012. arXiv: 1402.4375 [hep-ph].

[414] C. Garcia-Cely and A. Rivera. "General calculation of the cross section for dark matter annihilations into two photons". *JCAP* 03 (2017), p. 054. DOI: 10.1088/1475-7516/2017/03/054. arXiv: 1611.08029 [hep-ph].

[415] J. Goodman et al. "Gamma Ray Line Constraints on Effective Theories of Dark Matter". *Nucl. Phys. B* 844 (2011), pp. 55–68. DOI: 10.1016/j.nuclphysb.2010.10.022. arXiv: 1009.0008 [hep-ph].

[416] K. N. Abazajian et al. "Lower Limits on the Strengths of Gamma Ray Lines from WIMP Dark Matter Annihilation". *Phys. Rev. D* 85 (2012), p. 123543. DOI: 10.1103/PhysRevD.85.123543. arXiv: 1111.2835 [hep-ph].

[417] X. Chu et al. "What if Dark Matter Gamma-Ray Lines come with Gluon Lines?" *Phys. Rev. D* 86 (2012), p. 083521. DOI: 10.1103/PhysRevD.86.083521. arXiv: 1206.2279 [hep-ph].

[418] L. Wang and X.-F. Han. "130 GeV gamma-ray line and enhancement of $h \to \gamma\gamma$ in the Higgs triplet model plus a scalar dark matter". *Phys. Rev. D* 87.1 (2013), p. 015015. DOI: 10.1103/PhysRevD.87.015015. arXiv: 1209.0376 [hep-ph].

[419] Y. Bai and J. Shelton. "Gamma Lines without a Continuum: Thermal Models for the Fermi-LAT 130 GeV Gamma Line". *JHEP* 12 (2012), p. 056. DOI: 10.1007/JHEP12(2012)056. arXiv: 1208.4100 [hep-ph].

[420] A. Rajaraman, T. M. P. Tait, and D. Whiteson. "Two Lines or Not Two Lines? That is the Question of Gamma Ray Spectra". *JCAP* 09 (2012), p. 003. DOI: 10.1088/1475-7516/2012/09/003. arXiv: 1205.4723 [hep-ph].

[421] A. Rajaraman, T. M. P. Tait, and A. M. Wijangco. "Effective Theories of Gamma-ray Lines from Dark Matter Annihilation". *Phys. Dark Univ.* 2 (2013), pp. 17–21. DOI: 10.1016/j.dark.2012.12.001. arXiv: 1211.7061 [hep-ph].

[422] E. Dudas, L. Heurtier, and Y. Mambrini. "Generating X-ray lines from annihilating dark matter". *Phys. Rev. D* 90 (2014), p. 035002. DOI: 10.1103/PhysRevD.90.035002. arXiv: 1404.1927 [hep-ph].

[423] A. Coogan, S. Profumo, and W. Shepherd. "Monochromatic Gamma Rays from Dark Matter Annihilation to Leptons". *JHEP* 08 (2015), p. 074. DOI: 10.1007/JHEP08(2015)074. arXiv: 1504.05187 [hep-ph].

[424] M. Duerr, P. Fileviez Perez, and J. Smirnov. "Gamma Lines from Majorana Dark Matter". *Phys. Rev. D* 93 (2016), p. 023509. DOI: 10.1103/PhysRevD.93.023509. arXiv: 1508.01425 [hep-ph].

[425] S. Fichet. "Shining Light on Polarizable Dark Particles". *JHEP* 04 (2017), p. 088. DOI: 10.1007/JHEP04(2017)088. arXiv: 1609.01762 [hep-ph].

[426] V. Hirschi et al. "Automation of one-loop QCD corrections". *JHEP* 05 (2011), p. 044. DOI: 10.1007/JHEP05(2011)044. arXiv: 1103.0621 [hep-ph].

[427] M. Backović et al. "Higher-order QCD predictions for dark matter production at the LHC in simplified models with s-channel mediators". *Eur. Phys. J. C* 75.10 (2015), p. 482. DOI: 10.1140/epjc/s10052-015-3700-6. arXiv: 1508.05327 [hep-ph].

[428] C. Arina et al. "A comprehensive approach to dark matter studies: exploration of simplified top-philic models". *JHEP* 11 (2016), p. 111. DOI: 10.1007/JHEP11(2016)111. arXiv: 1605.09242 [hep-ph].

[429] G. Das et al. "NLO predictions for the production of a spin-two particle at the LHC". *Phys. Lett. B* 770 (2017), pp. 507–513. DOI: 10.1016/j.physletb.2017.05.007. arXiv: 1605.09359 [hep-ph].

[430] C. Arina et al. "Closing in on t-channel simplified dark matter models". *Phys. Lett. B* 813 (2021), p. 136038. DOI: 10.1016/j.physletb.2020.136038. arXiv: 2010.07559 [hep-ph].

[431] V. Hirschi and O. Mattelaer. "Automated event generation for loop-induced processes". *JHEP* 10 (2015), p. 146. DOI: 10.1007/JHEP10(2015)146. arXiv: 1507.00020 [hep-ph].

[432] O. Mattelaer and E. Vryonidou. "Dark matter production through loop-induced processes at the LHC: the s-channel mediator case". *Eur. Phys. J. C* 75.9 (2015), p. 436. DOI: 10.1140/epjc/s10052-015-3665-5. arXiv: 1508.00564 [hep-ph].

[433] A. Geringer-Sameth, S. M. Koushiappas, and M. Walker. "Dwarf galaxy annihilation and decay emission profiles for dark matter experiments". *Astrophys. J.* 801.2 (2015), p. 74. DOI: 10.1088/0004-637X/801/2/74. arXiv: 1408.0002 [astro-ph.CO].

[434] N. Baro, F. Boudjema, and A. Semenov. "Full one-loop corrections to the relic density in the MSSM: A Few examples". *Phys. Lett. B* 660 (2008), pp. 550–560. DOI: 10.1016/j.physletb.2008.01.031. arXiv: 0710.1821 [hep-ph].

[435] C. Hellmann and P. Ruiz-Femenía. "Non-relativistic pair annihilation of nearly mass degenerate neutralinos and charginos II. P-wave and next-to-next-to-leading order S-wave coefficients". *JHEP* 08 (2013), p. 084. DOI: 10.1007/JHEP08(2013)084. arXiv: 1303.0200 [hep-ph].

[436] J. Harz et al. "Theoretical uncertainty of the supersymmetric dark matter relic density from scheme and scale variations". *Phys. Rev. D* 93.11 (2016), p. 114023. DOI: 10.1103/PhysRevD.93.114023. arXiv: 1602.08103 [hep-ph].

[437] M. Beneke et al. "Relic density of wino-like dark matter in the MSSM". *JHEP* 03 (2016), p. 119. DOI: 10.1007/JHEP03(2016)119. arXiv: 1601.04718 [hep-ph].

[438] L. Hernquist. "An Analytical Model for Spherical Galaxies and Bulges". *Astrophys. J.* 356 (1990), p. 359. DOI: 10.1086/168845.

[439] H. Zhao. "Analytical models for galactic nuclei". *Mon. Not. Roy. Astron. Soc.* 278 (1996), pp. 488–496. DOI: 10.1093/mnras/278.2.488. arXiv: astro-ph/9509122.

[440] V. Lefranc et al. "Dark Matter in γ lines: Galactic Center vs dwarf galaxies". *JCAP* 09 (2016), p. 043. DOI: 10.1088/1475-7516/2016/09/043. arXiv: 1608.00786 [astro-ph.HE].

[441] G. Passarino and M. J. G. Veltman. "One Loop Corrections for e+ e- Annihilation Into mu+ mu- in the Weinberg Model". *Nucl. Phys. B* 160 (1979), pp. 151–207. DOI: 10.1016/0550-3213(79)90234-7.

[442] G. Ossola, C. G. Papadopoulos, and R. Pittau. "Reducing full one-loop amplitudes to scalar integrals at the integrand level". *Nucl. Phys. B* 763 (2007), pp. 147–169. DOI: 10.1016/j.nuclphysb.2006.11.012. arXiv: hep-ph/0609007.

[443] G. 't Hooft and M. J. G. Veltman. "Scalar One Loop Integrals". *Nucl. Phys. B* 153 (1979), pp. 365–401. DOI: 10.1016/0550-3213(79)90605-9.

[444] G. Ossola, C. G. Papadopoulos, and R. Pittau. "On the Rational Terms of the one-loop amplitudes". *JHEP* 05 (2008), p. 004. DOI: 10.1088/1126-6708/2008/05/004. arXiv: 0802.1876 [hep-ph].

[445] C. Degrande, V. Hirschi, and O. Mattelaer. "Automated Computation of One-Loop Amplitudes". *Ann. Rev. Nucl. Part. Sci.* 68 (2018), pp. 291–312. DOI: 10.1146/annurev-nucl-101917-020959.

[446] A. Denner, S. Dittmaier, and L. Hofer. "Collier: a fortran-based Complex One-Loop LIbrary in Extended Regularizations". *Comput. Phys. Commun.* 212 (2017), pp. 220–238. DOI: 10.1016/j.cpc.2016.10.013. arXiv: 1604.06792 [hep-ph].

[447] P. Mastrolia, E. Mirabella, and T. Peraro. "Integrand reduction of one-loop scattering amplitudes through Laurent series expansion". *JHEP* 06 (2012). [Erratum: JHEP 11, 128 (2012)], p. 095. DOI: 10.1007/JHEP11(2012)128. arXiv: 1203.0291 [hep-ph].

[448] T. Peraro. "Ninja: Automated Integrand Reduction via Laurent Expansion for One-Loop Amplitudes". *Comput. Phys. Commun.* 185

(2014), pp. 2771–2797. DOI: 10.1016/j.cpc.2014.06.017. arXiv: 1403.1229 [hep-ph].

[449] V. Hirschi and T. Peraro. "Tensor integrand reduction via Laurent expansion". *JHEP* 06 (2016), p. 060. DOI: 10.1007/JHEP06(2016)060. arXiv: 1604.01363 [hep-ph].

[450] G. Ossola, C. G. Papadopoulos, and R. Pittau. "CutTools: A Program implementing the OPP reduction method to compute one-loop amplitudes". *JHEP* 03 (2008), p. 042. DOI: 10.1088/1126-6708/2008/03/042. arXiv: 0711.3596 [hep-ph].

[451] A. van Hameren. "OneLOop: For the evaluation of one-loop scalar functions". *Comput. Phys. Commun.* 182 (2011), pp. 2427–2438. DOI: 10.1016/j.cpc.2011.06.011. arXiv: 1007.4716 [hep-ph].

[452] S. Carrazza, R. K. Ellis, and G. Zanderighi. "QCDLoop: a comprehensive framework for one-loop scalar integrals". *Comput. Phys. Commun.* 209 (2016), pp. 134–143. DOI: 10.1016/j.cpc.2016.07.033. arXiv: 1605.03181 [hep-ph].

[453] A. Alloul et al. "FeynRules 2.0 - A complete toolbox for tree-level phenomenology". *Comput. Phys. Commun.* 185 (2014), pp. 2250–2300. DOI: 10.1016/j.cpc.2014.04.012. arXiv: 1310.1921 [hep-ph].

[454] T. Hahn. "Generating Feynman diagrams and amplitudes with FeynArts 3". *Comput. Phys. Commun.* 140 (2001), pp. 418–431. DOI: 10.1016/S0010-4655(01)00290-9. arXiv: hep-ph/0012260.

[455] M. Garny et al. "Top-philic dark matter within and beyond the WIMP paradigm". *Phys. Rev. D* 97.7 (2018), p. 075002. DOI: 10.1103/PhysRevD.97.075002. arXiv: 1802.00814 [hep-ph].

[456] S. Colucci et al. "Top-philic Vector-Like Portal to Scalar Dark Matter". *Phys. Rev. D* 98 (2018), p. 035002. DOI: 10.1103/PhysRevD.98.035002. arXiv: 1804.05068 [hep-ph].

[457] T. Sjöstrand et al. "An introduction to PYTHIA 8.2". *Comput. Phys. Commun.* 191 (2015), pp. 159–177. DOI: 10.1016/j.cpc.2015.01.024. arXiv: 1410.3012 [hep-ph].

[458] M. Cirelli et al. "PPPC 4 DM ID: A Poor Particle Physicist Cookbook for Dark Matter Indirect Detection". *JCAP* 03 (2011). [Erratum: JCAP 10, E01 (2012)], p. 051. DOI: 10.1088/1475-7516/2012/10/E01. arXiv: 1012.4515 [hep-ph].

[459] L. Bergstrom. "Radiative Processes in Dark Matter Photino Annihilation". *Phys. Lett. B* 225 (1989), pp. 372–380. DOI: 10.1016/0370-2693(89)90585-6.

[460] S. Rudaz. "On the Annihilation of Heavy Neutral Fermion Pairs Into Monochromatic gamma-rays and Its Astrophysical Implications". *Phys. Rev. D* 39 (1989), p. 3549. DOI: 10.1103/PhysRevD.39.3549.

[461] M. Garny et al. "Internal bremsstrahlung signatures in light of direct dark matter searches". *JCAP* 12 (2013), p. 046. DOI: 10.1088/1475-7516/2013/12/046. arXiv: 1306.6342 [hep-ph].

[462] M. Actis et al. "Design concepts for the Cherenkov Telescope Array CTA: An advanced facility for ground-based high-energy gamma-ray astronomy". *Exper. Astron.* 32 (2011), pp. 193–316. DOI: 10.1007/s10686-011-9247-0. arXiv: 1008.3703 [astro-ph.IM].

[463] A. Hryczuk et al. "Testing dark matter with Cherenkov light - prospects of H.E.S.S. and CTA for exploring minimal supersymmetry". *JHEP* 10 (2019), p. 043. DOI: 10.1007/JHEP10(2019)043. arXiv: 1905.00315 [hep-ph].

[464] A. M. Sirunyan et al. "Search for direct production of supersymmetric partners of the top quark in the all-jets final state in proton-proton collisions at $\sqrt{s} = 13$ TeV". *JHEP* 10 (2017), p. 005. DOI: 10.1007/JHEP10(2017)005. arXiv: 1707.03316 [hep-ex].

[465] A. M. Sirunyan et al. "Search for new phenomena with the M_{T2} variable in the all-hadronic final state produced in proton–proton collisions at $\sqrt{s} = 13$ TeV". *Eur. Phys. J. C* 77.10 (2017), p. 710. DOI: 10.1140/epjc/s10052-017-5267-x. arXiv: 1705.04650 [hep-ex].

[466] A. M. Sirunyan et al. "Search for top squark pair production in pp collisions at $\sqrt{s} = 13$ TeV using single lepton events". *JHEP* 10 (2017), p. 019. DOI: 10.1007/JHEP10(2017)019. arXiv: 1706.04402 [hep-ex].

[467] M. Aaboud et al. "Search for a scalar partner of the top quark in the jets plus missing transverse momentum final state at $\sqrt{s}$=13 TeV with the ATLAS detector". *JHEP* 12 (2017), p. 085. DOI: 10.1007/JHEP12(2017)085. arXiv: 1709.04183 [hep-ex].

[468] M. Aaboud et al. "Search for top-squark pair production in final states with one lepton, jets, and missing transverse momentum using 36 fb^{-1} of $\sqrt{s} = 13$ TeV pp collision data with the ATLAS detector". *JHEP* 06 (2018), p. 108. DOI: 10.1007/JHEP06(2018)108. arXiv: 1711.11520 [hep-ex].

[469] M. Aaboud et al. "Search for direct top squark pair production in final states with two leptons in $\sqrt{s} = 13$ TeV pp collisions with the ATLAS detector". *Eur. Phys. J. C* 77.12 (2017), p. 898. DOI: 10.1140/epjc/s10052-017-5445-x. arXiv: 1708.03247 [hep-ex].

[470] R. Barbieri, L. J. Hall, and V. S. Rychkov. "Improved naturalness with a heavy Higgs: An Alternative road to LHC physics". *Phys. Rev. D* 74 (2006), p. 015007. DOI: 10.1103/PhysRevD.74.015007. arXiv: hep-ph/0603188.

[471] L. Lopez Honorez et al. "The Inert Doublet Model: An Archetype for Dark Matter". *JCAP* 02 (2007), p. 028. DOI: 10.1088/1475-7516/2007/02/028. arXiv: hep-ph/0612275.

[472] L. Lopez Honorez and C. E. Yaguna. "The inert doublet model of dark matter revisited". *JHEP* 09 (2010), p. 046. DOI: 10.1007/JHEP09(2010)046. arXiv: 1003.3125 [hep-ph].

[473] A. Pierce and J. Thaler. "Natural Dark Matter from an Unnatural Higgs Boson and New Colored Particles at the TeV Scale". *JHEP* 08 (2007), p. 026. DOI: 10.1088/1126-6708/2007/08/026. arXiv: hep-ph/0703056.

[474] E. Lundstrom, M. Gustafsson, and J. Edsjo. "The Inert Doublet Model and LEP II Limits". *Phys. Rev. D* 79 (2009), p. 035013. DOI: 10.1103/PhysRevD.79.035013. arXiv: 0810.3924 [hep-ph].

[475] M. Baak et al. "The global electroweak fit at NNLO and prospects for the LHC and ILC". *Eur. Phys. J. C* 74 (2014), p. 3046. DOI: 10.1140/epjc/s10052-014-3046-5. arXiv: 1407.3792 [hep-ph].

[476] D. Eriksson, J. Rathsman, and O. Stal. "2HDMC: Two-Higgs-Doublet Model Calculator Physics and Manual". *Comput. Phys. Commun.* 181 (2010), pp. 189–205. DOI: 10.1016/j.cpc.2009.09.011. arXiv: 0902.0851 [hep-ph].

[477] A. Goudelis, B. Herrmann, and O. Stål. "Dark matter in the Inert Doublet Model after the discovery of a Higgs-like boson at the LHC". *JHEP* 09 (2013), p. 106. DOI: 10.1007/JHEP09(2013)106. arXiv: 1303.3010 [hep-ph].

[478] A. Ilnicka, M. Krawczyk, and T. Robens. "Inert Doublet Model in light of LHC Run I and astrophysical data". *Phys. Rev. D* 93.5 (2016), p. 055026. DOI: 10.1103/PhysRevD.93.055026. arXiv: 1508.01671 [hep-ph].

[479] A. Belyaev et al. "Anatomy of the Inert Two Higgs Doublet Model in the light of the LHC and non-LHC Dark Matter Searches". *Phys. Rev. D* 97.3 (2018), p. 035011. DOI: 10.1103/PhysRevD.97.035011. arXiv: 1612.00511 [hep-ph].

[480] B. Eiteneuer, A. Goudelis, and J. Heisig. "The inert doublet model in the light of Fermi-LAT gamma-ray data: a global fit analysis". *Eur. Phys. J. C* 77.9 (2017), p. 624. DOI: 10.1140/epjc/s10052-017-5166-1. arXiv: 1705.01458 [hep-ph].

[481] M. Klasen, C. E. Yaguna, and J. D. Ruiz-Alvarez. "Electroweak corrections to the direct detection cross section of inert higgs dark matter". *Phys. Rev. D* 87 (2013), p. 075025. DOI: 10.1103/PhysRevD.87.075025. arXiv: 1302.1657 [hep-ph].

[482] D. Dercks and T. Robens. "Constraining the Inert Doublet Model using Vector Boson Fusion". *Eur. Phys. J. C* 79.11 (2019), p. 924. DOI: 10.1140/epjc/s10052-019-7436-6. arXiv: 1812.07913 [hep-ph].

[483] P. A. R. Ade et al. "Planck 2015 results. XIII. Cosmological parameters". *Astron. Astrophys.* 594 (2016), A13. DOI: 10.1051/0004-6361/201525830. arXiv: 1502.01589 [astro-ph.CO].

[484] F. Feroz, M. P. Hobson, and M. Bridges. "MultiNest: an efficient and robust Bayesian inference tool for cosmology and particle physics". *Mon. Not. Roy. Astron. Soc.* 398 (2009), pp. 1601–1614. DOI: 10.1111/j.1365-2966.2009.14548.x. arXiv: 0809.3437 [astro-ph].

[485] F. Feroz et al. "Importance Nested Sampling and the MultiNest Algorithm". *Open J. Astrophys.* 2.1 (2019), p. 10. DOI: 10.21105/astro.1306.2144. arXiv: 1306.2144 [astro-ph.IM].

[486] A. E. Egorov et al. "Dark matter searches by the planned gamma-ray telescope GAMMA-400". *JCAP* 11 (2020), p. 049. DOI: 10.1088/1475-7516/2020/11/049. arXiv: 2005.09032 [astro-ph.HE].

[487] D. Hooper and T. Linden. "On The Gamma-Ray Emission From Reticulum II and Other Dwarf Galaxies". *JCAP* 09 (2015), p. 016. DOI: 10.1088/1475-7516/2015/09/016. arXiv: 1503.06209 [astro-ph.HE].

[488] O. Buchmueller, C. Doglioni, and L. T. Wang. "Search for dark matter at colliders". *Nature Phys.* 13.3 (2017), pp. 217–223. DOI: 10.1038/nphys4054. arXiv: 1912.12739 [hep-ex].

[489] V. Silveira and A. Zee. "SCALAR PHANTOMS". *Phys. Lett. B* 161 (1985), pp. 136–140. DOI: 10.1016/0370-2693(85)90624-0.

[490] J. McDonald. "Gauge singlet scalars as cold dark matter". *Phys. Rev. D* 50 (1994), pp. 3637–3649. DOI: 10.1103/PhysRevD.50.3637. arXiv: hep-ph/0702143.

[491] C. P. Burgess, M. Pospelov, and T. ter Veldhuis. "The Minimal model of nonbaryonic dark matter: A Singlet scalar". *Nucl. Phys. B* 619 (2001), pp. 709–728. DOI: 10.1016/S0550-3213(01)00513-2. arXiv: hep-ph/0011335.

[492] H. Davoudiasl et al. "The New minimal standard model". *Phys. Lett. B* 609 (2005), pp. 117–123. DOI: 10.1016/j.physletb.2005.01.026. arXiv: hep-ph/0405097.

[493] S. W. Ham, Y. S. Jeong, and S. K. Oh. "Electroweak phase transition in an extension of the standard model with a real Higgs singlet". *J. Phys. G* 31.8 (2005), pp. 857–871. DOI: 10.1088/0954-3899/31/8/017. arXiv: hep-ph/0411352.

[494] D. O'Connell, M. J. Ramsey-Musolf, and M. B. Wise. "Minimal Extension of the Standard Model Scalar Sector". *Phys. Rev. D* 75 (2007), p. 037701. DOI: 10.1103/PhysRevD.75.037701. arXiv: hep-ph/0611014.

[495] S. Profumo, M. J. Ramsey-Musolf, and G. Shaughnessy. "Singlet Higgs phenomenology and the electroweak phase transition". *JHEP* 08 (2007), p. 010. DOI: 10.1088/1126-6708/2007/08/010. arXiv: 0705.2425 [hep-ph].

[496] V. Barger et al. "LHC Phenomenology of an Extended Standard Model with a Real Scalar Singlet". *Phys. Rev. D* 77 (2008), p. 035005. DOI: 10.1103/PhysRevD.77.035005. arXiv: 0706.4311 [hep-ph].

[497] R. N. Lerner and J. McDonald. "Gauge singlet scalar as inflaton and thermal relic dark matter". *Phys. Rev. D* 80 (2009), p. 123507. DOI: 10.1103/PhysRevD.80.123507. arXiv: 0909.0520 [hep-ph].

[498] P. Athron et al. "Status of the scalar singlet dark matter model". *Eur. Phys. J. C* 77.8 (2017), p. 568. DOI: 10.1140/epjc/s10052-017-5113-1. arXiv: 1705.07931 [hep-ph].

[499] P. Athron et al. "Impact of vacuum stability, perturbativity and XENON1T on global fits of $\mathbb{Z}_2$ and $\mathbb{Z}_3$ scalar singlet dark matter". *Eur. Phys. J. C* 78.10 (2018), p. 830. DOI: 10.1140/epjc/s10052-018-6314-y. arXiv: 1806.11281 [hep-ph].

[500] T. Binder et al. "Dark matter relic abundance beyond kinetic equilibrium". *Eur. Phys. J. C* 81 (2021), p. 577. DOI: 10.1140/epjc/s10052-021-09357-5. arXiv: 2103.01944 [hep-ph].

[501] *SingletScalar-DM*. URL: https://dimauromattia.github.io/SingletScalar_DM/ (visited on Jan. 31, 2024).

[502] J. M. Cline et al. "Update on scalar singlet dark matter". *Phys. Rev. D* 88 (2013). [Erratum: Phys.Rev.D 92, 039906 (2015)], p. 055025. DOI: 10.1103/PhysRevD.88.055025. arXiv: 1306.4710 [hep-ph].

[503] S. Dittmaier et al. "Handbook of LHC Higgs Cross Sections: 1. Inclusive Observables" (Jan. 2011). DOI: 10.5170/CERN-2011-002. arXiv: 1101.0593 [hep-ph].

[504] G. Aad et al. "Measurement of the Higgs boson mass in the $H \to ZZ^* \to 4\ell$ decay channel using 139 fb^{-1} of $\sqrt{s} = 13$ TeV pp collisions recorded by the ATLAS detector at the LHC". *Phys. Lett. B* 843 (2023), p. 137880. DOI: 10.1016/j.physletb.2023.137880. arXiv: 2207.00320 [hep-ex].

[505] J. Heisig et al. "Probing Higgs-portal dark matter with vector-boson fusion". *JHEP* 03 (2020), p. 183. DOI: 10.1007/JHEP03(2020)183. arXiv: 1912.08472 [hep-ph].

[506] M. Duerr, P. Fileviez Pérez, and J. Smirnov. "Scalar Dark Matter: Direct vs. Indirect Detection". *JHEP* 06 (2016), p. 152. DOI: 10.1007/JHEP06(2016)152. arXiv: 1509.04282 [hep-ph].

[507] M. Backovic, K. Kong, and M. McCaskey. "MadDM v.1.0: Computation of Dark Matter Relic Abundance Using MadGraph5". *Physics of*

the Dark Universe 5-6 (2014), pp. 18–28. DOI: 10.1016/j.dark.2014.04.001. arXiv: 1308.4955 [hep-ph].

[508] M. Backović et al. "Direct Detection of Dark Matter with MadDM v.2.0". *Phys. Dark Univ.* 9-10 (May 2015), pp. 37–50. DOI: 10.1016/j.dark.2015.09.001. arXiv: 1505.04190 [hep-ph].

[509] C. Bierlich et al. "A comprehensive guide to the physics and usage of PYTHIA 8.3". *SciPost Phys. Codeb.* 2022 (2022), p. 8. DOI: 10.21468/SciPostPhysCodeb.8. arXiv: 2203.11601 [hep-ph].

[510] A. Gizhko et al. "Running of the Charm-Quark Mass from HERA Deep-Inelastic Scattering Data". *Phys. Lett. B* 775 (2017), pp. 233–238. DOI: 10.1016/j.physletb.2017.11.002. arXiv: 1705.08863 [hep-ph].

[511] M. Laine. "Resonant s-channel dark matter annihilation at NLO". *JHEP* 01 (2023), p. 157. DOI: 10.1007/JHEP01(2023)157. arXiv: 2211.06008 [hep-ph].

[512] J. McDonald. "Thermally generated gauge singlet scalars as self-interacting dark matter". *Phys. Rev. Lett.* 88 (2002), p. 091304. DOI: 10.1103/PhysRevLett.88.091304. arXiv: hep-ph/0106249.

[513] T. Asaka, K. Ishiwata, and T. Moroi. "Right-handed sneutrino as cold dark matter". *Phys. Rev. D* 73 (2006), p. 051301. DOI: 10.1103/PhysRevD.73.051301. arXiv: hep-ph/0512118.

[514] L. J. Hall et al. "Freeze-In Production of FIMP Dark Matter". *JHEP* 03 (2010), p. 080. DOI: 10.1007/JHEP03(2010)080. arXiv: 0911.1120 [hep-ph].

[515] LHC Higgs Cross Section Working Group. "BSM Higgs production cross sections at $\sqrt{s} = 13$ TeV (update in CERN Report4 2016)" (2016). URL: %7Bhttps://twiki.cern.ch/twiki/bin/view/LHCPhysics/CERNYellowReportPageBSMAt13TeV%7D.

[516] Y. Wu et al. "Uncertainties in Direct Dark Matter Detection in Light of Gaia's Escape Velocity Measurements". *JCAP* 10 (2019), p. 034. DOI: 10.1088/1475-7516/2019/10/034. arXiv: 1904.04781 [hep-ph].

[517] P. Salucci et al. "The dark matter density at the Sun's location". *Astron. Astrophys.* 523 (2010), A83. DOI: 10.1051/0004-6361/201014385. arXiv: 1003.3101 [astro-ph.GA].

[518] F. Nesti and P. Salucci. "The Dark Matter halo of the Milky Way, AD 2013". *JCAP* 07 (2013), p. 016. DOI: 10.1088/1475-7516/2013/07/016. arXiv: 1304.5127 [astro-ph.GA].

[519] M. Benito, A. Cuoco, and F. Iocco. "Handling the Uncertainties in the Galactic Dark Matter Distribution for Particle Dark Matter Searches". *JCAP* 03 (2019), p. 033. DOI: 10.1088/1475-7516/2019/03/033. arXiv: 1901.02460 [astro-ph.GA].

[520] R. Guo et al. "Measuring the local dark matter density with LAMOST DR5 and Gaia DR2". *Mon. Not. Roy. Astron. Soc.* 495.4 (May 2020), pp. 4828–4844. DOI: 10.1093/mnras/staa1483. arXiv: 2005.12018 [astro-ph.GA]. URL: https://doi.org/10.1093/mnras/staa1483.

[521] R. Abbasi et al. "Improved Characterization of the Astrophysical Muon–neutrino Flux with 9.5 Years of IceCube Data". *Astrophys. J.* 928.1 (2022), p. 50. DOI: 10.3847/1538-4357/ac4d29. arXiv: 2111.10299 [astro-ph.HE].

[522] M. Korsmeier, F. Donato, and N. Fornengo. "Prospects to verify a possible dark matter hint in cosmic antiprotons with antideuterons and antihelium". *Phys. Rev. D* 97.10 (2018), p. 103011. DOI: 10.1103/PhysRevD.97.103011. arXiv: 1711.08465 [astro-ph.HE].

[523] T. A. Porter et al. "Inverse Compton Origin of the Hard X-Ray and Soft Gamma-Ray Emission from the Galactic Ridge". *Astrophys. J.* 682 (2008), pp. 400–407. DOI: 10.1086/589615. arXiv: 0804.1774 [astro-ph].

[524] F. Kahlhoefer et al. "Constraining dark matter annihilation with cosmic ray antiprotons using neural networks". *JCAP* 12.12 (2021), p. 037. DOI: 10.1088/1475-7516/2021/12/037. arXiv: 2107.12395 [astro-ph.HE].

[525] M. Aguilar et al. "The Alpha Magnetic Spectrometer (AMS) on the international space station: Part II — Results from the first seven years". *Phys. Rept.* 894 (2021), pp. 1–116. DOI: 10.1016/j.physrep.2020.09.003.

[526] E. C. Stone et al. "Voyager 1 Observes Low-Energy Galactic Cosmic Rays in a Region Depleted of Heliospheric Ions". *Science* 341.6142 (2013), p. 1236408. DOI: 10.1126/science.1236408.

[527] S. Balan et al. "Fast and accurate AMS-02 antiproton likelihoods for global dark matter fits". *JCAP* 08 (2023), p. 052. DOI: 10.1088/1475-7516/2023/08/052. arXiv: 2303.07362 [hep-ph].

[528] R. Bartels et al. "The Fermi-LAT GeV excess as a tracer of stellar mass in the Galactic bulge". *Nature Astron.* 2.10 (2018), pp. 819–828. DOI: 10.1038/s41550-018-0531-z. arXiv: 1711.04778 [astro-ph.HE].

[529] O. Macias et al. "Galactic bulge preferred over dark matter for the Galactic centre gamma-ray excess". *Nature Astron.* 2.5 (2018), pp. 387–392. DOI: 10.1038/s41550-018-0414-3. arXiv: 1611.06644 [astro-ph.HE].

[530] K. N. Abazajian et al. "Strong constraints on thermal relic dark matter from Fermi-LAT observations of the Galactic Center". *Phys. Rev. D* 102.4 (2020), p. 043012. DOI: 10.1103/PhysRevD.102.043012. arXiv: 2003.10416 [hep-ph].

[531] A. Esmaili and P. D. Serpico. "Gamma-ray bounds from EAS detectors and heavy decaying dark matter constraints". *JCAP* 10 (2015), p. 014. DOI: 10.1088/1475-7516/2015/10/014. arXiv: 1505.06486 [hep-ph].

[532] C. A. Argüelles et al. "Dark matter decay to neutrinos". *Phys. Rev. D* 108.12 (2023), p. 123021. DOI: 10.1103/PhysRevD.108.123021. arXiv: 2210.01303 [hep-ph].

[533] K. Murase and J. F. Beacom. "Constraining Very Heavy Dark Matter Using Diffuse Backgrounds of Neutrinos and Cascaded Gamma Rays". *JCAP* 10 (2012), p. 043. DOI: 10.1088/1475-7516/2012/10/043. arXiv: 1206.2595 [hep-ph].

[534] A. Esmaili, A. Ibarra, and O. L. G. Peres. "Probing the stability of superheavy dark matter particles with high-energy neutrinos". *JCAP* 11 (2012), p. 034. DOI: 10.1088/1475-7516/2012/11/034. arXiv: 1205.5281 [hep-ph].

[535] T. Cohen et al. "γ -ray Constraints on Decaying Dark Matter and Implications for IceCube". *Phys. Rev. Lett.* 119.2 (2017), p. 021102. DOI: 10.1103/PhysRevLett.119.021102. arXiv: 1612.05638 [hep-ph].

[536] O. K. Kalashev and M. Y. Kuznetsov. "Constraining heavy decaying dark matter with the high energy gamma-ray limits". *Phys. Rev. D* 94.6 (2016), p. 063535. DOI: 10.1103/PhysRevD.94.063535. arXiv: 1606.07354 [astro-ph.HE].

[537] A. U. Abeysekara et al. "A Search for Dark Matter in the Galactic Halo with HAWC". *JCAP* 02 (2018), p. 049. DOI: 10.1088/1475-7516/2018/02/049. arXiv: 1710.10288 [astro-ph.HE].

[538] M. Kachelriess, O. E. Kalashev, and M. Y. Kuznetsov. "Heavy decaying dark matter and IceCube high energy neutrinos". *Phys. Rev. D* 98.8 (2018), p. 083016. DOI: 10.1103/PhysRevD.98.083016. arXiv: 1805.04500 [astro-ph.HE].

[539] K. Ishiwata et al. "Probing heavy dark matter decays with multi-messenger astrophysical data". *JCAP* 01 (2020), p. 003. DOI: 10.1088/1475-7516/2020/01/003. arXiv: 1907.11671 [astro-ph.HE].

[540] O. Kalashev, M. Kuznetsov, and Y. Zhezher. "Constraining superheavy decaying dark matter with directional ultra-high energy gamma-ray limits". *JCAP* 11 (2021), p. 016. DOI: 10.1088/1475-7516/2021/11/016. arXiv: 2005.04085 [astro-ph.HE].

[541] C. Guépin et al. "Indirect dark matter searches at ultrahigh energy neutrino detectors". *Phys. Rev. D* 104.8 (2021), p. 083002. DOI: 10.1103/PhysRevD.104.083002. arXiv: 2106.04446 [hep-ph].

[542] Z. Cao et al. "Constraints on Heavy Decaying Dark Matter from 570 Days of LHAASO Observations". *Phys. Rev. Lett.* 129.26 (2022),

p. 261103. DOI: 10.1103/PhysRevLett.129.261103. arXiv: 2210.15989 [astro-ph.HE].

[543] R. Abbasi et al. “Search for neutrino lines from dark matter annihilation and decay with IceCube”. *Phys. Rev. D* 108.10 (2023), p. 102004. DOI: 10.1103/PhysRevD.108.102004. arXiv: 2303.13663 [astro-ph.HE].

[544] D. F. G. Fiorillo et al. “Searches for dark matter decay with ultrahigh-energy neutrinos endure backgrounds”. *Phys. Rev. D* 108.10 (2023), p. 103012. DOI: 10.1103/PhysRevD.108.103012. arXiv: 2307.02538 [astro-ph.HE].

[545] V. Berezinsky, M. Kachelriess, and A. Vilenkin. “Ultrahigh-energy cosmic rays without GZK cutoff”. *Phys. Rev. Lett.* 79 (1997), pp. 4302–4305. DOI: 10.1103/PhysRevLett.79.4302. arXiv: astro-ph/9708217.

[546] V. A. Kuzmin and V. A. Rubakov. “Ultrahigh-energy cosmic rays: A Window to postinflationary reheating epoch of the universe?” *Phys. Atom. Nucl.* 61 (1998), p. 1028. arXiv: astro-ph/9709187.

[547] V. Berezinsky, M. Kachelriess, and M. A. Solberg. “Supersymmetric superheavy dark matter”. *Phys. Rev. D* 78 (2008), p. 123535. DOI: 10.1103/PhysRevD.78.123535. arXiv: 0810.3012 [hep-ph].

[548] K. Griest and M. Kamionkowski. “Unitarity Limits on the Mass and Radius of Dark Matter Particles”. *Phys. Rev. Lett.* 64 (1990), p. 615. DOI: 10.1103/PhysRevLett.64.615.

[549] R. Allahverdi et al. “Superheavy dark matter from string theory”. *JHEP* 02 (2021), p. 026. DOI: 10.1007/JHEP02(2021)026. arXiv: 2010.03573 [hep-ph].

[550] F. Denef and M. R. Douglas. “Distributions of nonsupersymmetric flux vacua”. *JHEP* 03 (2005), p. 061. DOI: 10.1088/1126-6708/2005/03/061. arXiv: hep-th/0411183.

[551] I. Broeckel et al. “Moduli Stabilisation and the Statistics of SUSY Breaking in the Landscape”. *JHEP* 10 (2020), p. 015. DOI: 10.1007/JHEP09(2021)019. arXiv: 2007.04327 [hep-th].

[552] M. Cicoli et al. “Joint statistics of cosmological constant and SUSY breaking in flux vacua with nilpotent Goldstino”. *JHEP* 01 (2023), p. 013. DOI: 10.1007/JHEP01(2023)013. arXiv: 2211.07695 [hep-th].

[553] R. Kallosh and A. D. Linde. “Landscape, the scale of SUSY breaking, and inflation”. *JHEP* 12 (2004), p. 004. DOI: 10.1088/1126-6708/2004/12/004. arXiv: hep-th/0411011.

[554] M. Cicoli et al. “String cosmology: From the early universe to today”. *Phys. Rept.* 1059 (2024), pp. 1–155. DOI: 10.1016/j.physrep.2024.01.002. arXiv: 2303.04819 [hep-th].

[555] B. S. Acharya et al. “Non-thermal Dark Matter and the Moduli Problem in String Frameworks”. *JHEP* 06 (2008), p. 064. DOI: 10.1088/1126-6708/2008/06/064. arXiv: 0804.0863 [hep-ph].

[556] R. Allahverdi et al. “Nonthermal dark matter in string compactifications”. *Phys. Rev. D* 88.9 (2013), p. 095015. DOI: 10.1103/PhysRevD.88.095015. arXiv: 1307.5086 [hep-ph].

[557] R. Allahverdi et al. “Correlation between Dark Matter and Dark Radiation in String Compactifications”. *JCAP* 10 (2014), p. 002. DOI: 10.1088/1475-7516/2014/10/002. arXiv: 1401.4364 [hep-ph].

[558] L. Aparicio et al. “Non-thermal CMSSM with a 125 GeV Higgs”. *JHEP* 05 (2015), p. 098. DOI: 10.1007/JHEP05(2015)098. arXiv: 1502.05672 [hep-ph].

[559] L. Aparicio et al. “Light Higgsino Dark Matter from Non-thermal Cosmology”. *JHEP* 11 (2016), p. 038. DOI: 10.1007/JHEP11(2016)038. arXiv: 1607.00004 [hep-ph].

[560] M. Cicoli, K. Sinha, and R. Wiley Deal. “The dark universe after reheating in string inflation”. *JHEP* 12 (2022), p. 068. DOI: 10.1007/JHEP12(2022)068. arXiv: 2208.01017 [hep-th].

[561] A. Maharana and E. Palti. “Models of Particle Physics from Type IIB String Theory and F-theory: A Review”. *Int. J. Mod. Phys. A* 28 (2013), p. 1330005. DOI: 10.1142/S0217751X13300056. arXiv: 1212.0555 [hep-th].

[562] L. E. Ibanez and A. M. Uranga. “Neutrino Majorana Masses from String Theory Instanton Effects”. *JHEP* 03 (2007), p. 052. DOI: 10.1088/1126-6708/2007/03/052. arXiv: hep-th/0609213.

[563] L. E. Ibanez, A. N. Schellekens, and A. M. Uranga. “Instanton Induced Neutrino Majorana Masses in CFT Orientifolds with MSSM-like spectra”. *JHEP* 06 (2007), p. 011. DOI: 10.1088/1126-6708/2007/06/011. arXiv: 0704.1079 [hep-th].

[564] J. P. Conlon and F. Quevedo. “Kahler moduli inflation”. *JHEP* 01 (2006), p. 146. DOI: 10.1088/1126-6708/2006/01/146. arXiv: hep-th/0509012.

[565] M. Cicoli et al. “Higher derivative corrections to string inflation”. *JHEP* 02 (2024), p. 115. DOI: 10.1007/JHEP02(2024)115. arXiv: 2309.11697 [hep-th].

[566] M. Cicoli et al. “Moduli Vacuum Misalignment and Precise Predictions in String Inflation”. *JCAP* 08 (2016), p. 006. DOI: 10.1088/1475-7516/2016/08/006. arXiv: 1604.08512 [hep-th].

[567] G. Cowan et al. “Asymptotic formulae for likelihood-based tests of new physics”. *Eur. Phys. J. C* 71 (2011). [Erratum: Eur.Phys.J.C 73, 2501 (2013)], p. 1554. DOI: 10.1140/epjc/s10052-011-1554-0. arXiv: 1007.1727 [physics.data-an].

[568] *The Minimal Supersymmetric Standard Model with R-parity violation*. URL: https://feynrules.irmp.ucl.ac.be/wiki/RPVMSSM (visited on Jan. 31, 2024).

[569] B. Fuks. "Beyond the Minimal Supersymmetric Standard Model: from theory to phenomenology". *Int. J. Mod. Phys. A* 27 (2012), p. 1230007. DOI: 10.1142/S0217751X12300074. arXiv: 1202.4769 [hep-ph].

[570] C. W. Bauer, N. L. Rodd, and B. R. Webber. "Dark matter spectra from the electroweak to the Planck scale". *JHEP* 06 (2021), p. 121. DOI: 10.1007/JHEP06(2021)121. arXiv: 2007.15001 [hep-ph].

[571] J. Alwall et al. "A Standard format for Les Houches event files". *Comput. Phys. Commun.* 176 (2007), pp. 300–304. DOI: 10.1016/j.cpc.2006.11.010. arXiv: hep-ph/0609017.

[572] S. Ashok and M. R. Douglas. "Counting flux vacua". *JHEP* 01 (2004), p. 060. DOI: 10.1088/1126-6708/2004/01/060. arXiv: hep-th/0307049.

[573] F. Denef and M. R. Douglas. "Distributions of flux vacua". *JHEP* 05 (2004), p. 072. DOI: 10.1088/1126-6708/2004/05/072. arXiv: hep-th/0404116.

[574] L. Heurtier, Y. Mambrini, and M. Pierre. "Dark matter interpretation of the ANITA anomalous events". *Phys. Rev. D* 99.9 (2019), p. 095014. DOI: 10.1103/PhysRevD.99.095014. arXiv: 1902.04584 [hep-ph].

[575] T. Gherghetta et al. "Evaluating the price of tiny kinetic mixing". *Phys. Rev. D* 100.9 (2019), p. 095001. DOI: 10.1103/PhysRevD.100.095001. arXiv: 1909.00696 [hep-ph].

[576] J. R. Batley et al. "Search for the dark photon in π^0 decays". *Phys. Lett. B* 746 (2015), pp. 178–185. DOI: 10.1016/j.physletb.2015.04.068. arXiv: 1504.00607 [hep-ex].

[577] D. Banerjee et al. "Search for vector mediator of Dark Matter production in invisible decay mode". *Phys. Rev. D* 97.7 (2018), p. 072002. DOI: 10.1103/PhysRevD.97.072002. arXiv: 1710.00971 [hep-ex].

[578] P. Fayet. "U-boson production in e+ e- annihilations, psi and Upsilon decays, and Light Dark Matter". *Phys. Rev. D* 75 (2007), p. 115017. DOI: 10.1103/PhysRevD.75.115017. arXiv: hep-ph/0702176.

[579] R. Essig, P. Schuster, and N. Toro. "Probing Dark Forces and Light Hidden Sectors at Low-Energy e+e- Colliders". *Phys. Rev. D* 80 (2009), p. 015003. DOI: 10.1103/PhysRevD.80.015003. arXiv: 0903.3941 [hep-ph].

[580] S. N. Gninenko. "Search for MeV dark photons in a light-shining-through-walls experiment at CERN". *Phys. Rev. D* 89.7 (2014), p. 075008. DOI: 10.1103/PhysRevD.89.075008. arXiv: 1308.6521 [hep-ph].

[581] A. Berlin et al. "Sub-GeV dark matter production at fixed-target experiments". *Phys. Rev. D* 102.9 (2020), p. 095011. DOI: 10.1103/PhysRevD.102.095011. arXiv: 2003.03379 [hep-ph].

[582] D. Banerjee et al. "Search for invisible decays of sub-GeV dark photons in missing-energy events at the CERN SPS". *Phys. Rev. Lett.* 118.1 (2017), p. 011802. DOI: 10.1103/PhysRevLett.118.011802. arXiv: 1610.02988 [hep-ex].

[583] C. Cazzaniga et al. "Probing the explanation of the muon (g-2) anomaly and thermal light dark matter with the semi-visible dark photon channel". *Eur. Phys. J. C* 81.10 (2021), p. 959. DOI: 10.1140/epjc/s10052-021-09705-5. arXiv: 2107.02021 [hep-ex].

[584] S. N. Gninenko and N. V. Krasnikov. "The Muon anomalous magnetic moment and a new light gauge boson". *Phys. Lett. B* 513 (2001), p. 119. DOI: 10.1016/S0370-2693(01)00693-1. arXiv: hep-ph/0102222.

[585] G. Mohlabeng. "Revisiting the dark photon explanation of the muon anomalous magnetic moment". *Phys. Rev. D* 99.11 (2019), p. 115001. DOI: 10.1103/PhysRevD.99.115001. arXiv: 1902.05075 [hep-ph].

[586] M. Duerr et al. "Invisible and displaced dark matter signatures at Belle II". *JHEP* 02 (2020), p. 039. DOI: 10.1007/JHEP02(2020)039. arXiv: 1911.03176 [hep-ph].

[587] M. Duerr et al. "Long-lived Dark Higgs and Inelastic Dark Matter at Belle II". *JHEP* 04 (2021), p. 146. DOI: 10.1007/JHEP04(2021)146. arXiv: 2012.08595 [hep-ph].

[588] G. D. Kribs, G. Lee, and A. Martin. "Effective field theory of Stückelberg vector bosons". *Phys. Rev. D* 106.5 (2022), p. 055020. DOI: 10.1103/PhysRevD.106.055020. arXiv: 2204.01755 [hep-ph].

[589] M. Hostert, K. Kaneta, and M. Pospelov. "Pair production of dark particles in meson decays". *Phys. Rev. D* 102.5 (2020), p. 055016. DOI: 10.1103/PhysRevD.102.055016. arXiv: 2005.07102 [hep-ph].

[590] A. Filimonova et al. "Inelastic Dirac dark matter". *JHEP* 06 (2022), p. 048. DOI: 10.1007/JHEP06(2022)048. arXiv: 2201.08409 [hep-ph].

[591] D. Tucker-Smith and N. Weiner. "Inelastic dark matter". *Phys. Rev. D* 64 (2001), p. 043502. DOI: 10.1103/PhysRevD.64.043502. arXiv: hep-ph/0101138.

[592] Y. Cui et al. "Candidates for Inelastic Dark Matter". *JHEP* 05 (2009), p. 076. DOI: 10.1088/1126-6708/2009/05/076. arXiv: 0901.0557 [hep-ph].

[593] E. Izaguirre, G. Krnjaic, and B. Shuve. "Discovering Inelastic Thermal-Relic Dark Matter at Colliders". *Phys. Rev. D* 93.6 (2016), p. 063523. DOI: 10.1103/PhysRevD.93.063523. arXiv: 1508.03050 [hep-ph].

[594] A. Berlin and F. Kling. "Inelastic Dark Matter at the LHC Lifetime Frontier: ATLAS, CMS, LHCb, CODEX-b, FASER, and MATHUSLA".

Phys. Rev. D 99.1 (2019), p. 015021. DOI: 10.1103/PhysRevD.99.015021. arXiv: 1810.01879 [hep-ph].

[595] Y.-D. Tsai, P. deNiverville, and M. X. Liu. "Dark Photon and Muon $g-2$ Inspired Inelastic Dark Matter Models at the High-Energy Intensity Frontier". *Phys. Rev. Lett.* 126.18 (2021), p. 181801. DOI: 10.1103/PhysRevLett.126.181801. arXiv: 1908.07525 [hep-ph].

[596] D. Kim, J.-C. Park, and S. Shin. "Dark Matter "Collider" from Inelastic Boosted Dark Matter". *Phys. Rev. Lett.* 119.16 (2017), p. 161801. DOI: 10.1103/PhysRevLett.119.161801. arXiv: 1612.06867 [hep-ph].

[597] E. Ma. "Derivation of Dark Matter Parity from Lepton Parity". *Phys. Rev. Lett.* 115.1 (2015), p. 011801. DOI: 10.1103/PhysRevLett.115.011801. arXiv: 1502.02200 [hep-ph].

[598] R. T. D'Agnolo et al. "Exponentially Light Dark Matter from Coannihilation". *JHEP* 08 (2018), p. 079. DOI: 10.1007/JHEP08(2018)079. arXiv: 1803.02901 [hep-ph].

[599] A. M. Abdullahi et al. "The present and future status of heavy neutral leptons". *J. Phys. G* 50.2 (2023), p. 020501. DOI: 10.1088/1361-6471/ac98f9. arXiv: 2203.08039 [hep-ph].

[600] P. Minkowski. "$\mu \to e\gamma$ at a Rate of One Out of 10^9 Muon Decays?" *Phys. Lett. B* 67 (1977), pp. 421–428. DOI: 10.1016/0370-2693(77)90435-X.

[601] R. N. Mohapatra and G. Senjanovic. "Neutrino Mass and Spontaneous Parity Nonconservation". *Phys. Rev. Lett.* 44 (1980), p. 912. DOI: 10.1103/PhysRevLett.44.912.

[602] M. Gell-Mann, P. Ramond, and R. Slansky. "Complex Spinors and Unified Theories". *Conf. Proc. C* 790927 (1979), pp. 315–321. arXiv: 1306.4669 [hep-th].

[603] T. Yanagida. "Horizontal gauge symmetry and masses of neutrinos". *Conf. Proc. C* 7902131 (1979). Ed. by O. Sawada and A. Sugamoto, pp. 95–99.

[604] G. Lazarides, Q. Shafi, and C. Wetterich. "Proton Lifetime and Fermion Masses in an SO(10) Model". *Nucl. Phys. B* 181 (1981), pp. 287–300. DOI: 10.1016/0550-3213(81)90354-0.

[605] R. N. Mohapatra and G. Senjanovic. "Neutrino Masses and Mixings in Gauge Models with Spontaneous Parity Violation". *Phys. Rev. D* 23 (1981), p. 165. DOI: 10.1103/PhysRevD.23.165.

[606] J. Schechter and J. W. F. Valle. "Neutrino Masses in SU(2) x U(1) Theories". *Phys. Rev. D* 22 (1980), p. 2227. DOI: 10.1103/PhysRevD.22.2227.

[607] T. P. Cheng and L.-F. Li. "Neutrino Masses, Mixings and Oscillations in SU(2) x U(1) Models of Electroweak Interactions". *Phys. Rev. D* 22 (1980), p. 2860. DOI: 10.1103/PhysRevD.22.2860.

[608] R. Foot et al. "Seesaw Neutrino Masses Induced by a Triplet of Leptons". *Z. Phys. C* 44 (1989), p. 441. DOI: 10.1007/BF01415558.

[609] P. Ballett, M. Hostert, and S. Pascoli. "Neutrino Masses from a Dark Neutrino Sector below the Electroweak Scale". *Phys. Rev. D* 99.9 (2019), p. 091701. DOI: 10.1103/PhysRevD.99.091701. arXiv: 1903.07590 [hep-ph].

[610] D. Banerjee et al. "Search for Axionlike and Scalar Particles with the NA64 Experiment". *Phys. Rev. Lett.* 125.8 (2020), p. 081801. DOI: 10.1103/PhysRevLett.125.081801. arXiv: 2005.02710 [hep-ex].

[611] S. N. Gninenko et al. "The exact tree-level calculation of the dark photon production in high-energy electron scattering at the CERN SPS". *Phys. Lett. B* 782 (2018), pp. 406–411. DOI: 10.1016/j.physletb.2018.05.010. arXiv: 1712.05706 [hep-ph].

[612] E. Izaguirre et al. "Testing Light Dark Matter Coannihilation With Fixed-Target Experiments". *Phys. Rev. D* 96.5 (2017), p. 055007. DOI: 10.1103/PhysRevD.96.055007. arXiv: 1703.06881 [hep-ph].

[613] J. Blumlein and J. Brunner. "New Exclusion Limits for Dark Gauge Forces from Beam-Dump Data". *Phys. Lett. B* 701 (2011), pp. 155–159. DOI: 10.1016/j.physletb.2011.05.046. arXiv: 1104.2747 [hep-ex].

[614] J. Blümlein and J. Brunner. "New Exclusion Limits on Dark Gauge Forces from Proton Bremsstrahlung in Beam-Dump Data". *Phys. Lett. B* 731 (2014), pp. 320–326. DOI: 10.1016/j.physletb.2014.02.029. arXiv: 1311.3870 [hep-ph].

[615] Y. Li. "Search for Beyond Standard Model Physics at BaBar". PhD thesis. Caltech, 2022. DOI: 10.7907/tz7n-d662.

[616] F. Bossi et al. "Precision Kaon and Hadron Physics with KLOE". *Riv. Nuovo Cim.* 31.10 (2008), pp. 531–623. DOI: 10.1393/ncr/i2008-10037-9. arXiv: 0811.1929 [hep-ex].

[617] G. Amelino-Camelia et al. "Physics with the KLOE-2 experiment at the upgraded DAφNE". *Eur. Phys. J. C* 68 (2010), pp. 619–681. DOI: 10.1140/epjc/s10052-010-1351-1. arXiv: 1003.3868 [hep-ex].

[618] M. Ablikim et al. "Future Physics Programme of BESIII". *Chin. Phys. C* 44.4 (2020), p. 040001. DOI: 10.1088/1674-1137/44/4/040001. arXiv: 1912.05983 [hep-ex].

[619] N. F. Bell, G. Busoni, and I. W. Sanderson. "Loop Effects in Direct Detection". *JCAP* 08 (2018). [Erratum: JCAP 01, E01 (2019)], p. 017. DOI: 10.1088/1475-7516/2018/08/017. arXiv: 1803.01574 [hep-ph].

[620] F. Bishara et al. "DirectDM: a tool for dark matter direct detection" (Aug. 2017). arXiv: 1708.02678 [hep-ph].

[621] R. Agnese et al. “Projected Sensitivity of the SuperCDMS SNOLAB experiment”. *Phys. Rev. D* 95.8 (2017), p. 082002. DOI: 10.1103/PhysRevD.95.082002. arXiv: 1610.00006 [physics.ins-det].

[622] M. F. Albakry et al. “A Strategy for Low-Mass Dark Matter Searches with Cryogenic Detectors in the SuperCDMS SNOLAB Facility”. *Snowmass 2021*. Mar. 2022. arXiv: 2203.08463 [physics.ins-det].

[623] N. F. Bell et al. “Observing the Migdal effect from nuclear recoils of neutral particles with liquid xenon and argon detectors”. *Phys. Rev. D* 105.9 (2022), p. 096015. DOI: 10.1103/PhysRevD.105.096015. arXiv: 2112.08514 [hep-ph].

[624] R. Essig, J. Mardon, and T. Volansky. “Direct Detection of Sub-GeV Dark Matter”. *Phys. Rev. D* 85 (2012), p. 076007. DOI: 10.1103/PhysRevD.85.076007. arXiv: 1108.5383 [hep-ph].

[625] C. Kouvaris and J. Pradler. “Probing sub-GeV Dark Matter with conventional detectors”. *Phys. Rev. Lett.* 118.3 (2017), p. 031803. DOI: 10.1103/PhysRevLett.118.031803. arXiv: 1607.01789 [hep-ph].

[626] M. Ibe et al. “Migdal Effect in Dark Matter Direct Detection Experiments”. *JHEP* 03 (2018), p. 194. DOI: 10.1007/JHEP03(2018)194. arXiv: 1707.07258 [hep-ph].

[627] K. V. Berghaus et al. “The Migdal effect in semiconductors for dark matter with masses below ~ 100 MeV”. *JHEP* 01 (2023), p. 023. DOI: 10.1007/JHEP01(2023)023. arXiv: 2210.06490 [hep-ph].

[628] D. S. Akerib et al. “Results of a Search for Sub-GeV Dark Matter Using 2013 LUX Data”. *Phys. Rev. Lett.* 122.13 (2019), p. 131301. DOI: 10.1103/PhysRevLett.122.131301. arXiv: 1811.11241 [astro-ph.CO].

[629] L. Barak et al. “SENSEI: Direct-Detection Results on sub-GeV Dark Matter from a New Skipper-CCD”. *Phys. Rev. Lett.* 125.17 (2020), p. 171802. DOI: 10.1103/PhysRevLett.125.171802. arXiv: 2004.11378 [astro-ph.CO].

[630] E. Aprile et al. “Search for Light Dark Matter Interactions Enhanced by the Migdal Effect or Bremsstrahlung in XENON1T”. *Phys. Rev. Lett.* 123.24 (2019), p. 241803. DOI: 10.1103/PhysRevLett.123.241803. arXiv: 1907.12771 [hep-ex].

[631] P. Agnes et al. “Search for Dark-Matter–Nucleon Interactions via Migdal Effect with DarkSide-50”. *Phys. Rev. Lett.* 130.10 (2023), p. 101001. DOI: 10.1103/PhysRevLett.130.101001. arXiv: 2207.11967 [hep-ex].

[632] E. Aprile et al. “Light Dark Matter Search with Ionization Signals in XENON1T”. *Phys. Rev. Lett.* 123.25 (2019), p. 251801. DOI: 10.1103/PhysRevLett.123.251801. arXiv: 1907.11485 [hep-ex].

[633] E. Aprile et al. “Emission of single and few electrons in XENON1T and limits on light dark matter”. *Phys. Rev. D* 106.2 (2022), p. 022001. DOI: 10.1103/PhysRevD.106.022001. arXiv: 2112.12116 [hep-ex].

[634] C. Cheng et al. “Search for Light Dark Matter-Electron Scatterings in the PandaX-II Experiment”. *Phys. Rev. Lett.* 126.21 (2021), p. 211803. DOI: 10.1103/PhysRevLett.126.211803. arXiv: 2101.07479 [hep-ex].

[635] T. Bringmann and M. Pospelov. “Novel direct detection constraints on light dark matter”. *Phys. Rev. Lett.* 122.17 (2019), p. 171801. DOI: 10.1103/PhysRevLett.122.171801. arXiv: 1810.10543 [hep-ph].

[636] Y. Ema, F. Sala, and R. Sato. “Light Dark Matter at Neutrino Experiments”. *Phys. Rev. Lett.* 122.18 (2019), p. 181802. DOI: 10.1103/PhysRevLett.122.181802. arXiv: 1811.00520 [hep-ph].

[637] Y. Ema, F. Sala, and R. Sato. “Neutrino experiments probe hadrophilic light dark matter”. *SciPost Phys.* 10.3 (2021), p. 072. DOI: 10.21468/SciPostPhys.10.3.072. arXiv: 2011.01939 [hep-ph].

[638] W. Yin. “Highly-boosted dark matter and cutoff for cosmic-ray neutrinos through neutrino portal”. *EPJ Web Conf.* 208 (2019). Ed. by B. Pattison et al., p. 04003. DOI: 10.1051/epjconf/201920804003. arXiv: 1809.08610 [hep-ph].

[639] N. F. Bell et al. “Cosmic-ray upscattered inelastic dark matter”. *Phys. Rev. D* 104 (2021), p. 076020. DOI: 10.1103/PhysRevD.104.076020. arXiv: 2108.00583 [hep-ph].

[640] J.-C. Feng et al. “Revising inelastic dark matter direct detection by including the cosmic ray acceleration”. *JHEP* 04 (2022), p. 080. DOI: 10.1007/JHEP04(2022)080. arXiv: 2110.08863 [hep-ph].

[641] E. Cortina Gil et al. “Search for heavy neutral lepton production in K+ decays to positrons”. *Phys. Lett. B* 807 (2020), p. 135599. DOI: 10.1016/j.physletb.2020.135599. arXiv: 2005.09575 [hep-ex].

[642] J. P. Lees et al. “Search for heavy neutral leptons using tau lepton decays at BaBaR”. *Phys. Rev. D* 107.5 (2023), p. 052009. DOI: 10.1103/PhysRevD.107.052009. arXiv: 2207.09575 [hep-ex].

[643] K. Abe et al. “Search for heavy neutrinos with the T2K near detector ND280”. *Phys. Rev. D* 100.5 (2019), p. 052006. DOI: 10.1103/PhysRevD.100.052006. arXiv: 1902.07598 [hep-ex].

[644] K. J. Kelly and P. A. N. Machado. “MicroBooNE experiment, NuMI absorber, and heavy neutral leptons”. *Phys. Rev. D* 104.5 (2021), p. 055015. DOI: 10.1103/PhysRevD.104.055015. arXiv: 2106.06548 [hep-ph].

[645] G. Bernardi et al. “FURTHER LIMITS ON HEAVY NEUTRINO COUPLINGS”. *Phys. Lett. B* 203 (1988), pp. 332–334. DOI: 10.1016/0370-2693(88)90563-1.

[646] C. A. Argüelles, N. Foppiani, and M. Hostert. "Heavy neutral leptons below the kaon mass at hodoscopic neutrino detectors". *Phys. Rev. D* 105.9 (2022), p. 095006. DOI: 10.1103/PhysRevD.105.095006. arXiv: 2109.03831 [hep-ph].

[647] D. Gorbunov, I. Krasnov, and S. Suvorov. "Revisiting PS191 limits on sterile neutrinos". *Phys. Lett. B* 830 (2022), p. 137173. DOI: 10.1016/j.physletb.2022.137173. arXiv: 2112.06800 [hep-ph].

[648] F. Bergsma et al. "A Search for Decays of Heavy Neutrinos in the Mass Range 0.5-GeV to 2.8-GeV". *Phys. Lett. B* 166 (1986), pp. 473–478. DOI: 10.1016/0370-2693(86)91601-1.

[649] J. Orloff, A. N. Rozanov, and C. Santoni. "Limits on the mixing of tau neutrino to heavy neutrinos". *Phys. Lett. B* 550 (2002), pp. 8–15. DOI: 10.1016/S0370-2693(02)02769-7. arXiv: hep-ph/0208075.

[650] I. Boiarska et al. "Constraints from the CHARM experiment on heavy neutral leptons with tau mixing". *Phys. Rev. D* 104.9 (2021), p. 095019. DOI: 10.1103/PhysRevD.104.095019. arXiv: 2107.14685 [hep-ph].

[651] R. Barouki, G. Marocco, and S. Sarkar. "Blast from the past II: Constraints on heavy neutral leptons from the BEBC WA66 beam dump experiment". *SciPost Phys.* 13 (2022), p. 118. DOI: 10.21468/SciPostPhys.13.5.118. arXiv: 2208.00416 [hep-ph].

[652] P. Astier et al. "Search for heavy neutrinos mixing with tau neutrinos". *Phys. Lett. B* 506 (2001), pp. 27–38. DOI: 10.1016/S0370-2693(01)00362-8. arXiv: hep-ex/0101041.

[653] P. Abreu et al. "Search for neutral heavy leptons produced in Z decays". *Z. Phys. C* 74 (1997). [Erratum: Z.Phys.C 75, 580 (1997)], pp. 57–71. DOI: 10.1007/s002880050370.

[654] M. Acciarri et al. "Search for heavy isosinglet neutrinos in e^+e^- annihilation at 130-GeV less than $S^{(1/2)}$ less than 189-GeV". *Phys. Lett. B* 461 (1999), pp. 397–404. DOI: 10.1016/S0370-2693(99)00852-7. arXiv: hep-ex/9909006.

[655] P. Achard et al. "Search for heavy isosinglet neutrino in e^+e^- annihilation at LEP". *Phys. Lett. B* 517 (2001), pp. 67–74. DOI: 10.1016/S0370-2693(01)00993-5. arXiv: hep-ex/0107014.

[656] P. Ballett, S. Pascoli, and M. Ross-Lonergan. "U(1)′ mediated decays of heavy sterile neutrinos in MiniBooNE". *Phys. Rev. D* 99 (2019), p. 071701. DOI: 10.1103/PhysRevD.99.071701. arXiv: 1808.02915 [hep-ph].

[657] D. W. Kang, P. Ko, and C.-T. Lu. "Exploring properties of long-lived particles in inelastic dark matter models at Belle II". *JHEP* 04 (2021), p. 269. DOI: 10.1007/JHEP04(2021)269. arXiv: 2101.02503 [hep-ph].

[658] D. Babusci et al. "Search for light vector boson production in $e^+e^- \to \mu^+\mu^-\gamma$ interactions with the KLOE experiment". *Phys. Lett. B* 736 (2014), pp. 459–464. DOI: 10.1016/j.physletb.2014.08.005. arXiv: 1404.7772 [hep-ex].

[659] A. Anastasi et al. "Limit on the production of a new vector boson in $e^+e^- \to U\gamma$, $U \to \pi^+\pi^-$ with the KLOE experiment". *Phys. Lett. B* 757 (2016), pp. 356–361. DOI: 10.1016/j.physletb.2016.04.019. arXiv: 1603.06086 [hep-ex].

[660] D. Babusci et al. "Study of the Dalitz decay $\varphi \to \eta e^+e^-$ with the KLOE detector". *Phys. Lett. B* 742 (2015), pp. 1–6. DOI: 10.1016/j.physletb.2015.01.011. arXiv: 1409.4582 [hep-ex].

[661] A. Anastasi et al. "Search for dark Higgsstrahlung in $e^+e^- \to \mu^+\mu^-$ and missing energy events with the KLOE experiment". *Phys. Lett. B* 747 (2015), pp. 365–372. DOI: 10.1016/j.physletb.2015.06.015. arXiv: 1501.06795 [hep-ex].

[662] J. P. Lees et al. "Search for Low-Mass Dark-Sector Higgs Bosons". *Phys. Rev. Lett.* 108 (2012), p. 211801. DOI: 10.1103/PhysRevLett.108.211801. arXiv: 1202.1313 [hep-ex].

[663] B. Batell et al. "Inelastic dark matter at the Fermilab Short Baseline Neutrino Program". *Phys. Rev. D* 104.7 (2021), p. 075026. DOI: 10.1103/PhysRevD.104.075026. arXiv: 2106.04584 [hep-ph].

[664] C. A. Argüelles, N. Foppiani, and M. Hostert. "Efficiently exploring multidimensional parameter spaces beyond the Standard Model". *Phys. Rev. D* 107.3 (2023), p. 035027. DOI: 10.1103/PhysRevD.107.035027. arXiv: 2205.12273 [hep-ph].

[665] N. W. Kamp et al. "Dipole-coupled heavy-neutral-lepton explanations of the MiniBooNE excess including constraints from MINERvA data". *Phys. Rev. D* 107.5 (2023), p. 055009. DOI: 10.1103/PhysRevD.107.055009. arXiv: 2206.07100 [hep-ph].

[666] T. Schwetz, A. Zhou, and J.-Y. Zhu. "Constraining active-sterile neutrino transition magnetic moments at DUNE near and far detectors". *JHEP* 21 (2020), p. 200. DOI: 10.1007/JHEP07(2021)200. arXiv: 2105.09699 [hep-ph].

[667] M. Atkinson et al. "Heavy Neutrino Searches through Double-Bang Events at Super-Kamiokande, DUNE, and Hyper-Kamiokande". *JHEP* 04 (2022), p. 174. DOI: 10.1007/JHEP04(2022)174. arXiv: 2105.09357 [hep-ph].

[668] P. Coloma et al. "Double-Cascade Events from New Physics in Icecube". *Phys. Rev. Lett.* 119.20 (2017), p. 201804. DOI: 10.1103/PhysRevLett.119.201804. arXiv: 1707.08573 [hep-ph].

[669] P. Coloma. "Icecube/DeepCore tests for novel explanations of the MiniBooNE anomaly". *Eur. Phys. J. C* 79.9 (2019), p. 748. DOI: 10.1140/epjc/s10052-019-7256-8. arXiv: 1906.02106 [hep-ph].

[670] E. Bertuzzo, A. Scaffidi, and M. Taoso. "Searching for inelastic dark matter with future LHC experiments". *JHEP* 08 (2022), p. 100. DOI: 10.1007/JHEP08(2022)100. arXiv: 2201.12253 [hep-ph].

[671] M. Hostert and M. Pospelov. "Novel multilepton signatures of dark sectors in light meson decays". *Phys. Rev. D* 105.1 (2022), p. 015017. DOI: 10.1103/PhysRevD.105.015017. arXiv: 2012.02142 [hep-ph].

[672] T. Åkesson et al. "Light Dark Matter eXperiment (LDMX)" (Aug. 2018). arXiv: 1808.05219 [hep-ex].

[673] A. Berlin et al. "Dark Matter, Millicharges, Axion and Scalar Particles, Gauge Bosons, and Other New Physics with LDMX". *Phys. Rev. D* 99.7 (2019), p. 075001. DOI: 10.1103/PhysRevD.99.075001. arXiv: 1807.01730 [hep-ph].

[674] T. Åkesson et al. "Current Status and Future Prospects for the Light Dark Matter eXperiment". *Snowmass 2021*. Mar. 2022. arXiv: 2203.08192 [hep-ex].

[675] C. A. Argüelles et al. "MicroBooNE and the νe Interpretation of the MiniBooNE Low-Energy Excess". *Phys. Rev. Lett.* 128.24 (2022), p. 241802. DOI: 10.1103/PhysRevLett.128.241802. arXiv: 2111.10359 [hep-ph].

[676] A. M. Abdullahi et al. *Pandora based search for exotic e^+e^- production due to new "Dark Sector" physics in the Booster Neutrino Beam*. Tech. rep. MicroBooNE Collaboration and MoU with MicroBooNE, 2023.

[677] *GitHub - mhostert/DarkNews-generator: A lightweight event generator for new physics in neutrino-nucleus scattering*. URL: https://github.com/mhostert/DarkNews-generator (visited on Jan. 31, 2024).

[678] *DarkNews · PyPI*. URL: https://pypi.org/project/DarkNews (visited on Jan. 31, 2024).

[679] G. Altarelli, R. Kleiss, and C. Verzegnassi, eds. *Z PHYSICS AT LEP-1. PROCEEDINGS, WORKSHOP, GENEVA, SWITZERLAND, SEPTEMBER 4-5, 1989. VOL. 3: EVENT GENERATORS AND SOFTWARE*. CERN Yellow Reports: Conference Proceedings. Sept. 1989. DOI: 10.5170/CERN-1989-008-V-3.

[680] *LArSoft Collaboration | Software for LArTPCs*. URL: https://larsoft.org/ (visited on Jan. 31, 2024).

[681] E. D. Church. "LArSoft: A Software Package for Liquid Argon Time Projection Drift Chambers" (Nov. 2013). arXiv: 1311.6774 [physics.ins-det].

[682] R. Pordes and E. Snider. "The Liquid Argon Software Toolkit (LArSoft): Goals, Status and Plan". *PoS* ICHEP2016 (2016), p. 182. DOI: 10.22323/1.282.0182.

[683] E. L. Snider and G. Petrillo. "LArSoft: Toolkit for Simulation, Reconstruction and Analysis of Liquid Argon TPC Neutrino Detectors". *J. Phys. Conf. Ser.* 898.4 (2017). Ed. by R. Mount and C. Tull, p. 042057. DOI: 10.1088/1742-6596/898/4/042057.

[684] T. Chen and C. Guestrin. "XGBoost: A Scalable Tree Boosting System". *arXiv e-prints*, arXiv:1603.02754 (Mar. 2016), arXiv:1603.02754. DOI: 10.48550/arXiv.1603.02754. arXiv: 1603.02754 [cs.LG].

[685] E. Fernández-Martínez et al. "Effective portals to heavy neutral leptons". *JHEP* 09 (2023), p. 001. DOI: 10.1007/JHEP09(2023)001. arXiv: 2304.06772 [hep-ph].

[686] K. Moffat, S. Pascoli, and C. Weiland. "Equivalence between massless neutrinos and lepton number conservation in fermionic singlet extensions of the Standard Model" (Dec. 2017). arXiv: 1712.07611 [hep-ph].

[687] P. S. B. Dev and A. Pilaftsis. "Minimal Radiative Neutrino Mass Mechanism for Inverse Seesaw Models". *Phys. Rev. D* 86 (2012), p. 113001. DOI: 10.1103/PhysRevD.86.113001. arXiv: 1209.4051 [hep-ph].

[688] P. S. Bhupal Dev and A. Pilaftsis. "Light and Superlight Sterile Neutrinos in the Minimal Radiative Inverse Seesaw Model". *Phys. Rev. D* 87.5 (2013), p. 053007. DOI: 10.1103/PhysRevD.87.053007. arXiv: 1212.3808 [hep-ph].

[689] J. Lopez-Pavon, S. Pascoli, and C.-f. Wong. "Can heavy neutrinos dominate neutrinoless double beta decay?" *Phys. Rev. D* 87.9 (2013), p. 093007. DOI: 10.1103/PhysRevD.87.093007. arXiv: 1209.5342 [hep-ph].

[690] A. C. Vincent et al. "Revisiting cosmological bounds on sterile neutrinos". *JCAP* 04 (2015), p. 006. DOI: 10.1088/1475-7516/2015/04/006. arXiv: 1408.1956 [astro-ph.CO].

[691] V. Domcke et al. "MeV-scale Seesaw and Leptogenesis". *JHEP* 01 (2021), p. 200. DOI: 10.1007/JHEP01(2021)200. arXiv: 2009.11678 [hep-ph].

[692] N. Sabti et al. "Refined Bounds on MeV-scale Thermal Dark Sectors from BBN and the CMB". *JCAP* 01 (2020), p. 004. DOI: 10.1088/1475-7516/2020/01/004. arXiv: 1910.01649 [hep-ph].

[693] D. B. Newell and E. Tiesinga. *The International System of Units (SI): 2019 Edition*. Tech. rep. NIST SP 330-2019. Gaithersburg, MD: National Institute of Standards and Technology, 2019. DOI: 10.6028/NIST.SP.330-2019.